Wrocław University of Technology
Centre of Advanced Materials and Nanotechnology

Materials Science-Poland

Vol. 28 • No. 1 • 2010

Oficyna Wydawnicza Politechniki Wrocławskiej

Materials Science-Poland is an interdisciplinary journal devoted to experimental and theoretical research into the synthesis, structure, properties and applications of materials.

Among the materials of interest are:

- glasses and ceramics
- sol-gel materials
- photoactive materials (including materials for nonlinear optics)
- laser materials
- photonic crystals
- semiconductor micro- and nanostructures
- piezo-, pyro- and ferroelectric materials
- high-T_c superconductors
- magnetic materials
- molecular materials (including polymers) for use in electronics and photonics
- novel solid phases
- other novel and unconventional materials

The broad spectrum of the areas of interest reflects the interdisciplinary nature of materials research. Papers covering the modelling of materials, their synthesis and characterisation, physicochemical aspects of their fabrication, properties and applications are welcome. In addition to regular papers, the journal features issues containing conference papers, as well as special issues on key topics in materials science.

Materials Science-Poland is published under the auspices of the Centre of Advanced Materials and Nanotechnology of the Wrocław University of Technology, in collaboration with the Institute of Low Temperatures and Structural Research of the Polish Academy of Sciences and the Wrocław University of Economics.

All accepted manuscripts are placed on the Web page of the journal and are available at the address: http://MaterialsScience.pwr.wroc.pl

All published papers are placed on the Web page of the journal and are **freely accessible** at the address: http://MaterialsScience.pwr.wroc.pl

Materials Science-Poland is abstracted/indexed in: Chemical Abstracts, Materials Science Citation Index, Science Citation Index Expanded, Scopus.

The Journal is supported by the State Committee for Scientific Research

Editorial Office

Daniel Davies
Marek Łata

Printed in Poland

Drukarnia Oficyny Wydawniczej Politechniki Wrocławskiej
Zam. nr 276/2010.

Materials Science-Poland, *Vol. 28*, *No. 1*, *2010*

Synthesis and characterization of nanocrystalline hydroxyapatite obtained by the wet chemical technique

H. ESLAMI, M. SOLATI-HASHJIN, M. TAHRIRI*, F. BAKHSHI

Amirkabir University of Technology, Faculty of Biomedical Engineering,
Biomaterial Group, P.O. Box: 15875-4413, Tehran, Iran

Hydroxyapatite was synthesized by the wet chemical technique. Diammonium hydrogen phosphate and calcium nitrate 4-hydrate were used as starting materials and sodium hydroxide solution was used as the agent for pH adjustment. The powder sample was characterized by the commonly used bulk techniques of scanning electron microscopy (SEM), transmission electron microscopy, Fourier transform infra-red spectroscopy, differential thermal analysis, thermal gravimetric analysis, X-ray diffraction, atomic absorption spectroscopy and EDTA titration analyses. With respect to the results achieved from the above analyses, it was found that nanocrystalline hydroxyapatite can successfully be produced through the wet precipitation method. The bulk Ca/P molar ratio of synthesized hydroxyapatite was determined as 1.71, which was higher than the stoichiometric ratio (1.667) that is expected for a pure HA phase. SEM investigations revealed that, there is a distribution of small particles and large agglomerates consisting of fine particles cold welded together. Lastly, the TEM technique demonstrated that the crystallites of the prepared powder were nanosized and had a needle-like morphology. The aspect ratio of the crystallites was about 8.

Keywords: *hydroxyapatite; precipitation; nanocrystalline material; synthesis*

1. Introduction

In recent years, significant effort has been devoted to developing inorganic nanocrystals because of their potential applications in biology, electronics, optics, transport and information technology. Although there have been some investigations into ways of fabricating such nanocrystals, ways now need to be found of controlling their size, shape and crystallinity. This requires the identification of the various parameters influencing these features [1].

*Corresponding author, e-mail: m-tahriri@aut.ac.ir

Synthetic ceramic materials based on calcium phosphates (CaP), particularly those in the composition of tricalcium phosphate (TCP, $Ca_3(PO_4)_2$) and hydroxyapatite (HA, $Ca_{10}(PO_4)_6(OH)_2$), have been extensively studied and clinically used. These ceramics have been the focus of over three decades of biomaterials research in orthopedics and dentistry [2–7]. They are considered to be suitable biomaterials due to their biological affinity and activity to surrounding host tissues, when implanted [5]. Furthermore, according to the literature, calcium phosphates are widely used in medicine and oral biology, due to the apatite-like structure of enamel, dentin and bones, usually called "hard tissues". To date, in spite of the availability of several sophisticated characterization techniques for the investigation of tooth and bone tissues, their exact composition, phase distribution and structure remain unresolved [3]. The aim of the preparation of synthetic CaP is to understand the properties and physicochemical behaviour of biological mineral phases found in human hard tissues because they share many similarities [4]. In addition, these materials are also important in the study of biomineralization, since they are precursors and are the major components of bone and teeth [8]. In order to gain insights into the complex structure found in biological mineral phases, it would be necessary to establish a well-defined system for the characterization of the synthetic CaP, in which the composition, crystallinity and nanostructure would have to be properly addressed. These properties play a major role in the bioactivity of CaP based materials in terms of enhanced contact areas and degradation [5]. Detailed characterization indicates that an apatite layer is usually formed on the ceramic surface when implanted. This layer consists of a carbonate-ion-containing apatite, named "bone-like" apatite, forming a bond with the human bone [2]. These ceramic materials can also be used as coating on implants to improve the biocompatibility [1, 8] and can be injected in bone with non-invasive surgical techniques [9]. Bioactivity of CaP materials is dependent on many factors during the synthesis procedure, such as precursor reagents, impurities, crystal size and morphology, concentration and mixture order of reagents, pH and temperature. Also, the bioactivity response of CaP materials will depend on the type of thermal treatment selected for drying and sintering. These conditions are controlled by parameters of synthesis and consequently for each application a specific route is selected [6, 10].

In this investigation we report on the synthesis of nanocrystalline hydroxyapatite by the wet precipitation technique.

2. Experimental

Materials and methods. The flowchart for the synthesis of the hydroxyapatite is shown in Fig. 1. 0.09 M diammonium hydrogen phosphate ($(NH_4)_2HPO_4$, 99%, Merck; No. 1207) and 0.15 M calcium nitrate 4-hydrate ($Ca(NO_3)_2{\cdot}4H_2O$, 98%, Merck PROLABO, No. 22 384 298) were prepared and the pH of the both solutions was brought to about 11, by adding 1 M sodium hydroxide (NaOH, 99%, Merck, No. 5 226 926). The phosphate solution was added drop-wise into the calcium ni-

trate solution, resulting in the precipitation of HA according to reactions (1) and /or (2) [11].

$$10Ca^{2+} + 6HPO_4^- + 2OH^- \rightarrow Ca_{10}(PO_4)_6(OH)_2 + 6H^+ \quad (1)$$

$$10Ca^{2+} + 6H_2PO_4^- + 2OH^- \rightarrow Ca_{10}(PO_4)_6(OH)_2 + 12H^+ \quad (2)$$

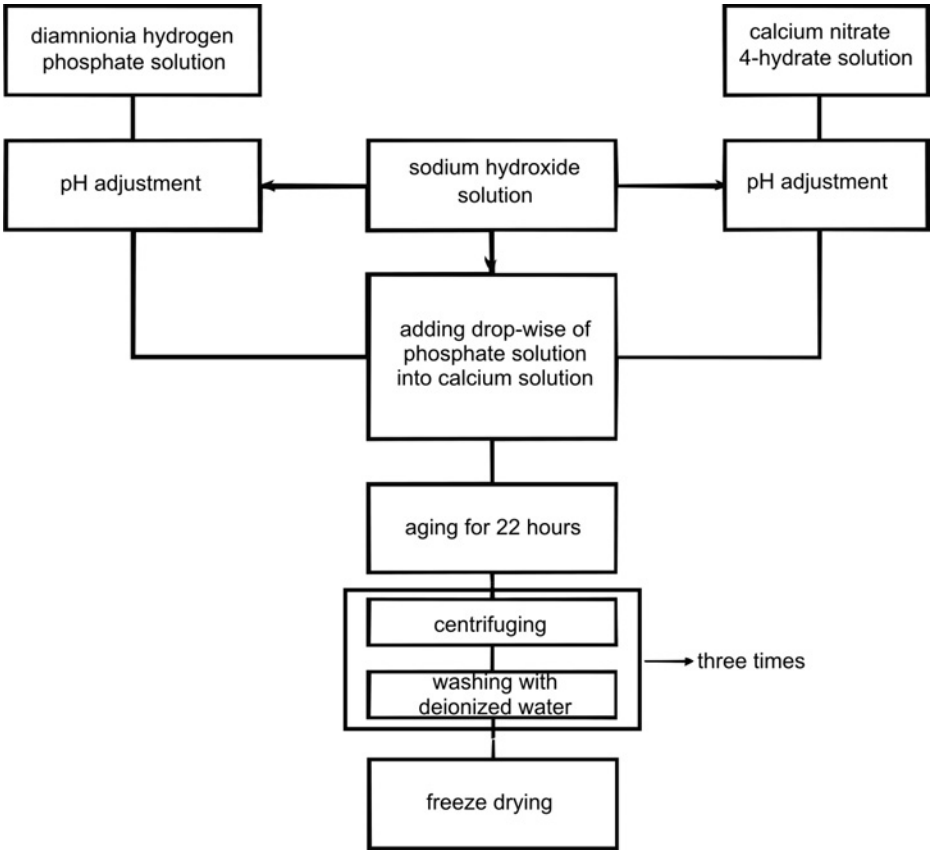

Fig. 1. Flowchart for the synthesis of the hydroxyapatite powder

The precipitate was aged for 22 h at room temperature. In the next step, the precipitated HA was centrifuged and then washed with de-ionized water. The processes of centrifuging and washing were carried out three times. The resulting powder was dried in a freeze-drier system (Alpha 1-2 LD, Germany) for 10 h. Lastly, dried powder was calcined in an electrical box furnace at 900 °C for 1 h at the rate of 5 °C/min in air.

Powder characterization. The powder sample was subjected to Fourier Transform infra-red analysis with a Bomem MB 100 spectrometer. For IR analysis, at first 1 mg

of the powder sample was carefully mixed with 300 mg of KBr (infrared grade) and palletized under vacuum. The pellets were analyzed in the range of 500 to 4000 cm^{-1} at the scan speed of 23 scan/min at the resolution of 4 cm^{-1}.

The resulting powder was analyzed by the X-ray diffraction (XRD) with a Siemens-Brucker D5000 diffractometer. This instrument works with voltage and current settings of 40 kV and 40 mA, respectively, and uses CuK_α radiation (1.540600 Å). For qualitative analysis, XRD diagrams were recorded in the interval $7° \leq 2\theta \geq 60°$ at the scan speed of 2 °C/min, the step size being 0.02° and the time step being 1 s.

The thermal behaviour of hydroxyapatite was studied by simultaneous thermal analysis (STA). A thermoanalyzer (Polymer Laboratories PL-STA 1640) was started at room temperature and measurements were subsequently taken up to 1200 °C; the heating rate of 10 °C/min was used to record the conventional DTA and TGA curves.

In order to calculate the Ca/P molar ratio of the precipitated powder, the contents of Ca and P were chemically analyzed by the quantitative chemical analysis via the EDTA titration technique and atomic absorption spectroscopy (AAS) with a Shimadzu UV-31005 instrument, respectively.

The powder sample was coated with a thin layer of Gold (Au) by sputtering (EMITECH K450X, England) and then the microstructure of the powder sample was observed under a scanning electron microscope (SEM, Tescan Vega 2XMU) that operated under the acceleration voltage of 15 kV.

Transmission electron microscopy (TEM, CM200-FEG-Philips) was used for characterizing the particles. For this purpose, particles were deposited onto Cu grids, which support a carbon film. The particles were deposited onto the support grids by deposition from a dilute suspension in acetone or ethanol. The particle shapes and sizes were characterized by diffraction (amplitude) contrast and, for the crystalline materials, by high resolution (phase contrast) imaging.

3. Results and discussion

3.1. FTIR analysis

Figure 2 shows the FT-IR spectrum of HA powders. Characteristic bands (listed in Table 1) exhibited in the sample spectrum are as follows: Two bands were observed at 3555 cm^{-1} and 622 cm^{-1} and were due to the stretching mode of hydrogen-bonded OH^- ions and liberational mode of hydrogen-bonded OH^- ions, respectively. The band at 1040 cm^{-1} has been attributed to ν_3 PO_4, the bands at 603 cm^{-1} and 561 cm^{-1} to ν_4 PO_4. The FTIR analysis showed all typical absorption bands of hydroxyapatite. In addition, some carbonate content also was seen (CO_3^{2-} peak around 1600 cm^{-1}), which is an indication of the presence of carbonate apatite. This might originate from absorption of carbon dioxide from the atmosphere [12, 14]. Therefore according to this reasoning, it is obvious that the synthesized powder is certainly hydroxyapatite.

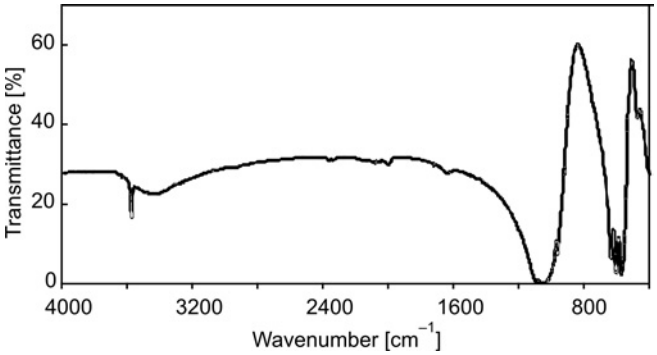

Fig. 2. FT-IR spectrum of the synthesized hydroxyapatite

Table 1. Infrared frequencies
for the synthesized hydroxyapatite powder

Frequency [cm^{-1}]	Assignment
561	PO_4 bending ν_4
622	OH structural
1040	PO_4 bending ν_3
3555	OH structural

3.2. XRD analysis

The XRD analysis was performed using the X-ray diffractometer. The straight base line and sharp peaks of the diffractogram in Fig. 3 confirmed that the product was well crystallized. The XRD pattern indicated that hydroxyapatite was formed in this sample and traces of other calcium phosphate impurities were not detected by this technique. This can also be seen in this figure, secondary CaO phase was observed.

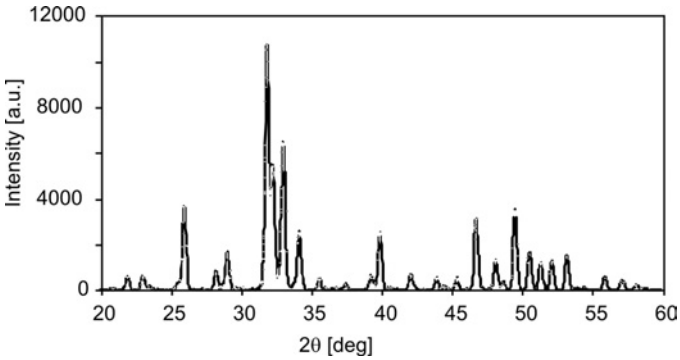

Fig. 3. XRD pattern of the synthesized hydroxyapatite

The intensity of the (200) CaO peaks on the XRD pattern of HA powder was used as a direct indicator of its purity as in the research of Afshar et al. [10]. The ratio of

the peak intensities in the XRD pattern of CaO/HA ($I_{(200)}$ CaO/$I_{(002)}$ HA) was calculated. The amounts of ($I_{(200)}$ CaO/$I_{(002)}$ HA) in the sample was about 0.08. The CaO presence, however, does not necessarily mean that HA has lower biocompatibility [15]. The control of parameters of the synthesis is the key to developing HA purity as well as to indentifying other phases in bioceramics [15].

3.3. Thermal analysis

Exemplary DTA and TGA curves for the hydroxyapatite powder are shown in Fig. 4. The first endothermic region ranges from 90 to 295 °C with a peak at about 250 °C, which corresponds to the dehydration of the precipitating complex and loss of physically adsorbed water molecules of the hydroxyapatite powder. The weight loss in this region is 16%. With increase in temperature from 295 to 1200 °C, no peak was observed, except that a weight loss of 6% is observed in the TGA curve in the temperature range which is assumed to be the result of gradual dehydroxylation of hydroxyapatite powder. This can be explained by the following reaction [13]:

$$Ca_{10}(PO_4)_6(OH)_2 \rightarrow Ca_{10}(PO_4)_6(OH)_{2-2x}O_x + xH_2O \quad (3)$$

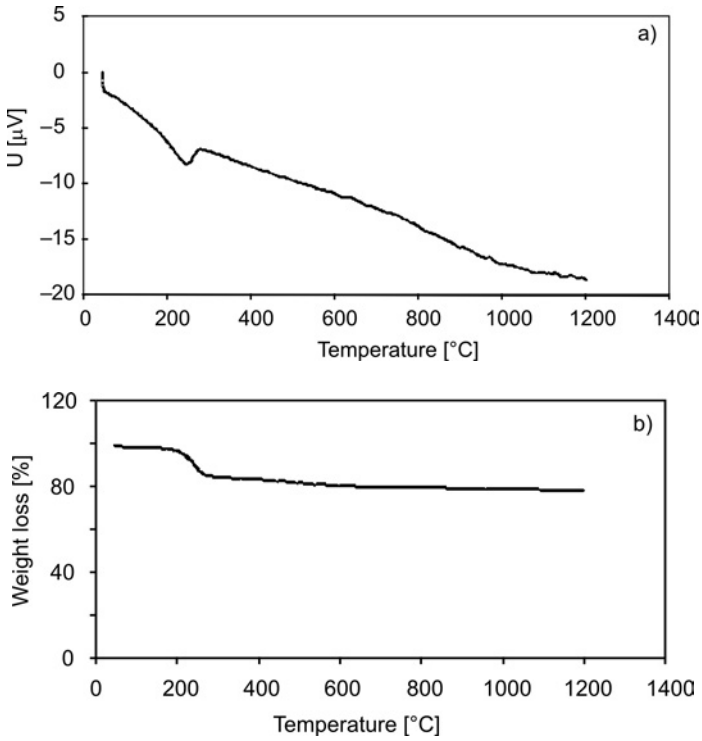

Fig. 4. DTA (a) and TGA (b) traces of the hydroxyapatite powder

3.4. Elemental analysis

The results of measurement for the elemental composition (Ca and P content) and Ca/P molar ratio are given in Table 2.

Table 2. Ca and P content in the synthesized hydroxyapatite powder and Ca/P molar ratio

Element	Measured content [wt%]	Ca/P molar ratio
Ca	38.63	1.71

The bulk Ca/P molar ratio was determined as 1.71. The measured Ca/P ratio for this synthesized powder was higher than the stoichiometric ratio (1.667) expected for a pure HA phase that can arise from the local presence of carbonate apatite in which the Ca/P molar ratio can be as high as 3.33 [14] or from the presence of impurities such as CaO. According to the XRD pattern that showed the existence of small amounts of CaO phase, the second case is much more probable.

3.5. SEM observations

The microstructure of the powder prepared by the present process was analyzed using SEM. SEM micrographs of synthesized powder under two magnifications are shown in Fig. 5.

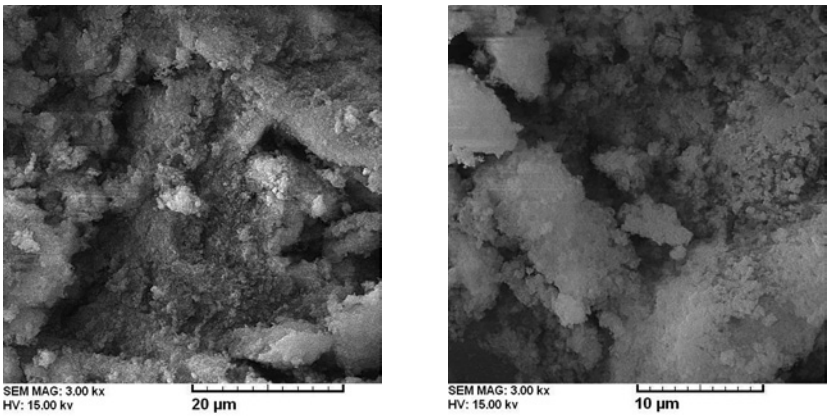

Fig. 5. SEM of the synthesized hydroxyapatite powder: magnification 3000× (left) and 5000× (right)

As can be seen from the morphologies of particles, there is a distribution of small particles and large agglomerates. These agglomerates consist of fine particles that are cold welded together.

3.6. TEM observations

TEM was used to examine the hydroxyapatite crystallites. TEM micrographs of the hydroxyapatite powder under two magnifications are shown in Fig. 6. The microstructure of the hydroxyapatite crystallites was observed to be almost like a needle, with the mean crystallite size of 60 nm. The aspect ratio of needle-like hydroxyapatite was measured to be about 8.

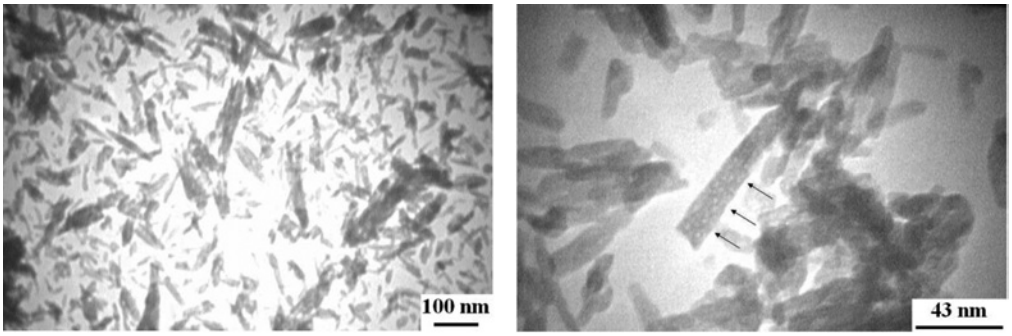

Fig. 6. TEM micrographs of the synthesized hydroxyapatite powder magnification 3500× (left) and 100 000× (right)

4. Conclusions

Hydroxyapatite was synthesized by the wet precipitation method. The hydroxyapatite powder was characterized at a macroscopic level by XRD, FTIR, DTA, TGA and chemical analysis (AAS and EDTA titration technique), while SEM and TEM provided detailed information at the microscopic (individual grain) level. The XRD analysis showed that the prepared hydroxyapatite sample was nearly a pure hydroxyapatite. Only low levels of specific impurities (such as CaO) were detected. FTIR investigations also showed all typical absorption characteristics of hydroxyapatite. The thermal behaviour of hydroxyapatite was studied by simultaneous thermal analysis (STA) which confirmed that the obtained powder was hydroxyapatite. Chemical analyses (for example AAS and EDTA titration) were used for the determination of Ca/P molar ratio. The bulk Ca/P molar ratio was determined as 1.71, which showed that the measured Ca/P ratio for the synthesized powder was higher than the stoichiometric ratio (1.667) expected for a pure HA phase. SEM revealed that there is a distribution of small particles and large agglomerates, and these agglomerates consist of fine particles that are cold welded together. Finally, TEM analysis ascertained that the crystallites of prepared powder were nano-sized and needle-like, with an aspect ratio of about 8.

References

[1] BOSE S., SAHA S.K., Chem. Mater., 15 (2003), 4464.
[2] JONES F.H., Surf. Sci. Rep., 42 (2001), 75.
[3] KIKUCHI M., ITOH S., ICHINOSE S., SHINOMIYA K., TANAKA J., Biomater., 22 (2001), 1705.
[4] SCHNETTLER R., ALT V., DINGELDEIN E., PFEFFERLE H.J., KILIAN O., MEYER C., HEISS C., WENISCH S., Biomater., 24 (2003), 4603.
[5] LIOU S.C., CHEN S.Y., LIU D.M., Biomater., 24 (2003), 3981.
[6] MAVROPOULOS E., ROSSI A.M., ROCHA N.C.C., SOARES G.A., MOREIRA J.C., MOURE G.T., Mater. Charact., 50 (2003), 203.
[7] LI Y., KLEIN C.P.A.T., J. Mater. Sci. Mater. Med., 5 (1994), 263.
[8] CHUSSEI C.C., GOODMAN D.W., Anal. Chem., 71 (1999), 149.
[9] WEISS P., OBADIA L., MAGNE D., BOURGS X., RAU C., WEITKAMP T., KHAIROUN I., BOULER J.M., CHAPPARD D., GAUTHIER O., DACULSI G., Biomater., 24 (2003), 4591.
[10] AFSHAR A., GHORBANI M., EHSANI N., SAERI M.R., SORRELL C.C., Mater. Design, 24 (2003), 197.
[11] MORALES J.G., BURGUES J.T., BOIX T., FRAILE J., CLEMENTE R.R., Cryst. Res. Technol., 36 (2001), 15.
[12] KOMATH M., VARMA H.K., Bull. Mater. Sci., 4 (2003), 415.
[13] MURRAY M.G.S., WANG J., PONTOON C.B., MARQUIS P.M., J. Mater. Sci., 30 (1995), 3061.
[14] WEI M., EVANS J.H., BOSTROM T., GRONDAHL L., J. Mater. Sci. Mater. Med., 14 (2003), 311.
[15] RAMESHBABU N., KUMAR T.S.S., RAO K.P., Bull. Mater. Sci., 29 (2006), 611.

Received 18 September 2007
Revised 10 January 2008

Materials Science-Poland, *Vol. 28*, *No. 1*, *2010*

Structure and optical properties of $(Alq_x)/Al_2O_3$ ethanol colloids

Q.-H. CHEN[1, 2*], W.-J. WANG[1], W.-G. ZHANG[1]

[1]College of Chemistry and Materials Science, Fujian Normal University, Fuzhou 350007, P. R. China

[2]Fujian Key Laboratory of Polymer Materials, Fuzhou 350007, Fujian, P. R. China

An investigation into the structure and chemical stability of green light emitting aluminum complexes of 8-hydroxyquinoline $(Alq_x)/Al_2O_3$ colloids was performed. $(Alq_x)/Al_2O_3$ ethanol colloid was characterized by the high resolution transmission electron microscopy (HRTEM), Fourier transform infrared spectroscopy, thermogravimetric and simultaneous differential thermal analysis, and thermogravimetric analysis coupled to Fourier transform infrared spectroscopy (TGA/FTIR). The results show that the $(Alq_x)/Al_2O_3$ nanoparticles are composed of an inner core of crystalline Al_2O_3 and an outer layer of 8-hydroxyquinoline (Q) coordinated to the surface aluminum ions of Al_2O_3 the nanoparticles. The luminescence intensity of the $(Alq_x)/Al_2O_3$ ethanol colloids decreased upon the increasing aging time, and is accompanying by the presence of a brown material and a dark brown deposit produced in the colloids. The main component of the deposit was polystyrene. These findings can be explained by a process where Q coordinates to the surface ions of the Al_2O_3 particles, followed by degradation of the pyridine ring of 8-hydroquinonline, leading to the formation of polystyrene.

Keywords: *$(Alq_x)/Al_2O_3$ nanoparticles; ethanol colloids; pulsed laser ablation; optical properties; structure*

1. Introduction

Aluminum complex of 8-hydroxyquinoline (Alq_3) is a stable metal complex that can be sublimed to yield a thin film and stands as one of the most useful materials used in organic light emitting devices for display applications [1–3] and panel displays [1, 4]. Organic-polymeric light emitting diodes (LEDs) exhibit many advantages over inorganic LEDs driven by low dc voltage, high luminous efficiency, high brightness and multicolour emission. Although much progress has been made in improving emission efficiencies and brightness and in prolonging the lifetime of the devices, they still suffer from a limited lifetime due to degradation of Alq_3 molecules [5]. Degradation of luminescence materials in organic light emitting diodes (OLED) is an area of intense

*Corresponding author, e-mail: qhchen@fjnu.edu.cn

scientific interest. Baldacchini et al. [6] suggested that accelerated failure of OLEDs at elevated temperatures was attributed to degradation of materials and electrode–organic interfaces, together with morphological change (crystallization) of the organic layers. Papadimitrakopoulos et al. [7–9] have recently published a chemical degradation mechanism for Alq_3, where the presence of moisture and oxygen was found to be detrimental to the production of luminescence quenching by-products. This was attributed to a condensation polymerization of the freed Q (8-hydroxyquinoline), to form a dark, non-emissive residue, whose structure has not yet been fully determined. Determination of this unknown polymer is very important because it might contribute to detail degradation of the Alq_3. Xu and his coworker [10] have systematically investigated the nature of the bright clusters, which can be classified as protrusion and grown grain, in/on the moisture-exposed Alq_3 thin film. The protrusion is most likely to be a hydrated Alq_3 species, whereas, the grown grain is attributed to a crystalline Alq_3 structure.

Our laboratory has recently discovered that alumina 8-hydroxyquinoline complexes $(Alq_x)/Al_2O_3$ nanocolloids prepared by focused pulsed laser ablation at the solid Al_2O_3 target and a flowing ethanol solution of Q can radiate intense green light under ultraviolet radiation. The fluorescence intensity of the $(Alq_x)/Al_2O_3$ nanocolloids decreases with the increase in the aging time in the presence of oxygen and moisture [11]. Because of similar properties and the luminescence mechanism between Alq_3 and the coordinated $(Alq_x)/Al_2O_3$ nanoparticles, studying the degradation of the coordinated $(Alq_x)/Al_2O_3$ nanoparticles may be helpful for understanding the detail degradation of the Alq_3.

In this paper, Fourier transform infrared spectroscopy (FTIR), thermogravimetric and simultaneously differential thermal analysis (TG/SDTA), thermogravimetric analysis coupled to Fourier transform infrared spectroscopy (TGA/FTIR) and high resolution transmission electron microscopy (HRTEM) were used to study the structure and chemical stability of the $(Alq_x)/Al_2O_3$ nanocolloids. Increasing the aging time of colloids resulted in changes in the luminescence colour and produced a brown polymer, accompanied by decrease in the photoluminescence intensity. The results show that polystyrene is formed, and leads to fluorescence quenching when the coordinated $(Alq_x)/Al_2O_3$ nanocolloids have been deposited for five months.

2. Experimental

8-hydroxyquinoline (Q) (Sinopharm Chemical Reagent Co., Ltd, SCRC) in ethanol solution (4.2×10^{-4} M) was used as a flowing liquid over the submerged Al_2O_3 target. The Al_2O_3 (SCRC) target was irradiated by a focused laser beam with 532 nm light from a DCR-3G Nd:YAG laser (Spectra Physics Inc.), operating at 10 Hz, at the fluence of 200 mJ/pulse with a pulse width of 8 ns. The spot size of the laser beam on the surface of the target was about 1 mm, and the flowing liquid was flowing over the target at the speed of about 0.05 cm^3/s. Al_2O_3 was submerged at the depth of 1–2 mm, thus the power density of the pulsed laser beam in the focus spot was approximately as

high as 3.18×10^9 W/cm^2. Considering the reflection loss from the focused lens, the actual power density is still higher than 10^8 W/cm^2. The whole preparation process was done in a very pure nitrogen atmosphere.

The light yellow granular deposit can be obtained from the $(Alq_x)/Al_2O_3$ ethanol colloids by centrifugal settling and removing the supernatant liquid. The obtained deposit was washed with ethanol (repeated eight times), dried in vacuum, and finally a light yellow powder was obtained and used for characterization by FTIR and TG/SDTA. After aging of $(Alq_x)/Al_2O_3$ ethanol colloids for five months, a deposit material with brown colour can be found at the bottom and inner wall of the vessel. The deposit (ca. 6mg) was used for TG-FTIR characterization.

The HRTEM photographs and selected area electron diffraction (SEAD) were obtained on the FEI F20 transmission electron microscope (Philips Company). Electron micrographs were recorded using 2 drops of $(Alq_x)/Al_2O_3$ nanocolloid solution, applied onto a copper mesh coated with an amorphous carbon film. FTIR was performed on an Avata 360 FT-IR spectrometer. TG/FTIR measurements were recorded with a Mettler Toledo TGA/SDTA 851^e and Nicolet 5700 FT-IR. TG measurements were performed at a 10 °C/min scanning rate, employing a 50 cm^3/min flow of dry nitrogen as a purge gas for the sample and reference cells.

3. Results and discussion

3.1. Structure of the nano Al_2O_3 particles

Figure 1 shows the HRTEM image of the $(Alq_x)/Al_2O_3$ clusters after being prepared for 1 h. It can be seen from Fig. 1a that the aggregated nanoparticles consist of many smaller, irregular 5–10 nm particles. It was previously shown that, over time, the particles produced by pulsed laser ablation grew in size while undergoing a change in shape, from irregular spherical forms [11]. The size of the particles in Fig. 1c is about 5 nm and it is obvious that the nanoparticles are enwrapped by an amorphous layer, because of the absence of sharp edges. The amorphous material is mostly composed of Q or Q on the surface of $(Alq_x)/Al_2O_3$ clusters. Crystal lines are visible in the enwrapped area of Fig. 1d and the calculated interplanar spacing is 0.3421 nm, which corresponds with the (110) (Fig. 1e) diffraction planes, revealing that the $(Alq_x)/Al_2O_3$ clusters consist of Al_2O_3 crystals. From Figure 1b, it is found that the SEAD pattern of the coordinated Al_2O_3 cluster has a distinctive diffraction pattern with many diffraction points. These findings show that the coordinated Al_2O_3 clusters consist of many smaller Al_2O_3 crystals of disordered arrangement. The interplanar spacing and diffracting planes, together with that of JCPDS card are listed in Table 1. It was found that the *d* spacing is similar for the Al_2O_3 and the $(Alq_x)/Al_2O_3$ clusters, and that the $(Alq_x)/Al_2O_3$ clusters have slightly higher *d* spacing. This also indicates that the original particles, produced by pulsed laser ablation of the Al_2O_3 target immersed into

flowing liquid, are Al_2O_3 crystals with the size of 5–10 nm. Original particles are co-ordinated by Q in the liquid, and very soon they congregate and form larger particles.

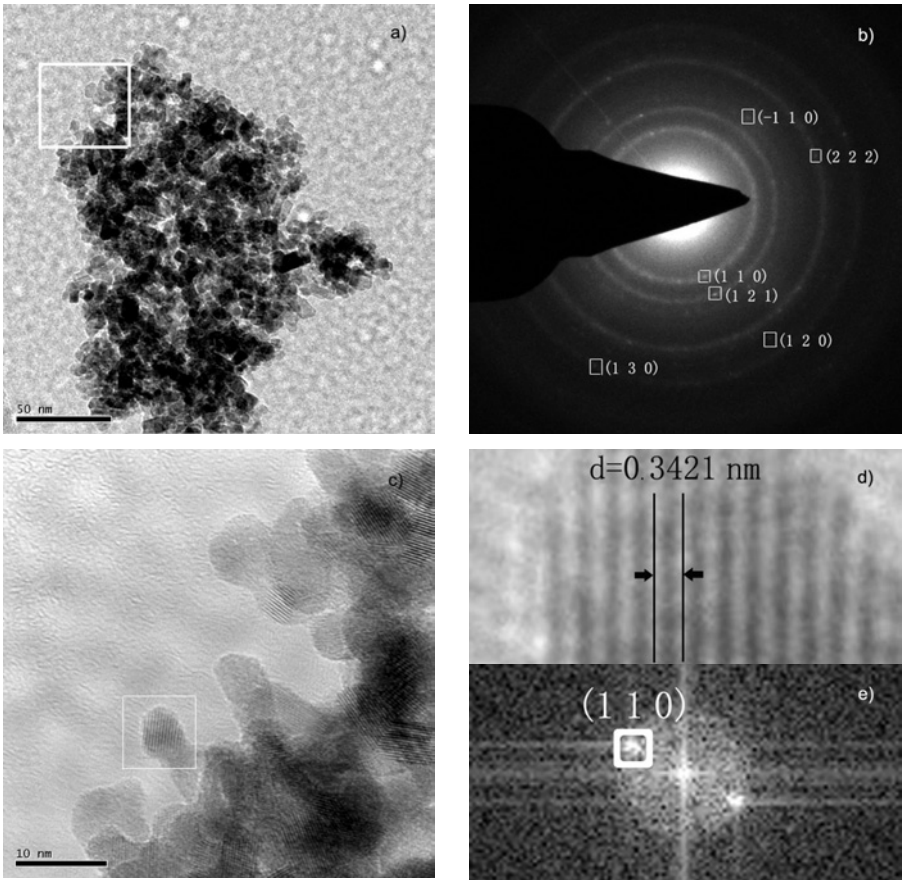

Fig. 1. HRTEM images of the $(Alq_x)/Al_2O_3$ clusters (a), and selected areas (b) of electron diffraction (SAED) patterns of (a), enlarged images (c) and (d) corresponding to the areas marked by the solid line in (a) and (c), and (e) is FFT image of (d)

Table 1. The interplanar spacing and diffraction planes together with that of the JCPDS card

Diffracting planes	Interplanar spacing [nm]	
	Al_2O_3 (JCPDS card 76-0144)	Alq_x/Al_2O_3 cluster
(110)	0.34804	0.3835
(121)	0.25515	0.2976
$(\bar{1}10)$	0.23794	0.2649
(222)	0.21660	0.2281
(120)	0.20855	0.2171
(130)	0.14046	0.1593

Figure 2 shows the FTIR spectra of $(Alq_x)/Al_2O_3$ clusters and Q from the Aldrich FTIR library. As compared with the spectra of Q and Alq_3 reported in the literature [12], the $(Alq_x)/Al_2O_3$ cluster has much weaker absorbance peaks at about 2920 cm^{-1} ($–CH_2$), 1200–1400 cm^{-1} (quinoline group) and 1580 cm^{-1} (–OH), but has two stronger peaks at 561 and 841 cm^{-1}, which can be attributed to the asymmetric vibrations of Al_2O_3. It is obvious that the $(Alq_x)/Al_2O_3$ clusters consist of Al_2O_3 and Q.

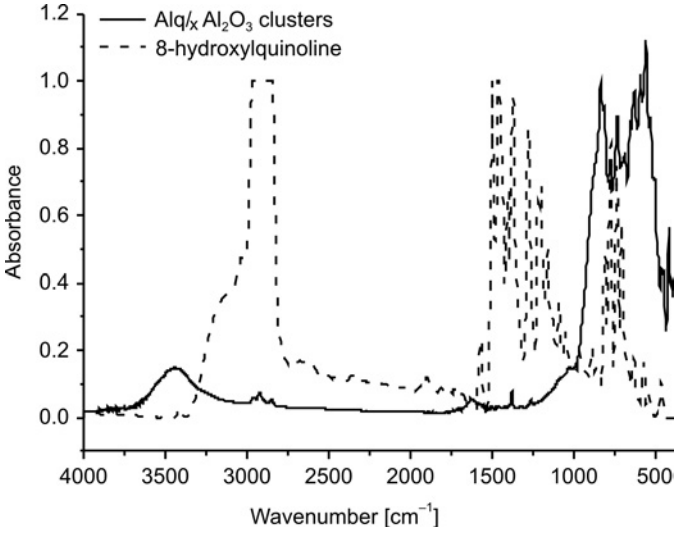

Fig. 2. FTIR spectra of the $(Alq_x)/Al_2O_3$ clusters and Q from the library of the Aldrich condensed phases

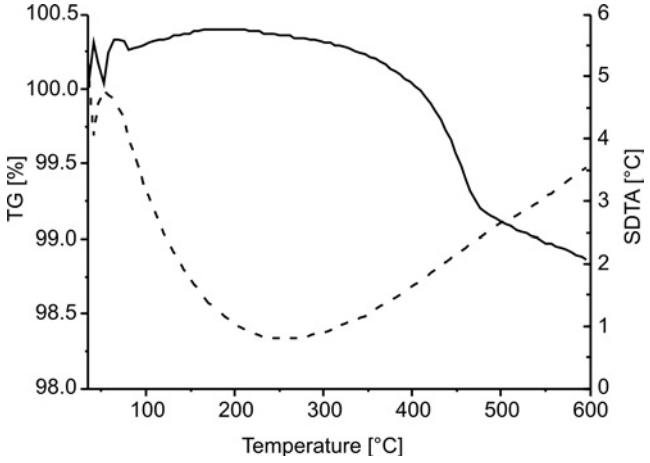

Fig. 3. TG/SDTA image of the $(Alq_x)/Al_2O_3$ clusters

Figure 3 shows the TG-SDTA image of the $(Alq_x)/Al_2O_3$ clusters. Above 200 °C $(Alq_x)/Al_2O_3$ clusters show obvious weight loss (ca. 1.5%) in the temperature range

over which the TG-SDTA measurements were conducted. $(Alq_x)/Al_2O_3$ clusters have large surface areas, thus they adsorb much gases (about 0.4%) at temperatures below 200 °C, released at higher temperatures. Thus the weight loss originates from the absorbed gas (about 0.4%) and the thermolysis of Q coordinated to the surface ions of the $(Alq_x)/Al_2O_3$ clusters or simply from its sublimation [8] (1.1%).

3.2. Optical properties of the $(Alq_x)/Al_2O_3$ ethanol colloids

The $(Alq_x)/Al_2O_3$ ethanol colloids can emit strong green fluorescent light under UV irradiation; however, the fluorescence colour changed upon the increasing aging time.

Table 2. The colour of the $(Alq_x)/Al_2O_3$ ethanol colloids with the various aging times under strong white light and UV irradiations

Aging time	The colour under strong white light	The colour under UV radiations
1 h	white	green
1 month	white	light Kelly green
2 months	light brown	Kelly green
5 months	brown	black

Table 2 shows the colour of the $(Alq_x)/Al_2O_3$ ethanol colloids corresponding to various aging times under strong white light and UV irradiations. Under irradiation, differing in time, $(Alq_x)/Al_2O_3$ ethanol colloids display various colours. These findings indicate with the increase in the aging time, a brown, non-fluorescent material is produced in the colloids, and the luminescence intensity decreases. After five months of aging, a deposit material with brown colour can be found at the bottom and inner walls of the vessel. Because the coordinated Znq_2/ZnO ethanol colloids prepared by the same method have very stable chemical properties, and have the same fluorescent green colour during aging [13], alumina was believed to be related to the fluorescence quenching of the coordinated Alq_x/Al_2O_3 colloids. The subsection immediately below describes how FTIR and TG-FTIR were used to characterize the brown deposit material.

Figure 4 shows the FTIR spectra of the deposits of the $(Alq_x)/Al_2O_3$ ethanol colloids and polystyrene (M. W. 50000) from the Aldrich FTIR library. Using pattern-matching software (Omnic 7.2, Thermo Electron corporation), the match value of these two spectra is as high as 95.5%, which shows that the main component of the deposit is polystyrene. In addition, the stronger absorption peak at 3400 cm^{-1} can be attributed to the hydroxyl group, which indicates there is little amount of material containing hydroxyl, which may be the result of Q being absorbed by the deposit.

Figure 5 shows the TG/SDTA image of the deposits of the $(Alq_x)/Al_2O_3$ clusters, and Figure 6 shows FTIR spectra of the thermal products released at 1.1 min, 8.6 min, 41.4 min and also styrene from the flavours and fragrances FTIR library. Weight losses indicating the release of some materials occurred at 1.1, 8.6 and 41.4 min.

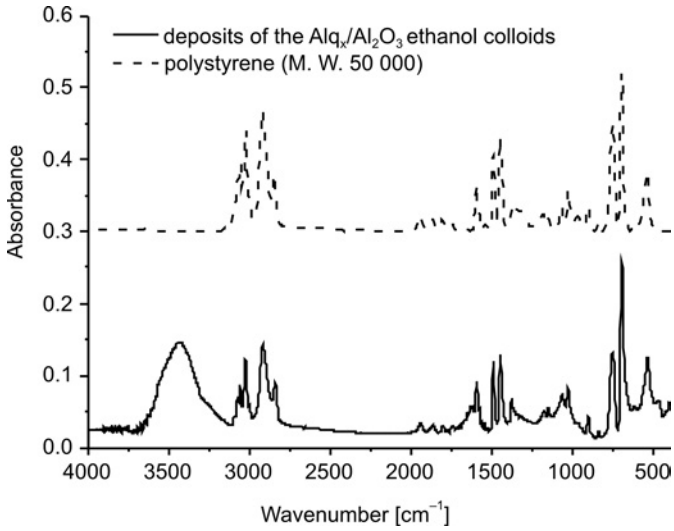

Fig. 4. FTIR spectra of the deposit of the Alq_x/Al_2O_3 ethanol colloids and polystyrene (M. W. 50000) from the Aldrich Condensed Phase Supplement

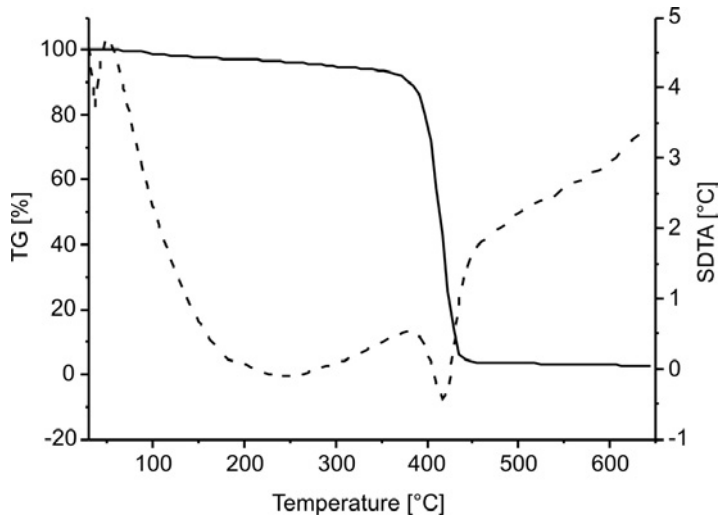

Fig. 5. TG/SDTA image of the deposits of the $(Alq_x)/Al_2O_3$ ethanol colloids

Table 3 shows the weight loss for an $(Alq_x)/Al_2O_3$ cluster in function of time and temperature. The materials released were identified by comparing their spectra with FT-IR spectra from the Aldrich FTIR library. As can be seen from Table 3, a close match of the product released after 41.4 min with styrene indicates these two materials are the same. The small quantity of water was probably absorbed during formation of the colloidal deposits, and ethanol would be expected to absorb into the colloidal deposits as well. As can be seen from Fig. 6 and Table 3, styrene was released in the

temperature range of 350–450 °C. It most likely originates from Q coordinated to the surface of the Al_2O_3 particles and also from Q in the colloids.

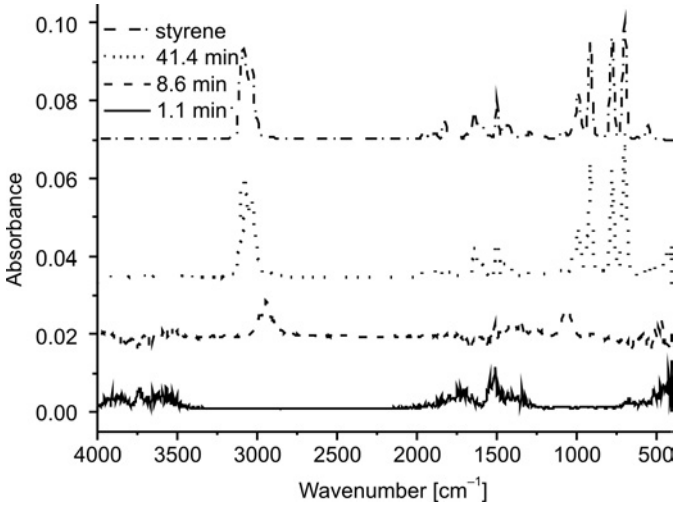

Fig. 6. FTIR spectra of the released thermal products from the deposit at 1.1 min, 8.6 min, 41.4 min and styrene spectrum from the library of flavours and fragrances

Table 3. Weight loss for $(Alq_x)/Al_2O_3$ clusters as a function of time and temperature

Heating time [min]	Temperature [°C]	Weight loss [%]	Rest weight [%]	Match value [%]	Possible released product
1.1	46	–0.34	100.34	45%	water without CO_2
8.6	121	1.7	98.3	60%	ethanol and water
41.4	449	96.29	3.71	96.1	styrene
61.5	650	97.33	2.67		

3.3. Process of decreasing luminescence of the $(Alq_x)/Al_2O_3$ ethanol colloids

It has been shown that $(Alq_x)/Al_2O_3$ nanoparticles are composed of the Al_2O_3 crystal core and Q coordinated with the surface ions of the Al_2O_3 nanoparticles. The luminescence intensity decreases with the increase in the aging time accompanied by the production of a brown material and a dark brown deposit in the colloids. The main component of the deposit is polystyrene. These findings can be explained if Q, coordinated to the surface of Al_2O_3 particles, was catalysed by Al_2O_3 nanoparticles having high surface areas, to form polystyrene. As Q coordinates to the surface Al ions of nanoparticles, some inner bonding energy becomes weaker, some bonds are broken and new ones are formed. The high surface energy of nano Al_2O_3 particles accelerates this change. During the bond changing process, polystyrene and a brown material are formed and Alq_x vanishes. Because this brown material is still unknown, further inves-

tigations are presently underway to elucidate the details of luminescence attenuation in $(Alq_x)/Al_2O_3$ ethanol colloids.

4. Conclusions

An investigation into the structure and chemical stability of ethanol colloids of aluminum 8-hydroxyquinoline complexes $(Alq_x)/Al_2O_3$ emitting green light under ultraviolet radiation was performed. The $(Alq_x)/Al_2O_3$ ethanol colloid product was characterized by HRTEM, FTIR, TG/SDTA, TGA/FTIR. The HRTEM and FTIR results showed that crystalline Al_2O_3 is the core of the $(Alq_x)/Al_2O_3$ nanoparticles, with Q coordinated to the surface of aluminum ions of the Al_2O_3 nanoparticles. $(Alq_x)/Al_2O_3$ ethanol colloids with different aging times show different luminescence colours under ultraviolet radiation. The luminescence intensity decreases as the aging time increases, accompanied by the formation of a brown material and a dark brown deposit. TG-FTIR and FTIR results show that the main component of the deposit is polystyrene. These findings can be explained by a process in which Q coordinated to the surface ions of Al_2O_3 particles, is catalysed by Al_2O_3 nanoparticles to form polystyrene.

Acknowledgements

The authors are indebted for the financial support of the National Natural Scientific Foundation of China (Grant No. 50272014), the Key Nano Special Item of Fujian Province of China (Grant No. 2005HZ01-5), the Natural Scientific Foundation of Fujian Province of China (Grant No. A0710001) and the Education Department of the Fujian Province of China (Grant No. JB07061). We also acknowledge Professor Richard D. Foust for helpful discussions.

References

[1] TANG C.W., VANSLYKE S.A., Appl. Phys. Lett., 51 (1987), 913.
[2] CÖLLE M., DINNEBIER R.E., BRÜTTING W., Chem. Commun., (2002), 2908.
[3] PRIESTLEY R., WALSER A.D., DORSINVILLE R., Opt. Commun., 158 (1998), 93.
[4] BURROUGHES J.H., BRADLEY D.D.C., BROWN A.R., MARKS R.N., MACKAY K., FRIEND R.H., BURNS P.L., HOLMES A.B., Nature, 347 (1990), 539.
[5] YU G., SHEN D.Z., LIU Y.Q., ZHU D.B., Chem. Phys. Lett., 333 (2001), 207.
[6] BALDACCHINI G., BALDACCHINI T., GAGLIARDI S., MONTEREALI R.M., PACE A., PODE R.B., Thin Solid Films, 417 (2002), 72.
[7] PAPADIMITRAKOPOULOS F., ZHANG X.M., Synth. Met., 85 (1997), 1221.
[8] HIGGINSON K.A., ZHANG X.M., PAPADIMITRAKOPOULOS F., Chem. Mater., 10 (1998), 1017.
[9] PAPADIMITRAKOPOULOS F., ZHANG X.M., THOMSEN D.L., HIGGINSON K.A., Chem. Mater., 8 (1996), 1363.
[10] XU M.S., XU J.B., Synth. Met., 145 (2004), 177.
[11] CHEN Q.H., ZHANG W.G., J. Colloid Interf. Sci., 309 (2006), 531.
[12] LI H.R., ZHANG F.J., WANG Y.Y., ZHENG D.S., Mat. Sci. Eng. B, 100 (2003), 40.
[13] CHEN Q.H., ZHANG W.G., Appl. Surf. Sci., 253 (2007), 3751.

Received 16 January 2008
Revised 22 January 2009

Materials Science-Poland, *Vol. 28*, *No. 1*, *2010*

Methods of manufacturing of potassium titanate fibres and whiskers. A review

T. ZAREMBA, D. WITKOWSKA*

Silesian University of Technology, Department of Chemistry, Inorganic Technology and Fuels, ul. Krzywoustego 6, 44-100 Gliwice, Poland

Titanate fibres and whiskers are new materials with high heat resistance and good chemical stability. They have found numerous applications such as ion exchanger materials, thermal insulators, reinforcements, catalysts, photocatalysts and substitutes of asbestos. In this paper, the methods of fabricating potassium titanate fibres and whiskers have been discussed, e.g., calcination, hydrothermal reaction, flux growth, sol -gel technique, and others. Because asbestos fibres are known to cause fibrotic diseases in lungs we also refer to studies into the toxicity and carcinogenicity of potassium titanate fibres and whiskers.

Keywords: *potassium titanate; fibres; whiskers; production;*

1. Introduction

Two types of fibres are encountered into human society: natural fibres, which have existed for 4 000 years or more, and synthetic fibres developed 100 years ago, when Count Chardonnet invented artificial silk, an achievement that had been only a pipe-dream up to then [1].

A fibre can be defined as a thin and long substance which has both strength and the capacity to be elongated to a certain extent. Because it is by definition thin, the fibre is able to bend. To characterise the thinness and the length of fibres numerically, the ratio L/D of their length L to their diameter D is commonly used to characterize the geometry of a fibre (this is known as the aspect ratio). A fibre can be then defined as a material that has an aspect ratio of 100 or more. Fibre diameters can be used to classify various fibre morphologies, which include whiskers (< 1 μm), staples (1–10 μm), continuous multifilament yarns (5–25 μm), and continuous monofilaments (> 100 μm). A whisker or microcrystalline fibre can be defined as a material having small diameters and minimal flaws or imperfections, which have very high strength and modulus values [1, 2].

*Corresponding author, e-mail: dagmara.witkowska@polsl.pl

During the last thirty years important progress has been made on inorganic fibres and whiskers. This progress appertains to the synthesis of new fibres and whiskers which have a high tensile strength, tenacity, stiffness, modulus of elasticity and heat resistance. First of all, they have found application in production of metal, organic and ceramic matrix composites. Composite materials are fundamental materials for supporting the technologies required for the 21st century, as demanded by the automobile/aircraft industries, space technology and in the leisure field, such as golf, tennis, skiing and sailing. They may therefore have a great impact on many human activities [1, 3, 4].

Glass and asbestos fibres were initially inorganic fibres. The discovery that asbestos has carcinogenic properties has motivated the search for new kinds of fibres. The technical processes of fabricating fibres like aluminosilicate, alumina, boron and silicon carbide have been developed, some of these fibres in the shape of whiskers. Fibres and whiskers are now widely applied in the field of aerospace technology, automobile technology, marine technology, optical networks, the leisure industry, and for the production of materials such as safety/protective garments and friction materials. These applications are mainly to replace metal parts and to reduce the weight for the purpose of energy conservation [1, 3, 4].

In the last decade, a new generation of inorganic fibres and whiskers – titanates – has been discovered. A series of titanates having the chemical formula $M_2O{\cdot}nTiO_2$ (where M = alkali metal and n = 2–8) are well-known. All of them have tunnel or layered crystal structures constructed out of TiO_6 octahedra sharing edges with interlaying cations. Because of their excellent chemical and mechanical properties, they have been used in a wide range of applications in industry as ion exchange materials, reinforcements, heat insulators, friction materials, catalysts, photocatalysts and as substitutes of asbestos [5, 6]. The following titanates have been described:

$M_2O{\cdot}2TiO_2 - M_2Ti_2O_5$ (M = Li, Na, K, Cs) [7], $M_2O{\cdot}4TiO_2 - M_2Ti_4O_9$ (M = Li, Na, K, Rb, Cs) [8], $M_2O{\cdot}6TiO_2 - M_2Ti_6O_{13}$ (M = Na, K, Rb, Cs) [9–11], $M_2O{\cdot}8TiO_2 - M_2Ti_8O_{17}$ (M = K, Rb) [12], as well as $KTiO_2(OH)$ [12], $K_3Ti_8O_{17}$ [13], $K_4Ti_3O_8$ [7], $Na_2Ti_3O_7$ [14], $Na_2Ti_9O_{19}$ and others [15].

Among alkali titanates, potassium titanates such as $K_2Ti_2O_5$, $K_2Ti_4O_9$, $K_2Ti_6O_{13}$ and $K_2Ti_8O_{17}$ have attracted much attention, due to their specific photochemical properties or their artificial cage-type structure. They have been recognized as important functional materials with wide applications [5, 6].

Among whiskers, potassium titanate whisker has several advantages compared with other ceramic whiskers. One of its most desirable features is low production cost of the whisker itself, which is one of the critical factors for commercial applications of composites [16].

2. Potassium titanates

The crystal structure and properties of potassium titanates, $K_2O{\cdot}nTiO_2$ (n = 2–8), are dependent on the value of n. Characteristic feature of potassium titanates with

a high potassium content (n = 2, 4) is the existence of a layer structure. They exhibit a distinctive intercalation capacity and catalytic activity. However, in the case of potassium titanates with a low potassium content (n = 6, 8), they have a tunnel structure and exhibit good thermo-insulation properties and good chemical stability [17].

Many methods have been developed to synthesize potassium titanate fibres and whiskers, including calcination, slow-cooling calcinations, hydrothermal reactions, flux growth (melting), flux evaporation and the combinative route of flux evaporation and the slow-cooling process. Among many methods of synthesis, the slow-cooling calcination method has advantages in that it uses no flux; therefore, production costs could be reduced compared with other methods [17, 18].

2.1. Potassium dititanate $K_2Ti_2O_5$

Potassium dititanate $K_2Ti_2O_5$ has been the focus of intense research because of the interchangeable crystal structure that facilitates subsequent conversions into inorganic-organic/inorganic composites and new layered or three-dimensionally bonded compounds with a high photocatalytic activity [19, 20]. The crystal structure of $K_2Ti_2O_5$ consists of $(Ti_2O_5)^{2-}$ layers in which titanium atoms have fivefold coordination, separated by potassium ions (Fig. 1) [19, 21].

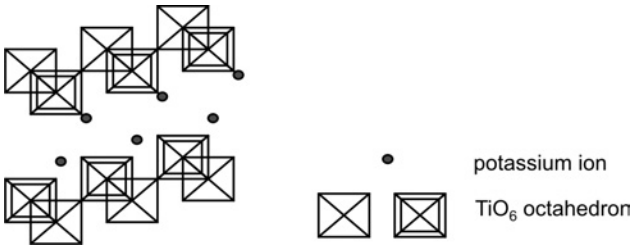

Fig. 1. Idealized crystal structure of $K_2Ti_2O_5$

According to Andersson and Wadsley [21], $K_2Ti_2O_5$ was obtained as colourless needles by melting K_2CO_3 and TiO_2 (anatase) in a platinum crucible. Whilst the crystals were kept for long periods in a desiccator, they decomposed on exposure to moist air. The layered structure of $K_2Ti_2O_5$ is not stable in water or acid solutions [20].

Bao et al. [22] synthesized $K_2Ti_2O_5$ single crystals using K_2CO_3 and nano TiO_2 (anatase) powders as starting materials with the TiO_2/K_2CO_3 molar ratio of 3.0. The precursors were mixed, and a small amount of water and surfactants was introduced to the mixture. The obtained paste was formed into 20 mm × 20 mm × 10 mm disks by mechanical pressing and dried in a oven at 100 °C for 10 h. The disks were then sintered in a muffle furnace at a calcination temperature of 830 °C for 10 h, and quickly removed at the end of the calcination for air-cooling. Monocrystals of $K_2Ti_2O_5$ obtained in the above way had the same size, morphology and surface; at 852 °C they

transformed into $K_2Ti_4O_9$ whiskers. The following steps of their synthesis have been reported:

$$K_2CO_{3(solid)} \rightarrow K_2O_{(solid)} + CO_{2(gas)} \text{ at } T < 828\ ^\circ C$$

$$2TiO_{2(solid)} + K_2O_{(solid)} \rightarrow K_2Ti_2O_{5(solid)} \text{ at } T = 828\ ^\circ C$$

$$2K_2Ti_2O_{5(solid)}) \rightarrow K_2Ti_4O_{9(solid)} + K_2O_{(liquid)} \text{ at } T = 952\ ^\circ C$$

Similarly as in the previous work, hydrous titanium dioxide $TiO_2 \cdot nH_2O$ and K_2CO_3 were used to fabricate $K_2Ti_2O_5$ single crystals [18]. A reactant mixture with the TiO_2/K_2CO_3 molar ratio of 3.0 was dried in an oven at 90 °C for 10 h, calcination was performed in a muffle furnace at 820 °C for 30 min. Then the sintered mixture was removed from the furnace and cooled in air. The synthesized $K_2Ti_2O_5$ single crystals had the same properties as that fabricated by Bao et al. [22].

Masaki et al. [23] obtained potassium dititanate by the hydrothermal method, by oxidation of titanium metal powder in concentrated potassium hydroxide solution. 50 cm^3 of KOH aqueous solution and 10 g of Ti powder were placed in an autoclave with a magnetic stirrer. After being sealed, the autoclave was set into an electric furnace for 2 h at a desired temperature. Then it was taken out from the furnace and cooled immediately in air. The product was separated from the solution by the use of centrifuge, then rinsed with methanol, and finally dried at 105 °C for 12 h in an oven to remove the absorbed water. Well crystallized platelet crystals of hydrated $K_2Ti_2O_5$ were formed as single phases having KOH concentrations ranging from 20 to 25 mol/kg H_2O at temperatures from 150 to 200 °C. Crystalline $K_2Ti_2O_5$ was also obtained from the amorphous compound synthesized at KOH concentration above 80 mol/kg H_2O at 150 °C by heating at 800 °C.

2.2. Potassium tetratitanate $K_2Ti_4O_9$

Crystalline potassium tetratitanate ($K_2Ti_4O_9$), with a characteristic layered structure, consists of TiO_6 octahedra linked with K ions (Fig. 2) [24, 25]. Considering its strong ion exchange properties, $K_2Ti_4O_9$ can be widely used as an ion exchanger for alkali metal ions, alkali earth metal ions and divalent transition metal ions. Furthermore, $K_2Ti_4O_9$ shows good catalytic and photocatalytic activity which enables their application as catalysts and photocatalysts. Potassium tetratitanate fibres and whiskers have been prepared among others by calcination, slow cooling calcination and sol- gel technique [26].

Andersen et al. [26] synthesized potassium tetratitanate by a conventional solid state reaction. Potassium carbonate (K_2CO_3) and anatase (TiO_2) in the molar ratio of 1:4 were milled together in slurry with absolute ethanol saturated with potassium carbonate. The solid was separated, air dried, and 2 g tablets were formed by mechanical pressing. The tablets were then heated at 900 °C for 48 h.

Andersen et al. [26] also synthesized $K_2Ti_4O_9$ by the sol-gel method. The solution of titanium isopropoxide in dry *n*-propanol was added slowly to a solution of potassium *t*-butoxide in dry methanol. The molar ratio of KOC_4H_9 to $Ti(OC_3H_7)_4$ was 1:2. This clear solution was hydrolyzed with a solution of water in *n*-propanol. The amount of water for hydrolysis was 4 mol H_2O per mol $Ti(OC_3H_7)_4$ plus 1 mol H_2O per 1 mol KOC_4H_9. The obtained gel was stirred for three days. Most of the liquid phase was then removed by centrifugation and decantation. The gel was dried in air at room temperature on a glass plate. The resulting white powder was heated for 1 h at 100 °C and then at 900 °C for 60 h. $K_2Ti_4O_9$ fabricated by Andersen et al. [26] was hydrolyzed to obtain hydrous titanium(IV) oxide ($H_2Ti_4O_9{\cdot}nH_2O$) which is an ionic conductor like other hydrous metal oxides ($Sb_2O_5{\cdot}nH_2O$, $ZrO_2{\cdot}nH_2O$, $SnO_2{\cdot}nH_2O$).

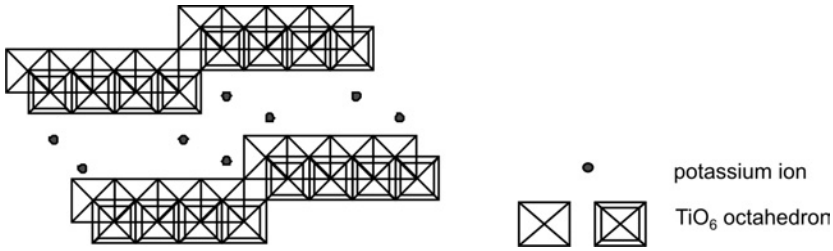

Fig. 2. Idealized crystal structure of $K_2Ti_4O_9$

Bao et al. [18] obtained $K_2Ti_4O_9$ whiskers by the calcination process. Hydrous titanium dioxide was mixed with K_2CO_3, and then the reactant mixture was dried in an oven at 90 °C for 10 h. Also, a mixture of anatase–K_2CO_3 was applied. Calcination was carried out in a muffle furnace at 920 °C for 30 min. The stirred mixtures were then removed at the corresponding calcination temperature, cooled in air and leached in boiling water for 2 h. $K_2Ti_4O_9$ whiskers had a uniform size and good morphology. Compared with anatase, amorphous hydrous titanate lowered the phase change temperature.

Another method to synthesize $K_2Ti_4O_9$ fibres is based on ion exchange and gelation of sodium alginate $(C_5H_7O_4COONa)_x{\cdot}yH_2O$, which is well known as an ion exchangeable organic polymer. This method does not require expensive reagents. In addition, viscous solutions of sodium alginate have an advantage in that it gel in any shape, such as fibre, film, and bead, by ion exchange with protons or multivalent metal ions. 5 g of sodium alginate was added slowly to 100 g of vigorously stirred deionized water. Stirring was continued for 5 h, and then the solution was degassed with a vacuum pump, after which it was left for 24 h to remove air bubbles. An aqueous solution of 5% sodium alginate was extruded from a nozzle into 1 M HCl. The extruded sodium alginate sol turns into alginic acid gel fibre through the ion exchange of its sodium ions with protons in the HCl solution. The alginic acid (H-alginate) fibre was rinsed in deionized water three times, dried in air for 24 h, and then immersed into a mixture of titanium sulfate ($Ti(SO_4)_2$) and potassium nitrate (KNO_3) for more than

10 h. The obtained K-Ti alginate fibre was rinsed in deionized water, dried at ambient temperature and then heated at 800 °C for 3 h in air. The average length and thickness of the potassium tetratitanate fibres were about 2.5 cm and 150 μm, respectively [27].

According to Fujiki and Yoshinori [28], $K_2Ti_4O_9$ fibres can be produced at low cost without using any flux or catalyst. Starting materials, TiO_2 and K_2CO_3, are mixed at the ratio satisfying the general formula $K_2O{\cdot}nTiO_2$ with n ranging from 3 to 5. The mixtures of powders were then heated in the temperature range from 950 °C to 1300 °C and then cooled slowly to 900–950 °C and left for decomposition for 3 to 5 h. Afterwards the crucibles were taken out of the furnace into open air, and allowed to cool to room temperature. The products were washed with cold or warm distilled water and dried at 100 °C. The production process is strongly dependent on the molar ratio of TiO_2/K_2O, the starting materials and the cooling rate. In order to obtain potassium tetratitanate fibres on an industrial scale, it is advisable to apply the decomposition temperature in the range 1100–1150 °C. The product must be held at this temperature for at least 4 h and then cooled at a low rate of 15–35 °C per h for satisfactory growth rate of fibres.

Recently, fibrous potassium tetratitanate was obtained at the Silesian University of Technology in the following way: The substrates, K_2CO_3 and TiO_2, were first ground in an agate mortar in isopropyl alcohol and dried. A powdered stoichiometric mixture was then placed into platinum crucibles and heated to 900–1000 °C in a box furnace. Obtained $K_2Ti_4O_9$ formed short and tightly packed rod-like crystals. Further $K_2Ti_4O_9$ syntheses were carried out by heating the mixture of raw materials to 1150 °C for 3 h thus, causing $K_2Ti_4O_9$ to melt incongruently. $K_2Ti_4O_9$ melts at 1114 ± 15 °C decomposing to $K_2Ti_6O_{13}$ stable solid phases and K_2O-rich liquid phases, which creates $K_2Ti_2O_5$. Then the samples were cooled to 950 °C in a furnace at the cooling rate within the range 50–25 °C·h^{-1}. On cooling, $K_2Ti_4O_9$ whiskers were formed and the association reaction occurred as follows:

$$K_2Ti_6O_{13(s)} + K_2Ti_2O_{5(l)} \rightarrow 2\ K_2Ti_4O_{9(s)}$$

Fig. 3. SEM of $K_2Ti_4O_9$ whiskers synthesized by the calcination at 1150 °C for 3 h and cooled to 950°C at the rate of 35°C·h^{-1} [29]

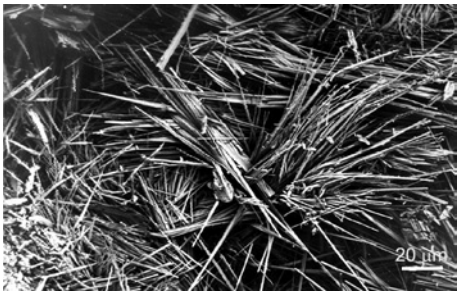

Fig. 4. SEM of $K_2Ti_4O_9$ whiskers synthesized by the calcination at 1150 °C for 3 h and cooled to 950 °C at the rate of 25°C·h^{-1} [29]

The cooling rate was found to be a determining factor of the size of $K_2Ti_4O_9$ whiskers. At the cooling rate of 50 °C·h^{-1}, the whisker length was up to 60 μm. The cooling at 35 °C·h^{-1} caused $K_2Ti_4O_9$ to decompose more quickly (Fig. 3). At the lowest cooling rate (25 °C·h^{-1}), whiskers of a high aspect ratio, exceeding the minimum value required for whiskers, were obtained (Fig. 4) [29–32].

2.3. Potassium hexatitanate $K_2Ti_6O_{13}$

Potassium hexatitanate belongs to materials attracting a growing interest, due to its potential economic importance. This relatively cheap, fibrous material has good thermal durability, chemical resistivity and dispersibility and has been found to be useful as a reinforcement material for plastic and ceramics, heat-insulating paints and automotive brake linings [17, 25, 33–37]. The structure of this material is one in which the structural unit of three TiO_6 octahedra forms the tunnels with sharing edges and joining through the corners as shown in Fig. 5 [25]. Because potassium ions in $K_2Ti_6O_{13}$ are enclosed by the tunnelling structure and isolated from the environment, potassium ions can not escape from the tunnelling structure in the solution [35]. This tunnel structure has also attracted additional interest because of its possible application as a photocatalytic material [25, 33, 38].

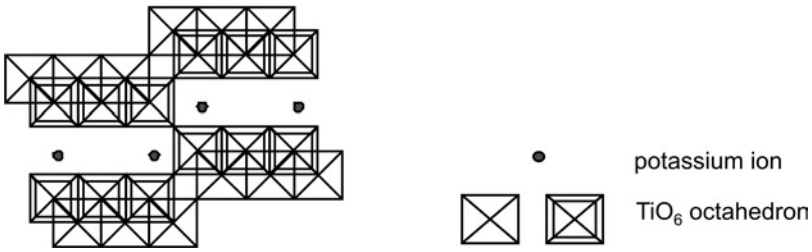

Fig. 5. Idealized crystal structure of $K_2Ti_6O_{13}$

$K_2Ti_6O_{13}$ whiskers may be synthesized by the calcination and slow cooling method. As starting materials, K_2CO_3 and TiO_2 were used in the molar ratio K_2O/TiO_2 1:3. The powder mixture was milled for 24 h with ethanol and subsequently dried. Then a platinum crucible was filled with the mixture and heated to 1150 °C for 6 h. After having been stored for a specified time at an assigned temperature, the specimens were slowly cooled to 950 °C at the rate of 16 °C·h^{-1} in a furnace and quenched in water. During calcination at 1150 °C, rod-like $K_2Ti_6O_{13}$ particles were formed, and $K_2Ti_4O_9$ whiskers were formed from K_2O-rich phase and $K_2Ti_6O_{13}$ during slow cooling (by the splitting of $K_2Ti_6O_{13}$ layers). The final $K_2Ti_6O_{13}$ whiskers were obtained from $K_2Ti_4O_9$ after treatment with boiling distilled water for 4 h and subsequent reheating to 1000 °C for 1 h. The $K_2Ti_6O_{13}$ whiskers had a clean surface and the length exceeding 100 μm [17].

Potassium hexatitanate fibres were fabricated by the combinative route of flux evaporation and slow cooling. 1 wt. % of Li_2CO_3 was added to K_2MoO_4 flux to enhance evaporation of the flux, then the flux (Li_2O–K_2MoO_4) and raw materials (K_2O:TiO_2 = 1:6) were mixed in an agate mortar. The molar ratio of flux to raw materials was kept at 7:3, which was found to lead to the optimum growth condition. After calcining at 1150 °C for 4 h, the sample was slowly cooled to 900 °C in a furnace at the rate of 10 °C·h^{-1}, and then quenched in air. The product was washed with distilled hot water and dried at 110 °C. The $K_2Ti_6O_{13}$ fibres grown by this process had a columnar type shape with very smooth and clean surface. They had a very uniform size, 1.5 mm in length and 2–3 μm in diameter [36].

Yokoyama et al. [37] synthesized $K_2Ti_6O_{13}$ long fibres by the flux evaporation method using Na_2O–K_2O–B_2O_3 flux fabricated from Na_2CO_3, K_2CO_3 and B_2O_3 in various molar ratios. Non-fibrous $K_2Ti_6O_{13}$ was prepared by solid-state reaction of K_2CO_3 and anatase (TiO_2) at 1450 °C. The mixture of $K_2Ti_6O_{13}$ and flux was put into a platinum crucible, heated at 1050 °C for 1–15 h, and then rapidly cooled to room temperature in air. The products were separated by dissolving the flux with HCl. It was found that the addition of Na_2O to $3K_2O{\cdot}5B_2O_3$ flux was highly conducive to the growth of long $K_2Ti_6O_{13}$ fibres.

Synthesis of potassium hexatitanate fibres was also carried out by hydrothermal reactions by using potassium hydroxide solution and titanium tetraisopropoxide as raw materials in a K:Ti molar ratio of 1:2. Both reactants were thoroughly stirred for 30 min to 1 h before heating in the autoclave using a nickel tube. Heating temperatures of 350 °C, 400 °C and 450 °C and heating durations of 2.5 and 25 h were employed. The products were allowed to cool slowly in an autoclave followed by filtering, washing with distilled water and ethanol, and finally drying at 50 °C for about 24 h. $K_2Ti_6O_{13}$ fibres synthesized hydrothermally were stable, long, felt-like, thin, of large surface area as compared with the fibres obtained from the solid state method. The heating temperature and duration employed in the hydrothermal synthesis do not seem to have much effect on the crystal morphology and structure of the fibres, but do have an effect on their size [38].

$K_2Ti_6O_{13}$ fibres were fabricated by ion exchange reaction from potassium tetratitanate fibres ($K_2Ti_4O_9$) based on the thermodynamic model. K_2CO_3 and hydrous titania ($TiO_2{\cdot}nH_2O$) at the molar ratio of 3.0 were mixed and then dried in an oven at 90 °C for 10 h. To prepare $K_2Ti_4O_9$ fibres (initial material), the mixture was sintered in a muffle furnace at 960 °C for 10 h. The sample was then removed from the furnace and cooled in air. Fibrous $K_2Ti_4O_9$ was suspended in vigorously stirred water, simultaneously while adding 1 M HCl continuously, the pH value and the concentration of potassium ions were controlled, to obtain the hydration intermediates which were separated by filtration and washed with distilled water, followed by drying at room temperature in a desiccator. The final product, $K_2Ti_6O_{13}$ fibres, were synthesized by heat treatment of intermediate ($K_{1.33}H_{0.67}Ti_4O_9{\cdot}H_2O$) at 850 °C in a muffle furnace for 2 h. Fibres had a structure similar to that of $K_2Ti_4O_9$ which was used as a precursor [39].

Liu et al. [40] also obtained potassium hexatitanate fibres by the ion exchange approach using fibrous potassium titanate ($K_4Ti_3O_8$) as an initial material. Synthesis of $K_4Ti_3O_8$ was carried out by mixing TiO_2 with 80 wt. % concentrated KOH solution at 220 °C for 2 h under atmospheric pressure. The hydrolytic process was carried out, while controlling the pH value from 10.9 to 12.00, to obtain the hydrolytic intermediates from $K_4Ti_3O_8$ fibres, which next were heated at 610 °C in a muffle furnace for 2 h and then fibrous $K_2Ti_6O_{13}$ was formed. Fibres had an average length of 10–30 μm and the mean diameter of 0.3–1.0 μm.

Potassium hexatitanate ($K_2Ti_6O_{13}$) whiskers were also synthesized by the calcination and slow cooling method in the Department of Chemistry, Inorganic Technology and Fuels at the Silesian University of Technology. Starting materials were dry K_2CO_3 and TiO_2 reagent grade. The molar ratio of K_2O to TiO_2 was 1:6. After being ground in an agate mortar under isopropyl alcohol and subsequent drying, platinum crucibles were filled with the powder mixture and heated to 1150 °C at the rate of 300 °C·h^{-1} in a box furnace. After calcination at 1150 °C for 3 h various methods and rates of cooling were applied. The mixture containing an excessive amount of K_2CO_3 was also examined (molar ratio K_2O:TiO_2 = 1:2). The samples of such mixture were also heated to 1150 °C. After 3 h of calcinations, these samples were slowly cooled to 950 °C at an adjusted rate and quenched in water or treated in distilled boiling water (for 1 or 4 h). Then it was decanted, dried at 50 °C and reheated at 1000 °C for 1 h. The residual water after decantation was checked for the presence of potassium ions, by conducting conventional reactions, characteristic of K^+ ions. The samples (K_2O:TiO_2 = 1:6) calcined at 1150°C proved that $K_2Ti_6O_{13}$ final product was created regardless of the cooling conditions. A slow cooling rate resulted in more crystalline $K_2Ti_6O_{13}$ in comparison with samples cooled rapidly.

Fig. 6. SEM of $K_2Ti_6O_{13}$ whiskers synthesized by the calcination and slow cooling [31]

The samples of the mixture with an excess of K_2CO_3 after heat treatment at 1150 °C, cooling and quenching in water and drying, were not homogeneous, they were partially compact and X-ray amorphous. Secondary heat treatment at 1000 °C caused crystallization of $K_2Ti_6O_{13}$, but the crystals had the shape of weakly split prisms. The applied treatment of the samples in boiling water, before secondary heating, contributed to splitting of the prisms into single whiskers. The longest $K_2Ti_6O_{13}$ crystals, up to 550 μm long (Fig. 6), were obtained using initial heat treatment of the mixture with

excess of K_2CO_3 at 1150 °C, followed by cooling to 950 °C at the rate of 25°C·h^{-1}, treatment of the sample in boiling water for 4 h and subsequent reheating to 1000°C for 1 h [31, 33, 34, 43].

2.4. Potassium octatitanate $K_2Ti_8O_{17}$

Potassium octatitanate $K_2Ti_8O_{17}$ possesses a stable tunnel-like structure, i.e. it has a framework enclosing tunnel structures formed by edge- and corner-shared TiO_2 octahedra (Fig. 7) [12]. $K_2Ti_8O_{17}$ exhibits characteristic properties such as a high thermal insulating ability, chemical stability and, compared with potassium hexatitanate ($K_2Ti_6O_{13}$), high ion conductivity. $K_2Ti_8O_{17}$, difficult to obtain, may be used as a novel functional material, also as an advanced reinforcement material, for example as a composite or friction material for braking systems.

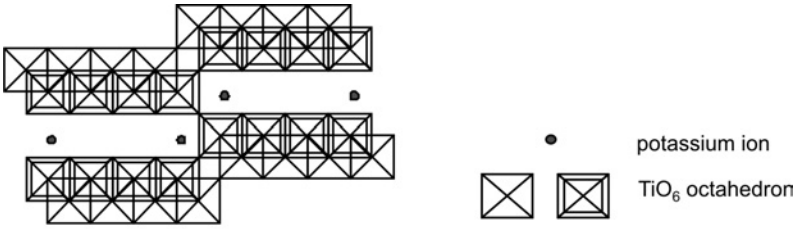

Fig. 7. Idealized crystal structure of $K_2Ti_8O_{17}$

One of the methods to synthesize $K_2Ti_8O_{17}$ is the hydrolysis of $K_2Ti_4O_9$. The starting material, $K_2Ti_4O_9$, was obtained by heating a mixture of KNO_3 and TiO_2 (anatase) in the molar ratio 1:2 at 1000 °C for two days. Then the hydrolysis of potassium tetratitanate was carried out by heating it with H_2O at 100 °C for three days. After thermal treatment of $KH_3OTi_4O_9$ previously obtained at 500 °C, potassium octatitanate was formed [12].

Fibrous octatitanate ($K_2Ti_8O_{17}$) was obtained from fibres of $K_2Ti_4O_9$, which were fabricated by melting of a mixture of TiO_2 and KCl (molar ratio 3:1) with addition of flux K_2MoO_4 at 1100 °C. Then the mixture was cooled slowly at the rate of 4 °C·min^{-1}. Next fibrous $K_2Ti_4O_9$ was converted into a protonated form by treatment with HCl aqueous solution. The resulting product, $H_2Ti_4O_9{\cdot}nH_2O$, was dried and shaken with a mixed solution of KCl and KOH to obtain $KHTi_4O_9{\cdot}0.5H_2O$, which next was dehydrated by heating at 500 °C. The final product was fibrous $K_2Ti_8O_{17}$ with fibres 0.5–1.0 mm long and 0.01–0.03 mm thick [42].

Whiskers of potassium octatitanate were fabricated by thermal treatment of $KHTi_4O_9{\cdot}nH_2O$, which was prepared by exchanging one-half of the K^+ ions in fibrous $K_2Ti_4O_9$ with H^+ ions using aqueous HCl. Pure $KHTi_4O_9$ was obtained by treating of $K_2Ti_4O_9$ with 0.005 M HCl for 30 min. The thermal treatment at temperatures ranging from 250 °C to 500 °C for 3h, however, enables obtaining only $K_2Ti_8O_{17}$. This com-

pound was decomposed above 600 °C to $K_2Ti_6O_{13}$ and TiO_2. The average length and diameter of the $K_2Ti_8O_{17}$ whiskers were 125 and 1 μm, respectively [41].

In a similar way, He et al. [39] synthesized $K_2Ti_8O_{17}$ fibres by ion exchange, starting from potassium tetratitanate ($K_2Ti_4O_9$) fibres. To obtain $K_2Ti_4O_9$, dried mixture of K_2CO_3 and hydrous titania ($TiO_2 \cdot nH_2O$), in a molar ratio TiO_2/K_2O of 3.0, was sintered in a muffle furnace at 960 °C for 10 h. The so-produced, fibrous $K_2Ti_4O_9$ was vigorously stirred under water while 1 M HCl was introduced continuously. pH value of the resulting solution was 0.5. The hydration intermediate was then filtered, washed with distilled water and dried at room temperature in a desiccator. The further thermal treatment at 500 °C for 2 h produced fibres of $K_2Ti_8O_{17}$ of the diameter of 0.2–1 μm and 10–30 μm long.

In the Department of Chemistry, Inorganic Technology and Fuels, Silesian University of Technology, a research aimed at identifying possible routes of synthesis of potassium octatitanate was conducted [43]. It was carried out by two methods: solid state reaction (conventional) and ion-exchange reaction. In the former case, a mixture of starting materials (K_2CO_3 and TiO_2) was subject to thermal treatment in two separate ways: one method was based on gradual linear heating of the precursors right up to the target temperature, at which calcinations were promptly aborted, and the other was based on isothermal processing of the precursors for a specified time period. Next, the samples were dried and heated at 400–700 °C. Obtaining of $K_2Ti_8O_{17}$ by a conventional method was not possible, pure $K_2Ti_8O_{17}$ could be synthesized, however, using the method based on ion-exchange reaction. Samples of $K_2Ti_4O_9$ were treated with hydrochloric acid to remove potassium ions from the structure. Next, the samples were heated in the temperature range 400–500 °C. The shape of the obtained $K_2Ti_8O_{17}$ crystals was the same as the primary shape of $K_2Ti_4O_9$ crystals. The experiment confirmed that $K_2Ti_8O_{17}$ decomposes above 600 °C.

3. Nano potassium titanate

In the past decade, the design and fabrication of nanostructures (structures with one of the characteristic sizes not exceeding 100 nm) based on metal oxides has attracted much attention because of their unique physical, mechanical and chemical properties and their potential applications in nanodevices. Nanofibres, nanorods, nanotubes and nanowires based on alkali metal titanates have been widely used as semiconductors in dye-sensitized solar cells, water treatment materials, catalysts, photocatalysts, gas sensors, nanoelectronic and optoelectronic nanodevices [44, 45].

$K_2Ti_6O_{13}$ nanowires were synthesized by a simple hydrothermal reaction between $Na_2Ti_3O_7$ and KOH. Sodium trititanate was made by solid state reaction at 1000 °C using Na_2CO_3 and TiO_2 (anatase) as raw materials. Then aqueous solution of KOH or KCl (concentrations from 3 to 10 M) was introduced to the $Na_2Ti_3O_7$ and the obtained paste was heated in a furnace at 150–250 °C for 24–72 h. A large quantity of

nanowires, with the uniform diameter around 10 nm and the length ranging from several hundred to several thousand nanometers, were obtained by using 10 M KOH and heating the mixture at 200 °C for 72 h. A lower heating temperature (150 °C) resulted in low quantity of nanowires, while at a higher temperature (250 °C) the nanowires were shorter. For comparison, 3 M KOH or KCl solutions were used for the reaction and the results obtained were similar [46].

Potassium hexatitanate nanowires were fabricated by the hydrothermal synthesis under supercritical conditions using a plug-flow reactor. The starting materials, sols of titanium hydroxide and potassium hydroxide, were prepared by mixing these materials into distilled water. Concentration of titanium ion was 0.02 M and concentration of potassium hydroxide was varied in the range of 0.002–0.4 M. Reactants and the preheated distilled water were supplied to the reactor and mixed, and then heated rapidly (to 350, 400 and 420 °C). Residence time was 2–3 s under the pressure of 30 MPa. The resulting product was dried in an oven at 60 °C for 24 h. Well crystallized nanowires 10 nm in diameter and the length ranging from 500 to 1000 nm were obtained at 400 °C under 30 MPa. In comparison with the conventional hydrothermal method which proceeds for several hours, this method enables fabrication of nanoscaled potassium hexatitanate particles, even at nearly the same temperature and pressure, since the reaction time is limited to the order of several seconds [47].

Titanate nanowires of $K_2Ti_8O_{17}$were synthesized hydrothermally via a reaction of titania particles and KOH solution (the concentration of KOH solution was in the range of 4–25 M). Hydrothermal treatment was carried out in a teflon-lined autoclave for one or two days in the temperature range of 130–240 °C. The nanowires were almost uniform with the diameter of 5–10 nm and the length in the range from several micrometers to several tens micrometers. During calcination in a conventional muffle above 600 °C, $K_2Ti_8O_{17}$ nanowires tend to decompose to $K_2Ti_6O_{13}$ and TiO_2 [48, 49].

$K_2Ti_8O_{17}$ nanowires have also been prepared in a one-step hydrothermal reaction between pure Ti and KOH solution. In a typical experiment, commercially available TiO_2 powder was added to 20 ml of ca. 1 M aqueous solution of KOH. Then the mixture was heated in a sealed autoclave at 200 °C for 3 days. After heating, the products were filtered and washed with deionized water. Nanowires were the final product. In another experiment, instead of Ti powder, Ti plates were used. During the process the whole Ti plate was consumed. The product was a brown coloured block composed of layered structures with a lot of open pores. The layers consisted of nanowires. The length of the nanowires ranged from several hundred nanometres to more than 8 μm and the diameter was around 40 nm [50].

Alkali titanate nanorods ($K_2Ti_8O_{17}$ and $Na_2Ti_3O_7$) were fabricated by the hydrothermal synthesis. 1.5 M HCl was used to adjust pH of distilled water to 2. Titanium tetrachloride ($TiCl_4$) was then dissolved in 30 ml of acid solution to get a concentration of 0.04 M, to which 10 ml, 25 M AOH (A = Na and K) aqueous solution was added. The mixture was stirred for 10 min and then transferred into a Teflon-lined stainless autoclave, sealed and maintained at 180 °C for 48 h. The product obtained

was thoroughly washed with distilled water until all the chloride was removed, and finally dried at 60 °C for 3 h. Sodium and potassium titanate nanorods had average diameters of 50 nm and 30 nm, respectively, with the lengths of up to several micrometers [51].

4. Influence of inorganic fibres on living organisms

Pulmonary fibrosis (asbestosis), lung cancer and mesothelioma are known to occur after exposure to asbestos in both humans and animals. Therefore, inorganic (man-made) and natural fibres have been often substituted for asbestos. Although numerous inhalation studies demonstrated no significant increase in tumour incidence in animals exposed to such substitutes, several mineral fibres (refractory ceramic fibres and fibre glass) were carcinogenic in rodent chronic inhalation studies. Moreover, in animal intraperitoneal studies, the fibre length of asbestos and other mineral fibres has been found to be one of the major descriptors of tumorigenicity.

Fibre dimension, durability, chemical composition and surface properties are thought to be important factors in the evaluation of potential fibre toxicity. Fibre diameter is a critical determinant of respirability. Respirable fibres have a mass median aerodynamic diameter not higher than 3.5 μm, the length over 5 μm and the ratio of the length to diameter of over 3 [52].

A variety of inorganic fibres such as mineral wool, continuous filament, superfine and refractory or ceramic MMMF are known as man-made mineral fibres (MMMF). The names of these classes of materials have different origins and are not necessarily mutually exclusive.

4.1. Influence of ceramic fibres on living organisms

Ceramic fibres comprise a wide range of amorphous or crystalline synthetic mineral fibres characterized by their refractory properties (i.e., stability at high temperatures). They are typically made of alumina, silica and other metal oxides, or less commonly of nonoxide materials such as silicon carbide. Since there are several types of ceramic fibres there is also a range of chemical and physical properties [53]. Their trade names are Zirlane, Kerlane, Pyronap, Keronap, Kaowoll, Fibrefrax, Pyroblok, Cartolane, Fibremax, Mattec, Saffil, Rubill, Nextel, aluminosilicate, aluminium oxide silicate, aluminium silicom polder, DOT, ceramic fibre, cyanite, Disthene, Kaopolite, Kyanite, Mullite, Oil-Dri, SafeN-Dri, Silicotic, Acid Aluminium Salt, Snow Tex, UN 1389, Valfor, Fybex, MAN, PKT, Langfaster, Thermowool [53].

The primary route of potential human exposure to ceramic fibres is by inhalation, mainly during manufacture and formation, especially in the workplace. The workplace population is exposed to potential contact with ceramic fibres mainly in the manufacturing environment, during installation, and during removal. Epidemiological research

on relatively large populations exposed to ceramic fibres strongly suggests that these fibres can act as skin irritants as well as eye irritants, affecting the conjunctiva and possibly causing focal pleura fibrosis. At present, such research has not provided convincing proof which indicates that there is a growing risk of tumour illness associated with these fibres. This viewpoint is based upon consideration of a relatively short period of exposure, as well as from the fact that a significant proportion of employees working in this industry was exposed to asbestos previously [53–57].

Results of experimental research carried out on laboratory animals (rats and hamsters) exposed via inhalation to ceramic fibres or on animals that had been given ceramic fibres via surgical implantation in trachea indicate that some ceramic fibres can induce tumours of lungs (adenomas and cancers) and pleura (mesotheliomas). Tumours of lungs and pleura occurred principally in single animals, the number of diseased animals was linked to the concentration (or dose) of fibres relative to the duration of exposure. Also, some kinds of fibres that had been inserted directly into body cavities (pleural or abdominal) did induce tumours – mesotheliomas. Research on the solubility of the fibres has not provided convincing data that those fibres of low solubility are strongly carcinogenic influence [53–57].

Results from numerous studies lead to the conclusion that basically all types of elongated dust particles can induce tumours if they are sufficiently long, thin and durable in the tissue [54].

Experts at the International Agency for Research on Cancer (IARC) maintain that a documentary evidence of the results of experimental research on animals does exist, showing that ceramic fibres do have a carcinogenic influence. However, there is no information about the carcinogenic influence of ceramic fibres on humans. Thus, according to the IARC, they have been classified to group 2B, this is possibly carcinogenic to humans [58]. However, experts at the European Union have classified refractory ceramic fibres for special purposes, for substances of category 2, this is for substances investigated as carcinogenic for humans with attributed expression R49 which can cause cancer in repercussion of exposing respiratory tract [58].

4.2. Influence of titanate fibres and whiskers on living organisms

It is well known that the inhalation of asbestos in the working environment leads to pulmonary fibrosis, lung cancer and mesothelioma. Various kinds of asbestos substitutes are now being produced, but the fibrous nature of these substances similar to asbestos, and their health effects, are still being investigated. One of these substitutes are fibres and whiskers of potassium octatitanate. These materials have a wide range of industrial applications due to their high tensile strength, weight advantage over metals, and stability at high temperatures [59–61].

Animal studies, which were carried out in 1981, show that whiskers of potassium octatitanate which are used in filters, separators and catalyst carriers, cause fibrosis, suggesting fibrogenic potential similar to that of asbestos [59].

Chronic inhalation toxicity/carcinogenicity studies on fibres of potassium octatitante (TISMO) have been carried out in the last few years on rats. Fibre dimension was mostly lower than 50 μm in length and lower than 2 μm in width. Rats were exposed via whole-body inhalation of fibres in concentrations of 0, 20, 60, or 200 fibres/cm^3 6 h/day, 5 day/week for 24 months. Some rats were killed after 3, 6, 12, 18 and 24 months of exposure for lung damage evaluations. Other rats were removed from the exposure after 6 months and then from this group 6 rats were killed at 3, 6, 9, 12 and 18 months later to study lung clearance. Results of studies have shown that there were no abnormalities in the fibre retention and the lung clearance rate. There was only negligible macrophage response to TISMO at 20 fibres/cm^3 exposure. Also, sometimes minimal collagenized pulmonary fibrosis was found at 60 or 200 fibres/cm^{3}for 24 month inhalation exposure, but neither pulmonary neoplasm nor pleural mesotheliomas were present [62].

Also a study was carried out of airborne concentration and the exposure-related potential hazard of potassium octatitanate fibres (TISMO). The airborne fibres were measured at 14 designated production workplaces once a year for a period of 2 days from 1994 to 1999. A health hazard evaluation was carried out on 27 current employees and 18 former employees. The average employment of the current employees was 7.6 years while that of the former was 5.9 years. In 1994, the fibre concentrations ranged from 0.2 to 1.6 fibres/cm^3 and decreased to 0.10–0.14 fibres/cm^3 in 1999. There were no exposure-related abnormalities in both pulmonary function and radiographic screening in the fibres found in production workers. Based on the animal experiments and medical surveys on workers, exposure to fibre concentrations not higher than 1 fibre/cm^3 would not constitute a significant health hazard to humans in the workplace [62].

In 2005, the WHO Workshop on Mechanism of Fibre Carcinogenesis and Assessment of Chrysotile Asbestos Substitutes considered that respirable potassium octatitanate fibres are likely to pose a great hazard to humans after inhalation exposure [63].

References

[1] HONGU T., PHILLIPS G.O., *New fibres,* Woodhead Publ. Ltd, Cambridge, 1997.
[2] SCHWARTZ M. M., *Handbook of structural ceramics,* McGraw-Hill, Inc., New York, 1992.
[3] COOKE T.F., J. Am. Ceram. Soc*.,* 74 (1991), 2959.
[4] WILCZEWSKA T., Materiały ogniotrwałe, 2 (1994), 66 (in Polish).
[5] JANES R., KINGHTLEY L.J., J. Mater. Sci., 39 (2004), 2589.
[6] MASAKI N., UCHIDA S., YAMANE H., SATO T., Chem. Mater., 14 (2002), 419.
[7] BAMBERGER C.E., BEGUN G.M., MACDOUGALL C.S., Appl. Spectrosc., 44 (1990), 30.
[8] REID A.F., WATTS J.A., J. Solid State Chem., 1 (1970), 310.
[9] KAZAMATA, TAKASHI, INOUNE, TSUNEO, HIROTA, EIICHI, US Patent 4,064,224 (1977).
[10] SHIMIZU, TADAO, HASHIMOTO, KOSHIRO, YANAGIDA, HIROAKI, US Patent 3,952,090 (1976).
[11] DION M., PIFFARD Y., TOURNOUX M., J. Inorg. Nucl. Chem., 40 (1978), 917.
[12] MARCHAND R., BROHAN L., TOURNOUX M., Mater. Res. Bull., 15 (1980), 1129.
[13] WATTS J.A., J. Solid State Chem., 1 (1970), 319.

[14] KENJI A., JP Patent 8,049,119 (1996).
[15] CLEARFIELD A., LEPTO J., J. Solid State Chem., 73 (1988), 98.
[16] LI J.H., NING X.G., YE H.Q., PAN J., FUKUNAGA H., J. Mater. Sci., 32 (1997) 543.
[17] LEE J.-K., LEE K.-H., KIM H., J. Mater. Sci., 31 (1996), 5493.
[18] BAO N., SHEN L., FENG X., LU X., J. Am. Ceram. Soc., 87 (2004), 326.
[19] BAO N., FENG X., LU X., SHEN L., YANAGISAWA K., AIChE J., 50 (2004), 1568.
[20] LIU CH., HE M., LU X., ZHANG Q., XU Z., Cryst. Growth Des., 5 (2005), 1399.
[21] ANDERSSON S., WADSLEY A.D., Acta Chem. Scand., 15 (1961), 663.
[22] BAO N., FENG X., LU X., YANG Z., J. Mater. Sci., 37 (2002), 3035.
[23] MASAKI N., UCHIDA S., YAMANE H., SATO T., J. Mater. Sci., 37 (2000) 3307.
[24] TERASAKI K., SHIMIZU T., IGARASHI K., J. Ceram. Soc. Japan, 111 (2003), 461.
[25] KANG S.O., JANG H.S., KIM Y.I., KIM K.B., JUNG M.J., Mater. Lett., 61 (2007), 473.
[26] ANDERSEN E.K., ANDERSEN G.K., SKOU E., Solid State Ionic, 27 (1988), 181.
[27] JUNG K.T., SHUL Y.G., MOON J.K., JUNG S.Y., PARK W.Z., OH W.Z., J. Mater. Sci. Lett., 17 (1998), 1045.
[28] FUJIKI, YOSHINORI, US Patent 4, 390 (1983), 513.
[29] ZAREMBA T., HADRYŚ A., J. Mater. Sci., 39 (2004), 4561.
[30] ZAREMBA T., J. Therm. Anal. Cal., 91 (2008), 911.
[31] ZAREMBA T., KRZĄKAŁA A., Pol. J. Chem. Tech., 8 (2006) 54.
[32] ZAREMBA T., 9th European Symposium on Thermal Analysis and Calorimetry ESTAC 9, Cracow, 27–31 August 2006, Book of Abstracts, 289.
[33] WANG B., SHI Y., XUE D., J. Solid State Chem., 180 (2007), 1028.
[34] LIU CH., LU X., YU G., FENG X., ZHANG Q., XU Z., Mater. Chem. Phys., 94 (2005), 401.
[35] XIE J., LU X., ZHU Y., LIU CH., BAO N., FENG X., J. Mater. Sci., 38 (2003), 3641.
[36] CHOY J.-H., HAN Y.-S., Mater. Lett., 34 (1998), 111.
[37] YOKOYAMA M., OTA T., YAMAI I., J. Mater. Sci. Lett., 13 (1994), 369.
[38] YAHYA R.B., EBINA T., HAYASHI H., NAGASE T., OODERA Y., SAITHO N., Chem. Mater., 13 (2001), 842.
[39] HE M., FENG X., LU X., JI X., LIU CH., BAO N., XIE J., J. Mater. Sci., 39 (2004), 3745.
[40] LIU Y., QI T., ZHANG Y., Mater. Res. Bull., 42 (2007), 40.
[41] LEE C.-T., UM M.-H., KUMAZAWA H., J. Am. Ceram. Soc., 83 (2000), 1098.
[42] SASAKI T., FUJIKI Y., J. Solid State Chem., 83 (1989), 45.
[43] ZAREMBA T., WITKOWSKA D., Polish Ceramic Bull., 103 (2008), 789 (in Polish).
[44] MENG X., WANG D., LIU J., ZHANG S., Mater. Res. Bull., 39 (2004) 2163.
[45] PAVASUPREE S., SUZUKI Y., YOSHIKAWA S., KAWAHATA R., J. Solid State Chem., 178 (2005), 3110.
[46] WANG B.L., CHEN Q., WANG R.H., PENG L.-M., Chem. Phys. Lett., 376 (2003), 726.
[47] HAKUTA Y., HAYASHI H., ARAI K., J. Mater. Sci., 39 (2004), 4977.
[48] YUAN Z.-Y., SU B.-L., Coll. Surf. A: Physicochem. Eng. Aspects, 241 (2004), 173.
[49] YUAN Z.-Y., ZHANG X.-B., SU B.-L., Mater. Sci. & Proc. Appl. Phys. A, 78 (2004), 1063.
[50] WANG B.L., CHEN Q., HU J., LI H., HU Y.F., PENG L.-M., Chem. Phys. Lett., 406 (2005), 95.
[51] SONG H., JIANG H., LIU T., LIU X., MENG G., Mater. Res. Bull., 42 (2007), 334.
[52] OYABU T., YAMATO H., OGAMI A., MORIMOTO Y., AKIYAMA I., ISHIMATSU S., HORI H., TANAKA I., J. Occup. Health, 46 (2004), 382.
[53] IARC Monographs on the Evaluation of Carcinogenic Risks to Humans. Man-made Mineral Fibres and Radon, Lyon, 43 (1988), 39.
[54] STEENLAND K., STAYNER L., Cancer Cause, Control, 8 (1997), 491.
[55] OHYAMA M., OTAKE T., MORINAGA K., Environ. Health Persp., 109 (2001), 1033.
[56] TANAKA I., YAMATO H., OYABU T., OGAMI A., Ind. Health, 39 (2001), 114.
[57] ADAXHI S., KAWAMURA K., TAKEMOTO K., Ind. Health, 39 (2001), 168.
[58] IARC Man-made Mineral Fibres. Summary and Evaluation 81 (2002).

[59] DING L., MORIMOTO Y., OYABU T., KIM H., OHGAMI A., YATERA K., HIROHASHI M., YAMATO H., HORI H., HIGASHI T., TANAKA I., J. Occup. Health, 43 (2001), 111.
[60] WATANABE M., SHIBATA K., OKADA M., KUDO Y., NIITSUYA M., SATOH T., KOTANI M., AIZAWAY., J. Occup. Health, 44 (2002), 321.
[61] ISHIHARA Y., KYONO H., KOHYAMA N., OTAKI N., SERITA F., TOYA T., Inhal. Toxicol., 14 (2002), 503.
[62] IKEGAMI T., TANAKA A.K., TANIGUCHI M., CLARK M.L., RAGAN H.A., MAST T.J., LEE K.P., Inhal. Toxicol., 16 (2004), 291.
[63] WHO Workshop on Mechanisms of Fibre Carcinogenesis and Assessment of Chrysotile Asbestos Substitutes (Summary Consensus Report), Lyon 8–12 November 2005).

Received 10 March 2008
Revised 9 September 2009

Materials Science-Poland, *Vol. 28*, *No. 1*, *2010*

Electronic mechanism of dehydrogenation of the Mg–Ge mixture during milling under hydrogen

D.W. ZHOU[1*], J.S. LIU[2], J. ZHANG[1], Z.G. HUANG[1], P. PENG[2]

[1]State Key Laboratory of Advanced Design and Manufacturing for Vehicle Body, Hunan University, Changsha, 410082, China

[2]School of Materials Science and Engineering, Hunan University, Changsha 410082, China

The energy and electronic structure of the hydride phase are calculated by using the first-principles plane-wave pseudopotential method to explain experimental results of milling of a Mg–Ge mixture under hydrogen. The electronic mechanism of dehydrogenation of the Ge alloying system is also considered. By calculating heats of formation of MgH_2 and $(MgGe)H_2$ solid solutions, it is found that the structural stability of the alloying system is reduced when a little Ge dissolves in MgH_2. As the Ge content increases, Mg_2Ge may be formed by the reaction: $2MgH_2 + Ge \leftrightarrow Mg_2Ge + 2H_2$, at the same time, the dehydrogenating properties of the system are improved compared with that of MgH_2, but are reduced by contrast with that of $(MgGe)H_2$ solid solutions. Based on the analysis of the densities of states (DOS) of MgH_2 before and after Ge alloying, it is found that the improvement of the dehydrogenating properties of MgH_2 dissolved into a little Ge is attributed to the weakened bonding between magnesium and hydrogen caused by the interactions between Ge and Mg.

Keywords: *Mg–Ge mixture; heat of formation; electronic structure; first-principles calculation*

1. Introduction

Nowadays, many efforts have been made to develop hydrogen storage materials for non-polluting applications. Magnesium-based hydrogen storage alloys have been extensively researched, due to their high hydrogen storage capacity, light weight and low cost. However, the slow hydriding and dehydrogenating kinetics and high dissociation temperature caused by its relatively high stability limits its practical application for hydrogen storage. The reaction kinetics of Mg and hydrogen is strongly dependent on the method of synthesis and the presence of additives. Samples can be synthesized by melting, sintering or mechanical milling, each method having its own characteristics. In particular, ball milling produces special microstructures, metastable phase, modified surfaces, defects, etc., which generally improve the hydriding

*Corresponding author, e-mail: ZDWe_mail@yahoo.com.cn

–dehydrogenating process [1, 2]. Recent experimental investigations [1, 3–10] have shown that the mechanical alloying of MgH_2 and 3d elements such as Ni, Co, Mn, Cu, Ti, Fe, V, non-3d elements – Ge, Nb, intermetallic compounds – $LaNi_5$, FeTi, $ZrFe_{1.4}Cr_{0.6}$, effectively improves the hydriding and dehydrogenating kinetics of MgH_2 at high temperature. In this work, at first, experimental results of milling of Mg–Ge mixture under hydrogen as described by Gennari et al. [5], are introduced, then, the energy and electronic structure of the hydride phases are calculated by using the first-principles plane-wave pseudopotential method to explain the experimental results from Gennari et al., Moreover, the dehydrogenating properties of milling the Mg–Ge mixture under hydrogen and the electronic mechanism of the Ge alloying system are analyzed and discussed.

2. Experimental results

Mg was initially milled for up to 100 h under a hydrogen atmosphere, and sequential XRD patterns were obtained after various milling times with Ge addition, which is the same method as that used by Gennari et al. [5]. It can be found that the tetragonal β-MgH_2 and orthorhombic γ-MgH_2 were synthesized by RMA of Mg after 75 h, and the broadening of the β-MgH_2 and γ-MgH_2 peaks was observed for a milling time of between 75 to 100 h.

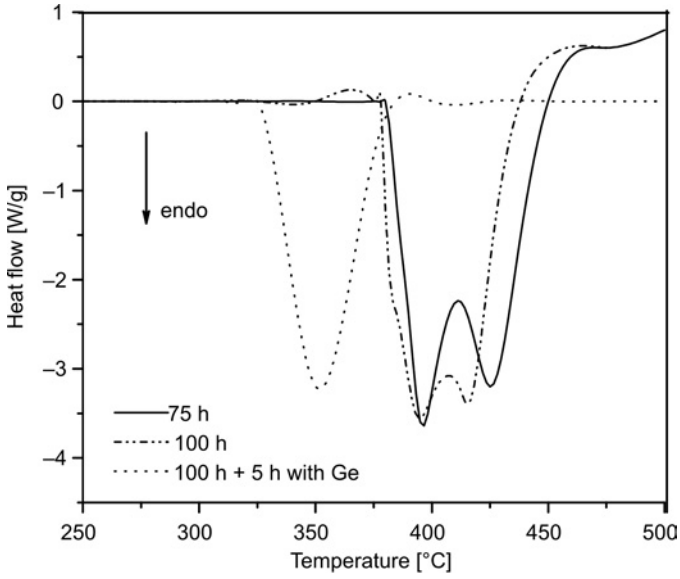

Fig. 1. DSC curves from Mg milled with and without Ge under hydrogen atmosphere for different milling time

Figure 1 shows the DSC curves of Mg initially milled for up to 100 h under a hydrogen atmosphere. For 75 and 100 h of milling, the curve shows a double endother-

mic peak located around 400 °C. When Ge (5 at. %) was added to Mg after 100 h of RMA, significant structural modifications were observed by Gennari et al. [5]. The XRD pattern shows that after 5 h of milling, compound Mg_2Ge appears. From the intensity of the peaks, the amount of Mg_2Ge increases with the milling time, whereas the amount of Ge decreases. In addition, the DSC curve (Fig. 1) shows a sharp endothermic peak at 355 °C. Thus, Ge addition decreases the temperature for hydrogen desorption at about 50 °C compared with pure Mg after 100 h of RMA.

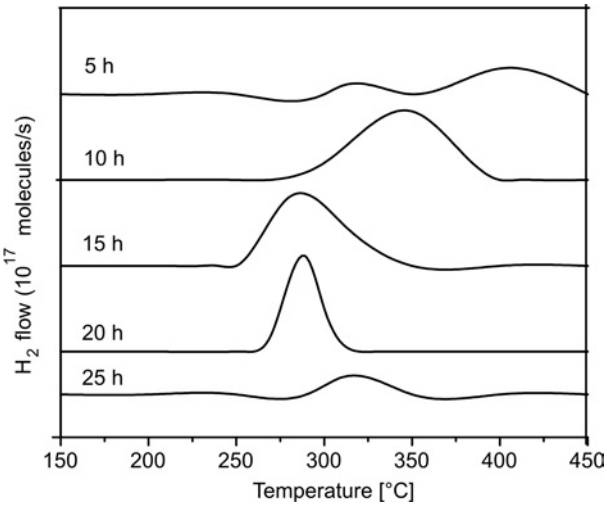

Fig. 2. TDS hydrogen spectra of Mg–Ge after RMA for different milling times

The Mg–Ge mixture was milled under a hydrogen atmosphere for various times. As the milling time increases, the intensity of the peaks corresponding to Mg and Ge decreases. The Mg_2Ge and β-MgH_2 hydride appear after 5 h of milling. The intensity of the peaks associated with Mg_2Ge grows with the milling time, whereas the peaks corresponding to the hydride initially increase and then decrease. The TDS spectra that describe the entire evolution of the hydrogen desorption kinetics for between 5 and 25 h of milling are shown in Fig. 2. For 5 to 15 h of milling, desorption peaks shift towards lower temperatures. In this range of milling time, the amount of hydride grows and desorption improves as a consequence of better Ge and MgH_2 intermixing. After 15 h or more, such as after 20 h, the effect reverses which can be seen in Fig. 2. Desorption begins at higher temperatures. This is a consequence of the consumption of Ge to form Mg_2Ge, as can be seen from the XRD patterns given by Gennari et al. [5]. After 25 h of milling, the amount of hydride that remains on the sample is hardly detected.

The above experimental results from Gennari et al. [5] show that Ge has an important effect on the hydrogen desorption process. This effect is enhanced with the milling time, probably due to a better Ge intermixing or because a little Ge is dissolved in

the magnesium hydride. As the Ge content increases, Mg_2Ge may be formed by the reaction:

$$2MgH_2 + Ge \leftrightarrow Mg_2Ge + 2H_2$$

at the same time the dehydrogenating properties of the system are improved compared with those of MgH_2, but reduced by contrast with those of $(MgGe)H_2$ solid solutions. However, more effort is needed to explain the experimental results shown in Figs. 1 and 2. Moreover, electronic mechanism on the dehydrogenating properties of Ge alloying magnesium hydride is also worth studying.

3. Method and models of computation

The Cambridge Serial Total Energy Package (CASTEP) [11], a first-principles plane-wave pseudopotentials method, based on density functional theory, was used in this work. The CASTEP uses a plane-wave basis set for the expansion of single particle Kohn–Sham wave functions, and pseudopotentials to describe the computationally expensive electron–ion interaction, in which the exchange-correlation energy with the generalized gradient approximation (GGA) of Perdew was used for all elements in our models by adopting the Perdew–Burke–Ernzerhof parameters [12]. The ultrasoft pseudopotential, represented in the reciprocal space, was used [13]. In the present calculations, the cutoff energy of atomic wave functions (PWs) E_{cut}, was set at 310 eV. Sampling of the irreducible wedge of the Brillouin zone was performed with a regular Monkhorst–Pack grid of special *k*-points, in a 6×6×6 configuration. A finite basis set correction and the Pulay scheme of density mixing [14, 15] were applied for the evaluation of energy and stress. All atomic positions in our model have been relaxed according to the total energy and force, using the BFGS scheme [16], based on the cell optimization criterion (RMs force of 0.05e V/Å, stress of 0.1 GPa, and displacement of 0.002 Å). The calculation of the total energy and electronic structure are followed by the cell optimization with the SCF tolerance of 2.0×10^{-6} eV.

In this work, the unit cell, super cell model of MgH_2 and the crystal model of Mg_2Ge are used for studying the dehydrogenating properties of milling the Mg–Ge mixture under a hydrogen atmosphere and for studying the electronic mechanism of Ge alloying magnesium hydride. The lattice parameters of MgH_2 with a tetragonal symmetry ($P4_2/mnm$, Group No.136) are a = 4.501Å and c = 3.010 Å. The positions of atoms are + 2Mg(0,0,0) and + 4H(0.304,0.304,0), respectively [17], as shown Fig. 3a. Two hypothesised super cells with 3 and 5 times in c axis of MgH_2 unit cell are shown in Figs. 3b, and 3c, respectively. When a little Ge is dissolved in MgH_2, it is thought that $(MgGe)H_2$ solid solutions are formed. As far as the solution concentration of Ge in MgH_2 is concerned, one Mg atom in threefold unit cell (Fig. 3b) or fivefold unit cell (Fig. 3c) is replaced by Ge atoms. Therefore, the corresponding super cell with Ge additions is $(Mg_5Ge)H_{12}$ with 8.33 at. % of Ge or $(Mg_9Ge)H_{20}$ with 5.0 at. % of Ge.

Two Mg atoms in threefold unit cell (Fig. 3b) or fivefold unit cell (Fig. 3c) are replaced by Ge atoms. Hence, the corresponding super cells are $(Mg_4Ge_2)H_{12}$ with 16.67 at. % of Ge or $(Mg_8Ge_2)H_{20}$ with 10.0 at. % of Ge.

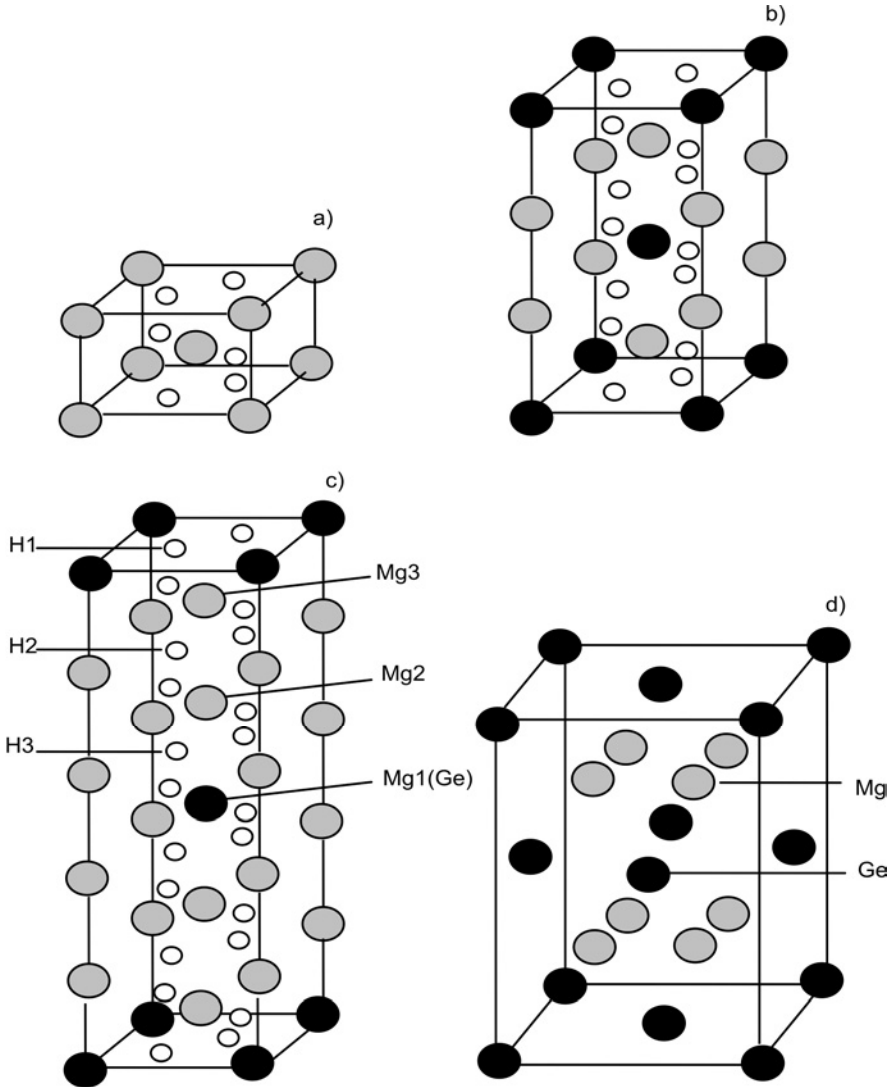

Fig. 3. Model of a unit cell of MgH_2 phase(a), threefold (b), and fivefold unit cells (c) of MgH_2 phase, cell of Mg_2Ge (d), where the nonequivalent atoms are denoted by the numbers 1–3

The lattice parameters of Mg_2Ge with CaF_2-type structure (*Fm*3*m*, group No. 225) are $a = b = c = 6.370$ Å. The positions of atoms are +8Mg (0.25,0.25,0.25) and +4Ge(0,0,0), respectively [18] (Fig. 3d). Hence, the chemical formula of Mg_2Ge crystal cell can be expressed as Mg_8Ge_4. Here, it must be pointed out that when the Ge

content of the $(MgGe)H_2$ solid solution is 20.0 at. %, the following reaction may proceed:

$$2MgH_2 + Ge \leftrightarrow Mg_2Ge + 2H_2$$

4. Results from first-principles calculations

4.1. Dehydrogenating properties

Thermodynamic aspects of formation/decomposition of magnesium hydride can be described by pressure–composition isotherms at a given temperature. The overall reaction of hydride formation consists of three steps. Firstly, the host metal dissolves some H atoms to form a solid solution, i.e., α-Mg(H) phase. Secondly, under increasing pressure of hydrogen or oncentration of H in the host metal, the interactions between H atoms locally strengthen and lead to nucleation and growth of the tetragonal β-MgH_2 phase. While the two phases of α and β coexist, the isotherms appear as a flat plateau, their lengths show how many H_2 can be stored with small pressure variations. This plateau or equilibrium pressure depends strongly on temperature and is related to the changes of enthalpy (ΔH) and of entropy(ΔS). Finally, the concentration of H in the host metal shows no further change if the hydrogen pressure continues to increase. The reaction of hydride decomposition is opposite to hydride formation, but occurs in time retardation compared with hydride formation. During the second step, it is often related to the equilibrium hydrogen pressure through the van't Hoff equation [19]:

$$\ln\left(\frac{P}{P_0}\right) = \frac{\Delta H}{RT} - \frac{\Delta S}{R} \tag{1}$$

where P is a flat plateau pressure for decomposition, P° is the standard pressure (0.1 MPa), ΔH is the heat of formation, ΔS is the entropy change, T is temperature and R is the gas constant. The entropy change in Eq. (1) is dominated by the entropy loss of gaseous hydrogen, roughly 130.8 J/mol [19] for the MgH_2 under consideration. Hence, Eq. (1) can be expressed as

$$\frac{\partial\left(\ln\frac{P}{P^\circ}\right)}{\partial\left(\frac{1}{T}\right)} = \frac{\Delta H}{R} \tag{2}$$

From Equation (2), it can be found that ΔH of magnesium hydride determines the flat plateau pressure of decomposition of magnesium hydride at a given temperature. The smaller the heat of formation, the lower the pressure is, which indicates the enhanced dehydrogenating properties of magnesium hydride [20, 21]. Hence, one need

only concentrate on the heat of formation in order to understand the dehydrogenating properties of magnesium hydride.

4.2. Heat of formation

The lattice constants of Mg_2Ge, MgH_2, Ge and hcp-Mg are estimated from the minimized total energy (Table 1). It can be found that the lattice parameter a of Mg_2Ge is 6.370Å, which is close to the experimental values (6.3849Å) in Ref. [18], and also in agreement with the calculated results (6.309Å [18], 6.12Å [22]). At the same time, we can calculate that the lattice parameters a and c of MgH_2 are 4.533 Å and 3.022 Å, respectively, which are close to the experimental values of a = 4.501 Å and c = 3.010 Å in Ref. [17] and are also in agreement with the results (a = 4.535Å and c = 3.023Å) calculated by Song et al. [20]. Moreover, the calculated lattice parameters a and c of hcp-Mg are 3.152 Å and 5.435 Å, respectively, which are close to the experimental values of a = 3.211Å and c = 5.215Å in Ref. [23]. Hence it can be concluded that the computational methods used in the present work are indeed effective.

Table 1. Equilibrium lattice constants and total energies of the crystal and super cell model

Material	Lattice parameter [Å]		Total energy of the crystal cell [eV]	Total energy of the primitive cell [eV]
	a	c		
Mg	3.152	5.435	–977.8677	
Ge	5.658	–	–109.2592	
MgH_2	4.533	3.022	–2020.1572	–1010.0786
MgH_2	4.533	9.069	–6060.4722	
	4.533	15.104	–10100.7856	
$(Mg_5Ge)H_{12}$	4.556	9.218	–5189.0300	
$(Mg_4Ge_2)H_{12}$	4.545	9.371	–4317.8333	
$(Mg_9Ge)H_{20}$	4.543	15.282	–9229.3451	
$(Mg_8Ge_2)H_{20}$	4.566	15.378	–8357.9166	
Mg_8Ge_4	6.370	–	–8263.2466	–2065.8117

The heat of formation of MgH_2 can be calculated from [20]

$$\Delta H_{\mathrm{MgH_2}} = E_{\mathrm{tot}}\left(\mathrm{MgH_2}\right) - E_{\mathrm{tot}}\left(\mathrm{Mg}\right) - E_{\mathrm{tot}}\left(\mathrm{H_2}\right) \tag{3}$$

where $E_{tot}(MgH_2)$ is the energy of the primitive cell of MgH_2, $E_{tot}(Mg)$ is a single atomic energy of hcp-Mg in the solid state, and $E_{tot}(H_2)$ is the total energy of the hydrogen molecule. The calculation energies of Mg atoms are also listed in Table 1 using the same code as for the primitive cell model. The total energy of the hydrogen molecule was calculated as –2.320Ry (ca. –31.5652 eV) [24], using the von Barth-Hedin exchange correlation potential. The $\Delta H(MgH_2)$ value (–62.30 kJ/(mol H_2)) in

this work is slightly higher than –73.5 kJ/(mol H_2) deduced from the thermodynamic data at $T \approx 673$ K and reported by Bogdanović et al. [24]. Taking into account that the temperature of computation is different from that of the experiment, the present results of computation should be suitable.

The heat of formation of $(MgGe)H_2$ solid solution is calculated from [25, 26]

$$\Delta H_1 = \frac{1}{6}\left[E_{\text{tot}}\left(\text{Mg}_{6-x}\text{Ge}_x\text{H}_{12}\right) - (6-x)E_{\text{tot}}\left(\text{Mg}\right) - xE_{tot}\left(\text{Ge}\right) - 6E_{tot}\left(\text{H}_2\right)\right] \quad (4)$$

$$\Delta H_2 = \frac{1}{10}\left[E_{\text{tot}}\left(\text{Mg}_{10-x}\text{Ge}_x\text{H}_{20}\right) - (10-x)\text{E}_{\text{tot}}\left(\text{Mg}\right) - xE_{\text{tot}}\left(\text{Ge}\right) - 10E_{tot}\left(\text{H}_2\right)\right] \quad (5)$$

Here $E_{\text{tot}}(Mg_{6-x}Ge_xH_{12})$ and $E_{\text{tot}}(Mg_{10-x}Ge_xH_{20})$ are the energies of three or five MgH_2 unit cells with Ge addition, respectively. $E_{\text{tot}}(Ge)$ is the energy of per Ge atom, X denotes the number of atoms replaced by Ge. The total energies of the $(Mg_5Ge)H_{12}$, $(Mg_9Ge)H_{20}$, $(Mg_4Ge_2)H_{12}$, $(Mg_8Ge_2)H_{20}$ super cell are calculated and the results are also listed in Table 1. The heat of formation of $(MgGe)H_2$ solid solutions, calculated from Eq. (4) and Eq. (5), are shown in Fig. 4. When the Ge content changes from 0 to 10.0 at. %, the heat of formation of the system is negative but the absolute value gradually decreases compared with that of MgH_2. However, when the Ge content is above 10.0 at. %, its value is positive, which means the system is unstable.

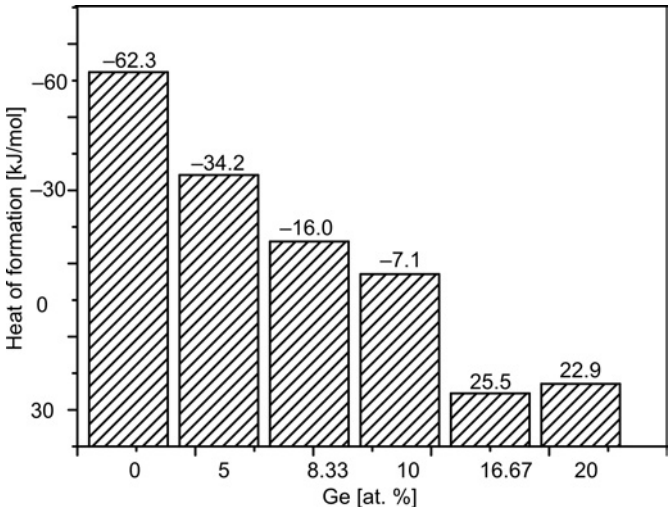

Fig. 4. Heat of formation of MgH_2 and $(MgGe)H_2$

The change of the energy from the reaction of

$$2MgH_2 + Ge \leftrightarrow Mg_2Ge + 2H_2$$

is calculated from [23]

$$\Delta H_3 = \frac{1}{2}\left[E_{\text{tot}}(\text{Mg}_2\text{Ge}) + 2E_{\text{tot}}(\text{H}_2) - 2E_{\text{tot}}(\text{MgH}_2) - E_{\text{tot}}(\text{Ge})\right] \quad (6)$$

Here $E_{\text{tot}}(\text{Mg}_2\text{Ge})$ is the energy of the primitive cell of Mg_2Ge. The calculated energy of Mg_2Ge is listed in Table 1. Its value is 22.9 (kJ/mol H_2) from Eq. (6), which means that the amount of released heat during the reaction

$$2\text{MgH}_2 + \text{Ge} \leftrightarrow \text{Mg}_2\text{Ge} + 2\text{H}_2$$

is smaller than 25.5 kJ/mol H_2 of $(\text{Mg}_4\text{Ge}_2)\text{H}_{12}$ solid solutions containing 16.7 % Ge. Hence, as the Ge content increases, Mg_2Ge may be formed in the above reaction.

The parameter $\Delta E_r(\text{Mg}_2\text{Ge})$ is used to estimate the influence of Mg_2Ge on the dehydrogenating properties of MgH_2. It is calculated from [20]:

$$\Delta E_r\ (\text{Mg}_2\text{Ge}) = E_{tot}(\text{Mg}_8\text{Ge}_2\text{H}_{20}) - 10E_{\text{tot}}(\text{MgH}_2) - 2E_{\text{tot}}(\text{Mg}_2\text{Ge}) + 6E_{\text{tot}}(\text{Mg}) \quad (7)$$

Here the calculated value of $\Delta E_r(\text{Mg}_2\text{Ge})$ is 69.3 kJ/mol H_2.

4.3. Electronic structure

Analysis of the total and partial density of states (DOS) of three- and fivefold Ge alloying MgH_2 unit cells is performed to understand the electronic mechanisms of the change of structural stability. The total and partial DOSs of $\text{Mg}_{10}\text{H}_{20}$, $(\text{Mg}_9\text{Ge})\text{H}_{20}$ and $(\text{Mg}_8\text{Ge}_2)\text{H}_{20}$ are plotted in Figs. 5a–c, respectively. The signs of Mg, Ge, H atoms are as shown in Fig. 3c. Figure. 5a shows the DOS of MgH_2 system without Ge addition. It is found that the main bonding peaks lie in the energy region between the Fermi energy (E_F) and –7.0 eV. The bonding peak between E_F and –3.0 eV mainly originates from the contribution of valence electrons of H(s), Mg(p) and a few Mg(s) orbitals. The bonding peak between –4.0 eV and –3.0 eV corresponds to the interaction between H(s) and Mg(s) as well as a few Mg(p) electrons. The bonding peak between –7.0 eV and –4.0 eV results from the bonding of valence electrons of H(s) and Mg(s). For Ge alloying the MgH_2 unit cell, a distinct difference in DOS between Fig. 5b and Fig. 5c can be seen:

- Compared with the MgH_2 super cell without Ge addition, the gap between the –2.0e V and –1.0 eV in the MgH_2 super cell disappears.
- The bonding electron numbers between –2.0 eV and 2.0 eV result mainly from the presence of Ge(s) orbits. For the $(\text{Mg}_9\text{Ge})\text{H}_{20}$ model, the bonding peaks increase the contribution of a few Mg2(p) and H3(s). For the $(\text{Mg}_8\text{Ge}_2)\text{H}_{20}$ model, not including the contribution of Mg2(p) and H3(s), the bonding peaks increase the contribution of valence electrons of a few Mg3(p), H1(s) and H2(s) orbitals.
- For the $(\text{Mg}_9\text{Ge})\text{H}_{20}$ model, compared with the MgH_2 super cell without Ge addition, the heights of the bonding peaks of H3 significantly increase between –9.0eV and

–11.0eV, and the bonding peaks increase the contribution of Ge(s) orbitals. For the $(Mg_8Ge_2)H_{20}$ model, not including the contribution of valence electrons of Ge(s), the height of the bonding peaks of H3 and H1 both significantly increase in the same region. In addition, the height of the bonding peaks of Mg(s), Mg(p) and H(s) decrease near E_F . Hence, when a little Ge dissolves in magnesium hydride, the weakened bonding between magnesium and hydrogen is caused by the interactions between Ge and Mg [20].

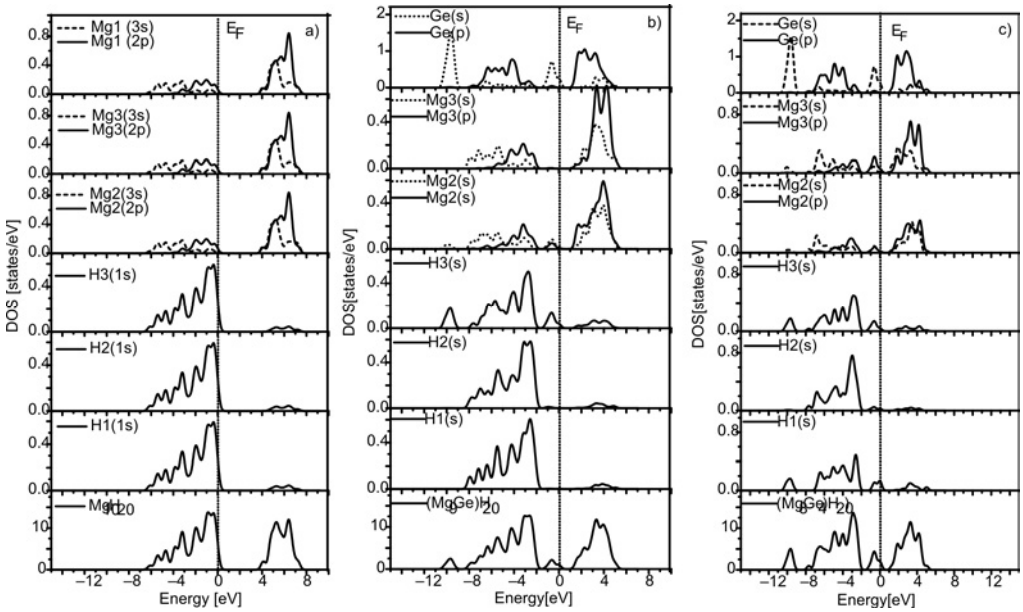

Fig. 5. Total and partial densities of states of: a) $Mg_{10}H_{20}$, b) $(Mg_9Ge)H_{20}$, c) $(Mg_8Ge_2)H_{20}$

4.4. Influence of Ge on dehydrogenating properties of MgH_2

In Section 4.2, it can be found that when the Ge content changes from 0 to 10.0 at. %, the heat of formation of the Ge alloying system is negative but the absolute value gradually decreases compared with that of MgH_2. However, in case the Ge content exceeds 10.0 at. %, its value is positive because the heat of formation of magnesium hydride determines the flat plateau pressure of magnesium hydride decomposition at a given temperature *T*. The smaller the heat of formation, the lower the pressure is. Hence, for Mg–Ge powder mixtures, with increasing milling time, a small amount of Ge are dissolved into MgH_2 to form $(MgGe)H_2$ solid solutions. Hence, for Mg–Ge powder mixtures, as the milling time increases, a small amount of Ge is dissolved in the MgH_2 to form $(MgGe)H_2$ solid solutions. As the concentration of the Ge solution in the MgH_2 lattice increases, the dehydrogenating properties of the system are improved compared with the system without Ge addition, which is in good agree-

ment with the results shown in Fig.1 and Fig.2 from the analysis of Gennari et al. [5]. The value 22.9 (kJ/mol H_2) from Eq. (6) is smaller than 25.5 (kJ/mol H_2) for $(Mg_4Ge_2)H_{12}$ solid solutions. Hence, as the Ge content increases, Mg_2Ge may be formed by the reaction: $2MgH_2 + Ge \leftrightarrow Mg_2Ge + 2H_2$ (Fig. 4). As the Ge content increases, the dehydrogenating properties of the system are improved compared with those with the system without Ge addition but not as good as those of $(MgGe)H_2$ solid solutions, which is in good agreement with the results of milling for 20 h, as shown in Fig. 2 from the analysis of Gennari et al. [5]. Moreover, the calculated value for $\Delta E_r(Mg_2Ge)$ from Eq. (7) is 69.3 kJ/mol H_2. Since the modified MgH_2 phase is still the major phase in the coexistence mixtures of two types of hydrides: β-MgH_2 and Mg_2Ge [5], which indicates that Mg_2Ge phase acts as a catalyst, it can therefore reduce the structural stability of MgH_2 and further improve its dehydrogenating properties, which is in good agreement with the results from the analysis of Gennari et al. [5] (Fig. 3).

5. Conclusions

Based on the experimental results of milling the Mg–Ge mixture under a hydrogen atmosphere, as obtained by Gennari et al., the energy and electronic structure of the hydride phase are calculated by using a first-principles plane-wave pseudopotential method based on the density functional theory. The main conclusions are summarized as follows: (1) when a little Ge dissolves in magnesium hydride, the structural stability of the alloying system is reduced compared with that of MgH_2; (2) as the Ge content increases, Mg_2Ge may be formed in the reaction: $2MgH_2 + Ge \leftrightarrow Mg_2Ge + 2H_2$, while at the same time the dehydrogenating properties of the system are improved compared with that of MgH_2 but are reduced by contrast with that of $(MgGe)H_2$ solid solutions; (3) the improvement in the dehydrogenating properties of MgH_2 in which a small quantity of Ge is dissolved, results in weakened bonding between magnesium and hydrogen caused by the interactions between Ge and Mg.

Acknowledgements

The work was supported by the Hunan University basic scientific research and operational costs of central colleges (No. 531107040038).

References

[1] LIANG G., HUOT J., BOILY S., SCHULZ R., J. Alloys Compd., 305 (2000), 239.
[2] SELVAM P., MOHAPATRA S.K., SONAVANE S.U., JAYARAM R.V., Appl. Catal. B Environ., 49 (2004), 251.
[3] SHANG C.X., BOUOUDINA M., SONG Y., GUO Z.X., Int J. Hydr. En., 29(2004), 73.
[4] AKIBA E., HAYAKAWA H., HUOT J., J. Alloys Compd, 248 (1997), 164.
[5] GENNARI F.C., CASTRO F.J., URRETAVIZCAYA G., MEYER G., J. Alloys Compd, 334 (2002), 277.

[6] TESSIER J.P., PALAU P., HUOT J., SCHULZ R., GUAY D., J. Alloys Compd，376 (2004), 180.
[7] LIANG G., HUOT J., BOILY S., VAN N.A., SCHULZ R., J. Alloys Compd., 292 (1999), 247.
[8] LIANG G., HUOT J., BOILY S., VAN N.A., SCHULZ R., J. Alloys Compd., 297 (2000), 261.
[9] MANDAL P., DUTTA K., RAMAKRISHNA K., SAPRU K., SRIVASTAVA O.N., J. Alloys Compd., 184 (1992), 1.
[10] WANG P., WANG A.M., DING B.Z., HU Z.Q., J. Alloys Compd, 334 (2002), 243.
[11] LINDAN P.L.D., SEGALL M.D., PROBERT M.J., PICKARD C.J., HASNIP P.J., CLARK S.J., PAYNE M.C., J. Phys: Cond. Matter, 14 (2002), 2717.
[12] MARLO M., MILMAN V., Phys. Rev. B, 62 (2000), 2899.
[13] VANDERBILT D., Phys. Rev. B, 41 (1990), 7892.
[14] HAMMER B., HANSEN L.B., NORKOV J.K., Phys. Rev. B, 59 (1999), 7413.
[15] FRANCIS G.P., PAYNE M.C., J. Phys. Cond. Matter, 2 (1990), 4395.
[16] MONKHORST H.J., PACK J.D., Phys. Rev. B, 13 (1976), 5188.
[17] BORTZ M., BERTHEVILLE B., BÖTTGER G., YVON K., J. Alloys Compd., 287 (1999), L4.
[18] GROSCH G.H., RANGE K.J., J. Alloys Compd., 235 (1996), 250.
[19] NAKAMURA H., NGUYEN M.D., PETTIFOR D.G., J. Alloys Compd., 281 (1998), 81.
[20] SONG Y., GUO Z.X., YANG R., Phys. Rev. B, 69 (2004), 094205.
[21] NAMBU T., EZAKI H., YUKAWA H., MORINAGA M., J. Alloys Compd., 293–295 (1999), 213.
[22] CORKILL J. L., COHEN M.L., Phys. Rev. B, 48 (1993), 17138.
[23] HUOT J., BOILY S., AKIBA E., SCHULZ R., J. Alloys Compd., 280 (1998), 306.
[24] BOGDANOVÍC B., BOHMHAMMELK., CHRIST B., REISER A., SCHLICHTE K., VEHLEN R., WOLF U., J. Alloys Compd., 282 (1999), 84.
[25] MEDVEDEVA M.I., GORNOSTYREV Y.N., NOVIKOV D.L., MRYASOV O.N., FREEMAN A.J., Acta Mater., 46 (1998), 3433.
[26] SAHU B.R., Mater. Sci. Eng. B, 49, (1997), 74.

Received 4 April 2008
Revised 24 November 2009

Materials Science-Poland, *Vol. 28*, *No. 1*, *2010*

Influence of cenospheres of fly ash on the mechanical properties and wear of permanent moulded eutectic Al–Si alloys

N. SURESH[1*], S. VENKATESWARAN[1], S. SEETHARAMU[2]

[1]Department of Mechanical Engineering, BMS Institute of Technology, Avalahalli, Doddaballapur Main Road, Bangalore-560 064, India

[2]Central Power Research Institute, Bangalore-560 080, India

In recent years, aluminium matrix composites reinforced with ceramic particulates have attracted considerable interest due to their inherent good mechanical properties and low cost. In this investigation, composites have been produced with cenospheres of fly ash as a reinforcement material and eutectic Al–Si alloy as a matrix. Stir casting route has been adopted to disperse cenospheres of fly ash (from 1% to 10%) in the Al–Si alloy matrix. The results indicate that with increase the content of fly ash, hardness and ultimate tensile strength increase by 34.7% and 44.3% respectively, while the density decreases by 13.2%. The wear loss decreases by 33% at the highest sliding distance. However, percentage elongation showed only a marginal decrease for various percentages of fly ash studied in this investigation.

Keywords: *metal matrix composites; fly ash; cenospheres; mechanical properties; wear*

1. Introduction

Metal–matrix composites are materials in which tailored properties are achieved by systematic combinations of various constituents [1]. Conventional monolithic materials generally have limitations in terms of their strength, stiffness, coefficient of expansion, and density. Eutectic Al–Si alloy (LM6) is one of the commonly used alloys in the non-heat treated condition for automotive engines because of its good mechanical properties, high strength-to-weight ratio, wear resistance and low coefficient of expansion. Apart from stress relieving and improvement in ductility, heat treatment does not significantly change the properties of such alloys [2]. Several authors re-

[*]Corresponding author, e-mail: suresh_n59@yahoo.co.in

ported that particulate reinforced composites exhibit superior mechanical properties compared to unreinforced alloys.

Particulates such as SiC, TiC, TiB_2 and fly ash have been used to reinforce Al alloys to improve their mechanical properties and wear resistance [3–8, 16, 17]. In recent years, the use of fly ash as a reinforcement material in Al alloys has been reported to be desirable from both environmental and economic points of view due to its availability as a low cost waste material [9]. Mahendra et al. [10] reported a higher tensile strength and hardness for Al–4.5% Cu alloy–fly ash based composites. Ramachandra et al. [11] in a study on the mechanical properties of hypoeutectic Al–Si/Fly ash composites showed that an increase in the percentage content of fly ash particulates results in an increase in the hardness and tensile strength but the density decreases as the fly ash content increases.

Fly ash is a byproduct of coal combustion collected from electrostatic precipitators and bottom ash at the bottom of furnaces. It is a fine-grained, powder material that is carried off in flue gas and usually collected by means of electrostatic precipitators, bag housings, or mechanical collection devices such as cyclones. Fly ash obtained from electrostatic precipitators varies in size from 5 μm to 75 μm [17]. It consists of hollow microspheres known as cenospheres which generally float on water in the ash collection ponds. Since the particles solidify in suspension, cenospheres of fly ash are generally spherical in shape and more uniform in quality, shape and size compared to normal fly ash. The density of cenospheres is 0.6–0.9 $g \cdot cm^{-3}$.

A detailed study of available literature reveals that very few systematic investigations have been carried out to investigate the influence of fly ash particulates, especially cenospheres, on the mechanical properties and wear of eutectic Al–Si alloys.

In this investigation, an attempt has therefore been made to study the influence of cenospheres of fly ash on the hardness, density, ultimate tensile stress (UTS), elongation, surface roughness and wear of eutectic Al–Si alloys.

2. Experimental

Matrix used. Eutectic Al–Si alloy LM6 containing 12.2% Si was used as a matrix. The composition of the alloy is given in Table 1.

Table 1. Composition of LM6 alloy [wt. %] designated as a base alloy

Si	Fe	Cu	Mn	Mg	Zn	Al
12.2	0.32	0.002	0.62	0.065	0.021	Bal

A typical microphotograph of cenospheres of fly ash is shown in Fig. 1 and the composition of cenospheres of fly ash used in this study is shown in Table 2.

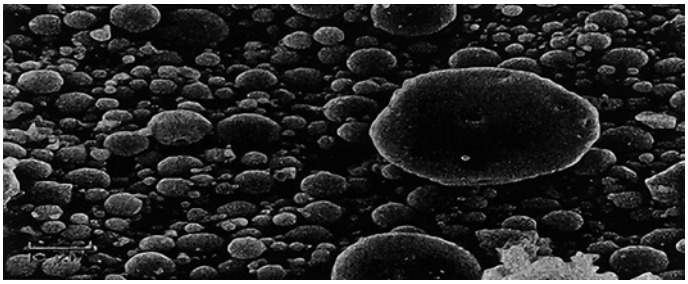

Fig. 1. Typical microphotograph of cenospheres of fly ash

Table 2. Composition of cenospheres of fly ash [wt. %]

Al_2O_3	SiO_2	Fe_2O_3	TiO_2	Carbon/LOI
29.9	56.92	8.44	2.75	1.99

Reinforcement used. Cenospheres of fly ash were used as a reinforcement material in this investigation. They are formed in the temperature range of 920–1200 °C [9]. The particle size distribution and cumulative distribution of the cenospheres used in this study was measured using ASTM standard sieves [18] and is shown in Table 3 and Fig. 2.

Table 3. Results of sieve analysis as per ASTM standards

ASTM sieve	Sieve opening [μm]	Cenospheres retained (R) [wt. %]	Cumulative cenospheres [wt. %]	Multiplier S	Product RS
12	1700	0.22	0.22	5	1.1
20	850	1.38	1.6	10	13.8
30	600	2.12	3.72	20	42.4
40	425	2.28	6	30	68.4
50	300	8.34	14.34	40	333.6
70	212	25.86	40.2	50	1293
100	150	50.68	90.88	70	3547.6
140	106	7	95.88	100	700
200	75	1.44	97.42	140	201.6
270	53	0.58	100	200	116
PAN	PAN	0	100	300	0
Total		$\sum R = 99.9$			$\sum RS = 6317.5$

The average grain fineness number was computed from the data given in Table 3:

$$\frac{\sum RS}{\sum R} = \frac{6317.5}{99.9} = 63.23$$

It was found experimentally that about 75% of the cenospheres particles have particle size in the range of 150 to 212 micrometers

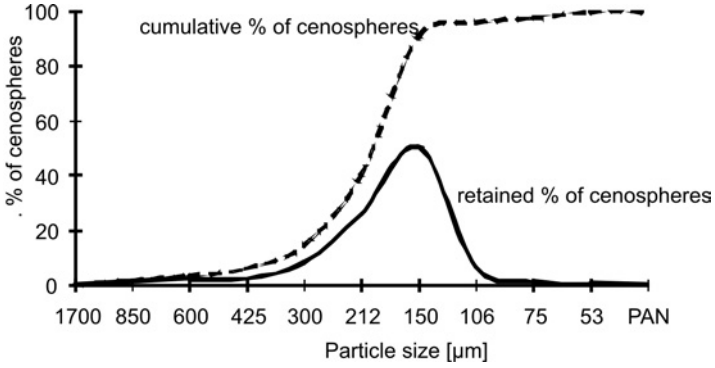

Fig. 2. Retained and cumulative % of cenospheres vs. particle size

Melting procedure. 2 kg of eutectic Al–Si alloy (LM6) ingots were melted in graphite crucibles using an electric resistance furnace. When the temperature of the molten alloy reached 850 °C, the crucible containing the melt was taken out for degassing. For degassing, hexachloroethane tablets, wrapped in a paper was plunged into the bottom of the crucible containing the molten metal and held at the bottom using a perforated plunger, until the bubbling action ceased. The metal was allowed to stand for a few minutes and the dross from the surface of the molten metal was skimmed using a perforated flat spoon. The temperature of the melt was checked using an alumel–chromel thermocouple. The molten metal was cast in a metallic die of 147×125×25 mm^3, which was pre-heated to 200 °C and coated with a protective layer of china clay, water and sodium silicate to prevent contamination. The pouring was carried out at 650 °C. In order to check for reproducibility, three sets of castings were poured under identical conditions.

Preparation of composites. The melting procedure, indicated above, was adopted until degassing of the molten metal. After degassing, 5 g (0.0025 wt. %) of magnesium ribbons were added to the melt to improve the wettability of the particles with the matrix. A vortex was created by rotation of stirrer blades at an optimum speed for a predetermined time period. A vortex forming in the molten metal helps to distribute the reinforcement particles uniformly throughout the matrix. Cenospheres were slowly added to the molten metal while continuously stirring with a mechanical stirrer. Once again, three sets of castings were poured under identical conditions to check for reproducibility.

Test procedure. The castings, produced as mentioned above, were taken out of the die, cooled and then cut into 5 equal sections along the length from one end to the other as shown in Fig. 3. The samples were then machined to get standard test specimens for determining hardness, UTS and percentage elongation, surface roughness

and slide wear. The densities of the samples were determined by the well known Archimedes principle.

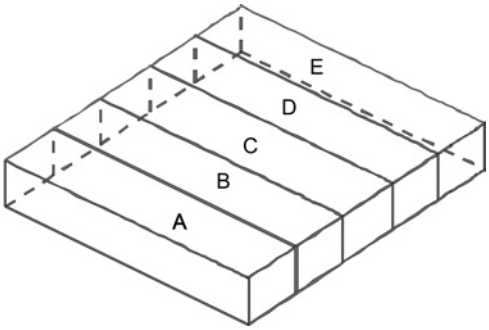

Fig. 3. Casting cut into sections along its length

Hardness. A Brinnel hardness test was conducted on the specimen using a standard Brinnel hardness tester. A load of 500 kg was applied on the specimen for 30 s using a 10 mm ball indenter and the indentation diameter was measured using a micrometer microscope. The Brinnel hardness number (BHN) was computed using the formula:

$$BHN = \frac{2P}{\pi D\left(D - \sqrt{D^2 - d^2}\right)}$$

where P is the load applied, D the diameter of the ball indenter and d the diameter of indentation.

Ultimate tensile strength (UTS) and elongation. An electronic tensometer of the Monsanto type W was used for tensile testing. The tensometer specimen was loaded between two grips that were adjusted manually. A constantly increasing force was applied to the specimen by electronic means. The load and elongation were continuously recorded. The UTS and percentage elongation were calculated.

Surface roughness. The surface imperfections consist of a succession of hills and valleys which vary both in height and spacing. These are measured using a Tally surf instrument. The surface roughness parameters R_a (*average roughness value*) and R_q (root mean square roughness) were selected. The stylus was moved over the surface and the readings were noted.

Dry sliding wear. A dry sliding wear test was conducted at ambient temperature using a pin-on-disc wear testing machine with a data acquisition system. Wear was determined by the weight loss method. Specimens of 6 mm diameter and 20 mm long were used for the dry sliding wear tests. The wear tests were carried out at a constant sliding velocity of 125.6 m·min^{-1} (500 rpm) for a track radius of 40 mm, load of 1 kg and sliding distances of 3768 m, 5652 m and 7536 m corresponding to 30, 45 and 60 min, respectively. A hardened steel disc of 60 HRC was used as the counterface.

3. Results and discussion

3.1. Hardness

Figure 4 shows an increase in hardness with the increase in the percentage of cenospheres of fly ash, when compared with the unreinforced eutectic Al–Si alloy. For instance, the hardness was found to be 50 BHN for 1% fly ash (an increase of 8.6% over the base alloy) and 62 BHN for10% fly ash (an increase of 34.7% over the base alloy).

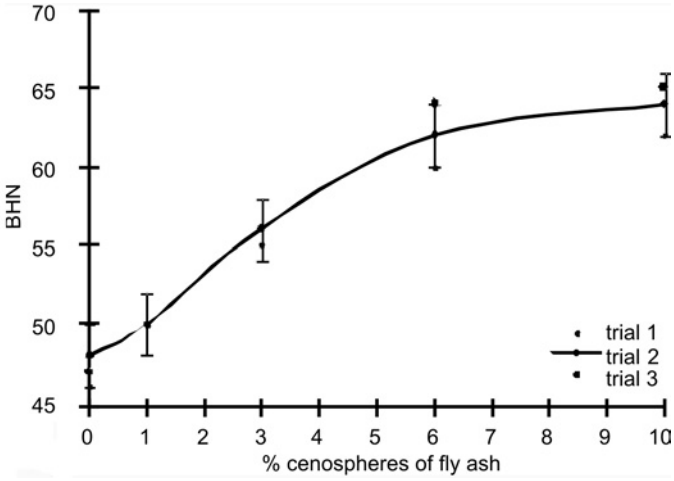

Fig. 4. BHN vs. % cenospheres of fly ash

It has been reported that addition of ceramic particles increases the hardness of composites [3, 5–8, 10, 11]. The increase in hardness is expected because of the presence of ceramic reinforcements which are very hard, and act as barriers to the movement of dislocations within the matrix and exhibit greater resistance to indentation [8]. This trend is also observed in our study.

3.2. Density

The density of the eutectic alloy was found to be 2.65 g·cm^{-3}. This is in agreement with reported literature [2]. The densities of the cast composites, at various percentages of fly ash are shown in Fig. 5. The scatter of three readings was within 2%. It is observed that the density decreases as the percentage of fly ash increases, when compared with the unreinforced eutectic Al–Si alloy. For example, the density of the composite was found to be 2.62 g·cm^{-3} for 1% fly ash (decrease of 1.13% compared with LM6. Similarly, the density for 10% fly ash was 2.31 g·cm^{-3} (decrease of 13.2%). Several investigators have reported a similar trend with the addition of particulates like fly ash [10, 11]. This can be attributed to the difference in densities of aluminium and fly ash.

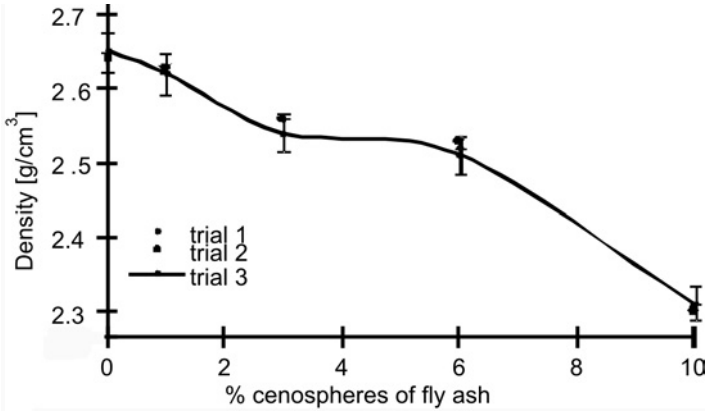

Fig. 5. Density for varying percentages of fly ash

3.3. Recovery of cenospheres

The recovery of cenospheres in the laboratory made Al–Si alloy–cenosphere composite system was calculated using the linear interpolation method, taking into account the density, volume of the alloy as well as of cenospheres. Linear interpolation is the simplest method of reliably estimating values at positions in between the data points [19]. It is observed that the recovery is 98.5% at 1% addition and decreases gradually as the percentage addition of cenospheres increases, as shown in Table 4.

Table 4. Recovery of cenospheres

Content of cenospheres [%]	1	3	6	10
Recovery [%]	98.5	95.6	93.6	83.4

3.4. Ultimate tensile strength and percentage elongation

Figure 6 shows the variation in UTS with the increase in the percentage content of fly ash. It was noted that the UTS for 1% fly ash is 158.8 MPa (16.2 kg·mm^{-2}) (an 8.5% increase over the untreated alloy). Similarly the UTS for 10% fly ash is 211 MPa (21.54 kg·mm^{-2}) and shows an increase of 44.3% when compared with the unreinforced eutectic Al–Si alloy (LM6).This could be due to the fact that the lighter microspheres of fly ash act as barriers to the movement of dislocation, thereby increasing the ultimate tensile strength of the composite [7].

Further, dispersion of hard ceramic particles in a soft ductile matrix results in improvement in strength. This may be attributed to large residual stress developed during solidification and to the generation of density of dislocations due to mismatch of thermal expansion between hard ceramic particles and soft Al matrix [16]. The reason

for the improved strength may perhaps be due to a good bonding between the cenosphere particles and also with the matrix [18]. Thus it can be seen that our results are in agreement with those reported in the literature.

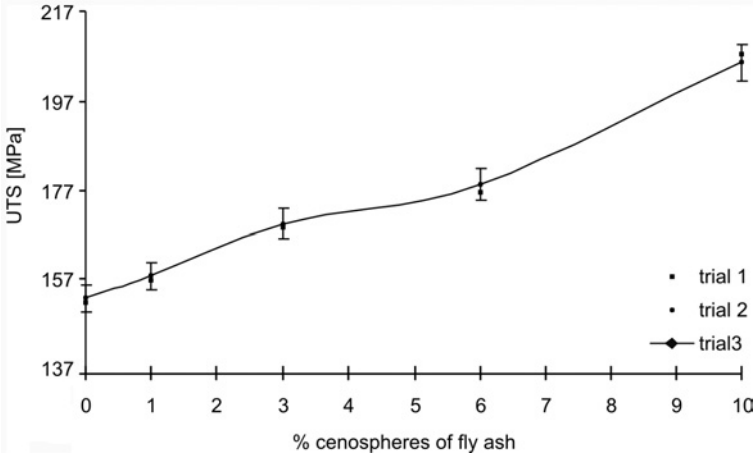

Fig. 6. Variation in UTS vs. % cenospheres of fly ash

Figure 7 shows that there is a marginal decrease in percentage elongation with the percentage increase in the fly ash. For instance, it can be seen that the elongation for 1% fly ash is 2.01%, while the elongation for 10% fly ash is 1.96%. This is in agreement with literature data [1, 6].

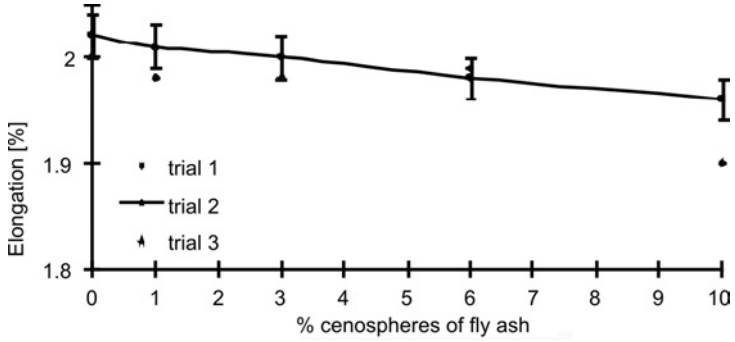

Fig. 7. Elongation vs. % cenospheres of fly ash

3.5. Surface roughness

A review of the literature reveals that no investigation seems to have been carried out to measure the surface roughness. From Figure 8 it is observed that the surface roughness increases as the percentage content of fly ash cenospheres increases, when compared with the unreinforced eutectic Al–Si alloy (LM6).

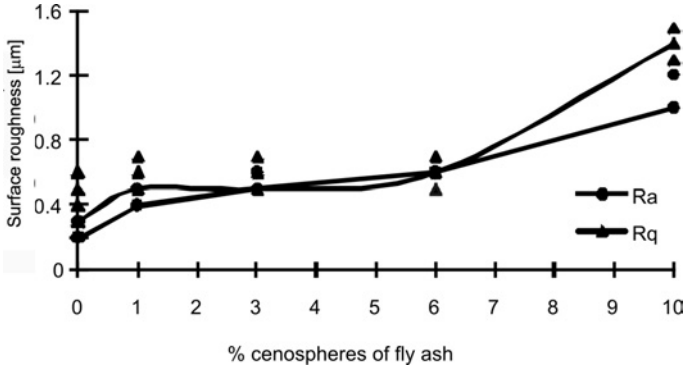

Fig. 8. Average surface roughness vs. % cenospheres of fly ash

For instance, R_a increases from 0.4 µm for 1% fly ash to 1 µm for 10% fly ash and R_q increases from 0.3 µm for 1% fly ash to 1.4 µm for 10% fly ash. Cenospheres of fly ash are extremely hard and contain much unburnt carbon [17]. This tends to have an adverse effect on the surface roughness.

3.6. Wear

In general, it is observed that the wear increases with the increase in time and distance. Figure 9 depicts the wear weight loss of the composites under different sliding distances. For instance, the weight loss is 0.06g at a sliding distance of 3768m, while the weight loss is 0.13g. at 7536m for 1% fly ash. A similar trend is observed for 3, 6 and 10% fly ash. This is due to the fact that cenospheres are hard, abrasive particles and resist wear better than the matrix. It is observed that, for a given sliding distance, the weight loss is lower for a higher percentage of fly ash. For example, the weight loss is 0.13g for 1% fly ash and 0.1g for 10% fly ash for a sliding distance of 7536 m. Similar trends were observed by other researchers [12–16].

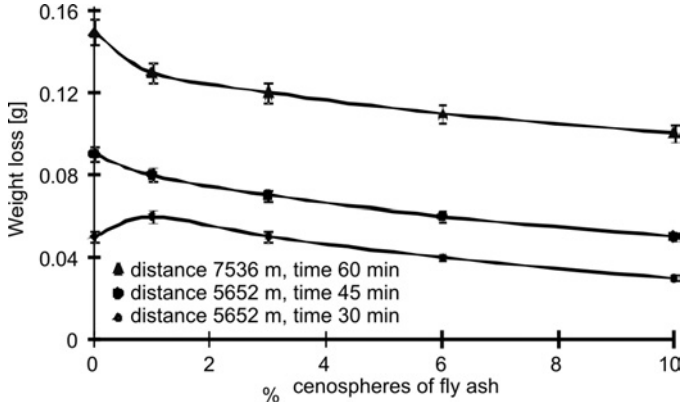

Fig. 9. Wear at 30, 45 and 60 min

The results shown in Figs. 4–9 indicate that fly ash cenospheres can increase hardness and UTS, while reducing density and wear. However, the surface roughness is found to increase, resulting in a poor surface finish, while the percentage elongation showed only a marginal variation for the various percentages of fly ash investigated.

4. Conclusion

An attempt has been made to evaluate the effect of various percentages of cenospheres of fly ash on the hardness, density, UTS, ductility, surface finish and wear, when compared with the unreinforced eutectic Al–Si alloy (LM6). The results of this investigation reveal the following:

It is observed that the hardness increases by 8.6% for 1% fly ash and by 34.7% for 10% fly ash based composite, compared with the base alloy.

Density decreases upon increasing percentage of fly ash addition. For instance, it decreases from 1.13% for 1% fly ash to 13.2% for 10% fly ash.

The ultimate tensile strength of the composite showed an increase ranging from 8.5% for 1% cenospheres of fly ash to 44.3% for 10% with the addition of cenospheres of fly ash.

The percentage elongation of the composite showed only a marginal decrease for the various percentages of fly ash studied in this investigation. It is found to decrease from 2.01% for 1% fly ash to 1.96% for 10% fly ash.

Sample analysis revealed there was a direct correspondence between the fly ash percentage and the wear loss: the higher the fly ash percentage, the lower the wear loss, and vice versa. For instance, the wear loss was found to be 0.1g for 10% fly ash compared with 0.13g for 1% fly ash for a sliding distance run of 7536m.

The surface roughness increases with the addition of cenospheres of fly ash. R_a increases from 0.4μm for 1% fly ash to 1μm for 10% fly ash and R_q increases from 0.3μm at 1% fly ash to 1.4μm at 10% fly ash.

Acknowledgements

The authors gratefully acknowledge the support provided by the M/S Central Power Research Institute, Indian Institute of Science, Bangalore and BMS Educational Trust for providing the facilities and technical help for carrying out this work.

References

[1] *ASM Handbook Composites*, ASM Int., 21 (2001) 3.
[2] The Foseco Foundryman's Handbook, Pergamon Press, Oxford, 1965, p. 110.
[3] SINGH M., MONDAL D.P., JHA A.K., DAS S., Composites, Part A, 32 (2001), 787.
[4] VENKATESWARAN S., MALLYA R.M., SHESHADRI M.R., Cast Metals, UK, (1991), 72.
[5] SARAVANAN R.A., SURAPPA M.K., PRAMILA BAI B.N., Wear, 202 (1997), 154.
[6] BENAL M.M., SHIVANAND H.K., MURALIDHARA M.K., Indian Foundry J., 52 (2006), 37.
[7] LEE H.S., YEO J.S., HONG S.H., YOON D.J., NA K.H., J. Mat. Proc. Techn., 113 (2001), 202.

[8] WONG W.L.E., GUPTA M., LIM C.Y.H., Mater. Sci. And Eng. A., 423 (2006), 148.
[9] NAGESHA, *Preparation of Al (6061) Fly Ash Composites*, B.E. Thesis, Visvesvaraya Technological University, Belgaum, India, 2006.
[10] MAHENDRA K.V., RADHAKRISHNA K., Mater. Sci.-Poland, 25 (2007), 57.
[11] RAMACHANDRA M., RADHAKRISHNA K., Mater. Sci. Techn. 21 (2005), 1.
[12] PRAMILA BAI B.N., BISWAS S.K., *Characterization of Dry Sliding Wear of Aluminum–Silicon Alloys*, Elsevier, Sequoia, 1987, p. 61.
[13] MURALI T.P., PRASAD S.V., SURAPPA M.K., ROHATGI P.K., Wear, 80 (1982), 149.
[14] PRAMILA BAI B.N., RAMASESH B.S., SURAPPA M.K., Wear, 157 (1992), 295.
[15] ROHATGI P.K., GUO R.Q., IKSON H., BORCHELT E.J., ASTHANA R., Mater. Sci. Eng. A., 244 (1998), 22.
[16] SURESH K.R., NIRANJAN H.B., MARTIN JEBARAJ P., CHOWDIAH M.P., Wear, 255 (2003), 638.
[17] PRASHANTH T., SHEKAR KUMAR., SURYANARAYAN., Intl. Conf on Advanced Materials and Composites ICAMC 2007, 24–27 October, CSIR, Trivandrum, India.
[18] GUO R.Q., ROHATGI P.K., J. Mater. Sci., 32 (1997), 3971.
[19] BOURKE P., *Interpolation Methods*, December 1999, http:// local.wasp.uwa.edu.au/~pbourke/.

Received 28 March 2008
Revised 11 September 2009

Materials Science-Poland, *Vol. 28*, *No. 1*, *2010*

Tribological properties of oxidation modified carbon fibre–reinforced polyamide 6 composites

W.Z. NIE[1], J. LI[2], X.H. SHENG[3*]

[1]School of Mechanical and Automation Engineering, Shanghai Institute of Technology, Shanghai 200235, P.R. China

[2]School of Mechanical and Electronic Engineering, Shanghai Second Polytechnic University, Shanghai 201209, P.R. China

[3]Shanghai Zhuzong Company, Shanghai 200032, P.R. China

The ozone modification method and air-oxidation were used for the surface treatment of polyacrylonitrile-based carbon fibre. The interfacial properties of carbon fibre–reinforced polyamide 6 (CF/PA6) composites were investigated by means of single fibre pull-out tests. It was found that the IFSS values of the composites with ozone treated carbon fibre are increased by 60% compared with that without treatment. The effect of surface treatment of carbon fibres on the tribological properties of CF/PA6 composites was also investigated for comparison. Experimental results revealed that surface treatment can effectively improve the interfacial adhesion between carbon fibre and PA6 matrix. Thus the wear resistance was significantly improved.

Keywords: *ozone; CF/PA6 composite; single fibre pull-out; interfacial adhesion*

1. Introduction

The application of carbon fibres–polymer composites has been rising during the last decade, mainly in the car and aerospace industry, due to the improvement of the electrical conductivity and mechanical stiffness. Polyamide, due to its unusual properties such as good thermal stability, low electric permittivity, high mechanical strength and chemical inertness, is becoming a strong competitor of matrix in the manufacture of advanced composite materials. Fibre-reinforced polyamide matrix composites with high performance have especial applications in aerospace, robots, sports goods, etc. Carbon fibres possess exceptional specific strength and stiffness, and hence they have important applications in structural composites. The performance of such composites depends on the properties of the fibres which depend not only on the type ofthe manu-

*Corresponding author, e-mail: shengxiaohong2@sina.com

facturing process [1–3] and the surrounding matrix, but also on the interface between them [4, 5]. However, as a composite material reinforcement, the full potential of carbon fibres has not yet been realized. This is due primarily to fibre–matrix adhesion. In order to harness the properties of carbon fibres and ensure good stress transfer, there must be adequate adhesion between the fibres and the matrix. Consequently, a variety of surface treatments of carbon fibres are developed such as oxidation, coating, grafting [6–11], etc. All surface treatments enhance the interfacial shear strength (IFSS) by introducing chemically active groups on the fibre surfaces which increases the reactivity with the matrix, enhancing surface roughness to produce better mechanical interlocking as well as increasing the surface energy for improved wetting. The ozone modification method is a kind of simple and efficient method for carbon fibre modification.

In this work, the ozone modification method is used for the surface treatment of carbon fibre. The purpose of this study was to examine the influence of ozone surface treatment methods on the interfacial adhesion properties of CF/PA6 composites and the surface characteristics of carbon fibre before and after treatment. And further research on ozone modification method is necessary for the application of this method.

2. Experimental

Materials. For the present investigation, the reinforcement materials were continuous polyacrylonitrile (PAN)-based carbon fibres manufactured by Shanghai Sxcarbon Technology Co. Ltd. prior to use, and polyamide-6 supplied by YueYang Juli Engineering Plastic Co. Hunan with the following properties: tensile strength – 85 MPa, flexural strength – 115 MPa, the density of the matrix – 1150 kg/m^3

Fibre surface treatment. Oxidation of the carbon fibres was carried out at 450 °C in an oxidation furnace for 10 min. The selected oxidation condition has been proved to be the most effective one for this kind of carbon fibre. Ozone surface treatment of the carbon fibres was carried out in a XFZ-5BI generator for 3 min [12]. The concentration was 10–36 mg/dm^3.

Single fibre pull-out test. A microbond test was performed to evaluate the interfacial shear strength (IFSS) between carbon fibre and matrix by pulling out a fibre from a PA6 resin droplet. The composite specimens were prepared by a screw in-line type injection moulding machine with the help of a special embedding machine, in which the fibre can be embedded perpendicular to the surface of the matrix globe with a defined embedded length.

The sample for the single fibre pull-out measurement is a few millimetres long fibre, partly embedded at one end in a polymer and orientated perpendicular to the polymer surface (Fig. 1). On a metal surface a small amount of polymer in the form of a hemisphere supported a vertically positioned fibre, which was embedded by using a special embedding machine [13]. The embedding depth of the carbon fibre filament in the PA6 resin was 105 μm, which is ca.15 times the size of the fibre diame-

ter(7μm).This makes it possible to ensure that the stress distribution around the fibre–matrix interface is nearly homogeneous.

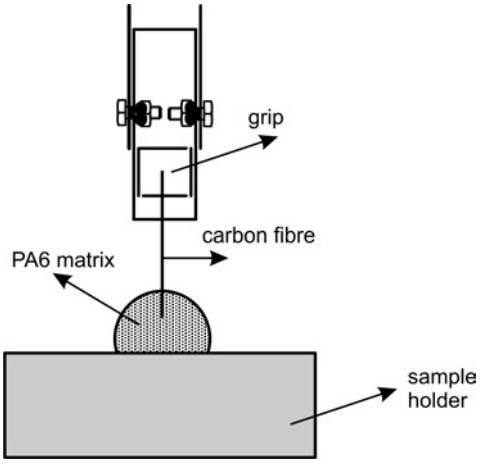

Fig. 1. Single fibre pull-out model

The pull-out test was performed at a crosshead displacement rate of 0.5 μm·s^{-1}. The value of IFSS was calculated according to the equation

$$\text{IFSS} = \frac{F}{\pi dl}$$

where F is the maximum load, d – the diameter of the carbon fibre, l – the length of the fibre embedded in the resin. The recorded value of IFSS was calculated from the normal distribution of more than 10 successful measurements

Friction and wear tests. Friction and wear tests were done using a ball-on-block reciprocating UMT-2MT tribometer at room temperature with a relative humidity of 45–55%. The specimen disks, cut from the above sintered composites, were 30 mm long, 20 mm wide and 5 mm thick. The disks were polished using a fine grade SiC emery paper and cleaned ultrasonically with acetone and dried before testing. The counterpart was a GCr15 steel ball of the hardness HRC61 and surface roughness *R*a ca. 0.05 μm with the diameter of 3 mm. The reciprocating friction stroke was 5 mm and tests were conducted at a normal spring-driven load. The test duration was 2 h and the friction coefficient was taken to be the average value of the whole process. During tests, the friction coefficient was continuously measured using a load cell. The cross-section of the wear scars were measured using a surface profilometer (model 2206, Harbin Measuring and Cutting Tool Group Co. Ltd., China). The wear volume of the specimen was calculated from the equation $V = Sl$, where V is the wear volume in m^3, S is the cross-section area, l is the length of the stroke. The specific wear rate of the composite was calculated using the equation $K = V/LF$, where V is the wear volume [m^3], L is the sliding distance [m], F is the applied load [N]. Five tests were conducted

under each test condition and the average values of the measured friction coefficient, and the specific wear rate were used for further analysis. The worn surfaces of CF/PA6 composites were investigated with a scanning electron microscope (SEM).

Preparation process. The hot moulding technique was employed to fabricate composite specimens, which is the most common technique for the sintering of pure PA6 without any sintering aids. In this process, the filler carbon fibres and the PA6 were churned together in a mixer. Mixing was done for a few minutes at the addition of each component for about 20 min. Sintering powder (20 vol. % of carbon fibres and 80 vol. % of PA6) was placed inside a stainless mould with its inner walls coated with a BN slurry to avoid any interaction between the powder and steel and also to facilitate the demoulding process. The compounds were put into the QLB-D170×170 vulcanizing machine at 280 °C for 1 h under a constant pressure of 12 MPa, then heated from 280 °C to 340 °C in 1 h. When the temperature reached 340 °C, it remained constant for 1 h. Then the compounds were cooled from 340 °C to 200 °C in 70 min. During the whole process, the pressure of ozone was constant. The obtained materials were then cooled to room temperature to get the composites.

3. Results and discussion

3.1. IFSS of CF/PA6 composites

Figure 2 shows that the IFSS values of the composites with ozone treated carbon fibre are increased by 60% compared with those without treatment. It is proved that the better interfacial adhesion can be obtained through surface modification.

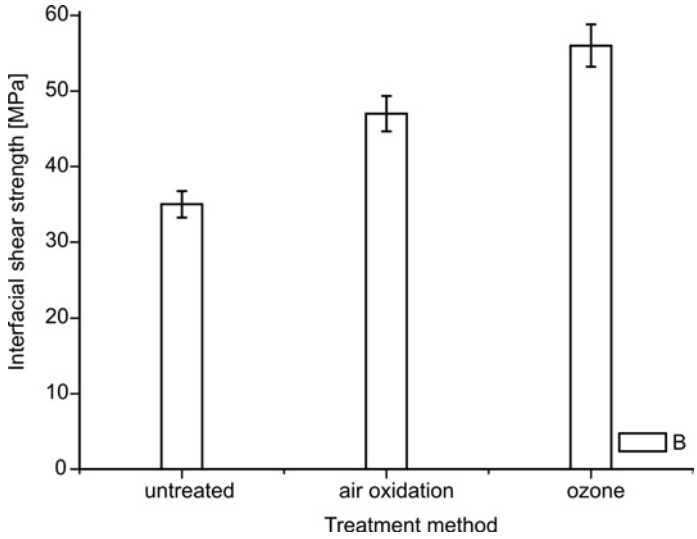

Fig. 2. IFSS of CF/PA6 composites

The reasons attributed to this is that the ozone treatment is a method to bind oxygen functional groups on carbon fibre surfaces, which increase the interlock between the fibre and matrix, leading to the increase of the IFSS of composites, which can effectively transfer the stress from matrix to the fibre, thus the fibre can provide more reinforcement. Therefore, the IFSS of the composite reinforced by ozone treated carbon fibres are considerably improved.

3.2. Friction and wear properties

Figure 3 shows the variation of the friction coefficient of the CF/PA6 composites with load. The friction coefficient of all PA6 composites increases as the load increases from 6 N to 15 N under the same reciprocating sliding frequency 8 Hz. This can be explained by the friction-induced thermal and mechanical effects, which may increase the actual contact area between the frictional pair as the load increases. Changes in the friction coefficient of CF/PA6 composites with reciprocating sliding frequency are shown in Fig. 4. The friction coefficient decreases as the reciprocating sliding frequency increases from 1 Hz to 12 Hz under the same load of 12 N. This was attributed to the increased softening and plastic deformation of the polymer matrix which was caused by the increased reciprocating sliding frequency. The ozone treated CF/PA6 composite exhibits the lowest friction coefficient and the untreated PA6 composite exhibits the highest friction coefficient both under the same reciprocating sliding frequency (Fig. 3) and at the same load (Fig. 4). The modification of the carbon fibres strengthens the combination of the interface between the fibres and the PA6 matrix and increases the elastic modulus of the PA6 composites. This will be the reason why the friction coefficient of the modified carbon fibre reinforced PA6 composites is reduced.

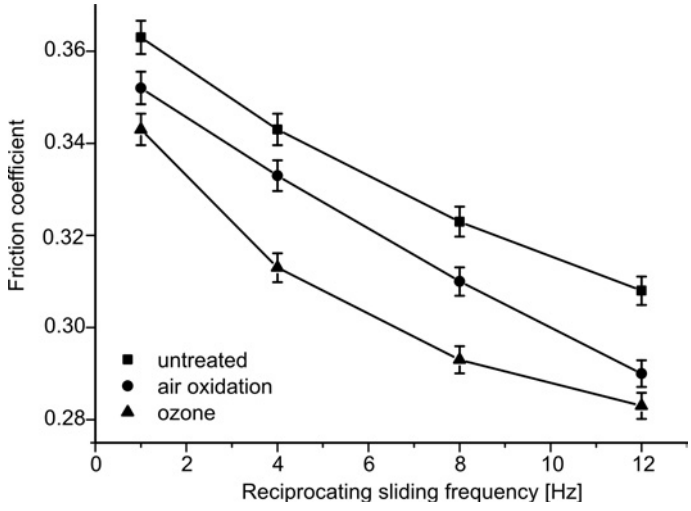

Fig. 3. Dependences of the friction coefficients on load for the PA6 composites

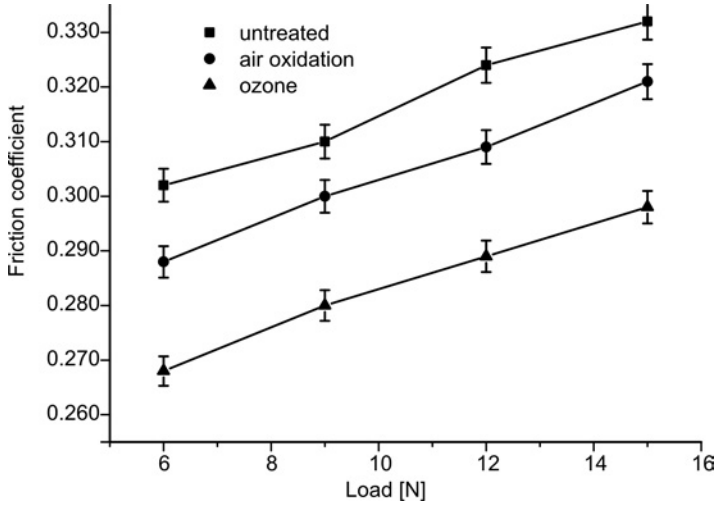

Fig. 4. Dependences of the friction coefficients on reciprocating sliding frequency for the PA6 composites

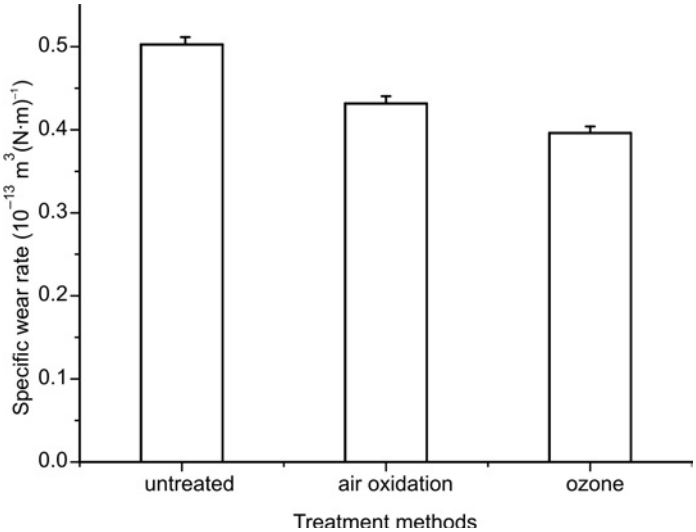

Fig. 5. Specific wear rate of PA6 composites under the load of 12 N and a reciprocating sliding frequency of 8 Hz

Figure 5 gives the specific wear rate of three CF/PA6 composites under the load of 12 N and reciprocating sliding frequency of 8 Hz. It is seen that the untreated composite has the highest specific wear rate, while the ozone treated composite has the lowest one. The specific wear rate itself depends on the properties of the filler, of the matrix and of the filler/matrix bond strength. In addition, the relative hardness of the filler to that of the counterface, the content, shape, size, distribution and orientation of the filler, and the abrasiveness of filler against the matrix are important parameters. In this

system, the difference of specific wear rate mainly comes from the bond strength between the reinforcement and the matrix. It can be seen from Fig. 5 that the modification of the carbon fibres can improve the wear resistance of the PA6 composites, reflecting the effectiveness of the modification of the carbon fibres on increasing the combining strength of the interface between the carbon fibres and PA6 matrix. The above experimental results reveal that ozone treatment greatly improves the friction-reducing and wear-resistance properties of PA6 composite under dry sliding conditions.

The normal load and reciprocating sliding frequency were fixed at 12 N and 8 Hz, respectively. SEM images of the worn surfaces of PA6 composites filled with carbon fibres that had been subjected to different surface treatments are shown in Fig. 6.

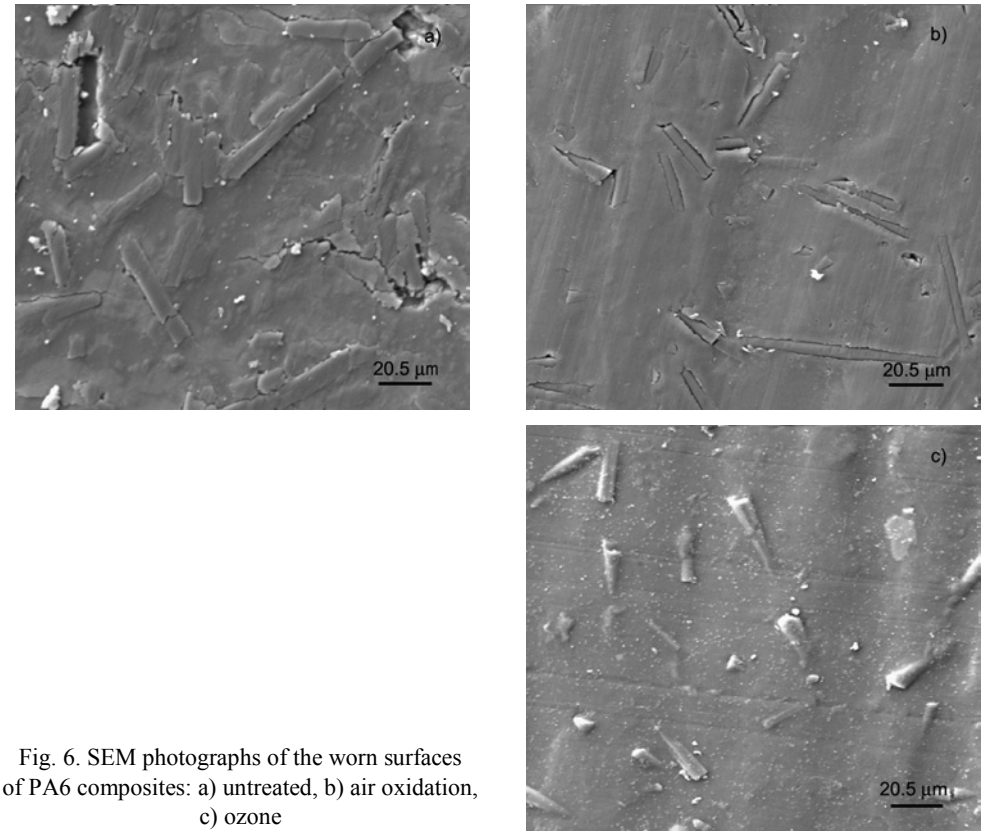

Fig. 6. SEM photographs of the worn surfaces of PA6 composites: a) untreated, b) air oxidation, c) ozone

For the PA6 composite filled with untreated carbon fibres, there are many cracks located near the carbon fibres, as shown in Fig. 6a. Deep pores exist between carbon fibres and PA6 matrix, which indicates that there is a very poor interfacial adhesion between the fibre and the PA6 matrix. Thus the untreated fibres are more prone to be peeled off due to the weak interface bonding. The fillers are easily detached from the matrix under the load of 12 N leaving cavities whose boundaries are the same shape as the filler fibres removed. Many cavities within the matrix material structure lead to

stress concentrations in the matrix resulting in higher local stress, microcracking, and in consequence a high specific wear rate. Furthermore, the detachment of fillers causes the adjacent matrix to be poorly supported and hence is subjected to greater stress and thus is more susceptible to fracture. Therefore, the load-carrying capability of the composite is reduced, resulting in a decrease in the/its wear resistance property.

On the worn surfaces of the PA6 composites containing the modified fibres, the damage became weaker, indicating how effectively surface modification of carbon fibres improves the wear resistance of the PA6 composites, as shown in Figs. 6b, c. For the air oxidated CF/PA6 composite, the worn surface is smoother than the untreated one, as seen in Fig. 6b. There are also pores between carbon fibres and PA6. This indicates that the interfacial adhesion between carbon fibres and PA6 is not strong enough, even though carbon fibres are air oxidated. Poor interaction leads to high abrasion wear due to the ease of fibre cracking or displacement. The reinforcing fibres are apt to be pulled-out if the resultant force of applied load and friction force exceeds the interface bonding strength during wear. Microcracks are observed at the surface either at the fibre–matrix boundary or at weak spots in the matrix and eventually lead to delamination of the matrix material. Poor adhesion of the filler to the matrix gave rise to the initiation of these cracks and hence increased the wear rate [12]. Probably, a crack follows the fibre–matrix interface and passes between the fibres at their closest distance. The crack propagates under the original surface matrix layer and causes fragments of the matrix to be broken off, leaving the fibres bare. The driving force for the crack comes from the friction forces being applied on the matrix surface. Where the fibres are close to each other the matrix between the fibres are often fragmented and broken off when the crack propagates along the fibre surface. Additionally, the cavity shown in the PA6 matrix is the result of a filler carbon fibre detaching from the matrix due to loss of matrix around it and poor adhesion between the filler and matrix.

For the composite filled with ozone treated carbon fibres, as shown in Fig. 6c, the worn surface is quite smooth and no cracks are visible. CF and PA6 are compactly bonded and no pores exist between the fibre and the matrix. This indicates that the filler carbon fibres in ozone treated CF/PA6 have good bonding to the matrix and support the load from the counterbody effectively. The carbon fibres are not easily detached from the PA6 matrix in the friction process, due to the improvement in the interfacial adhesion between the carbon fibres and PA6 matrix after ozone treatment. Thus, the load is effectively supported by carbon fibres and the large-scale transfer and rub off of PA6 will be restrained. Accordingly, the wear of the PA6 composite filled with ozone treated carbon fibres was reduced.

4. Conclusions

The effect of ozone treatment has been investigated on interfacial and tribological properties of carbon fibre–reinforced PA6 composites. The IFSS of the composites

were improved by ozone treatment. Ozone treatment effectively promotes the interfacial adhesion between the carbon fibre and PA6 matrix. IFSS values of the composites with ozone treated carbon fibre are increased by 60% compared with those of untreated composites. The friction coefficient and specific wear rate of CF/PA6 composite can be decreased after surface treatment of carbon fibres. The ozone treated composite has the lowest friction coefficient and specific wear rate under a given applied load and reciprocating sliding frequency.

Acknowledgements

The authors acknowledge the help from School Fund (Project No. JD208001), Shanghai Second Polytechnic University.

References

[1] JANG J., YANG H., J. Mater. Sci., 35 (2000), 2297.
[2] WILSON M.A., PATNEY H.K., KALMAN J., Fuel, 81 (2002), 5.
[3] KATSUMATA M., YAMANASHI H., USHIJIAMA H., Proc. SPA6E-Int. Soc. Opt. Eng., (1993), 140.
[4] FITZER E., GEIGL K.H., HÜTTNER W., WEISS R., Carbon, 18 (1979), 389.
[5] SHERWOOD P.M.A., Relat. Phenom., 81 (1996), 319.
[6] RASHKOVAN I.A., KORABELNIKOV Y.G., Comp. Sci. Technol., 57 (1997), 1017.
[7] DILSIZ N., EBERT E., WEISWEILER W., AKOVALI G., J. Colloid Interf. Sci., 170 (1995), 241.
[8] YUE Z.R., JIANG W., WANG L., GARDNER S.D., PITTMAN C.U., Carbon, 37 (1999), 1785.
[9] PAMULA E., ROUXHET P.G., Carbon, 41 (2003), 1905.
[10] FIELDLY A., OLSEN T., RYSJEDAL J.H., BERG J.E., Composites A, 32 (2001), 373.
[11] VARELIDIS P.C., MCCULLOUGH R.L., PAPASPYRIDES C.D., Comp. Sci. Technol., 59 (1999), 1813.
[12] YANG Y.G., HE F., WANG M.Z., LI Z.J., ZHANG B.J., Carbon Technol., 6 (1997), 12 (in Chinese).
[13] HAMPE A., KLINKA G., MERETZ S., SCHULZ E., Composites, 26 (1995), 40.
[14] SHERWOOD P.M.A., in: D. Brigg, Seah MP(Eds.), *Practical Surface Analysis*, 2nd Ed., Wiley, New York, 1995, p. 555.
[15] POLOVINA M., BABIĆ B., KALUDEROVIĆ B., DEKANSKI A., Carbon, 35 (1997), 1047.
[16] ZHANG Z.Q., LIU Y.W., HUANG Y.D., Comp. Sci. Technol., 62 (2002), 331.

Received 20 July 2008
Revised 17 November 2008

Materials Science-Poland, *Vol. 28*, *No. 1*, *2010*

Fabrication of core-shell Ge–GeO_2 nanoneedles

L.Z. PEI[1], H.S. ZHAO[1], W. TAN[2], H.Y. YU[1], Q.-F. ZHANG[1*]

[1]School of Materials Science and Engineering, Institute of Molecular Engineering and Applied Chemistry, Anhui University of Technology, Ma'anshan, Anhui 243002, P.R. China

[2]Henkel Huawei Electronics Co. Ltd., Lianyungang, Jiangsu 222006, P.R. China

Core-shell Ge–GeO_2 nanoneedles were prepared by a hydrothermal deposition using Ge and GeO_2 as starting materials. The samples were characterized by scanning electron microscopy, energy dispersive X-ray spectroscopy, transmission electron microscopy and high-resolution transmission electron microscopy. The results demonstrate that the length of the samples with typical needle structure is higher than 10 μm. The obtained nanoneedles are composed of single crystalline Ge with diamond cubic structure and amorphous oxide outer layers. An explanation of the formation and growth of Ge nanoneedles is proposed, and is based on the metallic-catalyst vapour-liquid-solid and oxide-assisted growth mechanisms.

Keywords: *Ge–GeO_2 nanoneedles; hydrothermal deposition; characterizations*

1. Introduction

Germanium is an important semiconductor with a direct band gap of 0.8 eV and an indirect band gap of 0.66 eV. Recently, interest in germanium has intensified as the migration from silicon to other materials is contemplated for enhanced functionality of future transistors for logic and other functions. Compared with bulk silicon, bulk germanium offers several advantages such as higher intrinsic carrier mobilities, promising faster switching and higher frequency devices, higher intrinsic carrier concentrations, larger bulk excitonic Bohr radii (24.3 nm for Ge versus 4.7 nm for Si), etc. Also, compatibility of germanium with the group of III–V materials (e.g., good lattice matching with GaAs) and optical properties of germanium oxide allow fabrication of radical integrated optoelectronic circuitry designs [1, 2]. Therefore, the one-dimensional nanoscale materials of Ge have many potential applications such as in nanoscale probes, nanoscale electron devices and nanoscale sensors. Ge nanowires and nanoneedles with core-shell structure are two kinds of one-dimensional solid forms of Ge. Ge nanowires with uniform diameter can be prepared easily by the laser ablation method [3], chemical vapour deposition (CVD) [4, 5], thermal evaporation [6], the

*Corresponding author, email: zhangqf@ahut.edu.cn

template method [7, 8] and the supercritical fluid method [9, 10]. In comparison with semiconductor Ge nanowires, Ge nanoneedles are also particularly interesting because their tips exhibit a sharp curvature. Due to their tapered shapes, nanoneedles can potentially be applied as probe tips with high spatial resolution but any damage to probed microstructures should be minimal. They can also be used as field-emission tips with outstanding field enhancement factors [11–13]. Unlike nanowires of uniform diameter, nanoneedles with sharp tips are difficult to prepare. Only a few kinds of semiconductor nanoneedles have been reported, such as silicon [14, 15], ZnO [13, 16, 17], Se [18] and ZnSe [19]. Therefore, the fabrication of Ge nanoneedles is still challenging. In this paper, we report a simple hydrothermal deposition route for the preparation of Ge nanoneedles with Ge–GeO_2 core-shell structure. The products have been characterized by scanning electron microscopy (SEM), energy dispersive X-ray spectroscopy (EDS), transmission electron microscopy (TEM), selected area electron diffraction (SAED) and high-resolution transmission electron microscopy (HRTEM). The growth mechanism of Ge–GeO_2 core-shell nanoneedles is also discussed.

2. Experimental

The preparation of Ge–GeO_2 core-shell nanoneedles was performed in an autoclave. The autoclave is composed of stainless steel (1Cr18Ni9Ti) with maximum pressure of 22 MPa, maximum temperature – 500 °C, volume 1000 cm^3, power – 1.5 kW and stirring velocity of the stirrer from 0 to1000 rpm. 2 wt. % Ge and GeO_2 (purity of both $\geq$ 99.99%) were mixed with 48 cm^3 of distilled water. The mole ratio of Ge and GeO_2 was 1:1. Then the mixture was placed in the autoclave. The copper sample of the dimensions 4 × 2 cm^2 was cleaned in distilled water for 10 min using supersonic wave apparatus in order to ensure the cleanliness in the surface of the copper substrate. Then, the latter was fixed in the stainless steel bracket in the centre of the autoclave. After the autoclave was sealed safely, it was heated to 480 °C, subject to a pressure of 9–10 MPa, and stirred at the rate of 100 rpm. The constant temperature and pressure were maintained for 24 h. Subsequently the autoclave was cooled in air. Finally, the copper substrate with bulk deposit was obtained after the experiment. SEM and TEM confirmed that the product were Ge–GeO_2 core-shell nanoneedles.

Scanning electron microscopy observations were performed using a JEOL JSM5410 scanning electron microscope with the 15 kV accelerating voltage. Chemical analysis was performed with an energy dispersive X-ray spectroscope attached to the scanning electron microscope. The product was mechanically scrapped from the copper substrate. Transmission electron microscopy and high-resolution transmission electron microscopy samples were prepared by putting several drops of solution containing nanoneedles onto a standard copper grid with a porous carbon film after the nanoneedle samples had been dispersed in distilled water and treated for about 10 min using a supersonic wave apparatus. Transmission electron microscopy and high-resolution transmission electron microscopy observations were performed using

a JEOL JEM-2100 transmission electron microscope operating with 1.9 Å point-to-point resolution, and a 200 kV accelerating voltage, equipped with a GATAN digital photography system.

3. Results and discussion

SEM observations show an abundant number of cluster-like nanoneedles on the substrate. In Figure 1, typical SEM images of the nanoneedles under various magnifications are seen. It was found that the substrate is uniformly covered by pure nanoneedle structures.

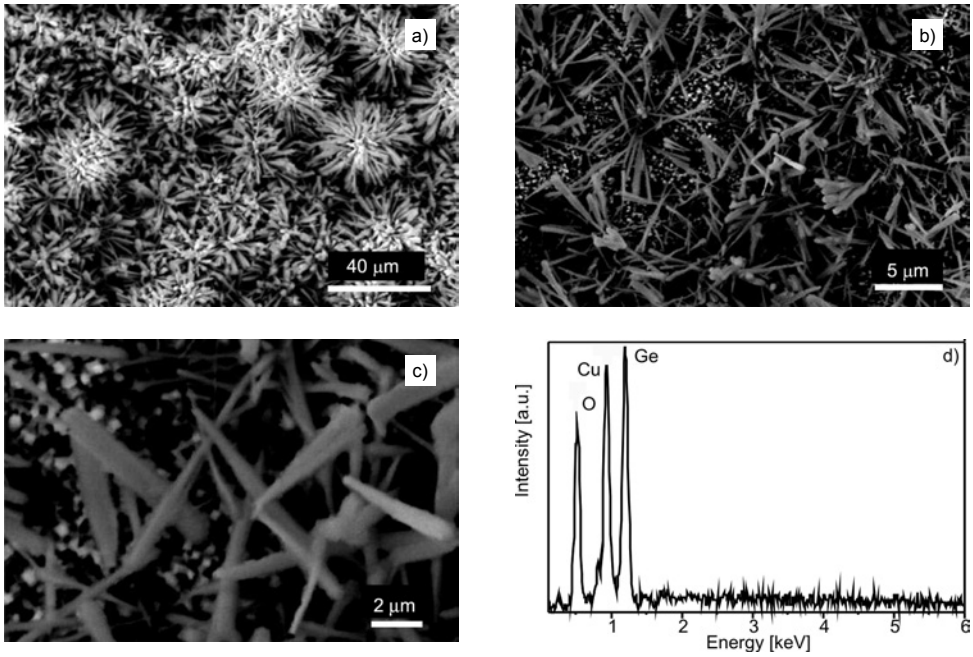

Fig. 1. General SEM images of the obtained nanoneedles with various magnifications (a)–(c) and the corresponding EDS spectra of the nanoneedles (d)

The length of each nanoneedle exceeds 10 μm. The diameter of each nanoneedle is continuously smaller towards one end, and the average diameter of needle tips is lower than 1 μm. Most nanoneedles have sharp tips and smooth surfaces, showing that their morphology is similar to that of other kinds of nanoneedles [14–19]. In order to determine the components of the obtained nanoneedles, the products are analyzed with an EDS spectrometer equipped with the SEM (Fig. 1d). According to the EDS data, the obtained nanoneedles are composed of Ge, O and Cu. No other elements are observed from the EDS spectroscopy.

Figure 2a shows a typical TEM image of the nanoneedles, which is similar to the SEM results. The corresponding SAED is shown in the inset of Fig. 2a. The SAED displays typical diffraction patterns of the {111}, {220} and {311} planes, which indicate that the nanoneedles are in a single crystalline form with a cubic diamond phase. Figure 2b is a typical high magnification TEM image of a single nanoneedle, revealing a sharp tip.

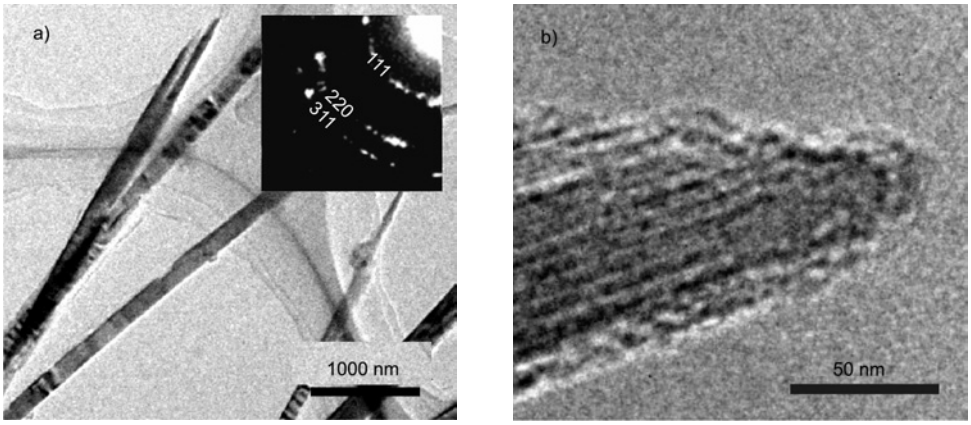

Fig. 2. General TEM image of the sample (a), the inset is the corresponding SAED pattern, and typical TEM image at the tip of a single nanoneedle (b)

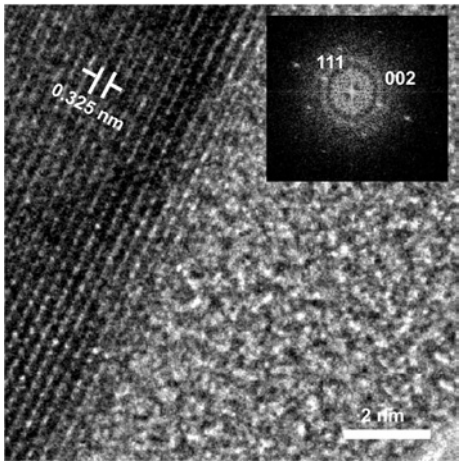

Fig. 3. HRTEM image of the sample, the inset is the corresponding diffraction pattern obtained by fast Fourier transformation (FET)

Figure 3 shows the HRTEM image of a single nanoneedle. The core-shell structure can distinctly be observed and the outer layer is amorphous, measuring several dozen nanometres. The crystalline interplanar spacing is about 0.325 nm, according to the HRTEM measurement and the subsequent calculation using the software of a digital micrograph (Gatan Inc., Pleasanton, CA) applied to the HRTEM, matching well with the {111} plane of Ge. In addition, the HRTEM image further confirms that the nanoneedles are single crystalline. The two-dimensional lattice image further reveals

that the obtained nanoneedles consist of single crystalline Ge cores and amorphous GeO_2 shell. The corresponding diffraction pattern obtained by fast Fourier transformation (FET) is shown in the inset of Fig. 3. [111] is the growth direction of the nanoneedles which is similar to that observed for Ge nanowires [9, 10, 20, 21].

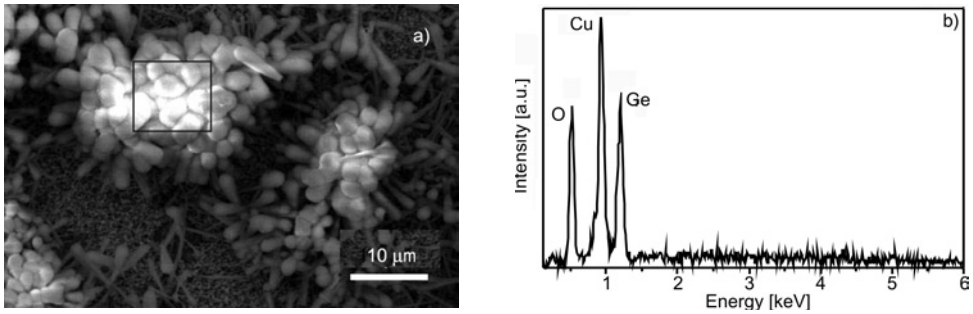

Fig. 4. SEM image of the tips of the nanoneedles (a) and the corresponding EDS spectra (designated by the black frame) (b)

The growth tips of the nanoneedles are shown in Fig. 4a. Sphere structures of various sizes are observed. The sphere structures are similar to the tips of catalyst alloys of other one-dimensional nanoscale materials, such as carbon nanotubes [22], silicon nanowires [23] and germanium nanowires [20] fabricated by metallic catalyst vapour-liquid-solid (VLS) growth methods. In addition, the corresponding EDS spectra (Fig. 4b) show that the sphere structures are composed of Ge, O and Cu. The content of Ge is obviously lower than that of Cu. The results show that the sphere structures at the tips are a kind of Cu/Ge/O catalyst alloy sphere. It is well known that the presence of solidified catalyst droplets of one-dimensional nanostructures is an evidence for the effective operation of the VLS mechanism, and the size of the droplet commonly governs the diameter of one-dimensional nanostructures [19]. Therefore, the formation of the Ge nanoneedles is believed to be very close to the metallic catalyst VLS growth mechanism. The increase in size of catalyst droplets during the growth probably results in the formation and growth of Ge nanoneedles. However, the peculiar needle-like structure of our grown products indicates that the growth of the nanoneedles does not seem to be governed solely by the VLS mechanism, although Cu/Ge/O catalyst spheres do exist. The Cu/Ge/O catalyst droplets contain a significant amount of oxide. It is also well known that it plays a vital role in the formation and growth of one-dimensional nanomaterials, such as silicon nanowires and germanium nanowires. The formation and growth process can be explained by the oxide-assisted growth (OAG) mechanism proposed by Lee et al. [6, 24–27]. Therefore, oxide is also considered to play an important role in the formation and growth of the nanoneedles. Both mechanisms show an approximately equal probability of occurrence. The possible growth mechanism is proposed below.

The starting materials, Ge and GeO_2 are a stable monoatomic element and oxide in a normal atmospheric environment at room temperature. The melting points of Ge and

GeO_2 are 937.4 °C and 1115 °C, respectively. Therefore, the starting materials are difficult to be gasified, reacting each other under the ambient atmospheric pressure and at experimental temperature under consideration here. The deposition process, however, was conducted under the pressure of 9–10 MPa at the temperature of 480 °C, which is higher than the critical temperature of water (374 °C) [28]. Therefore, the experiments are considered to be carried out under the supercritical hydrothermal conditions. Supercritical water has sufficient density to dissolve materials, a higher diffusivity than in liquid state, low viscosity facilitating mass transport, and high compressibility allowing easy changes in density and dissolving power [29, 30]. Thus the supercritical hydrothermal conditions may play an essential role in the reaction and gasification of Ge and GeO_2. The hydrothermal pressure can also enhance the reaction according to chemical reaction theory. Therefore, the reaction of Ge and GeO_2 should proceed, forming GeO under the present supercritical hydrothermal conditions.

GeO is an unstable compound and disproportionates into Ge atoms and GeO_2 molecules forming Ge/GeO_2 nanoscale clusters. The nanoclusters are suspended in the supercritical hydrothermal environment under continuous stirring. The melting temperature of these nanoclusters may be reduced due to their nanoscale size and the effect of the supercritical hydrothermal environment [28–30]. The nanoclusters might be liquid-like, in a semi-molten or molten state. They deposit onto the substrates continuously as the air flows into the autoclave. The supercritical hydrothermal conditions also enhance the oxidation and melting of Cu on the surface of the substrate. Cu reacts with O in the hydrothermal environment to form a large amount of molten Cu oxide nanoclusters on the surface of the substrate. The Cu/Ge/O catalyst droplets form from the molten nanoscale Cu oxide and from deposited Ge, Ge oxide nanoscale clusters. Therefore, the formation and growth of Ge nanoneedles are believed to follow simultaneously the metallic-catalyst VLS and OAG growth mechanisms.

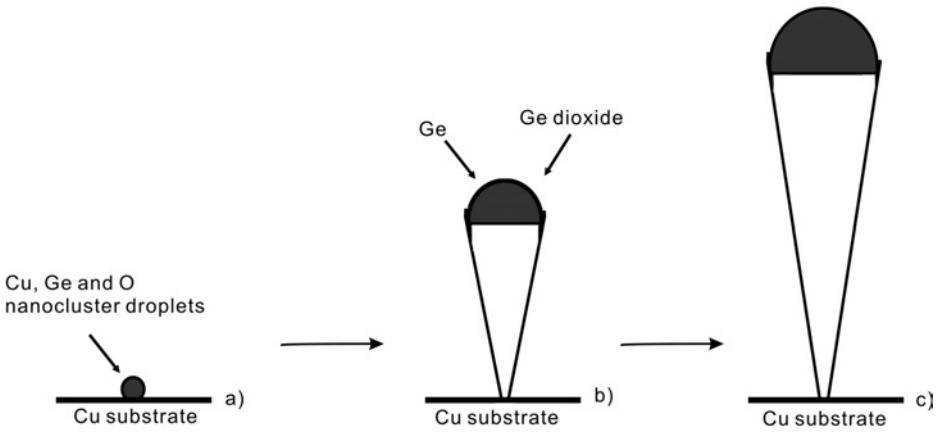

Fig. 5. The proposed metallic catalyst VLS and OAG growth scheme of the nanoneedles: a) the nucleation of the Cu/Ge/O catalyst droplets, b) the growth of the nanoneedles according to the metallic catalyst VLS and OAG growth mechanism, c) the final formation of the nanoneedles

Figure 5 shows the metallic-catalyst VLS and OAG growth scheme of the core-shell nanoneedles. The can be divided into the nucleation and growth of liquid Cu/Ge/O catalyst droplets. The Cu/Ge/O catalyst droplets form from the molten nanoscale Cu oxide and are deposited as Ge, Ge oxide nanoscale clusters (Fig. 5a). Liquid metallic catalyst droplets limit the diameter of the Ge nanoneedles. With the further absorption of Ge atoms and GeO_2 molecules into the droplets from the environment, the Ge atoms are in the supersaturation state and move across the interface between the catalyst and the nanoneedles, thereby resulting in the growth of Ge nanoneedles (Figs. 5b, c). According to the VLS mechanism, the diameter of one-dimensional nanomaterials depends on the size of the nanoclusters that are formed initially [31]. The relation between the nanocluster diameters and the ambient gas pressure is governed by the inertia fluid model proposed by Yoshida et al. [32], which is as follows:

$$d \propto p^n, \quad n = \frac{1}{3} \tag{1}$$

Here d is the diameter of the catalyst alloy nanoclusters, p is the ambient gas pressure. Therefore, the diameter of the Cu/Ge/O nanoclusters at the top of one-dimensional Ge nanoscale structures increases as the ambient gas pressure p increases to 10 MPa. Finally, special nanoneedle structures with sharp tips form. In addition, similar to the metallic catalyst VLS growth mechanism, liquid-like Ge oxide in the Ge/Cu/O nucleus plays also the role of metallic catalysts, according to the OAG mechanism. The Ge/Cu/O nucleus continuously absorbs Ge atoms and Ge oxide molecules from the atmosphere and undergoes recrystallization with phase separation into Ge and Ge oxide. Crystallized Ge stays inside and amorphous Ge oxide diffuses towards the nanoneedle surface. Subsequently, an amorphous GeO_2 shell will be formed [6]. From the thermodynamic viewpoint, recrystallization with phase separation is the result of free energy minimization of the system [6]. The crystalline structure will extend continuously in the axial direction, due to the rapid deposition of nanoclusters at the tip resulting in the growth of the nanoneedles. Therefore, the obtained nanoneedles with the single crystalline Ge cores are covered with oxide outer layers measuring several dozen nanometres.

4. Conclusions

Nanoneedles with Ge–GeO_2 core-shell structure longer than 10 μm have been synthesized by a simple hydrothermal deposition using Ge and GeO_2 as the starting materials. The obtained nanoneedles are covered with oxide outer layers measuring several dozen nanometres, and have single crystalline Ge cores with diamond cubic structure. The nanoneedle diameters become smaller towards one end: the average diameter of the tips is lower than 1 μm. Most needles have sharp tips and smooth surfaces. The formation and growth of the nanoneedles are believed to follow a similar profile to that of the metallic-catalyst VLS and OAG.

Acknowledgements

This work was supported by the National Basic Research Program of China (973 Program, 2008CB617605) and the Program for New Century Excellent Talents in University of China NCET-06-0556).

References

[1] NGUYEN P., NG H.T., MEYYAPPAN M., Adv. Mater., 17 (2005), 549.
[2] WANG L., WANG X.S., TANG J.C., CUE N., Mater. Charact., 48 (2002), 189.
[3] MORALS A.M., LIEBER C.M., Science, 279 (1998), 208.
[4] WANG D., DAI H., Angew. Chem. Int. Ed., 41 (2002), 4783.
[5] DAILEY J.W., TARACI J., CLEMENT T., SMITH D.J., DRUCKER J., PICRAUX S.T., J. Appl. Phys., 96 (2004), 7556.
[6] ZHANG Y.F., TANG Y.H., WANG N., LEE C.S., BELLO I., LEE S.T., Phys. Rev. B, 61 (2001), 4518.
[7] COLEMAN N.R.B., RYAN K.M., SPALDING T.R., HOLMES J.D., MORRIS M.A., Chem. Phys. Lett., 343 (2001), 1.
[8] HAN W.Q., WU L.J., ZHU Y.M., STRONGIN M., Microsc. Microanal., 11 (2005), 1506.
[9] HANRATH T., KORGEL B.A., J. Am. Chem. Soc., 124 (2002), 1424.
[10] HANRATH T., KORGEL B.A., Small, 1 (2005), 717.
[11] KIM P., LIEBER C.M., Science, 286 (1999), 2148.
[12] ZHU Y.W., ZHANG H.Z., SUN X.C., FENG S.Q., XU J., ZHAO Q., XIANG B., WANG R.M., Appl. Phys. Lett., 83 (2003), 144.
[13] PARK W.I., YI G.G., KIM M., PENNYCOOK S.J., Adv. Mater., 14 (2002), 1841.
[14] CHEN Y.W., JIANG S.H., SHAO B.X., WANG W., WANG R.C., J. Electron Mater., 37 (2008), 176.
[15] JUNG S., YOO J., KIM Y., KIM K., DHUNGEL S.K., YI J., Mater. Sci. Eng. C, 26 (2006), 813.
[16] LEE W., JEONG M.C., KIM M.J., MYOUNG J.M., Phys. Lett., 370 (2007), 345.
[17] ZHANG J., YANG Y.D., JIANG F.H., LI J.P., Physica E, 27 (2005), 302.
[18] XIONG S.L., XI B.J., WANG W.Z., WANG C.M., FEI L.F., ZHOU H.Y., QIAN Y.T., Cryst. Growth Des., 6 (2006), 1711.
[19] FU H.Z., LI H.Y., JIE W.Q., YANG L., J. Cryst. Growth, 289 (2006), 440.
[20] MATHUR S., SHEN H., SIVAKOV V., WERNER U., Chem. Mater., 16 (2004), 2449.
[21] LU X.M., FANFAIR D.D., JOHNSTON K.P., KORGEL B.A., J. Am. Chem. Soc., 127 (2005), 15718.
[22] JIANG Y., WU Y., ZHANG S.Y., XU C.Y., J. Am. Chem. Soc., 122 (2000), 12383.
[23] FENG S.Q., YU D.P., ZHANG H.Z., BAI Z.G., DING Y., J. Cryst. Growth, 209 (2000), 513.
[24] MA D.D.D., LEE C.S., AU F.C.K., TONG S.Y., LEE S.T., Science, 299 (2003), 1874.
[25] LEE S.T., ZHANG Y.F., WANG N., TANG Y.H., BELLO I., LEE C.S., CHUNG Y.W., J. Mater. Res., 14 (1999), 4503.
[26] LEE S.T., WANG N., ZHANG Y.F., TANG Y.H., MRS Bull., 24 (1999), 36.
[27] ZHANG Y.F., TANG Y.H., WANG N., LEE C.S., BELLO I., LEE S.T., J. Cryst. Growth, 197 (1999), 136.
[28] CUMMINGS P.T., COCHRAN H.D., SIMONSON J.M., MESMER R.E., KARABORNI S., J. Chem. Phys., 94 (1991), 5606.
[29] TANG Y.H., PEI L.Z., CHEN Y.W., GUO C., Phys. Rev. Lett., 95 (2005), 116102.
[30] PEI L.Z., TANG Y.H., ZHAO X.Q., CHEN Y.W., GUO C., J. Appl. Phys., 100 (2006), 046105.
[31] YANG Y.H., WU S.J., CHIU H.S., LIN P.I., CHEN Y.T., J. Phys. Chem. B, 108 (2004), 846.
[32] YOSHIDA T., TAKEYAMA S., YAMADA Y., MUTOCH K., Appl. Phys. Lett., 68 (1996), 1772.

Received 8 October 2008
Revised 9 November 2009

Materials Science-Poland, *Vol. 28*, *No. 1*, *2010*

Fabrication of yttria stabilized zirconia nanoparticles by the reverse microemulsion method for SOFC applications

S. VATANSEVER[1], F. ÖKSÜZÖMER[1*], S. NACI KOÇ,
M. SOMER[2], H. DELIGÖZ[1], M. A. GÜRKAYNAK[1]

[1]Department of Chemical Engineering, Istanbul University, 34320, Istanbul, Turkey

[2]Department of Chemistry, Koç University, 34450, Istanbul, Turkey

Yttria stabilized zirconia powders were synthesized by the reverse microemulsion method. Powders were calcined from 600 °C to 1000 °C and sintered at 1450 °C. Crystalline properties and microstructure of samples were characterized by X-ray diffraction and scanning electron microscopy, respectively. Oxygen ionic conductivity was measured by electrochemical impedance spectroscopy. Sizes of yttria stabilized zirconia particles calcined at 1000 °C are lower than 100 nm, and approximately, 1 μm grain was obtained after sintering at 1450 °C.

Keywords: *yttria stabilized zirconia; chemical synthesis; electron microscopy; ionic conductivity*

1. Introduction

High performance ceramic material, yttria stabilized zirkonia (YSZ) is the most commonly used as an electrolyte. YSZ is an important material for oxygen sensors, oxygen pumps, catalysts and fuel cells. When doped with 8 mol % of yttria, the structure is stabilized and this modified electrolyte shows high ionic conductivity as well as high thermal stability, and has excellent mechanical properties. In recent decades, there has been great interest in the conductivity of YSZ based electrolytes [1–4].

Many different methods exist for the preparation of nanosized YSZ such as sol -gel technique, precipitation, spark-plasma sintering and hydrothermal synthesis leading to final products differing in properties. Therefore, the choice of preparation route and particular heat treatment strongly influence the synthesis, sintering and properties of the YSZ powders, and are very important for optimizing the properties of the YSZ electrolytes.

[*]Corresponding author, e-mail: fufu@istanbul.edu.tr

In recent years, a relatively new microemulsion method has been used for preparation of ultrafine powders [5, 6]. It was invented in the 1980s as an effective process of fabrication of nanoparticles. Microdroplets containing solved reactants act as nanoreactors in the microemulsion system. When the droplets collide with each other, the precipitation occurs. A powder of spherical particles, with a uniform size distribution and good dispersibility can be obtained. The size and shape of reverse micelles would change with the molar ratio of the water to surfactant value (w_0), the type of ions and electrolyte concentration in the aqueous phase, and the type of co-surfactant used. Droplets with spherical, ellipsoidal, rod-like, cylindrical, or planar shapes would appear, depending on the w_0 value or the electrolyte concentration in the aqueous phase. By further addition of the aqueous solution or by increasing the ionic strength in aqueous phase, a bicontinuous structure or normal micelles might even be formed [5–11]. Fang et al. [6] obtained ultrafine YSZ using 1-hexanol–water–CTAB microemulsion system. Ultrafine powders of tetragonal crystalline zirconia having particle diameters of 40–70 nm were obtained. Ma et al. [7] employed cyclohexane–water–TritonX-100 –hexyl alcohol system to fabricate ultrafine spherical particles of 30–40 nm tetragonal zirconia powders. Tai et al. [8] obtained yttria stabilized zirconia by the reverse microemulsion technique using a system of water–CTAB–hexanol.

The aim of this study was to investigate the fabricate nanoscale uniform YSZ powder by the reverse microemulsion method. The microstructure and ionic conductivity of YSZ material were studied in detail.

2. Experimental

Reverse micelles were fabricated by using Triton X-100 (Merck, 99%) as a surfactant, hexanol (Merck, 98%) as co-surfactant, isooctane (Sigma, 99.5%) as an oil phase. $ZrOCl_2 \cdot 8H_2O$ (Merck, 99.9%), $Y(NO_3)_3 \cdot 6H_2O$ (Sigma, 99.9%) were used as inorganic precursors. Two organic phases containing equal amounts of Triton X-100, hexanol and isooctane were prepared separately. The mixture of inorganic salts containing 8 moles of Y_2O_3–92% mol ZrO_2 was dissolved in an appropriate amount of water and added dropwise into one of organic phases. NH_4OH was added dropwise into the other organic phase. Finally, these two transparent microemulsions were mixed together and refluxed. The mixture was magnetically stirred at 80 °C for 3 h. The stability of the mixture was broken by adding ethanol and then centrifuging. The residue was washed with ethanol repeatedly until no Cl^- ions could be detected with $AgNO_3$ solution, and sample was then dried in an oven at 180 °C for 12 h. The dried product was calcined at 1000 °C for 6 h. After calcination, the powders were ground using a ball milling system (Retsch-S100).

Differential and thermogravimetric analyses (DTA/TGA) of the dried product were carried out using a thermal analyzer (Linseis) at thea heating rate of 10 °C/min in air. The phase identification was performed by X-ray diffraction (XRD) using a Rigaku D/max-2200 diffractometer with CuK_α radiation (λ = 0.15418 nm) and, operat-

ing at 30 kV, 20 mA. The crystallite size of the calcined powders was calculated by the X-ray line broadening technique, performed on the (220) diffraction pattern of YSZ, using the Scherer equation: $D_{XRD} = (0.9\lambda)/(\beta\cos\theta)$, where D_{XRD} is the crystallite size (nm), λ is the radiation wavelength (0.15418 nm), θ is the diffraction peak angle and β is the corrected half-width at a half-maximum (FWHM).

In order to further investigate high temperature behaviour of this 8YSZ powder, a disk-shaped sample of 15 mm diameter and 1 mm thickness was obtained by cold isostatic pressing (CIP) at 95 MPa. Subsequently, the sample was sintered at 1450 °C for 6 h. The morphology of powders calcined at 1000 °C and of discs sintered at 1450 °C were examined using a scanning electron microscope (SEM, JEOL 6335F). The oxygen conductivity measurements were performed on a sintered sample using a two-probe ac impedance analyzer (Solartron 1260 FRA and 1296 interface) at 300 °C. Pt wire and Pt paste (Alfa Aesar) were used as electrode materials. The data were analysed in the impedance mode using a computer software (Z view, Scribner Associates).

3. Results and discussion

TGA and DTA curves of the analysed samples are shown in Fig. 1. The exothermal peak at 325 °C in DTA, and the rapid weight loss between 260 °C and 380 °C in TGA can be attributed to the decomposition of organic compounds [7]. The endothermal peak at 468 °C should be due to the dehydration process of $Zr(OH)_x$. The crystallization of zirconia began with a slight exothermal peak at around 550 °C.

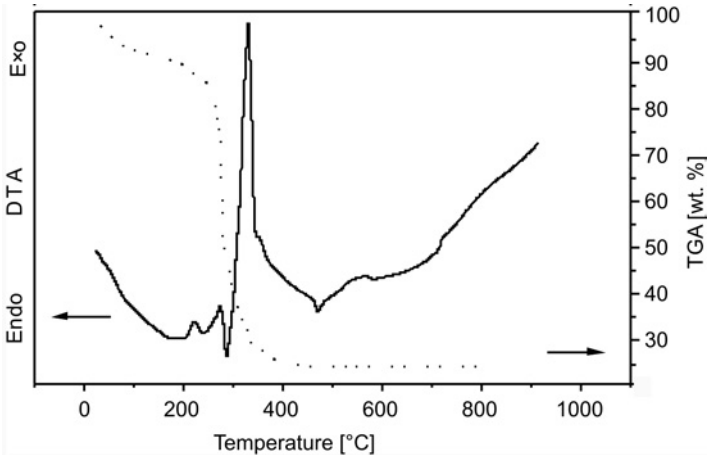

Fig. 1. The TGA/DTA curves of as prepared YSZ samples

The XRD patterns of samples calcined between 600 and 1000 °C are shown in Fig. 2, and those sintered at 1450 °C are in Fig. 3. The peak intensities increase and

get sharper as the calcination temperature increases. The YSZ sample shows the cubic phase of ZrO_2 Tetragonal and cubic phases can be distinguished with the characteristic (212) peak of tetragonal phase. This peak, as reported previously, has not been observed for any cubic samples [1, 2, 5, 12, 13]. The peaks observed in this study are attributed to the cubic phase, and it can therefore be concluded that the Y_2O_3 was completely dissolved in the zirconia structure.

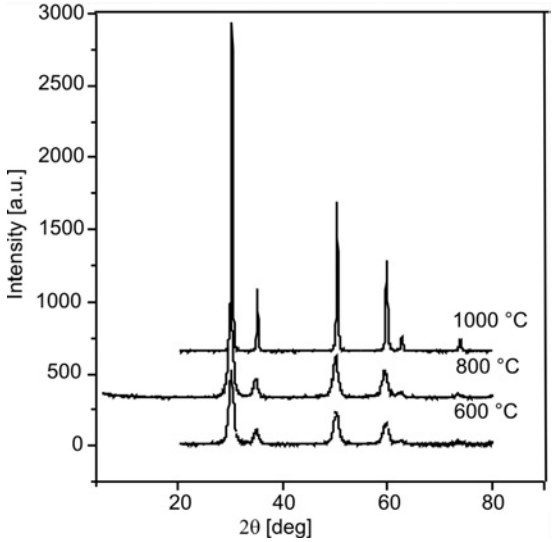

Fig. 2. XRD results in YSZ samples calcined at 600, 800 and 1000 °C

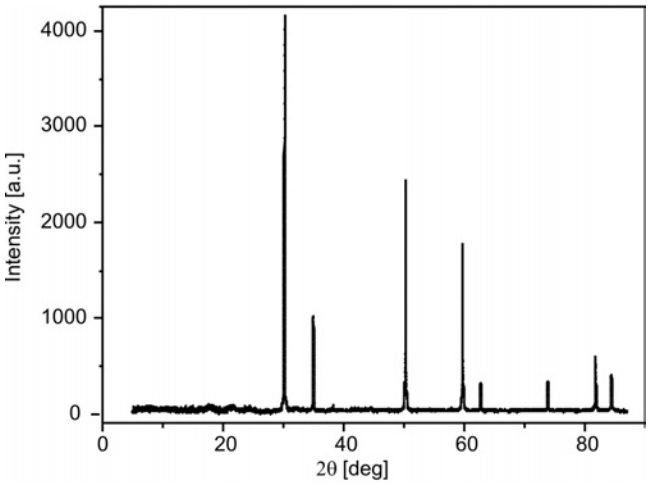

Fig. 3. XRD results for an YSZ sample sintered at 1450 °C for 6 h

The lattice constants of YSZ were found to be 5.135 Å and 5.133 Å, for samples calcined at 1000 °C and sintered at 1450 °C, respectively. It is generally known that

the lattice parameter of ZrO_2 increases with Y_2O_3 doping because ionic radii of Y^{3+} are higher than those of Zr^{4+}. When the coordination number is equal to 8, the ionic radii are 0.84 Å in Zr^{4+} and 1.02 Å in Y^{3+} [14].

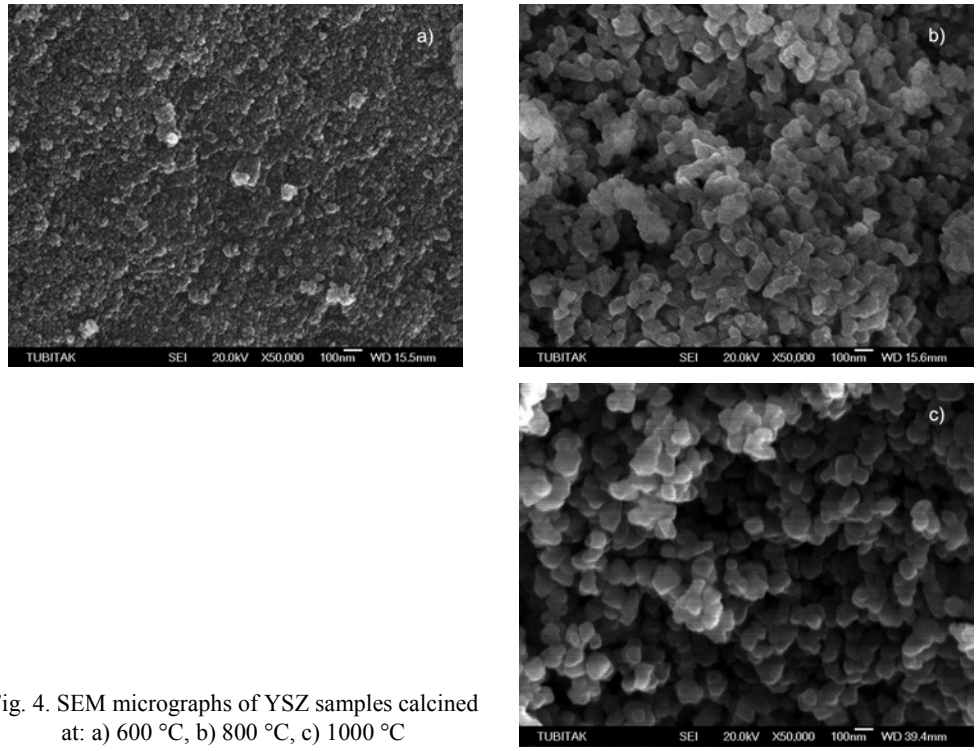

Fig. 4. SEM micrographs of YSZ samples calcined at: a) 600 °C, b) 800 °C, c) 1000 °C

SEM results of as-prepared samples are shown in Fig. 4. The particle size of powders calcined between 600 °C and 1000 °C increased. In the case of 600 °C calcinations, mean particle size is below 50 nm and it is approximately 80 nm at 1000 °C . The crystal sizes were calculated from the Debye–Scherer equation and they were found to be 10.6, 11.5, 30.9 nm for calcination temperatures of 600, 800 and 1000 °C, respectively. Consistently, both crystallite and particle sizes increased with the temperature of calcinations. It is also observed that all the calcined powders prepared with reverse-micelles have uniform and spherical particles. Powders calcined at 1000 °C were subjected to cold isostatic pressing at 95 MPa and were sintered at 1450 °C. The density of sintered discs was measured by the Archimedes method and calculated as being 92% of the theoretical density. The SEM data of the disc-shape sintered sample can be seen in Fig. 5. Sintering at 1450 °C resulted in sub-micrometer grain size. In addition, grains are uniform in size and shape, and there is no evidence of exaggerated grain growth. The grain uniformity of sintered samples is important for stable conductivity of YSZ exposed to high temperature. As is seen from Fig. 5, most of the particle sizes are approximately 1 μm after sintering.

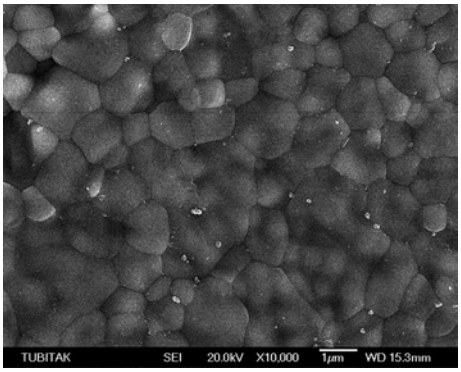

Fig. 5. SEM micrograph of an YSZ sample sintered at 1450 °C

The complex impedance plot of YSZ at 300 °C is shown in Fig. 6. It was observed that grain boundary resistivity is lower than the grain interior resistivity. The ratio of these resistivities is 1.62. It is generally believed that the grain boundary resistivity is higher than the grain interior resistivity of YSZ. In other words, in the case of YSZ, the key factor determining conductivity is the grain boundary resistivity.

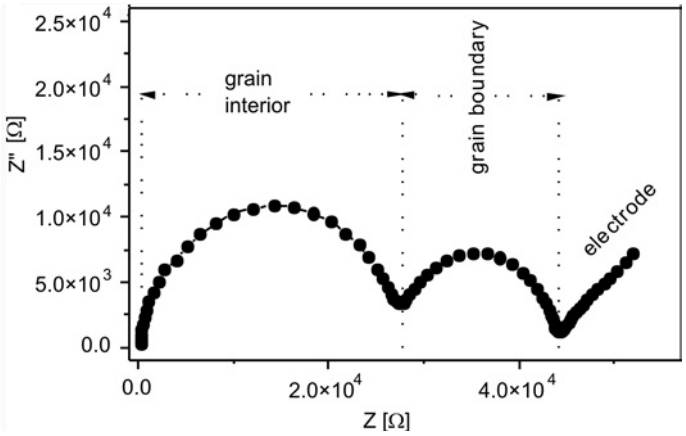

Fig. 6. An impedance plot of a sintered YSZ disc at 300 °C

Higher grain resistivity is attributed to bigger grain size and thicker grain interior. The small grain size, e.g. 1 μ, of YSZ obtained from microemulsions is associated with a thinner grain interior. Therefore it provides higher grain boundary conductivity. It has been reported that the conductivity of YSZ increases when grains are of submicron size. It can be increased by a factor of almost 2 with nanoscale grains [15–17].

4. Conclusions

8YSZ powder was synthesized by the reverse microemulsion method. Uniform, nanosized YSZ particles of the sizes brlow 100 nm were obtained. Most of the

particles were observed to be around 1 μm in grain size when sintered at 1450 °C, which would be suitable for thin film electrolyte applications.

Acknowledgement

The study has been supported by the Istanbul University Research Fund, Project No. 469/27122005 as wellas by the by TUBITAK Project No. 105M051

References

[1] POLITOVA T.I., IRVINE J.T.S., Solid State Ionics, 176 (2004), 153.
[2] KONDOH J., TOMII Y., KAWACHI K., J. Am. Ceram. Soc., 86 (2003), 2093.
[3] SINGHAL S.C., KENDALL K., H*igh Temperature Solid Oxide Fuel Cells: Fundamentals, Design and Applications*, Elsevier, Oxford, 2003.
[4] HUNG I-M., HUNG D-T., FUNG K-Z., HON M-H., J. Europ. Ceram. Soc., 26 (2006), 2627.
[5] LI L., SHI L., CAO S., ZHANG Y., WANG Y., Mater. Lett., 62 (2008), 1909.
[6] FANG X., YANG C., J. Colloid Interface Sci., 212 (1999), 242.
[7] MA T., HUANG Y., YANG J.L., HE J.T., ZHAO L., Mater. Design, 25 (2004), 515.
[8] TAI C.Y., HSIAO B.Y., CHIU H.Y., Mater. Lett., 61 (2007), 834.
[9] PILENI M.P., J. Exp. Nanosci., 1 (2006), 13.
[10] ERIKSSON S., NYLEN U., ROJAS S., BAUTONNET M., Appl. Cat. A, General, 265 (2004), 207.
[11] HUANG Y., MA T., YANG J.L., ZHANG L.M., HE J.T., LI H.F., Ceram. Int., 30 (2004), 675.
[12] HE T., HE Q., WANG N., J. Alloy Comp., 396 (2005), 309.
[13] KUO C.W., LEE Y.H., FUNG K.Z., WANG M.C., J. Non-Cryst. Solids, 351 (2005), 304.
[14] TAYLOR M.A., ARGIRUSIS C., KILO M., BORCHARDT G., LUTHER K.-D., ASSMUS W., Solid State Ionics, 173 (2004), 51.
[15] HAN M., TANG X., YIN H., PENG S., J. Power Sources, 165 (2007), 757.
[16] MONDAL P., KLEIN A., JAEGERMANN W., HAHN H., Solid State Ionics, 118 (1999), 331.
[17] CHEIKH A., MADANI A., TOUATI A., BOUSETTA H., MONTY C., J. Eur. Ceram. Soc., 21(2001), 1837.

Received 5 November 2008
Revised 22 May 2009

Materials Science-Poland, *Vol. 28*, *No. 1*, *2010*

Characterization of electrochemically deposited thin Mo–O–C–Se film layers

N. DUKSTIENE[1*], L. TATARISKINAITE[2], M. ANDRULEVICIUS[3]

[1]Department of Physical Chemistry, Kaunas University of Technology, LT-50254 Radvilenu pl. 19, Kaunas, Lithuania

[2]AB Achema, LT-55550, Jonavos r., Ruklos sen., Jonalaukio k., Lithuania

[3]Institute of Physical Electronics of Kaunas University of Technology, LT-50131 Savanoriu pr. 271 Kaunas, Lithuania

The paper reports on the composition, morphology and optical properties of thin Mo–O–C–Se film electrodeposited onto SnO_2–glass substrate (R = 292 Ω/cm^2). The composition of films was estimated based on X-ray photoelectron spectroscopy and Fourier transform infrared spectral analysis. Structural elements similar to molybdenum oxides and/or hydroxides, $MoSe_2$, Se and SeO_2 were identified on the surface and in the bulk of the electrodeposits. The studies of surface morphology by scanning electron microscopy and atomic force microscopy showed long-sized wires distributed over all the surface. The optical absorption studies revealed the films to be highly absorptive ($10^4\alpha$ cm^{-1}) with a direct band transition and the bang gap energy of 1.75 eV.

Keywords: *thin film electrodeposition; XPS; $MoSe_2$; selenium; molybdenum oxides and hydroxides; optical properties*

1. Introduction

A rapid progress in modern technologies induces the search for new compounds possessing advanced physicochemical properties. Thin films of molybdenum chalcogenide and oxide based compounds present considerable interest for many research fields including electrocatalysis [1, 2], fuel cells [3] and batteries [4]. This interest is related to the capacity of Mo atoms to assume various oxidation states, depending on the methods of syntheses. Therefore, there is continuous research into exploring new processing techniques which fulfil low-cost, scalability and production criteria. Electrodeposition satisfies all these conditions and hence accelerated efforts are made in

[*]Corresponding author, e-mail: nijole.dukstiene@ktu,lt

many laboratories [4–6]. Thin amorphous MoO_yS_x films, applied in lithium battery cells, have been successfully obtained by the electrodeposition technique [4]. The cathodic deposition of complex Mo_4O_{11}–MoS_2 systems has been described in the paper [5].

Results regarding simultaneous electrodeposition of Mo and Se onto SnO_2 coated glass electrodes from sodium citrate solutions have been recently reported [6]. Mirror-like, uniform and adhesive thin Mo–O–C–Se films were electrodeposited on the surface of SnO_2–glass electrode. However it was impossible to characterize the crystallographic structures of the deposits: the only lines corresponding to polycrystalline SnO_2 have been observed in X-ray diffractograms. Therefore, in this paper we continue our recent investigations and characterize electrodeposited Mo–O–C–Se films. Our motivation for characterizing these films is driven by their potential as promising candidates for photovoltaic applications. To establish the suitability of these thin films as a photovoltaic material, it is essential to study the distribution and nature of compounds present in the deposits and their optical properties.

2. Experimental

A commercially available ISE-2 three-electrode system with a PI-1-50 potentiostat coupled to a PR-8 programmer (ZIP, Russia) was adopted to deposit thin films on commercially available SnO_2 coated glass plates. The thickness of the SnO_2 layer was 1 μm and the sheet resistance was 292 Ω/cm^2. A plate was fixed in a stainless steel cylindrical holder, and a copper stick served as the contact. The working area of the SnO_2 plate was 4.5 cm^2. The conducting SnO_2 coated glasses were cleaned with acetone and then cleaned chemically in 0.1 M HNO_3, rinsed with distilled water and dried. A standard $KCl_{(sat)}$|AgCl, Ag electrode was used as the reference electrode. A platinum wire with the diameter of 1.0 mm and the active surface area of 12.5 cm^2 was used as the counter electrode.

Electrolyte solutions, pH = 8.3, containing H_2SeO_3 of fixed concentrations (0.0005 M), Na_2MoO_4 (0.05 M) and sodium citrate (0.22 M) were employed. The chemicals used were $Na_2MoO_4{\cdot}2H_2O$, H_2SeO_3 and $Na_3C_6H_5O_7{\cdot}2H_2O$, all of analytical grade. Each solution was freshly prepared with twice distilled water. The deposition was carried out at a constant potential E = –1.0 V and the deposition temperature of 15 ± 1 °C. The deposition time was 100 min. The thickness of the electrodeposited film was measured with a GAERTNER L115 laser ellipsometer (USA, Gaertner Scientific Corporation). The morphology of deposits was examined with a JOEL-SEM-1C25S (Japan) scanning electron microscope (SEM). For each sample, 10 surface points were examined.

An atomic force microscope Nanotop-206 (Microtestmashines Belarus) operating in a contact state mode was used to investigate the roughness of the surface. It used a silicon cantilever, with the force constant of 5.0 N/m. The image processing and analysis of the scanning probe microscopy data were performed using the Windows based program Surface View, Version 1.0.

X-ray photoelectron spectroscopy (XPS) and Fourier transform infrared (FTIR) spectroscopy experiments were performed to obtain information on the exact composition of electrodeposits. X-ray photoelectron spectra were obtained with a Kratos Analytical XSAM800 spectrometer. The energy scale of the spectrometer was calibrated using Au $4f_{7/2}$ and Cu $2p_{3/2}$ Ag $3d_{5/2}$ peaks. The source was operating in aluminium anode mode: non-monochromatized AlK_α with the photon energy of 1486.6 eV. The O 1s, C 1s, Mo 3d, and Se 3d spectra were determined at the 20 eV pass energy (0.05 eV energy increment) of the hemispherical analyser. The fixed analyser transmission (FAT) mode was used. The resolution of the instrument was 0.2 eV. The charging effects were corrected by referring the binding energies to that the of C 1 s line at 284.8 eV. The relative atomic concentrations of oxygen, carbon, molybdenum, and selenium were calculated from an appropriate peak area with respect to the sensitivity factors, using the original Kratos software. The XPSPEAK41 software was employed for the peak fitting procedure [7]. The Shirley background with Lorenz to Gauss rate 0:100 and a symmetric line shape for all peaks were used. Assignation of the signals to specific structures or given oxidation states of elements analysed was done by comparison with data available from the NIST standard Reference Database 20, Version 3.4 [8] and to literature references. All samples were scanned as received – without undertaking ion beam surface cleaning procedure.

Mo–O–C–Se deposits were scraped with a non-metallic scraper, and then scrapings were solid-mixed with KBr, modulated into pellets and investigated by the FTIR spectroscopy to determine the chemical structure and binding configuration of a thin film. Spectra were recorded on a Perkin–Elmer FTIR system spectrum GX with the resolution of 1 cm^{-1} in the 4000–400 cm^{-1} spectral range.

UV–Vis spectrometry was used to investigate the optical behaviour of the films. UV–Vis spectra were recorded with a UV/Visible Spectronic Genesis spectrophotometer in the range 200–800 nm. The absorption spectra of thin films were recorded using an identical transparent tin oxide coated glass plate as a reference, and the values of the optical absorption coefficient α were not corrected for the reflectance from the film surface. The optical bandgap energy, E_{og}, was obtained by studying the absorption edge behaviour.

3. Results and discussion

3.1. XPS analysis

The composition of deposits has been determined by the XPS measurements. The recorded Mo 3d, Se 3d, O 1s and C 1s core level (CL) spectra are shown in Figs. 1–4, respectively. The line shape of measured Mo 3d CL spectrum (Fig. 1) is highly asymmetric, indicating the presence of mixed oxidation states of Mo. The molybdenum oxidation state was estimated by deconvolution of the peaks in the Mo 3d region. The spin–orbit splitting between Mo $3d_{5/2}$ and Mo $3d_{3/2}$ signals was set to 3.14 eV and the integral intensity of the doublet peaks was fixed before the fitting procedure was run.

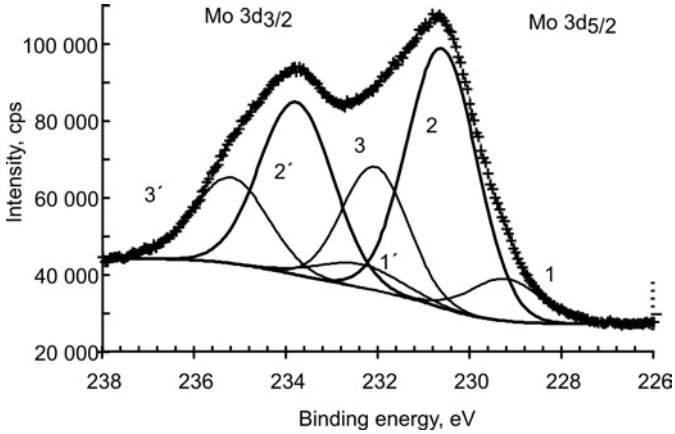

Fig. 1. Mo 3d XPS spectra from Mo–O–C–Se film electrodeposited on a SnO_2–glass plate: crosses – acquired data, dashed line – fitted curve, 1– $MoSe_2/Mo_2C$, 2 – $MoO_2/Mo_x(OH)_y$, 3 – MoO_3

Using the deconvolution technique, the best fit was obtained by resolving the spectrum into three pairs of Gaussian peaks, where 1, 2 and 3 represent the Mo $3d_{5/2}$ level of different molybdenum oxidation states. The primed peaks represent Mo $3d_{3/2}$ levels, respectively. The core level binding energy values of Mo $3d_{5/2}$ signals were compared with the values of corresponding states reported in the literature. When molybdenum is bound to selenium, the characteristic Mo $3d_{5/2}$ signal appears at E_b = 228.8 eV [9, 10]. It should be noted that the Mo $3d_{5/2}$ signal with a binding energy of 228.6 eV is typical of Mo^{2+} in Mo_2C [11, 12]. According to literature data, the energy values of the Mo $3d_{5/2}$ photoelectrons for MoO_2 and MoO_3 are ca. 229 eV [13–17] and 232 eV [13–15, 17, 18], respectively. A peak with the binding energy of 230.8 eV is midway between those Mo $3d_{5/2}$ values assigned to MoO_2 and MoO_3 and corresponds to the Mo^{5+} state associated with the mixture of oxides and hydroxides, mainly in the form of Mo^{4+} and Mo^{5+} [14, 19, 20].

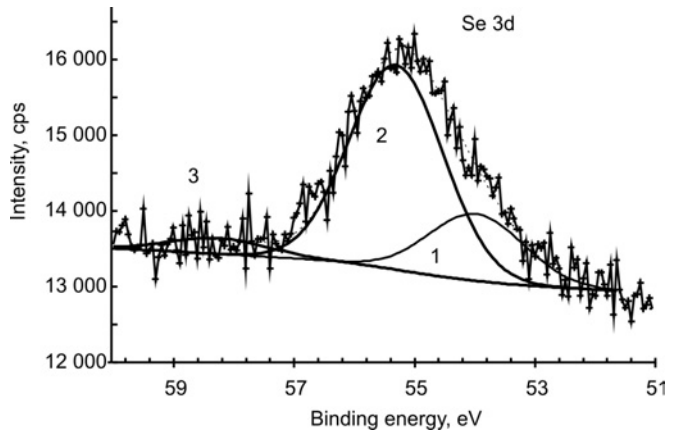

Fig. 2. Se 3d XPS spectra from Mo–O–C–Se film electrodeposited on a SnO_2–glass plate: crosses – acquired data, dashed line – fitted curve, 1– $MoSe_2$, 2 – Se, 3 – SeO_2

The Se 3d spectrum (Fig. 2) of a film sample shows the total peak envelope with the binding energy of 56 eV, which could be resolved into three peaks at 53.8, 55.9 and 58.3 eV. The Se 3d spectrum displaces the expected $MoSe_2$ peak with the binding energy 53.8 eV [21, 22]. This peak and the position of the signal from Mo $3d_{5/2}$ level at E_b = 228.7 eV strongly suggest the presence of $MoSe_2$ in thin film layers. It is known that the binding energy of elemental selenium is about 55.4 eV [22, 23]. A small peak centred at 58.3 eV indicates that the film layer may contain SeO_2 [24, 25].

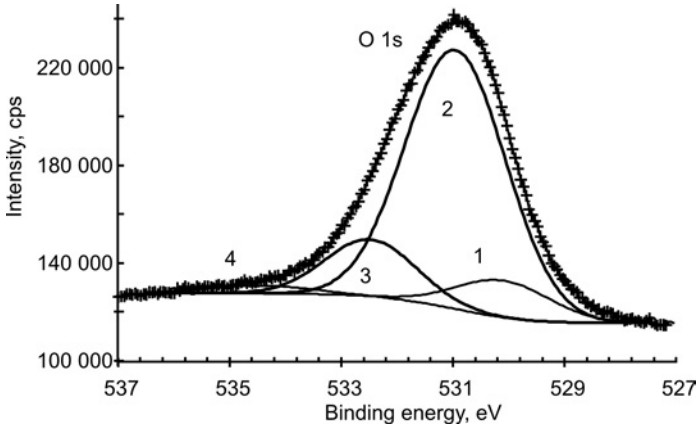

Fig. 3. O 1s XPS spectra from Mo–O–C–Se film electrodeposited on a SnO_2–glass plate: crosses – acquired data, dashed line – fitted curve, 1 – Mo–O, 2 – Mo–OH, 3 – H_2O, 4 – C=O

The O 1s spectrum (Fig. 3) can be deconvoluted into four contributions with the binding energies of 530.2, 531.1, 532.5 and 534.5 eV. The peaks at around 530 eV are known to result from oxides, and the peak at 532 eV may be assigned to the structural

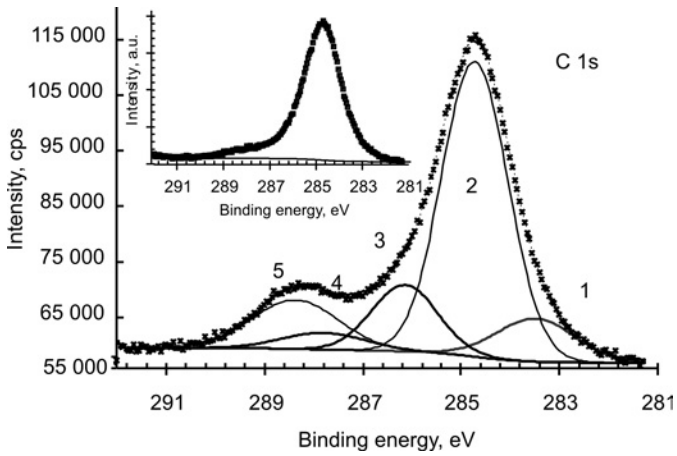

Fig. 4. C 1s XPS spectra from Mo–O–C–Se film electrodeposited on a SnO_2–glass plate: crosses – acquired data, dashed line – fitted curve, 1– Mo_2C, 2 – C–C or C–H, 3 – C–O, 4 – C=O, 5 – O– C=O. Inset: pure SnO_2–glass plate

water while the peak at 531 eV to hydroxide [17, 19]. Besides, the plot areas of peaks corresponding to oxides are small compared with the area of hydroxides. This observation suggests that the films consist largely of hydroxides. The O 1s peak component at 534.5 eV corresponds to C=O from citrate [26].

Figure 4 shows the C 1s region, after curve fitting to discriminate the various contributions. A very small peak at 283.6 eV is assigned to molybdenum carbide, in agreement with results published in the literature [15, 27]. The presence of small quantities of carbides, probably Mo_2C, has been observed in Mo–Co alloy electrodeposition from the sulphate–citrate medium [14]. The main signal at 284.8 eV corresponds to C–C and C–H bonds. Signals at 286.24, 287.88 and 288.46 eV are consistent with the presence of C–O, C=O and O–C=O groups, respectively. These bands mainly originate from the citrate ion [26]. The XPS data are summarised in Table 1.

Table 1. XPS results derived from the curve fitted deconvoluted spectra

Element	Atomic percentage, %	Binding energy, eV	FWHM, eV	NIST data	Oxidation state	Attribution to structural element found in	Relative percentage, %
Mo $3d_{5/2}$	20.81	229.2	1.8	228.3	4+/2+	$MoSe_2$. Mo_2C	10.18
		230.6	1.8	230.6	4+/5+	$MoO_2/Mo_x(OH)_y$	62.0
		232.0	1.7	232.6	6+	MoO_3	27.82
Se 3d	1.52	53.8	1.8	53.5	2–	$MoSe_2$	24.18
		55.9	1.8	55.7	0	Se	70.59
		58.3	1.9	58.0	4+	SeO_2	5.23
O 1s	60.19	530.1	2.0	530.8		Mo−O	7.14
		531.1	2.0	531.8		$Mo_x(OH)_y$	78.42
		532.3	1.9	532.8		H_2O	12.61
		533.7	2.0	535.1		C=O	1.83
C 1s	17.48	283.6	1.9	282.7		Mo_2C	10.19
		284.8	1.6	284.4		C−C, C−H	59.43
		286.24	1.6	286.4		C−O	13.33
		287.9	2.0	287.8		C=O	4.21
		288.5	2.0	289.0		O−C=O	12.84

3.2. FTIR studies

FTIR spectrum (Fig. 5) has been analysed in terms of the vibration of isolated molecular units and based on literature IR data on SeO_2 [28–31] and molybdenum oxides [32–36]. The results (cf. Table 2) strongly suggest that some selenium oxide exists in thin film layers, whereas weak absorption peaks indicate that the SeO_2 concentration is small.

The most pronounced absorption peak at 741 cm^{-1} is clearly related to Mo(IV) oxides [32–34]. The symmetric stretching modes of the terminal Mo=O bond of crystalline MoO_2 and crystalline MoO_3 appears at 985 cm^{-1} [35] and 990 cm^{-1} [36], respec-

tively. The terminal double bond peak downshift with respect to MoO_2 and MoO_3 might be assigned to the presence of OH groups in the structure of molybdenum oxide.

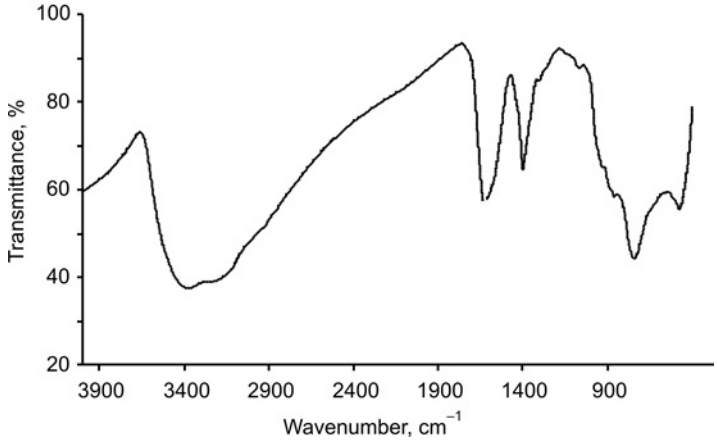

Fig. 5. FTIR spectrum of the Mo–O–C–Se film recorded in 4000–400 cm^{-1} spectral region

Table 2. Results from the analysis of FTIR spectrum of Mo–O–C–Se film

Wavenumber, cm^{-1}	Assignment
474	ν_s (Se–O–Se)
741	ν (Mo–O)
866	ν_{as} (O–Mo–O)
927	(Mo=O)
1065	(Se–O)
1398	COO^-
1621	δ (H–O–H), COO^-,
3373	ν (Mo–OH),

As a result of this interaction, a broad band assigned to the stretching mode ν_{OH} of adsorbed water molecule and OH groups linked in the form of Mo–OH is present at 3373 cm^{-1}.

3.3. Morphology of a thin film layer

Thin film layers with the thickness of 110 ± 60 nm were electrodeposited on a SnO_2–glass plate. Visually, the as-deposited films are mirror-like and coloured in a brown tint. Thin film layers were analysed without further treatment other than rinsing with distilled water. The micrograph of a thin film layer shown in Fig. 6 indicates

long-sized wires distributed all over the surface. AFM images (Fig. 7) show that wires cover the surface well, without any cracks and pinholes.

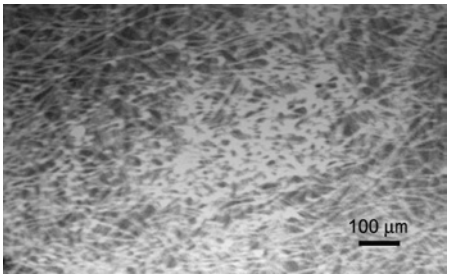

Fig. 6. SEM image of the Mo–O–C–Se film electrodeposited on a SnO_2–glass plate

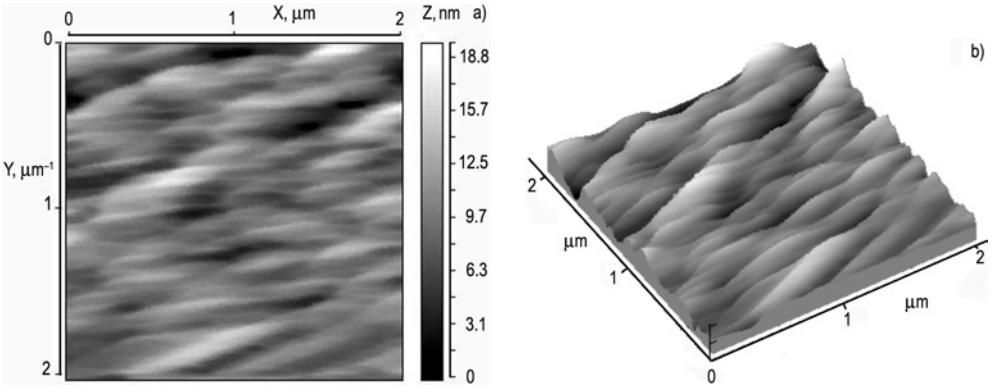

Fig. 7. AFM images of the Mo–O–C–Se film electrodeposited on a SnO_2–glass plate; a) 2D topography, b) 3D topography

3.4. UV–Vis studies

The optical absorption of the film was studied in the wavelength range from 200 to 800 nm without accounting for reflection and transmission losses. The UV–Vis transmittance spectrum of freshly deposited thin Mo−O–C–Se film is shown in Fig. 8. The transmission shows an intense minimum in the UV region. A less intense minimum in the red region is also observed. An absorption edge of the film is observed at 670 nm and lies in the visible wavelength range. Transmittance values higher than 100% between 670 and 800 nm can be ascribed to the fact that the Mo–O–C–Se film surface is smoother and less light-scattering than the SnO_2 surface used as a reference for optical transmission measurements.

The optical absorption coefficient α for the wavelength range near and below the absorption edge is found to have a value of 3.98×10^4 cm^{-1}. The variation of optical density with wavelength was analysed to find the nature of transition involved and the optical bandgap energy (E_{og}).

The variation of the optical absorption coefficient α near the absorption edge follows the power law in the form

$$\alpha = \frac{B(E - E_{og})^n}{E} \tag{1}$$

where: E is the photon energy, $h\nu$, E_{og} is the bandgap energy of the system, B is the function of the density of states near the conduction and valence band edges. The value of n is 2 for allowed direct transition and 1/2 for the allowed indirect transition.

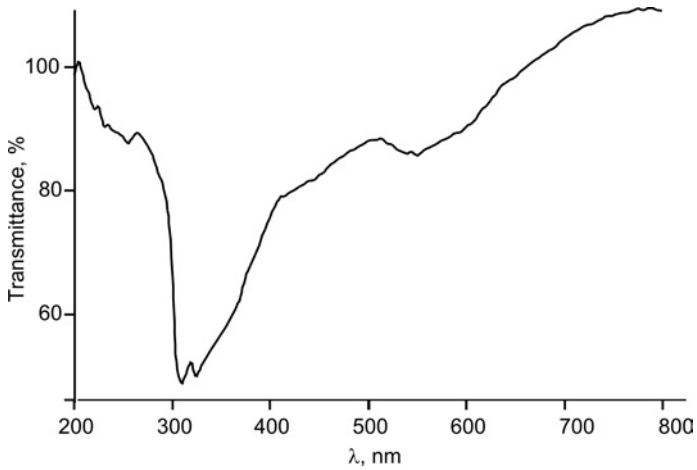

Fig. 8. UV-Vis spectrum of the Mo–O–C–Se film electrodeposited on a SnO_2–glass plate

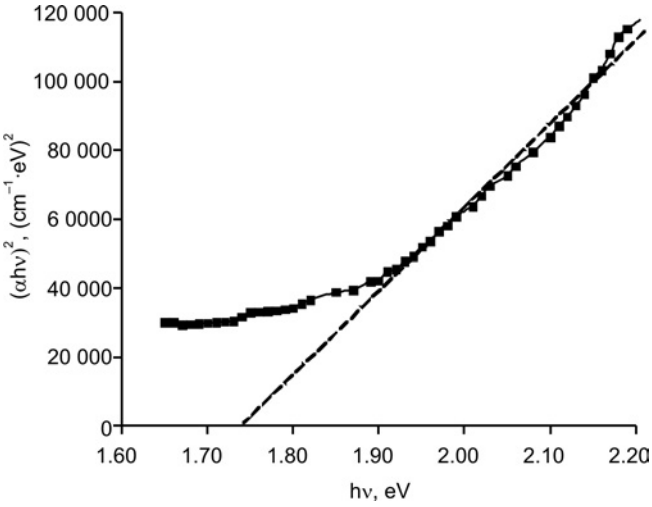

Fig. 9. Plot of $(\alpha h\nu)^2$ versus photon energy of the Mo–O–C–Se film electrodeposited on a SnO_2–glass plate

High α values suggest the existence of direct bandgap transition. The type of optical transition in the Mo–O–C–Se film has been determined from the dependence of $(\alpha h\nu)^2$ on the photon energy (Fig. 9). A linear rise near the absorption edge confirms the direct nature of transition. Extrapolating the linear part of the plot towards zero absorption, the intercept with the energy axis determines the optical bandgap energy (E_{og}) value of 1.75 eV.

4. Conclusions

XPS analysis confirms that Mo–O–C–Se film layers are heterogeneous and are composed of $MoSe_2$, Se, SeO_2 and molybdenum oxides and hydroxides. XPS core level analysis revealed the presence of Mo^{4+}, Mo^{5+} and Mo^{6+} oxidation states.

FT-IR spectra confirmed the hydrous nature of Mo–O–C–Se film.

SEM and AFM revealed the film surface to be of device-grade quality, and to be free of any pinholes.

Optical studies showed that thin Mo–O–C–Se film has a high optical absorption coefficient and direct band to band type optical transition. The bandgap energy E_{og} equals 1.75 eV.

References

[1] BOLIVAR H., IZQUIERDO S., TREMONT R., CABRERA C.R., J. Appl. Electrochem., 33 (2003), 1191.
[2] BEATO P., BLUME A., GIRGSDIES F., JENTOFT R.E., SCHOEGL R., TIMPE O., TRUNSCHE A., WEINBERG G., BASHER Q., HAMID F.A., HAMID S.B.A., OMA E., MOHOD SALIM L., Appl. Catal. A, 307 (2006), 137.
[3] US Patent No. 6214090, 2005.
[4] YUFIT V., NATHAN M., GOLODNITSKY D., PELED E., J. Power Sources, 122 (2003), 169.
[5] NAGIRNYI V.M., APOSTOLOVA R.D., BASKIEVICH A.S., SHEMBEL E.M., Russ. J. Appl. Chem., 76 (2003), 1438.
[6] DUKSTIENE N., TATARISKINAITE L., Polish J. Chem., 80 (2006), 1715.
[7] XPSPEAK41 software, http://www.phy.cuhk.edu.hk/~surface/ , April 2005.
[8] National Institute of Standard and Technology, NIST on line Databases. X-ray Photoelectron Spectroscopy Database. http://www.sr.data.nist.gov/xps (Accessed March 2007)
[9] GRIM S.O., MATIENZO L.J., Inorg. Chem., 14 (1975), 1014.
[10] BOLIVAR H., IZQUIERDO S., TREMONT R., CABRERA C.R., ASSMANN L., BERNEDE J.C., DRICI A., AMORY C., HALGAND E., MORSLI M., Appl. Surf. Sci., 246 (2005), 159.
[11] ZHANG Y., XIN Q., RODRIQUEZ-RAMOS I., GUERRERO-RIUZ A., Mat. Res. Bull., 34 (1999), 145.
[12] BRIGGS D., SEAH M.P., *Practical Surface Analysis*, Vol. 1, Wiley, New York, 1990.
[12] ZACH M.P., INAAZU K., NG K.H., HEMMINGER J.C., PENNER R.M., Chem. Mater., 14 (2002), 3206.
[14] GOMEZ E., PELLICER E., VALLES E., J. Electroanal. Chem., 580 (2005), 238.
[15] RUIZ F., BENZO Z., QUINTAL M., GARABOTO A., ALBORNAZ A., BRITO J.L., Appl. Surf. Sci., 252 (2006), 8695.
[16] DI G.G.D., SELMAN J.R., J. Electroanal. Chem., 559 (2003), 31.
[17] BARTOLOME J.F., DIAZ M., REQUENA J., MOYA J.S., TOMSIA P., Acta Mater., 47 (1999), 3891.
[18] PATISSIER-BLONDEAU V., DOMENICHINI B., STEINBRUN A., BOURGEOIS S., Appl. Surf. Sci., 175 (2001), 674.

[19] NAKAYAMA M., KOMATASU H., OZUKA S., OGURA K., Electrochim. Acta, 51 (2005), 274.
[20] SANCHES L.S., DOMINIGUES S.H., MARINO C.E.B., MASCARO L.H., Electrochem. Commun., 6 (2004), 543.
[21] BASOL B.M., KAPUR V.K., LEDIDHOLM C.R., MINICH A., HALANI A., First WCPEC, Dec. 5–9, 1994, Hawaii.
[22] SALTAS A., PAPAGEORGOPOULOS C.A., PAPAGEORGOPOULOS D.C., TONTI D., PETTENKOFER C., JAEGERMAN W., Thin Solid Films, 389 (2001), 307.
[23] SURODE P.R., RAO K.J., HEGD M.S., RAO C.N.R., J. Phys. C, 12 (1979), 4119.
[24] DIMITRIEV Y., YORDANOV ST., LAKOV L., J. Non-Crystal. Solids, 293 (2001), 410.
[25] IWAKURO H., TATSUYMA C., ICHIMURA J., Appl. Phys., 21 (1982), 9463.
[26] CHONGDAR S., GUNASEKARU G., KUMAR P., Electrochim. Acta, 50 (2005), 4655.
[27] LECLERCQ G., KAMAL K., LAMONIER J.F., FEIGENBOUM L., MALFOY P., LECLERCQ L., Appl. Catal. A, Gen., 121 (1995), 169.
[28] NAKAMOTO K., IR *Spectra of Inorganic and Coordination Compounds*, Mir, Moskva, 1991 (in Russian).
[29] SIMON A., PACTZOLD R., Anorg. Allg. Chem., 301 (1959), 246.
[30] BRABSON G.D., ANDREWS L., MARSDEN C., J. Phys. Chem., 100 (1996), 16487.
[31] CHEN Y.-W., LI L., D'ULIVO A., BELZILE N., Anal. Chim. Acta, 577 (2006), 126.
[32] NIU Z.J., YAO S.B., ZHOU S.M., J. Electroanal. Chem., 455 (1998), 205.
[33] GOMEZ E., PELLICER E., VALLES E., J. Appl. Electrochem., 33 (2003), 245.
[34] MELTS G., LINSEED CH., GOTTSCHALK R., DIETER M., FIND J, HEREIN D., JAEGR J., UCHIDA Y., SCHOLL R., J. Mol. Catal. A, 162 (2000), 463.
[35] MARTOS M., MORALES J., SANCHES L., J. Mater. Chem., 12 (2002), 2979.
[36] DU X., DONG L., LI CH., LIANG Y., CHEN Y., Langmuir, 15 (1999), 1693.

Received 20 November 2008
Revised 19 June 2009

Materials Science-Poland, *Vol. 28*, *No. 1*, *2010*

Advances in flash memory devices*

C. LUDWIG[1**], M.F. BEUG[2], K.-H. KÜSTERS[3]

[1]Q-Cells SE, OT Thalheim, Sonnenallee 17–21, 06766 Bitterfeld-Wolfen, Germany

[2]Physikalisch-Technische Bundesanstalt (PTB), Bundesallee 100, 38116 Braunschweig, Germany

[3]Conergy SolarModule GmbH, Conergy-Straße 8, 15236 Frankfurt (Oder), Germany

Fundamental challenges are discussed concerning the down-scaling of flash memory cells for mass storage applications. A general scaling issue for all various memory cell concepts is the structuring limit of conventional lithography. Therefore sub-lithographical structuring methods like e.g., double-patterning for future flash chips, have been evaluated. Another common scaling challenge of charge trapping (CT) and floating gate (FG) cells, the two future concurrent flash memory cell concepts, is the introduction of new materials such as high *k* dielectrics. Their implementation into CT and FG cells and the scaling related electrical issues of both cell concepts is also been discussed.

Keywords*: non-volatile memory; flash; charge trapping; SONOS; TANOS; high workfunction gate; high-k dielectric; double patterning; erase saturation*

1. Introduction

Flash memories enjoy a strongly growing demand. Further productivity improvements in the manufacture of flash devices have been achieved by continued scaling, recently formulated as Hwang's law [1]. Currently, the smallest flash products are available in the 50 nm generation. Attempts to increase the density of bits per area have addressed the challenges of designing as well as fabrication of the flash cell.

2. Lithography challenges for future flash technology nodes

Silicon structuring is currently facing a paradigm change. Considerable effort has been spent on techniques to enhance the resolution of the illumination systems, opti-

---

*The paper has been presented at the 3rd Workshop on Hybrid Nanostructured Materials, Prague, 5 November 2007.

**Corresponding author, e-mail: C.Ludwig@q-cells.com

mizing the usage of the 193 nm wavelength. The most prominent one is the successful development of immersion scanners, allowing numerical apertures larger than 1.

In order to achieve smaller features, a next step could be the introduction of extreme UV (EUV) scanners, operating at the wavelength of 13.5 nm. However, this spectral range comes along with a number of challenges as e.g. new diffraction elements, new mask materials and mask manufacturing, new resistance materials, and others. As an alternative, more conservative approach, so called double patterning techniques have been developed recently. These methods consist of process sequences which generate smaller pitches than the ones which are feasible by direct application of lithography tools. Basically, there are two options: one is subsequent printing of even and odd lines of an array separately, i.e. simply applying two subsequent lithography steps with an appropriate displacement. The other option uses spacers along the lines of a single lithography, and thus makes a pair of lines per one lithographically generated line. Figure 1 illustrates a possible process flow. In Figure 2, we show a part of a flash array including the fan out, resulting from this technique.

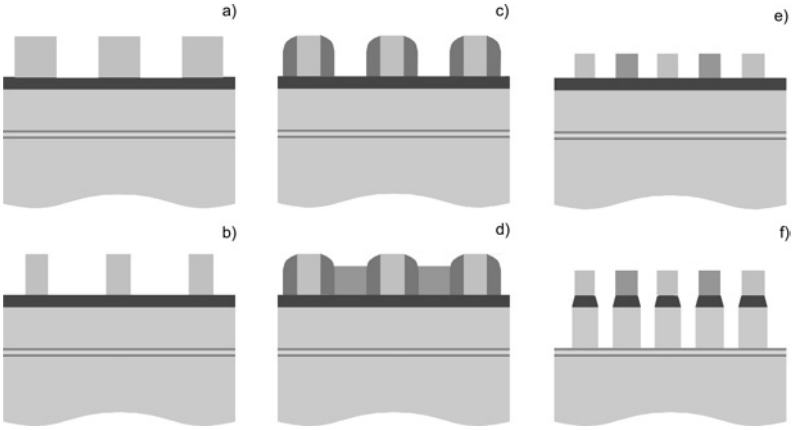

Fig. 1. Schematic process flow for double patterning: lithography defines an array with only half the number of lines, reflecting twice the desired pitch (a). The lines are narrowed by a trim etch (b) and a spacer is placed along the lines (c). The room between the lines is filled by the same material as the lithographically defined lines (d). After removing the spacers (e), a line array is obtained in the desired pitch (f)

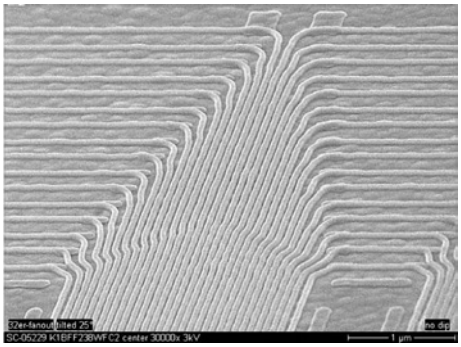

Fig. 2. Wordline fanout of a 36 nm half pitch array

This technique opens a new path to the next flash shrink generations without the need of expensive investment in lithography tools [2].

3. NAND shrink path

The highest bit densities have been continuously achieved in standard floating-gate (FG) NAND flash products, utilizing Fowler–Nordheim (FN) tunnelling for write and erase operations. However, there remain several challenges associated with persistently minimizing the dimensions of conventional floating gates (FG) in flash devices [3].

One of them is the crosstalk between adjacent FG cells [4], caused by the electrostatic interaction of the stored charge of all neighbouring floating gates on the FG and on the channel region of one particular flash cell. There is a significant capacitive coupling between neighbouring flash cells due to the relatively large height of FG poly silicon storage elements. Their height is typically in the order of twice the half-pitch, which is the distance between adjacent cells or even larger. As a result of this cross-talk, the unit elements of a Gbit scale flash memory array can no longer be considered independent.

Luckily, the coupling between adjacent FG is a deterministic effect. It can be treated by appropriate programming algorithms which extrapolate the cross-talk from the data pattern and adjust the amount of injected electrons for the individual flash cells accordingly.

Another challenge to be discussed here is related to the high wordline voltages needed for programming. During programming, selected and unselected wordlines may happen to be direct neighbours. Their difference in voltage becomes a challenge as soon as it reaches the level of the breakdown field strength of the insulating dielectric between them. A brief glance at numerous sub-50 nm flash devices shows that this is becoming a significant issue. The magnitude of the program pulse voltages is determined by two factors: the tunnelling oxide (TOX) thickness and the efficiency of the capacitive voltage transfer from the wordline to the FG body, called the gate coupling ratio [5, 6]. The latter depends on FG cell geometry and dielectric constants of the insulating materials around the FG. The TOX thickness dictates the voltage difference across the TOX barrier in order to achieve FN tunnelling. The data retention requirement of 10 years leads to a typical TOX thickness between 8 and 9 nm, resulting in a voltage difference of 10–13 V between FG and the channel region. With typical values of the gate coupling ratio of 0.5~0.6, wordline voltages typically exceed 20 V. Provided the voltage of an unselected wordline is kept at a half or a third of this value, the dielectric breakdown between selected and unselected wordlines during programming becomes an issue for technology generations below 30 nm. Therefore, the reduction of the programming voltage and the reduction of the FG–FG coupling deserve utmost attention.

Suggestions have been made to reduce the programming voltage by modifying the TOX barrier. Instead of a single SiO_2 layer, a tailored bandgap-engineered tunnelling

barrier can effectively enhance the tunnelling probability at high fields during programming, and still serve as a sufficient tunnelling barrier at low fields, keeping the escape rate low enough for good data retention [7–9]. Whatever material is investigated for this type of bandgap-engineering, it eventually must reach the high and mature quality of SiO_2 with respect to defect level and breakdown voltage.

Another possibility for a reduction of programming voltage is an increased capacitive coupling between control gate and floating gate. This can be achieved by inserting a high *k* material as interpoly dielectric (IPD) between the control gate and floating gate instead of the conventional oxide–nitride–oxide arrangement. Again, high electric breakdown fields and low trap density are important parameters. In addition, a large bandgap is desirable to act as an effective tunnelling barrier. Viable candidate materials are e.g. Al_2O_3 or HfSiO. Figure 3 shows an example of a 48 nm half pitch FG flash with Al_2O_3 IPD. Here, the programming voltage is reduced by 2 V.

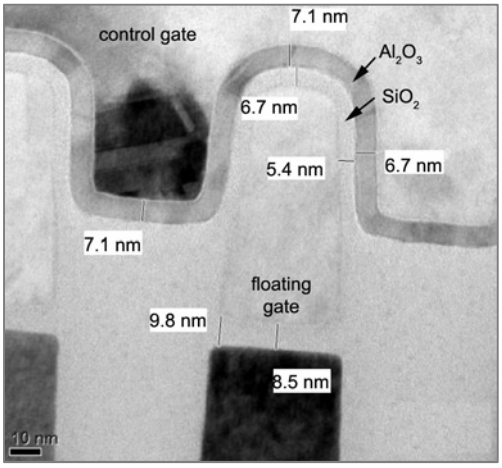

Fig. 3. TEM cross-section of a 48 nm half pitch floating gate flash. Interpoly dielectric between the floating gate and control gate consists of a bilayer of 5 nm oxide and 7 nm Al_2O_3

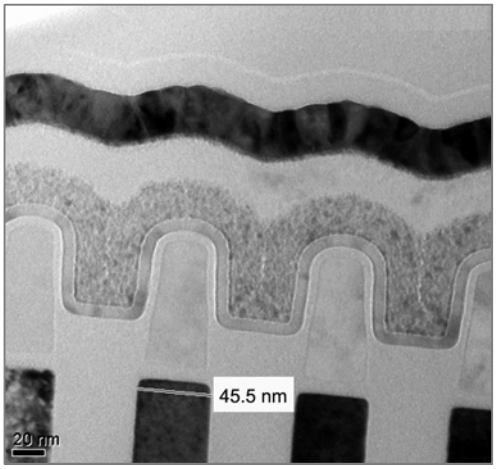

Fig. 4. 48 nm NAND flash with Ti(Si)N metal gate

Another very critical issue in FG flash cells beyond the 40 nm technology generation is the placement of the control gate (CG) plug between the cells [10]. This plug is important for the following two reasons. On the one hand, this increases the capacitive coupling area between CG and FG which allows gate coupling ratios in the range mentioned above. On the other hand, this CG plug electrically shields and therefore reduces the charge crosstalk in wordline direction between adjacent floating gates. But below 40 nm half pitch, there is literally not enough space between the flash cells for the CG plug. With a typical interpoly thickness of 12~15 nm, which has to fit twice into the intercell spacing, not much room is left to insert the CG poly as well. Furthermore, a conventional poly CG will always experience a depletion layer of a few

nm thickness once operating voltages are applied. Therefore a metallic conductor seems desirable. Figure 4 demonstrates such an example with Ti(Si)N as a CG electrode.

4. Charge trapping flash

An elegant way to address all the mentioned concerns in NAND flash is the replacement of the FG poly by a thin charge trapping layer, i.e. a SONOS-type (silicon –oxide–nitride–oxide–silicon) flash cell with proper material selections (see also Fig. 5). Both the programming voltage reduction and the coupling between adjacent flash cells can be significantly reduced in such a kind of charge trapping flash.

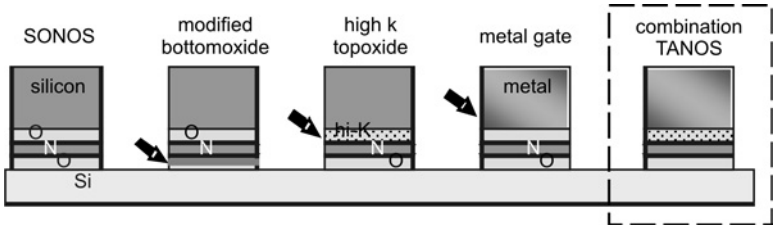

Fig. 5. Material options to improve the properties of a charge trapping flash

Here, the storage layer has a typical thickness in the order of 10 nm or below, much less than a typical FG poly. Therefore, the mere geometry of this stack provides a much smaller coupling area to accommodate an adjacent storage cell, thus minimizing the lateral cross-talk. We have used our Twinflash technology (see below) to quantify the cross-talk between charge trapping cells. Twinflash cells in the buried bit line (BBL) array configuration [16] are planar cells without shallow trench isolation (STI) between adjacent cells (or wordlines). Figure 6 shows the cross-talk analysis on a charge trapping cell with a 6 nm thick Si_3N_4 layer. As the worst case, the two neighbours of an erased flash cell (low V_t) are considered programmed (high V_t). The two neighbour cells are supposed to sit on the same bit line as the erased flash cell. Measured data and simulations show that for an extremely aggressive 20 nm spacing between the adjacent cells, the cross talk creates a V_t shift of 400~500 mV, whereas only a 100 mV cross-talk is observed for a 63 nm spacing. This result is generally also valid for the most commonly used NAND architecture. It shows that cross-talk between neighbouring CT cells cannot be neglected, as sometimes stated in the literature.

The programming voltage in charge trapping (CT) flash cells is generally reduced by the thinner tunnel oxide compared with FG cells (5 nm instead of 8 nm) and the overall smaller electrical thickness of the whole CT dielectric stack. A high *k* dielectric material as the top-oxide is introduced to solve the SONOS erase saturation issue [11] when tunnel oxides thicker than 4 nm are used.

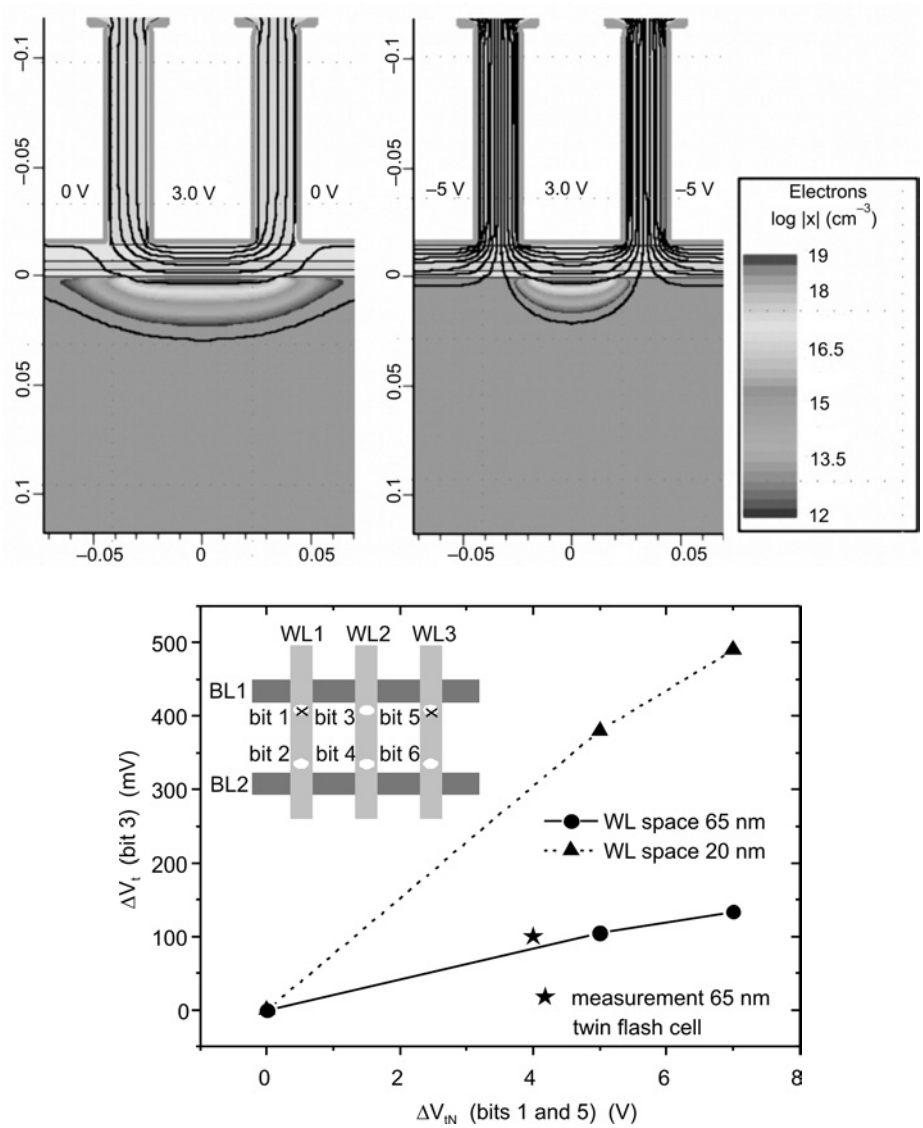

Fig. 6. Crosstalk in Twinflash 63 nm: simulation and measurement. Upperpart shows a sketch of the cross section perpendicular to the channel with simulated electron distributions in the channel. The gates are represented by white areas, with their respective voltages. The black lines are the simulated equipotential lines. The channel region of the central gate is in inversion. Obviously, the effective channel width strongly depends on the gate voltages of the left and the right gate. Lower part shows the simulated threshold voltage shifts in function of the gate potential on the neighbour cells and the measured shift of a 63 nm Twinflash cell array

The erase saturation is a fundamental challenge of the conventional silicon based SONOS flash with symmetrical materials and geometry. In such a standard structure, it turns out that the Vt after erasure cannot go much below the virgin value. The erase

voltage is supposed to create a hole tunnelling current from the substrate through the bottom oxide into the storage nitride. But as soon as the majority of stored electrons is neutralized, electrons out of the gate will start penetrating through the top oxide into the storage nitride and will eventually compensate the hole injection, as indicated in Fig. 7. Using a high *k* dielectric as a top oxide will improve the erase saturation issue compared to a SiO_2 top oxide, due to its lower internal field. Al_2O_3 is the preferred candidate because it acts as an effective tunnelling barrier due to its high bandgap and its relatively low trapping state density.

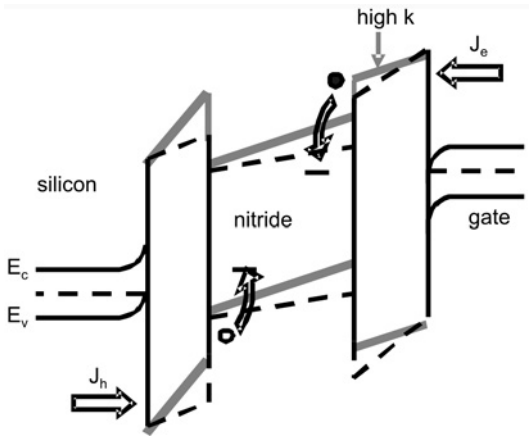

Fig. 7. Erase saturation

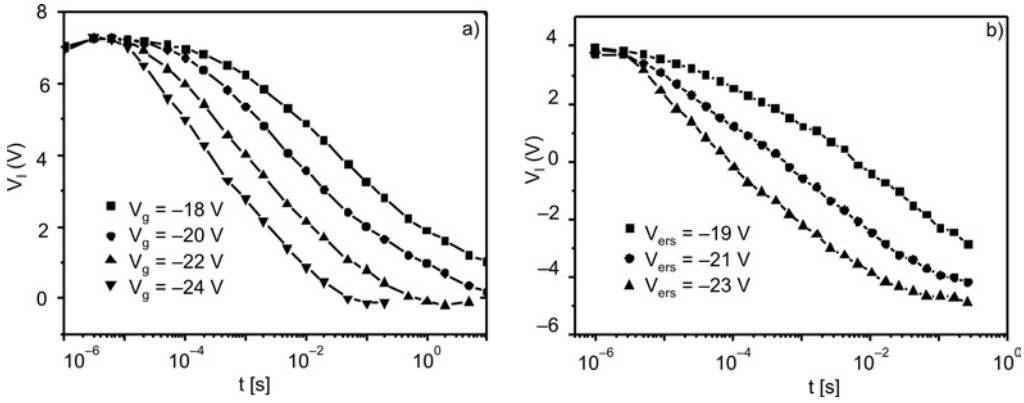

Fig. 8. Erase efficiency for charge trapping flash: a) with Al_2O_3 as high *k* top oxide, b) with Al_2O_3 as high *k* top oxide and in addition TaN as a gate electrode. Sample (b) with the high work function metal gate reaches significantly lower erase V_t. See also K.H.Küsters et al., MSE2008

The most recent developments of charge trapping flash, however, utilize a gate material with a large work function in addition to high *k* top oxide dielectric. Typical materials are TaN, TiN, W, WN [10, 12]. The reason for the need of a high work func-

tion gate is the problem of the erase saturation. If the band offsets of the high *k* top oxide and the work function of the gate material are large enough, tunnelling across the high *k* top oxide will be strongly suppressed, thus eliminating the erase saturation. Figure 8 demonstrates the improvement in erase level for a TANOS charge trapping flash (TaN gate–Al_2O_3 top oxide–Si_3N_4 charge storage–SiO_2 bottom oxide–Si channel) in comparison with a SANOS stack (with standard *n*+ gate instead of the TaN gate).

However, in the TANOS flash, the erase performance and the data retention seem to be two conflicting target parameters. The introduction of Al_2O_3 top oxide turns out to degrade the data retention. This effect can be ascribed to the somewhat lower band-gap compared with SiO_2 and to some detrapping inside the Al_2O_3.

5. Localized charge trapping flash

The usage of trap centres in a dielectric for storing the charge provides an additional advantage over a poly FG flash. Electrically confined local storage of more than one bit per flash cell is feasible if localized charge injection mechanisms are used. Hot electron (CHE) and hot hole injection into a trapping layer like Si_3N_4 are candidates for the write and erase mechanisms, as implemented in NROM™ [13], Twinflash™ [14–16], Mirrorbit™ [17] and other products. A typical process sequence consists of standard ONO deposition as trapping layer, buried bit lines, a standard gate, standard contact and standard metallization.

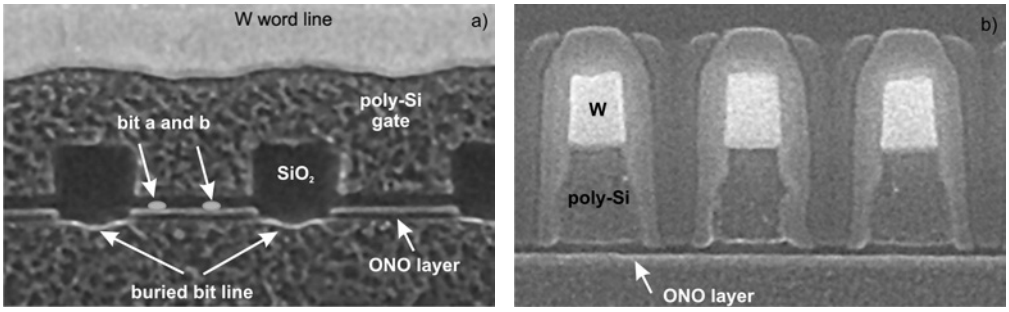

Fig. 9. Cross-section of a Twinflash 63 nm cell, along and perpendicular to the wordline. The wordline consists of a tungsten layer on top of a n type poly. Two charge packets, representing two locally confined bits a and b, can be stored in the nitride film of the oxide–nitride–oxide layer of one flash cell

A cross section of a 63 nm half-pitch Twinflash is shown in Fig. 9. A Twinflash shrink using double patterning should have an asymmetric cell layout geometry, as shown in Fig. 10. Only the width of the MOS channel is reduced, whereas the channel length is kept fixed to accommodate for the high source-drain potential difference during CHE programming. The voltage data of a Twinflash with sub-lithographical dimensions are shown in Fig. 11 and 12 [18]. The flash cells with a width of 45 nm exhibit reasonable programming and erase and can withstand 100 000 cycles without degradation.

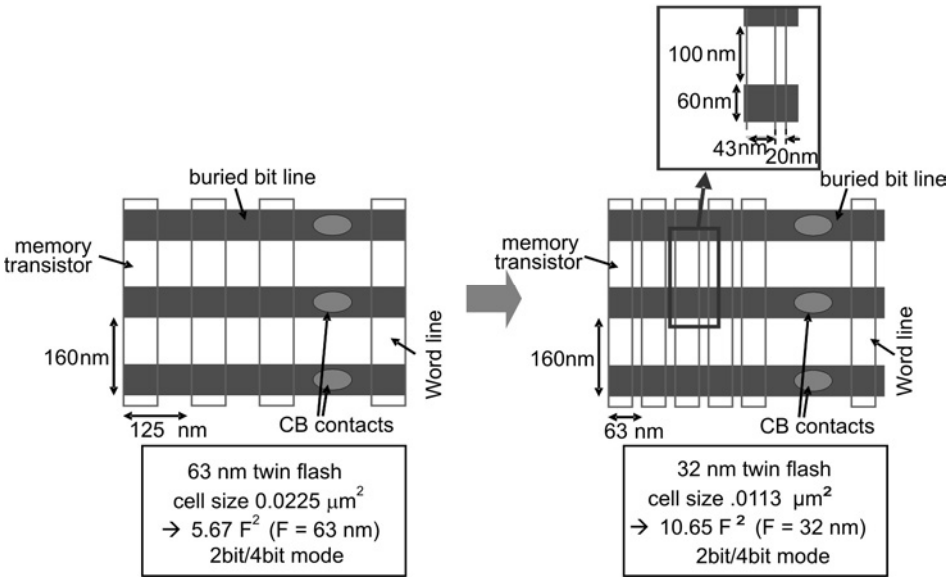

Fig. 10. Sub-lithographical shrink of Twinflash cells

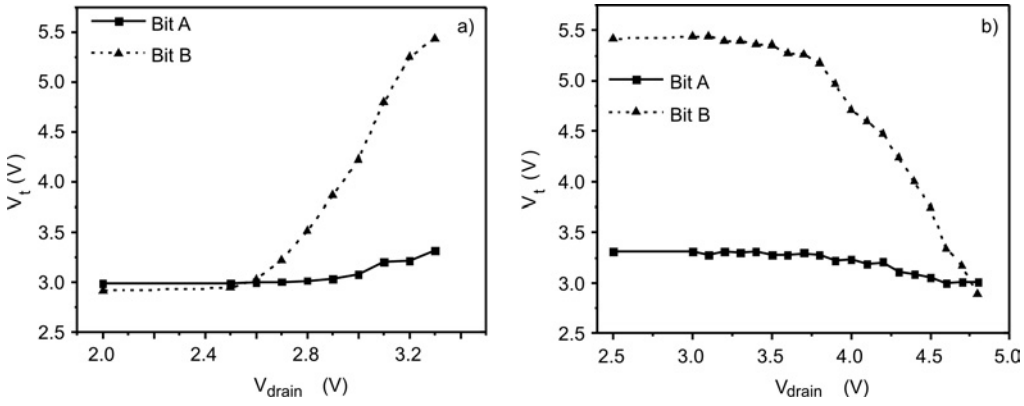

Fig. 11. Electrical results of narrow TwinFlash cells (45 nm width): Programming (a) and erase (b)

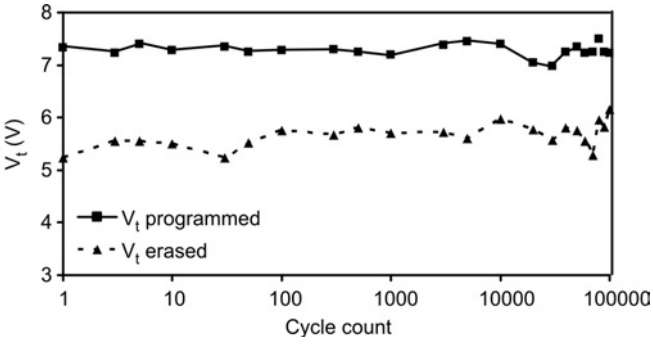

Fig. 12. Dependence of V_t on the cycle count. Narrow cells show good endurance behaviour up to 100 kcycles. The window between programmed and erased state remains without significant degradation

6. Conclusions

Next generations of flash will continuously be scaled down. Lithography being stuck at the 193 nm level is not considered an obstacle, since double patterning methods make sub-lithographical dimensions well below 40 nm accessible.

However, new materials will be needed to ensure robust operation of the flash devices. For both the conventional FG flash and charge trapping flash, high *k* dielectrics with large bandgap and low leakage at high fields need to be developed to a maturity good enough for reliable mass manufacture.

A charge trapping flash will in addition require high work function materials. A complete set of materials which achieve good data retention, good endurance, and good erase and program levels and write speed, is still to be discovered.

Acknowledgements

This work was financially supported by the Federal Ministry of Education and Research of the Federal Republic of Germany (Projects Nos. 01M3167 A and 01M3171 A).

References

[1] HWANG C.-G., International Solid State Circuits Conference, 2 (2002).
[2] BEUG M. F., PARASCANDOLA S., HOEHR T., MUELLER T., REICHELT R., MUELLER-MESKAMP L., GEISER P., GEPPERT T., BACH L., BEWERSDORFF-ARLETTE U., KENNY O., BRANDL S., MARSCHNER T., MEYER S., RIEDEL S., SPECHT M., MANGER D., KNOEFLER R., KNOBLOCH K., KRATZERT P., LUDWIG C., KUESTERS K.-H., Non Volatile Semiconductor Memory Workshop, 9 (2008), 77.
[3] KIM K., CHOI J., Non Volatile Semiconductor Memory Workshop, 21 (2006), 9.
[4] LEE J.-D., HUR S.-H., CHOI J.-D., IEEE Electron Dev. Lett., 23 (2002), 264.
[5] BEZ R., CAMERLENGHI E., CANTARELLI D., RAVAZZI L., CRISENZA G., International Electron Devices Meeting, (1990), 99.
[6] GHETTI A., BORTESI L., VENDRAME L., Solid State Elelctron., 49 (2005), 1805.
[7] LIKHAREV K., Appl. Phys Lett., 73 (1998), 2137.
[8] BLOMME P., AKHEYAR A., VAN HOUDT J., DE MEYER K., International Conference on Memory Technology and Design, (2005), 239.
[9] LUE H.-T., WANG S.-Y., LAI E.-K., SHIH Y.-H., LAI S.-C., YANG L.-W., CHEN K.-C., KU J., KUANG-YEU HSIEH K.-Y., LIU R., LU C.-Y., International Electron Devices Meeting, (2005), 547.
[10] CHAN N., BEUG M. F., KNOEFLER R., MUELLER T., MELDE T., ACKERMANN M., RIEDEL S., SPECHT M., LUDWIG C., TILKE A.T., Non Volatile Semiconductor Memory Workshop, 9 (2008), 82.
[11] BACHHOFER H., REISINGER H., BERTAGNOLLI E., VON PHILIPSBORN H., J. Appl. Phys., 89 (2001), 2791.
[12] LEE C.-H., CHOI J., KANG C., SHIN Y., LEE J.-S., SEL J., SIM J., JEON S., CHOE B.-I., BAE D., PARK K., KIM K., Symposium on VLSI Technology, (2006), 21.
[13] EITAN B., COHEN G., SHAPPIR A., LUSKY E., GIVANT A., JANAI M., BLOOM I., POLANSKY Y., DADASHEV O., LAVAN A., SAHAR R., MAAYAN E., International Electron Devices Meeting, (2005), 539.
[14] STEIN VON KAMIENSKI E. G., ISLER M., MIKOLAJICK T., LUDWIG C., SCHULZE N., NAGEL N., RIEDEL S., WILLER J., KUESTERS K.-H., NVMTS, (2005), 5.

[15] WILLER J., LUDWIG C., DEPPE J., KLEINT C., RIEDEL S., SACHSE J.-U., KRAUSE M., MIKALO R., STEIN VON KAMIENSKI E.G., PARASCANDOLA S., MIKOLAJICK T., FISCHER J.-M., ISLER M., KUESTERS K.-H., BLOOM I., SHAPPIR A., LUSKY E., EITAN B., Symposium on VLSI Technology, (2004), 76.

[16] NAGEL N., OLLIGS D., POLEI V., PARASCANDOLA S., BOUBEKER H., BACH L., MÜLLER T., STRASSBURG M., RIEDEL S., KRATZERT P., CASPARY D., DEPPE J., WILLER J., SCHULZE N., MIKOLAJICK T., KUESTERS K.-H., SHAPPIR A., REDMARD E., BLOOM I., EITAN B., International Symposium on VLSI Technology, Systems and Applications, 90 (2007), 120.

[17] KUO T.H., YANG N., LEONG N., WANG E., LAI F., LEE A., CHEN H., CHANDRA S., WU Y., AKAOGI T., MELIK-MARTIROSIAN A., POURKERAMATI A., THOMAS J., VAN BUSKIRK M., VLSI Circuits, Digest of Techn. Papers (2006), 114.

[18] BEUG M.F., KNOEFLER R., LUDWIG C., HAGENBECK R., T MÜLLER T., RIEDEL S., ISLER M., STRASSBURG M., HOEHR T., MIKOLAJICK T., KUESTERS K.-H., International Conference on Memory Technology and Design (2007), 191.

Received 6 October 2008
Revised 20 July 2009

Materials Science-Poland, *Vol. 28*, *No. 1*, *2010*

Optimization of MFIS structures containing poly(vinylidene-fluoride trifluoroethylene) for non-volatile memory applications

K. HENKEL*, B. SEIME, I. PALOUMPA, K. MÜLLER, D. SCHMEISSER

Brandenburgische Technische Universität, Angewandte Physik-Sensorik,
K.-Wachsmann-Allee 1, D-03046 Cottbus, Germany

In the paper, we report on ways to optimize metal–ferroelectric–insulator–semiconductor (MFIS) stacks in terms of the thickness combination of the ferroelectric and the buffering insulator layers in order to reduce the operation voltage of MFIS based non-volatile memory elements. The stack contains poly(vinylidene fluoride-trifluoroethylene) (P(VDF-TrFE)) as a ferroelectric layer. We discuss the optimization of the deposition of this material in order to produce thin films with high polarization. This must be accompanied by an adapted buffer layer, where reduction of thickness as well as increase of permittivity can be taken into account. We show the results based on capacitance voltage measurements (CV) on MFIS stacks, where SiO_2 and Al_2O_3 of different thicknesses have been used. Furthermore, we perform simulations of the CV characteristics and we are able to quantify the polarization and decline it from the CV curves. We observe for a 120 nm P(VDF-TrFE)/11 nm Al_2O_3 stack in a ±20V CV loop almost saturated polarization values as predicted by the simulations in that way.

Keywords: *P*(*VDF-TrFE*)*, MFIS, non-volatile memory, FeFET*

1. Introduction

Ferroelectric field effect transistors (FeFETs) are considered candidates for future non-volatile and non-destructive readout memory cells [1, 2]. The first attempt of combining the ferroelectricity with a field effect device has been demonstrated in [3]. The physics of the FeFET is described in [4]. The working principle of the device is based on bistable influence of different polarization states inside the ferroelectric insulator on the drain current (refer to Fig. 1a). The substitution of conventional perowskite type ferroelectrics by a polymer type material leads to possible low cost solutions of this kind of a memory cell. Furthermore, FeFETs composed of conven-

*Corresponding author, e-mail: henkel@tu-cottbus.de

tional materials have been shown to work in general but they need expensive high temperature and high oxygen partial pressure processing steps inducing also unintentional and undefined interfacial layers [2, 5]. Poly(vinylidene fluoride trifluoroethylene) P(VDF-TrFE) is an organic ferroelectric material. It is available for spin coating at room temperature after solving it in non-toxic 2-butanone. In this case, the substrates can have well defined buffer layers. The properties of P(VDF-TrFE) have extensively been reviewed in [6]. Recently, attempts at realizing organic FeFETs using P(VDF-TrFE) have been reported [7–9].

In this paper, we will mainly focus on steps to further improve the characteristic of metal–ferroelectric–insulator–semiconductor (MFIS) structures, which contain P(VDF -TrFE) as ferroelectric layers. Comparisons of results of measurements with predictions based on a simulation procedure proposed by Miller and McWorther [4] are discussed. We investigate the preparation procedure of the polymer layer as well as the influence of the buffer layer. We perform capacitance–voltage (CV) measurements on MFIS based structures. Due to the dipole switching of the P(VDF-TrFE) chains, the CV curves show a hysteresis [4] (refer to Fig. 1b), which depends on the maximum applied voltage in the CV loops [9], i.e. on the polarization of the ferroelectric material.

2. Experimental

Preparation. As a copolymer, we use P(VDF-TrFE) in a molar ratio of 70/30. The material was delivered as a film from Piezotech S.A., France. The film was solved in 2-butanone and spin coated onto the substrates. The thickness of the polymer film can be varied considerably, depending on the velocity and the concentration of the solution, as discussed in the results section. Annealing was performed for 2 h at 135 °C, and, for comparison also, samples without annealing were prepared. The thicknesses of the spin coated films were measured with a Taylor–Hobson profilometer (Talystep).

For electrical characterization, MFIS capacitors were fabricated on silicon p-type substrates with (100) orientation and the resistivity 1–20 Ω·cm. As buffer layer, 10–235 nm SiO_2 or 11 nm Al_2O_3 was used. As a top electrode, aluminum was used, which was thermally evaporated through a shadow mask with diameters between 500 μm and 900 μm. The set-up of a MFIS capacitor is shown in Fig. 1b.

The CV measurements were carried out with a LCR-Meter Agilent 4284A at the frequency of 1 MHz with a sweep of 0.1 V/s. Measurements at higher temperatures were performed keeping the sample holder in a common drying oven. All measurements were started in accumulation (negative gate bias) and finished there too, after driving the voltage in the investigated range to inversion and backwards (e.g., from –10 V to 10 V and back again to –10 V, we call this a "±10 V loop", for short). Other intermediate measurements were taken while driving the voltage over the investigated range in a "voltage loop" (e.g. , from –10 V to 10 V and back again).

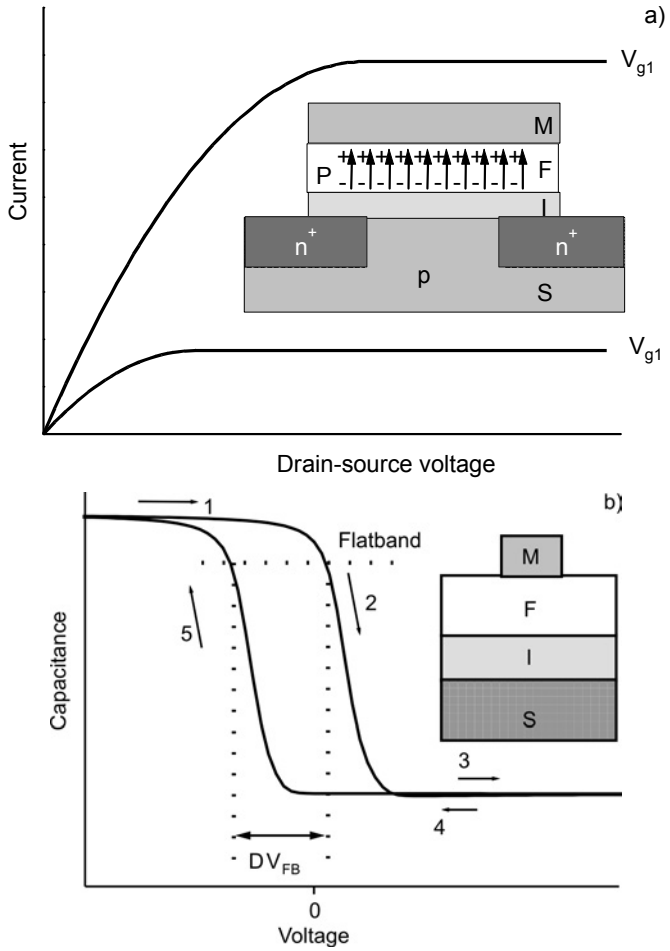

Fig. 1. Set-up and output characteristic of a FeFET. Due to switching of the dipoles after the programming, the current is showing two different states at the same gate voltage (a) as weel as set-up and CV characteristic of a MFIS capacitor (b), with a hysteresis caused by the polarization loop

Modulation. Miller and McWorther developed a method to include the ferroelectric polarization into the characteristics of FeFETs [4]. We use parts of it to model the CV characteristic of MFIS capacitors. The area capacitance of the MFIS system C''_{MFIS} can be written as follows:

$$\frac{1}{C''_{\mathrm{MFIS}}} = \frac{d_{\mathrm{PVDF}}}{\varepsilon_0 \varepsilon_{\mathrm{PVDF}}} + \frac{d_{\mathrm{buf}}}{\varepsilon_0 \varepsilon_{\mathrm{buf}}} + \frac{1}{C''_{\mathrm{S}}} = \frac{1}{C''_{\mathrm{stack}}} + \frac{1}{C''_{\mathrm{S}}} \tag{1}$$

where ε_0 is the permittivity of vacuum, $\varepsilon_{\mathrm{PVDF}}$ and $\varepsilon_{\mathrm{buf}}$ are the relative electric permittivities of the ferroelectric and the buffer layers, while d_{PVDF} and d_{buf} are their thick-

nesses. C''_S is the area depletion capacitance calculated from the derivative $d\sigma_S/d\phi_S$ of the semiconductor surface charge σ_S, which follows the same function of the silicon surface potential ϕ_S as that known for the CV characteristic of the MIS system[10]. The gate voltage V_g can then be written as

$$V_g = \phi_S - \frac{\sigma_S}{C''_{stack}} + V_{MS} - P(E_{PVDF})\frac{d_{PVDF}}{\varepsilon_0 \varepsilon_{PVDF}} \tag{2}$$

where V_{MS} is the work function difference between metal and semiconductor, C''_{stack} is the insulator capacitance calculated by the two first terms in Eq. (1), and P is the dipole polarization, which depends on the electric field E_{PVDF}

$$E_{PVDF} = \frac{-[\sigma_S + P(E_{PVDF})]}{\varepsilon_0 \varepsilon_{PVDF}} \tag{3}$$

in the ferroelectric and its history. The saturated polarization hysteresis $P^{\pm}_{sat}$ is defined by

$$P^{\pm}_{sat} = \pm P_S \tanh\left[\frac{\pm E_{PVDF} - E_c}{2\Delta}\right] \tag{4}$$

where P_S is the spontaneous polarization (i.e., the saturation polarization), E_c is the coercive field and Δ is a hysteresis loop parameter, being a function of the ratio of the remanent and saturated polarization. The dipole polarization at step t is then calculated by a numerical integration using the data known at step $t - 1$:

$$P(E_{PVDF}(t)) = P(E_{PVDF}(t-1)) + \left[(E_{PVDF}(t) - E_{PVDF}(t-1))\frac{d}{dE_{PVDF}}P(E_{PVDF}(t-1))\right] \tag{5}$$

The term $E_{PVDF}(t)$ is then eliminated by using Eq. (3). Furthermore, dP/dE_{PVDF} is a function of dP_{sat}/dE_{PVDF}, P_{sat}, P and P_S as:

$$\frac{dP^{\pm}}{dE_{PVDF}} = \left\{1 - \tanh\left[\sqrt{\frac{P - P_{sat}}{\xi P_S - P}}\right]\right\}\frac{dP^{\pm}_{sat}}{dE_{PVDF}} \quad \text{with} \quad \begin{array}{ll} \xi = 1 & \text{for } \dfrac{dE_{PVDF}}{dt} > 0, \\ \xi = -1 & \text{for } \dfrac{dE_{PVDF}}{dt} < 0 \end{array} \tag{6}$$

Knowing the actual polarization, the electric field E_{PVDF} and the gate voltage V_g can be determined from Eqs. (3) and (2), respectively, and the CV characteristic is given for every point of the loop. For further details refer to [4].

Data obtained by fitting methods which use this procedure will be shown in the paper. Additionally, we also use a simplified method to compare the results of measurements in a relative way being therefore more qualitative. As a value of the hystere-

sis of the CV loop we define the voltage window at flat band condition (ΔV_{FB}, refer to Fig. 1b), which is also called a memory window. Assuming, that this shift is caused by the dipole charges due to the polarization, ΔV_{FB} is then used to calculate the surface charge density N, which is a more qualitative value of the polarization

$$P \propto N = \frac{\Delta V_{FB}\, \varepsilon_0 \varepsilon_{PVDF}}{q d_{PVDF}} \tag{7}$$

where q is the elementary charge.

3. Results and discussion

3.1. Phase transition

Here, we establish whether the CV hysteresis is or is not controlled by the bistable polarization and not by charges, which are injected into the buffer or the polymer layer. As a first test, we perform CV measurements of reference samples without P(VDF-TrFE) and do not observe any hysteresis. Then, CV loops at elevated temperatures are recorded and we find a decrease in the flatband voltage window, while the hysteresis totally vanishes at temperatures around 100 °C (Fig. 2a) indicating a phase transition from the ferroelectric to the paraelectric phase. In Figure 2b, this effect is shown for two samples of different P(VDF-TrFE) thicknesses on a 100 nm SiO_2/Si substrate. For both samples the flatband voltage shift is reduced to almost zero values at ca. 100 °C. Furthermore, by analyzing the accumulation capacitance of the CV loop we estimate the temperature dependence of the dielectric constant. For P(VDF-TrFE) with more than 50% VDF content, the phase transition was found to be of thermodynamically first order [6, 11]. A classical theory (Landau theory) delivers the Curie –Weiss law describing the temperature dependence of the reciprocal permittivity near first order transition [6, 11, 12] as

$$\frac{1}{\varepsilon'} \propto \frac{\pm(T_0 - T)}{C_i} \tag{8}$$

where the sign (±) is positive for temperatures lower than the phase transition temperature (the Curie temperature, $T < T_c$) and negative for temperatures above it ($T > T_c$). C_i are the Curie constants ($i = 1$ for $T < T_c$, $i = 2$ for $T > T_c$). T_0 is not exactly the Curie temperature [6, 12] and in the case of a first order transition it is smaller than T_c [12]. Figure 2c shows the temperature dependence of the reciprocal permittivity for the same samples as in Fig. 2b. From the slope of these plots we determine the values of C_1 of around 1000 K. This is in the same order of magnitude as in other papers [11, 13, 14], but our values are higher by a factor of 1.5 to 2. Here we have to state, that the permittivity disperses with the VDF content as well as with the frequency [6].

The CV loops are recorded at 1MHz, while the corresponding values published elsewhere [11, 13, 14] are observed at lower frequencies.

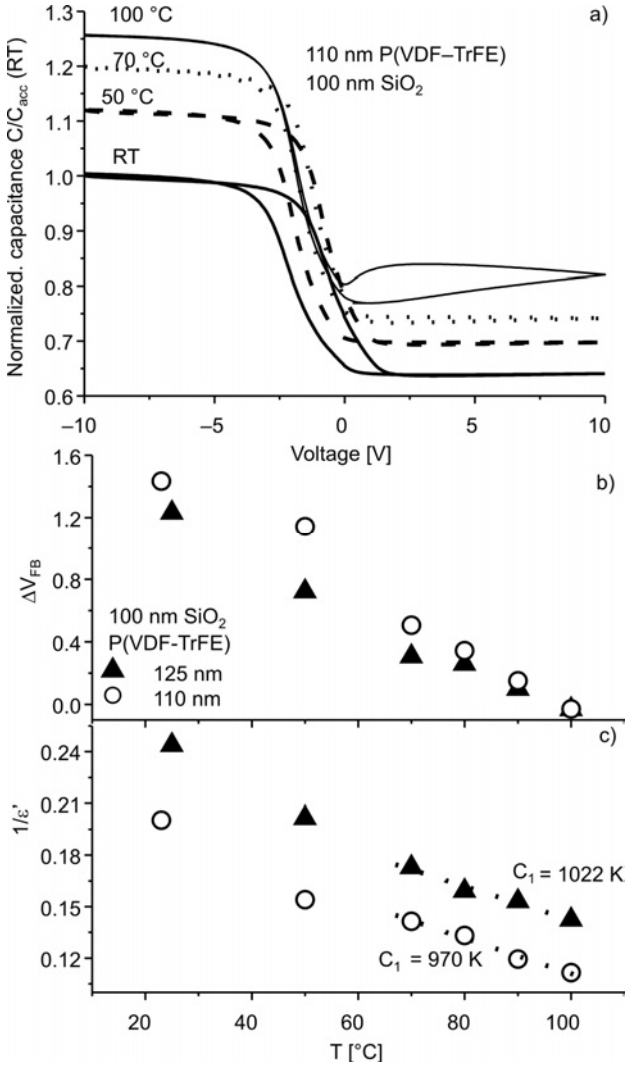

Fig. 2. CV curves of a 110 nm P(VDF-TrFE)/100nm SiO_2 stack at room temperature (RT) (a), the values of the capacitance are normalized to the accumulation capacitance (i.e. C_{Stack}) at room temperature; and flatband voltage shift (b) and the reciprocal permittivity (c) in dependence on temperature for a stack with 100 nm SiO_2 and 125 nm (filled triangle) or 110 nm (open circles) P(VDF-TrFE)

Furthermore, other VDF contents (52–55%, [11, 13, 14]) compared to our samples (70%) were used, and much thicker samples (11–100 μm in [13, 14]) have been analyzed. It was shown that the value of the C_1 constant increased as the layer thickness was reduced to 100 nm [11].

3.2. Optimization of the sample preparation

3.2.1. Polymer thickness, spin coating

In order to reduce the operation voltage of a memory device containing a P(VDF -TrFE) layer, due to its high coercive field (47–100 MV/m [6, 15]), the thickness of the ferroelectric layer should be downscaled below 100 nm.

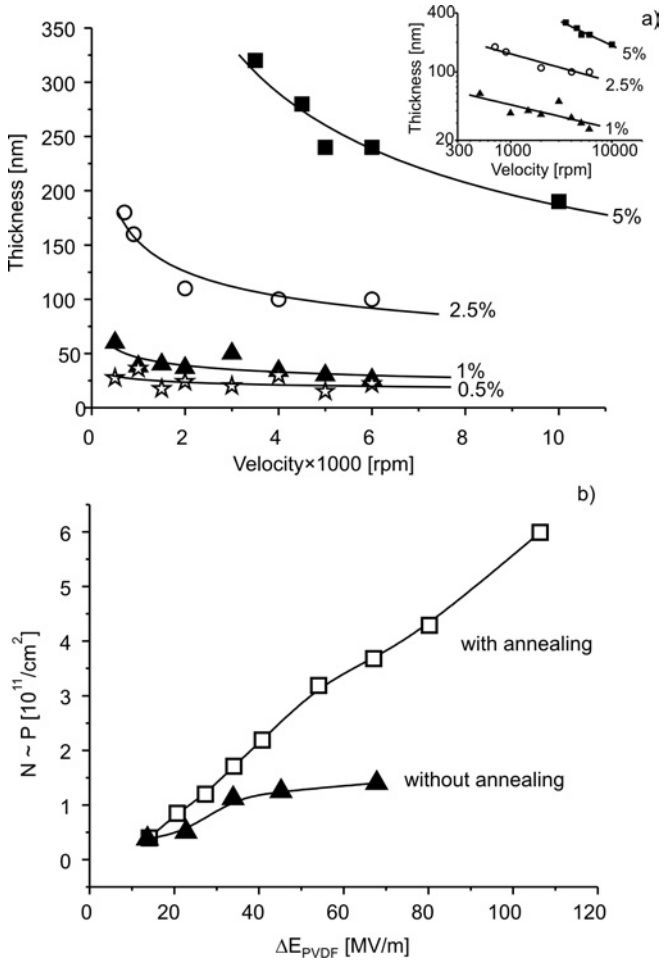

Fig. 3. Spin coating calibration of P(VDF-TrFE): thickness dependence on spin speed (a) at various solution concentrations. The inset depicts the log-log plot of the thickness versus the speed and dependence of the polarization proportional value *N* on the electric field loop (b) for one non-annealed sample (350 nm P(VDF-TrFE) and one annealed stack (220 nm P(VDF-TrFE)). Both layers were spun on a 235 nm SiO_2 buffer layer. The annealing was performed at 135 °C for 2 h

However, it should be noted that an increase of the coercive field of P(VDF-TrFE) with shrinking of the polymer thickness below 100 nm has been observed for this ma-

terial [6, 16]. Therefore, it should be possible to find an optimum solution for these two opposite trends. For that reason, it should be possible to adopt a wide range of applicable layer thickness.

In Figure 3a, the final film thickness versus the final spin speed is shown for various concentrations of the solution. In [17, 18] models for the spin coating have been developed, taking into account the solvent evaporation and a non-Newtonian character of the rheological behaviour of the resists. Jenekhe [18] introduced a parameter α, describing the influence of solvent evaporation on the viscosity of the fluid during spin coating. In a general dependence

$$d \propto w^{-p} \qquad \text{with} \qquad p = \frac{2}{2+a} \tag{9}$$

where d is the final thickness and ω is the angular frequency. By analyzing a log–log dependence of the thickness on the speed (inset of Fig. 3a) we determine mean values of p of 0.23 in the solution concentration range of 0.5–2.5%, while for the thicker solution of 5%, the value of 0.48 is found, which is in the typical range of 0.40–0.82 for resists discussed in [18]. Generally, we find an increased slope p by increasing the concentration of the solution. This is in good agreement with the modulations in the literature and is attributed to the increase in fluid viscosity and therefore to the more prominent non-Newtonian behaviour at higher concentrations [17].

With this calibrated spin coating procedure we are able to fabricate films in a wide range of thicknesses between 10 nm and 1 μm. Using it, we could recently identify interface reactions between aluminum electrodes and the P(VDF-TrFE) as the reason for decreased polarization values, when the polymer thickness is shrunk below 150 nm [15, 19]. Furthermore, we have recently shown that the ferroelectric switching shows still an extrinsic like behaviour in films as thin as 10 nm [20].

3.2.2. Annealing

We have already partially shown the effect of the annealing step on our CV measurements [21], where we find much more symmetric behaviour in the flatband voltage shift inside one CV loop after annealing. Conversely, the CV loops of non-annealed samples additionally shift due to a probable charge injection.

Here we analyze the impact of annealing to a higher polarization value. In Figure 3b, we show the dependence of N value – proportional to the polarization – calculated by Eq. (7) on the applied electrical field window of the CV loop for one annealed and one non-annealed sample. We observe much higher values of the polarizability for the annealed sample, while the non-annealed sample already shows saturation even here, where a thick SiO_2 buffer layer of 235 nm is used. In [6] a strong effect of annealing for improving the crystallinity of P(VDF-TrFE) was clearly discussed, which results in higher polarization values by a factor of 3 to 4. Our results are in good agreement with this finding.

3.3. Optimization of the buffer layer

As discussed above, a layer shrinking of the polymer is essential for a low voltage operation of a memory device based on MFIS like structures. However, in a MFIS stack a part of the programming voltage drops over the buffering insulator, which is necessary for the hindrance of depolarization, thereby causing leakage currents.

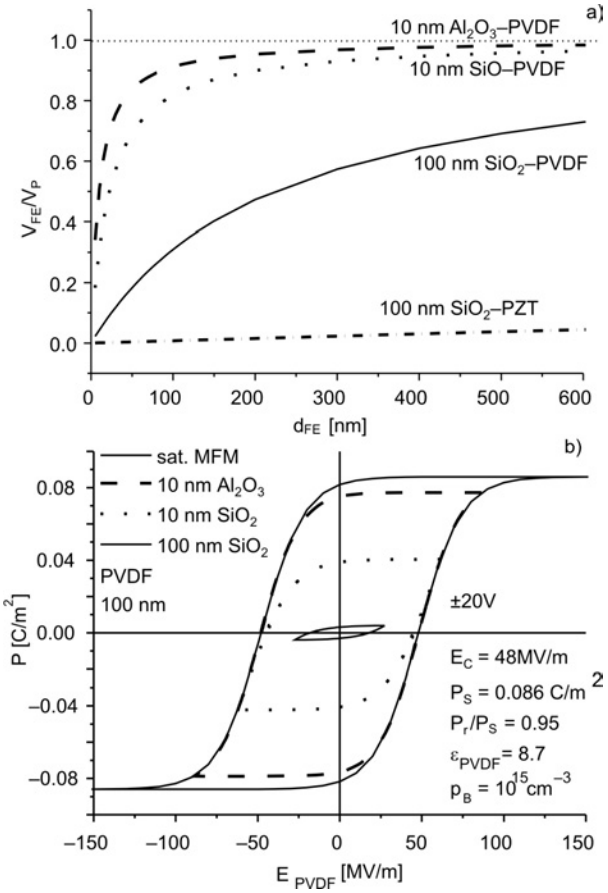

Fig. 4. Calculation of the ratio of the voltage over the ferroelectric layer V_{FE} and the applied voltage V_p in dependence on the ferroelectric thickness d_{FE} using Eq. (10) (a), and simulation of $P(E)$ curves of stacks with 100 nm P(VDF-TrFE) (b) for MFIS systems, which use various buffer layers: 100 nm SiO_2 (thick solid lines), 10 nm SiO_2 (dotted lines) and 10 nm Al_2O_3 (dashed lines). For comparison, results for a stack with a conventional PZT ferroelectric (dashed dotted line in part a) and for a MFM capacitor with the same thickness of the ferroelectric layer (thin solid line in part b) are shown. Because in part (a) PZT is used as a ferroelectric (FE) material as well, the plot shows the dependence of V_{FE}/V_P on d_{FE}, i.e. in Eq. (10) d_{PVDF}, $\varepsilon_{\mathrm{PVDF}}$ and V_{PVDF} should be substituted by d_{FE}, ε_{FE} and V_{FE}

Again for a low voltage operation, these programming losses should be as small as possible. Furthermore, in the "off state" of the memory, the gate is normally grounded.

Due to charge neutrality, the electric field caused by the polarization of the ferroelectric layer will be neutralized by an established field in the buffer layer, leading to depolarization fields, which can corrupt the saved information [5]. This fact meets the same requirements as for the low voltage operation, where a high capacitance of the buffer layer and a moderate permittivity value of the ferroelectric material are needed. In the accumulation regime of the MFIS structure, the ratio of the voltage drop over the ferroelectric layer (V_{PVDF} respectively V_{FE}) to the programming voltage (write, V_p) can be estimated by a simple model of two capacitors in series, and the following formula can be used:

$$\frac{V_{PVDF}}{V_p} = \frac{1}{1 + \frac{\varepsilon_{PVDF}}{\varepsilon_{buf}} \frac{d_{buf}}{d_{PVDF}}} \tag{10}$$

As is shown in Fig. 4a, this ratio depends on the thickness of the ferroelectric layer. The thickness of the ferroelectric layer could be increased so that a high voltage ratio is attained but this contradicts the criteria for low voltage operation. In the opposite direction, this ratio is reduced by making the polymer layer thinner. Therefore, the buffer layer should be adapted either by the reduction of its thickness (dotted line in Fig. 4a) or by increasing its permittivity (dashed line in Fig. 4a). In addition, Fig. 4a depicts also, that for the case in which a buffer layer is needed (see Sect. Introduction), a ferroelectric with a relatively small permittivity is preferable in terms of this voltage divider optimization. In terms of optimization of the buffer layer, it should be also taken into account that the fully saturated regime of the polarization of the ferroelectric should be achieved preferably in order to get a stable working MFIS memory stack. However, this simple model of the voltage divider does not consider the polarization inside the ferroelectric layer. Hence, we performed also simulations of $P(E)$ curves using the procedure described in Sect. 2.2 with the same thickness of the buffer layer and materials as used in Fig. 4a (refer to Fig. 4b). Assuming, that ±20 V CV loops are performed, we calculate the resulting $P(E)$ loop for a 100 nm P(VDF-TrFE) layer with a buffer layer of 100 nm SiO_2, 10 nm SiO_2, or 10 nm Al_2O_3. For comparison, the saturation loop of a pure 100 nm thick P(VDF-TrFE) capacitor (metal –ferroelectric–metal, MFM) is shown in Fig. 4b as well. The values of *Ec*, *Ps* and ε_{PVDF} are given in the legend of Fig. 4b and are taken from our former results [15]. The assumed values of the relative dielectric constants of SiO_2 and Al_2O_3 were 3.9 and 9, respectively. We clearly observe that for this configuration and a CV loop of ±20V, a 10 nm Al_2O_3 buffer layer almost leads to a complete saturation. This is confirmed by the results of measurements shown in Fig. 5a. Here, again we show the more qualitative polarization value *N* in dependence of the maximum applied voltage of the CV loop. We observe a similar behaviour as predicted by the simulation, the stack with 11 nm Al_2O_3 buffer layer shows a much higher polarization value than the stack with almost the same SiO_2 thickness and here the ferroelectric seems to be already more or less in saturation. This means that even this simplified calculation of the *N* value delivers good qualitative information about the polarization.

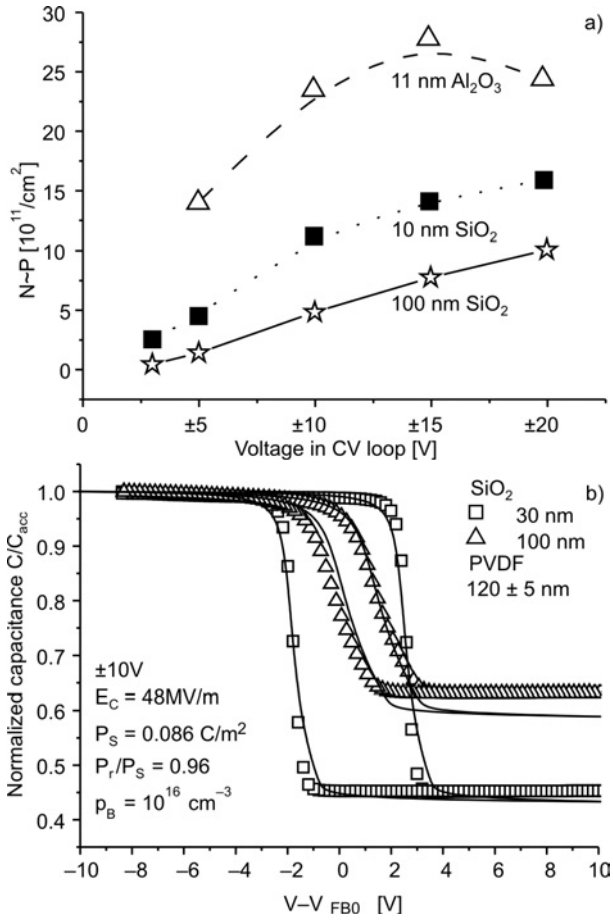

Fig. 5. Dependence of the polarization proportional value N on the maximal voltage applied in the CV loop (a) for MFIS stacks consisting of 120 nm P(VDF-TrFE) and 100 nm SiO_2, 10 nm SiO_2 or 11nm Al_2O_3 and measured (symbols) and calculated (lines) CV curves of stacks with 120 nm P(VDF-TrFE) and 30 nm or 100 nm SiO_2 (b). The values of the capacitance are normalized to the accumulation capacitance (i.e. C_{stack}) of each individual sample. The curves correspond to the initial flatband voltage (V_{FB0}) of every sample in order to visualize the hysteresis due to the ferroelectric switching more easy

To get more quantitative parameters of the polarization loop, the CV curve should be fitted to the model described above in Sect. 2.2. Here, we just show two examples of modelling, where a 120 nm P(VDF-TrFE) layer is combined with a 30 nm or 100 nm SiO_2 layer. In Figure 5b, the ±10V CV measurements on these stacks are marked by symbols, while the results of simulation are shown with solid lines. We use the same values as above for E_c, P_S and ε_{PVDF} (refer to the legend of Fig. 5b) as known values. The model is in very good agreement with the measurement. For a real fitting procedure the E_c and P_S values as well as the ratio of the remanent and saturated polarization should be adapted.

4. Conclusion

Ways to optimize a MFIS stack have been described. The optimization of a sequence of layer thickness of the ferroelectric and the buffer layer is discussed. We find that for a 120 nm P(VDF-TrFE)/11 nm Al_2O_3 stack in a ±20V CV loop, saturation of the polarization is almost reached. Here, we observe a very good match between the predicted and the measurement results. The application of the simulation proposed by Miller and McWorther [4] is a very useful tool to further optimize these stacks. Recently, we have shown retention of several days [15] and cycles of more than 10^5 (soon to be published). We expect even better values for optimized layers.

Acknowledgement

The authors acknowledge "Deutsche Forschungsgemeinschaft" for financial support within the priority program 1157 (SCHM745/11-1-2), and IHP Frankfurt/O, and AMD Saxony Dresden for providing us with oxidized wafers.

References

[1] BEZ R., PIROVANO A., Mat. Sci. Sem. Proc., 7 (2004), 349.
[2] KOHLSTEDT H., ISHIWARA H., *Ferroelectric Field Effect Transistors*, [in:] R. Waser (Ed.), *Nanoelectronics and Information Technology. Advanced Electronic Materials and Novel Devices*, Wiley –VCH, Weinheim, 2003, pp. 388–404.
[3] MOLL J.L., TAURI Y., IEEE T., Electron. Dev., ED10 (1963), 338.
[4] MILLER S.L., MCWORTHER P.J., J. Appl. Phys., 72 (1992), 5999.
[5] GNADINGER F.P., HUEBNER G.G., DERBENWICK G.F., DEVILBISS A.D., Ferroelectrics, 268 (2002), 729.
[6] FURUKAWA T., Phase Trans., 18 (1989), 143.
[7] NABER R.C.G., TANASE C., BLOM P.W.M., GELINCK G.H., MARSMAN A.W., TOUWSLAGER F.J., SETAYESH S., DE LEEUW D.M., Natur. Mater., 4 (2005), 243.
[8] UNNI K.N.N., DE BETTIGNIES R., DABOS-SEIGNON S., NUNZIA J.M., Appl. Phys. Lett., 85 (2004), 1823.
[9] MÜLLER K., HENKEL K., PALOUMPA I., SCHMEISSER D., Thin Solid Films, 515 (2007), 7683.
[10] SZE S.M., *Physics of Semiconductor Devices*, Wiley, New York, 1981.
[11] URAYAMA K., TSUJI M., NEHER D., Macromol., 33 (2000), 8269.
[12] KITTEL C., *Introduction to Solid State Physics*, 8th Ed., Wiley, New York, 2005.
[13] FURUKAWA T., DATE M., FUKADA E., TAJITSU Y., CHIBA A., Jpn. J. Appl. Phys., 19 (1980), L109.
[14]KOIZUMI N., HAIKAWA N., HABUKA H., Ferroelectrics, 57 (1984), 99.
[15] HENKEL K., LAZAREVA I., MANDAL D., PALOUMPA I., MÜLLER K., KOVAL Y., MÜLLER P., SCHMEISSER D., J. Vac. Sci. Technol. B, 27 (2009), 504.
[16] KIMURA K., OHIGASHI H., Jpn. J. Appl. Phys., 25 (1986), 383.
[17] FLACK W.W., SOONG D.S., BELL A.T., HESS D.W., J. Appl. Phys., 56 (1984), 1199.
[18] JENEKHE S.A., Ind. Eng. Chem. Fundam., 23 (1984), 425.
[19] MÜLLER K., MANDAL D., SCHMEISSER D., MRS Proc., 997 (2007), I6-02.
[20] MÜLLER K., MANDAL D., HENKEL K., PALOUMPA I., SCHMEISSER D., Appl. Phys. Lett., 93 (2008), 112901.
[21] HENKEL K., *Electrical Investigations on Praseodymium Oxide/Aluminum Oxynitride Containing Metal–Insulator–Semiconductor Stacks and on Metal–Ferroelectric–Insulator–Semiconductor Structures Consisting of Poly(vinylidene fluoride trifluoroethylene)*, PhD Thesis, Shaker-Verlag, Aachen, 2009, pp. 89–91.

Received 6 October 2008
Revised 20 July 2009

Materials Science-Poland, *Vol. 28*, *No. 1*, *2010*

Preparation and characterization of SiO_2 microspheres doped with $CoFe_2O_4$ nanocrystals

V. TYRPEKL[1, 2*], J. POLTIEROVÁ-VEJPRAVOVÁ[3], J. PLOCEK[1], D. NIŽŇANSKÝ[2]

[1]Institute of Inorganic Chemistry of the AS CR, v.v. i., 250 68 Řež, Czech Republic

[2]Faculty of Natural Sciences, Charles University, Department of Inorganic Chemistry, Albertov 6, 128 43 Praha 2, Czech Republic

[3]Faculty of Mathematics and Physics, Charles University, Department of Condensed Matter Physics, Ke Karlovu 5, 121 16 Praha 2, Czech Republic

Main goal of the reported work was to fabricate silica microspheres doped with magnetic nanocrystals. Cobalt ferrite nanocrystals were fabricated separately via surfactant-assisted coprecipitation. The sol-gel method in microemulsion was subsequently used for encapsulating of the magnetic nanonanocrystals into the silica microspheres. Final products were characterized by various techniques and magnetic measurements. The obtained silica microspeheres doped with $CoFe_2O_4$ were of average diameter 11 μm.

Keywords: *sol-gel; microemulsion; cobalt ferrite; microspheres; nanocomposite*

1. Introduction

Fabrication of new functional materials tailored for specific applications is a challenge for chemistry and material science. Magnetic nanoparticles have been of a great interest ever since pioneer works of their simple preparation, reported for example in [1]. The sol-gel chemistry, mainly of silicate precursors has been undergoing through a renaissance since 1980 [2–4]. Combination of ever more progressive techniques leads to a variety of new materials based on magnetic or superparamagnetic (SPM) nanoparticles with functionally modified surface. The presence of a silica gel surface layer could shift the point of zero charge (p.z.c.) into acidic one, while an amino-modified silica layer could shift it in a basic range [5, 6]. A silica layer could be introduced by a number of preparation methods, two of them being widely used. The Stöber method uses ammonia catalyzed gelation of tetraalkoxysilane [7, 8], and the so-called microemulsion method is based on the formation of droplets of the emulsion,

*Corresponding author, e-mail: tyrpekl@iic.cas.cz

stabilized by surfactants, that acts as a micro-reactor for the sol-gel process [5, 9]. The advantages of the microemulsion method are, for example, independence of a catalytic mechanism (acidic or basic) of the sol-gel process, easy variation of the droplet size (by changing the amount of the water phase or changing the surfactant type), thermodynamic stability of the system, etc.

The paper concentrates on the fabrication of silica microspheres with the diameter of a few micrometers containing nanocrystals of $CoFe_2O_4$. The magnetic Co-ferrite nanoparticles were prepared by coprecipitation of cobalt(II) and iron(II) dodecylsulphate solution using methylamine as the precipitant [10]. By this preparation route, many types of ferrite nanoparticles were synthesized, for example Fe_3O_4 [11], $NiFe_2O_4$ and $MnFe_2O_4$ [12]. Dodecylsulphate (an anionic surfactant) controls the shape and size of nanocrystals during the precipitation. A micellar system of water/CTAB (cetyltrimethylammonium bromide)/*n*-hexanol was used for encapsulation of the magnetic particles into silica spheres via the sol-gel microemulsion method. The proper pH acidic solution) of droplets and temperature around 40 °C, caused gelation of the silica precursor TMOS (tetramethoxysilane). In general, microemulsion, containing droplets of an acidic cobalt ferrite ferrofluid, is a suitable system for gelation of TMOS at higher temperatures.

Nowadays, a micro-scale processing is slightly ignored due to the greater emphasis placed on the nanosized features. However, this work is an illustrative example of a bottom-up approach, where the micro-objects are formed from molecular and nanoparticle building blocks.

2. Experimental

Syntheses and materials. All chemicals were of 98% purity or higher. Nanoparticles of $CoFe_2O_4$ were prepared by the coprecipitation method as described earlier [10]. Cobalt(II) and iron(II) dodecylsulphate, respectively, were prepared by crystallization of 1:1 volume mixture of 0.1 M cobalt acetate (Merck) or 0.1 M iron(II) chloride (Merck) solution, with 0.1 M sodium dodecylsulphate (Merck) at 2 °C. After adding of 2 M methylamine into the mixture of $8 \cdot 10^{-3}$ M $Co(DS)_2$ and $2{,}6 \cdot 10^{-2}$ M $Fe(DS)_2$, the mixture was stirred vigorously for 2 h. Co-ferrite particles were purified by several cycles of centrifugation and decantation.

A schematic diagram of the synthetic routes of $CoFe_2O_4/SiO_2$ microspheres is shown in Fig. 1. The non-aqueous part of the microemulsion consisted of 5 g of *n*-hexanol (Aldrich), 1.5 g of ethanol and 0.3 g of CTAB (Aldrich). Few droplets of distilled water (maximum 0.5 cm^3) were added to form appropriate emulsion. Furthermore, 3.87 g of TMOS (Aldrich) were pre-hydrolyzed with 3.6 g of 0.03% HNO_3 (Lachema) for 1 h at 40 °C. 1 g of formamide (Merck) with 30 mg of ultrasonically dispersed $CoFe_2O_4$ particles were added, and stirred for 1 h at room temperature. 1.5 g of this mixture was slowly added into stirred nonaqueous part and evenly heated up to 60 °C. Final product was washed with acetone and ethanol, and finally dried at 100 °C.

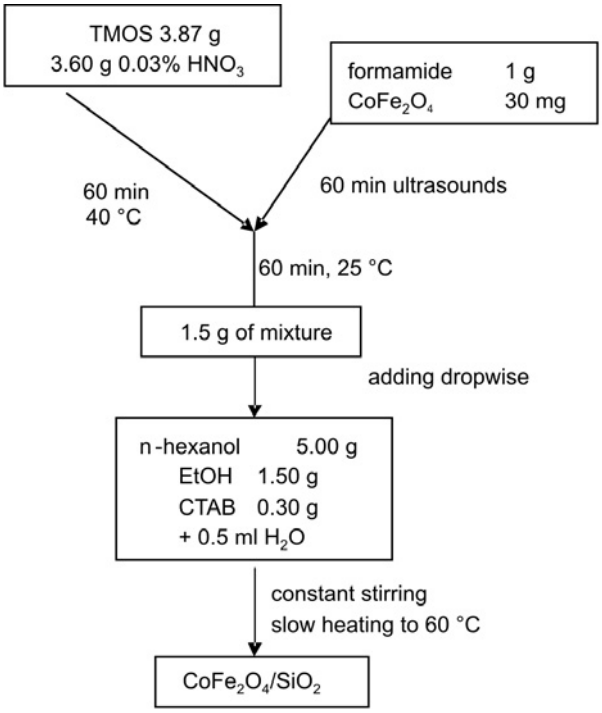

Fig. 1. The preparation scheme

Experimental techniques. Scanning electron microscopy (SEM) investigations were done on a SEM Philips XL 30 CP equipped with EDS (energy dispersive X-ray spectrometry), secondary and back-scattered electron detectors and a Robinson detector. Each powder sample was placed on the holder with an adhesive carbon slice and covered with a thin (<10 nm) Au/Pd layer. Microscale morphology was examined with a high-resolution transmission electron microscope HRTEM JEOL JEM 3010 and a conventional TEM Philips 80 kV. A copper grid coated with a perforated carbon support film was used to prepare samples for the TEM observation. The powdered sample was dispersed in ethanol and placed on the grid.

The powder X-ray diffraction (XRD) measurements were performed on the Seifert diffractometer using CuK_α radiation with a monochromator. The phase analysis was done using the PDIFF database.

Investigation of the magnetic behaviour of the final composite was performed with the PPMS 14T and PPMS 9 T devices (Quantum Design, San Diego). The temperature dependence of magnetization was recorded in the zero-field cooled (ZFC) and field-cooled (FC) regimes in an external magnetic field of 10 mT. The ac susceptibility measurements were done in strictly zero magnetic field conditions for which the amplitude of the ac field was set to 5 mT and the frequency was varied from 10 Hz to 10 kHz.

3. Results and discussion

3.1. Cobalt ferrite nanocrystals

Particles of cobalt ferrite nanocrystals had already been fully characterized earlier [10]. Briefly, the reported characteristics show the average diameter by TEM of 5 nm (σ = 23%). Magnetization measured at 10 K is 50 emu/g and the coercive field at 10 K is 9 kOe. The TEM micrographs were made in order to confirm that the desired particle size and morphology had been achieved (Fig. 2).

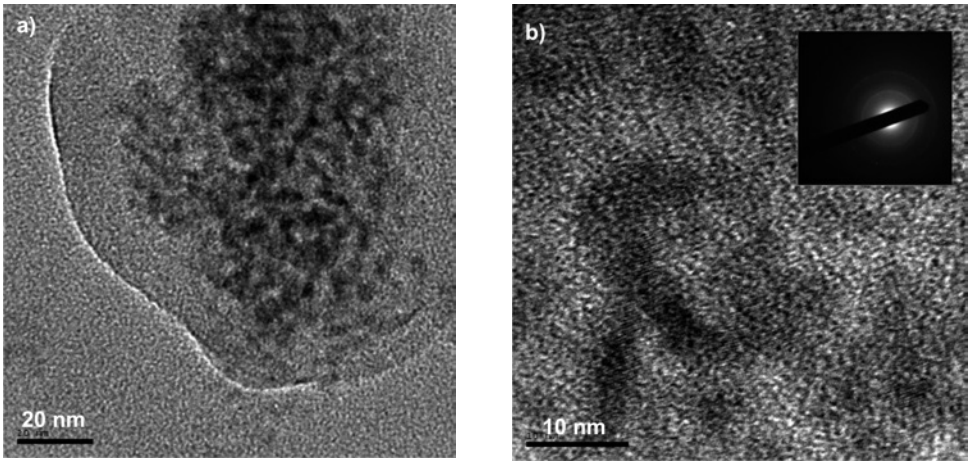

Fig. 2. TEM micrographs of $CoFe_2O_4$ nanocrystals: a) overview; b) details and electron diffraction pattern

3.2. $CoFe_2O_4/SiO_2$ microspheres

The morphology of the final composite microspheres is presented in Fig. 3. The silica particles are of regular spherical shape, as required.

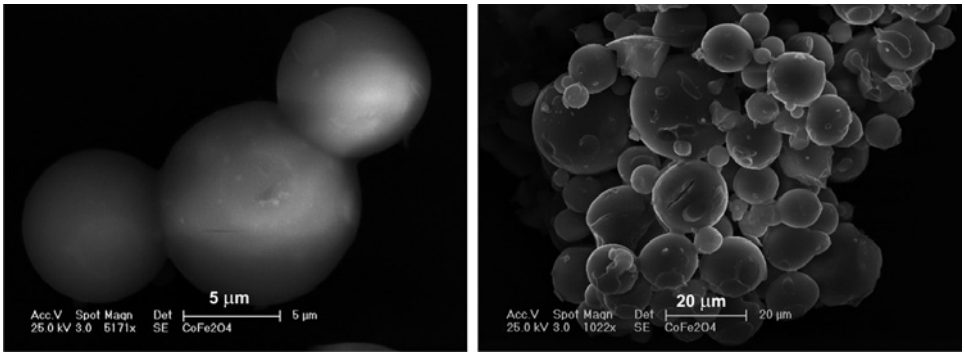

Fig. 3. SEM of the final $CoFe_2O_4/SiO_2$ composite morphology at various magnifications

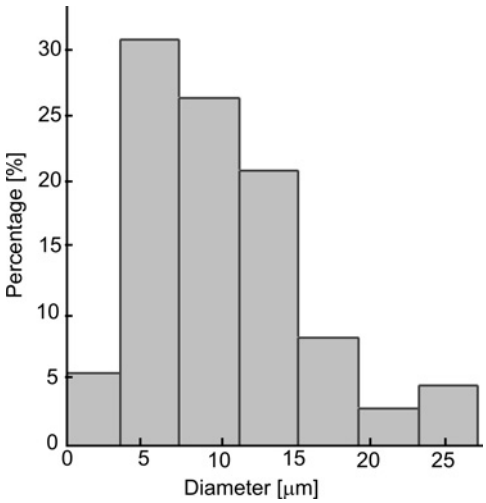

Fig. 4. Size distribution of $CoFe_2O_4$ doped silica spheres (calculated from SEM micrographs)

The size distribution calculated from the SEM measurements is shown in Fig. 4. The average diameter of the particles of the silica/ferrite composite was determined as 11.04 ± 7.7 μm. The size of the silica spheres is determined by the volume of the hydrophilic microdroplets of the microemulsion at ca. 60 °C, where silicon dioxide gel is formed from the pre-hydrolyzed TMOS.

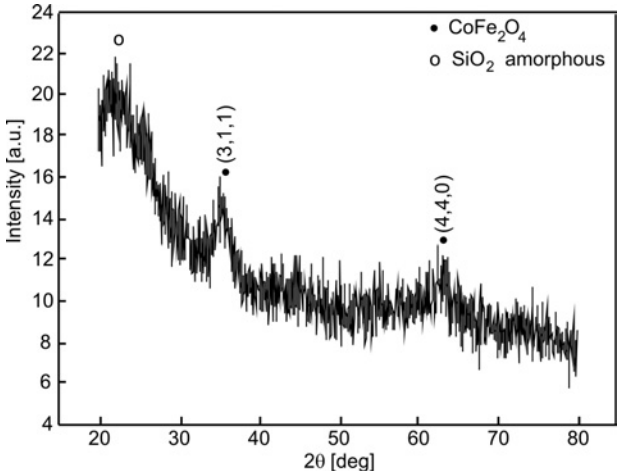

Fig. 5. Powder X-ray diffraction pattern of the final product. The two reflections above 30° are attributed to the Co ferrite nanoparticles, the broad maximum at around 25° corresponds to the contribution of the amorphous silica microspheres

The powder XRD measurements, shown in Fig. 5 proved the presence of the $CoFe_2O_4$ with the spinel structure, as demonstrated by the two strongest reflections in

the XRD pattern (PDF 22-1086), and amorphous silica, which contribute as a broad maximum at around 25°. The Co-ferrite related reflections are very broad and of low intensity, which points to a very small particle size.

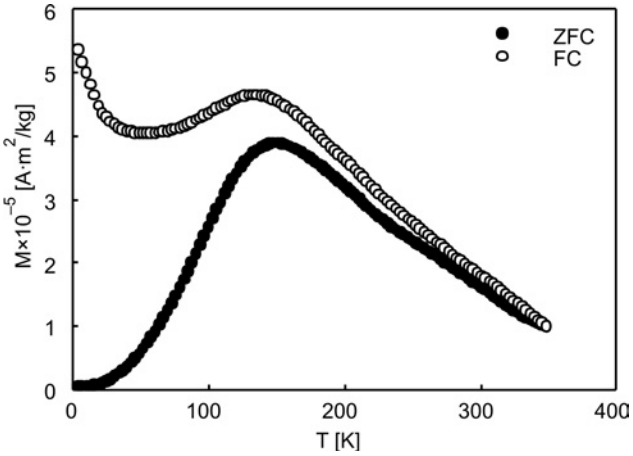

Fig. 6. Temperature dependence of the zero field cooled (ZFC) and field-cooled (FC) magnetization of SiO_2 microspheres doped with $CoFe_2O_4$measured at 10 mT

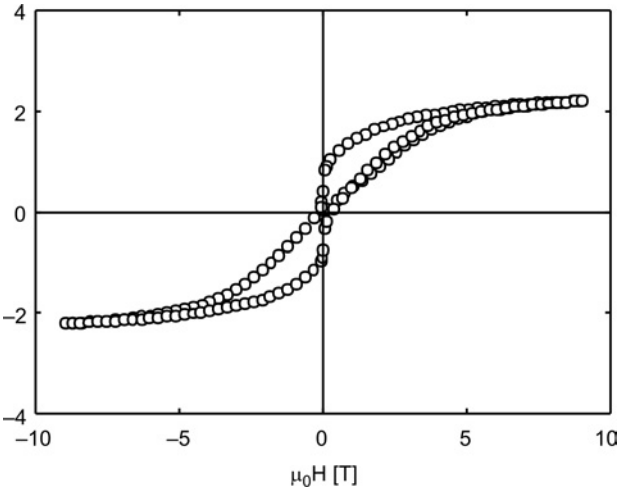

Fig. 7. Hysteresis loop of silica microspeheres doped with $CoFe_2O_4$ recorded at 2 K

Comprehensive investigations by means of magnetization and ac susceptibility measurements were performed in the temperature range 2–350 K. The temperature dependence of the ZFC and FC magnetization is shown in Fig. 6. The ZFC curve exhibits a broad maximum at ca. 150 K, which can be attributed to the blocking temperature, TB, of small Co-ferrite nanocrystals. The FC curve shows a similar maximum at a slightly lower temperature, and indicates an additional paramagnetic-like contribu-

tion at lower temperatures. The enhanced values on FC curve can be caused by the presence of particles below 2 nm, which do not interact with each other and follow the pure SPM trend. On the other hand, both curves correspond to slightly higher values than the proposed T_B level, which can be explained either by particle size distribution or rather by weak interparticle interactions between the majority particles of larger size, mediated by dipolar forces [13, 14].

The Co-ferrite particle diameter (R) of the majority fraction was estimated from the blocking temperature using the formula derived for a pure SPM system of non-interacting superspins: $V = 25k_BT_B/K_1$ and $R = (3V/4\pi)^{1/3}$, where V is the volume of one particle, K_1 is the first order anisotropy constant of the bulk Co-ferrite, k_B is the Boltzman constant and T_B is the blocking temperature. The estimated particle diameter was $R = (3.4 \pm 0.2)$ nm.

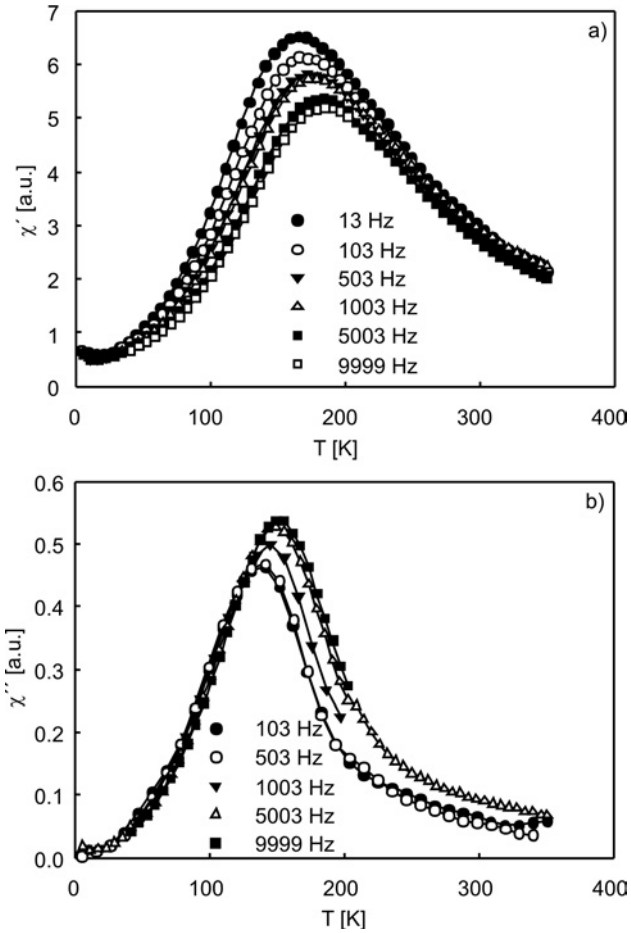

Fig. 8. Temperature dependence of the real χ' and imaginary χ'' parts of the ac susceptibility of silica microspeheres doped with $CoFe_2O_4$

The presence of hysteresis and remanence below the TB level was investigated by taking hysteresis loop measurements at 2 K (Fig. 7). The tapering of the loop in a magnetic field close to zero can be explained by the presence of a small proportion of small particles, as already suggested in the discussion of the temperature dependence of the ZFC/FC magnetization, which does not cause any hysteresis. The saturated magnetization at 2 K reaches ca. $2 \cdot 10^{-3}$ A·m^2/kg calculated relative to the total mass of the composite).

The dynamic properties of the system were examined by taking ac susceptibility measurements, and they are shown in Fig. 8. The character of the real and imaginary part of the ac susceptibility reflects the expected SPM behaviour, demonstrated by the frequency-dependent maximum at T_B at the corresponding frequency (T_f).

A useful criterion for classifying the observed freezing process is the empirical parameter Φ, which represents the relative shift of the blocking temperature per the frequency decade: $\Phi = \Delta T_f/[T_f \Delta \log 10(f)]$, where ΔT_f is the difference between the blocking temperature measured in the $\Delta \log 10f$. We obtained the value $\Phi = 0.04$, which is slightly lower than the 0.1 value expected for a superparamagnetic (SPM) system. Smaller values of Φ are usually caused by the spin-glass-like behaviour of the nanoparticle surface, or are simply due to non-negligible interparticle interactions, which corroborate the interpretation of the magnetization measurements. The Arrhenius plot of the ac susceptibility data, namely $\ln(1/f)$ vs. $1/T_B$, revealed an almost linear dependence, however, the obtained values are unrealistic fit, probably due to the dipolar phenomena proposed above.

4. Conclusion

We reported an easy route for the preparation of silica microspheres doped with cobalt ferrite magnetic nanocrystals. The synthesis was based on the acid-catalyzed sol -gel process in microemulsion. The final product consists of microspheres with average diameter of 11 μm, and very small Co-ferrite nanocrystals, as proved by SEM, HR TEM and XRD analyses. We have further demonstrated a full magnetic characterization of the resulting powder, which revealed that the size of the Co-ferrite nanocrystals is about 3.4 nm and suggested SPM behaviour, disturbed weak interparticle interaction of dipolar origin. Embedded magnetic particles in silica microspheres show different behaviour than pure co-particles 12]. Thanks to the limited concentration of the ferrofluid inside the microemulsion, the magnetic properties seem to be weaker. The composite may be used in the case when magnetic crystals have to be protected by a chemically inert matrix (SiO_2), which can be further functionalized, and simultaneously when manipulation in the micro-scale is required.

Acknowledgements

This work was supported by the project: *New preparation methods of magnetic nanocomposites (spinel ferrites) and study of their physical properties* by the Grant Agency of Czech Republic, GA106/07/0949.

References

[1] MASSART R., IEEE Trans. Magn., 17 (1981), 1247.
[2] POPE E.J.A., MACKENZIE J.D., J. Non-Cryst. Solids, 87 (1986), 185.
[3] CHEN K.C., TSUCHIYA T., MACKENZIE J.D., J. Non-Cryst. Solids, 81 (1986), 227.
[4] ARTAKI I., ZERDA T.W., JONAS J., J. Non-Cryst. Solids, 81 (1986), 381.
[5] MORNET S., GRASSET F., PORTIER J., DUGUET E., Europ. Cells Mater. Vol. 3., Supll. 2 (2002), 110.
[6] MORITAK S.E., TAIRA S., ICHIYANAGI Y., MORONE N., SONG S.-Y., HATANAKA T., YUASA S., SETOU M., J. Nanosci. Nanotechn., 7 (2007), 937.
[7] BORAK B., LASKOWSKI S., HECZKO O., AALTONEN A., BASZCZUK A., JASIORSKI M., SÖDERBERG O., MAZUREK B., OJA M., HANNULA S.-P., MARUZSZEWSKI K., Mater. Sci.-Poland, 25 (2007), 167.
[8] CHENG J., NI X., ZHENG H., LI B., ZHANG X., ZHANG D., Mater. Res. Bull., 41 (2006), 1424.
[9] TAGO T., HATSUTA T., MIYAJIMA K., KISHIDA M., TASHIRO S., WAKABAYASHI K., J. Am. Ceram. Soc., 85 (2002) 2188.
[10] NOUMEN M., PILENI M.P., J. Phys. Chem., 100 (1996), 1867.
[11] FELTIN M., PILENI M.P., Langmuir, 13(1997), 3927.
[12] JOLIVET J.-P., TRONC E., CHANEAC C., Chimie 5 (2002), 1.
[13] DJURBERG C., SVENDLINH P., NORDBLAD P., HANSEN M.F., BØDKER F., MØRUP S., Phys. Rev. Lett., 79 (1997), 51.
[14] DORMANN J.L. , FIORANI D., CHERKAOUI R., TRONC E., LUCARI F., D'ORAZIO F., SPINU L., NOGUES M., KACHKACHI H., JOLIVET J.-P., J. Magn. Magn. Mater., 203 (1999), 23.

Received 2 December 2008
Revised 2 July 2009

Materials Science-Poland, *Vol. 28*, *No. 1*, *2010*

Finite element stress analysis of forging dies to improve their fatigue life

K. DEHGHANI[1*], A. JAFARI[2, 3]

[1]Amirkabir University of Technology, Tehran, Iran

[2]Shahid Bahonar University of Kerman, Kernan, Iran

[3]University of Tehran, School of Mechanical Engineering, Tehran, Iran

The forging dies, and in a particular case a bolt die, were stress analyzed by the finite element method. Two possible modes of die failure, due to hoop and axial stresses, were investigated. The critical zones of highly concentrated stresses have been identified. Several approaches were studied to overcome the tensile stresses that result in a premature failure of a forging die. The results of the finite element simulations show that generating the compressive or negative stresses, as produced by the techniques applied, can completely remove, or at least significantly reduce the detrimental tensile stresses generated during forging. This can readily improve the fatigue life of dies. Numerical stress analysis was performed on critical elements lying in the transition zone of dies. Finally, advanced numerical methods, especially the finite element method, were used to determine the optimum mean stress and the optimum alternative stress as well as to analyze the compressive negative stresses generated by the applied techniques. The ABAQUS software was used for the finite element simulation. The optimum mean stress and the optimum alternative stress at the most critical finite element were determined to be 140–150 and 34–38 MPa, respectively.

Keywords: *die-life improvement; forging; extrusion; pre-stress; fatigue fracture*

1. Introduction

Forging is among the best techniques for the production of tools. However, the major concern is the fatigue life of forging dies, so that not only the selection of an appropriate material is very important in this regard, but also its proper design. That is because forging dies are usually subject to high cyclic stresses that can easily lead to a high level of internal pressure, local stress concentrations, localized deformation and finally premature failure of dies.

[*]Corresponding author, e-mail: dehghani@aut.ac.ir

Selecting a die material to satisfy all the properties required for a long life is not an easy task. Among the suggested materials, tungsten carbide has been widely used as the best choice [1–4]. However, there is a major concern remaining with this material, that is the lack of a long fatigue life. As tungsten carbide is a high strength, brittle material, the short fatigue life of dies might somehow be attributed to improper die design. That is because the high tensile stresses generated in the most critical regions of a die can readily reduce the fatigue strength, resulting in premature die failure. In other words, the importance of an appropriate die design to prevent or reduce the concentration of tensile stresses is just as important as die materials themselves.

It is reported that the decrease in the fatigue strength of dies, due to the presence of undesirable tensile stresses, can easily lead to the fracture of dies at a life shorter than expected [5–7]. As mentioned earlier, the main origin of detrimental tensile stresses is inadequate die design, resulting in undesirable stress concentrations. A high stress concentration leads in turn to crack initiation and fast crack growth, especially when the die material is brittle. This means that even if the best materials are selected, premature die failure can occur if a die is not designed properly.

Although a lot of papers have been published on the selection of suitable materials for dies [1–4], far fewer are available on the finite element modelling of die design. For example, reducing or eliminating the detrimental tensile stresses concentrated in the critical areas of dies is essential for improving the fatigue life of dies. Thus, the objectives of the present work were to determine and analyze the regions of highly concentrated stresses in forging dies, especially in the particular case of a bolt die. Then, attempts have been made for finite-element simulating the design of forging dies. To meet these goals, the practical approaches were studied, including die inserts, shrink rings, assembled dies and tapered dies. These alternative designs were investigated with regard to their effect on eliminating the tensile stresses concentrated in critical regions of a bolt die. The aforementioned techniques can significantly reduce the detrimental tensile stresses by imposing the pre-stresses leading to the prevention of premature failure of dies.

2. Experimental

Materials. Plastic deformation is not accepted to happen in the die because its occurrence in a die results in losing the dimension stability or size accuracy of produced bolts. In such a case, different bolts having various sizes may be produced with a large tolerance in dimensions. Consequently, tungsten carbide, which exhibits elastic behaviour rather than elastoplastic one due to its very high strength is considered for the die insert. Therefore, the material to be forged was considered AISI 1010 steel with elasto-plastic behaviour. The stress-strain relation for this steel is as follow [2]:

$$\sigma = 730\varepsilon^{0.22} \tag{1}$$

As for the die material, the characteristic parameters for tungsten carbide are, according to [3], as follows: E = 540 GPa, ν = 0.22.0. The result of the present simulation, applied for producing a M10 bolt made of AISI 1010, yielded the pressure of about 650 MPa.

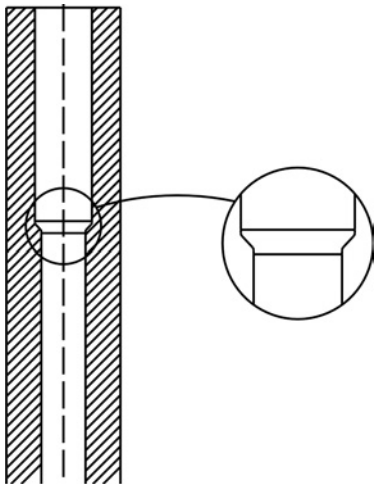

Fig. 1. Schematic of the design of an M10 bolt die

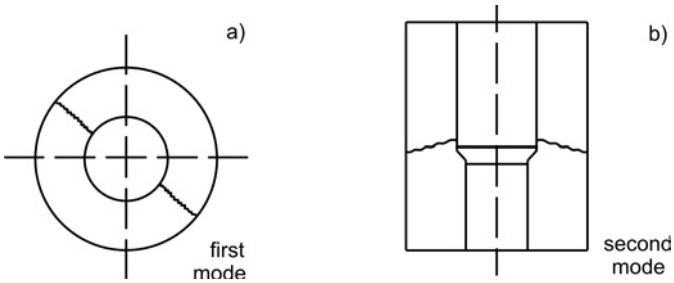

Fig. 2. Modes of possible failure due to: a) hoop stress and b) axial stress

A schematic design of the M10 bolt die studied in the present investigation is shown in Fig. 1. The design is based on existing standards [1, 2]. As any change in the cross section can cause stress concentration, therefore, in this case, the most significant fatigue failure is expected to occur at or near the transition section shown in Fig. 2. Due to the stress concentration, there are two possible origins for fatigue crack nucleation, as shown in Fig. 2. Contrary to the fact that the real life of forging dies should lie in the high cycle fatigue (HCF) range, here the premature fatigue failure is expected to occur in the low cycle fatigue (LCF) range. In other words, the undesirable tensile stress distribution in the die is responsible for this contravention and premature failure. As shown in Fig. 2, these tensile stresses are oriented in two directions; Figure 2a refers to the failure due to hoop stresses (first mode), whilst Fig. 2b indi-

cates the failure due to axial stresses (second mode). This is also in agreement with the previous works [6, 8].

This work is mostly focused on the methods used to eliminate the tensile stresses in the die. This technique is in accordance with the work of others [5, 9]. The proposed approach is based on the following steps:

- Analyzing the stresses distributed in both die and work-piece using the finite element method.
- Determining the critical points or regions of highest stress concentrations and/or of maximum tensile stresses in the die.

A crude representation of a die as a thick cylinder is sufficient for some mathematical models, but it is not an adequate for accurately identifying critical regions of fatigue stresses. As a result, advanced numerical methods, especially the finite element methods, were used in this regard [10, 11]. It should be emphasized that in the present work, the ABAQUS software was used for finite element simulation [12].

The assumptions made in the finite element modelling were: both die and workpiece were analyzed simultaneously, the rigid behaviour of the die during the workpiece deformation was ignored, the symmetrical condition was considered, and the boundary condition was considered as 15 mm vertical displacement of a hammer pin.

3. Results and discussion

3.1. Stress analysis

Although the die material (i.e., tungsten carbide) yields a high tensile strength, its fatigue strength is considerably reduced due to the tensile stress generated across the die during the forging cycles. Thus, as a first step, it is essential to determine the distribution of tensile stresses in the die. The regions of high tensile stresses are the so-called critical points of the die. To determine these regions, a simple die, without shrink ring, was considered. Figure 3 presents the axial stress distribution within the different portions of the die during forging, whereas Fig. 4 shows the distribution of hoop stresses, both obtained using the assumed models. As is obvious, the hoop stresses in most portions are positive (tensile) and reach the maximum level across the region α of the die (Fig. 4). With respect to axial stresses (Fig. 3), the situation is different; they are positive or tensile in a much fewer number of] regions. By contrast, in most places, the generated stresses are negative (compressive).

It is interesting that at the critical radius, i.e. at the point of cross-sectional change, where crack initiation is most likely to occur, the axial stresses are tensile (region β indicated in Fig. 3). Thus, these two regions (α and β) can be identified as the critical zones where the stress concentrations are the highest. That is why the first mode of fracture (Fig. 2a) can take place in the region α, while the second mode of failure (Fig. 2b) may occur in the region β.

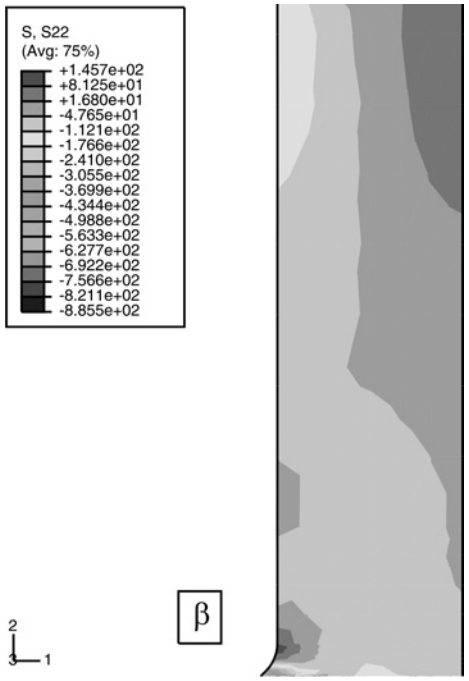

Fig. 3. Axial stress counter in the insert (MPa)

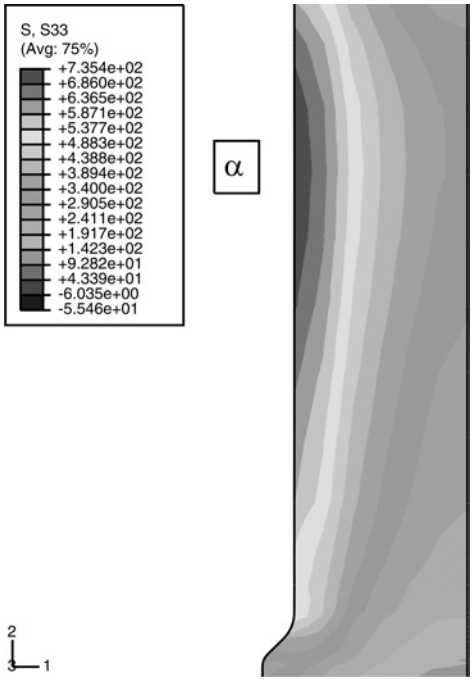

Fig. 4. Hoop stress counter in the insert (MPa)

Therefore, according to the fatigue analysis, the fatigue strength is reduced in the regions having positive stresses. As a result, premature fatigue failure is expected to occur anywhere in the die where the generated tensile stress is at its highest value [13, 14]. That is why the lifespan of forging dies is mainly considered to lie in the low-cycle fatigue (LCF) range rather than in the high-cycle fatigue (HCF) one. Nevertheless, as already mentioned, if these principal stresses could be changed to compressive stresses (negative), e.g. by using a shrink ring to induce pre-stresses, then a significant increase in the fatigue strength of dies could be readily attained. If however the tensile stresses, dominant during forging cycles, could not be eliminated, reduced, or replaced with compressive ones, then there is no alternative to using a tougher material.

3.2. First mode of failure caused by hoop stresses

In this section, the analysis and control, by means of FEM simulation, of the first mode of failure, as illustrated in Fig. 2a, caused by hoop stresses is discussed. One of the best approaches for converting the hoop tensile stresses (generated during cyclic forging) to compressive ones is use a shrink ring, which is simulated here. In such a case, there is a pre-stress imparted by the ring to the inner part of the die. This in turn causes the die to experience an overall negative hoop stress, even under the maximum inner pressure imposed on the die insert during service.

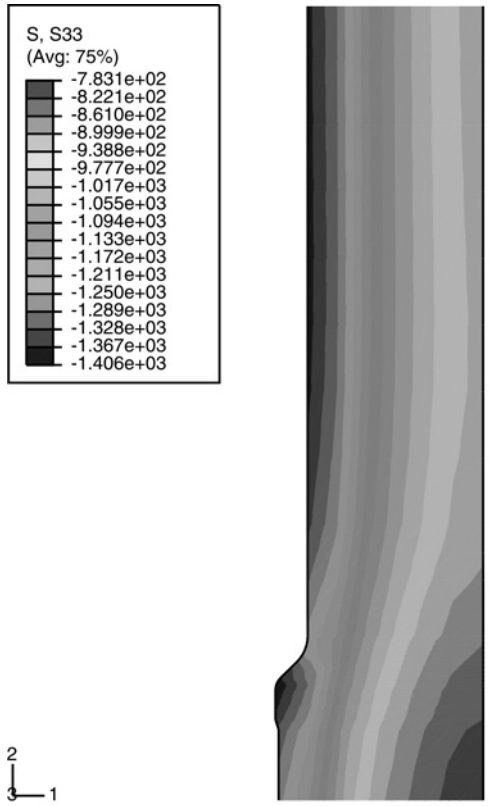

Fig. 5. Hoop stress counter imposed only by using shrink ring (MPa)

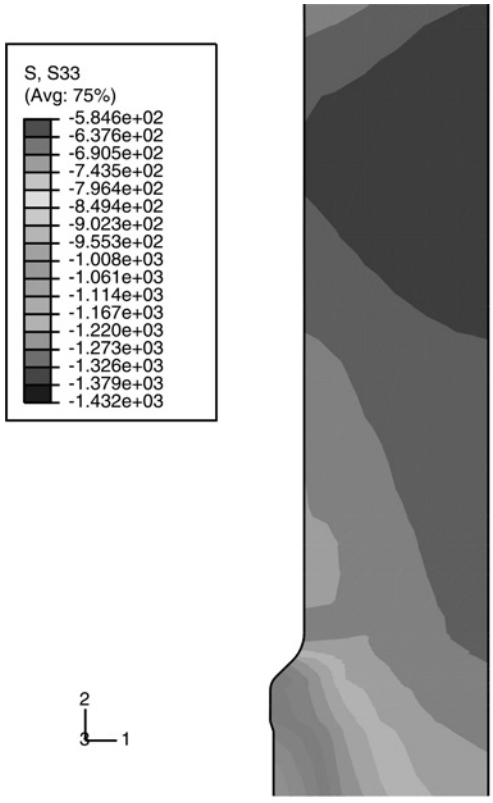

Fig. 6. Hoop stress counter when applying load along with using shrink ring (MPa)

Classical analysis, based on Lame's method [15], shows that it is possible to simulate and calculate the interference of a shrink ring. To illustrate the effect of a shrink ring, the results of FEM simulation regarding its hoop-stress counter are compared in Figs. 5 and 6. Figure 5 appertains only to the presence of the ring, but not to finer attributes, such as the inner pressure in the absence of loading. Figure 6 shows the simulated hoop stresses induced by both the ring load and the forging load. As is obvious, in both cases, the resultant hoop stress in all parts of the die is negative. As a result, the fatigue life of the die can be considerably increased if the first mode of die failure can be delayed by the use of shrink rings.

3.3. Second mode of failure caused by axial stresses

As previously mentioned, another cause of die failure (second mode) is due to the generation of tensile stresses in the transition region of the die, (Fig. 2b). In this case, three techniques may be applied to overcome the premature failure of the second mode. The first one is to use a multipart die, i.e. an assembled die. A schematic dia-

gram of a possible, assembled die for the M10 bolt is shown in Fig. 7. Here, the assembled die consists of only two parts. However, in the case of a complicated shape, a more elaborate assembly might consist of, for example, several parts, such as a case, sleeve, middle insert, back insert and front insert. In this procedure, the interface between various die parts may act as free surfaces that relieve the tensile stress, thereby reducing the stress concentrations at or near the critical sections. This is an important practical issue for increasing the fracture toughness of materials when a thick structure experiencing plane strain condition with low toughness is divided into thin layers experiencing plane stress condition with high toughness [16]. In the case of dies, this happens when they are manufactured of various interferences, e.g. an assembled die, which consists of a few parts or sections.

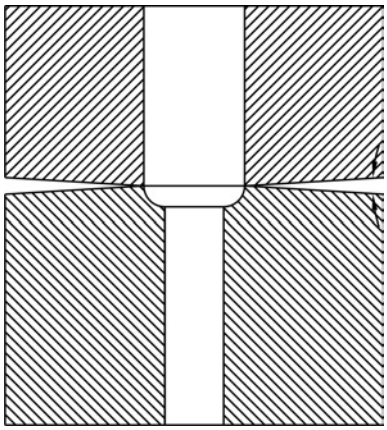

Fig. 7. The schematic of an assembled M10 bolt die consisting of two parts

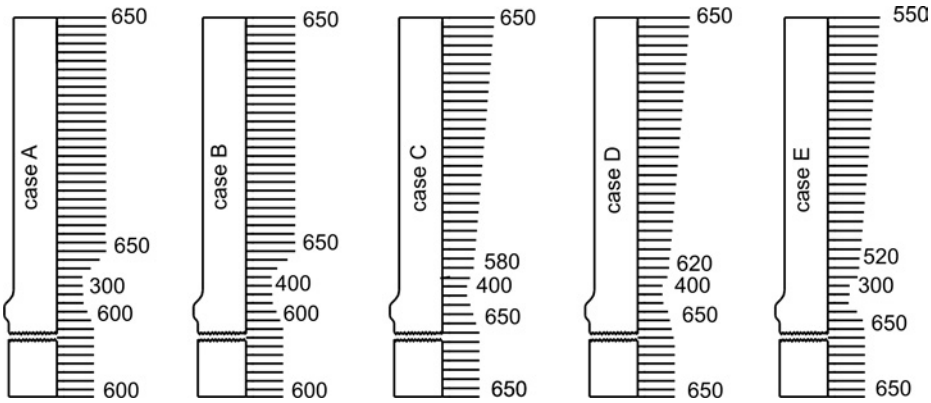

Fig. 8. Five different pressure distributions across the die wall (MPa)

The other method, already mentioned, is to impose a pre-stress (i.e., negative stress) across the die wall, especially at or near the cross-section change-zones or the critical transition zones. To model this case, five situations (A, B, C, D and E) of non-

uniform pre-stresses imposed on the die are assumed, and presented in Fig. 8. As the primary simulation, applied for producing a M10 bolt made of AISI 1010, yields the pressure of about 650 MPa, therefore, the upper limit of simulated pressure was considered 650 MPa,

For the cases C, D and E, the presumed pressure is reduced linearly from a maximum at the top, toward the transition section, and then remains constant at the bottom part of the bolt die. However for cases A and B, the pressure is reduced only at the transition section, while at both the top and bottom portions of the bolt die, it is kept constant. The reason for simulating such a pressure distribution was to generate a kind of negative bending moment, to counteract the positive one produced by the forming pressure, as shown in Fig. 9a. It should be emphasized that the simulated pressure distributions shown in Fig. 8 are obtained by the finite element method as well as by the ABAQUS software.

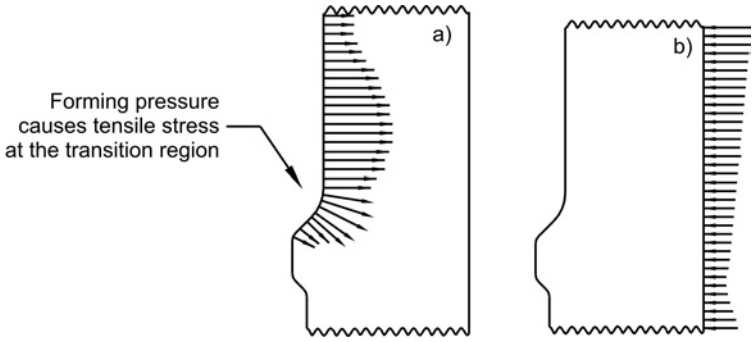

Fig. 9. Forging pressure that generates a bending moment (a) and imposed pressure that can eliminate bending effects (b)

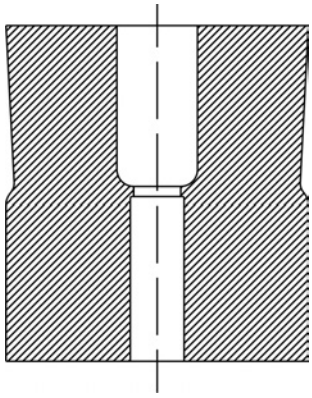

Fig. 10. Scheme of the proposed tapered die

In general, the forging pressure generates a positive bending moment that in turn causes positive tensile stresses at the cross-section change, as shown in Fig. 9a. These tensile stresses can readily result in fatigue crack initiation, leading to the premature

fracture of the die. That is because the generation of detrimental bending moments can result in the second mode of failure, as presented in Fig. 2b. As mentioned before, one useful technique to counteract these undesirable bending moments or tensile stresses is to employ one of the five pre-stresses described in Fig. 8, illustrated again in Fig. 9b to show the mechanism of compensation of bending effect. Such a condition can be created using a tapered insert. For instance, an alternative die design for an M10 bolt using a tapered insert is shown in Fig. 10.

3.4. Numerical analyses

As already mentioned, FEM was used to simulate the forging process for the tapered die design proposed in Fig. 10. As the overall stress should be negative in the critical regions, to prevent the premature failure, attempts were therefore made to identify the critical elements susceptible to crack initiation.

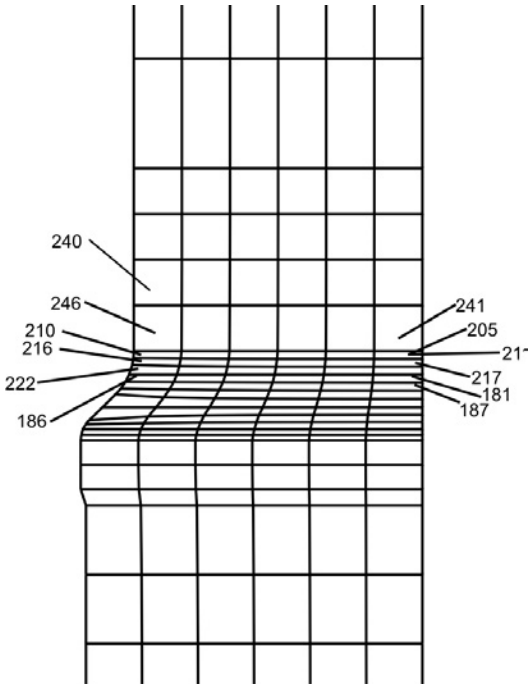

Fig. 11. Critical elements and their numbers

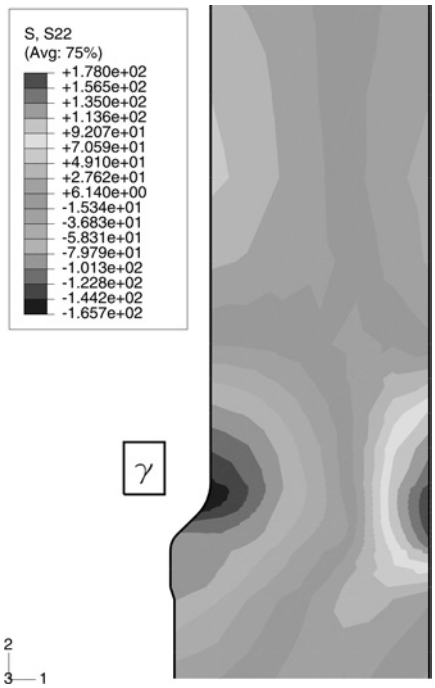

Fig. 12. Axial stress counters in the insert

Figure 11 shows the number of elements in the finite element simulation located at critical zones. Interestingly, for the different cases of A to E, illustrated in Fig. 8, the hoop stresses in all critical regions of the die insert, including the critical fillet region β, remain negative during a complete forging cycle. On the other hand, as shown in Fig. 12 and referring to the results summarized in Table 1, the axial stress at the

critical fillet region β remains negative during a complete cycle. This confirms the validity of the proposed approach in imposing the proper pre-stresses to generate negative stresses at critical zones of the die.

Table 1. Axial stresses in the critical elements in the fillet region (MPa)

Element number										Case
240		246		210		216		222		
After loading	Before loading	After loading	Before loading	After loading	Before loading	After loading	Before loading	After loading	Before loading	
–191	–135	–134	–177	–67	–203	–62	–208	–104	–208	A
–198	–114	–136	–157	–67	–185	–62	–191	–102	–193	B
–191	–103	–127	–136	–56	–159	–51	–164	–92	–165	C
–183	–114	–115	–151	–42	–177	–36	–182	–78	–183	D
–215	–141	–142	–167	–64	–183	–55	–185	–96	–182	E

As is obvious, due to this design, the imposed stresses on the die insert in the critical fillet region are negative. This again can lead to longer fatigue life of dies, by eliminating the undesirable tensile stresses. Therefore, generating negative or compressive stresses is the best method to increase the fatigue life of components. These stresses are typically produced by surface treatments such as shot preening, cold work, heat treatments, plating, etc. [16]. Generating the compressive stresses is practical not only for dies but also for other important rotating parts, including axles, shafts, crankshafts, etc. that are subjected to cyclic loading. However, there is a region in Fig. 12, labelled γ, where a positive axial stress is generated as well. Indeed, this region must be inspected and treated with care when being subject to forging cycles. The numerical simulations reveal that the axial stress varies from positive to negative in this region during a loading cycle.

In another attempt, the mean stress σ_m and alternative stress σ_a were simulated. The values for σ_m and σ_a, obtained using the finite element analysis for the critical elements numbered in Fig. 11, are summarized in Table 2. These elements are analyzed for five cases illustrated in Fig. 8. In general, the lower the σ_m and σ_a, the higher the fatigue life will be. On the other hand, it should be considered that it is impractical to lower both σ_m and σ_a for a process like forging.

The generation of cyclic stresses in the elements located in region γ in Fig. 12 enhances crack initiation at this region. That is because, due to the generation of tensile stress, this region is the area most susceptible to failure. As a quick approach, the values of σ_m and σ_a appertaining to the critical elements, can be used to determine the most critical case among the five cases, A–E, illustrated in Fig. 8. For instance, it can be concluded that by comparing the five cases, the optimum values, in terms of σ_m and σ_a, are probably those corresponding to cases B and C.

Table 2. Mean and alternative stresses in critical elements (MPa)

Element number										Case
205		211		217		181		187		
σ_a	σ_m	σ_a	σ_m	σ_a	σ_m	σ_a	σ_m	σ_a	σ_m	
44.5	153.5	44	154	45	152	45.5	149.5	47.5	145.5	A
37.5	145.5	37	149	38	150	39	149	41	146	B
31.5	133.5	32.5	138.5	34.5	140.5	36.5	140.5	39.5	138.5	C
46	131	49	135	51.5	135.5	53.5	133.5	57	132	D
37.5	151.5	38.5	152.5	40.5	152.5	42.5	149.5	50	146	E

On the other hand, another approach might be used to estimate the length of the life cycle for various stresses occurring in critical elements. The method enables determining the most critical element and finding the best case of A–E as well as estimating the life cycle numerically. In general, the fatigue life can be estimated from [17]:

$$N = \left(\frac{S_f}{a} \right)^{1/b} \tag{2}$$

where a and b are the constants defined below, and S_f is the fatigue strength for a specific life

$$a = \frac{\left(f S_{ut} \right)^2}{S_e} \tag{3}$$

$$b = -\frac{1}{3} \lg \left(\frac{f S_{ut}}{S_e} \right) \tag{4}$$

where f is a constant in the range 0.8–0.95, S_{ut} is the ultimate strength and S_e is the endurance strength of the material. On the other hand, according to Goodman's theory, the relation between the fatigue parameters is as follows [17]:

$$\frac{\sigma_a}{S_f} + \frac{\sigma_m}{S_{ut}} = 1 \tag{5}$$

Substituting Eq. (5) into Eq. (2) leads to the following formula for determining the fatigue life or the number of cycles N:

$$N = \left(\frac{\sigma_a S_{ut}}{a\left(S_{ut} - \sigma_m \right)} \right)^{1/b} \tag{6}$$

The values for σ_m and σ_a (Table 2) are obtained using FEM simulation. The assumed values for the ultimate and the endurance strengths were 800 MPa and 350 MPa, respectively. The value of 0.9 was used for the constant *f*. Now, the number of cycles to failure can be calculated.

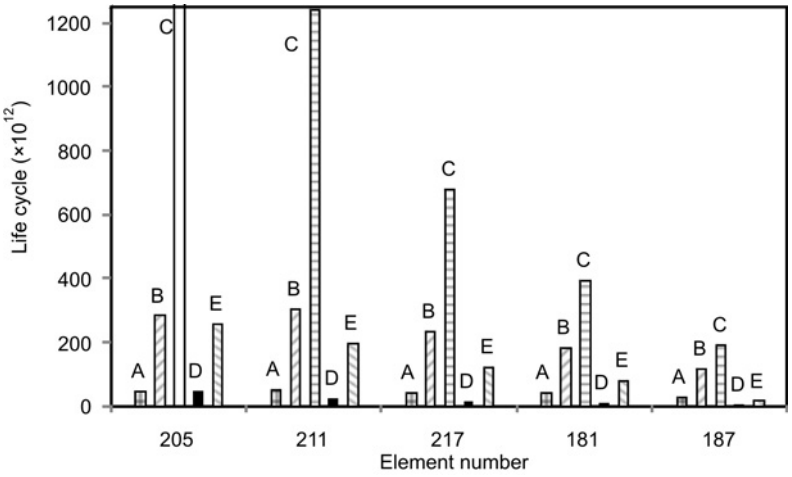

Fig. 13. Life cycle in accordance with cases A to E pertaining to critical elements

In Figure 13, the number of cycles to failure (the fatigue life) obtained for cases A–E are shown, pertaining to the critical elements subjected to cyclic positive/negative loading. The best case among A–E, the most critical element and the final life cycle can be readily determined by comparing the numbers of cycle to failure for various situations. To find the best case among the cases A–E, the number of cycles or fatigue life obtained for all states are compared in Fig. 14.

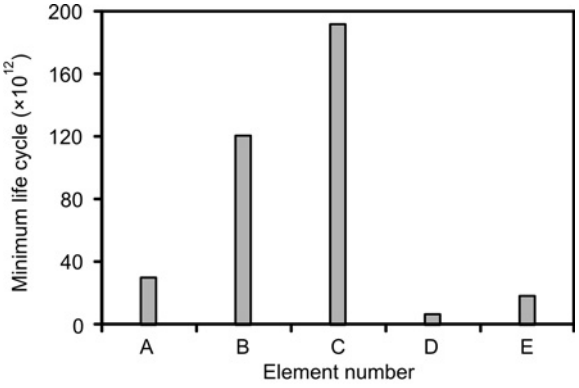

Fig. 14. Minimum life cycles for cases A–E

Obviously, the order C, B, A, E and D can be considered as the best to the worst case in terms of fatigue life. In other words, case C has the longest fatigue life because

it has the highest number of fatigue cycles (1.9×10^8 cycles). Besides, even for a given case, the most critical element can be determined in terms of the number f of cycles to failure. For example, referring to Fig. 13 and comparing the fatigue life of different elements in case C, the failure will most probably initiate at the element 187 which has the lowest cycle to failure.

From the industrial point of view, the application of numerical simulation, e.g. FE analysis, not only provides precise analysis of stresses, accurate calculation of forming loads and rapid solutions to technical problems , but it also saves costs and time.

4. Conclusions

The possible ways of improving the fatigue life and preventing the pre-mature failure of forging dies have been investigated, by using techniques such as imposing pre-stress by shrink rings, die inserts, shrink rings, assembled dies and tapered dies. The studies were carried out on a M10 bolt die made of AISI 1010 steel. The results of finite element simulation show that negative or compressive stresses are generated using the aforementioned approaches. In other words, the methods applied can reduce significantly the tensile stresses responsible for fatigue crack initiation. The fatigue life of dies can be significantly improved when the negative stresses, rather than tensile ones, are formed. In another approach, the critical regions of highly concentrated stresses are identified and appropriate solutions are provided. For example, changing the design of a die was considered as a practical approach that has significant influence on the fatigue life of dies.

References

[1] LANGE K., *Handbook of Metal Forming*, McGraw-Hill, New York, 1985.
[2] ALTAN T., OH S.I., GEGEL H.L., *Metal Forming: Fundamentals and Applications*, American Society for Metals, USA, 1983.
[3] HUR K.D., CHOI Y., YEO H.T., Finite Elem. Anal. Des., 40 (2003), 173.
[4] GRRAY A.G., *Source Book on Cold Forming*, American Society for Metals, USA, 1975.
[5] VAZQUEZ V., HANAN D., ALTAN T., J. Mater. Proc. Technol., 98 (2000), 90.
[6] YOH E.G., KIM Y.I., LEE Y.S., PARK H.J., NA K.H., J. Mater. Proc. Technol., 131 (2002), 647.
[7] COLLINS J.A., *Failure of Materials in Mechanical Design*, Wiley, New York, 1981.
[8] FALK B., ENGEL U., GEIGER M., J. Mater. Proc. Technol., 119 (2001), 158.
[9] KNOERR M., RENTSCH C., ALTAN T., *Application of 1-DEAS in CAE of Forging Dies*, Proc. ICCON User's Conference, OH, USA, 1991.
[10] YEO H.T., CHOI Y., HUR K.D., Int. J. Adv. Manuf. Technol., 18 (2001), 54.
[11] LONG H., BALENDRA R., J. Mater. Process. Techn., 81 (1998), 665.
[12] ABAQUS User's Manual. Version 6.3.1, Hibbitt, Karlson and Sorensen, Inc., USA, 2002.
[13] FUCHS H.O., STEPHENS R.I., *Metal Fatigue in Engineering*, Wiley, New York, 1980.
[14] GEIGER M., FALK B., ENGEL U., Prod. Eng., 6 (1999), 2.
[15] UGRAL A.C., FENSTER S.K., *Advanced Strength and Applied Elasticity*, Prentice-Hall, New Jersey, 1995.

[16] HERTZBERG R.W., *Deformation and Fracture Mechanics of Engineering Materials*, Wiley, New York, 1983.
[17] SHIGLEY J.E., MISCKE C.R., BUDYANS R.G., *Mechanical Engineering Design*, McGraw-Hill, New York, 2004.

Received 29 December 2008
Revised 12 October 2009

Materials Science-Poland, *Vol. 28*, *No. 1*, *2010*

Raman scattering of ZnO films prepared by the laser molecular beam epitaxy

C. WANG[1*], Z. CHEN[2], Y. HE[1], L. LI[1], D. ZHANG[1]

[1]School of Physics Science and Information Engineering, Liaocheng University, Liaocheng 252059, Shandong Province, P.R. China

[2]School of Materials Science and Engineering, Nanyang Technological University, Singapore 639798

A series of ZnO films have been prepared on Si (100) substrate at various oxygen pressures and at various substrate temperatures by using a laser molecular beam epitaxy system. Their structure was investigated by the Raman spectroscopy and X-ray diffraction. Raman spectra showed that only E_2 (low) and E_2 (high) modes were present in all ZnO films. The E_2 (low) mode peak changed from disperse to sharp at first and then became more dispersed as either the oxygen pressure or the substrate temperature increased. Its intensity reached a maximum either under the oxygen pressure of 1 Pa or at 773 K. The analyses showed that the sharper and stronger the E_2 (low) mode peak, the better the crystal quality, which was confirmed by the X-ray diffraction. Moreover, every E_2 (high) mode peak shifted to lower Raman frequencies compared with ZnO single crystal, implying that a tensile stress occurred in all films, which was also proved by the X-ray diffraction. All results indicated that Raman scattering is one of the most useful methods to investigate the structure of ZnO films. In addition, the intensity of Si Raman scattering was enhanced in our results, which might be due to surface-enhanced Raman spectroscopy.

Keywords: *Raman scattering; X-ray diffraction; ZnO films; laser molecular beam epitaxy*

1. Introduction

ZnO wjich has attracted much attention in recent years [1–4], is a versatile II–IV semiconductor material, with a variety of applications such as in ultraviolet (UV) emitters and detectors, surface acoustic wave (SAW) devices, gas sensors and transparent conducting electrodes. Many reports on ZnO films involved some techniques to study their structure, playing a key role in determining the properties of ZnO films. Raman scattering is considered to be a valuable technique for fast and nondestructive study of ZnO films. It can give information about the crystal structure at the scale of a few lattice constants. Any distortion of the lattice, excursion of the component, crystal defect and phase transformation can be shown in Raman bands. Therefore, the Ra-

[*]Corresponding author, e-mail: e-mail: wcz102@sjtu.org

man spectroscopic technique is one of the most useful methods for gaining insight into the microscopic structural effects of ZnO materials. In this paper, we have used Raman scattering to investigate the effects of both oxygen pressure and substrate temperature on ZnO films.

2. Experimental

All ZnO films were prepared on single crystals Si (100) substrates by using a laser molecular beam epitaxy system. The laser source was a KrF excimer laser with the wavelength of 248 nm. The pulse of the laser was 5 Hz and the energy was 100 mJ per pulse. A ZnO ceramic target with the diameter of 40 mm and the purity of 99.99% was installed parallel to the substrate surface and the distance between the target and the substrate was about 5 cm. The base pressure was ca. 5×10^{-6} Pa. When in position, all KrF excimer laser pulses were focused by a lens and were directed onto a ZnO ceramic target. In order to improve the crystal quality of ZnO films and to compensate the oxygen atoms in ZnO films, the oxygen gas with a purity of 99.999% was put into a deposition chamber. Both the target and the substrate were rotated at 30 rev/min in order to make the ZnO films homogeneous. The deposition time was about 2 h for all samples. The microstructure of ZnO films was investigated using both a Raman spectrometer and an X-ray diffractometer (XRD) with Cu K_α radiation ($\lambda = 0.15406$ nm). The cross-section morphologies were characterized by scanning electronic microscopy (SEM). The thicknesses of ZnO layers could also be determined by observing the cross-section morphologies of ZnO layers. The results showed that all ZnO layers are ca. 800 nm.

3. Results and discussion

Figure 1 shows the Raman spectra of ZnO films prepared on Si substrate under various oxygen pressures. The substrate temperatures are all 773 K and all the results could be obtained by the subtraction of signals of the Si substrate from total signals. It can be seen that the E_2 modes corresponding to ZnO films are represented besides some Raman peaks corresponding to single crystal Si, and no other Raman peaks corresponding to ZnO were discovered. The E_2 modes include an E_2(low) mode at about 99 cm^{-1} and an E_2(high) mode at about 437 cm^{-1} [5]. It was clear from Fig. 1 that the ZnO film exhibited a dispersed E_2(low) peak with low intensity at a low oxygen pressure of 10^{-5} Pa. As the oxygen pressure increased, the E_2(low) peak first became sharp and then dispersed, reaching its sharpest profile at 1 Pa oxygen pressure. At the same time, the intensity of the E_2(low) peak also reached a maximum. Meanwhile, it could be seen that the position of E_2(high) peaks for all ZnO films shifted to a lower frequency compared with ZnO single crystal [5]. In addition, it should be noted that a very strong Raman signal of Si substrate was present even if the substrate signal was

subtracted from the total signal. This might be attributed to the surface-enhanced Raman spectroscopy (SERS) [6] induced by the epitaxy layer ZnO films. Further comparative studies will be undertaken later.

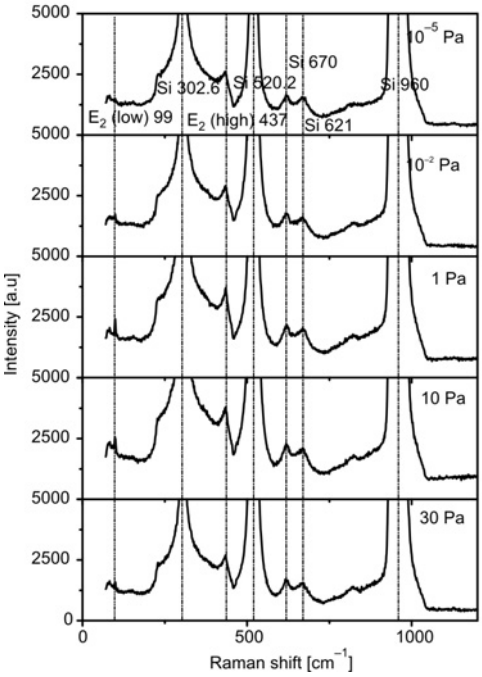

Fig. 1. Raman spectra of ZnO films prepared on Si substrate under various oxygen pressures. The substrate temperatures are all 773 K

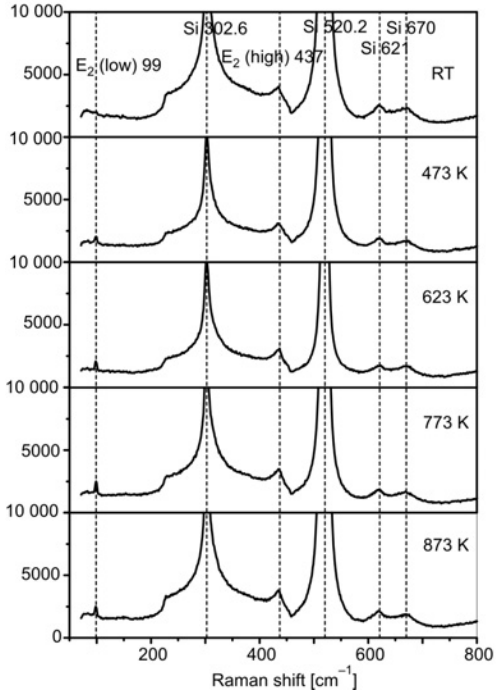

Fig. 2. Raman spectra of ZnO films prepared on Si substrate at various substrate temperatures. The oxygen pressures are all 1 Pa

Figure 2 shows the Raman spectra of ZnO films prepared on Si substrate at various substrate temperatures. The oxygen pressures were all 1 Pa and all the spectra were obtained by the subtraction of the Si substrate signal from the total signal. It can be seen that the results were similar to those in ZnO films prepared under various oxygen pressures. Besides some Raman peaks corresponding to single crystal Si, only E_2 modes corresponding to ZnO films were present in the spectra. At low substrate temperatures ZnO film exhibited a dispersed E_2 (low) peak with low intensity. As the substrate temperature increased, the profile of the E_2 (low) peak at first became sharp and then became dispersed, reaching its sharpest profile at 773 K. At the same time, the intensity of the E_2 (low) peak also reached a maximum. In addition, it can be seen from Fig. 2 that the position of each E_2 (high) peak also shifted to lower frequencies compared with ZnO single crystal [5].

It is well known that ZnO with a hexagonal wurtzite structure belongs to the space group C_{6v}^4. The group theory predicts that optical phonons at the Γ point of the Brillouin

zone belong to the following irreducible representation [7, 8]: $\Gamma = 1A_1 + 2B_1 + 1E_1 + 2E_2$. Both A_1 and E_1 modes are polar and split into transverse (TO) and longitudinal optical (LO) phonons with different frequencies, due to the macroscopic electric fields associated with the LO phonons. The two non-polar E_2 modes are Raman active only. The B_1 modes are infrared and Raman inactive (silent modes). As far as the phonon modes were concerned, different scattering geometry could generate different phonon modes in the Raman spectra. In this paper, the Raman spectra have been recorded with the scattering geometry in which incident and scattered polarizations are parallel. According to Raman selection rules [9], only the E_2 and A_1(LO) mode can be observed in the above geometry. The reason why the A_1(LO) mode did not occur in our experiments might be due to the fact that the A_1(LO) mode was subsumed by the strong Si substrate mode [10].

Some researchers [11–13] reported that the E_2 (low) peak could determine the crystal quality of films, while the E_2 (high) peak had a close relationship with the intrinsic stress in ZnO films. If the E_2 (low) peak is sharpest and has the highest intensity, the sample has the best crystal quality. Moreover, if a tensile stress occurs in the films, the E_2 (high) peak can shift to lower frequencies compared with the bulk value of 437 cm^{-1}, while the E_2 (high) peak can shift to higher frequencies with respect to 437 cm^{-1} if there exists a compressive stress in the films. Therefore, according to the Raman results above, we can draw the conclusion that ZnO films prepared on Si substrate both under 1 Pa oxygen pressure and at 773 K have the best crystal quality, and all ZnO films exhibited tensile stress, which can also be confirmed by XRD results.

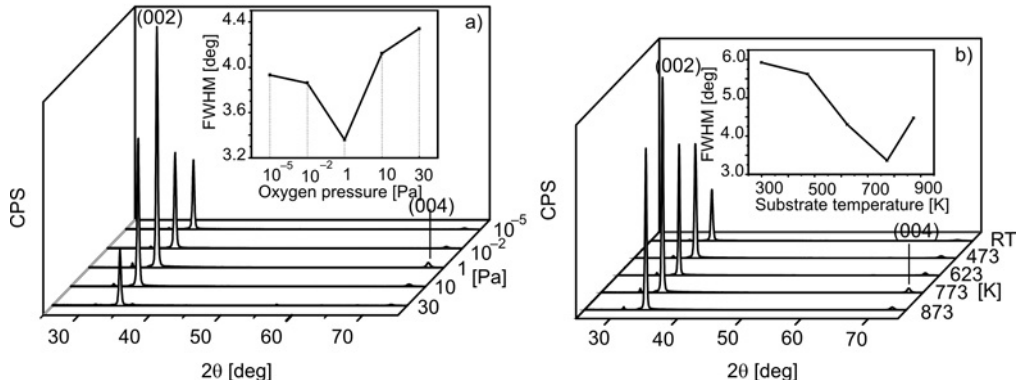

Fig. 3. XRD spectra of ZnO films prepared on Si substrate either at 773 K for various oxygen pressures (a) or under oxygen pressure of 1 Pa for various substrate temperatures (b). The inset shows the dependences of full widths at half maximum (FWHM) of the rocking curve of (002) diffraction peak on either the oxygen pressure (a) or the substrate temperature (b)

Figure 3 shows the XRD spectra of ZnO films prepared on Si substrate either at 773 K under various oxygen pressures or under 1 Pa oxygen pressure for various substrate temperatures. It can be seen that the ZnO films formed a wurtzite (*B*4) structure and there occurred a strong (002) diffraction peak at 2θ equal to ca. 34.5° for all ZnO films. A (004) diffraction peak also occurred for all ZnO films. However, its low in-

tensity compared the intensity of the (002) peak implied that ZnO films have strong (002) texture and grew along the [002] orientation. This is confirmed by SEM observation (Fig. 4). Figure 4 shows the cross-section morphologies of ZnO films prepared both at 773 K and under oxygen pressure of 1 Pa. It was apparent that ZnO films with the thickness of ca. 800 nm formed columnar grains, indicating that ZnO films grew in columnar form. By comparison of the XRD spectra, one can draw the conclusion that ZnO films grew along the [002] orientation, which is perpendicular to the substrate surface.

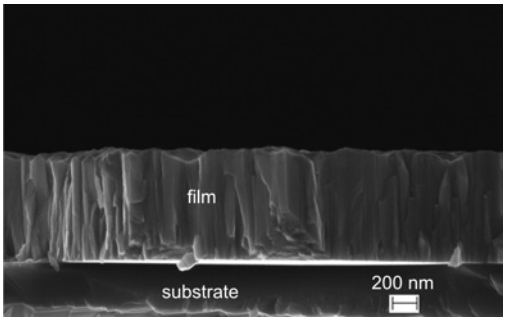

Fig. 4. The cross-section morphology of ZnO films prepared both at 773 K and at 1 Pa oxygen pressure

It is apparent from Fig. 3a that at a low oxygen pressure of 10^{-5} Pa, the intensity of the (002) diffraction peak was low. As the oxygen pressure increased, the intensity of the (002) diffraction peak increased and then decreased, reaching a maximum at the middle oxygen pressure of 1 Pa. In addition, at a low substrate temperature, the intensity of the (002) diffraction peak was also low. As the substrate temperature increased, the intensity of the (002) diffraction peak increased and then decreased, reaching a maximum at 773 K (Fig. 3b).

The intensity of a diffraction peak depends on both the crystal quality and the thickness of a film. Therefore it is insufficient to evaluate the crystal quality of ZnO films only from the intensity of the (002) diffraction peak. Another important factor is the full width at half maximum (FWHM) of the rocking curve of the (002) diffraction peak for ZnO films, through which we can easily determine the crystal quality of ZnO films prepared under various oxygen pressures. The smaller the FWHM, the better the crystal quality is. Accordingly, we measured the rocking curve of the (002) diffraction peak for ZnO films prepared under all conditions and showed the dependence of the FWHM values on either the oxygen pressure or the substrate temperature, as the insets in Fig. 3. It can be seen from the inset in Fig. 3a that as the oxygen pressure increased, the FWHM of the rocking curve of the (002) diffraction peak first decreased and then increased, reaching a minimum of about 3.36° at 1 Pa oxygen pressure, indicating that film had the best crystal quality. It can also be seen from Fig. 3b that as the substrate temperature increased, the FWHM of the rocking curve of the (002) diffraction peak first decreased and then increased, reaching a minimum of about 3.36° at 773 K, indicating that the film prepared at 773 K had the best crystal quality. All the above results showed that ZnO films prepared both at 1 Pa oxygen pressure and at 773 K have the

best crystal quality, which is in good agreement with the Raman spectra and confirmed the accuracy of the Raman results.

For all ZnO films, the diffraction angle of all ZnO (002) diffraction peaks shifted to higher values compared with the standard XRD spectrum of ZnO powder (2θ = 34.43°) [14], implying that the lattice constant c changed for all ZnO films. These changes were mainly caused by the intrinsic stress of ZnO films. For ZnO films with a wurtzite structure, the intrinsic stress could be obtained by the following formula [15]:

$$\sigma = \frac{2c_{13}^2 - c_{33}(c_{11} + c_{12})}{2c_{13}} \frac{c - c_0}{c_0} \tag{1}$$

where (i, j = 1, 2, 3) stands for the elastic constants in various orientations, c_0 is the lattice constant of ZnO films without defects and c is the lattice constant of ZnO film in our experiments, which can be computed by the following formulae:

$$\frac{1}{d^2} = \frac{4}{3}\frac{h^2 + hk + k^2}{d^2} + \frac{l^2}{c^2} \tag{2}$$

$$2d \sin\theta = \lambda \tag{3}$$

where h = 0, k = 0, l = 0 for the ZnO (002) diffraction peak, therefore, c is expressed as follows:

$$c = 2d_{002} = \frac{\lambda}{\sin\theta} \tag{4}$$

where d_{002} is the interplanar spacing of the ZnO (002) crystal plane. λ and θ are the X-ray wavelength and the Bragg diffraction angle, respectively.

Substituting the value of $c_{i,j}$ (i, j = 1, 2, 3) in Eq. (1) with c_{11} = 208.8 GPa, $c_{1,2}$ = 119.7 GPa, $c_{1,3}$ = 104.2 GPa, c_{33} = 213.8 GPa [16], we could obtain the residual stress σ [GPa] in ZnO film by the following formula:

$$\sigma = -233\frac{c - c_0}{c_0} \tag{5}$$

Using the above formula, we calculated the intrinsic stress σ and the lattice constant c for various ZnO films, as shown in Fig. 5. Figure 5a showed the dependence of the intrinsic stress and the lattice constant on the oxygen pressure at 773 K and Fig. 5b the dependence of the intrinsic stress and the lattice constant on the substrate temperature under oxygen pressure of 1 Pa. The lattice constants of all ZnO films are smaller than that of bulk materials, thus resulting in tensile stresses in films, which was in good agreement with Raman data. These results confirmed that Raman scattering is a useful method for studying the structure of ZnO films. In addition, upon increasing the oxygen pressure, the stress first decreased and then increased, reaching a minimum

at 1 Pa (Fig. 5a). As the substrate temperature increased, however, the stress increased monotonically (Fig. 5b).

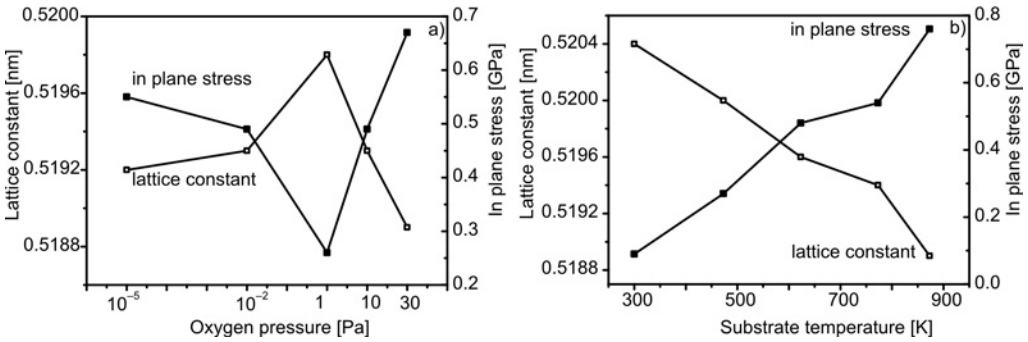

Fig. 5. Dependences of the lattice constant and the intrinsic stress on the oxygen pressure at 773 K (a), on the substrate temperature at 1 Pa oxygen pressure (b)

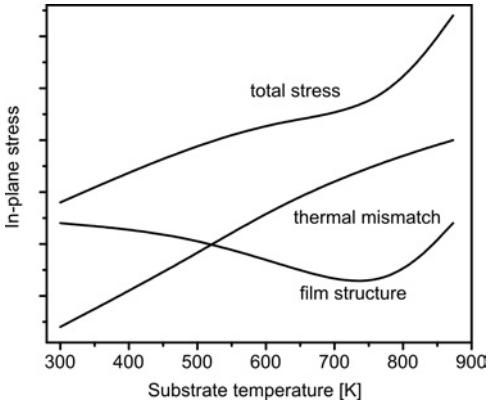

Fig. 6. Schematic illustration of the changes of stresses with the substrate temperature

In the ZnO film with the wurtzite structure, an intrinsic film stress in the direction perpendicular to the surface originated from a *C*-axis strain [17, 18]. Basically, this stress included an intrinsic stress originating from thermal mismatch between films and substrates and another intrinsic stress originating from the film structure. For ZnO films prepared with various oxygen pressures at 773 K, the intrinsic stress originating from thermal mismatch between films and substrates should be equal, while the intrinsic stress originating from the film structure changed non-monotonically with the film structure and should reach a minimum for films with the best crystal quality, thus resulting in the non-monotonic dependence of the stress on the oxygen pressure. For ZnO films prepared with various substrate temperatures under oxygen pressure of 1 Pa, two kinds of stresses changed with the substrate temperature. The intrinsic stress originating from thermal mismatch between films and substrates should increase monotonically as the substrate temperature increases, while another intrinsic stress originating from the film structure should change non-monotonically with the sub-

strate temperature and should reach a minimum for film with the best crystal quality. Therefore, the sum of the two kinds of stresses might give rise to the monotonic change of the stress with the substrate temperature (Fig. 6).

4. Conclusions

The structure and intrinsic stress of ZnO films have been investigated by using a Raman spectrometer and the X-ray diffraction. The results showed that only the E_2 mode occurred in ZnO films prepared either at 773 K for various oxygen pressures or at 1 Pa oxygen pressure for various substrate temperatures. The analyses showed that the sharper and the stronger the E_2 (low) mode peak, the better the crystal quality, and the E_2 (high) mode peak in all films shifted to lower frequencies compared with ZnO single crystal, implying that a tensile stress occurred in all films. These results confirmed by X-ray diffraction indicated that Raman scattering is one of the most useful methods to investigate the structure of ZnO films. The changes in intrinsic stress were also analyzed in detail.

Acknowledgement

This work was supported by the Research Foundation of Shandong Provincial Education Department of China (No. J08LI13) and by the Science Foundation for Distinguished Young Scientist of Shandong Province (No. 2008BS04036) of China. The authors also thank the Shandong Provincial Educational Department for providing a support base for College Teachers to research abroad.

References

[1] MANDALAPU L.J., XIU F., YANG Z., LIU J.L., Solid State Electr., 51 (2007), 1014.
[2] HUANG F.C., CHEN Y.Y., WU T.T., Nanotechn., 20 (2009), 065501.
[3] BASU P.K., JANA S.K., MITRA M.K., SAHA H., BASU S., Sens. Lett., 6 (2008), 699.
[4] MINAMI T., MIYATA T., Thin Solid Films, 517 (2008), 1474.
[5] ASHKENOV N., MBENKUM B.N., BUNDESMANN C., RIEDE V., LORENZ M., SPEMANN D., KAIDASHEV E.M., KASIC A., SCHUBERT M., GRUNDMANN M., J. Appl. Phys., 93 (2003),126.
[6] STILES P.L., DIERINGER J.A., SHAH N.C., VAN DUYNE R.R., Ann. Rev. Anal. Chem., 1 (2008), 601.
[7] ARGUELLO C.A., ROUSSEAU D.L., PORTO S.P.S., Phys. Rev., 181(1969), 1351.
[8] WANG X.B., SONG C., GENG K.W., ZENG F., PAN F., Appl. Surf. Sci., 253 (2007), 6905.
[9] ZHANG Y., JIA H.B., WANG R.M., CHEN C.P., LUO X.H., YU D.P., Appl. Phys. Lett., 83 (2003), 4631.
[10] BUNDESMANN C., ASHKENOV N., SCHUBERT M., SPEMANN D., BUTZ T., KAIDASHEV E.M., LORENZ M., GRUNDMANN M., Appl. Phys. Lett., 83 (2003), 1974.
[11] DCREMPS F., PELLICER-PORRES J., SAITTA A.M., CHERVIN J.C., POLIAN A., Phys. Rev. B, 65 (2002), 092101.
[12] SERRANO J., MANJÓN F.J., ROMERO A.H., WIDULLE F., LAUCK R., CARDONA M., Phys. Rev. Lett., 90 (2003), 055510.
[13] ZENG J.N., LOW J.K., REN Z.M., LIEW T., LU Y.F., Appl. Surf. Sci., 197/198 (2002), 362.
[14] CHEN Y., BAGNALL D.M., KOH H.J., PARK K.T., HIRAGA K.J., ZHU Z.Q., YAO T., J. Appl. Phys., 84 (1998), 3912.
[15] HONG R.J., HUANG J.B., HE H.B., FAN Z.X., SHAO J.D., Appl. Surf. Sci., 242 (2005), 346.

[16] CULLITY B.D., *Elements of X-ray Diffractions*, Addison–Wesley, Reading, MA, 1978.
[17] THORNTON J.A., HOFFMAN D.W., Thin Solid Films, 171 (1989), 5.
[18] HONG R.J., QI H.J., HUANG J.B., HE H.B., FAN Z.X., SHAO J.D., Thin Solid Films, 473(2005), 58.

Received 26 February 2009
Revised 14 June 2009

Materials Science-Poland, *Vol. 28*, *No. 1*, *2010*

Structure and properties of iron aluminide layers fabricated by the chemical vapour deposition on 316L steel

R. SITEK[1*], J. KAMIŃSKI[1], P. SALLOT[2], K.J. KURZYDŁOWSKI[1]

[1]Faculty of Materials Science and Engineering, Warsaw University of Technology, ul. Wołoska 141, 02-507 Warsaw, Poland

[2]Ecole Nationale Supérieure des Mines de Saint-Etienne, 158 Cours Fauriel, 42000 Saint-Etienne, France

The paper presents results of studies of structure and properties of the NiAl + FeAl type diffusion layers fabricated on 316L steel (00H17N14M2) by the chemical vapour deposition using aluminium chloride ($AlCl_3$) in a hydrogen atmosphere as a carrier gas. The layers were examined using light and scanning electron microscopy. Chemical composition analyses were carried out by EDS and phase content was investigated by XRD. Corrosion resistance was tested using the potentiodynamic method in 0.5 M NaCl, and layer/structure adhesion was tested by the scratch test. The results obtained indicate that the 50 μm thick layers fabricated on the 316L steel substrate show very good adhesion combined with very good corrosion resistance.

Keywords: *iron aluminides; FeAl; CVD; austenitic stainless steel; intermetallics*

1. Introduction

Austenitic stainless steel 316L, due to its high corrosion resistance, is frequently used in implant materials [1–5] and for surgical instruments. There is also a constant increase in the number of other fields of application, in the nuclear, shipping, chemical, power and food industries. Wider use of 316L steel in industry is limited by its low operating temperature (up to ca. 400 °C), unsatisfactory resistance to abrasive wear, and insufficient resistance to pitting corrosion (e.g., physiological fluids). To improve these properties, various technological processes are used, e.g. introduction of sufficient amounts of nitrogen and molybdenum, special heat-treatments [6] or surface treatments, i.e. nitriding or oxygen nitriding [7–10]. The advantage of the surface treatment is the ability to fully control the process used to produce layers with a spe-

*Corresponding author, e-mail: rsitek@inmat.pw.edu.pl

cific microstructure, phase content, and chemical composition. Fe-Al type intermetallic phases are increasingly more commonly used in the automotive, aircraft, and shipping industries because they have good heat resistance, are strongly resistant to abrasive wear, have a relatively low density compared with conventional iron and nickel alloys, and because of their high resistance to corrosion in environments containing sulphur or oxygen. It has been predicted [11] that Fe-Al type intermetallic phases can replace in future austenitic steels, used in the food industry, that contain chromium and nickel harmful to organisms. The feature that limits the application of bulk intermetallics is their fragility at room temperature, and hydrogen embrittlement caused by a high affinity of aluminium to water in vapour. These properties can be improved by the addition of alloy elements such as Mo, Si, Cr, Ta, or by grain refinement: this significantly increases the production cost of bulk intermetallic materials [11]. The fabrication of Fe-Al type intermetallics in the form of layers on austenitic steels is both simple and economical [12, 13]. Accordingly, this paper presents the results of research on the fabrication, using the chemical vapour deposition (CVD) method, of Fe-Al type intermetallic layers on 316L steel. Aluminium chloride ($AlCl_3$) was used as the source of aluminium, and the carrier gas was hydrogen.

2. Experimental

Samples for tests were cut out from a 4 mm thick cylindrical bar (diameter 20 mm) made of 316L steel (00H17N14M2) having the chemical composition presented in Table 1.

Table 1. Chemical composition of the 316L steel

Element	Cr	Ni	Mo	Si	Mn	C	Cu	P	S	Fe
Concentration [wt. %]	17.47	12.7	2.55	0.8	2.0	0.03	0.015	0.045	0.03	balance

Sample surfaces were polished using sandpapers (grit: 600, 800, and 1200) and were degreased using an ultrasonic washer in ethyl alcohol. The layers were deposited using the chemical vapour deposition (CVD) method in the IonBond device, in two stages, of one cycle. The first stage involved deposition of aluminium from $AlCl_3$ vapours with the addition of chromium in an hydrogen atmosphere at a temperature of 950 °C for a period of 1.5 h under the pressure of 350 hPa. The second stage entailed baking at 950 °C for 3 h under the pressure of 350 hPa in a N_2 atmosphere. This was to assure diffusion between the deposited aluminium and the steel substrate. In this process, an FeAl diffusion layer was formed. Sections of the samples were examined under scanning electron microscopes HITACHI 2600 and HITACHI 3500 equipped with a microarea microanalysers EDS from Thermo Noran. Cross sections were polished to a mirror-like finish using 0.05 μm silicate slurry. All samples were ultrasonically degreased in acetone and ethanol.

The phase analyses were performed with a Bruker D8 X-ray diffractometer using Cu K_α radiation. The samples were examined in a parallel beam from a parabolic mirror (Gobel Mirror Bruker) under the fixed angle $\omega = 10°$. A corrosion resistance test was conducted using impedance and potentiodynamic methods on an AutoLab PGSTAT 100 device in a deoxidised 0.5 M NaCl solution at room temperature. A deoxidised environment was obtained by running chemically pure argon through the solution. Oxygen concentration was measured using an Elmetron CO 401 oxygen meter. Impedance tests were performed in a three-electrode system (tested electrode –reference electrode (saturated calomel electrode – SCE)–counter electrode (platinum)) within the frequency range of 10^5–10^{-3} Hz at the sinusoidal signal amplitude of 20 mV. The impedance spectra for steel were analyzed using the equivalent circuits (EC). Figure 1a presents the EC for the one time constant model (R(RQ)) and Fig. 1b shows the EC for two time constants model R(Q[R(RQ)]).

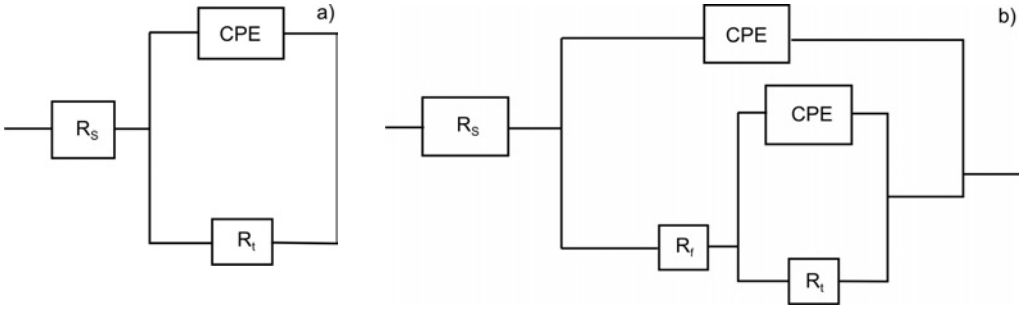

Fig. 1. Equivalent circuits: a) R(RQ), b) R(Q[R(RQ)]); CPE – constant phase element, R_s – solution resistance, R_f – resistance of the porous layer, R_t – charge transfer resistance through a double layer

The spectra were studied with the Baukamp's EQUIVCRT software. The potentiodynamic tests were performed in the same three-electrode system within the potential range from –400 mV to 500 mV in the anodic direction at the rate of 0.2 mV/s. Surface topography tests were conducted using a VEECO scanning profilometer. The microhardness measurements were carried out using the Vickers method and a ZWICK (Materialprüfung 3212002) hardness meter under the load of 200 g. The layer adhesion test was measured on a Micro-Combi-Tester device, with a variable load in the range from 0 to 100 N.

3. Results

The CVD method used in the study, employing $AlCl_3$ as an aluminium donor in a hydrogen carrier gas atmosphere, was good enough to produce a 50 μm layer on the 316L steel substrate. These layers of a complex substructure consisting of elongated grains exhibited geometrically perfect adhesion to the substrate (Fig. 2).

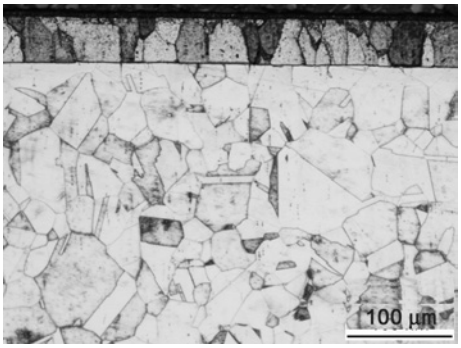

Fig. 2. Microstructure of the layer after the process at 950 °C on the 316L steel substrate

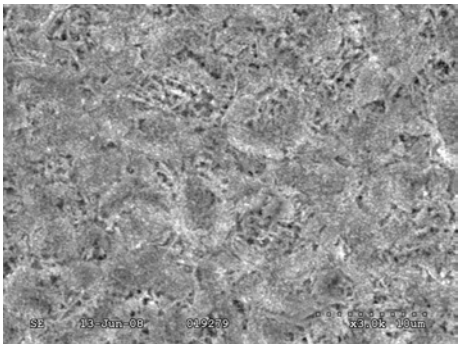

Fig. 3. Morphology of the surface of the layer at 950°C

Figure 3 shows that the surface of the layer was relatively smooth with an average surface roughness parameter R_a not exceeding 0.5 µm. Details on the data roughness is provided in Table 2. R_a is R_a is the average arithmetic standard deviation of the roughness profile, R_q is the average square deviation of the roughness profile and R_t is the maximum height of the roughness profile peak.

Table 2. Roughness parameters [µm] of the 316L steel surface before and after the CVD process

Materials	R_a	R_q	R_t
Before treatment	0.095	0.129	4.53
After treatment	0.412	0.526	6.18

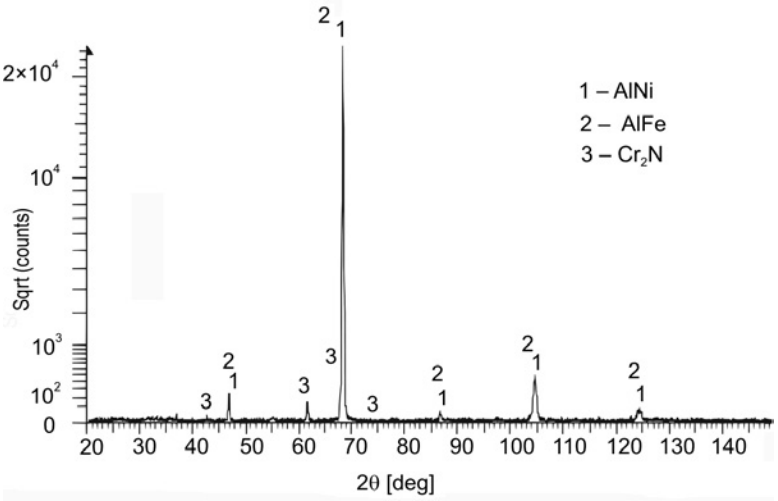

Fig. 4. Spectrum of the X-ray diffraction pattern from the layer produced in the CVD process at 950 °C on the 316L steel substructure

The surface microhardness of the layers was about 430$HV_{0.2}$. The results of X-ray analysis (Fig. 4), performed in the 20–150° range (2θ) revealed the presence of the AlFe, AlNi and Cr_2N phases.

The analysis of the chemical composition focusing on microareas of the transverse sections of the layers (Fig. 5, Table 3) showed the presence of two sub-layers. The outer sublayer is enriched in nickel appearing together with iron and aluminium. In the inner sublayer, the nickel content decreased while the iron content increased.

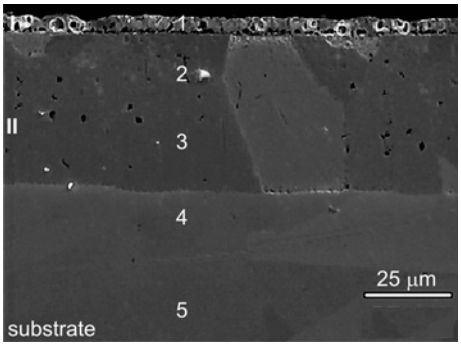

Fig. 5. SEM image of sublayer revealed on the transverse sections of the layers fabricated on the 316L steel in the CVD process at 950 °C (for details, see Table 3)

Table 3. Chemical composition in microareas of the transverse section of the layer produced on 316L steel in the CVD process at 950 °C

Microarea	Chemical composition [wt. %]					
	Fe	Cr	Ni	Mo	Al	C
1	47.61	9.80	23.77	1.70	10.02	6.84
2	67.51	17.19	6.63	2.30	3.42	2.87
3	68.99	18.86	5.06	2.17	2.02	2.91
4	67.01	16.81	8.79	2.07	-	3.21
5	66.67	16.69	9.32	1.87	-	2.88

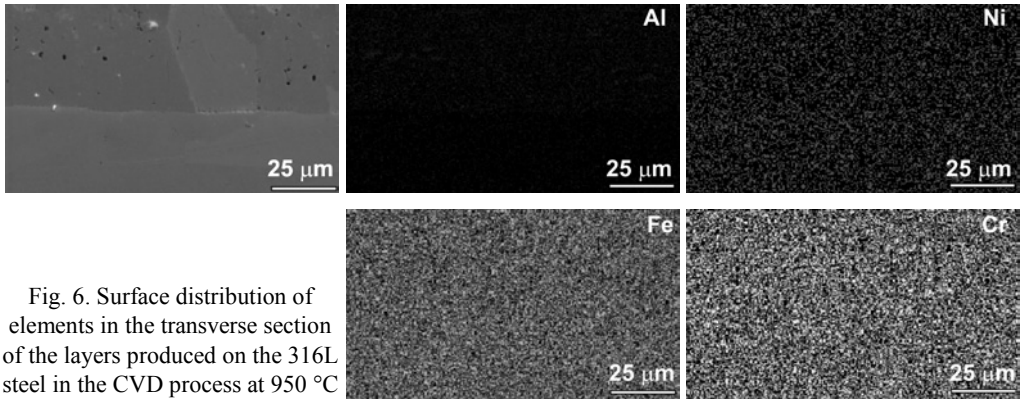

Fig. 6. Surface distribution of elements in the transverse section of the layers produced on the 316L steel in the CVD process at 950 °C

The distribution of the elements on a transverse section of the layer is shown in Fig. 6. It reveals that the layer was made mainly of aluminium, iron, chromium and nickel. The increased concentration of aluminium and nickel in the outer part of the layer indicates the formation of an intermetallic layer containing those two elements. The inner sublayer consists most probably of an intermetallic layer made of iron, and aluminium. However, the presence of some Cr_2N in both sublayers cannot be excluded.

The polarization curves for the 316L steel substrate and samples with the layer (FeAl) produced upon it are shown in Fig 7. Table 4 presents the characteristic electrochemical parameters of the tested materials; i_{corr} is the corrosion current density, E_{corr} – corrosion potential, and E_{np} – nucleated pit.

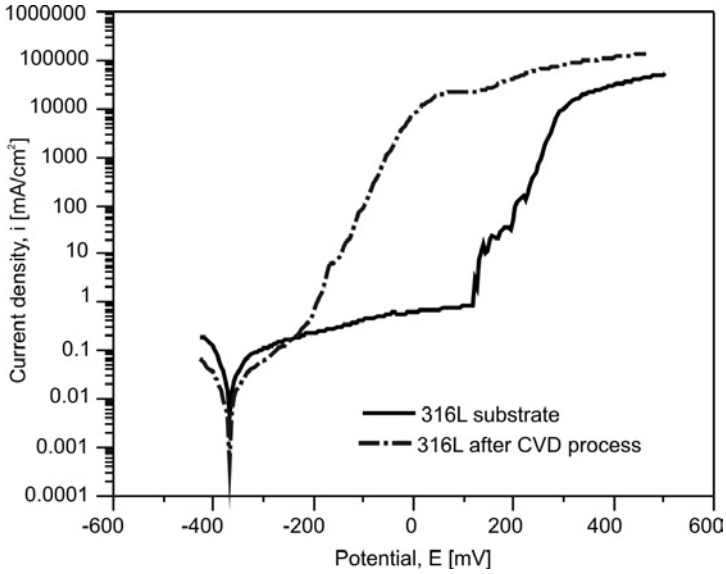

Fig. 7. The anodic polarisation curve in 0.5 M NaCl for NiAl + FeAl type diffusion layer and for 316L steel substrate

Table 4. Corrosion parameters describing the influence of layers fabricated in the CVD process on the corrosion resistance in comparison with the 316L steel

Material	i_{corr} [μA/cm^2]	E_{corr} [mV]	E_{np} [mV$_{SCE}$]
316L steel without a layer	0.08	–370	120
316L steel with a layer of the NiAl + FeAl type	0.028	–330	–180

As results from the data in Table 4 the layers of the NiAl + FeAl type increase the corrosion resistance of 316L steel. It is evidenced by a reduction in the density of corrosion currents with a simultaneous increase in the corrosion potentials. The durability

of this state was significant, as proved by both the low current densities in the passive area (ca. 0.8 μA/cm^2) and the relatively high breakthrough potentials (E_k = 120 mV), with pitting corrosion observed above this potential (Fig. 8a).

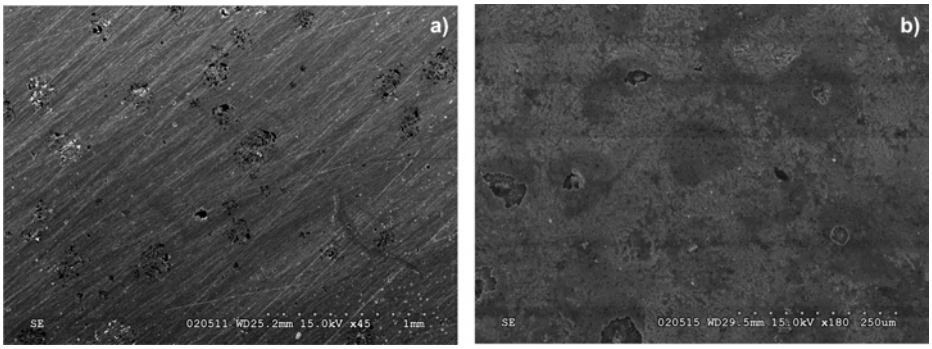

Fig. 8. Morphology of steel after potentiodynamic tests in deoxidised 0.5 M NaCl of the 316L steel substrate (a) and after the CVD process (b)

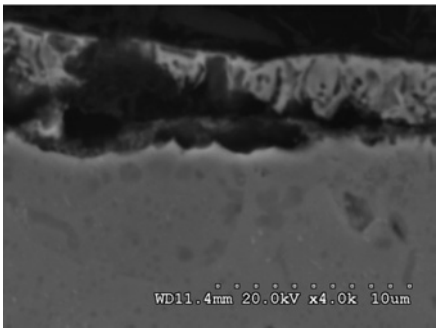

Fig. 9. Under-layer corrosion after being revealed by the potentiodynamic test in deoxidised 0.5 M NaCl solution in transverse sections

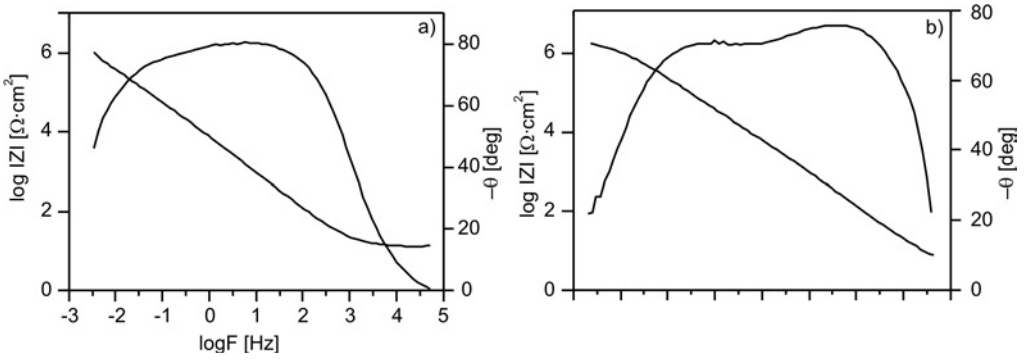

Fig. 10. Impedance spectra (Body's diagram) for the 316L substrate (a) and after the CVD process (b)

The FeAl layers had a significant influence on the 316L steel corrosion resistance. Although the data in Table 4 indicates an improvement in the corrosion resistance, the potentiodynamic tests showed that the durability of the passive state is very low.

A constant increase in densities of currents in the passive area was observed with a simultaneous reduction in the breakthrough potential. Moreover, the produced coatings have a cathodic potential with respect to the substrate which caused the material to be sensitive to underlayer corrosion (Fig. 9). The non-metallic intrusions observed on the layer surface seem to act as local corrosion initiation spots (Fig. 8b).

Table 5. Results of impedance measurement tests of the 316L substrate before and after the CVD process

Material	R [Ωcm^2]	Q_{CPE} [F/cm^2]	n
316L steel without a layer	1.47×10^{6}	7.04×10^{-6}	0.88
316L steel with layer of the NiAl+FeAl type	1.58×10^{6}	6.26×10^{-7}	0.82

Analysis of the spectra shown in Fig. 10 indicates a one time constant characteristic for a single electrochemical process taking place on the surface (i.e., the passage of an electron through a double layer). High angle values (ca. 80°) in a broad frequency range (10^{2}–10^{-1}Hz) confirmed the presence of the passive layer on the steel substrate.

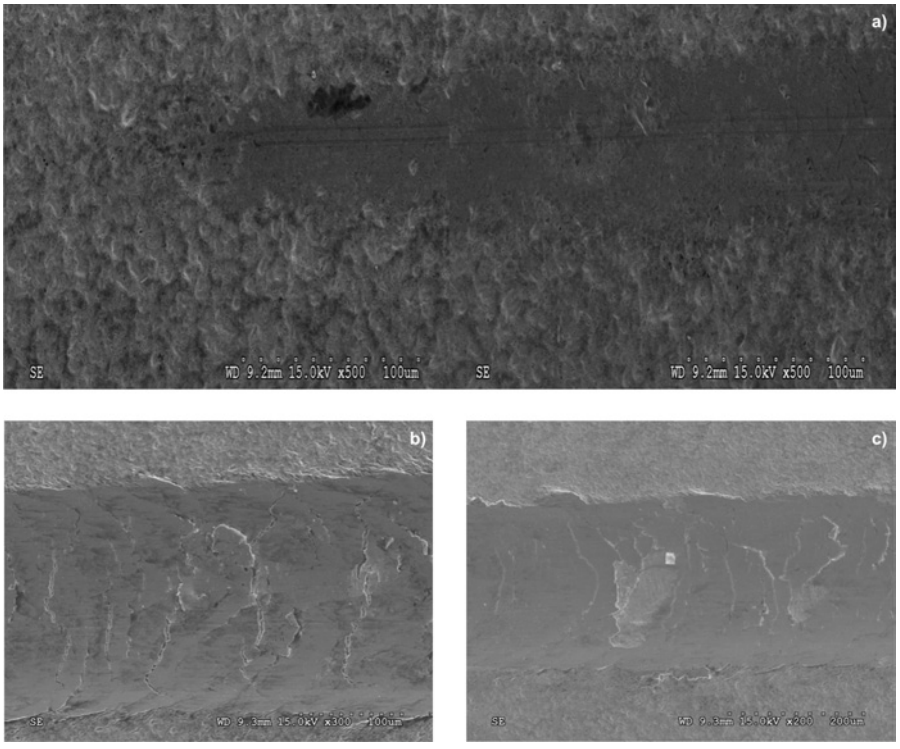

Fig. 11. Results of the scratch test of the resistance to abrasive wear. Details in the text

The layer characteristics (Table 5) were close to the values obtained for permanent passive layers. The impedance spectrum shown in Fig. 10b is different. The presence of two peaks in the impedance spectrum means that two electrochemical processes occurred on the surface, one of them being related to the passage of electrons through the double layer and the other to the electrochemical processes at the heterogeneous outer layer (zone 1 enriched with Al and Ni). According to the impedance spectrum and Fig. 4, it might be assumed that this layer was discontinuous (porous). This is the most likely explanation for the unsatisfactory durability of passive layers as observed during the potentiodynamic tests. The data in Table 5 (R is the resistance, Q – capacity) indicate that, despite the significant porosity of the outer layer, the Fe-Al coating was characterised by a similar corrosion resistance (slightly better) in comparison with the substrate.

Results of the adhesion tests (scratch-test) are presented in Fig. 11. The tested layers demonstrated a very good adhesion to the substrate and plasticity. The first cracks of the layer were observed under a critical force of Lc_1 = 24.1 N at the distance of 2.23 mm (Fig. 11a). Spalling (non-continuous perforation) was observed under a critical force of Lc_2=38.8 N at the distance of 7.63 mm (Fig. 11b). Continuous perforation and layer removal were observed under a critical force of Lc_3 = 73.57 N at the distance of 7.63 mm (Fig. 11c).

4. Summary

The CVD treatment with $AlCl_3$ vapour and hydrogen as carrier gas at 950 °C is satisfactory to produce ca. 50 μm thick layers of the NiAl + FeAl type 316L substrate in one-step. The layers are characterised by a very good adhesion to the substructure, and can be deposited on surfaces having complicated geometries. The NiAl + FeAl layer has a cathodic character in relation to the substrate. It improves the corrosion resistance of steel 316L but makes it more sensitive to the sublayer corrosion.

References

[1] *Engineering Materials for Biomedical Applications*, Teoh Swee Hin (Ed.), World Scientific, Singapore, 2004.
[2] BORDJI K., JOUZEAU J.Y., MAINARD D., PAYAN E., DELEGOUTTE J.P, NETTER P., Biomater., 17 (1996), 491.
[3] SUDHAKAR K.V., Eng. Fail. Anal., 12 (2005), 249.
[4] LIU C., LIN G., QI D.Y.M., Surf. Coat. Techn., 200 (2006), 4011.
[5] GERINGER J., FOREST B., COMBRADE P., Wear, 259 (2005), 943.
[6] ABDULUYAHED A.-A., ROŻNIATOWSKI K., KURZYDŁOWSKI K.J., Scripta Metal., 33 (1995), 1489.
[7] FOSSATI A., BORGIOLI F., GALVANETTO E., BACCI T., Surf. Coat. Technol., 200 (2006), 3511.
[8] LI G.-J., PENG Q., LI C., WANG Y., GAO J., CHEN S.-Y., WANG J., SHEN B.-L., Surf. Coat. Technol., 202 (2008), 2749.
[9] MINGOLO N., TSCHIPTSCHIN A.P., PINEDO C.E., Surf. Coat. Technol., 201 (2006), 4215.

[10] ZHAO C., WANG L.Y., HAN L., Surf. Eng., 24 (3) (2008), 188.
[11] *Metallic Materials Containing Intermetallic Phases*, W. Przetakiewicz, Z. Bojar (Eds.), Studio Bel, Warsaw, 2006 (in Polish).
[12] ZHANG Y., PINT B.A., COOLEY K.M., HAYNES J.A., Surf. Coat. Technol., 202 (2008), 3839.
[13] KAMACHI MUDALI U., BHUVANESWARAN N., SHANKAR P., RAJ B., Corr. Sci., 46 (2004), 2867.

Received 10 March 2009

Materials Science-Poland, *Vol. 28*, *No. 1*, *2010*

Optical properties of ternary tellurite glasses

M.K. HALIMAH*, W.M. DAUD, H.A.A. SIDEK, A.W. ZAIDAN, A.S. ZAINAL

Ultrasonic Laboratory, Department of Physics, Faculty of Science,
University Putra Malaysia, 43400 Serdang, Selangor, Malaysia

Test samples of ternary glass tellurite $[(TeO_2)_{65}(B_2O_3)_{35}]_y[Ag_2O]_y$ with y = 10, 15, 20, 25, 30 mol % have been fabricated and their physical and optical properties were investigated. The optical absorption was recorded at room temperature in the wavelength range from 200 to 800 nm. From the absorption edge data, the value of the optical band gap E_{opt} and the Urbach energy ΔE were evaluated. The value of E_{opt} lies between 2.15 eV and 1.85 eV for the indirect transition and for direct transition the values vary from 2.77 eV to 2.35 eV. From the experimental results, values of the optical band gap and Urbach energy were calculated. They were found to be dependent on the glass composition.

Keywords: *tellurite glasses; optical band gap; Urbach energy; density*

1. Introduction

Glasses have some unique properties such as high hardness and transparency at room temperature, along with sufficient strength and excellent corrosion resistance. Due to potential applications in various engineering and technological fields, the study of the properties of glasses is of great significance. Glassy materials have acknowledged advantages, like physical isotropy, the absence of grain boundaries, continuously variable composition they are practical to use [1].

Tellurite glasses are very promising materials for laser and non-linear applications in optics, due to some of their important characteristic features, such as high refractive index, low phonon maxima and low melting point [2]. TeO_2 is known as a conditional glass former; it needs a modifier ion to form the glassy state easily. The formation of glass on two glass formers such as borate glass and tellurite glass is of both scientific and practical interest. This may lead to the formation of new structural units [3]. The basic structural unit of tellurite glass is TeO_4 trigonal bipyramid (tbp) containing a lone pair of electrons and the structural units take the Te–O–Te bond for glass formation. The introduction of TeO_2 into the matrix of alkali borate glasses decreases its

*Corresponding author, e-mail: halimah@science.upm.edu.my

hygroscopicity, improves the quality of the glass (less brittle and free from bubbles) and enhances the IR transmission [4, 5]. Silver dioxide, Ag_2O in the borotellurite network modifies the host structure through the transformation of the structural units of the borate network from $[BO_3]$ to $[BO_4]$ and tellurite network from trigonal bipyramid $[TeO_4]$ to trigonal pyramid $[TeO_3]$[6].

The objective of the present work was to study the optical band gap of the silver borotellurite glass system. A systematic study has been performed on the variation of the optical band gap in function of the Ag_2O composition in borotellurite glasses. Densities were also determined, in order to investigate the correlation between density and molar volume in function of Ag_2O content in the silver borotellurite glass.

2. Experimental

The ternary $[(TeO_2)_{65}\ (B_2O_3)_{35}]_{1-y}(Ag_2O)_y$ glasses were prepared by mixing together tellurium dioxide (Aldrich 99.5%), boron oxide B_2O_3 (Alfa Aesar, 97.5%) and silver dioxide Ag_2O (Aldrich 99%), in a closed alumina crucible, y being 10, 15, 20, 25 and 30 mol %. Appropriate amounts of powder chemicals were weighed and placed in a crucible. The crucible was covered with a lid and then put inside an electric furnace set at 400 °C. The mixture was maintained at 400 °C for 30 min, the crucible was then transferred to another furnace for 60 min at 800 °C. The crucible was constantly stirred in order to obtain a homogeneous melt. The melt was then poured into a stainless steel, cylindrically shaped split mould which had been preheated, and then the sample was annealed at 350 °C. The samples were cut into pieces having appropriate dimensions for optical absorption and density measurements.

Optical absorption measurements in the wavelength range of 200–800 nm were performed at room temperature using a Camspec M350 double beam UV-visible spectrophotometer. The optical absorption coefficient $\alpha(\lambda)$ was calculated from the absorbance A, using the following equation

$$\alpha(\lambda) = 2.303\frac{A}{d} \tag{1}$$

where d is the sample thickness. Density measurements were made at room temperature based on Archimedes' Principle, involving weighing in air and in acetone as the buoyancy liquid. The samples were ground into powder for X-ray diffraction measurements, using an X'pert Pro Panalytical mill.

3. Results and discussion

The X-ray diffraction patterns of the studied glass system revealed the absence of any discrete or sharp crystalline peaks, indicating that the samples are amorphous (Fig. 1).

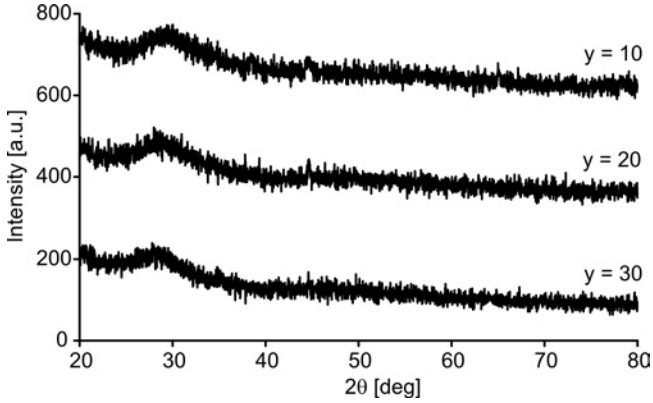

Fig. 1. XRD spectrum of $[(TeO_2)_{65}(B_2O_3)_{35}]_{1-y}[Ag_2O]_y$ glasses

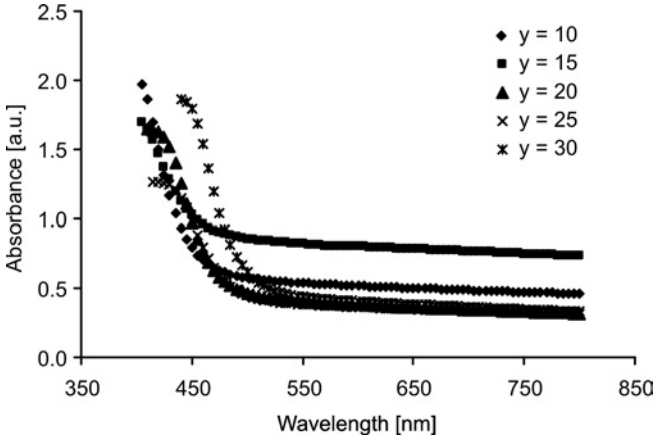

Fig. 2. Optical absorbance spectra of $[(TeO_2)_{65}(B_2O_3)_{35}]_{1-y[Ag2O]_y}$ glasses

The optical absorption spectra of Ag_2O–TeO_2–B_2O_3 are shown in Fig. 2. They do not display any sharp absorption edges, which is characteristic of the glassy state. As the X-ray diffraction spectra, they also show no distinguishable peaks or sharp lines but the pattern does exhibit a broad hump, which shows that the samples are essentially amorphous rather than crystalline (Fig. 1). It is also observed in Figure 2 that the fundamental absorption edge shifts to higher wavelengths as the concentration of Ag_2O increases. This may be due to the lower rigidity of the glass resulting from higher Ag_2O content. The data in Figs. 3 and 4 were obtained from the equation:

$$\alpha(\omega) = \frac{\text{const}\left(\hbar\omega - E_{\text{opt}}\right)^n}{\hbar\omega} \tag{2}$$

where E_{opt} is the energy of the optical band gap and $\hbar\omega$ is the photon energy. The values of n are 1/2 and 2 for the direct and indirect transitions, respectively. Both these

band gaps obtained from the above dependences are interband transitions, but the latter involves the phonon interaction. In order to check whether optical data on the present glasses fit better to the direct or indirect band gap formula; dependences $(\alpha\hbar\omega)^2$ on $\hbar\omega$ as well as $(\alpha\hbar\omega)^{1/2}$ on $\hbar\omega$ have been plotted in the absorption region for which the absorption $\alpha(\omega) \geq 10^4$ cm^{-1} as shown in Figs. 3 and 4.

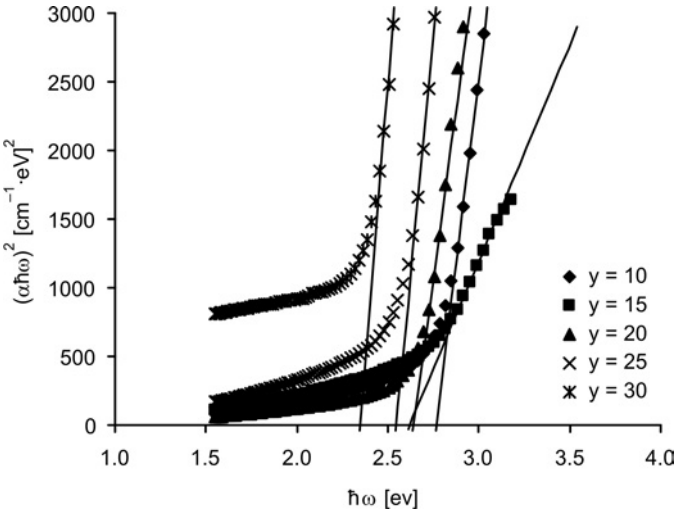

Fig. 3. Plot of $(\alpha h\omega)^2$ against photon energy for direct band gap measurement in $[(TeO_2)_{65}\ (B_2O_3)_{35}]_{1-y}[Ag_2O]_y$ glasses

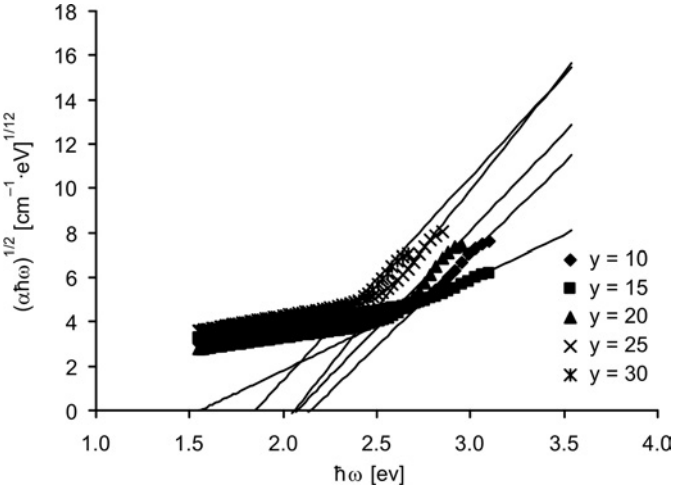

Fig. 4. Plot of $(\alpha h\omega)^{1/2}$ against photon energy for indirect band gap measurement in $[(TeO_2)_{65}\ (B_2O_3)_{35}]_{1-y[Ag2}O]_y$ glasses

The direct and the indirect energy band gaps are determined from the linear regions of the data plots, as shown in the figures, and the corresponding values are pre-

sented in Table 1. The values for the optical band gaps lie between 1.85 eV and 2.37eV for $n = 2$, whereas for $n = 1/2$ they lie between 2.35 eV and 2.82 eV.

Table 1. Results of optical measurements in $[(TeO_2)_{65}\ (B_2O_3)_{-35}]_{1-y[Ag2O]_y}$ glasses

y [mol %] $x = 65$	Direct transition E^1_{opt} [eV]	Indirect transition E^2_{opt} [eV]	Urbach energy ΔE [eV]
10	2.77	2.15	0.37
15	2.62	2.06	0.43
20	2.64	2.07	0.40
25	2.55	2.06	0.45
30	2.35	1.85	0.48

The optical band gaps for direct and indirect transitions for this ternary tellurite system both decrease as the Ag_2O content increases, as shown in Fig. 5.

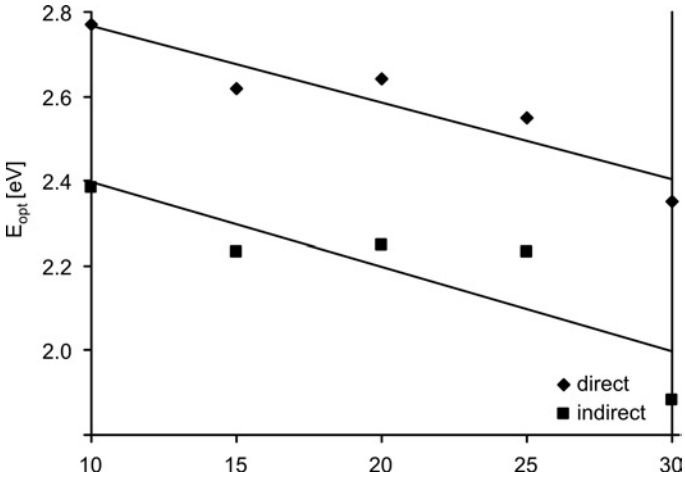

Fig. 5. Dependences of optical band gap on molar percentage of Ag_2O for direct and indirect transitions in $[(TeO_2)_{65}\ (B_2O_3)_{35}]_{1-y[Ag2O]_y}$ glasses

This behaviour may be associated with the structural changes occurring after addition of Ag_2O. In binary tellurite, non bridging oxygen atoms are already present, and with the addition of Ag_2O as a modifier, their concentration increases. The glass structure becomes less ordered; addition of Ag_2O causes breaking of the regular structure of borate and tellurite, leading to a decrease of the band gap [7]. The values of the obtained band gaps of tellurite glasses are quite close to the values reported in the literature [8, 9]. This decrease is due to an increase of the disorder and consequently the more extension of the localized states within the gap according to Mott and Davies [10].

From Table 1 and Figure 5, it is observed that the values of the direct band gap are larger than the corresponding values of the indirect band gap. For this ternary tellurite glass system, there are two optical transitions in **k** space. Assuming that the lowest minimum of the conduction band and the highest maximum of the valence band lie in different regions of the **k** space, direct allowed transitions may occur, as shown in Fig. 6, and the observed indirect transition may be associated with transitions from the top of the valence band to the bottom of the conduction band [11].

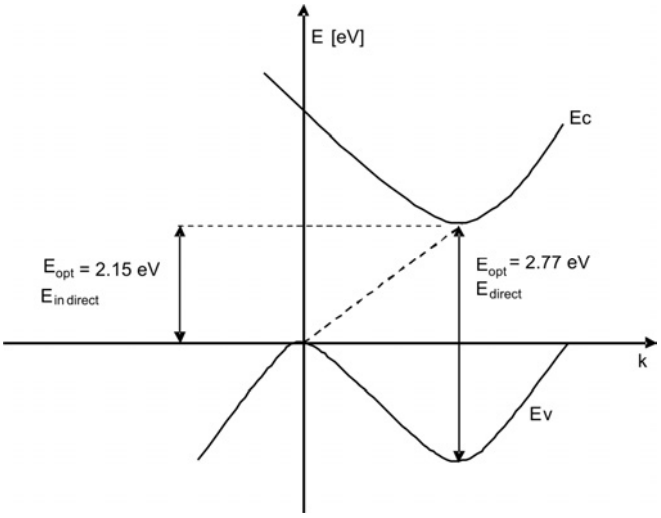

Fig. 6. Suggested energy band diagram (electron energy E against wave vector **k** in $[(TeO_2)_{65}\ (B_2O_3)_{35}]_{1-y}[Ag_2O]_y$ glasses

The fundamental absorption edge usually follows the Urbach rule [3]

$$\alpha(\omega) = B\exp\left(\frac{\hbar\omega}{\Delta E}\right) \tag{3}$$

where B is a constant, ΔE is a measure of the band tailing and is known as the Urbach energy. The values of the Urbach energy ΔE were calculated by taking the reciprocals of the slopes of the linear portion of the $\ln\alpha(\omega)$ versus $\hbar\omega$ curves in the lower photon energy regions. These values are given in Table 1.

The values of the Urbach energy increase as the quantity of Ag_2O increases (Fig. 7). An increase in the Urbach energy can be considered being due to a higher number of defects [12]. Hence, the increase in the Urbach energy with Ag_2O content confirms that the number of defects also increases. Mott and Davies [10] reported that the values of ΔE for a range of amorphous semiconductors are very close and the range of their values is between 0.046 eV and 0.066 eV. The ΔE value of Na_2O–TeO_2 glasses is reported by Prakash et al. [2] to lie between 0.09 eV and 0.26 eV, and in the case of V_2O_5–P_2O_5–TeO_2 glasses, Hogarth [8] reported that the value of ΔE varies between 0.31 eV to 0.41 eV. In the present work, the exponential behaviour is ob-

served and the value of ΔE varies between 0.37 eV and 0.48 eV. The obtained optical band gap energies are of the order reported in the literature, and the Urbach energy values are in the same range as that reported for tellurite glasses [13].

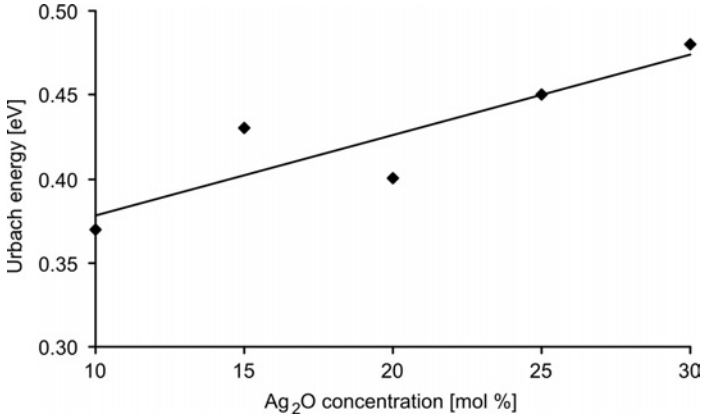

Fig.7. Dependence of Urbach energy on molar percentage of Ag_2O in $[(TeO_2)_{65}\ (B_2O_3)_{35}]_{1-y}[Ag_2O]_y$ glasses

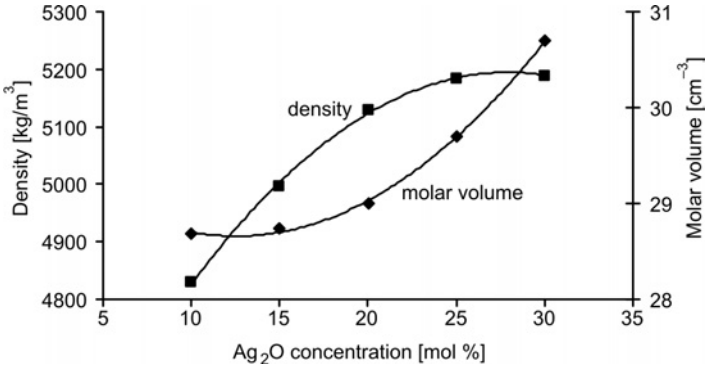

Fig. 8. Density and molar volume of $[(TeO_2)_{65}(B_2O_3)_{35}]_{1-y}[Ag_2O]_y$ glasses

The dependences of density and molar volume of $[(TeO_2)_{65}(B_2O_3)_{35}]_{1-y}[Ag_2O]_y$ glasses on Ag_2O content are shown in Fig. 8. They both increase as the molar percentage of Ag_2O increases. The atomic weight of TeO_2–B_2O_3 is 229.2 g and the atomic weight of Ag_2O is 231.7 g, the replacement of the borotellurite atom with the silver atom is explained by the increase in the density resulting from the increase in the content of Ag_2O. Generally, the density and the molar volume show opposite behaviours, but in this work it is not the case. This anomalous behaviour was shown in a study by Rajendran et al. [3] and Saddeek and Abdul El-Latif [14]. The increase in the molar volume, resulting from the presence of non-bridging oxygen atoms (NBO) causes bond breaking, and thereby leads to an increase in the number of spaces in the network [14]. The observed increase in the molar volume may be due to an increase in

the bond length or an increase in the interatomic spacing between the atoms. The values of the molar volume of the ternary tellurite glass system lie in the same range as those reported by El-Mallawany [15] for the tellurite glasses.

4. Conclusions

The ternary tellurite glass system $[(TeO_2)_{65}(B_2O_3)_{35}]_{1-y}(Ag_2O)_y$ was fabricated. The optical band gap values have been determined and from the theoretical fitting of the experimental absorption coefficient for all samples, it is concluded that both direct and indirect transitions occur. For both transition types, the values of the optical band gap, are found to decrease as the amount of Ag_2O increases. The Urbach energy is found to be between 0.37 eV and 0.48 eV. Urbach edge behaviour is observed in these glasses, and the slope of the edge was found to increase as the amount of Ag_2O increases. The density depends on the composition: the greater the compactness of the structure, the higher the density.

Acknowledgement

The financial support of the Ministry of Science, Technology and Innovation, Malaysia under FRGS grant No. 5523645 is gratefully acknowledged.

References

[1] JOSEPH C.M., BINU P.R., SHREEKRISNAKUMAR R., MENON C.S., Mat. Lett., 50 (2001), 251.
[2] VIJAYA PRAKASH G., NARAYANA RAO D., BHATNAGAR A.K., Solid State Commun., 119 (2001), 39.
[3] RAJENDRAN V., PALANIVELU N., CHAUDHURI B.K., GOSWANI K., J. Non-Cryst. Solids 320 (2003), 195.
[4] EL-MALLAWANY R., *Tellurite Glasses Handbook. Physical Properties and Data*, CRC Press, Boca Raton, 2002.
[5] SADDEEK Y.B., Phys. B, 344 (2004), 163.
[6] CHOWDARI B.V.R., PRAMODA KUMARI P., Solid State Ionics, 86–85 (1996), 521.
[7] SINDHU S., SANGHI S., ARGAWAL A., SONAM S.V.P., KISHORE N., Physica B, 365 (2005), 65.
[8] HOGARTH C.A., HOSSEINI A.A., J. Mater. Sci., 18 (1983), 2697.
[9] SHALTOUT I., YI TANG, BRAUNSTEIN R., SHAISHA E.E., J. Phys. Chem. Solids, 57 (1996), 1223.
[10] MOTT N.F AND DAVIS E.A., *Electronic Processes in Non-Crystalline Materials*, Oxford University Press, London, 1971, pp. 293.
[11] AL-ANI S.K.J., AL-HASSANY I.H.O., AL-DAAN Z.T., J. Mater. Sci., 20 (1995), 661.
[12] SREEKANTH CHAKRADAR R.P., SIVARAMAIAH G., LAKSHMANA R., GOPAL N.O., Spectrochim. Acta, Part A, 62 (2005), 761.
[13] EL-MALLAWANY R., J. Alloys. Compd., 394 (2005), 292.
[14] SADDEEK Y.B., ABD EL-LATIF L., Phys. B, 348 (2004), 475.
[15] EL-MALLAWANY R., Mater. Chem. Phys., 53 (1998), 93.

Received 10 April 2009
Revised 11 August 2009

Materials Science-Poland, *Vol. 28*, *No. 1*, *2010*

Fabrication and performance of carbon coated copper nanoparticles

L.-P. LI, H.-Y. ZHANG*, J.-S. PANG, J. LIN

Faculty of Material and Energy, Guangdong University of Technology, Guangzhou, 510006, P.R. China

Carbon coated copper nanoparticles were synthesized by the carbon arc discharge method using a powder mixture containing copper and carbon at the ratio different than in the raw material. The structure, topography, size distribution, phase composition and anti-oxidation property of the nanoparticles were characterized by X-ray diffraction, transmission electron microscopy, thermogravimetry and differential scanning calorimetry experiments. The results indicated that carbon coated copper nanoparticles had a clear core-shell structure, the core of the particles being copper single crystal, and the shell of the particles – a carbon layer with a graphite-like structure. Carbon coated copper nanoparticles had diameters of ca. 20–60 nm. As the copper content increased, the inner copper core became more crystallized. Copper promoted catalysis to the external carbon layers, the graphitization degree became more obvious as the content of copper increased. The outer graphitic carbon layers effectively prevented oxidation of the copper core inside. The oxidation resistance of carbon coated copper nanoparticles was superior to that of pure copper powder.

Keywords: *carbon coated; copper nanoparticles; carbon arc discharge; oxidation resistance*

1. Introduction

Compared with conventional materials, copper nanoparticles have some unusual properties, such as small dimensions, large specific surface area and low electric resistance. They display quantum size effect, macroscopic quantum tunnel effect. Therefore, copper nanoparticles have been the subject of much attention in recent years, due to their potential applications in several fields. Copper nanoparticles with low resistivity can be used for electronic connectivity, and this has aroused great interest in the field of electronics [1]. They are suitable for fabricating conductive paste, which can be applied to coating, electronic packaging in microelectronic industry [2]. Copper nanoparticles can be used as catalysts in metallurgical, petroleum and chemical indus-

*Corresponding author, e-mail: hyzhang@gdut.edu.cn

tries due to extremely high activity and selectivity in catalysis and hydrogenation of macromolecular polymers [3]. At the same time, owing to their low melting point, isotropy, weak shear strength and applicability over a wide temperature range, copper nanoparticles have been used as additives in lubricating oils, resulting in a very high quality of products [4–9]. Copper nanoparticles have anti-wear and anti-friction properties, are resistant to extreme pressure, are environment-friendly and also have self-repairing properties. Consequently they have become an indispensable and important, basic material for inorganic composites [10, 11].

Copper nanoparticles have a high activation state which is attributable to their special volume and surface properties. They are sensitive to various environmental factors such as instance, temperature and humidity, promoting strong interactions with substances exposed to air, thereby rendering the surfaces of copper nanoparticles vulnerable to oxidation. The chemical stability of nanoparticles decreases and their activity ceases, which makes copper nanoparticles inconvenient to store and use.

Carbon coating of metal nanoparticles can protect them from physicochemical changes. The technology can prevent metal particles from hydrolysis and oxidation. Carbon layers can improve the surface activity and electrical properties of the inner copper particles and effectively prevent their growth and agglomeration. Metal particles can be confined to a small place by the carbon shells, thereby preventing the metal particles from being oxidized. This solves the problem of how to make metal nanoparticles exist stably in air [12]. Carbon coated nanomaterials protection technology greatly extends the application range of metal nanomaterials in many fields such as chemistry, physics and materials science [13]. Many methods of fabrication of carbon coated metal nanoparticles have been reported, including arc discharging [14–17], ion beam method [18] and chemical vapour deposition [19, 20].

In the paper, we report on the preparation of carbon coated copper nanoparticles using dc carbon arc discharge under an argon atmosphere. The synthesized product is of high purity and has a small particle size the preparation route being rather simple.

2. Experimental

Micron size graphite powder (C, 98.0%) and micron copper powder (Cu, 99.8%) were used as staring materials. The powders in the weight ratio of graphite to copper 4:1 and 2:3 were mixed and pressed into a cylindrical sample of the diameter 24 mm, 20 mm high, which was placed at the bottom electrode of the reactor. The nanoparticle manufacturing apparatus consisted of the following parts: a stainless steel vacuum chamber cooled by circulating water; a water cooled copper anode on which the cylindrical metal to be evaporated is placed; a water cooled and moveable graphite cathode; a cold surface collector; a gas flow system; a two stage vacuum pump system; and a DC power supply. Before preparation, the chamber was vacuumed to 2–3 Pa by mechanical vacuum pump, pumped in argon to 1000 Pa and stopped, continued to vacuum to 2–3 Pa of the reactor, and then pumped in high purity argon. When the pressure

was 50 000 Pa, the distance of two electrodes for dc arc discharge was adjusted to 1–2 mm. When discharge current was 120 A, and discharge voltage was 22 V, the electrode began to discharge. The reaction caused ionization and a plasma fume was formed in the reaction chamber, which was deposited in the container wall and formed nanoparticles. After the reaction had finished, the product deposited on the container wall was collected, filtrated in toluene, and carbon coated copper nanoparticles were thus obtained.

Transmission electron microscopy (TEM; JEM-2000EX) and high-resolution transmission electron microscopy (HRTEM; JEM-2000EX) were applied to determine the morphologies and sizes of carbon coated copper particles. An X-ray diffractometer with CuK_α radiation under the applied power of 50 kV×30 mA was employed to detect phases and the crystal structure of the particles. The thermal effect and weight change analysis of the reaction were confirmed by differential thermal analysis (DTA) in the temperature range of 25–600 °C with the heating rate of 20 °C·min^{-1} was applied, under a nitrogen atmosphere.

3. Results and discussion

3.1. XRD analysis

Figure 1 shows X-ray diffraction profiles of carbon coated copper nanoparticles. Three sharp peaks at 2θ of 43.3°, 50.6° and 74.3° can be seen in the figure. The corresponding d value was 0.2087 nm, 0.1808 nm, 0.1278 nm, respectively. We consulted the PDF card (the PDF card number 04-0836), which corresponded to the (111), (200) and (220) plane of the face centred Cu, respectively. The carbon coated copper nanoparticles were found to match the diffraction peak characteristics of copper, whereas no peaks assigned to carbon were detected, suggesting that the carbon shell was amorphous.

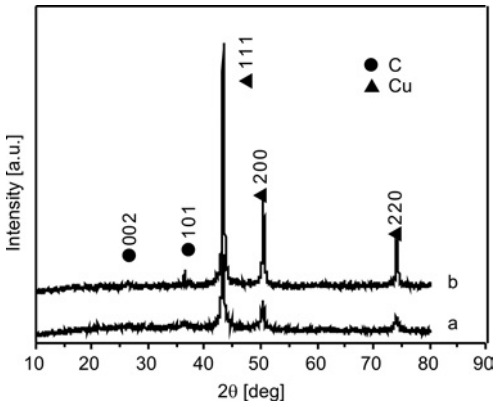

Fig. 1. X-ray diffraction patterns for carbon coated nanoparticles fabricated by using two different ratios of carbon to copper starting material: a) 4:1, b) 2:3

It is obvious from Fig. 1 that the increase in the copper content in the samples resulted in the marked increase in intensity of the copper diffraction peak. This indicated

that with an increase in the concentrations of copper nanoparticles, copper became more crystallized. At the same time, it can be seen that the carbon coated copper nanoparticles at 2θ of 36° are represented by a diffuse scattering peak in curve a, while at 2θ of 27° and 36° they are represented by a clear diffraction peak, for which the corresponding d values were 0.3364 nm and 0.2470 nm (the PDF card number 46-0945), which showed that the carbon of the former sample existed in amorphous form, while the surface of the latter sample of carbon coated copper nanoparticles changed to graphite state (a diffraction peak of graphite was present).

Obviously, carbon graphitization can be promoted by increasing the copper content, but XRD analysis of the powder did not reveal the presence of carbide or of copper oxide. During the preparation process, at first argon was ionized to form argon plasma and caused the release of electrons. The released electrons defined an electric field which caused the acceleration of Ar^+ ions from the anode, thereby producing a stream of high-speed ions. The ions bombarded the bottom electrode, so that their kinetic energy was converted to a thermal energy; the temperature of the reaction reached several thousand degrees, which enabled rapid gasification of copper and carbon atoms. The copper atoms agglomerated quickly, became radicals in container wall and left the discharge region. Since the diffusion rate of the copper atoms was larger than that of carbon, despite the role of surface tension, the copper atoms could spherodize and become spherical particles. At the same time, carbon atoms adhered to the molten Cu nanoparticles and eventually formed core-shell nanoparticles and were deposited on the container wall. As the copper content of the sample was increased, the quantity of copper atoms evaporating from the samples also increased, which led to an increase in the nanoparticle sizes. Therefore, the samples of higher Cu content exhibited stronger diffraction peaks of copper than those samples having a lower copper content.

3.2. TEM analysis

Typical TEM images for the obtained carbon-coated copper nanoparticles are shown in Fig. 2. The nanoparticles were spherical in shape (Fig. 2a), well dispersed, with the diameter of 50 nm. Particle surfaces were relatively smooth with no apparent traces of agglomeration.

According to HRTEM observation (Fig. 2b), we also found that these nanoparticles possessed a distinct core/shell structure. It was found that the carbon layers in carbon coated copper nanoparticles were 3–5 nm thick. The interlayer spacing of these graphitic planes was about 0.34 nm, therefore we can see that the shell of each nanoparticle possessed an ordered graphite structure.

The selected area electron diffraction (SAED) patterns of A and B areas from Fig. 2a are shown in Figs. 2c and 2d, respectively. According to the calculation of electron diffraction spots in Fig. 2c, it was revealed that the crystal plane spacing of the inner core region was 0.21 nm, which corresponded to the crystal plane distance of

the main diffraction peak of copper; the crystal plane is (111). It was proved to be the electron diffraction pattern of the face centred cubic single crystal copper. It is shown in Fig. 2d that the TEM diffraction pattern of B is an amorphous diffuse scattering ring. From the above analysis, we can see that the outer carbon layers were amorphous, which was consistent with the XRD spectrum.

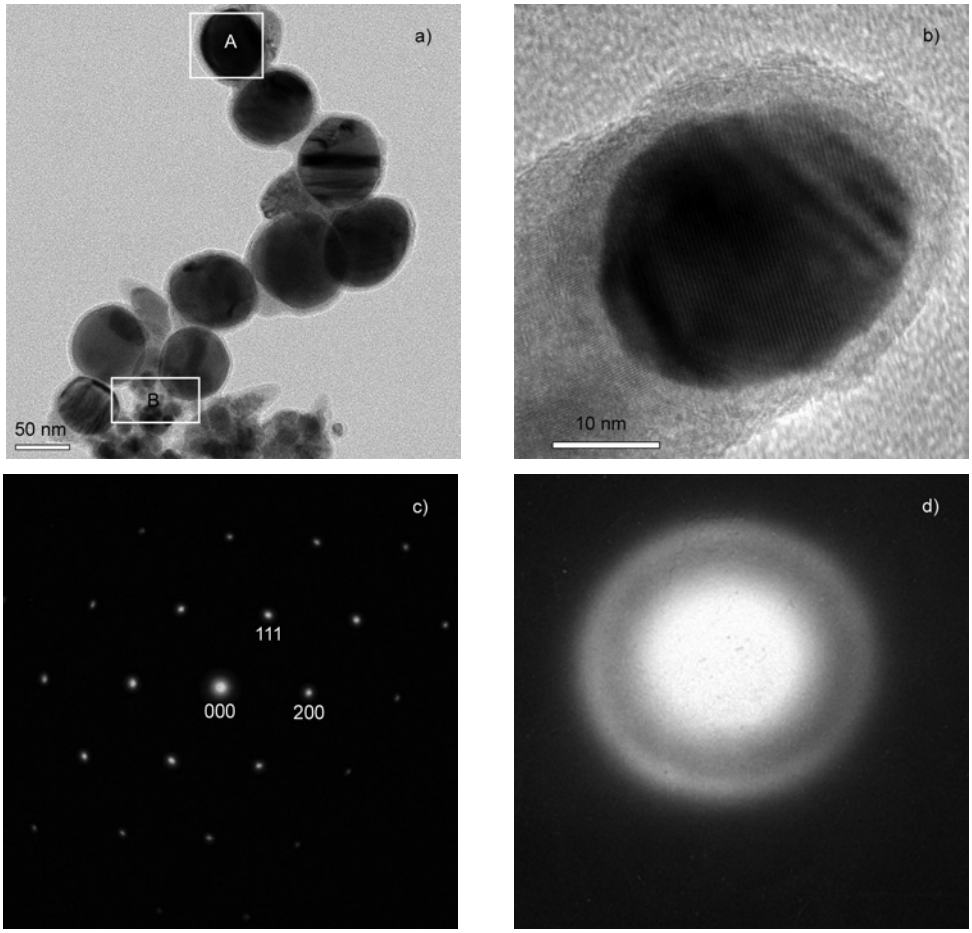

Fig. 2. TEM (a) and HRTEM (b) images of carbon coated copper nanoparticles as well SAED patterns of areas A (c) and B (d) in Fig. 2a

3.3. TGA-DSC analysis

The oxidation resistance of carbon coated copper nanoparticles was determined by thermogravimetric analysis (TGA) and differential scanning calorimetry (DSC). Figure 3a shows the TGA curves of the carbon coated copper nanoparticles. Between 35 °C and 293.9 °C, the mass of the sample slightly increased (ca. 1%) because at this

temperature the reaction of carbon with air occurred at a lower rate. This weight increase was attributed to the oxidation of the trace copper on the particle surface. From 293.9°C to 420.1° C, the outer amorphous carbon layer began to oxidize, which manifested in an exothermic peak at 321.5 °C with a radical weight loss. At 420.1 °C, the weight loss rate reached the maximum (weight loss rate of 1.5%). Upon increasing the temperature above 420.1 °C, due to the decrease of the outer carbon layer, a part of the copper nanoparticles exposed to air was oxidized, and thus the carbon coated copper nanoparticles had an obvious weight gain. From room temperature to 600 °C, the whole reaction caused a weight gain of 1.8 wt %.

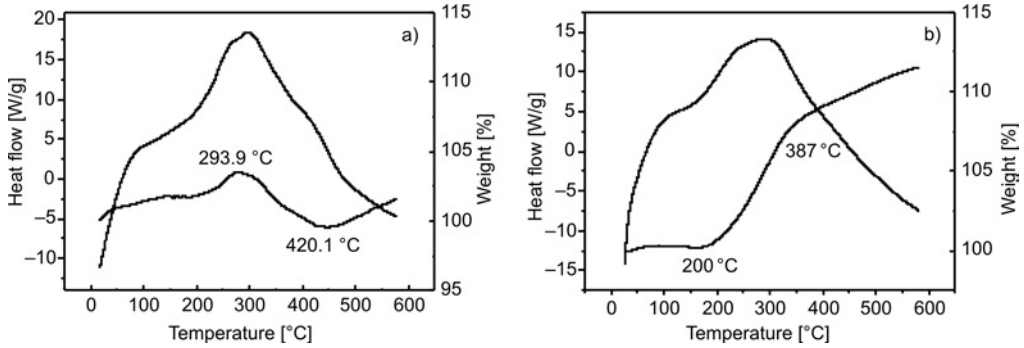

Fig. 3. TGA-DSC curves of carbon coated copper nanoparticles (a) and copper nanoparticles (b)

Figure 3b shows the TGA curves of copper nanoparticles. It was shown that the copper nanoparticles had an apparent weight gain at temperatures above 200 °C, there was an obvious exothermic peak associated with weight gain, which was observed at 310 °C. During the whole process, copper nanoparticles experienced a weight gain of 12%. The initial temperature of oxidation of carbon coated copper nanoparticles was superior to that of the copper nanoparticles.

From the above comparative analysis of both charts we can see that carbon coated copper nanoparticles have better oxidation resistance than that of copper nanoparticles. Copper nanoparticles experience very obvious weight gain, which revealed that they easily reacted with oxygen, while the weight gain of carbon coated copper nanoparticles was not obvious in the whole process, which demonstrates that carbon-coated copper nanoparticles have superior oxidation resistance. The carbon shell of graphite provides good protection for the copper particles in the core.

4. Conclusions

Carbon coated copper nanoparticles with the diameter of ca. 20–60 nm have been successfully fabricated by the carbon arc discharge method. The core shell nanoparticles had a graphitic carbon shell and face centred cubic copper core. The interlayer

spacing of the graphitic planes was about 0.34 nm. Copper catalyses graphitization of the external carbon layer, the higher the copper content, the more obvious the degree of graphitization is. The DSC experiments showed that the produced material exhibited an excellent oxidation resistance.

Acknowledgements

This work was supported by the National Natural Science Foundation of China (Grant No. 20971027) by the Special Research Fund for the Doctoral Program of Higher Education of China (Grant No. 20050562002), supported by the Guangdong Provincial Natural Science Foundation of China (Grant No. 9251009001000006), and by the Science and Technology Program of Guangdong Province of China (Grants Nos. 2009A030301008, No.2009B090300017).

References

[1] HEINO P., RISTOLAINEN E., J. NanoStruct. Mater., 11 (1999), 587.
[2] LI Z.Y., GONG P.W., ZHAI Y.C., J. Iron Steel Res. Int., 14 (2007), 125.
[3] CHU G., TANG Y.J., LIU W., LUO J.S., LI J., YANG T.Z., J. Metallic. Funct. Mater., 12 (2005), 18.
[4] HISAKADO T., IKUTA K., SUD A., KSAITOU K., J. Wear., 197 (1996), 280.
[5] WANG X.B., LIU W.M., YAN F., ZHANG Z., XU B., J. Chem. Lett., 33 (2004), 196.
[6] OU X.M., GE C.L., WANG J., WANG B., ZHU H., J. China Univ. Min. Technol., 34 (2005), 640.
[7] XIA Y.Q., J. Tribology., 24 (2004), 576.
[8] LI B., XIA Y.Q., WANG X.B., XUE J.J., J. Tribology., 25 (2005), 385.
[9] WANG X.L., XU B.S., XU Y., J. Cent. China Norm. Univ., 12 (2005), 203.
[10] LEE D.W., KIM B.K., J. Mater. Lett., 58 (2004), 378.
[11] LI Z.Y., ZHAI Y.C., TIAN Y.W., MA J.H., J. Rare Met. Mater. Eng., 34 (2005), 965.
[12] HUO J.P., SONG H.H., CHEN X.H., J. Chem., 68 (2005), 23.
[13] BANHART F., GROBERT N., TERRONES M., J. Int. J. Mod. Phys. B., 15 (2001), 4037.
[14] SUN X.C., GUTIERREZ A., YAEAMAN M.J., DONG X.L., JIN S., J. Mater. Sci. Eng. A., 286 (2000), 157.
[15] SUN X.C., TOLEDO J.A., J. Current Appl. Phys., 2 (2002), 113.
[16] SI P.Z., ZHONG Z.D., GENG D.Y., YOU C.Y., ZHAO X.G., ZHANG W.S., J. Carbon, 41 (2003), 247.
[17] SCHAPER A.K., HOU H., GREINER A., SCHNEIDER R., PHILLIPP F., J. Appl. Phys. A., 78 (2004), 73.
[18] TIAN Y.Y., NIWA O.S., TOMITA M., J. Electrochem. Commun., 4 (2002), 468.
[19] HAO G.H., SCHAPER A.K., WELLER F., GREINER A., J. Chem. Mater., 14 (2002), 3990.
[20] SANO N., AKAZWAA H., KIKUEHI T., J. Carbon, 41 (2003), 2159.

Received 25 April 2009
Revised 10 September 2009

Materials Science-Poland, *Vol. 28*, *No. 1*, *2010*

Nitrogen doped carbon nanotubes and curved lamellas produced via pyrolysis of melamine by direct current arc discharge

R.I. ZHAO[1, 2], Y. MA[1], J. ZHANG[1*], F. LI[1], W. LIU[1], Q. CUI[1]

[1]National Laboratory of Superhard Materials, Jilin University, Changchun 130012, China

[2]Computer College, Jilin Normal University, Siping 136000, China

Nitrogen doped carbon nanostructures, including nanotubes and barrel like curved lamellas, were fabricated via the pyrolysis of a solo precursor, melamine, in a direct current arc discharge. The samples were characterized by elemental analysis, using XRD, XPS, TEM and SEM in parallel. The nitrogen concentration, determined from the elemental analysis, was shown to be lower than 5%. Nitrogen-based functional groups such as pyridine like structures, the pyrrolic or pyridonic structures, N-amine like structures and substitutional nitrogen within the graphene layers, were observed to coexist in the turbostratic carbon matrix. XRD patterns showed characteristic features of turbostratic carbons. TEM analysis of morphologies showed that nanostructures such as tubes and conglomerations of barrel like curved lamellas were present. The formation of bundles of nanotubes was further confirmed by SEM studies. The inhomogeneity in the morphologies of the nanostructures was attributed to the differences in their growth mechanisms.

Keywords: *carbon nanotubes; pyrolytic carbon; arc discharge*

1. Introduction

The studies of doping of carbon materials with nitrogen atoms has shown that the nitrogen-doping can obviously enhance mechanical, conducting, field emission, energy storage and electron transport properties and the catalytic activity in oxidation reactions of carbon materials [1–3]. Carbon nanotubes doped with nitrogen should exhibit novel electronic, chemical and mechanical properties [4]. In fact, the N doped bulk graphite systems have been the subject of investigations for a long time, due to their enhanced oxidation resistance and the possibility to adjust the crystallinity and graphitization. Nowadays, thanks to advances in nanoengineering and nanotechnology, the study of doping carbon nanostructures has entered a boom phase because

*Corresponding author, e-mail: zhangjian_lxf@yahoo.com.cn

these materials have potential applications as field effect transistors, logic circuits [5], sensors [6], promising materials for gas storage and adsorption [7], and as filler materials for reinforced composites [8], etc. Thus considerable efforts have been made to study the fabrication and the growth mechanism of the related carbon nanostructures with nitrogen as the dopant.

Up to now, only small quantities of nitrogen ($\leq$ 15 at. %) have been incorporated into carbon networks [9–12], which implies that the formation of C–N bonds is somehow difficult. From a thermodynamic point of view, this is reasonable, since segregation into pure carbon phases and nitrogen gas is much enhanced due partly to the strong triple bond in the nitrogen molecule. However, multiform nanostructures and inaugurating prototypes of devices have been obtained through various techniques, such as chemical vapour deposition (CVD) [1, 13], solvothermal techniques [14], direct current arc discharge [15], etc.

It is desirable that nitrogenous organic compounds be used as precursors for the fabrication of nitrogen containing nanostructures. Melamine seems to be an appropriate precursor of such a kind. In this paper, we report a new method to synthesize nitrogen doped carbon nanostructures in which the pyrolysis of melamine in a direct current arc discharge is involved. In this method, the pyrolysis of melamine takes place in a fast heating process generated by the direct current arc with the nitrogen rich gases as the working media, and the final products are formed via a quenching process for which the rate of temperature decrease ranges between 10^3 and 10^5 $K \cdot s^{-1}$. It is shown that nanotubes and nanobarrel like curved lamellas and sponge like networks formed by the conglomeration of those nanolamellas can be grown directly by this method.

2. Experimental

A sketch map of the direct current arc discharge system we used is shown in Fig. 1. In a typical experimental run, fine powders of melamine (purity $\geq$ 99.9%) and magnesium (purity $\geq$ 99.9%) were mixed together in an agate mortar in an appropriate ratio and cold pressed into pellets. The deliberate addition of magnesium was to make the pellets conductive, so that a direct current arc might be started. Carbonaceous conductive materials such as carbon fibres or filaments were not used, so that the final carbon product was totally produced from melamine, taking into account that the weight loss of graphite electrodes was negligible. Then a pellet was loaded in the water cooled graphite crucible, acting as the anode. A graphite rod (6 mm in diameter and 25 cm in long) was employed as the cathode. The reaction chamber was first evacuated to less than 1 Pa and washed several times with nitrogen (N_2, 99.999%). Then working gases such as nitrogen or ammonia (NH_3, 99.95%) were introduced into the chamber until the inner pressure reached the target value of 10–30 kPa. After the direct current arc was ignited, the input current was maintained at 100 A during the whole process of synthesis. However, the arc voltage increased gradually from 35 V to 45 V until the reactants were exhausted and the arc was quenched. After being pas-

sivated in N_2 for 6 h, powders were collected from the water-cooled collecting wall, which is made of copper. The powders were washed with concentrated hydrochloric acid, distilled water and ethanol repeatedly to remove the remnant reactants and magnesium compounds. The final product, which was black and had a fleece like texture, was then gathered.

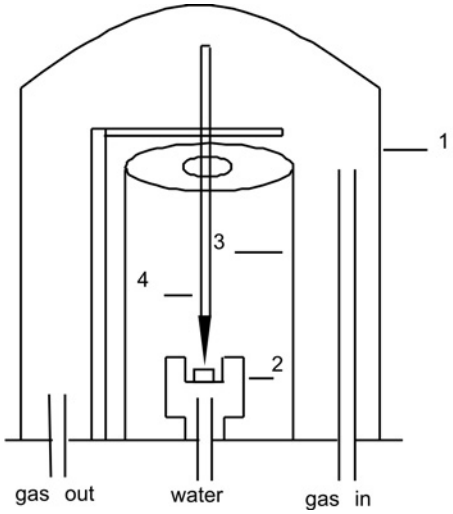

Fig. 1. A sketch diagram of the arc discharge system: 1 – reaction chamber, 2 – graphite crucible, 3 – copper collecting wall, 4 – graphite cathode. The crucible and the collecting wall are both cooled with water

The characterizations of the samples were carried out via elemental analysis, X-ray photoelectron spectroscopy (XPS), X-ray diffraction (XRD), transmission electron microscopy (TEM) and scanning electron microscopy (SEM). The compositions of the samples were examined by elemental analysis on a CHNS-O analyzer (Flash EA 1112 Series) through the conventional combustion method. The bonding states of the elements were studied via XPS on an EASY ESCA spectrometer (VG ESCA LAB MKII). The XRD patterns were obtained via a Rigaku Dmax-rA diffractometer operating with a copper target (λ = 1.54056 Å). The morphologies of the samples were taken on a H8100 transmission electron microscope operating at 200 KV and a Shimadzu Superscan SSX-550 scanning electron microscope operating at 15.0 kV.

3. Results and discussion

The chemical compositions of the samples synthesized under typical experimental conditions estimated through the combustion method are listed in Table 1. It can be seen that the products contain primarily carbon (82.51–89.37 wt. %). The doping level of nitrogen is relatively low (1.39–4.66 wt. %). Considerable amounts of hydrogen

(0.88–2.15 wt. %) are also present. The presence of other components of the products may be due to surface oxidation and absorption, which may be promoted by incorporating nitrogen in the carbon network. In addition, the influence of incomplete combustion of carbon species may not be ruled out entirely.

Table 1. Chemical compositions of the samples synthesized at typical experimental conditions estimated through the combustion method

Sample No.	Experimental conditions		Chemical composition [wt. %]			
	Gas	Pressure [kPa]	C	N	H	Other
1	N_2	10	86.54	2.39	0.97	10.10
2	N_2	30	89.37	1.39	0.88	8.36
3	NH_3	10	82.51	4.66	2.15	10.68
4	NH_3	30	86.58	3.19	1.01	9.22

The systematic variation of the compositions in relation to the experimental conditions may be roughly summarized as follows: (a) the powders produced in ammonia have higher nitrogen concentrations than those produced in nitrogen gas at the same gas pressure; (b) higher working gas pressures tend to lower the nitrogen concentration incorporated into the products. Taking the surface oxidation and adsorption into account, the contaminating oxygen and hydrogen are unavoidable. This effect may be enhanced by the intrinsic mesoporosity of the products, as shown below.

In fact, the compositions, structures, morphologies and other characteristics of the samples did not vary much, despite being subject to various experimental conditions. Hereafter, the samples obtained in the procedure under N_2 pressure of 10 kPa will be taken as the representative ones in the following discussions.

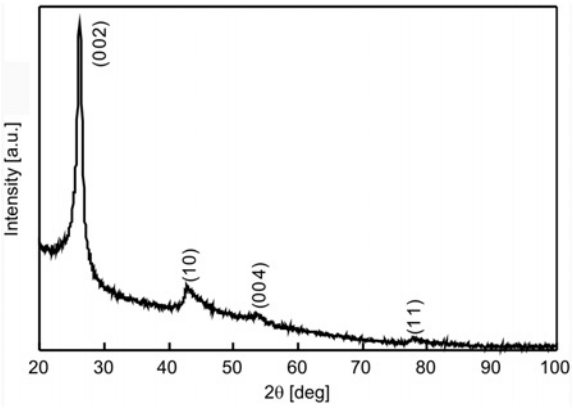

Fig. 2. A typical XRD pattern of the powders synthesized under the N_2 pressure of 10 kPa and I =100 A. The pattern is typical of all samples investigated in this study

The XRD pattern of the representative sample is shown in Fig. 2. A broadened peak at 26.22° and three weak diffraction bands at 42.91°, 53.48° and 78.03°, respec-

tively, are distinguished in the pattern. They can be indexed as typical (002), (10), (004) and (11) diffraction bands, respectively, for turbostratic carbons [16]. The (10) diffraction band shows a shape characteristic of a two-dimensionally ordered structure. The absence of (10l) bands or peaks indicates that there is no long range three-dimensional order of the graphite structure. The average thickness of the crystallized layers, L_c, can be roughly estimated to be about 10 nm through Scherrer's equation:

$$L_c = \frac{K\lambda}{B_{002}\cos\theta_{002}}$$

where θ_{002} is the diffraction angle and B_{002} is the full width at half maximum (FWHM) of (002) diffraction.

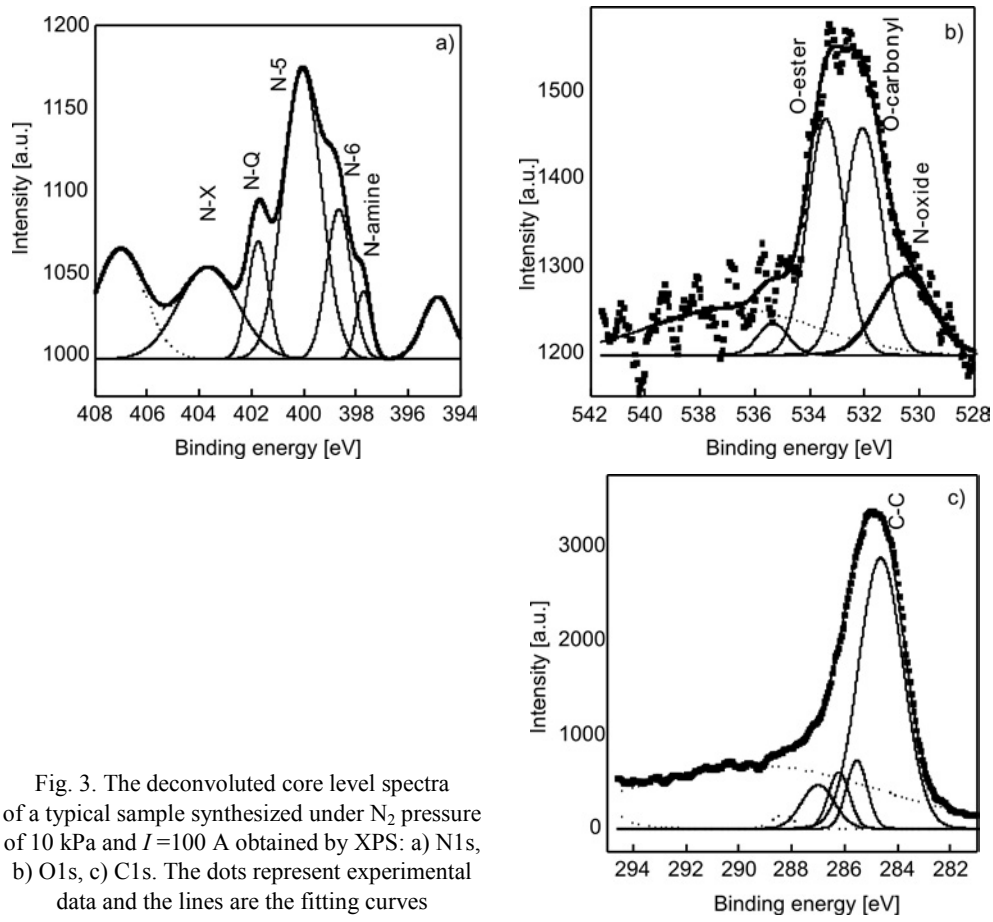

Fig. 3. The deconvoluted core level spectra of a typical sample synthesized under N_2 pressure of 10 kPa and I =100 A obtained by XPS: a) N1s, b) O1s, c) C1s. The dots represent experimental data and the lines are the fitting curves

The binding energy (BE) dispersion of the emitted core level electrons observed by XPS can reveal the chemical environment of the atoms in materials. In the present

case, turbostratic carbons are formed from radical atoms or small clusters in the arc discharge, thus one can assume that the experiments with other nitrogen containing carbons should be applied. Generally the results follow the observations with nitrogen-based functional groups of molecular organic compounds [17–19]. The N 1s core level spectra of our samples are fitted to Gaussian profiles, as shown in Fig. 3a. The component peaks are identified as nitride like species or aromatic N-amines with a BE of 397.7 eV, pyridinic nitrogen (N-6) with a BE of 398.7 eV, pyrrolic or pyridonic nitrogen (N-5) with a BE of 400.1 eV, substitutional nitrogen in the centre position in condensed polyaromatic systems, also called quaternary nitrogen (N-Q) with a BE of 401.7 eV, and nitrogen oxide or nitrate species (N-X) with a BE in the range of 402-405 eV. A schematic representation of the nitrogen based functional groups similar to those assigned in the present work may be found in the literature [19]. The O 1s core level spectra of our samples are also fitted to Gaussian profiles in a similar manner, as shown in Fig. 3b. Following the interpretation of XPS signals from oxygenated microporous carbons [20], the component peaks are identified as carbonyl oxygen atoms in esters, amides, anhydrides, and hydroxyls with a BE of 532.1 eV, ester oxygen atoms in esters and anhydrides with a BE of 533.4 eV, and nitrogen oxide or nitrate species (N-oxide) with a BE of 530.5 eV. These surface oxygen containing functional groups were most probably acquired during washing, since washing with acid solutions is a general way for modifying the surface chemistry of activated carbons to enable oxygen containing functional groups. Based on the above analyses, the deconvoluted C 1s core level spectra of the samples, as shown in Fig. 3c, can be readily explained. The major component with a BE of 284.6 eV is attributed to graphitic carbons (C–C). The minor component peaks are identified as carbons in C–N and/or C–O with a BE of 285.5 eV, carbons bonded to two N and/or O neighbours a BE of 286.3 eV, and carbons in C≡N and/or C=O with a BE of 287.1 eV, respectively.

The formation and mechanism of the bending and curling of graphene layers attracts considerable interest at present. In this study, nitrogen doped carbon nanostructures with exotic morphologies such as barrel like nanolamellas and bundles of nanotubes have been discovered. The so-called barrel like nanostructures are much shorter and less homogeneous with respect to their shapes and dimensions compared with ordinary nanotubes [16]. Typical TEM morphologies of the barrel like, or to be more precise in our case, bowl like curved lamellas, are shown in Fig. 4. It can be seen from Fig. 4a that the nanolamellas are curled and curved into irregular bowl like shapes. The characteristic calibre of these nanobowls is about 100 nm and the thickness is estimated to be about 10 nm. It is speculated that these curved lamellas may be the intermediate structures between the fully curled nanotubes and flat graphite planes. Structures with similar shapes but smaller sizes are also found (Fig. 4b). Presumably they are 10–20 nm in calibre and 2–5 nm thick. These curved lamellas conglomerated with one another, resulting in a sponge like structure with multitudinous mesopores and micropores. This structure may find potential usage in gas storage and catalyst support.

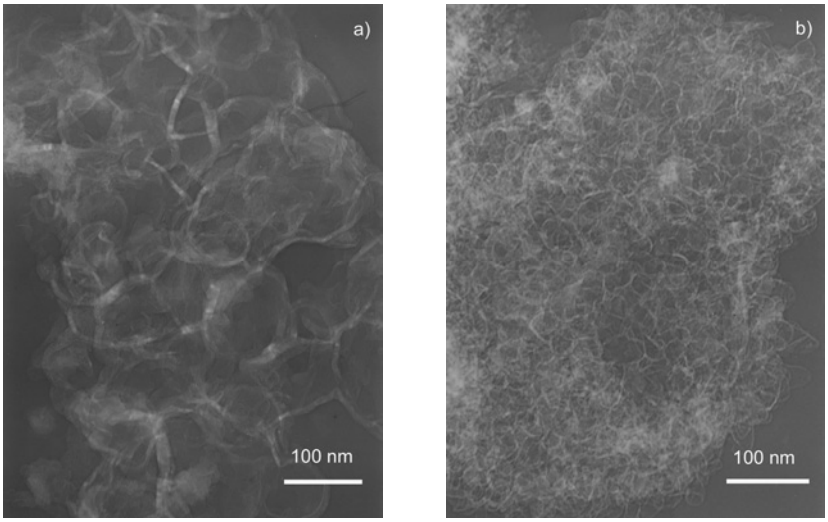

Fig. 4. TEM morphologies of N doped carbon nanomaterials with curved lamellar structures: a) the so-called barrel like nanolamellas with larger sizes, b) the sponge like conglomerations of smaller nanolamellas

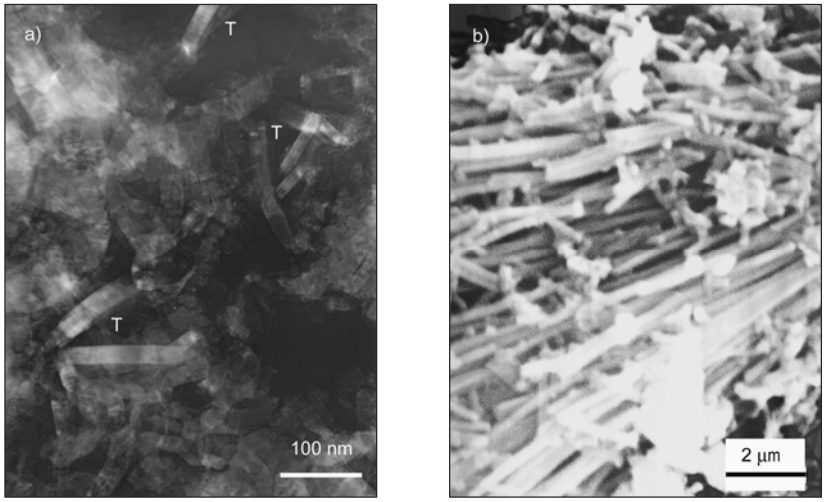

Fig. 5. The morphologies of nanotubes found in a representative sample synthesized under the N_2 pressure of 10 kPa and I =100 A: a) typical TEM morphology of several carbon nanotubes (marked as T) with their ends buried in amorphous clumps, b) typical SEM morphology of the nanotube bundles

Several nanotubes, 15–35 nm in diameter, are demonstrated in Fig. 5a (marked as T), with the coexistence of CN_x clumps. It is evident that the ends of the nanotubes are buried in those clumps. In Figure 5b, a typical SEM morphology of the nanotube bundles is demonstrated. The lengths of the nanotubes range from several micrometers to at least tens of micrometers. The nanotubes are somewhat crooked, indicating low

crystallinity. This is only reasonable, since the incorporation of nitrogen in the graphene network is anticipated to introduce large amounts of defects.

The growth of nanotubes and the clusters of nanolamellas seem to be mutually exclusive. In expansive regions, the nanotubes tend to coexist with only irregular-shaped particles (Fig. 5), absolutely non-concomitant with curved nanolamellas Meanwhile, the conglomerates seem to contain only species of barrel like nanolamellas. This phenomenon implies there is a difference between the growth mechanisms of the two kinds of nanostructures. As for the growth of carbon nanotubes, the so-called root-growth model has been proposed [1], in which vapours of the reactants dissolve in a molten catalyst to form eutectic particles and nanotubes then grow from these particles by supersaturation and segregation. From our TEM observations (Fig. 5), it can be seen that the ends of the nanotubes were embedded in surrounding clumps. Such a phenomenon implies that the root-growth model also provides a suitable explanation for the formation of N doped carbon nanotubes of our samples. Magnesium, melamine and the working gases such as nitrogen and ammonia react drastically with one another and nanosized particles of Mg_3N_2 and CN_x composites are formed. The vapours rich in carbon, nitrogen and CN radicals dissolve into these composite particles at the highly ionized central region of the arc plasma. The composite particles become supersaturated as they fly away from the high temperature arc region to the water-cooled collecting wall and the nucleation and segregation of the nanotubes take place.

As to the growth of the barrel like curved lamellas, a conceivable hypothesis is that they are formed with relatively low supersaturation of CN_x species, which results in low growth rates. They grow faster within the graphene planes than in the perpendicular direction and develop into lamellas with high aspect ratios. The lamellas are so thin that the rolling process could proceed easily via the combined effect of the extremely high temperature, the bombardment of radicals and the quenching process. However, the curling of the lamellas occurred in all direction simultaneously, due to the high defect density induced by the incorporation of N atoms. Thus, instead of seamless co-axial cylinders, irregular barrel like structures are formed.

It should be noted that no materials with the layered structure such as graphite were present in the starting materials. This implies that the direct formation of doped carbon nanostructures such as nanotubes, fullerenes, etc., using nitrogen-rich precursors via certain techniques such as arc discharge or laser ablation is possible. This may be a new and promising route for the synthesis of doped carbon nanostructures and further work has to be carried out for the optimization of the experiments.

4. Conclusion

Nanocrystalline carbon materials such as nanotubes, fullerenes and related structures are a high profile subject in science and technology, due to their potential usages in nanoengineering as well as their other attractive properties. The doping of these

materials opens up new routes to nanoscale electronics. Various techniques such as arc discharge laser ablation and CVD, etc. have been employed to produce those doped nanostructures. In this study, the preparation of N doped carbon nanostructures via the pyrolysis of a solo precursor, melamine, was demonstrated. The final product had been characterized by various techniques used in parallel. The doping level was shown to be lower than 5 wt. % by elemental analysis via the combustion method. XPS studies revealed that N atoms occupying the substitutional sites, the pyridine like sites, the pyrrolic or pyridonic sites and N-amine like sites coexisted in the carbon matrix. XRD patterns showed characteristic features of turbostratic carbons. In the TEM morphologies, nanostructures such as tubes and conglomerations of barrel like curved lamellas were found and attributed to different growth mechanisms. The formation of bundles of nanotubes was further confirmed by SEM studies.

Acknowledgements

This work was supported by the Natural Science Foundation of China (grant No. 50772043, 50372023, 50334030), the National Basic Research Program of China (grant No. 2001CB711201, 2005CB724400), the research startup foundation of Jilin University (No. 419080103460) and the Research Fund for the Doctoral Program of Higher Education of China (20070183175).

References

[1] TERRONES M., AJAYAN P.M., BANHART F., BLASE X., CARROLL D.L., CHARLIER J.C., CZERW R., FOLEY B., GROBERT N., KAMALAKALAN R., REDLICH PH., RŰHLE M., SEEGER T., TERRONES H., Appl. Phys. A, 74 (2002), 355.
[2] STÖHR B., BOEHM H., SCHLÖGL R., Carbon, 29 (1991), 707.
[3] BANDOSZ T., J. Colloid Interf. Sci., 246 (2002), 1.
[4] TERRONES M., JORIO A., ENDO M., RAO A.M., KIM Y.A., HAYASHI T., TERRONES H., CHARLIER J.C., DRESSELHAUS G., DRESSELHAUS M.S., Mater. Today, 7 (2004), 30.
[5] AVOURIS P., Chem. Phys., 281 (2002), 429.
[6] DOROZHKIN P.S., TOVSTONOG S.V., GOLBERG D., ZHAN J., ISHIKAWA Y., SHIOZAWA M., NAKANISHI H., NAKATA K., BANDO Y., Small, 1 (2005), 1088.
[7] YANG C.M., NOGUCHI H., MURATA K., YUDASAKA M., HASHIMOTO A., IIJIMA S., KANEKO K., Adv. Mater., 17 (2005), 866.
[8] THOSTENSON E.T., LI C., CHOU T.W., Compos. Sci. Technol., 65 (2005), 491.
[9] TERRONES M., REDLICH PH., GROBERT N., TRASOBARES S., HSU W.K., TERRONES H., ZHU Y.Q., HARE J.P., CHEETHAM A.K., RŰHLE M., KROTO H.W., WALTON D.R.M., Adv. Mater., 11 (1999), 655.
[10] TERRONES M., GROBERT N., OLIVARES J., ZHANG J.P., TERRONES H., KORDATOS K., HSU W.K., HARE J.P., TOWNSEND P.D., PRASSIDES K., CHEETHAM A.K., KROTO H.W., WALTON D.R.M., Nature, 388 (1997), 52.
[11] SEN R., SATISHKUMAR B.C., GOVINDARAJ S., HARIKUMAR K.R., RENGANATHAN M.K., RAO C.N.R., J. Mater. Chem., 7 (1997), 2335.
[12] SEN R., SATISHKUMAR B.C., GOVINDARAJ S., HARIKUMAR K.R., RAINA G., ZHANG J.P., CHETHAM A.K., RAO C.N.R., Chem. Phys. Lett., 287 (1998), 671.
[13] TERRONES M., TERRONES H., GROBERT N., HSU W.K., ZHU Y.Q., KROTO H.W., WALTON D.R.M., KOHLER-REDLICH PH., RŰHLE M., ZHANG J.P., CHEETHAM A.K., Appl. Phys. Lett., 75 (1999), 3932.
[14] WU C., GUO Q., YIN P., LI T., YANG Q., XIE Y., J. Phys. Chem. B, 109 (2005), 2597.

[15] GLERUP M., STEINMETZ J., SAMAILLE D., STÉPHAN O., ENOUZ S., LOISEAU A., ROTH S., BERNIER P., Chem. Phys. Lett., 387 (2004), 193.
[16] LEIS J., PERKSON A., ARULEPP M., KÄÄRIK M., SVENSSON G., Carbon, 39 (2001), 2043.
[17] STAŃCZYK K., DZIEMBAJ R., PIWOWARSKA Z., WITKOWSKI S., Carbon, 33 (1995), 1383.
[18] WEIDENTHALER C., LU A., SCHMIDT W., SCHÜTH F., Micropor. Mesopor. Mat., 88 (2006), 238.
[19] KAPTEIJN F., MOULIJN J., MATZNER S., BOEHM H., Carbon, 37 (1999), 1143.
[20] SU F., ZHAO X.S., LV L., ZHOU Z., Carbon, 42 (2004), 2821.

Received 27 April 2009
Revised 10 September 2009

Materials Science-Poland, *Vol. 28*, *No. 1*, *2010*

Characterization of laser ablated $AgInSe_2$ films

D. PATHAK[1*], R.K. BEDI[1], D. KAUR[2]

[1]Department of Physics, Guru Nanak Dev University, Amritsar, India

[2]Department of Physics and Center of Nanotechnology,
Indian Institute of Technology Roorkee, India

$AgInSe_2$ (AIS) thin films have been grown directly on silicon by means of a pulsed laser deposition technique. The X-ray diffraction studies show that the films are textured in the (112) direction. Increase of the substrate temperature results in a more ordered structure. Composition of the samples has been analysed by EDAX. It was found that the stoichiometry is better maintained with the PLD technique than with other traditional methods like thermal evaporation. The optical studies of the films show that the optical band gap is about 1.20 eV. The results of investigations may be of interest for a better understanding of the growth processes of chalcopyrite thin films on silicon materials.

Keywords: *pulse laser ablation; silicon wafers; heterojunction; FESEM; direct band gap materials*

1. Introduction

The I–III–VI_2 compounds are ternary analogues of II–VI compounds having high absorption coefficient and good thermal stability [1]. The chalcopyrite semiconductor $AgInSe_2$ (AIS) is one of the most attractive materials in thin film solar cell applications because of its high optical absorption coefficient. These compounds crystallize in chalcopyrite structure which is closely related to a zinc blend structure. Ternary chalcopyrite compounds have photovoltaic properties that have potential use in solar cells since their optical band gap lies between 0.8 eV and 2.0 eV and can be grown either as n or p type [2]. The efficiency of 19.5% has been reported by Contreras et al. in $CuInGaSe_2$ [3]. $AgInSe_2$ having a band gap of 1.20 eV and the melting point of 780 °C has applications in photovoltaic and optoelectronic devices. Matsuo et al. studied $AgInSe_2$ films grown by the thermal evaporation technique, taking Ag_2Se and In_2Se_3 as starting materials [4]. Ramesh et al. obtained the efficiency of 7.5% in p-$AgInSe_2$/n-CdS solar cells in which $AgInSe_2$ is used as the absorber material [5].

*Corresponding author, e-mail: dineshpathak80@gmail.com

A number of physical and chemical deposition techniques such as flash evaporation [6], radio frequency sputtering [7], thermal evaporation [8–10], solution growth [11, 12] and hot pressing [13] have been used for the preparation of $AgInSe_2$ under various experimental conditions. All these techniques have advantages and disadvantages, depending on the type of application intended for the films. It is important to obtain high quality AIS films for improving solar cell performance. However, the common problem encountered during synthesis is to preserve the stoichiometric amount of selenium due to high volatility in Se containing compounds. The pulsed laser deposition (PLD) technique has been shown to be an excellent way to fabricate high temperature superconductors [14] and multicomponent oxide films [15, 16], especially with respect to compositional reproduction and high deposition rate. PLD has many advantages and technological possibilities. These advantages are the effectiveness and simplicity of the deposition equipment, high deposition rates and low temperature deposition, a wide spectrum of deposition parameters for the control and optimization of film properties. In addition, PLD enables accurate control both the stoichiometry and the film thickness. The growth of AIS on Si substrates is of interest, since it is regarded to be a prerequisite for the direct integration of this material with the more dominant Si-based technologies. In this paper, an attempt has been made to grow $AgInSe_2$ films on Si substrates with (100) orientation by laser ablation. We report on the synthesis of AIS thin films using the (PLD) technique in which Se volatility can be minimized. Structural and optical properties depending on substrate temperature of films fabricated by pulse laser deposition have also been studied.

2. Experimental

Ablation of a polycrystalline target 25 mm in diameter was achieved using a multitarget, ultra high vacuum (UVH) pulse laser deposition (PLD), KrF excimer laser system (λ = 248 nm, the laser rate of 3 Hz and the pulse energy density of 1–2 J/cm^2). The complete set up of the system is shown in Fig. 1. The synthesis of the target was performed using a stoichiometric mixture of Ag, In and Se, followed by sealing in a quartz tube ampoule. The sealed quartz tube was heated at 900 °C for 48 h and cooled slowly. A polycrystalline chalcopyrite structure was obtained as the resulting compound. The details of the synthesis of the AIS target have been described elsewhere [10]. The target substrate distance was kept at 40 mm. The chamber was evacuated to the pressure lower than 2.7×10^{-6} Pa before ablation. The (100) oriented Si substrates were chemically cleaned and etched in a dilute HF solution prior to introduction into the chamber. All substrates were also cleaned in an ultrasonic bath before deposition. The ablated AIS was collected on a Si(100) wafer. The silicon substrates were then mounted on a direct heating sample holder made of a stainless steel sheet. AIS/Si films were grown with the deposition temperatures 300 K and 473 K. Laser pulses were incident at the angle of 45° on the target, over the surface scanned

by the focused laser beam. The deposited films were finally cooled to room temperature in vacuum.

Fig. 1. Complete PLD set up

The structure of the as prepared powder and pulse laser ablated films on Si(100) wafers was observed with a θ–2θ X-ray diffractrometer using CuK_α radiation to study the orientation and crystallinity of the films. The analysis of the composition of the product has been carried out by the energy dispersive analysis through X-rays (EDAX), together with field emission scanning electron microscopy (FESEM). The optical studies were performed on films grown on glass substrates, using the same conditions as used for the deposition on Si substrates [9, 17]. Glass was chosen only for the optical measurements. It is noted that AIS/glass exhibits a similar composition to that found in AIS/Si films. The absorption spectra of $AgInSe_2$ films were recorded in the wavelength range 200–1100 nm, using a UV-VIS Perkin-Elmer spectrophotometer.The microstructure was studied using field emission scanning electron microscopy (FESEM-FEI Quanta 200 F). To prevent the charge build up during FESEM observation, samples were coated with gold using a sputtering system.

3. Results and discussion

The XRD profile of the as-prepared powder is shown in Fig. 2a. The pattern indicates that AIS is polycrystalline in nature and exhibits a prominent (112) peak of chalcopyrite phase, in addition to other (220), (204), (312) and (116) peaks of very small intensity. The films prepared on the Si(100) wafers at room temperature are characterized by the absence of diffraction peaks, indicating their amorphous nature. However the AIS films obtained at 473 K indicate high orientation in the (112) plane, parallel to the silicon substrate along with a reflection from the (204) plane of comparatively small intensity (Fig. 2b).

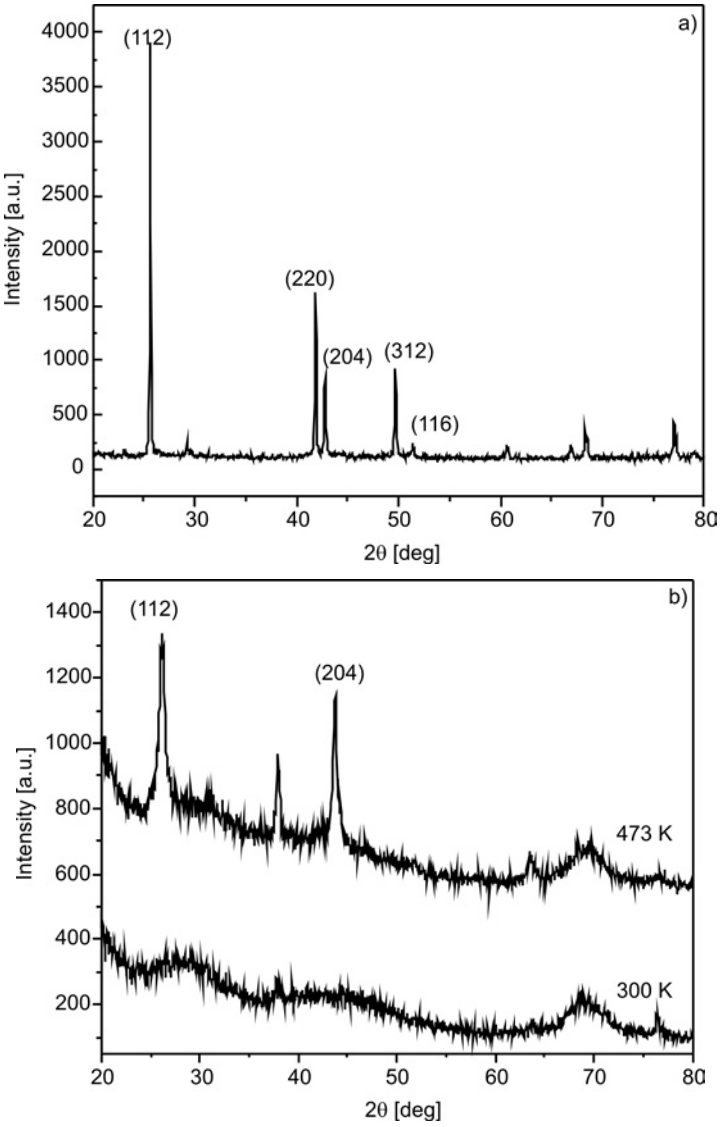

Fig. 2. XRD pattern of as synthesized powder (a) and films (b) fabricated by PLD on Si(100) wafers at 300 K and 473 K

The crystallite size is calculated from the FWHM value of the (112) peak by using Scherrer's formula

$$D = \frac{0.9\lambda}{\beta \cos\theta} \tag{1}$$

and is found to be 6 nm, where λ is the wavelength of X-rays, β is the FWHM in radians, θ is the Bragg angle. XRD studies confirm that by performing laser ablation,

$AgInSe_2$ can be grown on silicon wafers. These preliminary results indicate the possibility of producing device quality chalcopyrite–$AgInSe_2$/Si heterojunctions by pulse laser ablation for photovoltaic applications.

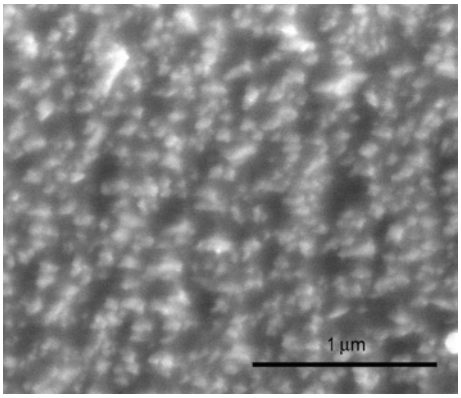

Fig. 3. FESEM of laser ablated AIS films on Si(100) wafer at 473 K

Field emission scanning electron micrograph of an AIS nanostructured film deposited by pulse laser deposition at 473 K on Si(100) substrate is shown in Fig 3. It delineates the shape and distribution of crystallites. Densely packed grains elongated in one direction are exhibited by AIS film grown at 473 K. It is also observed that grains are more homogeneous, uniformly distributed and densely packed as compared with the films deposited by thermal evaporation on the same substrate, Si(100), and at the same deposition temperature [9]: these are the major advantages of PLD, along with pore free growth.

Analysis of the composition of AIS films grown on 100 oriented silicon wafers was carried out by the energy dispersive analysis through X-rays. This elemental analysis showed that films obtained at 473K are almost as stoichiometric those prepared by thermal evaporation with Ag 28.96%, In 27.41% and Se 43.63%. The selenium percentage deviates to some extent due highly volatile nature of the element.

The optical studies were carried out on AIS films grown on glass substrates under the same conditions as those used for deposition on Si substrates [9, 17]. It is noted that AIS/glass has a similar composition to that found in AIS/Si films. The linear nature of the plot near the absorption edge confirms that ablated $AgInSe_2$ films show semi-conducting behaviour with direct band gap [18]. The band gap energy (E_g) was estimated based on the recorded optical spectra from the equation of Bardeen [19].

$$\alpha h\nu = A\left(h\nu - E_g\right)^n \tag{2}$$

where A is a constant, α is the absorption coefficient, $h\nu$ is the photon energy, and n depends on the nature of the transition. For direct transition, n =1/2 or 3/2, while for the indirect one n = 2 or 3, depending on whether they are allowed or forbidden, respectively. Here the best fit to the experimental data was obtained for n = 1/2. The

dependence of $(\alpha h\nu)^2$ on $h\nu$ yields a straight line, indicating that the fundamental absorption edge could be due to direct allowed transition.

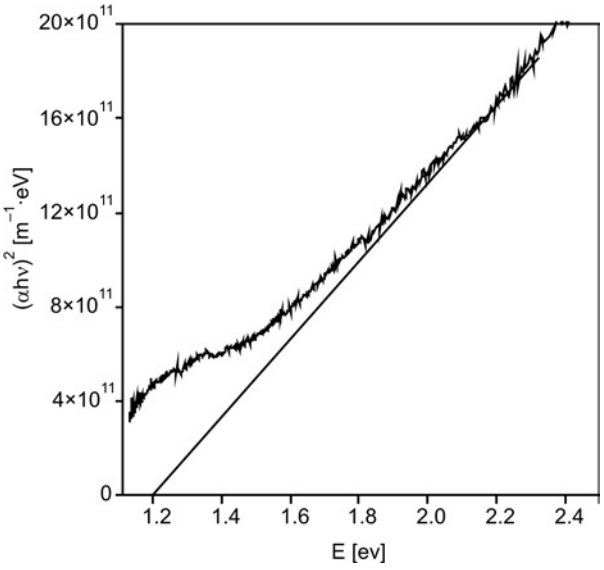

Fig. 4. Dependence of $(\alpha h\nu)^2$ on E

These results are in conformity with those reported earlier for thermally evaporated AIS [6, 8–10]. The band gap energy is estimated to be 1.20 ev (Fig. 4). Various authors reported different values for the band gap energy of $AgInSe_2$ films [6,8], which may be attributed to different proportions of Ag/In/Se in the composition.

4. Conclusions

We have successfully deposited silver indium selenide films directly on Si (100) substrates by the pulse laser deposition technique. The films show a tetragonally distorted chalcopyrite structure. Room temperature deposited films are amorphous in nature while AIS films deposited at 473 K appear to have preferential texture oriented in the (112) direction. Crystallites of 6 nm size were obtained. On silicon wafers, from optical measurements, the band gap energy is estimated to be 1.20 eV. We believe that these preliminary results may be of interest for a better understanding of the growth of chalcopyrite thin films on silicon materials, since it is regarded to be a prerequisite for the direct integration of these materials with the dominant Si-based technologies.

Acknowledgements

One of the authors (D. P.), acknowledges the Council of Scientific and Industrial Research (CSIR), New Delhi, India, for awarding a Senior Research Fellowship (SRF) grant to carry out this project.

References

[1] TELL B., SHAY J., KASPER H.M., J Appl. Phys., 43 (1972), 2469.
[2] JOSEPH C.M., MENON C.S., Semicond. Sci. Techn., 11 (1996),1668.
[3] CONTRERAS M.A.,RAMANATHAN K., ABUSHAMA J., HASOON F., KEANE J., YOUNG L., EGAAS B., NOUFI R., Prog. Photovolt. Res. Appl.,13 (2005), 209.
[4] MATSUO H., YOSHINO K., AND IKARI T., Phys. Stat. Sol. (c), 3 (2006), 2644.
[5] RAMESH P.P., UTHANA S., SRINIVASALU B.N., JAYARAMA P.R., Vacuum, 47 (1996), 211.
[6] PATEL S.M., PATEL A.D., Thin Solid Films, 111 (1984), 53.
[7] WEIR R.D., JESSOP P.E., GARSIDE B.K., Can. J. Phys., 65 (1987), 1033.
[8] KORASHY A.E., ABDEL-RAHIM M.A., ZAHED H.E., Thin Solid Films, 338 (1999), 207.
[9] PATHAK D., BEDI R.K., KAUR D., Appl. Phys. A, (2009), DOI 10.1007/s00339-009-5083-8.
[10] BEDI R.K., PATHAK D., DEEPAK, KAUR D., Z. Cristallogr. Suppl., 27 (2008), 177.
[11] SHARMA R.P., Indian J. Pure Appl. Phys., 33 (1995), 711.
[12] MENG A., CHRIS B., JAGDESE J.V., J. Am. Chem. Soc.,128 (2006), 7118.
[13] YOSHINO K., KINOSHITA A., SHIRAHTA Y., OSHIMA M., YOSHITAKE T., OZAKI S., IKARI T., J. Phys., Conf. Ser. 100 (2008), 042042.
[14] DIJKKAMP D., VENKATSAN T., WU X.D., Appl. Phys. Lett., 51 (1987), 619.
[15] OTUBO S., MAEDA U., MINAMIKAWA T., YONEZWA Y., MORIMOIO A., SHIMIZU.T., Jpn. J. Appl. Phys,. 29 (1990), 133.
[16] KIDOH H., YASHIMA H., MORIMOTO A., SHIMIZU T., Jpn J. Appl. Phys., 33 (1994), 4094.
[17] BECHIRI L., BENABDSLEM M., BENSLIM N., DIEKOUN A., OTMANI A., MAHADDJOUBI L., MADELON R., RUTERANA P., NOUET G., Catal. Today, 113 (2006), 226.
[18] PANKOVE J.I., *Optical Processes in Semiconductors*, Prentice Hall, New York, 1971.
[19] *Photoconductivity Conference*, J. Bardeen (Ed.), Wiley, New York, 1956.

Received 5 June 2009
Revised 13 October 2009

Materials Science-Poland, *Vol. 28*, *No. 1*, *2010*

On the design of biodegradable hydrogels both thermosensitive and pH sensitive

B. WANG[1, 2*], Y. GUO[1, 2], G. HU[1]

[1]Institute of Macromolecules and Bioengineering, North University of China, Taiyuan 030051, China

[2]Institute of Chemical Engineering and Environment, North University of China, Taiyuan 030051, China

A Pluronic oligo(ε-caprolactone) block copolymer has been synthesized by ring opening polymerization of ε-caprolactone monomers in the presence of poly(ethylene oxide)–poly(propylene oxide) –poly(ethylene oxide) triblock copolymers, using stannous octoate as a catalyst, and then the block copolymer was terminated with an acryloyl group. A novel biodegradable pH- and temperature sensitive hydrogel has been fabricated by free radical copolymerization of diacylated macromer–methacrylic acid aqueous solution initiated by a redox initiator. The structures of products were characterized by the Fourier transform infrared spectroscopy. Variations of the equilibrium swelling ratio in various environmental solutions confirmed the pH- and temperature sensitivity of hydrogel, which were affected by the MAA content.

Keywords: *biodegradable hydrogel; pH sensitivity; temperature sensitivity*

1. Introduction

During the last decade, a great attention has been focused on the controlled drug release technique, due to the appearance of protein drugs and their special structure. Among the current materials for controlled drug carriers, hydrogels are rather unique and especially suitable for the sustained release of hydrophilic macromolecular drugs [1]. Hydrogels are three-dimensional hydrophilic polymer networks that can be swollen to many times their mass and volume in aqueous environments [2]. As the term "network" implies, cross-linking has to be formed to avoid dissolving or losing their structural integrity in the aqueous phase [3]. Due to their diverse functionalities, intelligent hydrogels have been the subject of extensive investigations in recent years [4]. Most of the intelligent hydrogels reported respond to only one type of stimuli. Among these intelligent hydrogels, pH sensitive or temperature sensitive hy-

*Corresponding author, email: bbwang@nuc.edu.cn

drogels have been commonly investigated, because both parameters are important environmental factors in biomedical and other systems [5]. Body temperature often deviates from the normal one (near 37 °C) by the physiological presence of pathogens or pyrogens. This change of temperature may be a useful stimulus that can modulate the delivery of therapeutic drugs for diseases with accompanying fever [6]. pH sensitivity is another parameter that can be exploited in applications, and arguably has greater potential for use in biomedical devices, or biomaterials than thermosensitivity (see [7]).

From the application point of view, hydrogels, especially biodegradable hydrogels, would be highly useful if they simultaneously responded to two stimuli. Keeping this consideration in mind, our objective is to design and synthesize a novel biodegradable hydrogel that sensitive both to pH as well as to temperature. We selected Pluronic (Poloxamer), an ABA triblock copolymer of poly(ethylene oxide) –poly(propylene oxide)–poly(ethylene oxide) (PEO–PPO–PEO), as the central part of the hydrogel for its superior biocompatibility and temperature sensitivity [8–11]. Then extending it with of ε-caprolactone oligomer can endow the final product with biodegradability. Finally, end-capping with reactive acryloyl units allows the macromer to be polymerized. The PMAA is selected as a pH sensitive copolymer both because of its sharp pH induced volume transition in the physiological pH range and its broad range of applications in the biomaterial field [12, 13].

In the present work, the hydrogel was obtained by radical copolymerization of the diacrylated macromer–methacrylic acid aqueous solution initiated by a redox initiator. We also investigated the effect of MAA content on the temperature sensitivity and pH sensitivity of the biodegradable hydrogel.

2. Experimental

Materials. Pluronic F127 (PEO–PPO–PEO) triblock copolymer was obtained from BASF (Germany). ε-caprolactone monomer and tin(II)2-ethylhexanoate (stannous octoate) were purchased from Aldrich (Milwaukee, WI, USA) and Sigma (Dallas, Texas, US), respectively. All other chemicals were of analytical grades.

Synthesis of Pluronic–oligo(ε-caprolactone) block copolymers (PFCL). Pluronic –oligo (ε-caprolactone) amphiphilic block copolymers were synthesized by ring opening polymerization of ε-caprolactone monomers in the presence of PEO–PPO–PEO triblock copolymers, Pluronic F127, using stannous octoate as a catalyst. The Pluronic, ε-caprolactone monomers and stannous octoate with various weight ratios were placed into a flask connected with a vacuum outlet tube, and the mixture was preheated for 6 h at 60 °C under vacuum in order to obtain a well mixed melting phase. The mixture was purged several times with argon to displace the oxygen. Finally, the flask was sealed off under vacuum and the reactant was copolymerized at 150 °C for 24 h. The copolymerization product was cooled to the room temperature, dissolved

with dichloromethane, and then precipitated with an excess of anhydrous ether to remove unreacted Pluronic and ε-caprolactone monomers. The precipitate was collected by filtration and washed several times with absolute ether. The resulting product was dried under vacuum. The Pluronic–oligo(ε-caprolactone) block copolymer products are denoted as $PFCL_X$, where X is the degree of polymerization of ε-caprolactone at each end of the Pluronic molecule according to the feed ratio.

Synthesis of diacrylated macromer (PFCL-D). Dried Pluronic–oligo(ε-caprolactone) block copolymer product and triethylamine were dissolved in dichloromethane in a 250 cm^3 round bottom flask. Acryloyl chloride in dichloromethane was drop-wise added. The reaction mixture was stirred with an agitator at 0 °C for 12 h and then for next 12 h at room temperature. The reaction product was filtrated and extracted with an excess of anhydrous ether. The precipitate was collected by filtration and dried under vacuum. The diacrylated macromer of Pluronic–oligo(ε-caprolactone) block copolymer is denoted as $PFCL_X$-D.

Synthesis of pH- and temperature sensitive hydrogels (PFCL-MAA). Hydrogels were obtained by free radical copolymerization in distilled water. Ammonium persulfate (APS) was selected as a redox initiator and *N*,*N*,*N*′,*N*′-tetramethylene diamine (TEMED) was used as an accelerator. $PFCL_X$-D and MAA monomers were dissolved in distilled water. Then a appropriate amounts of APS and TEMED were added to the mixtures. The mixture solution was poured onto a glass dish and crosslinked to form a hydrogel film at 60 °C. The wet hydrogel films were dried under vacuum for several days. The hydrogels $PFCL_X$-MAA-*Y*, were obtained where *Y* is the wt. % of MAA in diacrylated macromer of Pluronic–oligo(ε-caprolactone).

FTIR characterization. The dried products were analyzed in KBr discs with a FTIR spectrophotometer (FTIR-8400S, Japan) in the range of 500–4000 cm^{-1}.

Temperature sensitivity. The temperature dependence of the swelling ratio in the range of 4–37 °C was investigated by the classical gravimetric method. Dried hydrogel samples were immersed in distilled water at a given temperature for at least 24 h. Then any excess water on the swollen hydrogel surface was removed by wet filter paper. The equilibrium swelling ratio (ESR) is defined as follows:

$$\mathrm{ESR} = \frac{m_s - m_d}{m_d} \tag{1}$$

where m_s is the weight of the equilibrium swollen hydrogel and m_d is its initial weight.

pH sensitivity. The hydrogels were immersed in buffer solutions of various pH (from 2 to 8) at 4 °C and 37 °C for at least 24 h, in order to achieve swelling equilibrium. Then the hydrogels were weighed, and the swelling ratio at each pH was calculated according to Eq. (1).

3. Results and discussion

3.1. Characterization of chemical structures of macromers

FTIR spectroscopy has been employed to characterize the chemical structure of Pluronic, a series of PFCL block copolymers and PFCL-D macromers (Fig. 1).

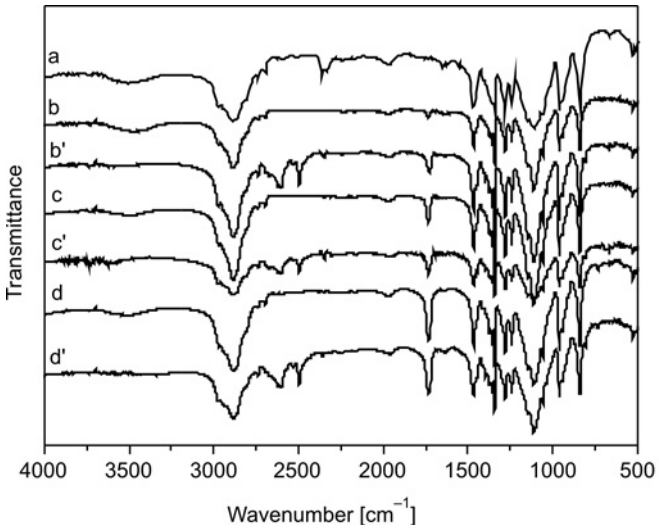

Fig. 1. FTIR spectra of: a) Pluronic F127, a series of PFCL block polymers – b), $PFCL_4$, c) $PFCL_8$, d) $PFCL_{12}$ and PFCL-D macromers – b′) $PFCL_4$-D, c′) $PFCL_8$-D, d′) $PFCL_{12}$-D

The peaks between 3000 and 4000 cm^{-1} are assigned to symmetric and asymmetric stretching vibration modes of the hydroxyl group. As compared with the FTIR spectra of F127, PFCL block copolymers (Fig. 1, b–e) display a new and strong carbonyl band at 1734 cm^{-1}, which is attributed to the C=O stretching mode of the ε-caprolactone units in the copolymers. The ε-caprolactone units are extended into the ends of Pluronic molecules. The intensity of the peaks at 1734 cm^{-1} increases as the number of ε-caprolactone units increases. Ding et al. reported similar results [14, 15]. Furthermore, the peaks at 3500 cm^{-1} disappear for PFCL-D macromers as shown in Fig. 1b′–d′. It may be concluded that the hydroxyl group at both ends of F127-oligoCL was substituted by the acryloyl group in the macromers.

3.2. Temperature sensitivity

The temperature dependence of the equilibrium swelling ratio (ESR) over a temperature range from 4 to 37 °C is shown in Fig. 2. All obtained hydrogels display

a good temperature response. For example, at 4 °C, the ESR value of the samples PFCL4-MMA-10, PFCL4-MMA-20, and PFCL4-MMA-30 is 7.22, 4.76 and 3.93, respectively, whereas the corresponding values at 37 °C are 3.99, 3.28 and 2.63, respectively.

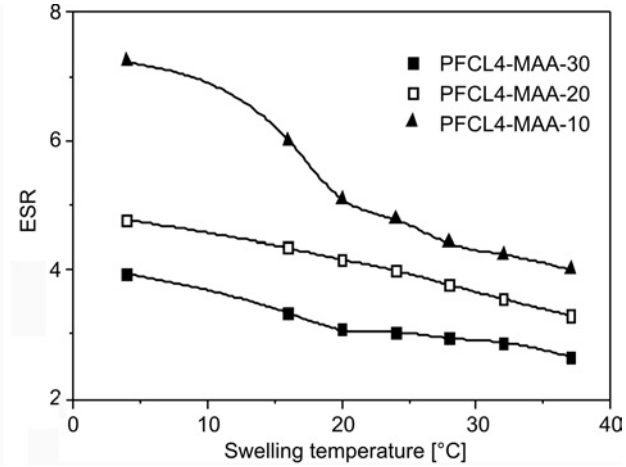

Fig. 2. Temperature dependence of the swelling ratio in hydrogels

The negative temperature sensitivity of the hydrogels originates from the lower critical solution temperature (LCST) behaviour of PEO–PPO–PEO block copolymers in water. Clearly, the swelling ratio of hydrogels decreases as the MAA content increases, which may be attributed to the formation of a more compact network after the incorporation of MAA segments.

3.3. pH sensitivity

The investigations of the swelling properties of the hydrogels were carried out in various buffer solutions (pH from 2 to 8) at 4 °C and 37 °C, respectively. An evident swelling transition is observed with pH change (Figs. 3 and 4). Additionally, with the increase in the MAA content, the ESR value decreases before the swelling transition: this is in contrast to the increase of ESR at high pH. For example, at pH = 5 and 4 °C (or 37 °C), the ESR values of PFCL8-MMA-10, PFCL8-MMA-20, and PFCL8-MMA-30 samples are 6.87 (3.91), 4.50 (3.20), and 3.01 (2.21), respectively. Their corresponding ESR values at pH = 8, however, are increased to 25.42 (18.61), 33.17 (27.07), and 38.66 (30.63), respectively. Such behaviours demonstrate that the PFCL –MMA hydrogels show both pH and temperature sensitivity. The pH sensitivity is related to the pH dependent ionization of side carboxylic acid (–COOH) groups of PMAA.

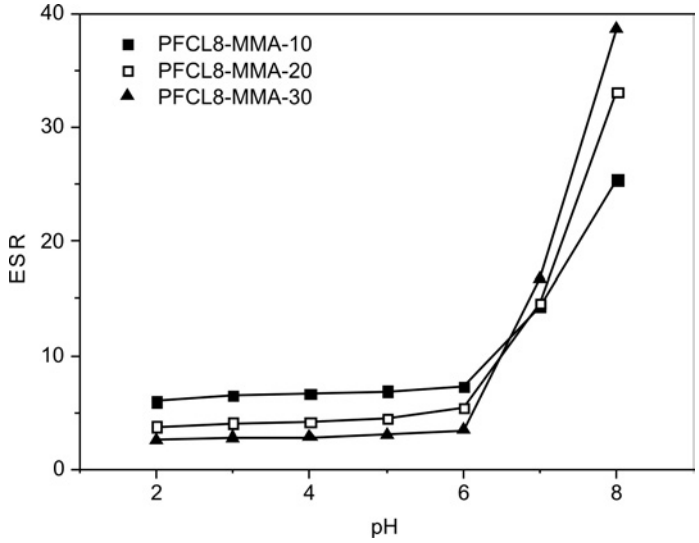

Fig. 3. Dependence of the swelling ratio on pH plot in hydrogels at 4 °C

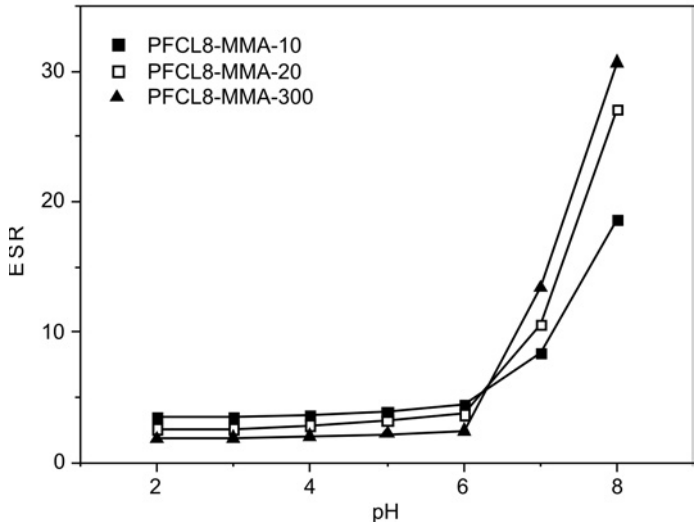

Fig. 4. Dependence of the swelling ratio on pH plot in hydrogels at 37 °C

3.4. The temperature and pH dependent swelling mechanism

Obviously, the temperature and pH-sensitivity of PFCL-MAA hydrogels are related with the network structure and the associated interactions (such as hydrophobic and hydrophilic interaction). We hypothesize that there are three different structures in the network of the PFCL-MAA hydrogel (Fig. 5).

The temperature sensitivity of PFCL-MAA hydrogel contributes to the moiety of Pluronic in the network. Hydrogen bonding between hydrophilic segments of the macromer chain and water molecules dominates at low temperatures, leading to enhanced dissolution in water of the copolymer hydrogel. Hydrophobic interactions among hydrophobic segments, especially PPO segments, however, are strengthened at high temperatures, resulting in association and shrinking of the network.

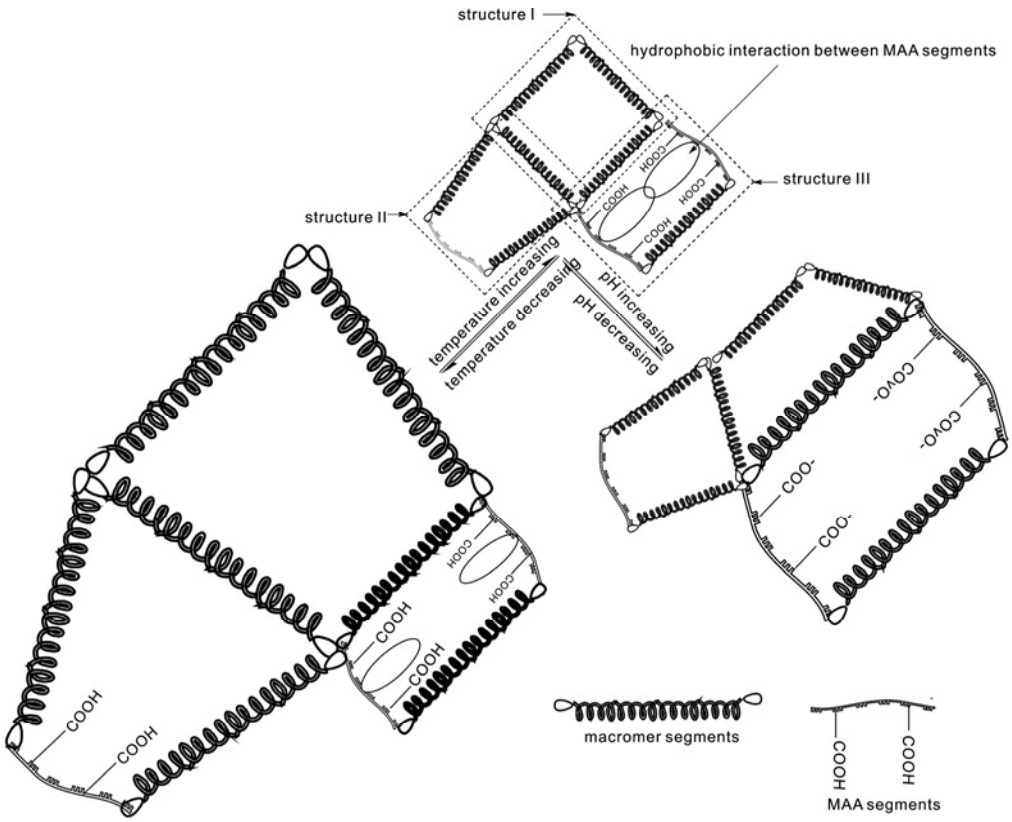

Fig. 5. Scheme of temperature and pH dependence of swelling mechanism of the PFCL–MAA hydrogel

As expected, using MAA as a pH sensitive co-monomer of PFCL-D macromer, the PFCL-MAA hydrogel is highly responsive to changes in pH, just like PMAA itself. Due to the existence of carboxylic acid groups in MAA segments, the hydrophobic units can undergo stable hydrophobic interaction in an acid medium. The hydrophobic interaction can restrict the movement or relaxation of network chains. Therefore, a more compact hydrogel network is formed, with a lower swelling capacity. But in a neutral and alkaline media, the ionization of the carboxylic acid groups of MAA occurs, disrupts the hydrophobic interaction and generates electrostatic repulsion among hydrogel chains. This repulsive force is strong enough to push the network

chain segments apart and attract more water into the hydrogel, so a higher swelling ratio is observed.

Moreover, it is easy to explain different swelling behaviour of PFCL-MAA hydrogel for different MAA contents, as is observed in Fig. 5. Clearly, all of these three structures in Fig. 5, are highly responsive to temperature changes. The swelling capacity, however, is different and is described by the sequence: structure I > structure II > structure III. Therefore, it is not surprising that the ESR values decrease as the MAA content increases, since the content of the latter two structures increases at high MAA content. We also suspect that only structure III can sensitively respond to the change of pH, since it can interact hydrophobically with MAA segments in an acidic medium which causes shrinkage of polymer chains, water molecules cannot easily diffuse and permeate into a more compact network. Since the hindrance effect increases as the MAA content in the PFCL-MAA hydrogel increases, the ESR values certainly decrease with MAA content increasing at acidic swelling solution. As the pH of the swelling solution increases, ionization of the carboxylic acid groups occurs and their electrostatic repulsions cause a great degree of swelling of the hydrogel. In this case, the resulting hydrophobic interaction between MAA segments becomes weaker and finally vanishes, leading to expansion of structure III and therefore an increase in the ESR value. The electrostatic repulsions become much stronger if the MAA content is high. As such, the degree of swelling of the hydrogel increases as the MAA content increases.

4. Conclusions

A series of Pluronic–oligo(ε-caprolactone) (PFCL) block copolymer was synthesized by ring opening polymerization of ε-caprolactone monomers in the presence of PEO–PPO–PEO triblock copolymers (Pluronic), and was then subsequently end-capped with the acryloyl groups. The FTIR spectra verified that the diacrylated macromer successfully has been synthesized.

This novel, pH-sensitive and temperature sensitive PFCL-MAA hydrogel was obtained by free radical copolymerization of the diacrylated macromer–methacrylic acid aqueous solution initiated by a redox initiator. The equilibrium swelling ratio of hydrogel in various solutions indicated that the PFCL-MAA hydrogel displayed both temperature- and pH sensitivity, which were affected by the MAA content. The MAA content caused the ESR values to decrease at specific swelling temperatures. With the increase in the MAA moiety of the PFCLMAA hydrogel, the degree of swelling at an acidic medium decreased due to the presence of hydrophobic interaction. It, however, decreased at neutral and alkaline media since lack of hydrophobic interaction offered the hydrogel much stronger electrostatic repulsions in the case of high MAA content.

Acknowledgements

This work was financially supported by the Science and Technology Foundation for Youth from Shanxi Sci and Tech Bureau (Grant No. 2006021011).

References

[1] PEPPAS N.A., BURES P., LEOBANDUNG W., ICHIKAWA H., Eur. J. Pharm. Biopharm., 50 (2000), 27.
[2] NI H., KAWAGUCHI H., ENDO T., Coll. Polym. Sci., 285 (2007), 873.
[3] ZHAO Y., KANG J., TAN T.W., Polymer, 47 (2006), 7702.
[4] SUN G.M., ZHANG X.Z., J. Mater. Sci.: Mater. Med., 18 (2007), 1563.
[5] ZHANG J., CHU L.Y., LI Y.K., LEE Y.M., Polymer, 48 (2007), 1718.
[6] KIM S.Y., HA J.C., LEE Y.M., J. Control. Release, 68 (2000), 345.
[7] NI H., KAWAGUCHI H., ENDO T., Coll. Polym. Sci., 285 (2007), 819.
[8] KABANOV A.V., LEMIEUX P., VINOGRADOV S., ALAKHOV V., Adv. Drug Deliv. Rev., 54 (2002), 223.
[9] HA J.C., KIM S.Y., LEE Y.M., J. Control. Release, 62 (1999), 381.
[10] CHANDAROY P., SEN A., HUI S.W., J. Control. Release, 76 (2001), 27.
[11] ZHANG Y., ZHU W., WANG B.B., YU L., DING J.D., J. Control. Release, 105 (2005), 260.
[12] TORRES-LUGO M., PEPPAS N.A., Macromolecules, 32 (1999), 6646.
[13] LIU Y.Y., LIU W.Q., CHEN W.X., SUN L., ZHANG, G.B.; Polymer, 48 (2007), 2665.
[14] ZHU W., WANG B.B., ZHANG Y., DING J.D., Euro. Polym. J., 41 (2005), 2161.
[15] WANG B.B., ZHU W., ZHANG Y., YANG Z.G., DING J.D; React. Funct. Polym., 66 (2006), 509.

Received 6 June 2009

Materials Science-Poland, *Vol. 28*, *No. 1*, *2010*

Influence of sol-gel matrices on the optical excitation of europium ions

M. BANSKI*, A. PODHORODECKI, J. MISIEWICZ

Institute of Physics, Wrocław University of Technology,
Wybrzeże Wyspiańskiego 27, 50-370 Wrocław, Poland

Photoluminescence (PL), total photoluminescence excitation (TPLE), transmission and decay photoluminescence experiments were done to establish the most efficient excitation mechanism of the europium (Eu^{3+}) ions in amorphous Al_2O_3 and $Y_3Al_5O_{12}$ host matrices. Both matrices were fabricated using the sol-gel technique, doped with Eu^{3+} ions and sputtered on a flat quartz plate. Because of relatively low temperatures of annealing (200 °C), after this treatment the matrices should remain in an amorphous phase. In such a system, Eu^{3+} ions occupy the points having different site symmetries. However, based on characteristic features of the PL spectra, the effective site symmetry (ESS) parameter was defined to describe the PL properties of the Eu^{3+} ions in various matrices. Low intensive direct f-f transitions at 392, 465, 530 nm were observed in the TPLE spectra. The most intensive, wide excitation bands were centred at around 250–260 nm and the charge transfer process was found to be related to these excitation bands. Finally, a good correlation between photoluminescence lifetimes, the PL intensity and CT energy was observed.

Keywords: *excitation mechanism; charge transfer; europium; amorphous matrix; photoluminescence*

1. Introduction

Nowadays, one of the leading research areas is the investigation of new light sources with high emission efficiency, low power consumption, stability in various environments, characterised with simple method of fabrication and low production costs.

In the last two decades, intensive investigations were performed with sol-gel materials as potential host matrices for the optically active centres [10]. One of its most important advantages of the sol-gel technology is the low cost. Another one is simplicity and the possibility of easily incorporating optical active centres (i.e., rare earth ions) [2] into sol-gel and later depositing them onto various substrates (including porous materials) [3]. It is well know that PL efficiency of rare earth (RE) ions increases

*Corresponding author, e-mail: mateusz.banski@pwr.wroc.pl

with increasing non-centrosymmetricity of host crystals. In practice, a big challenge is to find a combination of substrate, matrix and RE ions such that photoluminescence emission is enhanced.

The advantage of RE ions is luminescence being related to the internal 4f orbital transitions. The screening of the internal 4f orbitals from the external environment by the 5d orbital electrons provides the stability of the emission wavelength in various external conditions. In addition, the emissions of different RE ions cover almost all visible range of wavelengths. As a result, RE ions have already been found to have many applications, e.g. in large-scale display screens, television sets, lasers and amplifiers [4]. However, 4f–4f transitions are in principle electric dipole forbidden according to Laporte's rule, thus the RE ions have very small absorption cross sections, which limits their use in photo-activated systems [5]. Because of this limitation, in practical applications RE ions have to be doped in a host material which plays the role of a sensitizer and increases the RE excitation efficiency.

The main role of the matrix is to increase the efficiency of RE ion photoexcitation leading to the increase of the PL intensity from the ions. The PL intensity increases, because the crystal field slightly influences the 4f orbitals of RE which overlap and cause that forbidden electric dipole transitions become allowed. Thus, Laporte's rule no longer applies in the presence of the lattice. Simultaneously, the number of the possible excitation mechanisms increases. For RE ions in the host matrix, there are four various excitation mechanisms: direct excitation of the RE ions through 4f–4f and 4f–5d transitions, and excitation through the matrix by charge transfer (CT), or energy transfer (ET). However, depending on the matrix properties (absorption coefficient, refractive index, RE ion site symmetry, etc.), different excitation mechanisms can dominate. Thus, the determination of this mechanism is crucial from the point of view of excitation/emission optimization.

From the application point of view, we expected that the ideal host material would be transparent for the visible light, environmentally stable and not fragile. Only if all these criteria are satisfied, the proposed solution will have a viable chance of becoming a commercially available product.

$Y_3Al_5O_{12}$ matrices in a crystalline form are already known to be excellent scintillators. The phosphors based on this material are widely used in cathode ray tubes, and field emission display technologies because of their optical emission intensity and long lifetime [6]. Besides the good environmental stability and high electrical resistivity, the main advantage of the Al_2O_3 matrix is its ability to incorporate a high concentration of RE ions without clustering. This phenomenon is related to the cubic crystal structure of the γ-Al_2O_3 which is very similar to the RE_2O_3 structure. This matrix can significantly enhance the RE^{3+} fluorescence [7].

$Y_3Al_5O_{12}$ and Al_2O_3 matrices were prepared using the sol-gel technique [8]. Both of them were doped with Eu^{3+} ions and sputtered on flat quartz plates. In order to reduce the cost of the production, the samples were annealed at relatively low temperatures and thus they remained in the amorphous phase.

Better information about the most efficient excitation mode will be crucial to produce more efficient and low power consuming devices. Thus, the aim of this work was to investigate the influence of an amorphous sol-gel matrix, fabricated at low temperature, on the excitation mechanism of Eu^{3+} ions. The results of the photoluminescence (PL), the total photoluminescence excitation (TPLE), as well as the transmittance measurements and PL decay have been presented.

2. Experimental

In the experiment, two samples were investigated. They were prepared using different sol-gel compounds as the matrix material, i.e. Al_2O_3, $Y_3Al_5O_{12}$ (YAG). To obtain sol-gel matrices doped with europium ions, the following compositions were used: Al_2O_3:Eu^{3+} (30 wt. % of Eu_2O_3, 70 wt. % Al_2O_3), YAG:Eu^{3+} ($Eu_{0,15}Y_{2,85}Al_5O_{12}$). The exact preparation procedure has already been described elsewhere [8, 9]. The sol-gel derived xerogel films (matrices) were fabricated by spin-on deposition at the rate of 2700 rpm onto flat quartz substrates, followed by drying at 200 °C for 30 min [10, 11]. Finally all the just-prepared samples were heated at 200 °C.

The experimental setup consisted of a 450 W Xenon lamp, Jobin Yvon TRIAX 180 monochromator, OceanOptics HR4000 CCD detector. The incident light, in the range from 210 to 500 nm, coming from a monochromator, was focused on the sample. The photoluminescence signal was collected and transmitted with the fibre optic device to the CCD detector. The setup for transmission measurements were based on a broadband light source – a deuterium tungsten halogen lamp. The luminescence lifetimes were measured with the equipment made by the Photon International Instruments, where the flash halogen lamp was used as a pulse source. The wavelength of the incident light was chosen by the monochromator. The second monochromator dispersed the signal recorded by a photomultiplier tube. All the measurements were done at room temperature.

3. Results and discussion

Figure 1 shows PL spectra of Al_2O_3:Eu^{3+} and $Y_3Al_5O_{12}$:Eu^{3+} samples excited with the wavelength in the maximum of the excitation band. The recorded spectrum exhibits features characteristic of the RE ion 4f–4f intrashell transitions. Four emission bands related to transition from the lowest excited state ($^5D_0$) to the ground state ($^7F_1$, $^7F_2$, $^7F_3$ and $^7F_4$) are clearly resolved at the 593, 613, 650 and 701 nm, respectively. The $^5D_0$–$^7F_2$ transition gives the most intensive emission peak in the spectrum, because it is the most probable transition as it is the electric dipole transition [12]. Luminescence from the higher excited states such as $^5D_1$ is not observed at all, indicating very efficient non-radiative (multiphonon) relaxation to the $^5D_0$ level [13]. The most intensive Eu-related photoluminescence is found for the $Y_3Al_5O_{12}$ matrix. At this

point, a question arises which factors influence the emission. The understanding of these factors enables us to control the excitation properties of the Eu^{3+} ions in a sol-gel matrix.

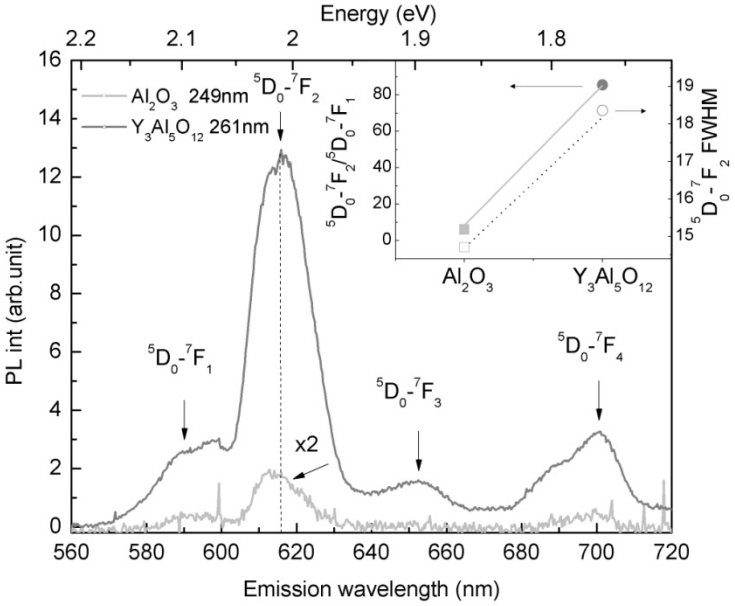

Fig. 1. The PL spectra of various sol-gel matrices doped by Eu^{3+} on the quartz substrate excited at the maximum of the excitation band. The inset shows the intensity ratio of the $^5D_0 \rightarrow {}^7F_2$ and $^5D_0 \rightarrow {}^7F_1$ and FWHM of $^5D_0 \rightarrow {}^7F_2$ transition

The emission efficiency of the RE ions depends on four factors, if they are excited non resonantly: absorption of the matrix, excitation energy transfer, emission properties of the ions and relaxation within an ion. First, the emission properties of the RE ions in two different matrices based on aluminum oxide is presented. Like the absorption, the first order emission among 4f orbitals is also forbidden by electric dipoles but it is allowed by the electric quadrupole, vibronic, magnetic dipole and forced electric dipole mechanisms. However, only the last two cases can be related to the observed emission intensities. From the experimental point of view, it was found that the emission efficiency of the ion itself depends strongly on the local symmetry of the ion site, and also on the energy difference between the excited 4f configuration and the $4f^{n-1}5d$ or CT state.

The crystal field of the host material influences not only the emission intensity from RE ions, but it also splits their ground energy levels. Because of that, few separate lines related to different transition could be observed and their number depends on the symmetry of the ion site in the matrix. In a less centrosymmetric system, the crystal lattice causes the energy levels of Eu^{3+} ions to split into a higher number of sublevels and the breadth of the emission peak increases [12]. However, in our PL spectra

it is impossible to distinguish these separate lines. They are observed as one peak at around 612.5 and 615.9 nm, with the FWHM parameter equal to 14.7 and 18.4 nm for Al_2O_3 and $Y_3Al_5O_{12}$ matrices, respectively. The observed inhomogeneous broadening is due to many site symmetries of the crystal structure, which can be occupied by the Eu^{3+} ions in an amorphous matrix, and it can be additionally enhanced by the lattice defects and contamination of the hydrous species. This is characteristic of the sol-gel structures annealed at low temperatures. They are like a disordered structure with a wide inhomogeneous broadening, like in glass [14].

As was already mentioned, in the amorphous phase it is impossible to determine the site symmetry of the Eu^{3+} incorporated into the matrix. However, the measured PL spectra exhibit different properties of the Eu^{3+} ions incorporated into various matrices. This fact allows us to determine the effective site symmetry (ESS) parameter, which describes not exactly the site symmetry of the ions in the crystal structure, but rather the response of the Eu^{3+} ions to the influence of average crystal field.

To determine the order of ESS of the Eu^{3+} incorporated into various matrices, the intensity ratio $I_2(^5D_0 \rightarrow {}^7F_2)/I_1(^5D_0 \rightarrow {}^7F_1)$ which serves as an effective spectroscopic probe could be used. The sensitivity of the intensity transition ratio (I_2/I_1) arises from the fact that the $^5D_0 \rightarrow {}^7F_1$ transition is mainly magnetically allowed (i.e., it is a magnetic-dipole transition) and is independent of the site symmetry at which any Eu^{3+} ion is situated [15], while the $^5D_0 \rightarrow {}^7F_2$ transition is a hypersensitive, forced electric-dipole transition which can occur only at low symmetries with no inversion centre [14]. Thus, the higher the I_2/I_1 ratio, the lower the effective site symmetry (ESS = I_1/I_2) [16]. In our case, the intensity ratio I_2/I_1 increases and thus the ESS decreases from Al_2O_3 to $Y_3Al_5O_{12}$ (inset of Fig. 1).

In addition, the information about centrosymmetry features of the matrices can be deduced also from FHWM parameters of the $^5D_0 \rightarrow {}^7F_2$ transition (inset of Fig. 1). The obtained results indicate that inhomogeneous broadening increase from Al_2O_3 to $Y_3Al_5O_{12}$, so the ESS at which the Eu^{3+} ions are incorporated into the matrices has to decrease. It is in the good agreement with our previous result.

To deeper analyze the excitation properties of Eu^{3+} ions embedded in the matrix, the total photoluminescence excitation (TPLE) map was measured and the results are shown in Fig. 2. Figure 2a shows the 2D map of PL intensity for the $Y_3Al_5O_{12}$:Eu^{3+} sample in function of both, the excitation and the emission wavelength. The $^5D_0 \rightarrow {}^7F_1$, $^5D_0 \rightarrow {}^7F_2$, $^5D_0 \rightarrow {}^7F_3$, $^5D_0 \rightarrow {}^7F_4$, optical transitions are well resolved and the most efficient excitation wavelength is indicated. The PLE spectra recorded for the most intensive $^5D_0 \rightarrow {}^7F_2$ transitions of Eu^{3+} in the Al_2O_3, $Y_3Al_5O_{12}$ matrices are plotted in Fig. 2b. The analysis of those spectra allows us to confirm or reject the suggestion that the sol-gel matrix is responsible for the efficient excitation of Eu^{3+} ions since obtained maxima vary with material of the matrix in which the Eu^{3+} ions are doped. Nevertheless, coming from a longer wavelength, there is a very weak absorption band (530 nm) at the PLE spectra of all the samples, related to direct excitation of europium ions by f–f transition. At 465 nm there is another optical transition related to direct excitation

of Eu^{3+} on the first excited term $^7F_0 \rightarrow {}^5D_2$. The excitation on the upper term $^7F_0 \rightarrow {}^5L_6$ takes place for the photons with 392 nm wavelength [16]. However, the main excitation peaks for $A_{l2}O_3$ and $Y_3Al_5O_{12}$ are at 249 and 261 nm, respectively.

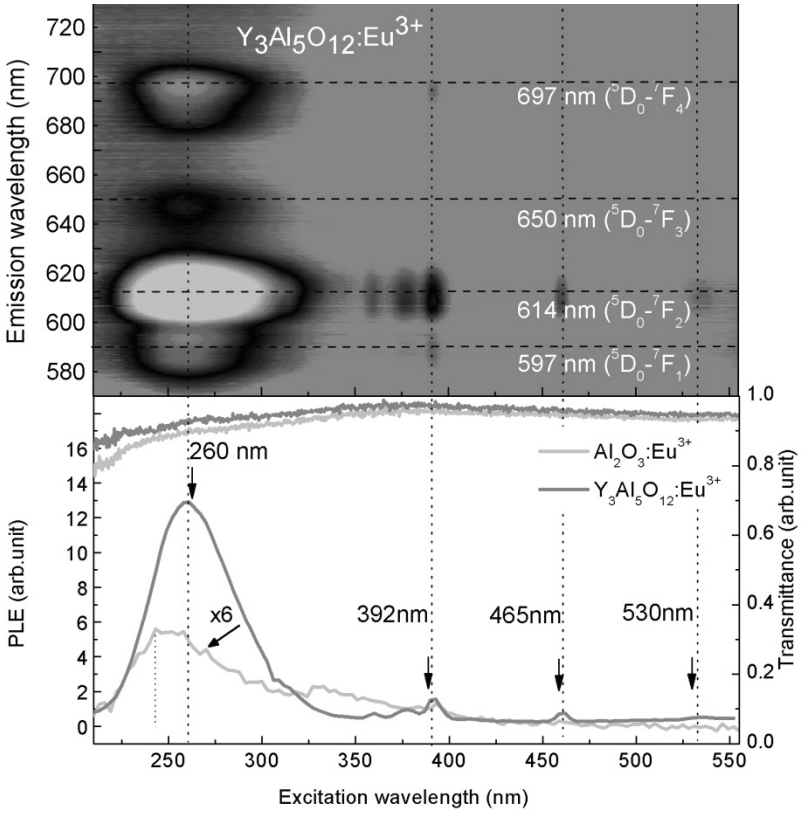

Fig. 2. TPLE map of the $Y_3Al_5O_{12}:Eu^{3+}$ on a quartz plate (a), and the PLE and transmittance spectra of Al_2O_3, $Y_3Al_5O_{12}$ matrices doped by Eu^{3+} on quartz

To analyze the influence of the energy transfer (ET) on the Eu^{3+} excitation, transmission spectra have been collected for both samples. The transmission experiment gives an effective matrix response, and at low Eu^{3+} concentration it is not possible to acquire any information about the Eu^{3+} absorption properties. For the samples fabricated with Al_2O_3 and $Y_3Al_5O_{12}$ matrices, results presented in Fig. 2b confirm that those materials have a high energy gap (*Eg*) and the light almost does not interact with these matrices in the investigated wavelength range. The transmittance of such structures is over 80% even for the photons of energy 6.0 eV, as the energy gaps equal 6.6 eV for Al_2O_3 [18] and 6.44 for $Y_3Al_5O_{12}$ [19]. It is clear that the ET from the matrix to Eu^{3+} is not involved in the excitation of the ions, since the band gap is far from the energy levels of the Eu^{3+} ions and no evidence of the defect states have been found. Thus, we suggest that the charge transfer (CT) transition or direct excitation of

Eu^{3+} ions, by f–d transition is responsible for efficient Eu^{3+} excitation in the case of Al_2O_3 and $Y_3Al_5O_{12}$ matrix. Moreover, since the absorption of the matrices is close to zero in the investigated range and the recombination of the ion itself does not depend on the excitation wavelength, the PLE spectra therefore correspond directly to the excitation efficiency of the Eu^{3+} ions.

The proposed mechanism responsible for the main excitation band is a direct f–d transition. The theory proposed by Nakazawa [20] makes it possible to establish the energy position of the lowest f–d transition, which for Eu^{3+} ion was determined as 7.94 eV (156 nm). Unfortunately, this result lies outside the scope of our investigation here, but certainly it is not the source of the observed excitation bands.

In the high-energy part of the optical spectra of f-compounds, not only f–d but also CT transitions give raise to strong absorption bands. The CT follows the transition of the electron from 2p full orbit O^{2-}, which energetically belongs to the top of the valence band, to a charge transfer state (CTS) of the trivalent RE ion, resulting in RE transition to a divalent form. As a result, the CT appears as an intense and wide band in absorption, and excitation spectra due to a spin and dipole allowed transition [21]. The stimulated emission process is not reversible. The Eu^{3+} ions are joined to the matrix, thus the electron comes back from CT state to its initial ion by transferring its energy to the Eu^{3+}. Eu^{3+} is stimulated to the ^5D_J ($J = 0, 1$) state from which the intra 4f orbital emission takes place. As was shown by Carnall [22], f–d and CT bands may largely overlap and their assignment is quite difficult and even impossible without the help of calculations. However, based on the Jørgensen formula [23], CT energy relative to the Eu^{3+} ground state in oxides is expected to be ca. 5.39 eV ($\lambda \approx 230$ nm). Among the lanthanide series, Eu^{3+} and Yb^{3+} have the highest optical electronegativity, thus much lower CT state due to the higher electron affinity of f^6 and f^{13} electronic configurations. In the more advanced Nakazawa approach [20], the established transition energy takes into account many electron effects and, for the O^{2-}–Eu^{3+} charge transfer excitation, the energy was calculated as corresponding to 227 nm. However, both estimated values of the charge transfer energy are far away from our measured values.

To explain the difference in the CT energy for the investigated matrices, the environment of the ions has to be taken into account. It has been already shown that the CT absorption band position depends on the covalence of matrix bonds. Hoefdraad [25] reported that the longer the bond length of Eu ligand, the longer the wavelength of the CT band position. Also other possible factors, i.e. the covalence or ionicity, the coordinate number, the potential field of the coordinate ions, the standard cation oxidation potential were identified as the factors influencing the position of the CT band [26]. As a result, the charge transfer position is sensitive to the ion environment and it can vary from matrix to matrix over a broad range. Dorenbos [27] showed that possible CT energy is in the range from 3.3 to 6.5 eV. The empirical formula proposed by Ling Li et al. [26] describes the relationship between CT energies and environmental factors, based on the dielectric theory of complex crystals. They introduced and calculated the environmental factor (h_e) for many crystal matrices to describe their

influence on the optical properties of Eu^{3+} ions. For example, h_e of $Y_3Al_5O_{12}$ is equal to 0.733 and the related CT energy is 5.54 eV (223 nm). However, this environmental factor is established for the fully crystallized $Y_3Al_5O_{12}$ matrix, where all the Eu^{3+} ions usually occupy the dodecahedral *c* site with D_2 symmetry [6]. In our case, the sol-gel matrices are in the amorphous phase. Thus, Eu^{3+} ions are substituted at many sites in the host materials, which leads to much broader charge transfer bands, which are red shifted in the PLE spectra, because of the weaker chemical bond Eu^{3+}–O^{2-}, compared with the crystallized matrix. The values of the CT energies obtained from PLE spectra of Al_2O_3:Eu^{3+} and $Y_3Al_5O_{12}$ are 4.98 eV and 4.75 eV, respectively. As we expected, the observed CT energy for $Y_3Al_5O_{12}$ is slightly lower than the CT energy in crystallized matrix (5.54 eV) [26].To the best of our knowledge, the CT energy in Al_2O_3 crystal has not been determined so far. Finally, the CT is considered to be responsible for the efficient excitation mechanism of the Eu^{3+} ions in all the investigated matrices.

CT states influence the emission properties of Eu^{3+} ions as well. The closer the CT state is to the 4f orbitals, the more intensive the spin-orbit interaction between them and the more intensive the emission related to electric dipole transition. This expectation is in good agreement with our samples containing the Al_2O_3 and $Y_3Al_5O_{12}$ matrices. The first matrix has higher CT energy (4.98 eV) and lower intensity of the $^5D_0$–$^7F_2$ transition (1.0 a.u.). For the latter matrix, the CT state is closer to 4f orbitals (4.75 eV) and higher intensity of the $^5D_0$–$^7F_2$ transition (12.8 a.u.) is observed.

To fully characterize the properties of our samples required for the phosphorous material, the photoluminescence lifetimes were measured. PL delay related to the $^5D_0$–$^7F_2$ (at 615 nm) transitions were observed for both samples, which were excited by the wavelength of the maximum of the excitation band, i.e. 249 and 260 nm for Al_2O_3 and $Y_3Al_5O_{12}$, respectively. The decay time of the Eu^{3+} ions depends mainly on the surrounding crystal field, and can change in a wide range, from several microseconds to milliseconds, when the ions are doped in various host materials (i.e. 4.0 ms for $Y_3Al_5O_{12}$) [28]. However, photoluminescence lifetime depends also on the excitation mechanism and non-radiative processes. Dai et al. [29] showed also that Eu^{3+} photoluminescence lifetime depends strongly on the ion concentration and he observed an exponential decrease from 162 to 32 μs. This decrease was attributed to the increase in the non-radiative relaxation rates due to the cross relaxation process among the Eu^{3+} ions. This decrease was more significant for the ions in the surrounding with more defected state. Knowing that our samples are in amorphous phase and the doping concentration is relatively high (30%), we expected that the observed photoluminescence lifetime would be relatively short. Figure 3 shows the PL decay for our samples with fitted theoretical curves. For both the samples, a fast recombination process with $t = 10$ μs was observed, however, the intrinsic properties of the setup were found to be the cause of it. For samples with Al_2O_3 and $Y_3Al_5O_{12}$ matrices, long lifetimes were determined as $\tau_{1CT} = 120$ μs and $\tau_{2CT} = 328$ μs. The discovered lifetimes confirm previous results, stating that the smaller CT energy, the stronger the interaction of the CT

state with 4f orbitals and the higher the observed PL intensity in the steady-state condition, which are related to the long lifetime emission.

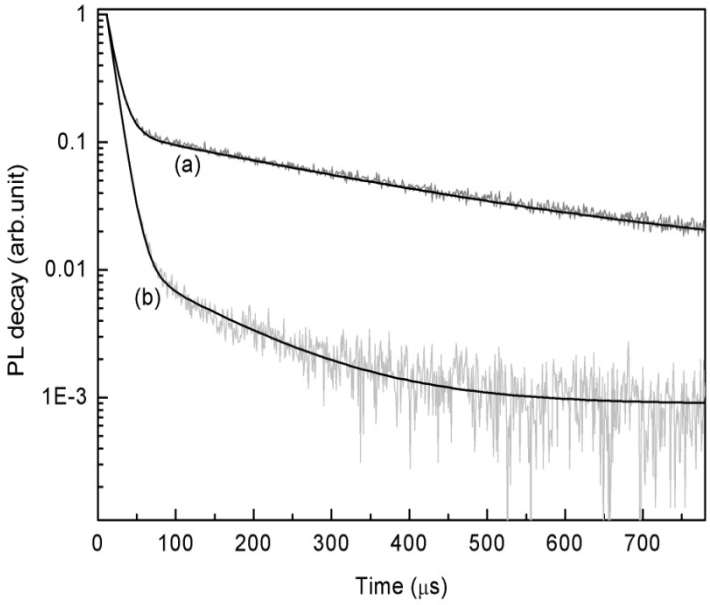

Fig. 3. PL decay spectra of $^5D_0$–$^7F_2$ transition in $Y_3Al_5O_{12}:Eu^{3+}$ (a) and $Al_2O_3:Eu^{3+}$ (b) samples excited at the maximum of PLE spectra (260 and 249 nm, respectively)

In Table 1, the PL and PLE intensity data have been summarized and compared with the reciprocal of the ESS parameter, the CT position and the photoluminescence lifetime. The agreement between the values of these parameters and the theory was found, which asserts that the efficiency of rare earth ion excitation increases as the centrosymmetricity of the ion environment decreases.

Table 1. PL, PLE intensities, ESS^{-1} parameter, CT position and photo-luminescence lifetime

Sample	PL [a.u.]	PLE [a.u.]	ESS^{-1}	CT [eV]	τ_{PL} [μs]
$Al_2O_3:Eu^{3+}$	1	1	6	4.98	120
$Y_3Al_5O_{12}:Eu^{3+}$	12.4	12.4	86	4.75	328

4. Conclusions

Eu^{3+} ions doped into an amorphous host material were proved to be effective light emitters. The samples were fabricated using the inexpensive sol-gel technology in conjunction with a low-cost after-treatment process. In the investigations, the f–f transitions were observed to be responsible for the intensive PL emission of Eu^{3+} ions in

any matrix. The ESS parameter was determined to describe the influence of the crystal field on the emission of Eu^{3+} ions in the amorphous matrix. It was found that the broad excitation band related to CT is responsible for efficient ion excitation, which gives us more flexibility in inducing efficient Eu^{3+} excitation. The knowledge of the origin of the excitation mechanism is important because various excitation mechanisms undergo different quenching processes, which can be optimized to influence the efficiency of the emitters.

Acknowledgement

The authors would like to thank to N.V. Gaponenko and G. K. Maliarevich from the Belarusian State University of Informatics and Radioelectronics (Minsk, Belarus) for the delivered samples. Moreover, one of the authors (A.P.) acknowledges financial support from the from fellowship co-financed by European Union within the European Social Fund and financial support from the Foundation for Polish Science within the START programme.

References

[1] KIM T., YOON Y., HWANG Y., CHUNG H., KIM I.H., AHN Y., Mater. Lett., 47 (2001), 290.
[2] MOLCHAN I.S., GAPONENKO N.V., KUDRAWIEC R., MISIEWICZ J., THOMPSON G.E., Mater. Sci. Eng. B, 105 (2003), 37.
[3] KUDRAWIEC R., MISIEWICZ J., BRYJA L., MOLCHAN I.S., GAPONENKO N.V., J Alloys Compd., 341 (2002), 211.
[4] WITTMANN H.F., GRUNER J., FRIEND R.H., SPENCER G.W.C., MORATTI S.C., HOLMES A.B., Adv. Mater., 7 (1995), 541.
[5] KENYON A.J., Prog. Quant. Electron., 26 (2002), 225.
[6] RAVICHADRAN D., ROY E., CHAKHOVSKOI A.G., HUNT C.E., WHITE W.B., ERDEI S., J. Lumin., 71 (1997), 291.
[7] MAEDA N., WADA N., ONODA H., MAEGAWA A., KOJIM K., Opt. Mater., 27 (2005), 1851.
[8] MALIAREVICH G.K., GAPONENKO N.V., MUDRYI A.V., DROZDOV Y.N., STEPIKHOVA M.V., STEPANOVA E.A., Semiconductors, 43 (2009), 158.
[9] MOLCHAN I.S., GAPONENKO N.V., KUDRAWIEC R., MISIEWICZ J., BRYJA L., THOMPSON G.E., SKELDON P., J. Alloys. Compd., 341 (2002), 251.
[10] MOLCHAN I.S., GAPONENKO N.V., KUDRAWIEC R., MISIEWICZ J., THOMPSON G.E., SKELDON P., J. Electrochem. Soc., 151 (2004), H16.
[11] GAPONENKO N.V., MOLCHAN I.S., SERGEEV O.V., THOMPSON G.E., PAKES A., SKELDON P., KUDRAWIEC R., BRYJA L., MISIEWICZ J., PIVIN J.C., HAMILTON B., STEPANOVA E.A., J. Electrochem. Soc., 149 (2002), H49.
[12] WALSH B.M., *Judd–Ofelt Theory: Principles and Practices*, [In:] B. di Bartolo, O. Forte (Eds.), *Advances in Spectroscopy for Lasers and Sensing*, Springer, New York, 2006, p. 403.
[13] BUNZLI J.-C.G., *Rare Earth Luminescence Centres in Organic and Biochemical Compounds*, [In:] G. Liu, B. Jacquier (Eds.), *Spectroscopic Properties of Rare Earths in Optical Materials*, Springer, New York, 2005, p. 462.
[14] HARADA M., GOTO M., J. Alloys. Compd., 408–412 (2006), 1193.
[15] PENG A., XIE E., JIA C., JIANG R., LIN H., Mater. Lett., 59 (2005), 3866.
[16] ZHAO Z., ZENGA Q.G., ZHANGA Z.M., DING Z.J., J. Lumin., 122 (2007), 862.
[17] ZHU Y., DING C., J. Solid State. Chem., 139 (1998), 124.
[18] SHIIKI K., IGARASHI M., KAIJYU H., Jpn. J. Appl. Phys., 42 (2003), 5185.

[19] XU Y.N., CHING W.Y., Phys. Rev. B, 59 (1999), 10530.
[20] NAKAZAWA E., J. Lumin., 100 (2002). 89.
[21] YU O., LIU Y., WU S., LU X., HUANG X., LI X., J. Rare Earth, 26 (2008), 783.
[22] CARNALL W.T., J. Less Common Met., 122 (1986), 1.
[23] KRUPA J.C., J. Solid State Chem., 178 (2005), 483.
[24] YAVETSKIY R., DUBOVIK M., TOLMACHEV A., TARASOV V., Phys. Stat. Sol. (c), 2 (2005), 268.
[25] HOEFDRAAD H.E., J. Solid State Chem., 15 (1975), 175.
[26] LI L., ZHANG S., J. Phys. Chem. B, 110 (2006), 21438.
[27] DORENBOIS P., J. Phys-Condens. Mater., 15 (2003), 8417.
[28] CHEN X.Y., LIU G.K., J. Solid State Chem., 178 (2005), 419.
[29] DAI Q., SONG H., WANG M., BAI X., DONG B., QIN R., QU X., ZHANG H., J. Phys. Chem. C, 112 (2008), 19399.

Received 10 August 2009

Materials Science-Poland, *Vol. 28*, *No. 1*, *2010*

First principles study on the improved dehydrogenating properties of MgH_2 systems with metal fluorides

D.W. ZHOU[1*], J.S. LIU[2], S.H. XU[2], G.Y. CHEN[1]

[1]State Key Laboratory of Advanced Design and Manufacturing for Vehicle Body, Hunan University, Changsha 410082, P.R. China

[2]School of Materials Science and Engineering, Hunan University, Changsha 410082, P.R. China

Energies and electronic structures of MgH_2 systems were determined from the first principles calculations to explain the improving of their dehydrogenating properties by addition of metal fluorides as catalysts. These calculations show that a Mg vacancy can improve the thermodynamics of MgH_2 systems and Mg atom replaced for Fe, Ti, Zr, V, Ni, Nb, Cr, Cu is energetically more favourable than formation of Mg vacancies at lower temperatures. Calculations of density of states (DOS) provide a particularly good explanation for a close agreement between the experimental results and theoretical predictions for improvements to the dehydrogenation kinetics of MgH_2 systems for NiF_2, NbF_5, ZrF_4 used as the catalysts.

Keywords: *MgH_2; density functional theory; dehydrogenating properties*

1. Introduction

Magnesium hydride (MgH_2) is a promising material for hydrogen storage applications, as it has high gravimetric (7.6 wt. %) and volumetric (110 kg·m^{-3}) densities. Moreover, its reversibility and cycle performance are quite good compared with other binary and complex hydrides of I and II groups. However, magnesium hydride has a high dissociation temperature and relatively high thermal stability, resulting in its slow re-hydrogenation and de-hydrogenation kinetics. This therefore limits its practical application as a good hydrogen storage material.

The kinetics of sluggish hydrogenation was found to be significantly improved by fabricating fine nanocrystalline Mg particles, by the mechanical alloying method [1, 2]. Although a high desorption temperature still remains a problem to be solved, the mechanical alloying of MgH_2 and 3d transition metals (Ni, Co, Mn, Cu, Ti, Fe, V, etc. [3, 4]), 3d non-transition metals (Ge, Nb, etc. [3, 5]), intermetallic compounds

*Corresponding author, e-mail: ZDWe_mail@yahoo.com.cn

($LaNi_5$, FeTi, $ZrFe_{1.4}Cr_{0.6}$, etc. [6–8]), metal oxides (Nb_2O_5, Fe_3O_4, etc [9]), effectively improve the hydriding and dehydrogenating kinetics of MgH_2 at high temperatures. Recently, Jin et al. [10] systematically investigated various metal fluorides (such as FeF_2, NiF_2, TiF_3, NbF_5, CuF_2, VF_4, ZrF_4, CrF_2, etc.) and their catalytic effect on the dehydrogenation and hydrogenation characteristics of MgH_2 powder. They have found that metal fluorides are the most suitable catalysts for the re/dehydrogenation of MgH_2. They ranked the following in order of increasing catalytic performance: CuF_2, CrF_2, ZrF_4, FeF_2, NbF_5, VF_4, TiF_3, NiF_2.

Some considerable experimental and theoretical investigations have been performed on the improved dehydrogenating properties of MgH_2 systems. Based on X-ray scattering measurements and phase structural change analysis, Pelletier et al. [9] suggested that the improved kinetics in Nb doped MgH_2 is due to the formation of niobium hydride, which leads to the nucleation of the α-Mg at the β-NbH/β-MgH_2 interface. Song et al. [11], Shang et al. [3] and Li et al. [12] calculated the total energy and electronic structure of MgH_2 solid solution in order to study the mechanism of the improvement to the dehydrogenating properties of MgH_2 systems with metal elements (Al, Ti, Fe, Ni, Cu, Nb, etc.) and metal oxides (Nb_2O_5, etc.). In the examined group, the energy and electronic structure of the adsorption of H_2 on a clean, vacancy defective Mg(0001) surface and iron alloying MgH_2 were calculated by using the first principles plane-wave pseudopotential method. The improved properties of MgH_2 systems are also analyzed with respect to the milling process and iron addition [13]. Moreover, based on the energy calculations of $VH_{0.81}$ phase, and the design and exploitation of a VH/MgH_2 interface model, the vanadium alloying effects on the dehydrogenating properties [14] and diffusion and adsorption of H atoms [15] of MgH_2–V system have been investigated [15].

Jin et al. [10] investigated the catalytic performance of different metal fluorides on MgH_2, and they concluded that NiF_2 performed best. Nevertheless, it is still not clear how these chemically different additives promote the dehydrogenation and hydrogenation reactions of MgH_2. As for as the improved dehydrogenating properties of MgH_2 systems with NiF_2 are concerned, MgF_2 and Mg_2NiH_4 are detected in the reaction products during high-energy milling process, as reported by Jin et al. [10]. It is believed that MgF_2 and Mg_2NiH_4 form by the following displacement reaction: $NiF_2 + 3MgH_2 = MgF_2 + Mg_2NiH_4$. One could assume that MgF_2 formation is caused by the Mg atom of MgH_2 and the F atom of NiF_3, thus some Mg vacancies which remain in the sample, may affect desorption of hydrogen. If an Ni atom of NiF_3 replaces a Mg atom of MgH_2, it forms $(Mg,Ni)H_x$ solid solution, which can be changed into Mg_2NiH_4 hydrides, thus the electronic structure of the considered systems is locally changed. Hence, both Ni substitution and Mg vacancies have an effect on the dehydrogenating properties of MgH_2 systems.

Based on the above analysis, in the present work, the bonding distance change for Mg–H and Ni–H, the energy to remove H atoms and electronic structure of MgH_2 systems have been calculated by using the Dmol 4.1 program based on the density

functional theory. The improved properties of MgH_2 systems with metal fluorides (NiF_2, TiF_3, VF_4, NbF_5,FeF_2, ZrF_4, etc.) have also been analyzed, some new results are expected to be of theoretical guidance for designing advanced magnesium-based hydrogen storage materials.

2. Models and method of computation

The energy and electronic structure of MgH_2 systems with metal fluorides were investigated by constructing 2×2×2 supercell models consisting of 48 atoms ($Mg_{16}H_{32}$) (Fig. 1a) [12]. Here, the lattice parameters of MgH_2 with a tetragonal symmetry (*P*4/*mnm*, group No.136) are a = 0. 4501 nm and c = 0.3010 nm [11].

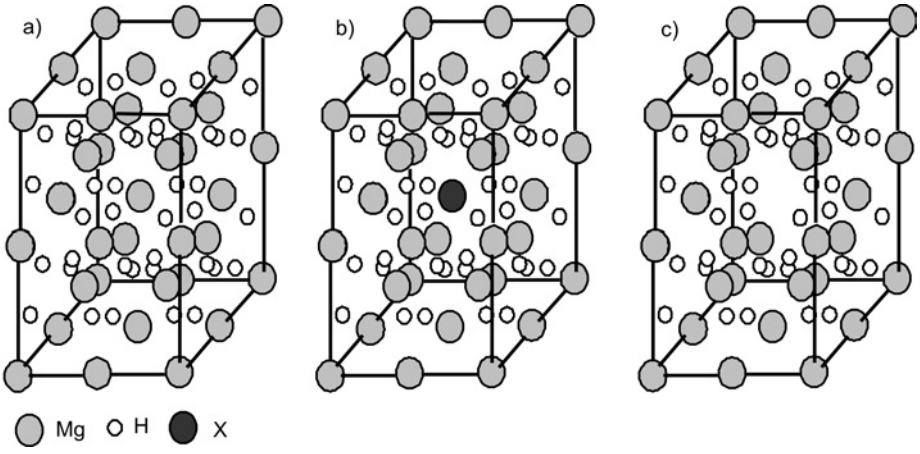

Fig. 1. Supercell model: a) $Mg_{16}H_{32,}$ b) $Mg_{15}XH_{32}$ (X = Ni, Ti, V, Nb, Fe, Zr, Cr, Cu), c) $Mg_{15}H_{32}$

To simulate element substitution or a vacancy at the Mg 2*a* site (0.5, 0.5, 0.5), we considered $Mg_{15}XH_{32}$ (X = Ni, Ti, V, Nb, Fe, Zr, Cr, Cu, Fig. 1b) and $Mg_{15}H_{32}$ (Fig. 1c) supercell models, respectively. In the present work, the optimized structure, the total energy and electronic structure calculations are performed by the the DMol^3 package, which is based on density functional theory (DFT). The PWC [16] exchange correlation functional is adopted for LDA correction [17]. Sampling of the irreducible wedge of the Brillouin zone is performed with a regular Monkhorst–Pack grid of special *k*-points [18]. The positions of selected atoms in the structures are relaxed to get the final structure with minimum total energy. The convergence criteria of optimization are 1.0×10^{-5} Ha, 0.004 Ha/Å and 0.005 Å for energy, gradient and atomic displacement, respectively. To assess the accuracy of the method as well as of the computational models, a series of calculations has been performed on the bulk properties of the *hcp*-Mg and H_2 molecules correlated with the MgH_2 supercell models. In Table 1, the calculated equilibrium lattice constants a, c are listed, and c/a of *hcp*-Mg bulk, the bond length ($d_{H–H}$) of a free H_2 molecule as well as their cohesive energies (E_{tot}). The

equilibrium lattice constants a, c and c/a of hcp-Mg bulk are estimated to be 0.31751 nm, 0.51504 nm and 1.6240, respectively; this is in good agreement with the experimental values [19] and other calculations [20], and the error of the c/a ratio, calculated here relative to the experimental result, is only 0.06%. The bond length of a free H_2 molecule is calculated to be 0.07490 nm, which gives a relative error of only 1.08% compared with the experimental value [21]. Meanwhile, their calculated cohesive energies (E_{tot}) are also close to the experimental data [19] and other calculated data [20]. Thus, the geometrical and electronic structures of the MgH_2 supercell models have been calculated the same conditions.

Table 1. The calculated equilibrium lattice constants a, c and c/a of *hcp*-Mg bulk, the bond length d_{H-H} of a free H_2 molecule as well as their cohesive energies E_{coh}

Source	*hcp*-Mg				H_2	
	Equilibrium lattice constants			E_{coh} /(eV·atom^{-1})	Bond length/nm	E_{coh} /(eV·atom^{-1})
	a/nm	c/nm	c/a			
Present work	0.31751	0.51504	1.6240	1.4942	0.07490	4.5502
Experimental [19, 21]	0.321	0.521	1.62	1.51	0.0741	4.74
Ref. [20]	0.318	0.524	1.65	1.48	0.075	4.56

In our calculations of the phase stability of the MgH_2 system with a Mg vacancy under high temperature, it is relaxed through NVT molecular dynamics for 0.01 ps with a time step of 1.0 fs. The BLYP exchange-correlation functional is adopted for GGA correction. All electron Kohn–Sham wave functions are expanded in a double numerical basis with a polarized orbital (DNP).

3. Results and discussion

3.1. Effect of Ni substitution on the dehydrogenating properties of MgH_2 systems

In MgH_2 (see Fig. 2), the bonding distances with Mg at the 2a site (Mg(0), Fig. 2b) and its first nearest neighbour H atom (H(A), Fig. 2b) and second nearest H atom (H(B), Fig. 2b) are analyzed, as shown in Fig. 3. The results show that the distance of Mg(0)–H(A) and Mg(0)–H(B) are 0.1935 nm and 0.1955 nm, respectively. We then replace one Mg atom at the 2a (0.5, 0.5, 0.5) site with a Ni atom (Fig. 1b). Similarly to the case of MgH_2, the corresponding Ni–H(A) and Ni–H(B) bond lengths are shorter compared with those of Mg–H(A) and Mg–H(B), and decrease by 0.0297 nm and 0.0245 nm, respectively. When H(A) is removed, there is no observable difference in the bonding distance between the H(B) and Mg(0) atoms (Fig. 4,

NO, NO1 denote MgH_2 systems with no H atom removed and one H atom removed, respectively). After Ni substitution, the distance between the Mg(0) and H(B) atom is 0.167 nm, which is also shorter compared with that (0.1710 nm) of the unchanged structure. Thus, one can visualize the Ni atom as playing the role of a magnet that continues to attract nearby H atoms as the very nearest ones are successively desorbed.

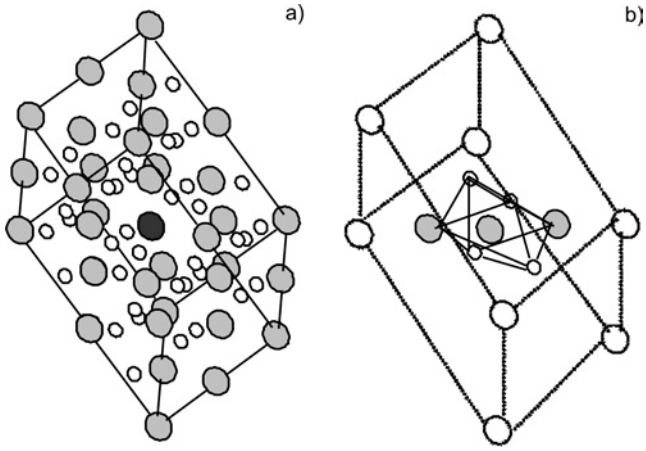

Fig. 2. Supercell model of MgH_2 (a) and supercell octahedral (b)

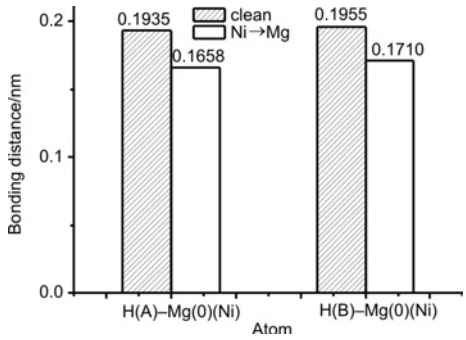

Fig. 3. The H–Mg(Ni) atom bonding distance change

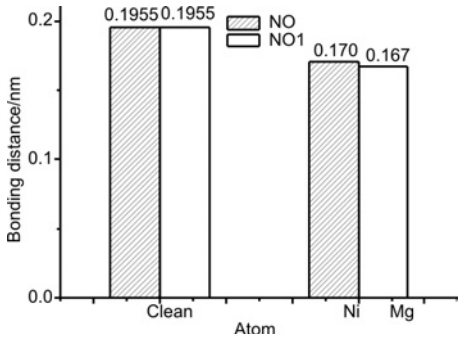

Fig. 4. The H(B–Mg(0)(Ni) atom bonding distance change

The energy costs to remove H atoms from intrinsic MgH_2 as well as the energy costs associated with Ni substitution at the Mg site are calculated by using the following equation [19]:

$$E_{coh} = E(Mg_{16-x}Ni_xH_{32-n}) - E(Mg_{16-x}Ni_xH_{32}) + (n/2)E(H_2) \quad (1)$$

The subscripts x and n refer to the number of Ni and H atoms, respectively, in the supercell that are removed, and E_{coh} refers to the cohesive energy at 0 K, defined with respect to the dissociated atoms. The calculated energies of MgH_2 systems are given in Fig. 5 (NO2 denotes MgH_2 system with two atoms removed). We find that 1.77 eV are

required to remove a hydrogen atom in pure MgH_2, and 1.90 eV are required to remove two hydrogen atoms from the vicinity of the same. In contrast, in Ni doped MgH_2, the energy cost of removing one or two H atoms is 0.75 eV and 1.61 eV at 0 K, respectively, which is marginally less than that required in the case of H atom removal from pure MgH_2. This dramatic decrease in energy costs originates from structural changes following hydrogen removal from different positions, which means that Ni substitution plays an important role in the dehydrogenation properties of MgH_2 systems.

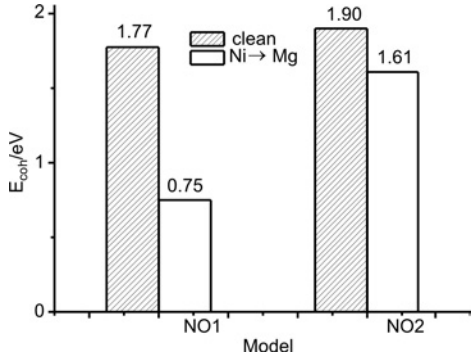

Fig. 5. The critical energy needed to remove H atoms in MgH_2 systems

3.2. Effect of Mg vacancy on the dehydrogenating properties of MgH_2 systems

Jin et al. [10] pointed out that the improved kinetics in MgH_2 systems for NiF_2 may be due to high density defects but the nature of these defects is not identified. Moreover, MgF_2 has been found to form during ball milling of MgH_2, which is also correlated to Mg vacancies. Here, we study the role of Mg vacancies on hydrogen desorption; a Mg vacancy is created from MgH_2 supercells, and the resulting changes in the H–H bonding distance are listed in Table 2.

Table 2. The differences in the H-H atom bonding distance for MgH_2 systems with/without Mg vacancy

Supercell model	Temperature/K	H(B)–H(B)/nm	H(A)–H(B)/nm	H(A)–H(A)/nm
$Mg_{15}H_{32}$	0	0.4134	0.2796	0.3766
$Mg_{15}H_{30}$	0	0.3087	0.2924	–
$Mg_{15}H_{30}$	325	0.2992	0.2789	–
$Mg_{15}H_{30}$	473	0.2960	0.2780	–
$Mg_{15}H_{30}$	673	0.2926	0.2773	–

Based on the data from the Table 2, it can be seen that the bonding distance between two H atoms in MgH_2 systems with a Mg vacancy is 0.2796 nm, longer compared with that (0.0741 nm) of hydrogen molecule. This therefore means that no hy-

drogen molecule formation is observed during 0 K optimization, because when two hydrogen atoms, i.e., H(A) and H(B) (Fig. 2b), are removed, the bonding distance is 0.2924 nm, meaning that no hydrogen molecule can form. To check whether there are energy barriers that cannot be overcome at 0 K during dehydrogenation, we consider temperatures of 325 K, 473 K or 673 K. The corresponding two H atoms are found to bond to each other at the distances of 0.2924 nm, 0.2780 nm and 0.2773 nm, respectively (Fig. 6). Although Mg vacancy is created, no hydrogen molecule formation is observed during optimization at 0–673 K, based on analysis of changes in the bonding distances. The H–H bonding distances at 325 K, 473 K or 673 K are all shorter than that at 0 K, lying in the trend for hydrogen molecule formation, which hints that the thermodynamics of the considered systems can be improved. This is consistent with the dynamics of hydrogen molecule formation, and suggests that the thermodynamics of the considered systems can be improved.

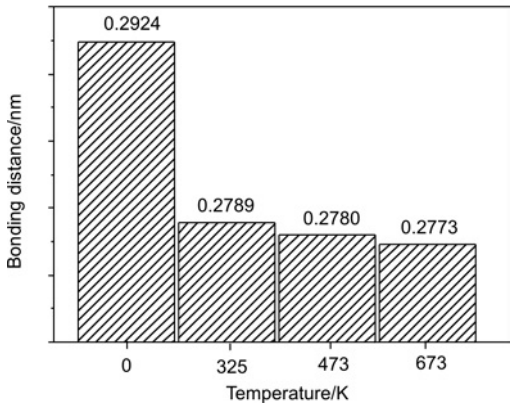

Fig. 6. The H–H atom bonding distance change at various temperatures

Further calculation is done to check whether there are benefits for the dehydrogenation of MgH_2 systems having a Mg vacancy, it is found that the energy cost of removing a hydrogen molecule from the vicinity of a Mg vacancy is –2.76 eV. The negative sign means that energy is gained if a hydrogen molecule is removed from the vicinity of a Mg vacancy and therefore the dehydrogenation process is exothermic. Based on the above analysis, a Mg vacancy also plays an important role in the dehydrogenation properties of MgH_2 systems [22].

3.3. Improved dehydrogenating properties of MgH_2 systems with NiF_2

Based on the analyses of sections 2.1 and 2.2, one can see that both Ni substitution as well as Mg vacancies both play an important role in dehydrogenation, so which of these two cases is most effective for desorbing hydrogen at lower temperatures? Clearly it is important to firstly know the energies of their formation. The

formation energy of a Ni atom substituted at the Mg site is calculated using the following equation [23]:

$$H_1 = \left[E\left(\mathrm{Mg_{15}NiH_{32}}\right) + E\left(\mathrm{Mg}\right)\right] - \left[E\left(\mathrm{Ni}\right) + E\left(\mathrm{Mg_{16}H_{32}}\right)\right] \quad (2)$$

The formation energy of a Mg vacancy is computed from cohesive energies for the $Mg_{16}H_{32}$ and and $Mg_{15}H_{32}$ supercells, using the following equation [23]:

$$E\left(\mathrm{Mg_{15}H_{32}}\right) + E\left(\mathrm{Mg}\right) - E\left(\mathrm{Mg_{16}H_{32}}\right) \quad (3)$$

The calculated energy of vacancy formation is 6.51 eV; this value is higher than the one obtained by Li (3.87 eV) [12], although different methods should produce similar results. The formation energy of the Mg vacancy is much higher than the 2.12 eV needed to substitute Ni at the Mg site assuming all other conditions remain unchanged. Thus, although both Ni substitution and Mg vacancies are found to be effective in desorbing hydrogen at lower temperatures, Ni substitution is more energy efficient than the formation of Mg vacancies. If an Ni atom of NiF_2 can replace a Mg atom belonging to a MgH_2 system, the reaction $NiF_2 + 3MgH_2 = MgF_2 + Mg_2NiH_4$, occurring during the milling process, is accelerated. Thus MgH_2 with the higher stability can be changed into Mg_2NiH_4. In Sect. 2.1, regarding the removal of one first nearest neighbouring H atom, the Ni atom plays the role of a magnet that continues to attract its second nearest H atom as the nearest ones are successively desorbed, thus, it can be thought that there lies in the trend for NiH_x cluster formation, MgH_2 may be changed into $(Mg,Ni)H_x$ solid solution due to the substitution of Ni at the Mg site, while $(Mg,Ni)H_x$ solution is a likely the pathway for dehydrogenation in MgH_2 [10], and which lead to Mg_2NiH_4 formation. In the experiment undertaken by Jin et al. [10], MgF_2 and Mg_2NiH_4 were detected in the reaction products during the milling process, which is in agreement with the above analysis. Moreover, the experimental value for the formation heat of Mg_2NiH_4 is –62.7 kJ/mol H_2 [24] which is larger than that (–76.15 ± 9.2 kJ/(mol H_2) [24]) for MgH_2, which means that the H atoms of MgH_2 can be released more easily than those in Mg_2NiH_4. Hence, when a Ni atom of NiF_2 replaces a Mg atom belonging to a MgH_2 system at lower temperatures, the reaction $NiF_2 + 3MgH_2 = MgF_2 + Mg_2NiH_4$ is accelerated. Thus, MgH_2 having higher stability can be changed into Mg_2NiH_4 with lower stability. Due to formation of ternary hydride Mg_2NiH_4 with the lower stability, the dehydrogenating properties of Ni doped MgH_2 systems are improved.

3.4. Improved dehydrogenating properties of MgH_2 systems with metal fluorides

As far as the improved dehydrogenating properties of MgH_2 systems with the addition of TiF_3, VF_4, NbF_5, FeF_2, ZrF_4 are concerned, the corresponding phase of MgF_2, TiH_2, V_3H_2, NbH, Mg_2FeH_6, ZrH_2 were also detected in the reaction products during

the milling process by Jin et al. [10]. It is believed that MgF_2, TiH_2, V_3H_2, NbH, Mg_2FeH_6, ZrH_2 are formed by the following displacement reactions:

$$TiF_3 + 3MgH_2 = 3MgF_2 + 2TiH_2 + H_2$$

$$3VF_4 + 6MgH_2 = 6MgF_2 + V_3H_2 + 5H2$$

$$2NbF5 + 5MgH_2 = 5MgF_2 + 2NbH + 4H_2$$

$$FeF_2 + 3MgH_2 = MgF_2 + Mg_2FeH_6$$

$$ZrF_4 + 2MgH_2 = 2MgF_2 + ZrH_2$$

Similarly, it is assumed that MgF_2 is formed by a Mg atom of MgH_2 and a F atom of TiF_3, VF_4, NbF_5, FeF_2, ZrF_4, respectively. Thus some Mg vacancies remain in the sample, while Ti, V, Nb, Fe, Zr atoms of TiF_3, VF_4, NbF_5, FeF_2, ZrF_4 replace a Mg atom of MgH_2, which will lead to formation of TiH_2, V_3H_2, NbH, Mg_2FeH_6 or ZrH_2.

Table 3. The energy to remove H atoms and the energy of the Mg atom replaced with other atoms for MgH_2 systems

Mg substitution	One H atom removed/eV	Two H atoms removed/eV	Substitution energy/eV
clean	1.7688	1.9021	–
Ni	0.7456	1.6136	2.1198
Ti	1.6463	2.4763	1.1946
V	1.7062	2.8872	2.0899
Nb	1.6490	1.7606	2.4354
Fe	1.9021	–	0.6912
Zr	1.5592	1.8368	1.3511
Cr	–	–	2.4626
Cu	–	–	2.6967

The energies needed for Ti, V, Nb, Fe, or Zr substitution (as well as Ni itself) at the Mg site are listed in Table 3. It is known that the higher the energy needed for the considered systems, the more difficult the atom substitution is. Hence, in the present work, the substituting elements can be ranked in the following order, according to increasing levels of energy required for substitution: Fe, Ti, Zr, V, Ni, Nb, Cr, Cu (Fig. 7) because the calculated vacancy formation energy is much higher than that (the highest value is 2.6967eV) needed to substitute Ti, V, Nb, Fe, Zr, Cr, Cu at the Mg sites. Hence, the substitution at the Mg site is more energy efficient than the formation of Mg vacancies at lower temperatures. According to the results of Jin et al. [10], neither CuF_2 nor CrF_2 have a significant effect on the dehydrogenation properties of MgH_2 systems, while the substitution of Cr, Cu at the Mg site is the most difficult among all other elements under consideration, thus, we believe that the catalytic effect of CuF_2 and CrF_2 is correlated to its substitution at the Mg site.

The energy costs of removing one or two H atoms from MgH_2 systems are calculated from Eq. (1) (Table 3). Here, Cr and Cu are not considered, due to the difficulty of substituting them at the Mg site. It was found that the energy needed for Ni, Zr, Ti, Nb, or V substitution (not including Fe) at the Mg site is lower than that (1.7688 eV) of pure MgH_2 systems with one H atom removed, which means that elemental substitution improves the dehydrogenation properties of MgH_2 systems and the influence of substitution on the dehydrogenating properties increases in the order Nb, Ni, Ti (Fig. 8).

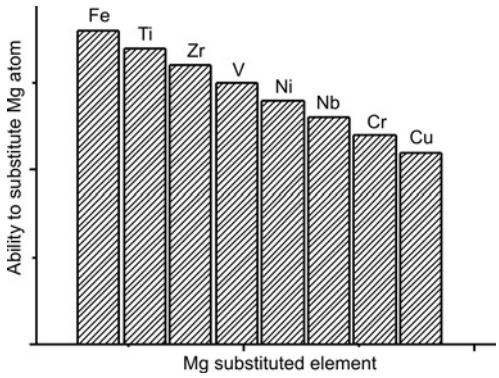

Fig. 7. The order of the Mg atom replaced with another atom

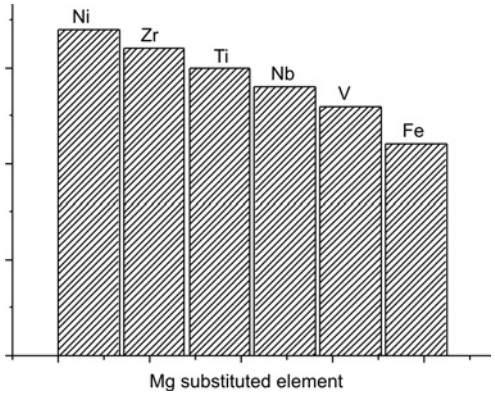

Fig. 8. The calculation order of one Mg atom replaced with other atom in the catalyst effect

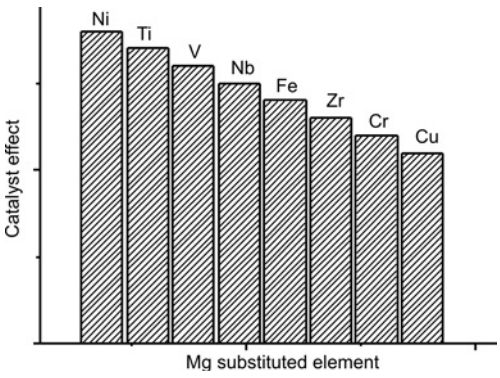

Fig. 9. The experimental order of one Mg atom replaced with another atom in the catalyst effect

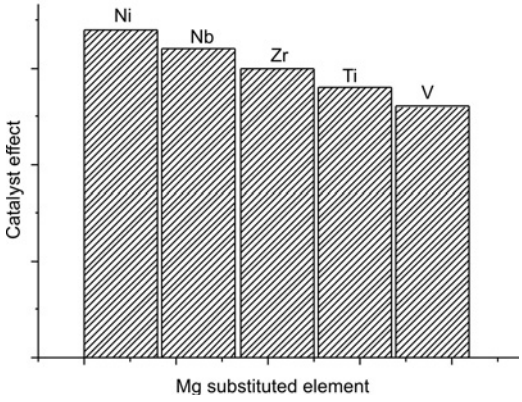

Fig. 10. The calculation order of two Mg atoms replaced with another atom in the catalyst effect

This is in agreement with the experimental results of Jin et al. [10] (Fig. 9). Fe substitution is not considered here, in the case when two H atoms are removed because dehydrogenation of MgH_2 systems is difficult in this case. It was found that the energy needed for Ni, Nb, or Zr substitution (not including Ti and V) at the Mg site is lower than that needed for pure systems (1.9021 eV), which means that Ni, Nb,

Zr substitution at the Mg site plays an important role in the dehydrogenation properties of MgH_2 systems. The substituting elements (assuming two H atoms are removed) can be ranked as follows, according to their increasing dehydrogenation efficiencies: Zr, Nb, Ni (Fig. 10). This is also in agreement with the experimental results of Jin et al. [10] (Fig. 9).

In the present work, since MgH_2 systems with removed two H atoms are close to the realistic case in which hydrogen molecule is released, they are investigated in detail as following. Based on Fig. 10, it can be seen that Ni, Nb, or Zr substitution at the Mg site improves the dehydrogenating process for MgH_2 systems, while it is not the case for Fe, Ti, or V substitution, which is not in agreement with the experimental results of Jin et al. [10]. In our group, the characterization of the synthesized duplex $MgH_2 + Mg_2FeH_6$ hydrides mixture has been investigated. We found that the structural stability of the alloying system is reduced when a little iron is dissolved in MgH_2, and further reduced when the iron additions form the compound Mg_2FeH_6. Consequently, the dehydrogenation properties of the corresponding systems are improved [24]. Moreover, based on the calculated energy results for the TiH_2 and $VH_{0.81}$ phase structures, TiH_2/MgH_2 and VH/MgH_2 interfaces were designed. The alloying effects of titanium [25] and vanadium [14] substitution on the dehydrogenating properties of MgH_2 were investigated. It was found that the improved dehydrogenating properties of MgH_2 were caused by titanium or vanadium alloying originates from the increasing of the valence electrons at the Fermi level (E_F) and the decreasing of the HOMO -LUMO gap (ΔE_{H-L}) after titanium or vanadium alloying. The catalysis effect of titanium or vanadium on the dehydrogenating kinetics of MgH_2 may be attributed to a stronger bonding between the Ti or the V atoms with the H atoms in comparison with the bonding between Mg and H atoms. This stronger bonding leads to easier nucleation of the α-Mg at the TiH_2/MgH_2 or the VH/MgH_2 interface in the MgH_2–Ti or the MgH_2–V systems, compared with the nucleation associated with pure MgH_2 phase. Ti and V both have higher affinity to hydrogen than Mg, and work as a hydrogen pump that chemisorbs hydrogen atoms and transfers them to the TiH_2/MgH_2 or the VH/MgH_2 interface. The nucleation barrier is relatively small. Based on our previous work, the catalytic effect of FeF_2, TiF_3, VF_4 on the dehydrogenation properties of MgH_2 systems (Fig. 9) cannot be caused by Fe, Ti, V substitution at the Mg site. With regard to Fe substitution, the Mg_2FeH_6 compound formed during the milling process acts as the catalyst that improves the dehydrogenation properties of MgH_2 systems [3, 13]. For Ti or V doped systems, the TiH_2/MgH_2 or VH/MgH_2 interfaces help improve the dehydrogenation properties of MgH_2 systems [14]. The effect of FeF_2, TiF_3 and VF_4 on the dehydrogenation properties will be discussed elsewhere. As far as NiF_2, NbF_5 and ZrF_4 are concerned, they are all beneficial for the dehydrogenating kinetics of MgH_2 systems, and the results of our calculations for the improved dehydrogenating kinetics are in agreement with experimental results. If a Ni, Nb, or a Zr atom replaces a Mg atom of a MgH_2 system, the corresponding reactions, namely

$$NiF_2 + 3MgH_2 = MgF_2 + Mg_2NiH_4$$

$$2NbF_5+5MgH_2 = 5MgF_2+2NbH+4H_2$$

or

$$ZrF_4+2MgH_2 = 2MgF_2+ZrH_2$$

that occur during the milling process are accelerated, thus, MgH_2 with the higher stability can be changed into other hydrides such as Mg_2NiH_4, NbH and ZrH_2.

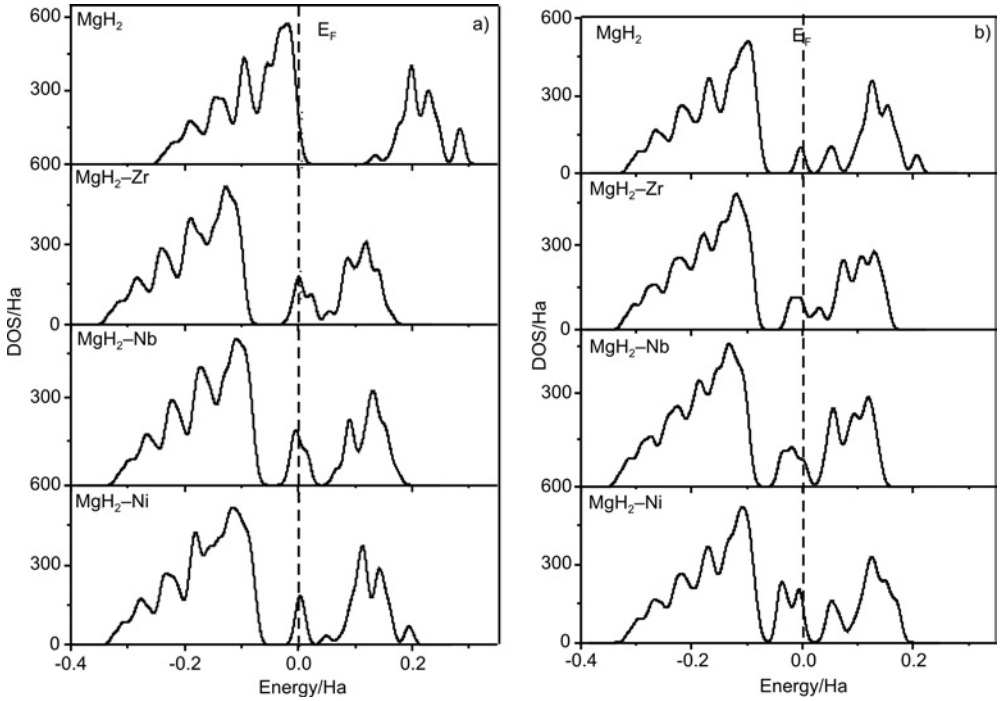

Fig. 11. DOS of MgH_2 systems with Mg atom replaced with another atom (a), and H atoms unchanged (b) two H atoms removed

An analysis was undertaken of the total density of states (DOS) of MgH_2 systems with two H atoms removed and replaced by other atoms, in order to understand the mechanism of the improved dehydrogenation kinetics of MgH_2 systems with metal fluorides (such as NiF_2, NbF_5 ZrF_4, etc.) (Fig. 11). With regard to Mg, with or without Ni, Nb or Zr substitution, it was found that before the dehydrogenation process, the bonding electron numbers below the Fermi energy are 72.14513, 67.13484, 66.13957, 64.10414, which are higher than the corresponding values, (70.11917, 65.06694, 64.07548, 62.07548) for the same systems after the dehydrogenation process. Hence, the bonding strengths/energies for Ni–H, Nb–H and Zr–H are stronger than that for Mg–H. Compared with the density of states (DOS) of MgH_2 systems (Fig. 12), it is found that when a Ni, Nb, or a Zr atom replaces a Mg atom, the valence electron numbers (Fig. 13) lying below the Fermi level in octahedral areas are made of the supercell

central atom and the first-nearest and second-nearest H atoms (Fig. 2b) reduce in the order of Ni, Ti, Zr.

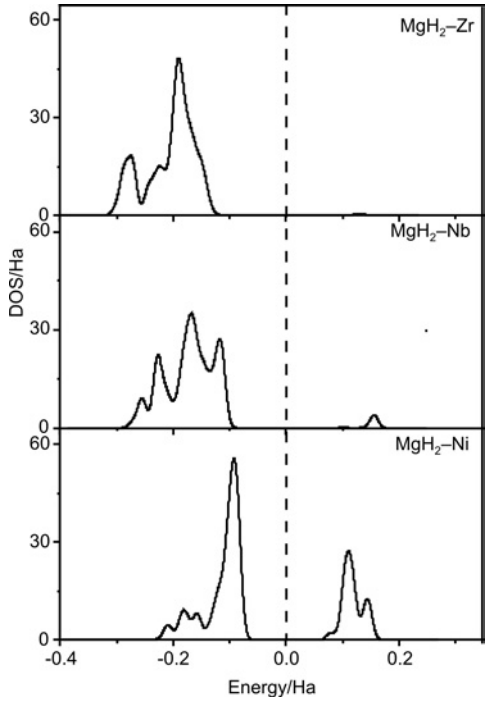

Fig. 12. DOS of octahedral areas in the MgH_2 supercell

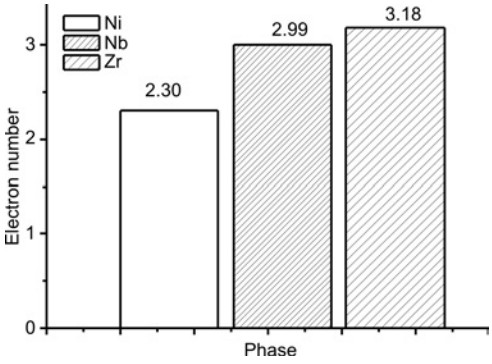

Fig. 13. The number of valence electrons lying below the Fermi level in octahedral areas in the MgH_2 supercell

The higher the bonding electron numbers are, the stronger the charge interactions, and other electron numbers in the low energy range, lying far below the Fermi level, will lead to a more stable structure. Hence, the corresponding structural stability is increased and the dehydrogenation kinetics is less energy-efficient. The density of states (DOS) theory of these MgH_2 systems also provides a very good explanation for the close agreement between the experimental results and the theoretical calculations for predicted improvements to the dehydrogenation kinetics of MgH_2 sytems, if NiF_2, NbF_5, or ZrF_4 are used as catalysts.

4. Conclusions

Density functional theory and the Dmol 4.1 software program were used to calculate the formation energy associated with the replacement of a Mg atom by a different atom, the formation energy of a Mg vacancy, the critical energy needed to remove two H atoms and the electronic structure of MgH_2 systems. The main conclusions are summarized as follows:

The formation energy of a Mg vacancy is higher than that of Fe, Ti, Zr, V, Ni, Nb, Cr, or Cu substitution, which means that the substitution of Fe, Ti, Zr, V, Ni, Nb, Cr, or Cu at the Mg site is more energy efficient than the formation of an Mg vacancy at lower temperatures.

NiF_2, NbF_5, ZrF_4 all improve the dehydrogenation kinetics of MgH_2 systems. The theoretical predictions for these kinetic improvements are in good agreement with the experimental results.

If a Ni, Nb, or a Zr atom replaces a Mg atom of an MgH_2 system, the corresponding reactions that occur during the milling process are accelerated, thus, MgH_2 with the higher stability can be changed into other hydrides such as Mg_2NiH_4, NbH and ZrH_2.

Compared with the density of states (DOS) theory of MgH_2 systems, it was found that when a Ni, Nb, or a Zr atom replaces a Mg atom, the valence electron numbers lying below the Fermi level in octahedral areas are made of the supercell central atom and its first-nearest, second-nearest H atom reduces in the order of Ni, Ti, Zr, meaning the corresponding structural stability is increased and the dehydrogenation kinetics become inferior. The density of states (DOS) theory of these MgH_2 systems also provides a very good explanation for the close agreement between the experimental results and the theoretical calculations for predicted improvements to the dehydrogenation kinetics of MgH_2 sytems, if NiF_2, NbF_5, or ZrF_4 are used as catalysts.

Acknowledgements

The work was supported by the Hunan Provincial Natural Science Foundation of China No. 09JJ6079, the PhD Programs Foundation of Ministry of Education of China No. 200805321032, the Science Fund of State Key Laboratory of Advanced Design and Manufacturing for Vehicle Body No. 60870005.

References

[1] ZALUSKA A., ZALUSKI L., STRÖM-OLSEN J.O., J. Alloys Compd., 288 (1999), 217.
[2] JURCZYK M., SMARDZ L., OKONSKA I., JANKOWSKA E., NOWAK M., SMARDZ K., Int. J. Hydrogen. En., 33 (2008), 374.
[3] SHANG C., X BOUOUDINA M., SONG Y., GUO Z., Int. J. Hydrogen. En., 29 (2004), 73.
[4] HUOT J., HAYAKAWA H., AKIBA E., J. Alloys Compd., 248 (1997), 164.
[5] GENNARI F.C., CASTRO F.J., URRETAVIZCAYA G., MEYER G., J. Alloys Compd., 334 (2002), 277.
[6] LIANG G., HUOT J., BOILY S., VAN NESTE A., SCHULZ R., J. Alloys Compd., 297 (2000), 261.
[7] MANDAL P., DUTTA K., RAMAKISHNA K., SAPRU K., SRIVASTAVA O.N., J. Alloys Compd., 184 (1992), 1.

[8] WANG P., WANG A.M., DING B.Z., HU Z.Q., J Alloys Compd., 334 (2002), 243.
[9] PELLETIER J.F., HUOT J., SUTTON M., SCHULZ R., SANDY A.R., LURIO L.B., MOCHRIE S.G.J., Phys. Rev. B., 63 (2001), 052103.
[10] JIN S.A., SHIM J.H., CHO Y.W., YI K.W., J. Power Sources, 172 (2007), 859.
[11] SONG Y., GUO Z., YANG R., Phys. Rev. B., 69 (2004), 094205.
[12] LI S., JENA P., AHUJA R., Phys. Rev. B., 74 (2006), 132106.
[13] ZHOU D.W., ZHANG J., LIU J.S., PENG P., Chin. Nonferr. Metal., 18 (2008), 2233.
[14] ZHOU D.W., PENG P., LIU J.S., Sci. China Ser. E., 49 (2006), 129.
[15] ZHOU D.W., LIU J.S., PENG P., Sci. China Ser. E., 51 (2008), 979.
[16] PERDEW J.P, BURKE K., ERNZERHOF M., *Phys. Rev. Lett.*, 77 (1996), 3865.
[17] PACK J.D., Phys. Rev. B., 16 (1977), 1748.
[18] DELLY B., J. Chem. Phys., 94 (1991), 7245.
[19] KITTEL C., *Introduction to Solid State Physics*, Wiley, New York, 1986.
[20] HOU Z.F., J. Power Sources, 159 (2006), 111.
[21] FUKAI Y., *The Metal–Hydrogen System*, Springer, Berlin, 1993.
[22] MEDVEDEVA M.I., GORNOSTYREV Y.N., NOVIKOV D.L., MRYASOV O.N., FREEMAN A.J., Acta. Mater., 46 (1998), 3433.
[23] SAHU B.R., Mater. Sci. Eng. B., 49 (1997), 74.
[24] BOGDANOVÍC B., BOHMHAMMEL K., CHRIST B., REISER A., SCHLICHITE K., J. Alloys Compd., 282 (1999), 84.

Received 18 August 2009

Materials Science-Poland, *Vol. 28*, *No. 1*, *2010*

Characterization of electrodeposited nanostructured macroporous cobalt films using polystyrene sphere templates

I.S. EL-HALLAG*

Chemistry Department, Faculty of Science, Tanta University, 31527, Tanta, Egypt

The electrodeposition of highly ordered macroporous films of cobalt with regular arrays of spherical pores of the diameters 200, 550, 600, 750 and 1000 nm was carried out into the interstitial spaces of a template formed by polystyrene latex spheres. The spheres were self-assembled on flat gold electrodes of 1 cm^2 surface area to produce a highly periodic, hexagonal close packed, interconnected network of monodisperse spherical pores within the metal film. The size of pores was determined by the diameter of the polystyrene latex particles used to prepare the template. The nanostructure of the films was studied by the scanning electron microscopy. Magnetic studies of the films were carried out with an Aerosonic 3001 vibrating sample magnetometer. The nucleation and the growth mode of cobalt were investigated via a chronoamperometry study.

Keywords: *electrochemical deposition; macroporous films; chronoamperometry; magnetic properties; polystyrene latex*

1. Introduction

Metal electrodeposition is of great importance, both for the basic science involving the process and for its major technological applications in electroplating, metal electrofining and electrowinning. Porous metals are important for many engineering applications such as filters, catalysts, supports, heat exchangers, fuel cells, electrolytic cells, thermal screens, and vibration dampers [1–4]. In many applications, a high specific surface area is required. The production of materials with micron and submicron scale structures in two and three dimensions is of importance in the range of applications such as photonic materials, high density magnetic data storage devices, microchip reactors and biosensors [5–9].

The electrochemical deposition of nanoscale Ni and Au meshes through templates made from a closely-packed silica sphere array have been described by Xu et al [10].

*E-mail: ielhallag@yahoo.co.uk

Several important differences were found between the method described in this work over that of Xu et al. These differences can be summarized as follows: (i) the polystyrene latex particles used are commercially available in a range of sizes; (ii) the closely-packed templates can be prepared by evaporation rather than by sedimentation over a period of several months; (iii) there is no need to sinter the template; (iv) the metal deposition is achieved in a few minutes rather than over 36 h; (v) the template can be removed by dissolving the polystyrene in toluene rather than requiring the use of HF.

In the paper, we report on the preparation of highly ordered macroporous metal films. The preparation of the structured macroporous films was carried out via the electrochemical reduction of $CoSO_4$ in aqueous solution within the interstitial spaces of a closely packed polystyrene latex sphere template, self assembled on a gold surface. The influence of the pore diameter of polystyrene latex spheres on the magnetic properties of the electrodeposited Co films is reported. The nucleation and the growth mode of Co onto gold substrates were investigated via current–time transient curves during potentiostatic deposition. The morphologies of the Co films were investigated by the scanning electron microscopy (SEM). Magnetic hysteresis curves were recorded with an Oxford Instruments Aerosonic 3001 vibrating sample magnetometer at room temperature.

2. Experimental

Materials. All solvents and chemicals were of reagent quality and were used without further purification. The monodisperse polystyrene latex spheres, with diameters of 200, 550, 600, 750 and 1000 nm were obtained from an Alfa Asear a 2.5 wt. % solution in water. Propanol and toluene were obtained from Aldrich. The gold electrodes used as substrates were prepared by evaporating 10 nm of a chromium adhesion layer, followed by evaporating 200 nm of gold, onto 1 mm thick glass microscope slides. The gold electrodes were cleaned by sonication in propanol for 1 h followed by rinsing with deionized water. All solutions were freshly prepared using reagent-grade water (18 MΩ·cm) from a Whatman RO 80 system coupled to a Whatman Still Plus system. The deposition solution was 0.1 mol·dm^{-3} $Co(Ac)_2$ with 0.1 mol·dm^{-3} KAc and 0.1 mol·dm^{-3} H_3BO_3 to produce pH 3.7. The deposition was carried out potentiostatically at the potential of –0.95 V vs. SCE.

Instrumentation. An analytical scanning electron microscope (JEOL 6400) was used to study the morphology and thickness of the electrodeposited cobalt films. Magnetic hysteresis loops were measured using an Oxford Instruments Aerosonic 3001 vibrating sample magnetometer. Electrochemical deposition was carried out in a conventional three electrode configuration using an EG G 273. A large area platinum gauze was used as the counter electrode, saturated calomel (SCE) as the reference electrode and the template coated gold substrate as the working electrode.

Assembly of the colloidal templates. The polystyrene sphere templates were assembled by sticking a 1.0 cm internal diameter Teflon ring onto the gold substrate using double-sided tape. Approximately 0.3 cm^3 of an aqueous suspension of the monodisperse polystyrene spheres of 200, 550, 600, 750 and 1000 nm in diameter diluted with water to 0.5 wt. % was spread over the area of the gold electrode surrounded by the Teflon ring (0.785 cm^2); this corresponds to a template layer about 2.0×10^4 nm thick. The sample was then kept in a controlled humidity chamber and allowed to dry slowly over a period of 3–4 days. After all the water had evaporated, the Teflon was removed to leave a circular area covered by the template. The templates are robust and adhere well to the gold substrate. There is no evidence for the resuspension of the latex particles when these are placed in contact with the deposition solutions.

Synthesis of highly ordered macroporous cobalt films. The electrochemical deposition was performed at fixed potentials of –0.95 V vs. SCE. The cobalt films were grown with a constant and gradient thickness. The gradient ranged from 0.0 to 1500 nm across the sample 1 cm in diameter. This was done in order to allow a systematic study, by SEM measurements, of the properties of the films, as a function of the film thickness. When the electrochemical deposition was complete (25–30 min), the cobalt films were soaked in toluene for 24 h to dissolve away the polystyrene template. All experiments were performed at room temperature (20–23 °C).

3. Results and discussion

3.1. Characterization by chronoamperometry

Chronoamperometry is a widely used technique for the deposition and observation of the growth process during the film formation. The chronoamperometric curve in Fig. 1a shows three different regions, in which *A* region corresponds to a rapid increase under an applied potential of –0.95 V vs. SCE. A slow current decay is observed in the B region which is followed by a constant current in C region. A rapid surge and exponential decay of the current observed in region A is due to double layer charging, which takes 6 s to reach the peak current of 4.7 μA. A continuous decay current observed in region B corresponds to the formation of cobalt films [11]. The current in region C is characteristic of diffusion controlled growth. In this region, the diffusion rate of Co^{2+} is equal to the reduction rate of Co^{2+} at the electrode surface, current keeps steady. This means that at longer time gradual increase of the diffusion zone increases the volume the depleted region. The diffusion zone between the electrode surface and the electroactive species in the bulk solution increase which leads to extension of the diffusion zone into the bulk solution (high population region of the electroactive species) causing linear diffusion of species to the electrode surface [1, 12, 13]. Thus, (i) cobalt deposition after double layer charging, (ii) critical nuclei

formation, and (iii) further diffusive controlled growth of the cobalt films, are the responsible steps for the nuclei formation and subsequent growth of cobalt thin films.

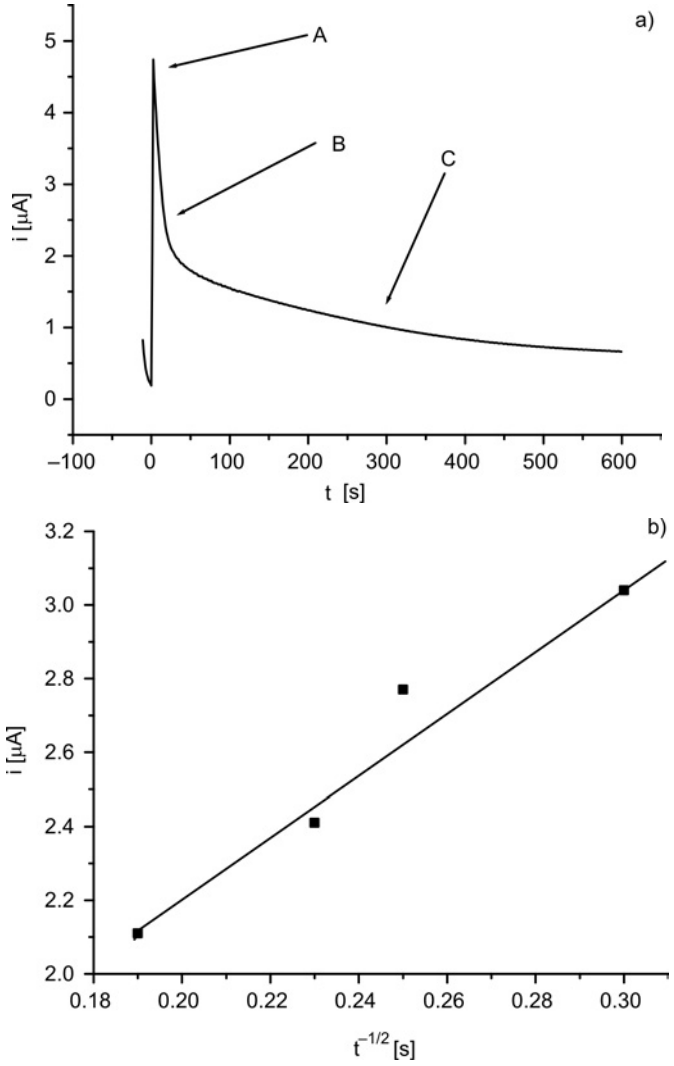

Fig. 1. Time dependences of current during deposition of cobalt at an applied potential of –0.95 V vs. SCE (a) and the Cottrel plot at E_f = –0.950 V (b)

By choosing the data for a short time from the experimental points selected in Fig. 1a, a Cottrel plot was obtained as a dependence of current on the reciprocal square root of time (Fig. 1b). The slope of the Cottrel plot yields the diffusion coefficient $D = 5.2\times10^{-10}$ $m^2 \cdot s^{-1}$. Cobalt thin films were deposited from an optimized bath composition by applying the –0.95 V vs. SCE deposition potential for various time durations. Figure 2 shows the plot of film thickness against the amount of charge re-

quired for the deposition of films. It was observed that the film thickness increases as the quantity of change increases.

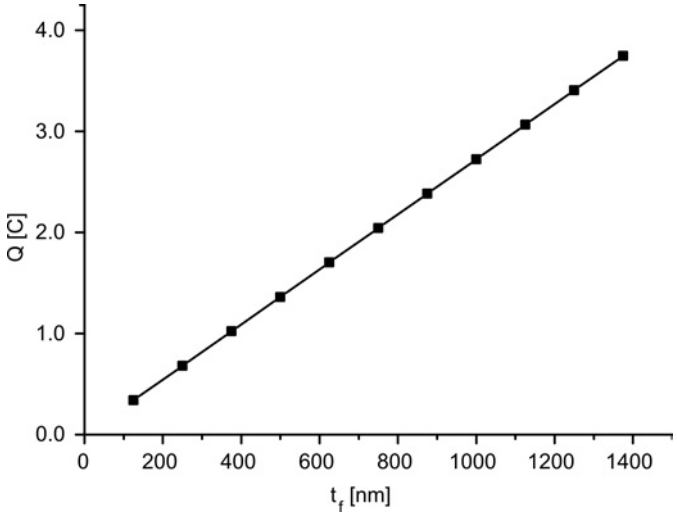

Fig. 2. Dependence of the charge required
for deposition of cobalt films on the film thickness

3.2. Characterization by SEM

Figure 3a shows an exemplary SEM image of the surface of a macroporous cobalt film on a gold substrate covered with templates made of 550 ± 20 nm diameter polystyrene spheres. The electrochemical deposition was carried out at potentials of –0.95 V vs. SCE (total charge passed 2 $C \cdot cm^{-2}$).

The SEM images show that the spherical voids left in the gold films after the removal of the polystyrene sphere are arranged in a well ordered, single domain, closely packed structure. Measurements of the centre-to-centre distances for the pores in Fig. 3a, and for similar images of other films, confirms that the spherical voids within the cobalt films have the same diameter as the polystyrene spheres used to fabricate the template. Figure 3b shows an image for a macroporous cobalt film prepared with a template of spheres 750 nm in diameter. Figure 3c shows a cross section of a cobalt film fabricated using templates formed from 750 nm polystyrene latex spheres. These micrographs also reveal the formation of three-dimensional macroporous films. The spherical voids have diameters determined by the diameter of the polystyrene latex spheres used for the template and are arranged as a part of an hexagonal lattice, again indicating that the polystyrene latex particles were arranged in a three-dimensional, hexagonal, closely packed structure. This was also confirmed by scanning electron micrographs of the template themselves before the deposition of the metal.

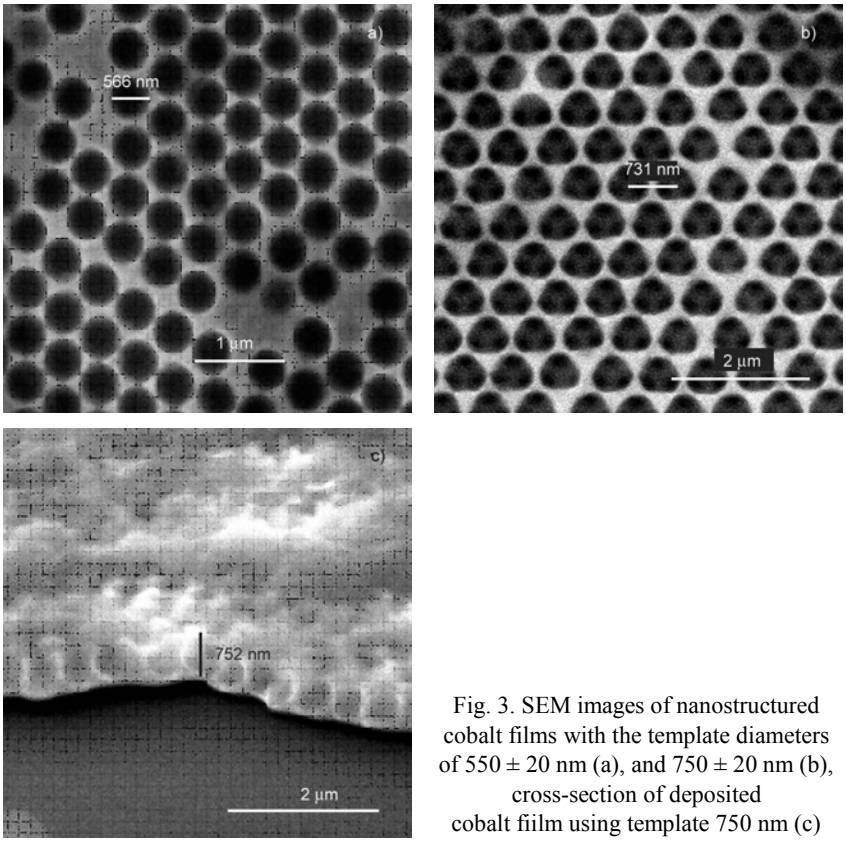

Fig. 3. SEM images of nanostructured cobalt films with the template diameters of 550 ± 20 nm (a), and 750 ± 20 nm (b), cross-section of deposited cobalt fiilm using template 750 nm (c)

It was noted that self-assembled layers of polystyrene latex particles formed on gold surfaces by slow evaporation of water from the latex suspension can be used as templates through electrochemical deposition of metal films. In the resulting metal/polystyrene composite, the polystyrene spheres are in contact and can be dissolved out of the metal to leave a regular array of interconnected spherical voids. The size of each of these voids is determined by the size of the polystyrene latex particles used. Polystyrene latex particles of tightly controlled size distribution are readily commercially available controlled. The final film thickness can be controlled by appropriately regulating the quantity of charge employed in the electrochemical deposition. Thus this method provides a simple route for the fabrication of ordered macroporous films of metals with potentially interesting and useful photonic, catalytic, magnetic, or other properties.

3.3. Magnetic properties of cobalt films

The film thicknesses were controlled by changing the diameter, *d*, of the polystyrene latex spheres, used to form the template, and the amount of charge passed during

the electrodeposition process [14]. Consequently, the grain structure and morphology of the electroplated cobalt films obtained from water and from the template mixture may be significantly different.

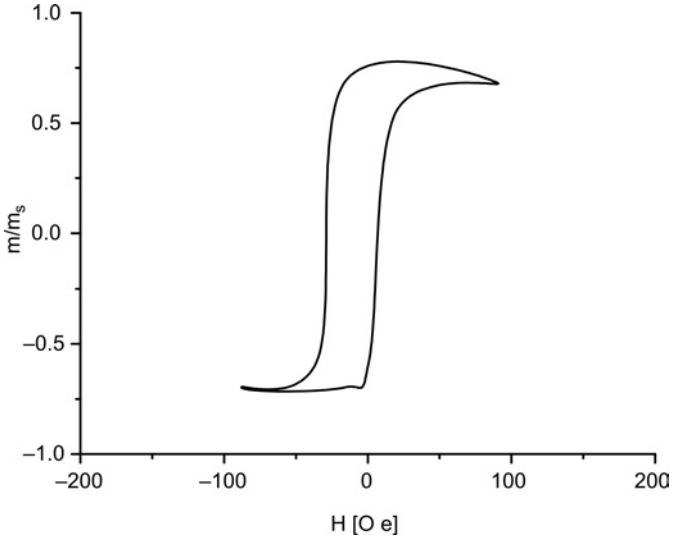

Fig. 4. Normalized in plane magnetic hysteresis loop at 550 nm

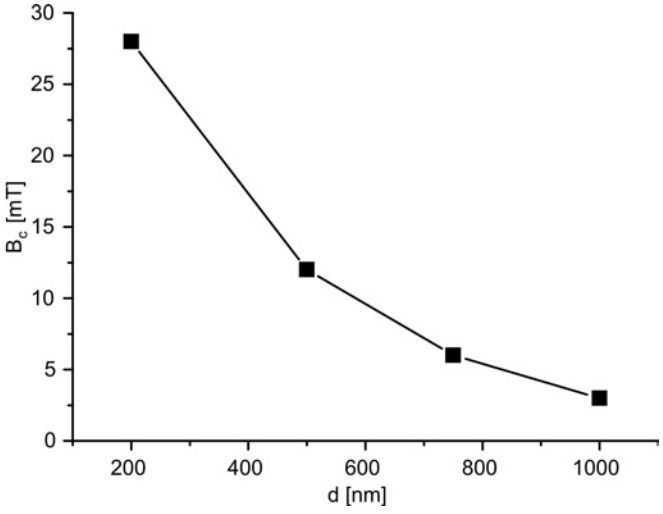

Fig. 5. Dependence of the measured coercivity on the diameter of the polystyrene sphere

Figure 4 shows an example of a normalized in plane magnetic hysteresis loop recorded at room temperature for cobalt film electrochemically deposited on a gold substrate using a polystyrene sphere of 550 nm in diameter. It was found that the hystere-

sis decreases as the the diameter of the polystyrene sphere increases. Figure 5 shows the dependence of the coercivity on the diameter of the polystyrene sphere. It is clear that the coercivity is proportional to the inverse of the diameter of polystyrene sphere. The nanostructuring significantly affects the shape of magnetization loops and drastically changes the coercive field β_c which found to show a maximum with variation of sphere diameter [15]. Measurements of the dependence of β_c on the thickness of the magnetic film, t_f, revealed that the coercive force changes periodically as a function of film thickness.

4. Conclusions

Using a simple method, we have successfully produced nanostructured films of cobalt via electrochemical deposition using templates prepared by assembling close packed arrays on monodisperse polystyrene spheres of various diameters (200, 550, 600, 750, and 1000 nm). The resulting electrochemical deposition is highly ordered. Three dimensional macroporous thin films of cobalt are robust and stable when the the template is removed. The diameter of the spherical voids is determined by the diameter of the polystyrene latex spheres employed to form the template. Scanning electron microscopy confirms the presence of a highly regular macroporous structure. The thickness of the films is controlled by varying the charge passed in their deposition. It was noted that the synthesis exhibits the Cotterellian behaviour at short time. This means that the diffusion controlled limiting current is proportional to $t^{-1/2}$.

Magnetic measurements show that the magnetic properties of cobalt films were strongly influenced by the diameter of the polystyrene sphere and the film thickness. It was found that the hysteresis loops and coercivity decrease with increasing the diameter of polystyrene sphere.

Acknowledgement

The author is grateful to Prof. P.N. Bartlett, School of Chemistry, University of Southampton, U.K., for providing the material for this work.

References

[1] KANG Y., ZHAQ J., TAO J., WANG X., LI Y., Appl. Surf. Sci., 254 (2008), 3935.
[2] YUN H.J., DULAL S.M.S.I., SHIN C.B., KIM C.K., Electrochim. Acta, 54 (2008), 370.
[3] ZHAO D.D., XU M.W., ZHOU W.J., ZHANG J., LI H.L., Electrochim. Acta, 53 (2008), 2699.
[4] MARTIN C.R., Chem. Mater., 8 (1996), 1739.
[5] HULTEEN J.C., MARTIN C.R., J. Mater. Chem., 7 (1997), 1075.
[6] MARTIN C.R., PATHASARATHY R.V., Adv. Mater., 7 (1995), 787.
[7] CHAN J.P., LEE K.M., SORENSEN C.M., J. Appl. Phys., 75 (1994), 5876.
[8] WESTON J.L., BUTERA A., BARNARD J.A., J. Magn. Magn. Mater., 193 (1999), 515.
[9] ATTARD G.S., BARTLETT P.N., COLEMAN N.R.B., ELLIOTT J.M, OWEN J.R., WANG J.H., Science, 278 (1997), 838.

[10] XU L., ZHOU W.L., FROMMEN C., BAUGHMAN R.H., ZAHKIDOV A.A., MALKINSKI L., WANG J.Q., WILEY J.B., Chem. Commun., (2000), 997.
[11] OKAM G., VEREECKEN P.M., SEARSON P.C., J. Electrochem. Soc., 146 (1999), 1436.
[12] VALIZADEH S., GEORGE J.M., LEISNER P., HULTMAN L., Electrochim. Acta, 47(2001), 865.
[13] *Instrumental Methods in Electrochemistry*, T.J. Kemp (Ed.), Hills Horwood, Chichester, UK, 1985.
[14] BARTLETT P.N., BIRKIN P.R., GHANEM M.A., Chem. Commun., (2000), 1671.
[15] DE GROOT P.A.J., ZHUKOV A.A., BOARDMAN R., BORDIGNON G., FANGOHR H., BARTLETT P.N., J. Magn. Magn. Mater., 310 (2007), e846.

Received 12 November 2008
Revised 22 June 2009

Materials Science-Poland, *Vol. 28*, *No. 1*, *2010*

Mechanical behaviour of glass during cyclic instrumented indentation

A. CHORFA[1*], M. HAMIDOUCHE[2], M.A. MADJOUBI[2], F. PETIT[3]

[1]Department of Mechanics, Faculty of Engineering Science, Skikda University, Algeria

[2]Departement O.M.P., Faculty of Engineering Science, Ferhat Abbas University, Algeria

[3]Belgian Ceramic Research Centre, Mons, Belgium

Indentation techniques are largely used nowadays for characterizing the intrinsic mechanical properties of brittle materials. A cyclic indentation tests have been carried out on soda lime glass and borosilicate glass using an instrumented indentation apparatus. Repeated post-threshold Vickers indentations were made using various peak loads. The hardness, elastic modulus and fracture toughness of the two glasses were evaluated using the consecutive load–displacement curves. Their properties of were compared and discussed.

Keywords: *glass; hardness; fatigue crack propagation; stress analysis*

1. Introduction

Indentation techniques are appropriate for characterizing the fracture behaviour of brittle materials. They are simple, economical and efficient methods that can be used to determine the material fracture parameters (toughness, and sub-critical crack-growth characteristics) and to analyse brittle contact damage problems (erosion, wear) [1]. Their applications have been extended over the last two decades with the development of instrumented equipments that allow the continuous measurement of the indenter depth under loading [2–4]. Instrumented indentation is a sensitive technique that can probe the mechanical properties of materials (Young modulus and hardness) at submicron scales from the load–displacement data (Fig. 1). Loads at the milli-Newton scale and displacements lower than 1 nm can be measured. It was used for studying metal dislocations [5, 6], toughened ceramics fracture behaviour [7], material coatings [8, 9], residual stresses [10] and the tribological behaviour of materials [11–13].

[*]Corresponding author, e-mail: a_chorfa@yahoo.fr

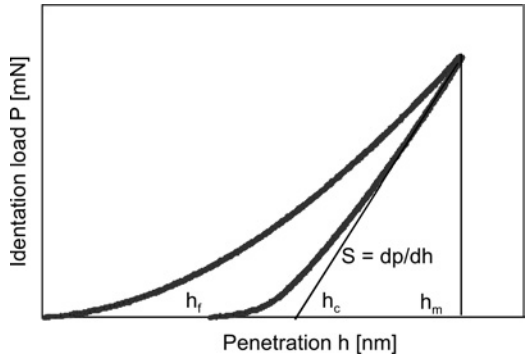

Fig. 1. Typical load–displacement indentation curve

When a Vickers indenter is loaded against a brittle material surface, it induces a plastic zone under the residual imprint. Above a critical loading level, in the post-threshold domain, two crack systems form during a loading–unloading cycle. A radial-median cracks system evolves normal to the surface along the imprint diagonals followed by a lateral crack system parallel to the surface [1] (Fig. 2).

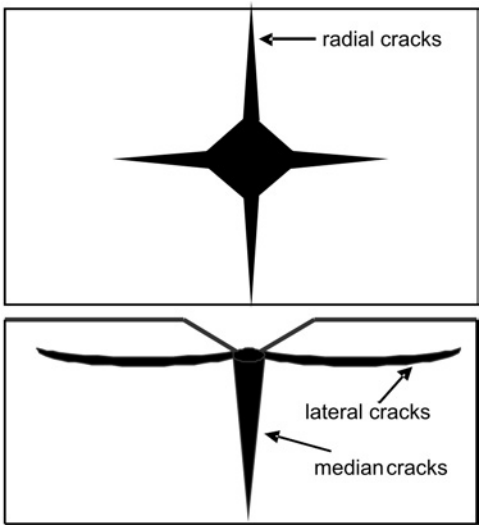

Fig. 2. Vickers indentation crack systems in glass

The material fracture toughness can be evaluated by measuring the radial cracks and the lengths of imprint diagonals with the knowledge of the applied load and the material elastic modulus using formula of Anstis et al. [14]:

$$K_{Ic} = 0.016\sqrt{\frac{E}{H_v}}\frac{P}{C^{3/2}} \tag{1}$$

where P is the peak applied indentation load, E is the elastic modulus, H_v is the material hardness and C is half the length of the two radial cracks (measured from the imprint centre).

Both the hardness and the elastic modulus can be derived from the load –displacement curve. Figure 1 shows a typical load–displacement indentation curve during a loading–unloading cycle. In this figure, h_m represents the displacement at the peak load $P_{\max}$, h_c is the depth along which the indenter is in contact with the sample during loading, h_f is the final displacement after complete unloading, S is the initial unloading contact stiffness. From the load–displacement curve, the hardness obtained at the peak load is defined as:

$$H = \frac{P_{\max}}{A} \tag{2}$$

where A is the projected contact area. Determining the projected contact area from a load–displacement curve requires the contact depth h_c to be known. The elastic modulus of the indented sample can be inferred from the initial unloading contact stiffness [15]:

$$S = \frac{dP}{dh} \tag{3}$$

Brittleness is crucial to ceramic and glass materials in contact damage issues. The ranking of susceptibilities of brittle materials to contact damage is based on indentation brittleness indexes. With the use of the Vickers indentation, Lawn and Marshall [16] proposed the brittleness index B, defined as the ratio of the hardness H to the fracture toughness K_{1c}:

$$B = \frac{H}{K_{1c}} \tag{4}$$

Cyclic fatigue characterization is usually used for describing the degradation of the mechanical properties of metals with time under repeated subcritical loads. Cyclic fatigue on brittle materials has not been extensively studied as for metals because it was thought insignificant in terms of their lack of plasticity. Some ceramics exhibit the mechanical fatigue effect related to the microstructure toughening mechanisms present in these materials [17–19]. Without any toughening mechanisms, glasses are considered resistant to mechanical cyclic fatigue. The observed glass mechanical strength deterioration under cyclic loading was explained by stress corrosion (environmentally assisted crack growth process).

However, recent works on borosilicate glass showed an evidence of a mechanical effect in addition to the stress corrosion effect at very low sub-critical crack growth velocities, using a standard fatigue test method [20]. In the context of brittle contact damage problems, repeated indentation was used to study the cyclic fatigue of ceramics [21–23]. The method is based on the relation between the applied indentation load and the number of subsequently repeated indentations needed to produce radial cracks (for sub-threshold loads) [23], or chipping (for post-threshold loads) [21].

2. Experimental

CSM indentation equipment (Micro-Combi-Tester, CSM Instruments, Switzerland) was used for our tests. It is essentially composed of three parts, as shown in Fig. 3. The first part corresponds to the indentation and scratch instrument. It has a sample holder table (4), an indenter holder (3) connected to the amplification and signal transformation system (1) and an acoustic probe (2). The second part consists of an optical system that enables imprint observation and magnification with the use of different objectives (6) and a display screen. The third part is the computer (7) used for test programming and data acquisition.

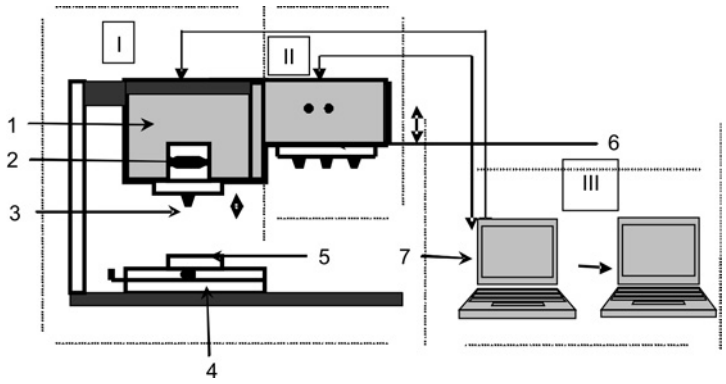

Fig. 3. Scheme of the CSM indentation tester. See the text for details

Table. 1. Chemical compositions [wt. %] of the tested glasses

Soda lime glass		Borosilicate glass	
Oxide	Content	Oxide	Content
SiO_2	72.851	SiO_2	69.734
Al_2O_3	1.354	Al_2O_3	2.549
Na_2O	12.729	Na_2O	6.761
K_2O	0.478	K_2O	3.071
CaO	8.249	CaO	1.508
MgO	4.097	B_2O_3	12.086
Fe_2O_3	0.098	ZrO_2	0.399
SO_3	0.151	SO_3	0.033
BaO	0.007	BaO	2.318
TiO_2	0.469	ZnO	1.115

Soda lime and borosilicate flat glass samples were used in this study. Their chemical compositions are given in Table 1. The sample thicknesses were 3 and 5 mm for the soda lime and borosilicate glasses, respectively. Samples of the dimensions 40×20 mm^2 were fabricated. They were annealed at 530 °C for 40 min in order to eliminate residual

stresses. Each sample was glued to a metallic pellet fixed on the sample holder. Its surface was previously cleaned before testing.

Indentations have to be spaced apart by 2 mm intervals in order to avoid their mutual interactions. The peak loads applied for the different indentations were: 1 N, 2 N, 3 N, 4 N and 5 N. For each load, the number of loading–unloading cycles was varied from 1 to 5. The loading and unloading speed was maintained at a constant rate of 1 N/min. A dwell time of 5 s at the peak load was used at every cycle. The minimal contact load during unloading was 0.2 N. Every test was repeated three times in order to get reliable results. Imprint micrographs were systematically taken for both glasses.

3. Results and discussion

The load–displacement curves obtained during repeated indentations under the 5 N peak load for the two glasses are presented in Fig. 4. It can be noticed that there is a hysteresis effect and a looping shift toward higher displacements as the number of repeated indentations increases, which are more pronounced for soda lime glass than for borosilicate glass.

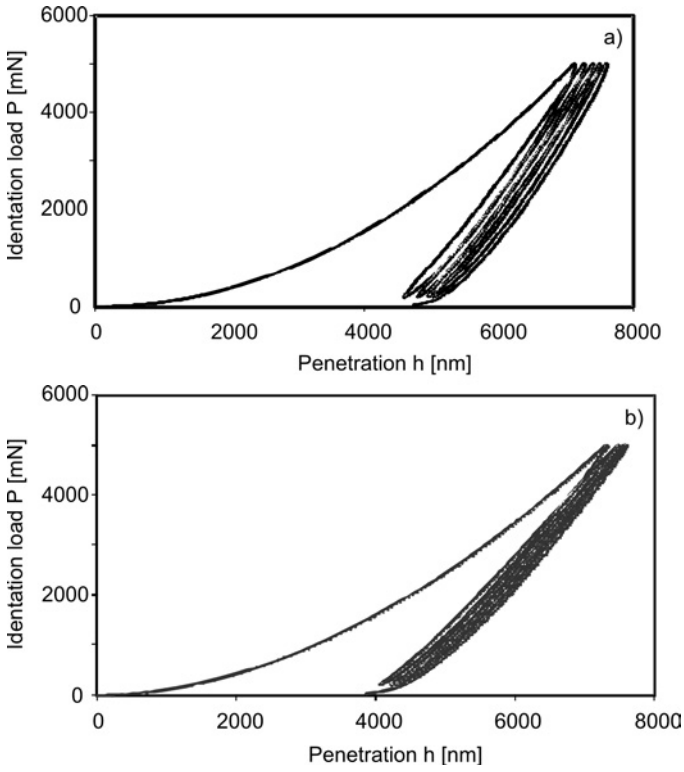

Fig. 4. Cyclic load–displacement curves for:
a) soda lime glass, b) borosilicate glass

The hysteresis effect reveals that the unloading is not only due to elastic recovery but includes also a certain amount of plastic reversibility. The dissipated energy related to non-elastic effects during the hysteresis process can be measured from the obtained closed loop surfaces. This energy, more important for soda lime glass, decreases as the indentation cycle number increases. The permanent penetration depth after the fifth cycle is 5 μm and 3.9 μm for the soda lime and the borosilicate glass, respectively. This leads to a smaller elastic recovery E_r for soda lime glass (E_r is the ratio of the recovered to the total surface of the loading displacement curve) [24].

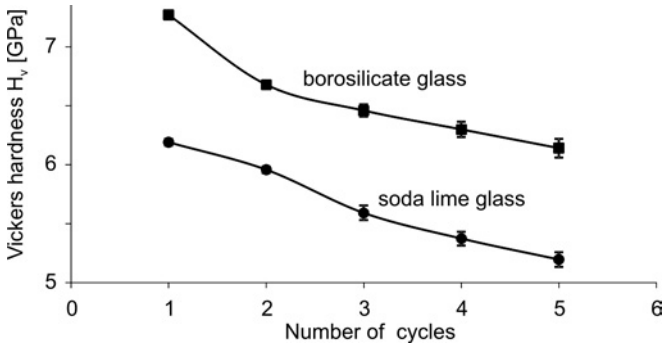

Fig. 5. Dependence of hardness on the number of indentation cycles for 5 N peak load

The hardness values (Fig. 5) reveal a similar decreasing trend upon the increasing number of indentation cycles for both glasses. It is probably related to the hysteresis effect. Such a trend was not observed with subthreshold loads in other papers when the three first cycles were avoided [3]. The measured values of hardness from the first load –displacement curve (6.2 GPa and 7.27 GPa for the soda lime glass and the borosilicate glass, respectively) are higher than the previously reported values (5 GPa and 6 GPa). The lower values obtained at the fifth indentation are closer to these values. Based on the mean value obtained from three measurements in every test, it is noticed that the hardness values obtained with instrumented indentation exhibit an insignificant variation between 0.4% and 0.94% for the first indentation and the fifth one, respectively.

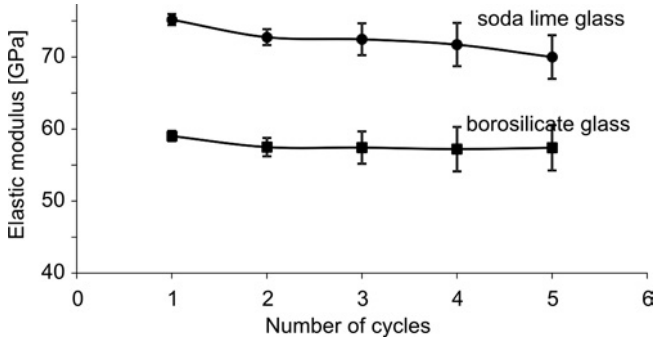

Fig. 6. Dependence of the elastic modulus on the number of indentation cycles for 5 N peak load

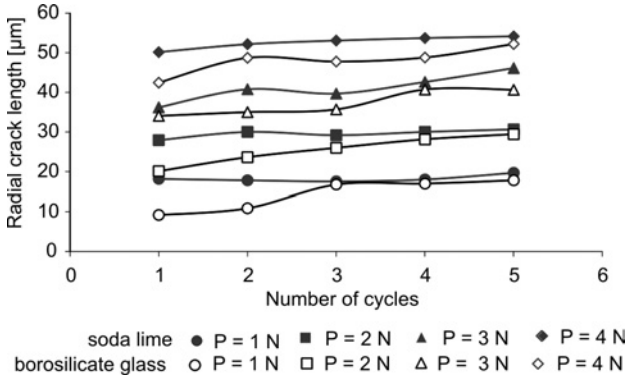

Fig. 7. Dependence of radial crack length
on the number of indentation cycles using different peak loads

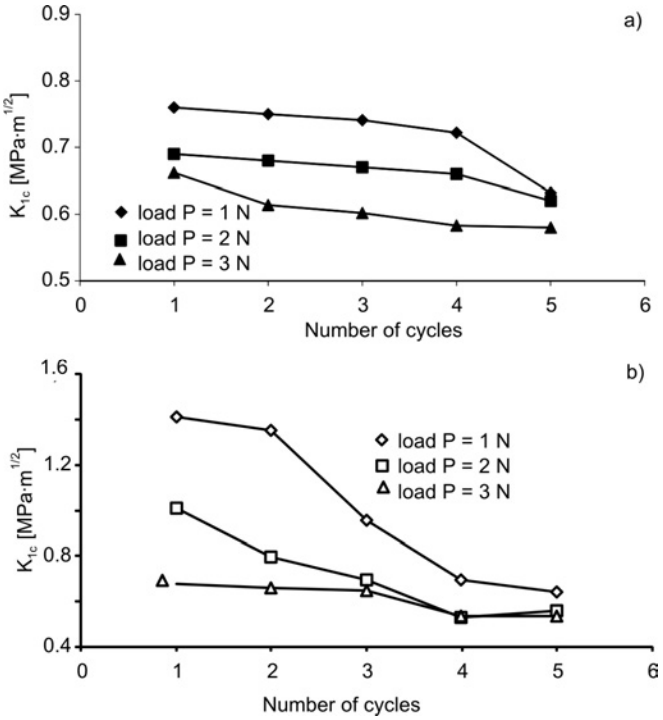

Fig. 8. Dependence of fracture toughness on the number
of indentation cycles for: a) soda lime glass, b) borosilicate glass

The obtained elastic moduli for the borosilicate glass seem to stabilize after the first indentation cycle, as seen in Fig. 6. Contrarily, the values obtained for the soda lime glass appear less consistent with the more pronounced hysteresis effect. It can be noted that Young's moduli obtained using instrumented indentation for both glasses, exhibit a significant scatter. Typical variations are in the range from 1% for the first

indentation to 6% for the fifth indentation. Nevertheless, it remains acceptable if one considers the fact that Young's moduli, obtained by instrumented indentation, rely on localized measurements, highly sensitive to local defects like micro-cracks, and cumulative residual stresses induced during the indentation cycles.

Figure 7 shows the radial crack length evolution with the cycle numbers for various peak loads corresponding to the two glasses. The same increasing trend of the radial crack lengths clearly appears for all peak indentation loads. This is probably due to the increase in the residual stresses as the number of cycles increases.

For both glasses, the obtained values of fracture toughness from the Anstis et al. formula (Fig. 8) are much lower than previously accepted values. The determination of fracture toughness is not only influenced by the variation of the hardness and Young modulus, but also by the cumulative residual stresses induced during the indentation cycles. With regard to the obtained variations of hardness and the Young modulus, the observed decrease in the fracture toughness with the cycle number can be explained by the effect of cumulative residual stresses on the propagation of the radial cracks. This effect is more apparent on the borosilicate glass.

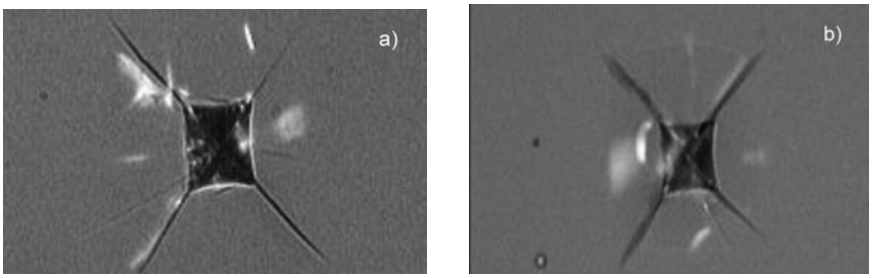

Fig. 9. Vickers indentation imprints for 4 N peak load after 5 cycles (×400): a) soda lime glass, b) borosilicate glass

For a peak load of 5 N, soda lime glass was found to have a brittleness index that increases from 9.98 $\mu m^{-1/2}$ at the first cycle up to 10.60 $\mu m^{-1/2}$ at the fifth cycle. For the same testing conditions, the borosilicate glass showed a variation from 10.19 $\mu m^{-1/2}$ up to 11.24 $\mu m^{-1/2}$. This increase of the brittleness index is clearly related to the changes in fracture toughness, which is more important than that of the hardness. Observations of the two glasses indentation imprints generated during the cyclic loading showed more pronounced scaling in the borosilicate case. The contact damage characteristics (imprints, radial cracks, etc.) for the soda lime glass did not vary that much during cycling. The photographs in Fig. 9 show longer radial cracks for soda lime glass under the same peak load (4 N).

4. Conclusions

For the mechanical properties obtained during repeated indentations, we observe a similar qualitative behaviour for both soda lime and borosilicate glasses. The hardness

evaluation is clearly influenced by the hysteresis effect affecting the load–displacement curves. The values obtained during the first four cycles are higher than those usually accepted. The values of the Young modulus seem to stabilize after the first cycle and are closer to expected values. It is therefore important to reduce the hysteresis effect, as was suggested in the literature, by using a longer dwell time at the peak load and avoid the first cycles, where this effect is preponderant. The obtained values for the fracture toughness are much lower than the accepted values for both glasses. They decrease, particularly for the borosilicate glass, as the cycle number increases. This is probably due to the cumulative residual stress effect on the radial crack propagation. From the brittleness index values, it appears that the use of instrumented Vickers indentation is appropriate for detecting the variation in the brittleness index.

References

[1] LAWN B.R., *Fracture of Brittle Solids*, 2nd Ed., Cambridge University Press, Cambridge, 1993.
[2] OLIVER W.C., PHARR G.M., J. Mater. Res., 7 (1992), 1564.
[3] PHARR G.M., Mater. Sci. Eng. A, 253 (1998), 151.
[4] FISHER-CRIPPS A.C., N*anoindentation*, 2nd Ed., Springer, New York, 2002.
[5] NIX W.D., GAO H., J. Mech. Phys. Solids., 46 (1998), 411.
[6] CORCORAN S.G., COLTON R.J., LILLEODDEN E.T., GERBERICH W.W., Phys. Rev. B, 55 (1997), 16057.
[7] CLARKE D.R., TANDON R., Mater. Sci. Eng. A, 195 (1995), 207.
[8] KRAFT O.K., SCHWAR Z., BAKER S.P., FREUND B., HULL R., Mater. Res. Soc., 673 (2001), 131.
[9] TSUI T.Y., PHARR G.M., J. Mater. Res., 14 (1999), 292.
[10] SWADENER J.G., TALJAT B., PHARR G.M., 16 (2001), 2091.
[11] RANDALL N.X., CONSIGLIO R., Rev. Sci. Instrum., 71 (2000), 2796.
[12] JARDRET V., LUCAS B.N., OLIVER W.C., RAMAMURTHY A.C., J. Coating Technol., 72 (2000), 79.
[13] LI X.D., BHUSHAN B., Thin Solid. Films, 398 (2001), 313.
[14] ANSTIS G.R., CHANTIKUL P., LAWN B.R., MARSHALL D.B., J. Amer. Ceram. Soc., 64, 9 (1981), 533.
[15] LI X.D., BHUSHAN B., J. Mater. Charact., 48 (2002), 11.
[16] LAWN B.R., MARSHALL D.B., J. Am. Ceram. Soc., 62 (1979), 347.
[17] EVANS A.G., FULLER E.R., Metall. Trans. A, 5 (1974), 27.
[18] GIGU F.J., Mater. Sci. Lett., 13 (1978), 1357.
[19] DAUSKARDT R.H., YU W., RITCHIE R.O., J. Am. Ceram. Soc., 70 (1987), 248.
[20] DILL S.J., BENNISON S.J., DAUSKARDT R.H., J. Am. Ceram. Soc., 80 (1997), 773.
[21] REECE M.J., GUIU F., J. Am. Ceram. Soc., 73 (1990), 1004.
[22] TAKAKURA E., HORIBE S., J. Mater. Sci., 27 (1992), 6151.
[23] BANERJEE R., SARKAR B.K., Glass Sci. Technol., 68 (1995), 177.
[24] SUZUKI K., BENINO Y., FUJIWARA T., KOMATSU T., J. Am. Ceram. Soc., 85 (2002), 3102.

Received 17 December 2008
Revised 25 August 2009

Materials Science-Poland, *Vol. 28*, *No. 1*, *2010*

A novel technique for the synthesis of $CaCu_3Ti_4O_{12}$ ceramics

S. SEN[1*], P. SAHU[1], K. PRASAD[2]

[1] Materials Science and Technology Division, National Metallurgical Laboratory, Jamshedpur-831007, India

[2]Material Research Laboratory, T.M. Bhagalpur University

A novel, low temperature synthesis technique is developed for fabrication of nanocrystalline $CaCu_3Ti_4O_{12}$ ceramic powders, using inexpensive and easily available reagents. Structural and microstructural characterization was undertaken by X-ray diffraction, scanning electron microscopy and transmission electron microscopy. The confirmation regarding the phase formation was done using the Reitveld analysis. The compound belongs to the cubic system with the lattice parameter a = 7.3985 Å, which agrees well with the values reported in the literature. The particles formed were spherical in shape, with the average size of 70 nm.

Keywords: *nanocrystalline materials; XRD; Reitveld analysis; SEM*

1. Introduction

Dielectric materials have many technological applications such as capacitors, resonators and filters. It is commonly accepted that high dielectric ceramic capacitors with Ba/Pb based perovskite oxides are indispensable for modern electronic devices and are found to be suitable for a wide range of applications. In general, these compounds belong to the perovskite structure where high electric permittivities are always associated with ferroelectric or relaxor properties, with a maximum depending on fu temperature, due to phase transition. $CaCu_3Ti_4O_{12}$ (CCTO) has the cubic perovskite crystal structure and unusual dielectric properties [1–3]. It exhibits an enormously large, low-frequency electric permittivity ε' (ca. 10^4), for both single crystal and ceramics at room temperature, and remains constant over 100–380 K at low frequencies. According to some researchers, this stunning dielectric behaviour is intrinsic [5], while others claim that it arises from external effects such as spatial inhomogene-

*Corresponding author, e-mail: shrabanee@nmlindia.org

ity [6], contact effect [7] or internal barrier-layer capacitors (IBLC). While the still exist controversies with respect to the mechanism, the IBLC explanation is rather widely accepted. Most of the reports were done on bulk materials, which were prepared by solid state reaction from metal oxides at higher temperature with several intermediate grindings. This method requires tedious work, relatively long reaction times and high temperature conditions, and still may result in unwanted phase because of limited atomic diffusion through micrometer sized grains. On the other hand, chemical methods provide atomic level mixing of individual components, and result in the formation of nanocrystalline materials at much lower temperatures compared with solid state reactions. There are many chemical methods, such as sol-gel, co-precipitation, precursor solution technique and hydrothermal process [8–13], which have already been reported for the synthesis of CCTO ceramics.

Here, we made a first time attempt to synthesize CCTO ceramics by precursor solution technique using easily available and inexpensive reagents at low temperature, and further characterize the compound by several different techniques.

2. Experimental

Nanocrystalline $CaCu_3Ti_4O_{12}$ powder was prepared by a metal ion–ligand complex based precursor solution evaporation method using high purity raw materials. Calcium carbonate ($CaCO_3$) (Merck), copper(II) acetate ($Cu(CH_3COO)_2$) (Merck), ethylenediaminetetraacetic acid (EDTA) (SRL, 99%), triethanolamine (TEA) (Merck, >97%) and titanium tartarate were used. The required amount of calcium carbonate was first dissolved in a minimum amount of dilute (6 M) nitric acid to make a clear solution. The solution was then boiled for 10 min to remove CO_2. The required amount of copper(II) acetate dissolved in water was then added, and finally EDTA was added to the solution and stirred. In order to get a clear solution, dilute ammonia solution [(2 M) was further added (pH ≈ 8). Titanium tartarate was obtained in the laboratory in the following way. Titanium oxide (Aldrich, 98%) was dissolved in HF (M/s Merck, 40% solution, 1:7 mole ratio) by heating on a water bath for 72 h. A clear solution of titanium fluoro complex was produced. The addition of dilute ammonia to that clear solution resulted in insoluble hydrous titanium hydroxide ($TiO_2{\cdot}nH_2O$) which was then separated from its solutions by filtration and was repeatedly washed with 5% ammonia to yield hydrous titanium oxide free from chloride ions. After estimating the amount of TiO_2 present in $TiO_2{\cdot}nH_2O$ by heating its small part at 1000 °C for 2 h, the hydrous TiO_2 was dissolved in tartaric acid (Quest, 99%) (1:4 mol) solution to obtain titanium tartarate through constant stirring at 60 °C for 8 h. Then a required amount of titanium tartarate and TEA was mixed. The final pH of this mixture was fixed at pH ca. 8 using dilute ammonia solution (2 M). Finally, both the solutions were mixed thoroughly and heated over a hot plate (ca. 200 °C) for complete evaporation under constant stirring. Continuous heating of the solution led to foaming and puffing. During evaporation, the nitrate ion provides an in situ oxidizing environment for TEA, which partially converts the hydroxyl groups

of TEA into carboxylic acids. On complete dehydration of the precursor solution, the metal complexes, TEA and EDTA, decomposed with the evaluation of dense fumes and resulted in a voluminous, fluffy, black carbonaceous mass, which was calcined at 700 °C to get the precursor powder.

The crystal structure of the pellet was confirmed by powder X-ray diffraction (XRD) using CuK_α radiation from a high resolution PANalytical X'Pert PRO diffractometer equipped with a secondary beam graphite monochromator and operating with the Bragg–Brentano geometry. For determination of the instrumental broadening function, a specially prepared Si sample was used [14]. The microstructural characterization was done using a JEOL-JSM 5800 microscope and JEOL-JSM-2010. In order to study the electrical properties, pellets were formed and sintered at 800 °C. The impedance properties were measured with an HIOKI 3532 LCR METER with a high temperature attachment.

3. Results and discussion

The phase formation of the compound was confirmed by XRD, which matched well with the results reported in the literature. It was further confirmed by the Reitveld analysis using the MAUD program (Version 2.044). The XRD pattern of CCTO was simulated with the cubic space group $Im\bar{3}$ and atoms at the following Wyckoff positions: Ca (0,0,0), Cu (0,1/2, 1/2), Ti (1/4,1/4,1/4), O (0, 1/4, 1/4) (ICDD PDF Card # 21-0140). The Rietveld analysis of the XRD pattern also confirmed the formation of the CCTO phase with the lattice parameter a = 7.3985 Å, which agreed well with the values reported in the literature. With regard to the microstructure analysis for the extraction of particle size and r.m.s. microstrain values using the Rietveld method from the 'size–strain' broadening, we considered the model proposed by Popa involving the expansions of spherical harmonics for the prediction of the particle shapes [154]. This model accounts for the anisotropic X-ray peak broadening, i.e. the model is capable of reproducing the case where in addition to the regular diffracting angle (2θ) dependent broadening, the broadening becomes a function of the diffracting planes (*hkl*) as well. From the 'size-strain' analysis, it turned out that the particle size values are nearly isotropic along all major [*hkl*] directions. In other words, it can be said that the particles are nearly spherical with average diameter ca. 70 nm having negligible r.m.s. strain (10^{-4}).

SEM micrographs of the calcined powders and sintered pellets are shown in Fig. 1. Due to the fineness of the particle, agglomeration took place, which resulted in the formation of a network resembling foam. The equation for grain growth at fixed temperature is:

$$G^m - \left(G(0)\right)^m = Kt$$

where G is the average size, $G(0)$ is the average size at $t = 0$, K is a constant and m is taken as 3. In nanomaterials, grain growth is inhibited by open porosity, growth inhibitors and grain boundary segregation. Thus the size of the grains does not increase much.

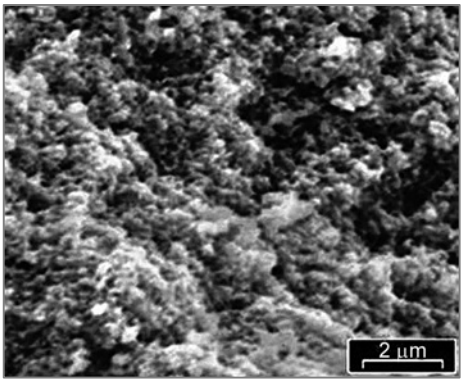

Fig. 1. SEM micrographs of calcined CCTO powders

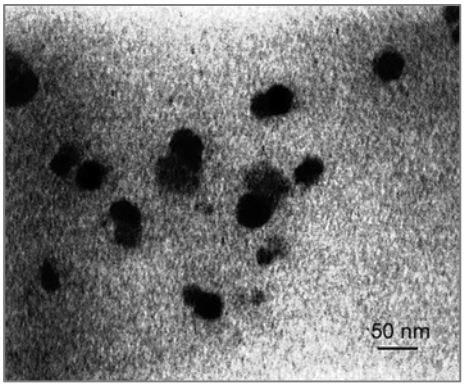

Fig. 2. TEM micrographs of calcined CCTO powders

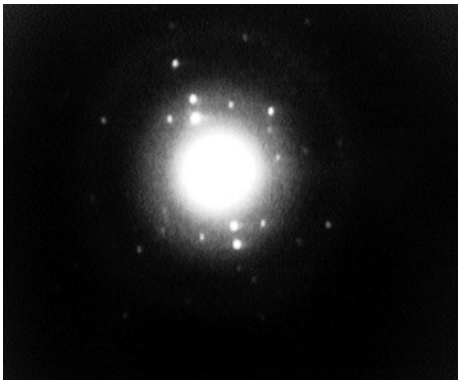

Fig. 3. Selected area electron diffraction (SAED) pattern of CCTO powders

The uniform distribution of the particles obtained from TEM is observed (Fig. 2) and the shapes of the particles are spherical. The particle size was calculated with the help of UTHSCA IMAGE TOOL considering 50 particles. After statistical analysis, the average particle size was found to be ca. 65 nm. This is in agreement with the particle size obtained from the Reitveld analysis. The corresponding selected area electron diffraction pattern (Fig. 3) shows a symmetrically dotted pattern, implying that the nanoparticles are well crystallized.

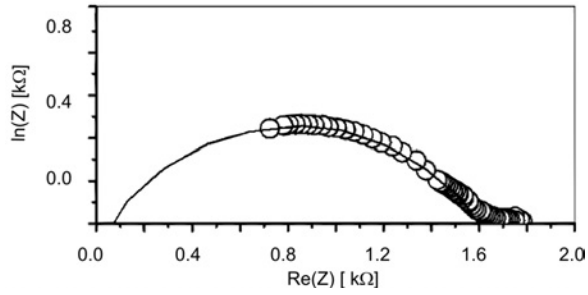

Fig. 4. Plot of the real and imaginary parts of impedance of CCTO powders

The electrical behaviour of the compound was studied using the ac technique of CIS. Figure 4 shows the plot of the real and imaginary parts of impedance at higher temperatures. The impedance spectrum is characterized by the appearance of semicircular arcs whose profile changes as the temperature increases. Also at higher temperatures only one semicircular arc was present, which clearly showed that only the bulk effect was prominent. The centre of the arcs lies below the real axis (Z'), which suggests that the relaxation is of polydispersive non-Debye type.

The complex impedance ($Z^*(\omega)$) can be expressed as:

$$Z^*(\omega) = \frac{R}{1 + \left(\frac{j\omega}{\omega_0}\right)^{1-n}}$$

where the exponent n represents the magnitude of the departure of the electrical response from the ideal condition, and is greater than zero for non-Debye type phenomena.

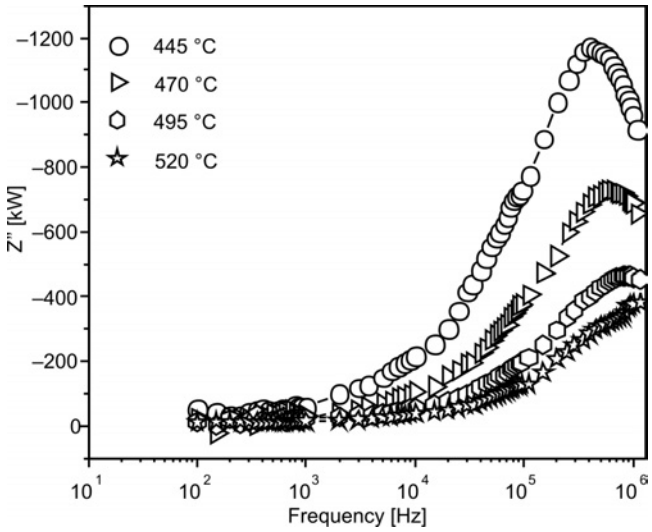

Fig. 5. Dependence of the imaginary part of impedance on frequency

The dependence of the imaginary part of impedance (Z″) on frequency at higher temperatures is shown in Fig 5. A typical peak broadening, which is slightly asymmetrical in nature, was observed at higher temperatures. This asymmetric broadening of the peaks suggests the presence of electrical processes in the material with a spread of the relaxation time. The relaxation species can be defect tanδ complexes. In the case of dielectric materials, the localized relaxation dominates [15, 16] (i.e., defect relaxation) because of the low dielectric ratio r, ($r = \varepsilon_s/\varepsilon_\infty$, ε_s and ε_∞, electric permittivity at low and high frequencies, respectively).

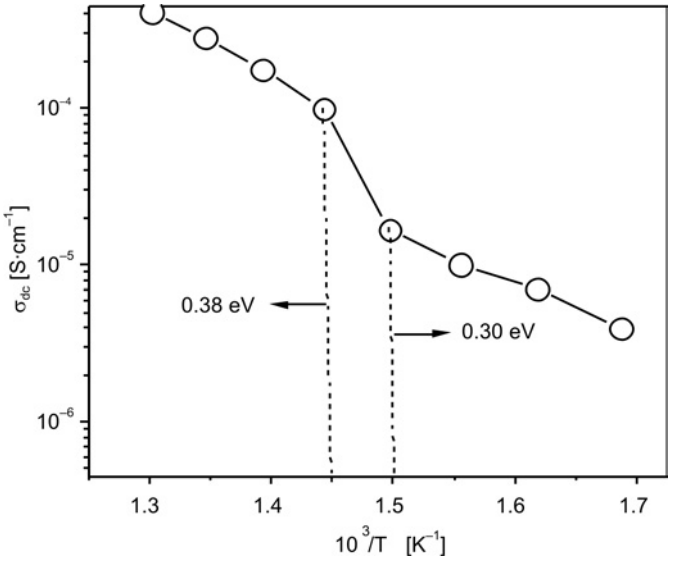

Fig. 6. Dependence of the dc conductivity on the reciprocal temperature

The bulk conductivity of the CCTO compound at higher temperatures was evaluated from the impedance data using the equation:

$$\sigma_{dc} = \frac{t}{R_b A}$$

where R_b is the bulk resistance, t the thickness and A the area of the electrode deposited on the sample. The value R_b is obtained from the low frequency intercept of the semicircle on the real axis Z' axis in the complex impedance plot. The value of the apparent bulk conductivity $(\sigma_b)_a$ determined from the complex impedance plots can be treated approximately as the true value σ_b because of the negligibly small thickness of the grain boundary layer in the sample. The dc conductivity also follows the Arrhenius law, and the activation energy was calculated from the slope of the linear portion of the plot of σ vs. 10^3/T (Fig. 6) [17]. It was found to be 0.3 eV at higher temperatures and 0.38 eV at lower temperatures. This value is close to the single crystal value of 0.24 eV, which again supports the existence of the internal barrier layers inside the grains [18, 19].

4. Conclusions

$CaCu_3Ti_4O_{12}$ ceramics were fabricated by the precursor solution technique. Keeping in mind the importance of this compound, this process provides a novel and reproducible route for preparation using two complexing agents (EDTA and TEA). XRD analysis confirmed the formation of cubic phase, with a lattice parameter value of

7.3985 Å. Spherical particles of average 65 nm size were observed from TEM micrographs after calcination at 700 °C. The presence of single semicircular arcs obtained from the impedance plots depicted the bulk effect only. The conductivity plot follows the Arrhenius law. The obtained activation energy was close to that of a single crystal.

References

[1] SUBRAMANIN M.A., DONG L., DUAN N., REISNER B.A., SLEIGHT A.W., J. Solid State Chem., 151 (2000), 323.
[2] RAMIREZ A.P., GARDEL M., BLUMBERG G., LI. D., VOGT T., SHAPIROS M., Solid State Commun., 115 (2000), 217.
[3] SINCLAIR D.C., ADAMS T.A., MORRISON F.D., WEST A.R., Appl. Phys. Lett., 80 (2002), 2153.
[4] HOMES C.C., VOGT T., SHAPIRO S.M., WAKIMOTO S., RAMIREZA P.R., Science, 293 (2001), 673.
[5] COHEN M.H., NEATON J.B., VANDERBIT D., J. Appl. Phys., 94 (2003), 3299.
[6] LUNKNHEIMER P., FICHTL R., EBBIMGHAUS S.G., LOIDL A., Phys. Rev. B, 70 (2004), 172102.
[7] LIU J., SUI Y., DUAN C., NEI W., SMITH R.W., HARDY J.R., Chem. Mater., 18 (2006), 3878.
[8] JHA P., ARORA P., GANGULY A.K., Mater .Lett., 57 (2003), 2443.
[9] JIN S., XIA H., ZHANG Y., XU J.G., J. Mater. Lett., 61 (2007), 1404.
[10] MASINGBON C., THONGBAI P., MAENSIRI S., YAMWONG T., SERAPHIN S., Mater. Chem. Phys., 109 (2008), 15.
[11] LIU J., SUI Y., DUAN C., MWI W.N., SMITH R.W., HARDY J.R., Chem. Mater., 18 (2006), 3878.
[12] YU H., LIU H., LUO D., CAO M., J. Mater. Res., 208 (2008), 145.
[13] BARBIER B., COMBETTES C., GUILLEMET-FRITSCH S., CHARTIER T., ROSSIGNOL F., RUMEAU A., LEBEY T., DUTARDE E., J. Eur. Ceram. Soc., 29 (2009), 731.
[14] VAN BERKUM J.G.M., SPRONG G.J.M., DE KEIJSER TH.H., DELHEZ R., SONNEVELD E.J., Powder Diffr., 10 (1995), 129.
[15] POPA N.C., J. Appl. Cryst., 31 (2006), 176.
[16] SEN S., CHOUDHARY R.N.P., TARAFDAR A., PRAMANIK P., J. Appl. Phys., 99 (2006), 124114.
[17] MACDONALD J.R., *Impedance Spectroscopy*, Wiley, New York, 1987.
[18] FANG T., MEI L.T., HO H.F., Acta Mater., 54 (2006) 2867.
[19] LI J., SLEIGHT A.W., SUBRAMANIAN M.A., Sol. Stat. Commun,135 (2005) 260.

Received 17 December 2008
Revised 1 April 2009

Materials Science-Poland, *Vol. 28*, *No. 1*, *2010*

Growth orientation transition and metal-like conductivity of Ti, Al co-doped ZnO films

M. JIANG*, X. LIU, H. WANG, J. XU

Guangxi Key Laboratory of Information Materials, Guilin University of Electronic Technology, Guilin, Guangxi 541004, P.R. China

Ti, Al co-doped ZnO thin films have been fabricated by radio frequency magnetron sputtering and post-vacuum-annealing techniques on glass substrates. For annealing temperatures below 723 K, the room temperature resistivity of these films was found to decrease as the annealing temperature increased. The lowest resistivity (6.75×10^{-4} Ω·cm), indicating metal-like conductivity, was found at 723 K. The post-annealing temperature dependent on the resistivity of these films also showed a metal –semiconductor transition at 723 K. It was also found a growth orientation transition of these films from (002) to (100) with the annealing temperature up to 773 K.

Keywords: *growth-orientation transition; metal-like conductivity; Ti, Al co-doped; ZnO thin film; vacuum annealing*

1. Introduction

Transparent conducting oxides (TCOs) have found applications in several opto-electronic devices such as light emitting diodes (LEDs), solar cells, and flat panels as well as flexible displays [1–3]. Indium tin oxide (ITO) is the most commonly used TCO for these applications because of its high transmittance in the visible region and the resistivity close to 1.0×10^{-4} Ω·cm [4, 5]. However, a high cost and scarce resources of In limit its usage in these devices. This has led researchers to explore alternative materials for TCO devices. Some of the TCOs which have shown transmittance and resistivity values close to those of ITO are ZnO:Al, ZnO:Ga, SnO_2:F, TiO_2:Nb etc. Among these, ZnO is the most favourable material, because of its benign nature, relatively low cost, good stability in hydrogen plasma process, and non-toxicity [5, 6]. Therefore, there is a considerable interest in understanding the electrical and transport properties of doped ZnO films which is critical for further improvement of TCOs characteristics.

*Corresponding author, e-mail: jiangmh@guet.edu.cn (M.H. Jiang)

Most of the careful doping studies have been performed by several techniques of various types in order to improve the performance of ZnO films [5, 7–10]. Doped ZnO, especially Al-doped ZnO (ZATO), shows excellent transparency over the entire visible spectrum and has better transport properties, due to higher electron mobility. For further improvement of properties of ZATO films, the co-doping effect of some impurity and Al^{3+} has been reported earlier [8, 11]. But the co-doping effect of Ti^{4+} and Al^{3+} has not been reported so far. TiO_2 has a particular and useful physical property for optical applications [12, 13]. TiO_2 was selected as dopant and expected to improve the transmittance and transport properties for ZATO film. In this paper, we have investigated the post-annealing, temperature dependent, transport properties of ZATO films grown on glass substrates at room temperature using the radio frequency (rf) magnetron sputtering technique. The investigation of a metal-like behaviour at low temperature has been investigated, being probably due to weak localization of the charge carries at the defect sites, surface scattering and the annealing temperature. In the paper, a new observation of the growth-orientation transition from (002) to (100) with an annealing temperature of up to 773 K has also been reported; it is probably related to the change of crystal surface energy induced by ionized impurities and massive formation of oxygen vacancies and defects in ZnO films grown on glass substrates during annealing.

2. Experimental

The ZATO ceramic sputtering targets, of which the raw materials were mechanical mixed powders, were fabricated by the conventional solid state sintering process in air. The following compositions were chosen: 97% ZnO + 1.5% Al_2O_3 + 1.5 TiO_2 (wt. %). The raw materials were commercially available ZnO, Al_2O_3 (99.95% in purity) and TiO_2 (99.96% in purity) powders. The compacted targets were sintered at 1573 K for 3 h in air.

ZATO thin films were grown on glass substrates at room temperature by the rf magnetron sputtering technique. The glass substrates were thoroughly cleaned using absolute ethanol, acetone and distilled water as solvents and ultrasonic technology, and then dried before loading in a deposition chamber. The chamber was evacuated to the pressure of 8×10^{-5} Pa, and the deposition was carried out under 1.6 Pa argon pressure. The ZATO films of 400–500 nm thick were annealed in the temperature range of 298–823 K for 3 h under vacuum (ca. 10^{-1} Pa).

Crystallographic and phase structures of the ZATO thin films were determined using a D8-Advance X-ray diffractometer with Cu K_α radiation. A JSM-5610LV scanning electron microscope (SEM) was used to investigate the surface morphologies of the deposited films. The electrical resistivity was measured using a standard four-point probe technique at room temperature.

3. Results and discussion

Figure 1 shows X-ray diffraction (XRD) patterns of the ZATO films annealed at various temperatures under vacuum for 3 h. The (100), (002) peaks are observed in the XRD patterns. The peaks correspond to a hexagonal wurtzite structure. The patterns show that the ZATO films deposited and annealed are highly textured along the *c* axis, except for the films annealed at 773 K. The absence of additional peaks excludes the possibility of any extra phases and/or large-size precipitates in the films. The above indicates that Al, Ti co-doping did not distort the original crystalline structure.

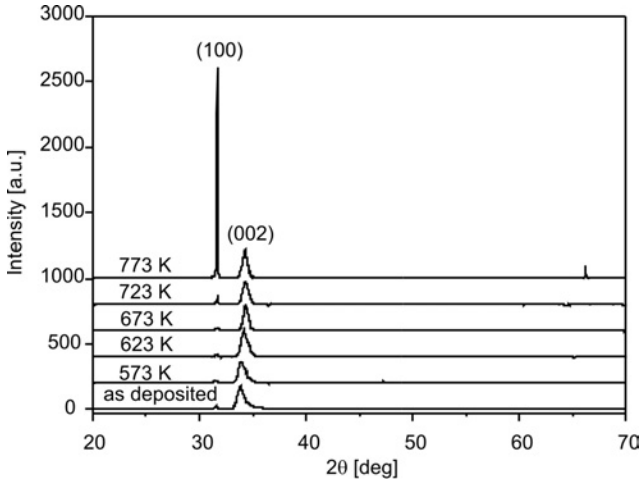

Fig. 1. X-ray diffraction (XRD) patterns OF ZATO films annealed at various temperatures under vacuum (ca. 10^{-1} Pa) for 3 h

However, for the film annealed at 773 K, very strong (100) and weak (200), (002) peaks were observed, which suggests that the preferred growth orientation undergoes a transition from (002) to (100), which is related to the change of surface energy of the film crystals during the annealing. Theoretically, for the ZnO films, (002) plane is the close-packed surface, and thus the value (1.6 J/m^2) of its surface energy is the lowest among all the planes, which is the reason that ZnO film crystals preferentially grow along the *c* axis [14, 15]. However, after the high temperature (773 K) annealing, Al, Ti ions sufficiently substitute the sites of Zn ions in the ZATO film, which probably results in the change of the closely-packed surface, and makes the surface energy value of the (100) plane be lowest being the reason for the change in the orientation of the recrystallization growth. In order to prove that Al^{3+}, Ti^{4+} ions occupy Zn substitutional sites, the dependences of the lattice parameters *a* and *c* and the step-scanned (002) XRD line profiles of ZATO films on the annealing temperature have been recorded (Fig. 2).

The lattice parameter *c* decreases as the annealing temperature increases to 723 K, and then it slightly increases till 773 K. The lattice parameter *a* also initially tends to decrease and then subsequently increases. This is a universal trend with the shift of 2θ

in the XRD patterns, as is seen from the (002) XRD line profiles of ZATO films at various annealing temperatures (Fig. 2) suggesting that the Al and Ti atoms occupy Zn substitutional sites.

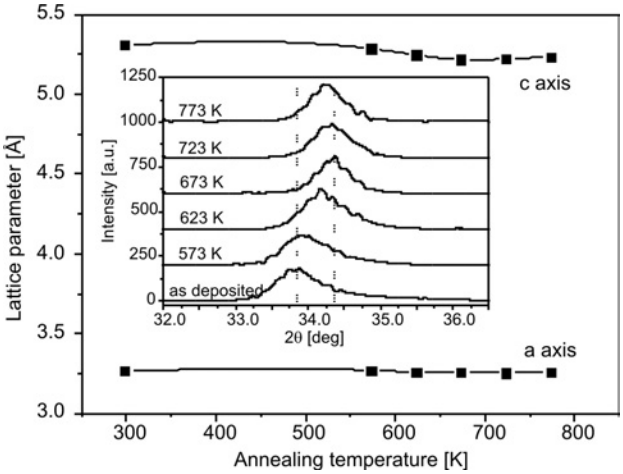

Fig. 2. Annealing temperature dependence of the lattice parameters (*a*, *c*) and step-scanned (002) XRD line profiles of ZATO films

Annealing of ZnO under vacuum at 773 K also leads to massive formation of oxygen vacancies and defects in ZnO films grown on glass substrates. In order to verify this supposition, ZATO films were annealed under oxygen atmosphere at 773 K for 3 h. In their XRD patterns (Fig. 3), only the (002) peak is observed, which supports the above supposition.

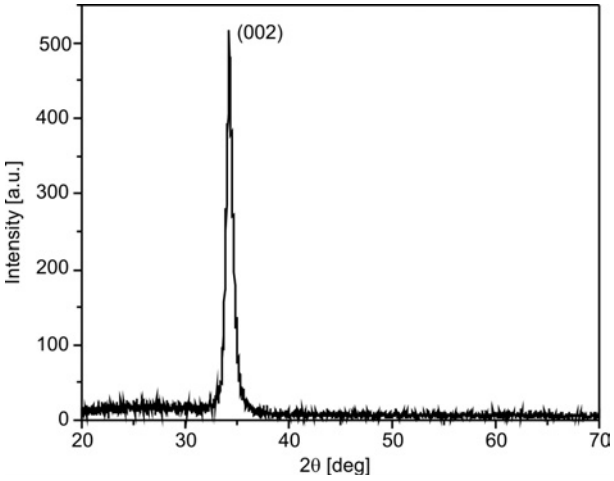

Fig. 3. X-ray diffraction (XRD) patterns OF ZATO films annealed at 773 K under oxygen atmosphere for 3 h

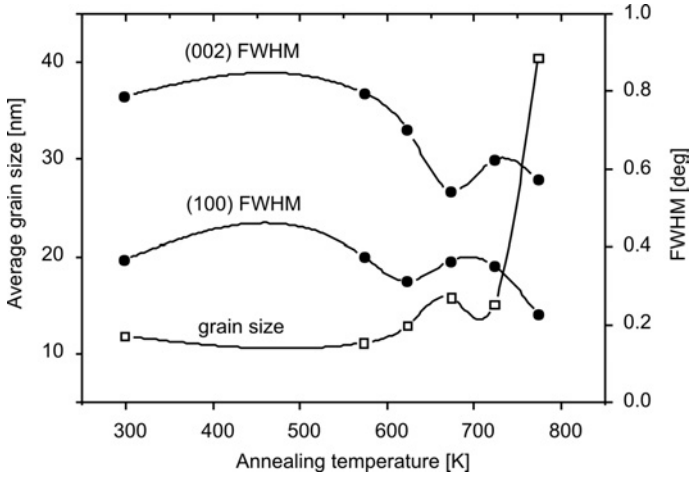

Fig. 4. Dependences of FWHM of (002) peak and average grain size of ZATO films on annealing temperature

Figure 4 shows the dependence of the full width at half maximum (FWHM) and average grain size on the annealing temperature. The FWHM decreased, that is, the average grain size became larger, as the annealing temperature increased. The smallest (100) peak FWHM exists when the annealing temperature is 773 K; this is the temperature at which the largest grain size can be obtained. Figure 4 also shows that the annealing temperature dependence of both the (100) peak FWHM and the (002) peak FWHM is similar, that is, initially both the (100) peak FWHM and the (002) peak FWHM decrease as the annealing temperature increases up to 623 K, then slightly increase till 673 K, and then decrease till 773 K.

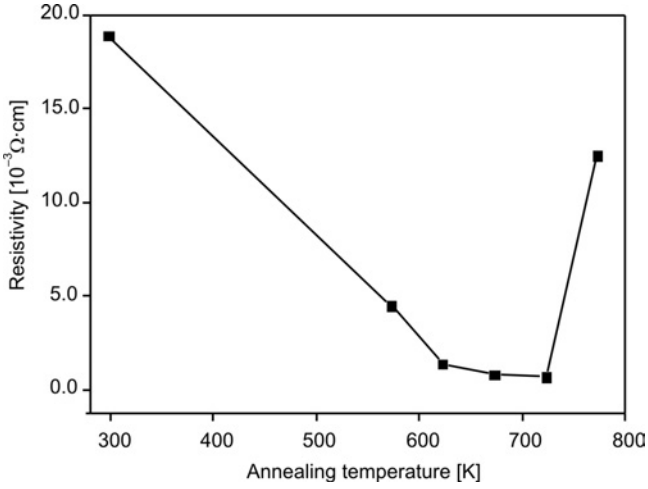

Fig. 5. Dependence of the resistivity of ZATO films on the annealing temperature

Figure 5 shows the dependence of the resistivity of ZATO films on the annealing temperature. The resistivity decreases as the annealing temperature increases up to 723 K, due to the increased grain size and the decreasing scattering to electrons. Then it clearly increases to 773 K, due to the growth-orientation transition from (002) to (100) as discussed previously, weak localization of the charge carriers at the defect sites and surface scattering. When the annealing temperature is 723 K, the semiconductor–metal transition appears, at which, the lowest resistivity, 6.75×10^{-4} Ω·cm, is achieved. The lower resistivity of ZATO films after thermal annealing can be explained by the presence of Al, Ti ions at the substitutional sites of Zn ions. Furthermore, Al, Ti interstitial atoms change the oxygen vacancy characteristics, and desorption of oxygen atoms under vacuum, thereby causing a shift in the Fermi level. By raising the annealing temperature, the atoms receive energy and migrate to relative equilibrium positions. This induces a series of effects, for example, it reduces the lattice strain and the oxygen defect levels. In particular, it results in the appearance of a more perfect crystallite, and a pilling-up of donor, thereby weakening the grain boundary scattering and increasing the number of current carriers. The other reason for the lower resistivity is the growth of the average grain size as the annealing temperature increases, which reduces the grain boundary scattering [3, 4]. When the annealing temperature is increased even further, a serious diffusion appears however between the glass substrates and the ZnO films, and consequently more defects are produced in the films. Excessive defect levels and disorder caused by the impurities strengthen the grain boundary scattering and reduce the number of current carriers.

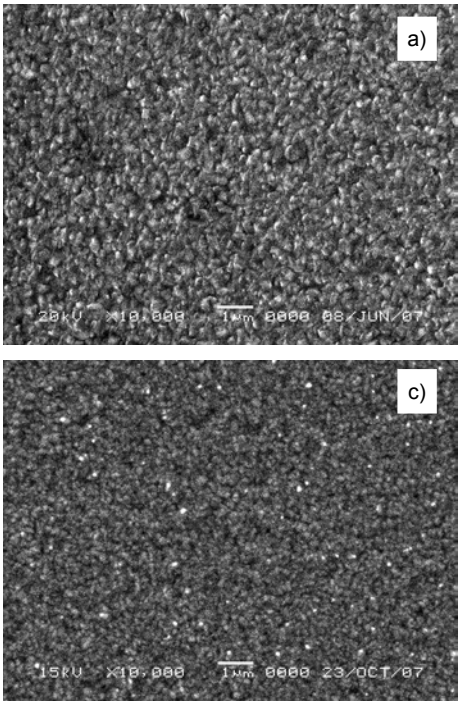

Fig. 6. SEM micrographs of ZATO films after annealing under vacuum at: a) room temperature, b) 673 K and c) 773 K for 3 h

Thus, the resistivity of the films starts to increase when annealing occurs at 773 K. Otherwise, the preferred growth orientation changes for a few grains in the films, and maybe also increases the resistivity of the films. A novel preferred orientation might offer different properties.

In order to illustrate the surface morphology of the ZATO films, scanning electronic microscopy (SEM) images are shown in Fig. 6. For the obtained ZATO films, uniform and dense surfaces with small grain sizes are observed, but these nanocrystalline surfaces do not show evident differences. The crystallite size, which can be estimated using the Scherrer formula, increases as the annealing temperature increases up to 773 K, as shown in Fig. 4 and is in the 10–45 nm range. This indicates the coalescence of the grains in ZATO films after thermal annealing at a different temperature. During deposition of ZATO films by sputtering onto glass substrates the growth took place by the nucleation and coalescence process. Randomly distributed nuclei may have formed first and then may have grown to form some observable "islands" which come closer to each other [8]. The larger ones appeared to grow by coalescence of smaller ones during annealing.

4. Conclusion

High-quality conducting ZATO films were grown on glass substrate by the rf magnetron sputtering technique, showing stronger *c* axis orientation. After thermal annealing in vacuum at 723 K, the preferred growth orientation of ZATO films changes from the (002) to the (100) plane. The resistivity of ZATO films decreases as the annealing temperature increases up to 723 K, and then clearly increases till 773 K. At 723 K, the semiconductor–metal transition appears, at which, the lowest resistivity, 6.75×10^{-4}, is achieved. For the obtained ZATO films, uniform and dense surfaces with small grain size are observed, but these nanocrystalline surfaces do not show evident differences. The crystallite size is in the 10–45 nm range.

Acknowledgements

The authors are grateful to the Education Department of Guangxi Zhuang Autonomous Region and to the Guangxi Key Laboratory of Information Materials for supporting this research under the grants Nos. 200807LX121 and 0710908-09-Z.

References

[1] LEE J., METSON J., EVANS P.J., KINSEY R., BHATTACHARYYA D., Appl. Surf. Sci., 253 (2007), 4317.
[2] AKHLESH G., COMPAAN A.D., Appl. Phys. Lett., 85 (2004), 684.
[3] BAMIDURO O., MUNDLE H., KONDA R.B., PRADHAN A.K., Appl. Phys. Lett., 90 (2007), 252108.
[4] WELLINGS J.S., CHAURE N.B., HEAVEHS S.N., DHARMADASA I.M., Thin Solid Films, 516 (2008), 3893.
[5] BHOSLE V., TIWARI A., NARAYAN J., J. Appl. Phys., 100 (2006), 033713.
[6] ASHOUR A., KAID M.A., EL-SAYED N.Z., IBRAHIM A.A., Appl. Surf. Sci., 252 (2006), 7844.

[7] KIM Y.S., TAI W.P., Appl. Surf. Sci., 253 (2007), 4911.
[8] LIN W., MA R.X., SHAO W., LIU B., Appl. Surf. Sci., 253 (2007), 5719.
[9] ZHU X.W., LI Y.Q., LU Y., LI Y.W., XIA Y.B., J. Inorg. Mater., 22 (2007), 359.
[10] SAITO K., HIRATSUKA Y., OMATA A., MAKINO H., KISHIMOTO S., YAMAMOTO T., HORIUCHI N., HIRAYAMA H., Superlattice Microst., 42 (2007), 172.
[11] TADATSGUMU M., SHINGO S., TOSHIHIRO M., Thin Solid Films, 398 (2001), 53.
[12] XU L.H., SHI L.X., LI X.Y., J. Phys. Chem. Solids, 70 (2009), 511.
[13] CHUNG J.L., CHEN J.C., TSENG C.J., J. Phys. Chem. Solids, 69 (2008), 535.
[14] PEI Z.L., ZHANG X.B., WANG T.G., GONG J., SUN C., WEN L.S., Acta Metall. Sinca, 41 (2005), 84.
[15] FUJIMURA N., NISHIHARA T., GOTO S., XU J., ITO T., J. Cryst. Growth, 348 (1993), 165.

Received 25 November 2008
Revised 8 May 2009

Materials Science-Poland, *Vol. 28*, *No. 1*, *2010*

Enhancement of photovoltaic performance of quasi-solid state dye sensitized solar cell with dispersion of a hole conducting agent

S. RANI[1], P.K. SHISHODIA[2], R.M. MEHRA[1*]

[1]Department of Electronic Science, University of Delhi, South Campus, New Delhi – 110 021, India

[2]Department of Physics & Electronics, Zakir Husain College,
University of Delhi, New Delhi – 110 002, India

The presence of a hole conducting agent in a quasi-solid state dye sensitized solar cell (DSSC) may improve cell parameters. The paper reports on the photovoltaic properties of two types of cells, one containing a layer of CuI on a dye coated ZnO electrode (cell A) and the other with CuI dispersed in a gel electrolyte (cell B). The cell A generated a short circuit current density of 7.45 mA·cm^{-2}, an open-circuit voltage of 0.56 V, a fill factor of 0.54 and an overall power conversion efficiency of 2.26% under 100 mW·cm^{-2} (air mass: 1.5). In cell B, an enhancement in its performance was observed. The cell showed 2.67% efficiency with a short circuit current density of 8.75 mA·cm^{-2}, an open-circuit voltage of 0.59 V and a fill factor of 0.52. The increase in the performance is attributed to the improvement in the hole transport in the electrolyte. The efficiency of cell B was further increased to 3.38% by introducing a compact layer of ZnO 106 nm thick.

Keywords: *ZnO DSSC; layered CuI; dispersed CuI; ZnO compact layer*

1. Introduction

Dye sensitized nanocrystalline solar cells have intensively been investigated, as they offer an attractive alternative to conventional p-n junction solar cells, because of their high efficiency, simple fabrication process and low production cost [1, 2]. In solid state versions, the electrolyte present in the pores of a mesoporous oxide film is replaced by a large band gap p-type semiconductor [3–6]. Light is absorbed by the dye adsorbed on the oxide surface. Upon excitation, the dye injects electrons into the conduction band of the oxide and is regenerated by injection of holes into the p-type conductor. A great advantage of such systems with regard to conventional p-n junctions is that only majority carriers are involved in the photoelectric conversion process.

*Corresponding author, e-mail: rammehra2003@yahoo.com

TiO_2 based quasi-solid state dye sensitized solar cell (DSSC) produce energy conversion efficiencies as high as ca. 11%, Typical DSSC are normally arranged in a sandwich configuration, that is the space between dye sensitized semiconductor (e.g., TiO_2) and counter electrodes is filled with an organic solution containing I^-/I_3^- redox couple as a cell electrolyte. Problems such as leakage and solvent evaporation associated with liquid electrolyte results in lower long-term stability and a decrease in cell performance. Many efforts have been made to replace liquid electrolytes with solid state or quasi-solid state ones such as inorganic p-type semiconductors [7], organic hole conductors [8], polymer/polymer gels [9, 10] and other new materials [11, 12]. Inexpensive ZnO powder is expected to be an alternating wide bandgap semiconductor because of its many important physical properties, such as large exciton binding energy of 60 meV at room temperature and good electrical conductivity [13]. Recently we reported results on ZnO based quasi-solid state DSSC fabricated using the sol-gel derived ZnO powder [14].

Solid state cells comprising CuI as a p-type semiconductor, to conduct away the holes, exhibit low conversion efficiencies [15], compared with the liquid version due to the low conductivity of charge carriers in the electrolytes and incomplete penetration of the solid electrolyte in the voids of the porous electrode. Therefore, quasi-solid state cells have received much attention because they have higher conductivities and higher conversion efficiencies compared with solid state cells. There are a number of reports on the use of organic or inorganic fillers in gel electrolytes in order to increase the efficiency of quasi-solid state dye sensitized solar cells. For example, Wang et al. [16] obtained a quasi-solid state electrolyte by solidifying the ionic liquid (1-methyl-3-propylimidazolium iodide) electrolyte with fluorine polymer (poly(vinylidenefluoride-co-hexafluoropropyl-ene)), achieving 5.3% overall conversion efficiency of the cells. Usui et al. [17] found improved conversion efficiency by dispersing TiO_2 nanoparticles in a ionic gel electrolyte. Kubo et al. [18] studied a quasi-solid state electrolyte by mixing the gelator with low molecular weight ionic liquid and achieved a cell with the conversion efficiency of 5%. Wang et al. reported DSSC with an ionic gel electrolyte containing dispersed silica nanoparticles [19]. The dispersion of various agents such as CNT, TiO_2, carbon black and graphite in ionic gel electrolyte enables the use of nanoparticles as "gelators" to solidify ionic liquid-based electrolytes and also increase the photovoltaic output [17].

In this paper, the authors have studied the effect of dispersion of hole conducting materials such as CuI in gel electrolyte to increase the photovoltaic performance of ZnO based quasi-solid state dye sensitized solar cells. The solar cell containing CuI as a layer on dye coated ZnO electrode and CuI dispersed in gel electrolyte were formed. The purpose of this work is to investigate various technologies which affect the photovoltaic performance, such as the application of CuI in various forms (layer or dispersion) to collect holes. The effect of a ZnO compact layer on photovoltaic performance was also investigated.

2. Experimental

Preparation of the polymer gel electrolyte. The polymer gel electrolyte was synthesized as follows: 3.0 g of poly ethylene glycol (PEG MW_{6000}), 0.03 g of tetra propyl ammonium iodide (TPAI), 0.003g of I_2, 0.15 g of ethylene carbonate (EC): propylene carbonate (PC) 1:1 in 25 cm^3 acetonitrile were used. TPAI and I_2 were firstly dissolved in a binary organic solvent mixture containing EC and PC (1:1) Then PEG was added and the solution was heated at 75–80 °C under vigorous stirring until a viscous gel was obtained, followed by cooling to room temperature.

Dispersion of CuI in polymer gel electrolyte. A composite polymer gel electrolyte was formed by dispersing 0.3 cm^3 of filtered acetonitrile solution of CuI (0.16 M) in the polymer gel electrolyte, prepared as above (0.9 cm^3) at 60 °C under continuous stirring. A DSSC using the dispersed CuI polymer gel-electrolyte was fabricated by spreading the composite electrolyte on a dye coated ZnO electrode and then applying a counter electrode.

Preparation of ZnO electrode and treatment with the dye. Porous ZnO films, produced using nanocrystalline ZnO powder, were deposited on indium tin oxide (ITO) coated glass from the synthesized ZnO powder by the doctor blade technique [14]. Rose Bengal (RB) dye was used to sensitize the ZnO film. RB is an organic dye in the xanthene class. It absorbs a wide spectrum of solar energy and energetically matches the ZnO and iodine/iodide redox couple for DSSC application [20, 21]. Thus ZnO performs particularly well when sensitized with Rose Bengal [22]. Being an organic dye, there are no concerns about environmental damage, as it does not contain any noble metal, such as ruthenium. RB dye has been successfully used by several groups for DSSCs structures. It has high extinction coefficients and its molecular structure contains anchoring groups that can be adsorbed onto the oxide surface [23]. For the particular case of ZnO–RB (or other anionic xanthenes dyes), it is highly probable that the dye is directly bound to the surface of a zinc ion. Such bonding will not only make the adsorptivity high but also facilitate the electron injection process by a strong overlap between the electron molecular orbitals of the dye and those of the conduction band of the semiconductor [22]. The ZnO film was immersed in a 0.3 mM solution of Rose Bengal dye in ethanol for 24 h. To minimize the adsorption of impurities from moisture in the ambient air, the electrodes were dipped in the dye solution while they were still warm (ca. 80 °C). The dye covered electrodes were then rinsed with ethanol, to remove excess dye on the surface, and dried at room temperature.

Formation of CuI layer. A solution of CuI (0.16 M) was prepared by dissolving 0.3 g of CuI in 10 cm^3 of moisture free acetonitrile. The dye coated ZnO electrode was placed on a hot plate (80–100 °C) and filtered (0.3 cm^3) acetonitrile CuI solution was spread over the dye coated ZnO electrode.

Preparation of ZnO compact layer. The ZnO compact layer was prepared by the sol-gel technique. Sols were prepared by dissolving zinc acetate ($Zn(CH_3COO)_2 \cdot 2H_2O$, 99.0% purity) in methanol to form 0.2 M solution. The mixture was stirred with an ultrasonic and magnetic stirrer at 25 °C for 120 min until a clear solution was formed. The sol prepared was found to be stable and transparent with no precipitate or turbidity. Monoethanolamine (MEA) was further added to the sol to achieve the pH of ca. 9. The modified sols were stirred ultrasonically for 60 min at room temperature. The sols were then kept for 48 h for aging in order to convert the sol into gel. The conductive glass substrate (ITO) was cleaned using acetone, methanol and distilled water in an ultrasonic bath. The ZnO film was spin coated on the substrate at a spinning speed of 3000 rpm for 20 s. The desired thickness of the ZnO compact layer was varied by repeatedly applying the appropriate number of coatings. The films were dried on a hot plate at 300 °C for 10 min in between each successive layer deposition. Since the boiling point of MEA and temperature of thermal decomposition of zinc acetate are 170 °C and 240 °C respectively [24], a preheat treatment temperature of 300 °C is sufficient for the complete evaporation of organics. The deposited ZnO compact layer films were annealed in air at 400 °C for 1 h. The thickness of the film was measured by the reflectance method.

Solar cell assembly. The assembled solar cells are: cell A: CuI in a layer form (ITO/ZnO/Rose Bengal/CuI layer/gel electrolyte/Pt), and cell B: CuI dispersed in a gel electrolyte (ITO/ZnO/Rose Bengal/dispersed CuI gel electrolyte/Pt). Pt sheet was used as a counter electrode. The active electrode area was typically 1 cm^2.

Characterization and J–V measurement. The crystalline nature of ZnO powder and ZnO electrode was determined by X-ray diffraction (XRD) using a Philips analytical Model No.-PW1830 with a CuK_α incident beam (λ = 1.54 Å). The presence of CuI on the ZnO surface and in gel electrolyte was confirmed by X-ray diffraction. The surface morphology of the ZnO electrode was analyzed by using a scanning electron microscope (SEM) (LEO 435 Vp, variable pressure scanning electron microscope, Cambridge UK). The absorbance of the ZnO electrode, sensitized with Rose Bengal dye was measured using a UV-VIS-NIR spectrophotometer (SolidSpec-3700, Shimadzu, Japan). The spectrophotometer was equipped with an integrating sphere which enabled recording the reflectance. The absorbance is obtained by transforming the diffused reflectance data using the Kubelka–Munk function.

The solar energy conversion efficiency (*J–V*) curve was measured by using a computerized digital Keithley source meter (Model 2400) and a tungsten halogen lamp as the light source. The lamp was calibrated close to AM1.5 SUN conditions from National Physical Laboratory (NPL, New Delhi). The IR radiation was attenuated using a water filter. A tungsten halogen lamp does not assure AM conditions since its source of light contains insufficiently small amounts of UV light. Therefore generally xenon arc lamps are used in solar simulators. Although in such a case the

absolute value of solar cell parameters would slightly differ from the actual one but this would not significantly affect the comparative study [25, 26].

Based on the *J–V* curve, the fill factor (*FF*) is defined as:

$$FF = \frac{I_{\max} V_{\max}}{I_{sc} V_{oc}}$$

where I_{max} and V_{max} are the photocurrent density and photovoltage for maximum power output (P_{max}), I_{sc} and V_{oc} are the short-circuit current density and open circuit voltage, respectively. The overall energy conversion efficiency η is defined as:

$$\eta = \frac{I_{sc} V_{oc} FF}{P_{in}}$$

where P_{in} is the power of the incident light.

The incident photon-to-current density conversion efficiency (IPCE) gives the ratio between the number of generated charge carriers contributing to the photocurrent density and the number of incident photons, and is given by

$$\text{IPCE} = \frac{1240 j_{sc}}{\lambda P_{in}} \%$$

where j_{sc} [mA/cm^2] is the short circuit current density, P_{in} [mW/cm^2] is the light power density and λ [nm] is the wavelength. j_{sc} of the cells was determined from the *J–V* characteristics of the cells obtained at various wavelengths of light using narrow bandwidth (10–12 nm) interference filters (Vin Karola Instruments, USA). The intensity of the incident monochromatic radiation was kept constant and measured using an optical power meter (Model 1815-C, Newport USA).

3. Results and discussion

3.1. Structural characterization

Figure 1 shows a SEM image of synthesized ZnO powder. Microstructural homogeneities are visible in the morphology of ZnO powder. The diameter of ZnO particles is approximately 1 μm. Figure 2 shows the SEM micrograph of the ZnO film on ITO sintered at 400 °C. The film is porous with a homogeneous distribution of particles, tightly packed with good connectivity between them.

Figure 3a shows the XRD pattern of synthesized ZnO powder. The powders showed their crystalline nature, with peaks corresponding to the (100), (002) and (101) planes. The preferred orientation corresponding to the (101) plane is observed for ZnO powder. The spacing values and relative intensities of the peak coincide with the JCPDS card No. 36-1451 for ZnO powder.

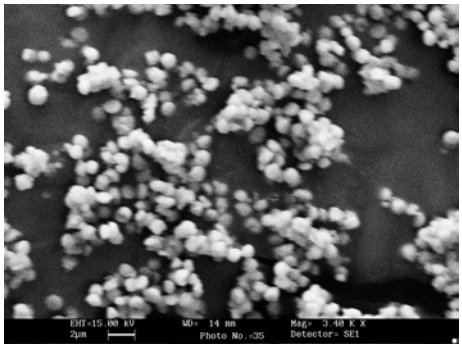

Fig. 1. SEM images of ZnO powder grown at pH = 9 in sol

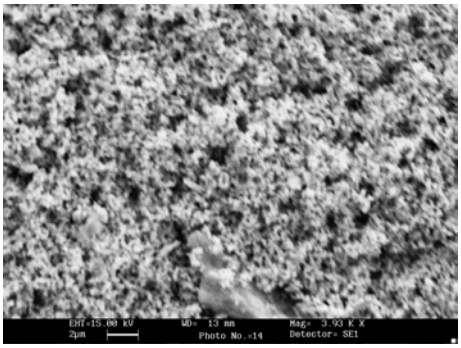

Fig. 2. SEM image of the ZnO film on ITO sintered at 400 °C

Crystallite size D was obtained from the full width at half maximum β of (101) peak using the Debye–Scherrer formula [27, 25]

$$D = \frac{0.94\lambda}{\beta \cos\theta}$$

where λ is the wavelength of CuK_α radiation and θ is the angle obtained from the 2θ value corresponding to the maximum intensity peak in the XRD pattern. The crystallite size of ZnO powder was found to be ca. 28 nm.

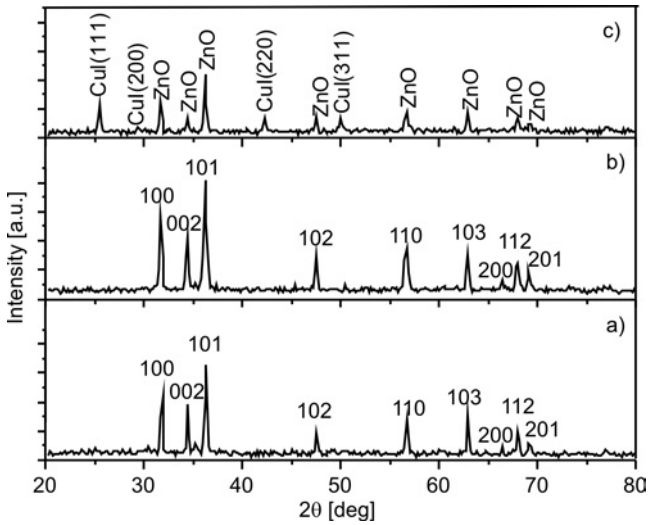

Fig. 3. XRD patterns of a synthesized ZnO powder (a), ZnO film on ITO (b), and after deposition of CuI layer on ZnO film(c)

Figure 3b shows the XRD pattern of ZnO films on ITO sintered at 400 °C. The film shows the polycrystalline nature with a preferred orientation corresponding to (101). Fig-

ure 3c shows the XRD pattern of ZnO electrode after deposition of CuI. It contains the peaks of both ZnO and CuI. CuI crystallizes in the zinc blende structure with γ-phase while the preferential orientation is the (111) direction.

To show the presence of CuI in gel electrolyte, films of gel electrolyte were deposited on Corning glass (7059) by the spin coating unit. Figure 4 shows the XRD pattern of the films before and after dispersion of CuI in gel electrolyte. It shows the presence of CuI in gel electrolyte with the preferential orientation in (111) direction.

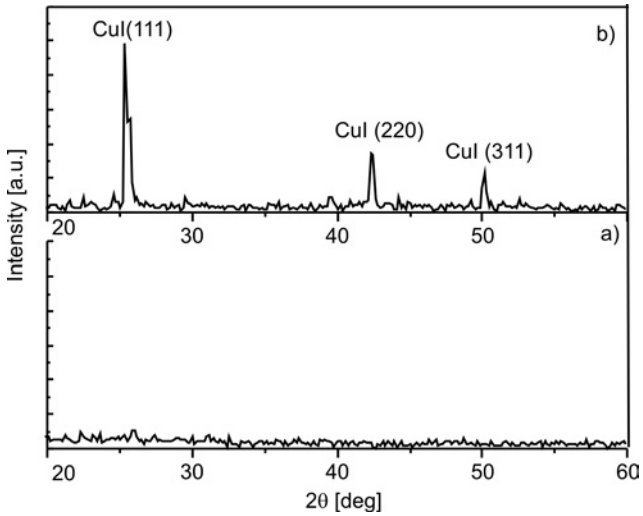

Fig. 4. XRD patterns of a gel electrolyte (a) and dispersed CuI (b) in gel electrolyte

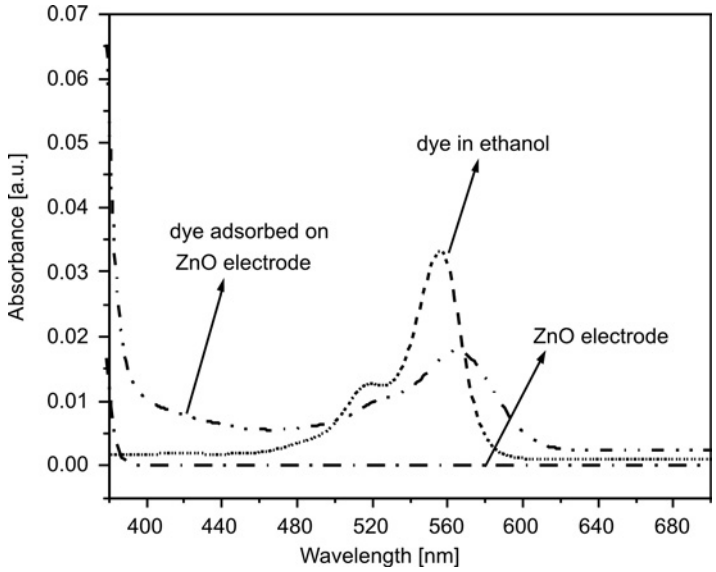

Fig. 5. UV-VIS absorption spectra of the Rose Bengal dye on ZnO surface

The absorbance of a ZnO electrode with and without dye is shown in Fig. 5. The absorption spectrum shows that the dye absorbs visible light in the 400–670 nm range with the maximum absorption at 564 nm. A broader absorption spectrum of the dye on the porous layer of ZnO is observed as compared with that in ethanol.

3.2. Effect of dispersion of CuI particles in gel electrolyte (*J–V* measurement)

Figure 6 shows the *J–V* characteristics of cells A and B. The *J–V* characteristic of a solar cell without CuI is also shown in the figure. The obtained solar cell parameters are given in Table 1. The cell made without the use of CuI was characterized by J_{sc} = 6.21 mA, V_{oc} = 0.58 and η = 1.92%. Enhancement in the photovoltaic performance is observed when CuI was used in the cell structure, and the increment in performance depends on the fabrication technique (layer or dispersed form). The J_{sc}, V_{oc}, *FF*, and η for the cell A having CuI in a layer form were found to be 7.45 mA·cm^{-2}, 0.56 V, 0.54, and 2.26% respectively while the solar cell B with CuI in a dispersed form by J_{sc} = 8.75 mA·cm^{-2},V_{oc} = 0.59 V, *FF* = 0.52 and η = 2.67%. It may be mentioned that various cells were fabricated under identical conditions. There was no significant change in the *J–V* characteristics, including the value of V_{oc} and J_{sc}.

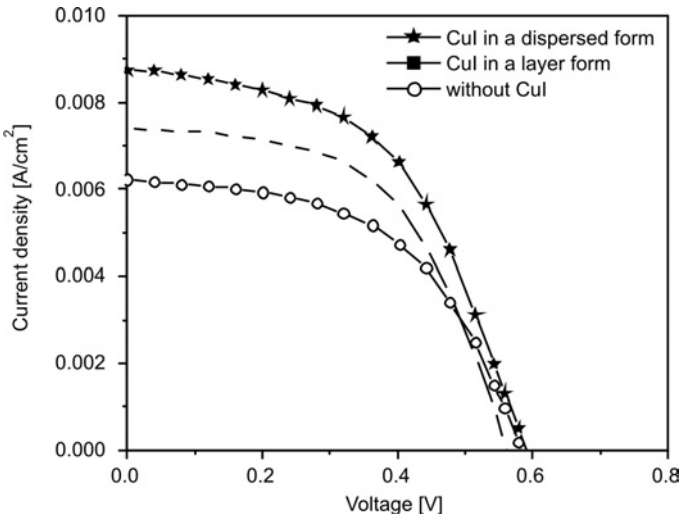

Fig. 6. *J–V* characteristics of solar cells showing the effect of addition of CuI on photovoltaic performance

Table 1. Photovoltaic parameters of DSSC employing CuI in various forms

Solar cell	J_{sc} [mA/cm^2]	V_{oc} [V]	FF	η [%]
Without CuI	6.21	0.58	0.53	1.92
CuI in a layer form	7.45	0.56	0.54	2.26
CuI in a dispersed form	8.75	0.59	0.52	2.67

Figure 7 shows the influence of CuI concentration on the performance of DSSC. When 0.3 cm^3 of CuI (0.16 M) was added to 0.9 cm^3 of gel electrolyte (the ratio of CuI to gel electrolyte was 1/3), V_{oc}, J_{sc} and η were found to have maximum values. V_{oc} decreases as the ratio of CuI/gel increases. J_{sc} and η also showed the same trend.

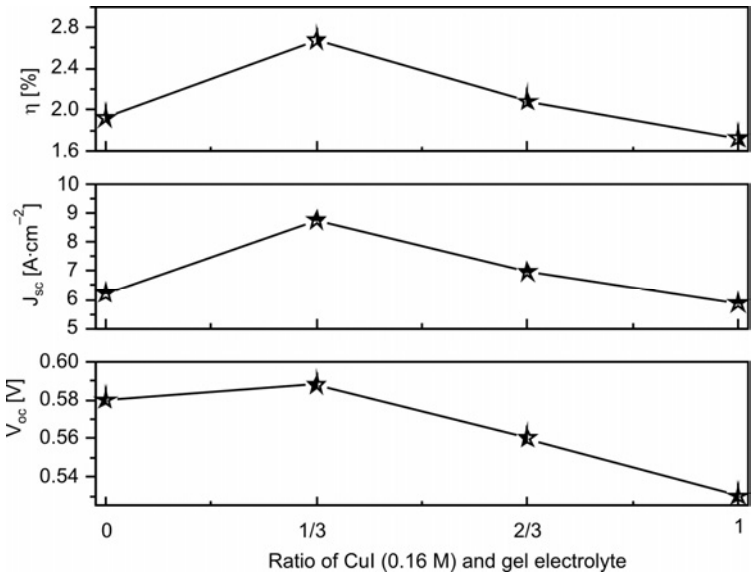

Fig. 7. Influence of the CuI concentration in gel electrolyte on the performance of DSSC

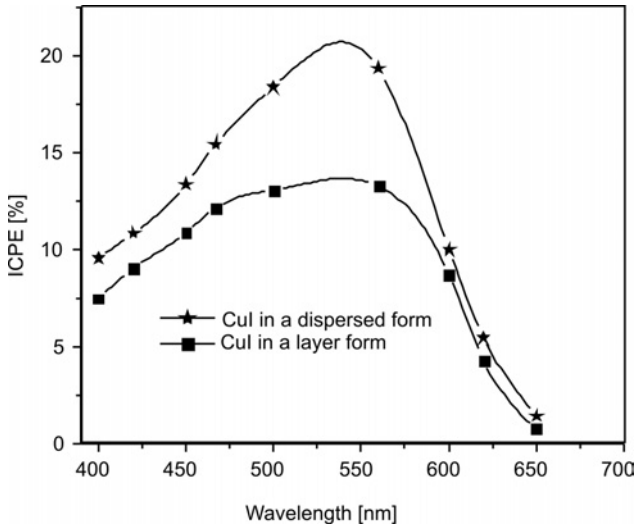

Fig. 8. Effect of layered and dispersed CuI on IPCE of a solar cell

Figure 8 shows the IPCE of the two solar cells A and B. Cells A and B show a maximum IPCE of ca. 14% and 20% at 564 nm, respectively. The peak in IPCE spectra

at ca. 564 nm is close to the observed peak in the absorbance of the ZnO electrode sensitized with RB dye. One of the recent papers also reports that the sensitization of TiO_2 layer with RB causes a widening of the spectral response covering the visible region, and results in high value of IPCE [28]. In the present case, also this could be the reason for a high value of IPCE in the range of 400–470 and 600–650 nm.

The IPCE is expressed in terms of the light harvesting efficiency of the dye (LHE), the quantum yield of electron injection (η_{inj}) and the efficiency of collecting the injected electrons (η_{cc}) at the transparent back contact, as described in [29]:

$$\mathrm{IPCE}(\lambda) = \mathrm{LHE}(\lambda)\eta_{inj}\eta_{cc}$$

A high IPCE is the result of either efficient light harvesting by the dye, efficient charge injection into ZnO, or efficient collection of injected electrons.

In the present case, only the conducting property of the electrolyte has been modified. The observed increase in the value of IPCE with the dispersion of CuI in TPAI+PEG gel electrolyte indicates an efficient collection of holes at the back contact.

3.3. Mechanism for achieving higher photocurrent density

Several workers have attempted to improve the properties of electrolytes by adding nanofillers such as TiO_2 particles, MWCNT and carbon black [17, 30–32]. It has been shown that the addition of nano fillers in the ionic liquid electrolyte reduces the resistance of the electrolyte and increases the redox couple mobility. Recently, Chen et al. [33] used CuI as an additive in an ionic liquid electrolyte (HMImI). It has been shown that CuI dissolves in HMImI and exists as Cu^+ and I^- in the electrolyte. Cu^+ ions are adsorbed on TiO_2 which results in the increase in I_{sc} and the decrease in V_{oc}.

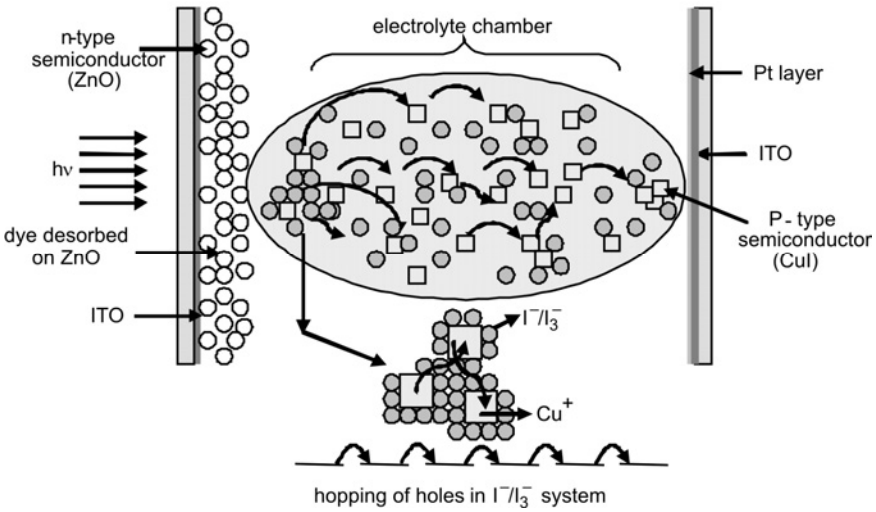

Fig. 9. Mechanism of hole transport in dispersed CuI gel electrolyte

In the present case (Cell B), the dispersion of CuI in the gel electrolyte (TPAI + PEG) resulted in the increase in I_{sc} without affecting V_{oc} unlike the values obtained for Cell A which had a layer of CuI on the ZnO electrode. It is assumed that the dispersed CuI dissociates into Cu^+ and I^- ions in the gel electrolyte and forms $Cu^+/I^-/ I_3^-$ complexes, thereby introducing local ordering of the redox couple as shown in Fig. 9. This local ordering facilitates the hole conduction at back electrode which results in the higher conversion efficiency of the solar cell B. The efficiency of DSSC increased from 1.92 to 2.67% (Table 1) by the introduction of hole conducting agent CuI to the gel electrolyte (TPAI + PEG). Figure 9 illustrates the hopping of positive charges (holes) between I^- / I_3^- and Cu^+.

3.4. Effect of ZnO compact layer on photovoltaic performance

The photovoltaic properties of fabricated solar cell B was further improved by applying ZnO compact layer on a conductive glass substrate. The introduction of a thin, ZnO compact layer in a dye sensitized solar cell can prevent a short circuit in the cell and therefore may inhibit the back transfer of electrons by blocking direct contact between the electrolyte and the conductive glass substrate [6]. Figure 10 shows the photocurrent density–voltage characteristics of solar cells, and the cell parameters are given in Table 2.

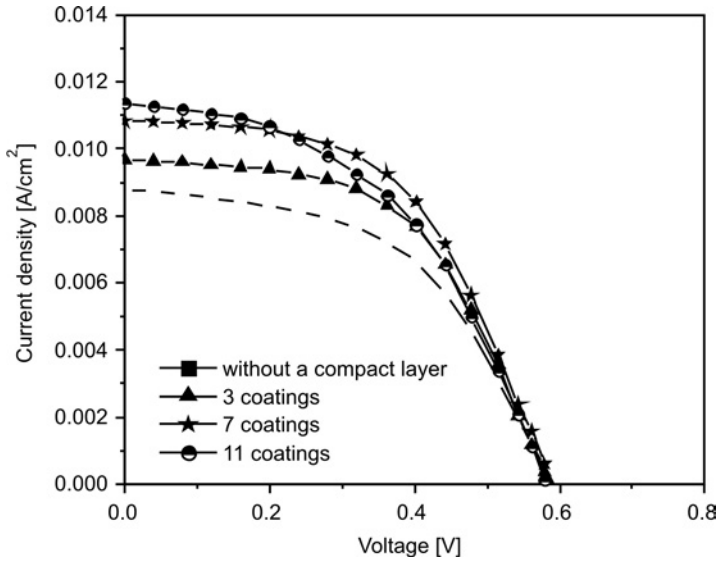

Fig. 10. *J–V* characteristics of a dispersed CuI solar cell with various numbers of compact layer coatings

When a ZnO compact layer was applied to cell B, the cell was found to exhibit an increase in efficiency from 2.67 to 3.38%. On applying 3 coatings of compact layer

(thickness ca. 42 nm), the efficiency increased from 2.67 to 3.06%. Efficiency was found to increase up to 3.38% with 7 numbers of coatings of compact layer corresponding to the thickness of 106 nm. With 11 coatings of compact layer (~140 nm) the efficiency decreases from 3.38% to 3.12%. At the thickness of 140 nm, the compact layer becomes thick enough to hinder the electrons from reaching the anode, which in turn worsens the performance of a solar cell [34].

Table 2. Photovoltaic parameters of DSSC with a ZnO compact layer

No. of compact layers	Thickness [nm]	J_{sc} [mA/cm^2]	V_{oc} [V]	FF	η [%]
Without layer	0	8.75	0.59	0.52	2.67
3	42±1	9.66	0.59	0.54	3.06
7	106±1	10.83	0.59	0.53	3.38
11	140±1	11.34	0.58	0.48	3.12

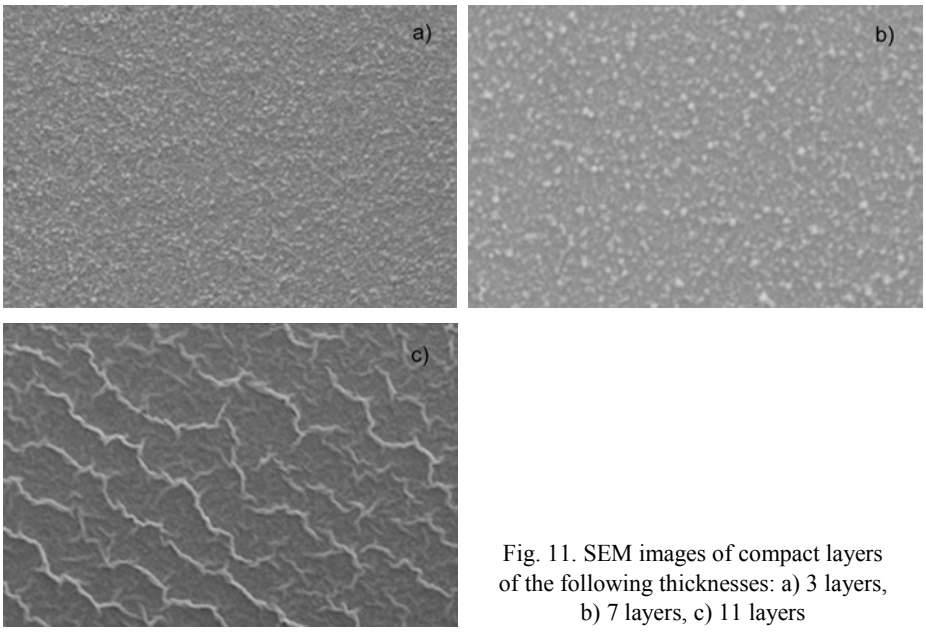

Fig. 11. SEM images of compact layers of the following thicknesses: a) 3 layers, b) 7 layers, c) 11 layers

Figure 11 shows the surface morphology (SEM images) of the compact layers 42, 106 and 140 nm thick. Uniformly tight packed grains of ZnO (Fig. 11a, b) convert into a tetrapod-like textured surface with sharp boundaries.

4. Conclusions

Dispersion of CuI in a gel electrolyte improves the cell parameters. It is envisaged that the dispersion of CuI in the gel electrolyte results in the formation of $Cu^+/I^-/I_3^-$

complexes thereby, introducing local ordering of the redox couple. This local ordering facilitates the hole conduction towards the back electrode, thereby improving the conversion efficiency of the DSSC. Use of a ZnO compact layer in ZnO/Rose Bengal/dispersed CuI gel electrolyte cell further increases the efficiency of the solar cell, due to prevention of back transfer of electrons by blocking direct contact between the electrolyte and the conductive substrate.

Acknowledgements

This work has been financially supported under the MNRE project No. 31/7/2004–05/PV-R&D, Govt. of India. One of the authors, S.R., gratefully acknowledges the financial support in the form of JRF from UGC, New Delhi.

References

[1] O'REGAN B., GRATZEL M., Nature, 353 (1991), 737.
[2] NAZEERUDDIN M.K., KAY A., RODICIO I., HUMPHRY-BAKER R., MULLER E., LISKA P., LACHCHOPOULOS N., GRATZEL M., J. Am. Chem. Soc., 115 (1993), 6382.
[3] O'REGAN B., SCHWARTZ DANIEL T., Chem. Mater., 10 (1998), 1501.
[4] TENNAKONE K., KUMARA G.R.R.A., KUMARSINGHE A.R., WIJAYANTHA K.G.U., SIRIMANNE P.M., Semicond. Sci. Technol., 10 (1995), 1689.
[5] MURAKOSHI K., KOGURE R., YANAGIDA S., Chem. Lett., 5 (1997), 471.
[6] BACH U., WEISSORTEL F., UEBE J., GRATZEL M., SALBECK D.W., Abstract Book, Bayreuth Polymer and Material Research Symposium, 1997, p. 28.
[7] MENG Q.B., TAKAHASHI K., ZHANG X.T., SUTANTO I., RAO T.N., SATO O., FUJISHIMA A., WATANABE H., NAKAMORI T., AND URAGAMI M., Langmuir 19 (2003), 3572.
[8] BACH U., LUPO D., COMTE P., MOSER J.E., WEISSORTEL F., SALBECK J., SPREITZER H.& GRATZEL M., Nature, 395 (1998), 583.
[9] NOGUERIA A.F., DURRANT J.R., DEPAOLI M.A., Adv. Mater., 13 (2001), 826.
[10] WANG P., ZAKEERUDDIN S.M., GRÄTZEL M., J. Fluorine Chem., 125 (2004), 1241.
[11] WANG H., LI H., XUE B., WANG Z., MENG Q., LIQUAN C., J. Am. Chem. Soc., 127 (2005), 6394.
[12] XUE B., WANG H., HU Y., LI H., WANG Z., QINGBO M., HUAN X.G., SATO O., CHEN L., FUJISHIMA A., Photochem. Photobiol. Sci., 3 (2004), 918.
[13] NAKAHARA K., TAKASU H., FONS P., YAMADA A., MATSUBARA K., HUNGER R., NIKI S., Appl. Phys. Lett., 79 (2001), 4193.
[14] RANI S., SURI P., SHISHODIA P.K., MEHRA R.M., Solar En. Mater. Solar Cells, 92 (2008), 1639.
[15] KUMARA G.R.A., KANEKO S., SHIRATSUCHI K., TSUKAHARA J., TENNAKONE K., Chem. Mater., 14 (2002), 954.
[16] WANG P., ZAKEERUDDIN S.M., EXNAR I., GRATZEL M., Chem. Commun., 24 (2002), 2972.
[17] USUI H., MATSUI H., TANABE N., YANAGIDA S., J. Photochem. Photobiol. A: Chem., 164 (2004), 97.
[18] KUBO W., KITAMURA T., HANABUSA K., WADA Y., YANAGIDA S., Chem. Commun., 4 (2002), 374.
[19] WANG P., ZAKEERUDDIN S.M., EXNAR I., GRATZEL M., J. Am. Chem. Soc., 125 (2003), 1166.
[20] PRADHAN B., BATABYAL S.K., PAL A.J., Solar En. Mater. Solar Cells 91 (2007), 769.
[21] DUFFY N.W., PETER L.M., RAJAPAKSE R.M.G., WIJAYANTHA K.G.U., J. Phys. Chem. B, 104 (2000), 8916.
[22] MLCHIO M., SHIGEYUKI M., HIROSHI T., Ind. Eng. Chem. Prod. Res. Dev., 19 (1980), 415.
[23] GUILLENA E., CASANUEVA F., ANTA J.A., VEGA-POOT A., OSKAM G., ALCANTARA R., FERNANDEZ -LORENZO C., MARTIN-CALLEJA J., J. Photochem. Photobiol. A: Chem., 200 (2008), 364.

[24] MAJUMDER S.B., AGARWAL D.C., MOHAPATRA Y.N., KULKARNI V.N., Integr. Ferroelectr., 9 (1995), 271.
[25] GODOVSKY D., CHEN L., PETTERSSON L., INGANAS O., ANDERSSON M.R., HUMMELEN J.C., Adv. Mater. Opt. Electron., 10 (2000), 47.
[26] BEREZNEV S., KOEPPE R., KONOVALOV I., KOIS J., GUNES S., OPIK A., MELLIKOV E., SARICIFTCI N.S., Thin Solid Films, 515 (2007), 5759.
[27] WEST A.R., *Solid State Chemistry and Its Application*, Wiley, New York, 1984, p. 174.
[28] ROY M.S., BALRAJU P., MANISH K., SHARMA G.D., Solar En. Mater. Solar Cells, 92, (2008), 909.
[29] SODERGREN S., HAGFELDT A., OLSSON J., LINDQUIST S.E., J. Phys. Chem., 95 (1994), 5522.
[30] BING L., PING C., CHANG-SHENG D., Chin. J. Chem. Phys., 20, (2007), 816.
[31] KANG M.-S., AHN K.-S., LEE J.-W., J. Power Sources, 180 (2008), 896.
[32] STERGIOPOULOS T., ARABATZIS I.M., KATSAROS G., FALARAS A.P., Nano Lett., 2 (2002), 1259.
[33] CHEN L.-H., XUE B.-F., LIU X.-Z., LI K.-X., LUO Y.-H., MENG Q.-B., WANG R.-L., CHEN L.-Q., Chin. Phys. Lett., 2 (2007), 555.
[34] BIN P., JUNGMANN G., JAGER C., HAARER D., SCHMIDT H.W., THELAKKAT M., Coord. Chem. Rev., 248 (2004), 1479.

Received 18 December 2008
Revised 10 July 2009

Materials Science-Poland, *Vol. 28*, *No. 1*, *2010*

Influence of CaO reactivity on the formation of low-base calcium silicate hydrates

K. BALTAKYS*, E. PRICHOCKIENE

Department of Silicate Technology, Kaunas University of Technology,
Radvilenu 19, LT – 50270 Kaunas, Lithuania

The influence of CaO reactivity on the formation of calcium silicate hydrates in the $CaO–SiO_2·nH_2O–H_2O$ system has been determined when the CaO/SiO_2 molar ratio was equal to 0.83 and 1.0. In a pure $CaO–SiO_2·nH_2O–H_2O$ system, with CaO/SiO_2 = 0.83, C–S–H (I) is rather stable, and at 175 °C, even after 72 h, only partially recrystallizes into 1.13 nm tobermorite. Meanwhile, in the mixtures with less reactive CaO (96%), the stoichiometric composition (CaO/SiO_2) of products of the synthesis varies from 0.66 to 0.83. When the CaO/SiO_2 molar ratio in the initial mixture is equal to 1.0, the CaO reactivity has a significant effect on the composition of products forming in hydrothermal conditions. The products of the syntheses were characterized by X–ray diffraction analysis, simultaneous thermal analysis and Fourier transform infrared spectroscopy.

Keywords: *calcium silicate hydrate; 1.13 nm tobermorite; gyrolite; CaO reactivity*

1. Introduction

The most common calcium silicate hydrates found in nature, produced in laboratories and formed in silicate products during hydrothermal treatment – or in autoclaved or hot-pressed materials – are C–S–H (I), 1.13 nm tobermorite, xonotlite, gyrolite. The formation of these calcium silicate hydrates depends on the duration and temperature of hydrothermal synthesis, stoichiometric composition of the initial mixture (CaO/SiO_2 (C/S) molar ratios), granulometric composition (grading) and strain of the raw materials, the additives used, mixing intensity and other factors [1–5].

Low-base (C/S = 0.6–1.5) and high-base (C/S = 1.5–2.0) calcium silicate hydrates belong to the set of key binding compounds [6]. They can be used as fillers for the production of rubber, plastics, paper, paint; for cleaning water contaminated with heavy and radioactive metal ions, for non-asbestos heat insulations, for adsorbents of

*Corresponding author, e-mail: kestutis.baltakys@ktu.lt

organic and inorganic effluents, cation exchangers [7]. Therefore, calcium silicate hydrates formed under hydrothermal conditions are the subject of numerous scientific studies.

The 1.13 nm tobermorite is the most prevalent among calcium silicate hydrates found in nature and obtained during autoclave treatment. This compound was first described by Heddle [8]. Tobermorite is known to have four different strains: 0.9 nm tobermorite – riversidite, 1.13 nm tobermorite, 1.4 nm tobermorite – plombierite, and clinotobermorite [9–11]. The 1.13 nm tobermorite $Ca_5(Si_6O_{18}H_2)\cdot 4H_2O$ can be reproduced in the laboratory in hydrothermal conditions when C/S = 0.8–1.0 [2]. The typical interplatelet distances *d* of 1.13 nm tobermorite are 1.13 and 0.297 nm.

From the wollastonite group of calcium silicate hydrates, xonotlites $Ca_6(Si_6O_{17})(OH)_2$ are of great practical importance and interest [3, 4]. This compound can be synthesized at 190–400 °C when the molar ratio of the mixture is C/S = 1.0. Xonotlite is characterized by an interplatelet distance *d* of 0.7 nm [12]. Nocuń–Wczelik reports that synthesis of xonotlite highly depends on the SiO_2 strain and the temperature and duration of synthesis [13] and that xonotlite may be formed directly, without the formation of an intermediate mineral – 1.13 nm tobermorite.

Gyrolite ($2CaO\cdot 3SiO_2\cdot 2.5H_2O$), calcium silicate hydrate, rarely occurs as a natural mineral together with with zeolites as low-temperature hydrothermal replacement product of basic igneous rock. Synthetic gyrolite was hydrothermally synthesized by Flint et al. [14]. They indicated that after 6–42 days of hydrothermal synthesis at 150–350 °C, the only product – gyrolite forms when the C/S ratio changes from 0.5 to 0.66. Mackay and Taylor [15] synthesized this compound by isothermal curing at 150 °C within 76 days of. Later on, other scientists continued studies on the synthesis of gyrolite [16–18]. It was declared that gyrolite is stable at 120–200 °C in hydrothermal conditions under a saturated steam pressure. Truscottite ($Ca_{14}Si_{24}O_{58}(OH)_8\cdot 2H_2O$) forms at the temperature higher than 200 °C, although metastable gyrolite may be obtained at temperatures up to 270 °C. It is assumed that gyrolite forms only at a temperatures higher than 120 °C. The parameters of hydrothermal synthesis of gyrolite in unstirred suspensions, when initial mixtures were composed from CaO and $SiO_2\cdot nH_2O$ or quartz, were determined elsewhere [19]. The results of the research showed that the optimal temperature of the synthesis of gyrolite is rather high (approximately 200 °C) and that the duration is long (ca. 32 h) when amorphous $SiO_2\cdot nH_2O$ is used as the SiO_2 component.

Much scientific research is focused on the influence of calcium strains SiO_2 on the formation of calcium silicate hydrate [2, 5, 20]. Not much data has been published on the effects of reactivity of another raw material, CaO, on the synthesis of calcium silicate hydrates.

The aim of this work was to analyse the influence of reactivity of CaO on the formation of 1.13 nm tobermorite and xonotlite, as well as to analyse and explain the sequence of formations of intermediary compounds.

2. Experimental

The following reagents were used as starting materials: fine-grained $SiO_2 \cdot nH_2O$ (Reachim, Russia, ignition losses 21.28%, specific surface area S_a = 1155 m²/kg by Blaine), CaO (free CaO = 99.96%, S_a = 548 m^2/kg, time of lime slaking τ = 135 s, temperature of lime slaking 96 °C, Reachim, Russia) and CaO (free CaO = 96%, S_a = 320 m^2/kg, time of lime slaking τ = 430 s, temperature of lime slaking 94 °C, Reachim, Russia) were additionally burned at 1000 °C for 0.5 h.

The syntheses of calcium silicate hydrates were carried out in unstirred suspensions in stainless steel vessels. Calcium silicate hydrates were synthesized within 8, 16, 24 and 72 h at 175 °C using stoichiometric compositions (CaO/SiO_2 molar ratios were equal to 0.83 and 1.0, the water/solid ratio of the suspension was equal to 10.0) of the initial CaO and $SiO_2 \cdot nH_2O$ mixture. The products of the syntheses were filtered, rinsed with ethyl alcohol to prevent carbonization of materials, dried at 50 ± 5 °C and filtered through a sieve with a mesh width of 50 μm.

The X-ray powder diffraction data was collected with a DRON–6 X-ray diffractometer with the Bragg–Brentano geometry using Ni-filtered CuK_α radiation and a graphite monochromator, operating at the voltage of 30 kV and delivering an emission current of 20 mA. The step scan covered the angular range 2–60° (2θ) in steps of 2θ = 0.02°.

Simultaneous thermal analysis (STA: differential scanning calorimetry – DSC and thermogravimetry – TG) was carried out on a Netzsch instrument STA 409 PC applying the heating rate of 15 °C/min. The temperature ranged from 30 °C up to 1000 °C under an air atmosphere. Ceramic sample handlers and crucibles of Pt–Rh were used.

FTIR spectra were obtained with the aid of a Perkin Elmer FTIR Spectrum X system. Specimens were prepared by mixing 1 mg of the sample with 200 mg of KBr. The spectral analysis was performed in the range of 4000–400 cm^{-1} with the spectral resolution of 1 cm^{-1}.

3. Results and discussion

After 8 h of isothermal curing at 175 °C in the Ca O–$SiO_2 \cdot nH_2O$–H_2O system, traces of 1.13 nm tobermorite (Fig. 1, curve 1, *d* spacing 1.1472, 0.5449, 0.3063, 0.2967, 0.2804, 0.1834, 0.1670 nm, the area of the endothermic effect at 220 °C is equal to 5.72 μV·s/mg, according to the tangent method) together with C–S–H (I) were formed (Fig. 1, curve 1, *d* spacing 0.3048, 0.1834 nm, the area of the exothermic effect at 833 °C is equal to 41.24 μV·s/mg according to the tangent method). By prolonging the duration of synthesis, an increasing amount of 1.13 nm tobermorite is formed in the product, due to an increase in the intensity of its characteristic diffraction peak, whose interplanar distance is *d* ~1.13 nm, and the area of the endothermic effect at 219 °C is 8.31 μV·s/mg (Fig. 1, curve 2). It should be underlined that even

after an isothermal exposure for 72 h, the identified endothermic effect (i.e., the area measuring 9.34 μV·s/mg) at 848 °C indicates that a small amount of C–S–H (I), which had insufficient time for recrystallisation into 1.13 nm tobermorite, remains in the products (Fig. 1b, curve 3). These data was confirmed by differential scanning calorimetry: at 225 °C the area of the endothermic effect increased to 18.97 μV·s/mg (Fig. 1b, curve 3).

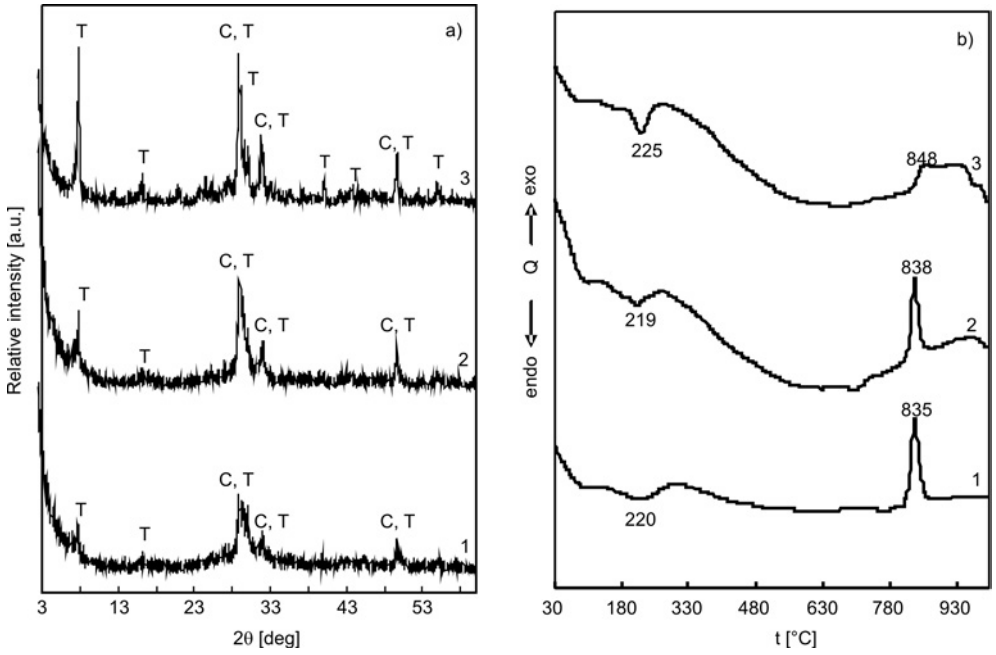

Fig. 1. X-ray diffraction patterns (a) and DSC curves (b) of the products of synthesis; the initial C/S molar ratio is equal to 0.83. Duration [h] of hydrothermal syntheses at 175 °C: 1 – 8; 2 – 16; 3 – 72; C – C–S–H (I), T – 1.13 nm tobermorite

Thus, in a pure CaO–SiO_2·nH_2O–H_2O system, C–S–H (I) which formed at the beginning of the synthesis, is sufficiently stable and at 175 °C, even after 72 h, it only partially recrystallizes into 1.13 nm tobermorite.

In mixtures with less reactive CaO (96%), changes occur not only in the sequence of the formed compounds, but also in their stability limits. After 8 h of hydrothermal synthesis, a semicrystalline calcium silicate hydrate C–S–H (I) and traces of 1.13 nm tobermorite were formed (Fig. 2, curve 1). It should be noted that 1.13 nm tobermorite becomes a dominant compound after 24 h of hydrothermal treatment (Fig. 2, curve 2). After extending the duration of isothermal curing to 72 h, unexpected results were obtained: the intensity of peaks characteristic of the 1.13 nm tobermorite in X-ray patterns decreased (Fig. 2, curve 3). Together with this compound, a low-base calcium silicate hydrate – gyrolite – begins to form (according to stoichiometry of this compound, the C/S molar ratio is equal to 0.66). Thermal conversions characteristic of this compound were identified in the DSC curve: endothermic (at 148 °C) and exothermic

(at 793 °C) (Fig. 3a). Presumably, one of the reasons for this is that the less active CaO is less soluble in water, moreover, that the water solubility of CaO, upon raising the temperature from 20 °C to 175 °C, decreases from 1.58 g/dm^3 to 0.17 g/dm^3 [21]. The larger amount of impurities and a smaller surface area of CaO change the time of lime slaking and thus influence the formation of calcium silicate hydrates. This means that the molar ratio of the reacting mixture is lower than in the raw materials, i.e. intermediate between 0.66 and 0.83, and there occur favourable conditions for the simultaneous crystallisation of the two compounds – gyrolite and 1.13 nm tobermorite.

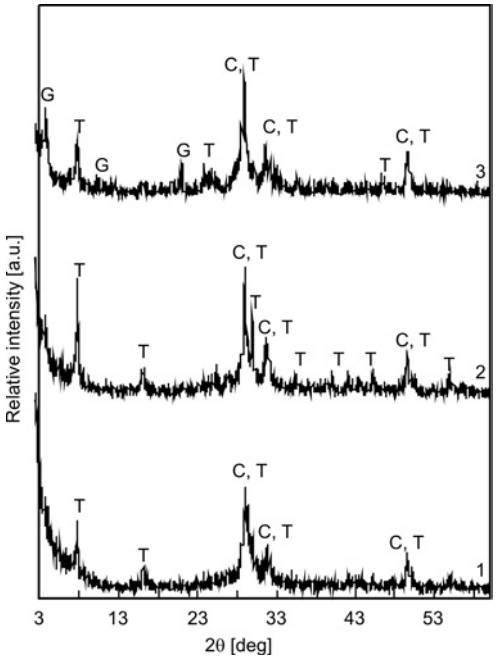

Fig. 2. X-ray diffraction patterns of the products of the synthesis; the C/S molar ratio is equal to 0.83 (less reactive CaO). Duration [h] of hydrothermal syntheses at 175 °C: 1 – 8; 2 – 24; 3 – 72; C – C–S–H (I), T – 1.13 nm tobermorite, G – gyrolite

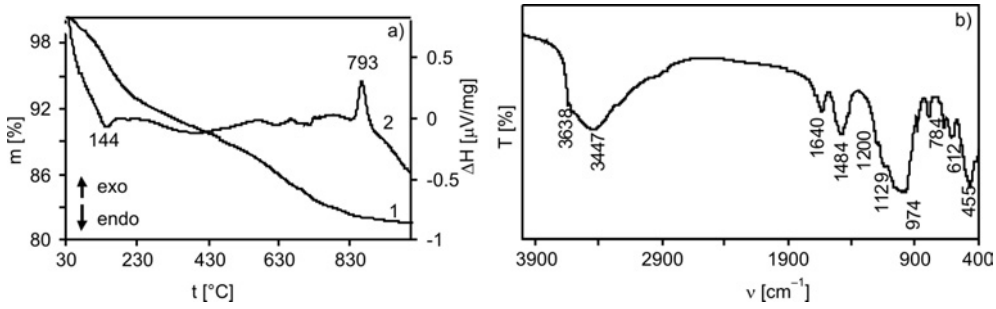

Fig. 3. STA curve (TGA – 1, DSC – 2) (a) and FTIR spectrum (b) of the products of the 72 h hydrothermal synthesis at 175 °C; the C/S molar ratio is equal to 0.83 (less reactive CaO)

All these results were confirmed by FTIR spectroscopy data, which can be used to distinguish gyrolite from other calcium silicate hydrates [22]. A sharp peak near

3635 cm^{-1} is visible only in the gyrolite spectrum (Fig. 3b). This clear band (3638 cm^{-1}) proves that clearly distinguished OH positions exist in the structure of gyrolite, which are connected only with Ca atoms and are not influenced by hydrogen bridge links. A wide band near 3447 cm^{-1} means the opposite – that molecular water forms hydrogen bridge links in the interlayers. The bands in the 1640 cm^{-1} frequency range are assigned to $\delta(H_2O)$ vibrations and confirm this presumption. Thus, the sequence of the formation of calcium silicate hydrates is highly dependent on the reactivity of the initial materials used for the preparation of the mixture – in this case, on the purity of CaO. It was found that in the mixtures with C/S = 0.83, the stoichiometric factor of products of the synthesis varies from 0.66 to 0.83 and depends on the CaO reactivity.

In order to evaluate the influence of higher CaO reactivity on the mixtures of higher basicity, i. e. with C/S = 1.0, similar hydrothermal syntheses were carried out. It was found that the reactivity of CaO has by far a great effect on the formation of monobasic calcium silicate hydrate. During the first 8 h of the synthesis, regardless of the CaO reactivity, a semicrystalline calcium silicate hydrate C–S–H (I) is formed (Fig. 4, curve 1, Fig. 6, curve 1).

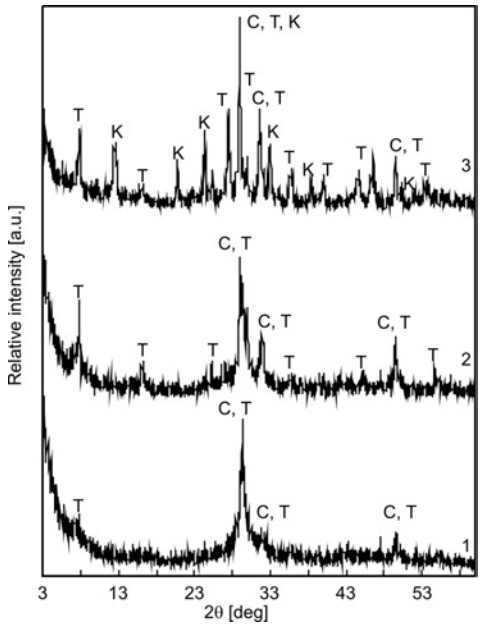

Fig. 4. X-ray diffraction patterns of the products of the synthesis; the C/S molar ratio is equal to 1.0. Duration [h] of hydrothermal syntheses at 175 °C: 1 – 8; 2 – 24; 3 – 72; C – C–S–H (I), T – 1.13 nm tobermorite, K – xonotlite

However, after 24 h of isothermal curing by using less reactive CaO, X-ray diffraction analysis curves showed only traces of 1.13 nm tobermorite (Fig. 6, curve 2), but if more reactive CaO is added to the initial mixture, 1.13 tobermorite having a noticeably higher degree of crystallization is formed (Fig. 4, curve 2). When the duration of the synthesis is prolonged even more, the effect of CaO reactivity on the composition of the product becomes even more obvious. When CaO of the lower reactivity is used in primary mixtures, 1.13 nm tobermorite and traces of gyrolite are formed

(Fig. 6, curve 3). The thermal conversion characteristic of gyrolite was identified in the DSC curve as an endothermic peak at 144 °C and an exothermic peak at 793 °C (Fig. 7a, curve 2). FTIR spectroscopy data supports the DSC results (Fig. 7b). It should be noted that typical peaks characteristic of xonotlite have not been identified in the X-ray diffraction analysis curves, even though the molar ratio C/S = 1.0 of the initial mixture corresponded specifically to the stoichiometric composition of this compound. In the mixture with more reactive CaO, both compounds – 1.13 nm tobermorite and xonotlite – are already formed after 72 h of synthesis (Fig. 4, curve 3). Thermal conversions characteristic of 1.13 nm tobermorite were identified in the DSC curve as an endothermic peak at 220 °C (Fig. 5a, curve 1).

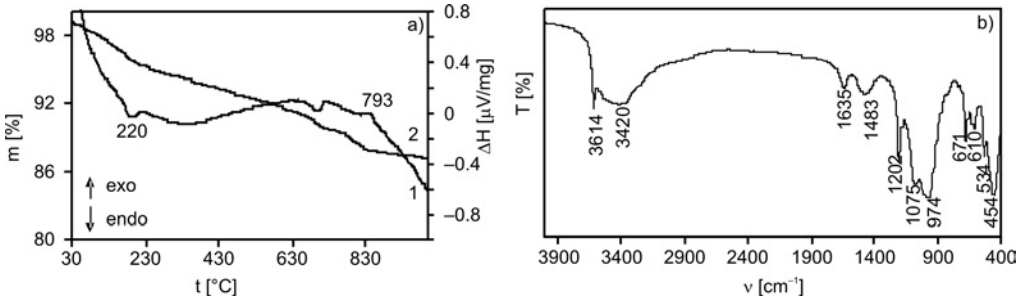

Fig. 5. STA curve (1 – DSC, 2 – TGA) (a) and FTIR spectrum (b) of the products of the 72 h hydrothermal synthesis at 175 °C when the C/S molar ratio is equal to 1.0

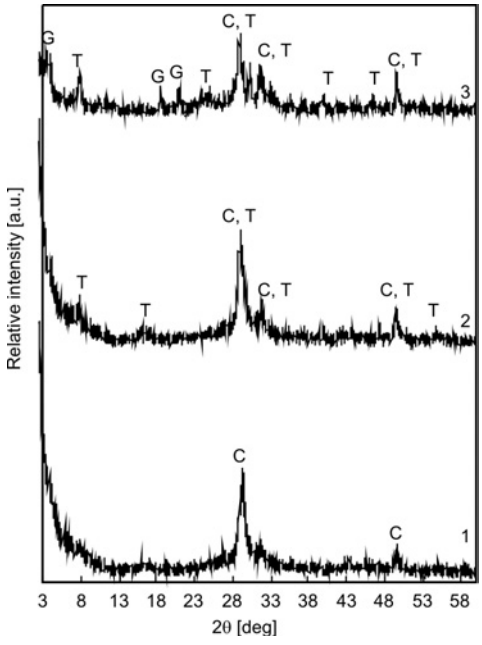

Fig. 6. X-ray diffraction patterns of the products of the synthesis; the C/S molar ratio is equal to 1.0 (less reactive CaO). Duration [h] of hydrothermal syntheses at 175 °C: 1 – 8; 2 – 24; 3 – 72; C – C–S–H (I), T – 1.13 nm tobermorite, G – gyrolite

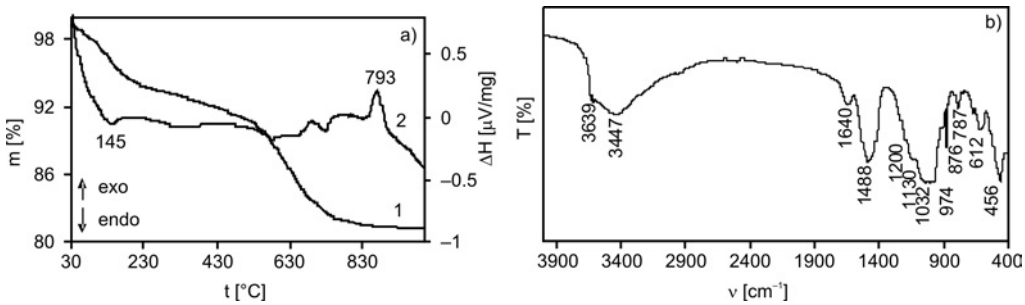

Fig. 7. STA curve (1 – DSC, 2 – TGA) (a) and FTIR spectrum (b) of the products of the 72 h hydrothermal synthesis at 175 °C when C/S molar ratio is equal to 1.0 (less reactive CaO)

Data that can be used to distinguish xonotlite from other calcium silicate hydrates [22] were confirmed by FTIR spectroscopy results: sharp peaks near 3614 cm^{-1} and near 1202 cm^{-1} are visible only in the xonotlite spectrum (Fig. 5b). Thus, when in the initial mixture the C/S molar ratio is equal to 1.0, CaO reactivity has a significant effect on the composition of products forming in hydrothermal conditions.

Thus the formation of calcium silicate hydrates proceeds during the reaction $CaO + SiO_2 \cdot nH_2O + H_2O$ under the outer surface of the particles of reagents. According to kinetic theory with influence of diffusion, when the crystallization products react at the outer surface of particles, the apparent order of reaction n is close to zero:

$$w_{app} = \frac{dx_{CaO}}{d\tau} = k_{app} F_R \left(\frac{dx}{dl}\right)^n$$

where w_{app} is the rate of reaction, k_{app} – a constant of apparent reaction, F_r – reactive surface of CaO, dx/dl – gradient of reagent concentration, n – apparent order of reaction.

$$\left(\begin{array}{c}\text{Particle of CaO}\\ O_{\text{Fr}}\end{array}\right) \xrightarrow{\tau,\ t, p, SiO_2 \cdot nH_2O} \text{C–S–H} \left(\begin{array}{l}\text{the former calcium silicate hydrate}\\ \text{composition depends}\\ \text{on the conditions of synthesis}\end{array}\right)$$

$$\downarrow$$

$$n \to 0$$

$$\left(\frac{dx}{dl}\right) \to 1;$$

$$w_{app.} = f(F_r)$$

It is obvious that the outer surface area of particles increases when the particles are milled. In this case, the apparent order of reaction increases as well. Therefore, the

factor limiting the formation of calcium silicate hydrate is the outer surface area F_r of calcium oxide particles.

It should be underlined that extra admixtures in the calcium oxide composition may have extra influence on the formation of products.

4. Conclusions

The reactivity of CaO changes the composition of intermediate and final products of the synthesis. In a pure Ca O–SiO_2·$n$$H_2O$–$H_2O$ system with CaO/SiO_2 = 0.83, the C–S–H (I) which forms at the beginning of synthesis is rather stable, and at 175 °C, even after 72 h, it only partially recrystallizes into 1.13 nm tobermorite. In the mixtures with less reactive CaO (96%), however, the stoichiometric composition of products of the syntheses varies from 0.66 to 0.83 because, together with 1.13 nm tobermorite, a low-base calcium silicate hydrate – gyrolite – begins forming.

When the CaO/SiO_2 molar ratio in the initial mixture is equal to 1.0, CaO reactivity has a significant influence on the composition of products forming in hydrothermal conditions. In the CaO–SiO_2·$n$$H_2O$–$H_2O$ system, after 72 h of synthesis at 175 °C in the mixture with more reactive CaO both compounds – 1.13 nm tobermorite and xonotlite – are formed. However, when the lower reactivity CaO is used in primary mixtures, only 1.13 nm tobermorite and traces of gyrolite are formed.

Acknowledgement

We gratefully thank A. Baltusnikas – a Head of X-ray diffraction analysis laboratory of KTU for carrying out X-ray analysis experiments and for his constructive comments on the paper.

References

[1] BALANDIS A., JASIUKEVICIUS V., MARTYNAITIS M., STRAZDAS K., *The Fundamentals of Silicate Technology*, The Institute of Scientific and Encyclopaedic Press, Vilnius, 1995 (in Lithuanian).
[2] TAYLOR H.F.W., *Cement Chemistry*, Academic Press, San Diego, 1997.
[3] MARTUSEVICIUS M., KAMINSKAS R., MITUZAS J., *The Chemical Technology of Binding Materials*, Technology, Kaunas, 2002 (in Lithuanian).
[4] MARTUSEVICIUS M., *Nonhydraulic Hydrated Binders,* Technology, Kaunas, 1993 (in Lithuanian).
[5] TAYLOR H.F.W., *Hydrothermal reactions in the system and autoclaved treatment of the products of cement and cement silicates*, Press of Constructional Literature, 4th National Congress of Cement Chemistry, Washington, 15 (1973), pp. 385–406 (in Russian).
[6] TAYLOR H.F.W., ROY D.M., *Structure and composition of hydrates*, Proc. 7th Int. Symposium on the Chemistry of Cement, Paris, 1 (1980), pp. 112/1–112/3.
[7] MOSTAFA N.Y., KISHAR E.A., ABO-EL-ENEIN S.A., J. Alloys Comp., 1–2 (2009), 538.
[8] HEDDLE M.F., Mineral. Mag., 30 (1954), 293.
[9] MERLINO S., BONACCORSI E., ARMBRUSTER T., Am. Mineral., 84 (1999), 1613.
[10] MERLINO S., BONACCORSI E., ARMBRUSTER T., Eur. J. Mineral., 12 (2000), 411.
[11] MERLINO S., BONACCORSI E., ARMBRUSTER T., Eur. J. Mineral., 13 (2001), 577.

[12] BUT YU.M., RASHKOVICH L.N., *The Hardening of Binding Materials at Higher Temperatures*, Constructional Press, Moscow, 1965 (in Russian).
[13] NOCUŃ-WCZELIK W., Cem. Concr. Res., 29 (1999), 1759.
[14] FLINT E.P., MCMURDIE H.F., WELLS L.S., J. Res. Natl. Bur. Stand., 21 (1938), 617.
[15] MACKAY A.L., TAYLOR H.F.W., Mineral Mag., 30 (1953), 80.
[16] STEVULA L., HARMAN M., HORVATH I., PUTYERA K., Ceramics – Silikaty, 34 (1990), 315.
[17] JAUBERTHIE R., TEMIMI M., LAQUERBE M., Cem. Concr. Res., 26 (1996), 1335.
[18] SHAW S., HENDERSON C.M.B., CLARK S.M., Am. Mineral., 87 (2002), 533.
[19] SIAUCIUNAS R., BALTAKYS K., Cem. Concr. Res., 34 (2004), 2029.
[20] BALTAKYS K., SIAUCIUNAS R., BALTUSNIKAS A., *Chemical Technology*, Kaunas, 1 (2004), 45.
[21] GUNDLACH H., *Dampfgehartete Baustoffe*, Bauverlag GmbH, Wiesbaden, 1973 (in German).
[22] SIAUCIUNAS R., BALTAKYS K., BALTUSNIKAS A., *The Instrumental Analysis of Silicate Materials*, Vitae Litera, Kaunas, 2007 (in Lithuanian).

Received 19 December 2008
Revised 9 June 2009

Materials Science-Poland, *Vol. 28*, *No. 1*, *2010*

Influence of frequency variations on the dielectric properties of Sm doped $Ba_4La_{9.33}Ti_{18}O_{54}$ dielectric ceramics at various temperatures

S. BINDRA NARANG*, S. BAHEL

Department of Electronics Technology B-18, Guru Nanak Dev University, Amritsar-143005, Punjab, India

The dependence of frequency variations on the dielectric properties of Sm substituted barium lanthanum titanate was investigated. Dielectric ceramics based on the $Ba_4(La_{1-y}Sm_y)_{9.33}Ti_{18}O_{54}$ system, where y = 0.0, 0.3, 0.5, 0.7, were synthesized and subsequently characterized for their structural and dielectric properties. The temperature dependences of the relative permittivity and the dielectric losses were measured in the frequency range from 10 kHz to 10 MHz, for temperatures ranging from 25 °C to 150 °C. The measurement system consisted of an impedance analyzer and a temperature chamber. Substituting Sm for La was an effective way to stabilize the variations in relative permittivity, within the temperature range of interest. No dielectric anomaly was observed in this temperature range. The temperature coefficient of the resonant frequency improved from 273.9 ppm/°C at y = 0.0 to 53.8 ppm/°C at y = 0.7. The relative permittivity of 90.33 and a dielectric loss of 0.09 were obtained at 25 °C for y = 0.5 at 10 MHz; the temperature coefficient of the resonant frequency was 106.8 ppm/°C. The materials under investigation have high relative permittivities, remaining constant under temperature variation, which therefore makes them suitable for applications in communication devices.

Keywords: *ceramics; relative permittivity; dielectric loss; temperature coefficient of resonant frequency*

1. Introduction

The revolution in microwave telecommunication and satellite broadcasting systems has created the need for good quality dielectric ceramics. The important properties required for these materials are a high electric permittivity ($\varepsilon_r > 70$) for miniaturization, low loss or a high quality factor ($Q > 2000$) for selectivity, and a low temperature coefficient of the resonant frequency (τ_f) for stability. The unique dielectric properties, namely high relative permittivity (70–100), low dielectric losses and low temperature coefficient of resonant frequency, of $Ba_{6-3x}R_{8+2x}Ti_{18}O_{54}$ (R is a rare earth atom such as La, Nd, Sm or Gd) solid solutions [1–3] make them very important

*Corresponding author, e-mail: sukhleen2@yahoo.com

for applications in communication devices. However, the requirements of modern communication technologies demand even greater improvements in the performance of the materials. Ohsato et al. [4–7] have extensively studied the structural and dielectric properties of $Ba_{6-3x}R_{8+2x}Ti_{18}O_{54}$ and found that the ordering of Ba^{2+} and R^{3+} ions at $x = 2/3$ leads to the lowest internal strain, which in turn results in a maximum quality factor. In this system, La based solid solutions [5, 7, 8] have the highest relative permittivity, but dielectric loss and the temperature coefficient of the resonant frequency (~300 ppm/°C) are also high. Some reports have been published on the improvement of dielectric properties of $Ba_{6-3x}R_{8+2x}Ti_{18}O_{54}$ solid solutions by A and/or B site substitution [9, 10]. In our previous paper [11], we have reported the required reduction in dielectric loss tangent by Sm substitution in $Ba_4La_{9.33}Ti_{18}O_{54}$ dielectric ceramic while keeping the high relative permittivity. Now, the main objective is the suppression of the temperature coefficient of the resonant frequency (τ_f) while retaining low dielectric loss and a high relative permittivity (ε_r). The goal of this study is to investigate the effect of various Sm substitutions on $Ba_6La_{9.33}Ti_{18}O_{54}$ solid solutions over a wide temperature and frequency range.

2. Experimental

Ceramic samples of $Ba_4(La_{(1-y)}Sm_y)_{9.33}Ti_{18}O_{54}$, where y = 0.0, 0.3, 0.5 and 0.7, were prepared using the high temperature solid state reaction technique. The stoichiometric mixtures of high purity powders of $BaCO_3$ (99.5%), La_2O_3 (99.9%), Sm_2O_3 (99.9%) and TiO_2 (99.5%) were weighed and ground for 12 h in methanol. The mixtures were then dried and calcined in air at 1100 °C for 2 h. The calcined powders were thoroughly re-ground, mixed with 3 wt. % of polyvinyl alcohol (PVA) as a binder and pressed into pellets of various shapes under the load of 98 kN. These pellets were then sintered at 1300 °C for 2h in air.

X-ray diffraction data were collected on a Philips, PWQ 1729 powder X-ray diffractometer using CuK_α radiation in the 2θ range from 20° to 80°. The microstructures of freshly fractured sintered samples were examined using a JEOL, JSM 6100 scanning electron microscope and an Oxford, INCA energy dispersive X-ray analyzer. The bulk densities of the sintered samples were measured by the Archimedes method.

Flat surfaces of the pellets were polished with high purity conductive silver paste. The dielectric properties, namely the relative permittivity and the dielectric loss in function of temperature in the range from 25 °C to 150 °C and frequency in the range from 10 kHz to 10 MHz, were calculated from the data recorded from an Agilent, HP 4192A impedance analyzer and a programmable temperature chamber interfaced with a PC. The temperature coefficients of the resonant frequency (τ_f) in the temperature range from 25 °C to 90 °C were estimated using the dependence [12]:

$$\tau_f = -\left(\frac{\tau_\varepsilon}{2} + \alpha\right)$$

where τ_ε is the temperature coefficient of the relative permittivity and α is the thermal expansion coefficient, which is about 10 ppm/°C [9] in the ceramics under study here.

3. Results and discussion

The XRD patterns and SEM micrographs of $Ba_4(La_{1-y}Sm_y)_{9.33}Ti_{18}O_{54}$ ceramics having different Sm content were reported earlier [11]. Detailed structural analysis, along with lattice parameters, has already been reported.

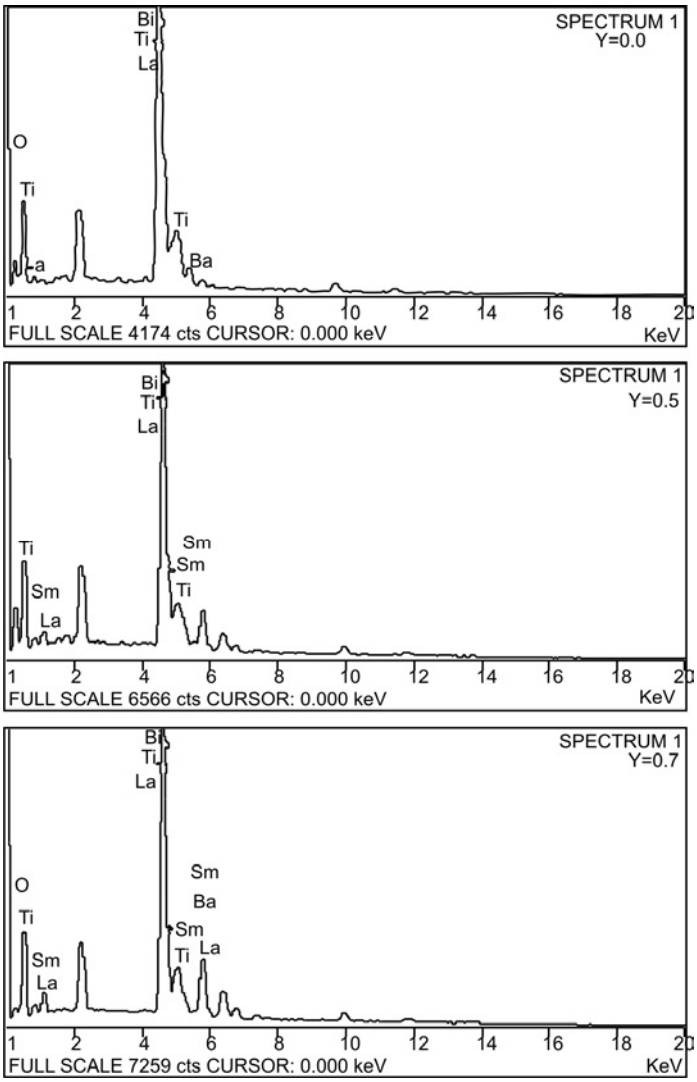

Fig. 1. Results of EDX analysis of $Ba_4(La_{(1-y)}Sm_y)_{9.33}Ti_{18}O_{54}$ for various Sm contents

It has been found that all the ceramic samples possess single phase of tungsten bronze-type compounds and have orthorhombic symmetry. Microstructural examination showed the presence of closely packed uniform hexagonal grains with low porosity. Figure 1 shows the results of the EDX analysis of three samples, with $y = 0.0$, 0.5 and y = 0.7. The observed and the calculated atomic concentration of various elements in $Ba_4(La_{(1-y)}Sm_y)_{9.33}Ti_{18}O_{54}$ solid solution are given in Table 1. This indicates the presence of expected elements (Ba, La, Sm, Ti and O) in the required proportions.

Table 1. Observed and calculated atomic concentrations [at. %] of various elements in $Ba_4(La_{(1-y)}Sm_y)_{9.33}Ti_{18}O_{54}$

Element	$y = 0.0$		$y = 0.5$		$y = 0.7$	
	Calculated	Observed	Calculated	Observed	Calculated	Observed
Ba	4.69	4.52	4.69	4.85	4.69	4.59
La	10.93	10.29	5.47	5.07	3.28	2.98
Sm	–	–	5.47	5.27	7.65	7.05
Ti	21.09	20.13	21.09	20.22	21.09	19.42
O	63.29	65.06	63.28	64.59	63.28	65.96

The bulk density for all the samples in function of Sm content is shown in Fig. 2. These ceramics have a high bulk density (>5.0 g/cm3), with a maximum of 5.46 gm/cc for y = 0.7, confirming the observed porosity diminution in the microstructures [11] (grain closeness).

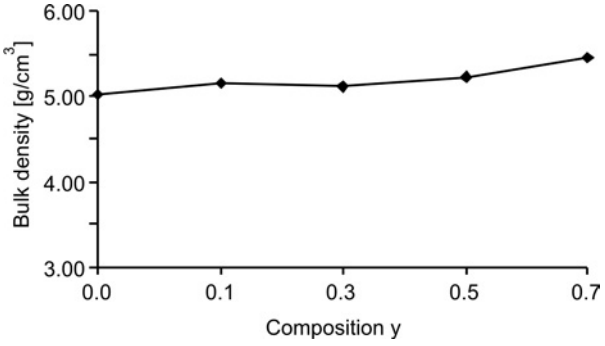

Fig. 2. Bulk densities of $Ba_4(La_{(1-y)}Sm_y)_{9.33}Ti_{18}O_{54}$ for various Sm contents

The dependences of relative permittivity and dielectric losses on frequency in the range of 10–10 MHz for various Sm contents at room temperature are shown in Figs. 3 and 4, respectively. The relative permittivity decreases from 106.44 for $y = 0.0$ to 90.33 for $y = 0.5$ and finally to 89.27 for $y = 0.7$ at 10 MHz. These results are in accordance with the variation in relative permittivity and loss at high frequencies (0.3 GHz–3.0 GHz) as previously reported [11]. The relative permittivity ε_r decreases

with the increase in Sm content, due to the substitution of Sm ions for La ions. The relative permittivity depends on the unit cell volume, tilting of octahedral strings along the *c* axis and polarizabilities of ions [5]. It is evident from previously reported results that the unit cell volume decreases with increase in Sm contents thereby decreasing ε_r. The tilting angle between the *c* axis and the central axis of the octahedra is smaller for larger sized ions [12]. The smaller ionic radii of Sm^{3+} ions (1.24 Å) than those of La^{3+} ions (1.36 Å) [13] cause an increase in the tilt of octahedra in solid solutions with higher Sm content, resulting in lower ε_r. Moreover, the third factor, i.e. the ionic polarizability of Sm^{3+} ions (4.74 $Å^3$), is lower than the ionic polarizability of La^{3+} ions (6.07$Å^3$) as reported by Shannon [14] also contributes towards decrease in ε_r.

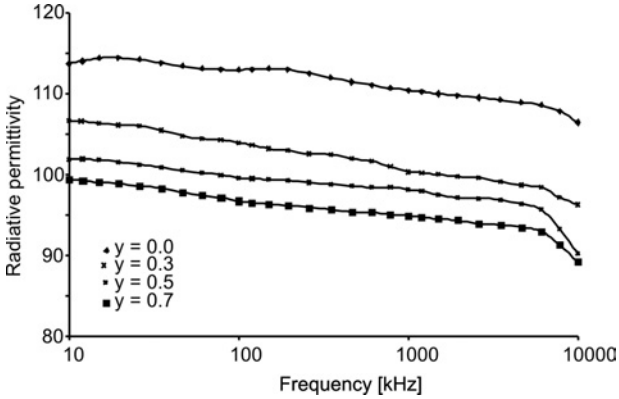

Fig. 3. Dependence of relative permittivity on frequency for various Sm contents at 25 °C

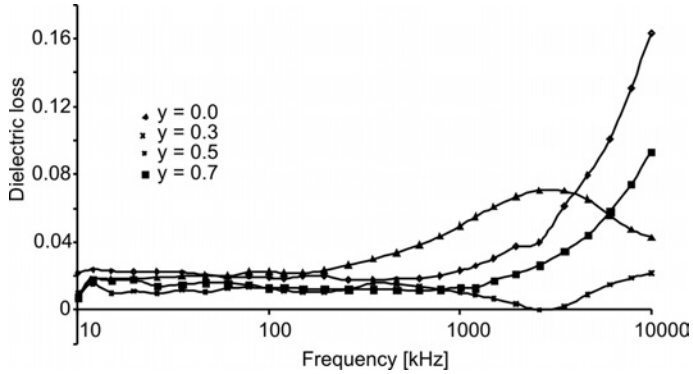

Fig. 4. Dependence of dielectric loss on frequency for various Sm contents at 25 °C

Figure 5 shows the dependence of the temperature coefficients of relative permittivity and resonant frequency on Sm contents. The estimated value of the temperature coefficient of relative permittivity decreases from –567.68 ppm/°C at $y = 0.0$, through –233.46 ppm/°C at $y = 0.5$ to –127.6 ppm/°C at $y = 0.7$. The corresponding values of τ_f also decrease from 273.9 ppm/°C at $y = 0.0$ to 106.8 ppm/°C at $y = 0.5$ and finally to 53.8 ppm/°C at $y = 0.7$.

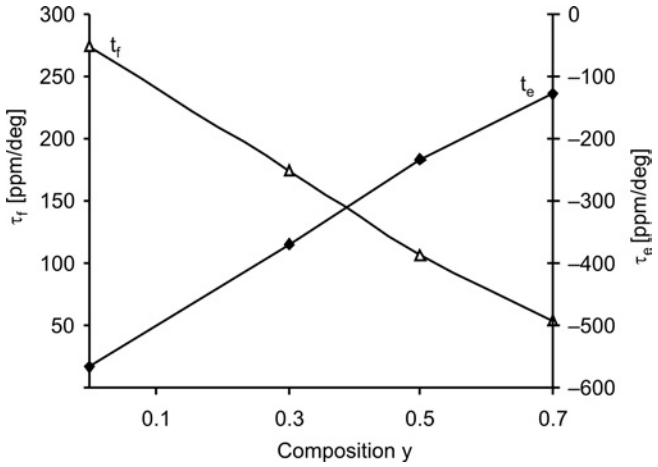

Fig. 5. Dependence of the temperature coefficient
of resonant frequency and relative permittivity for various Sm contents

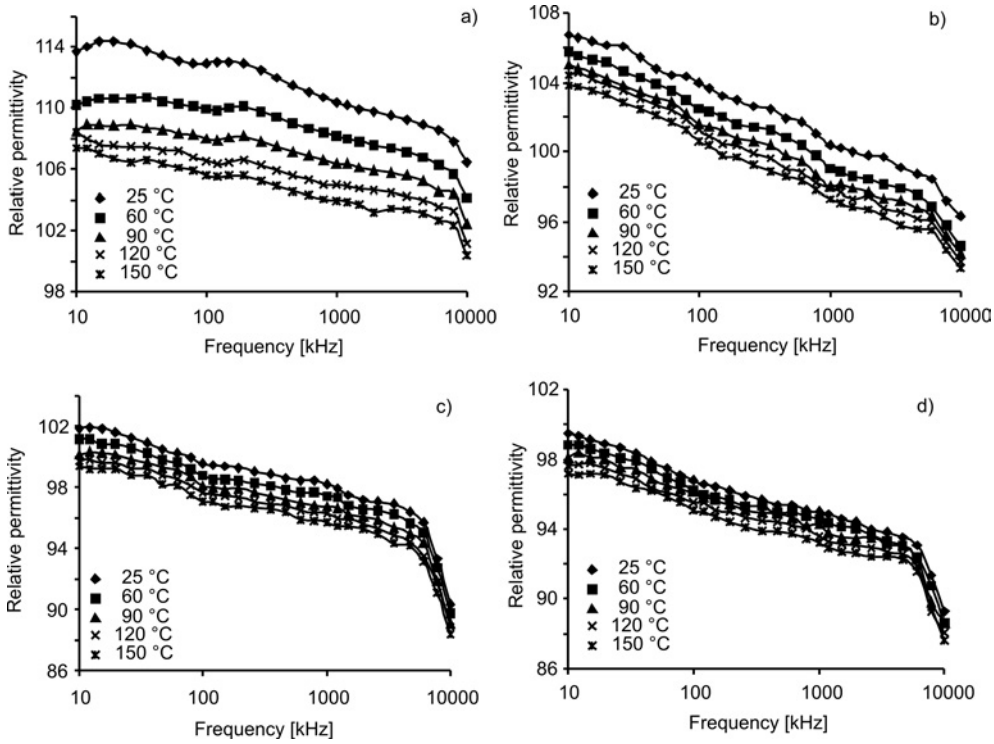

Fig. 6. Dependence of relative permittivity on frequency at various temperatures
for the following Sm contents *y*: a) 0, b) 0.3, c) 0.5, d) 0.7

With regard to the dependences of dielectric properties on ionic radii, the observed behaviour can be explained by the existence of the same intrinsic mechanism revealed

to govern the dielectric properties of undoped $Ba_{6-3x}R_{8+2x}Ti_{18}O_{54}$ solid solutions [12]. The extension of this study to Sm doped $Ba_{6-3x}La_{9.33}Ti_{18}O_{54}$ solid solutions suggests that the changes in the tilting of the octahedral due to substitution of small sized Sm ions for large sized La ions induce changes in the crystal field and consequently cause a decrease in τ_f.

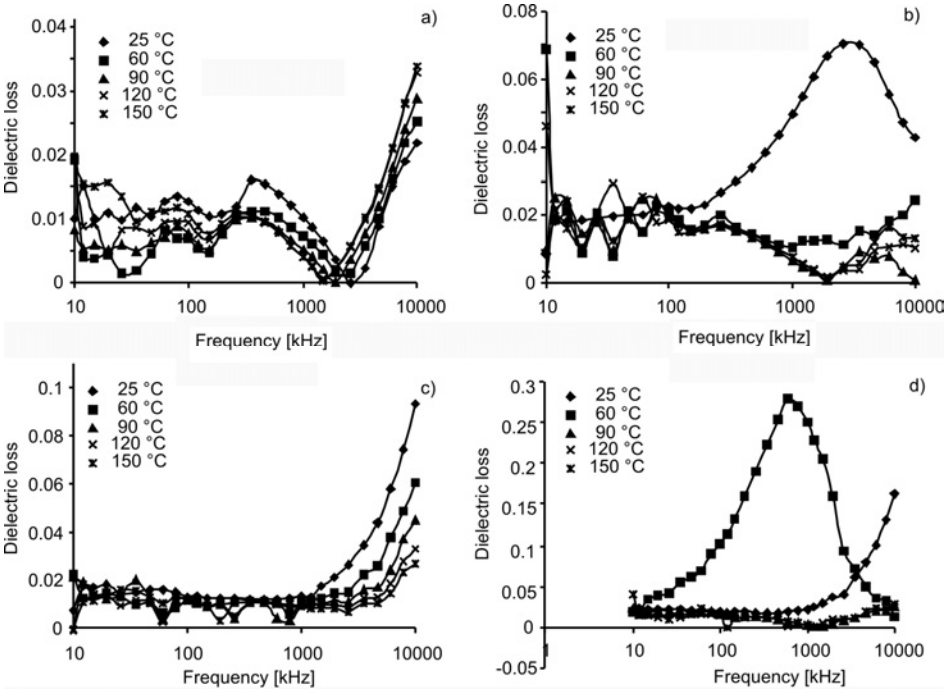

Fig. 7. Dependence of dielectric losses on frequency at various temperatures for the following Sm contents *y*: a) 0, b) 0.3, c) 0.5, d) 0.7

The dependences of the relative permittivity and dielectric losses with frequency for various temperatures and Sm contents of are shown in Figs. 6 and 7. No dielectric anomaly was observed for these materials in the temperature range 25–150 °C. It is assumed that there is no structural transition over the temperature range of interest which is in accordance with the results of other authors [15, 16]. The relative permittivity varies from 106.44 to 100.35 for $y = 0.0$ and from 89.27 to 87.62 for $y = 0.7$ as temperature increases from 25 °C to 150 °C at 10 MHz. However, it is also evident that the increase in the contents of Sm reduces the variations of relative permittivity with temperature, which is required for the thermal stability of ceramics having a high relative permittivity.

4. Conclusions

Dielectric ceramics of the general formula $Ba_4(La_{(1-y)}Sm_y)_{9.33}Ti_{18}O_{54}$, where $y = 0.0$, 0.3, 0.5 and 0.7 were synthesized by high temperature solid state reaction

technique and characterized for structural and dielectric properties. A detailed study related to the variation in the dielectric properties, namely the relative permittivity and the dielectric loss, as temperature increases from 25 °C to 150 °C, was carried out using an impedance analyzer in the frequency range 10 kHz–10 MHz. The relative permittivity decreased in the entire frequency range for all the three samples as the temperature increased. The variation in relative permittivity of $Ba_4(La_{(1-y)}Sm_y)_{9.33}Ti_{18}O_{54}$ solid solutions with temperature reduces as the concentration of Sm increases. The temperature coefficient of the resonant frequency was estimated to improve from 273.9 ppm/°C to 53.8 ppm/°C as the concentration of Sm increased.

Acknowledgements

The authors express their gratitude to Dr. A. Banerjee, UGC-DAE CSR, Indore, for providing the facility to study the dielectric properties in function of temperature and frequency.

References

[1] KOLAR D., STADLER Z., GABERSCEK S., SUVOROV D., Ber. dt. Keram. Ges., 55 (1978), 346.
[2] KOLAR D., GABERSCEK S., VOLAVSEK B., J. Solid State Chem., 38 (1981), 158.
[3] KAUR D., NARANG S.B., SINGH K., J. Ceram. Proc. Res., 7 (2006), 31.
[4] OHSATO H., OHHASHI T., NISHIGAKI S., OKUDA T., SUMIYA K., SUZUKI S., Jpn. J. Appl. Phys., 32 (1993), 4323.
[5] OHSATO H., J. Eur. Ceram. Soc., 21 (2001), 2703.
[6] OHSATO H., IMAEDA M., Mater. Chem. Phys., 79 (2003), 208.
[7] OHSATO H., J. Ceram. Soc. Japan, 113 (2005), 703.
[8] NARANG S.B., KAUR D., BAHEL S., Mater. Lett., 60 (2006), 3179.
[9] LI Y., CHEN X.M., J. Eur. Ceram. Soc. 22 (2002), 715.
[10] CHENG C.C., HSIEH T.E., NAN LIN I., Mat. Chem. Phys 79 (2003), 119.
[11] BAHEL S., BINDRA NARANG S., Mater. Sci.-Poland, 26 (2008), 555.
[12] VALANT M., SUVOROV D., RAWN C.J., Jpn. J. Appl. Phys., 38 (1999), 2820.
[13] SHANONON R.D., Acta Cryst., 32A (1976), 751.
[14] SHANNON R.D., J. Appl. Phys., 73 (1993), 348.
[15] BELOUS A.G., OVCHAR O., VALANT M., SUVOROV D., J. Appl. Phys., 92 (2002), 3917.
[16] BELOUS A.G., OVCHAR O.V., MISCHUK D.O., Cond. Mater. Phys., 6 (2003), 251.

Received 16 January 2009
Revised 7 June 2009

Materials Science-Poland, *Vol. 28*, *No. 1*, *2010*

Quantum computations for temperature variation of refractive indices of covalent semiconductors

B.K. SHARMA[1*], G. MISRA[2], S.C. GOYAL[3]

[1]Department of Physics, Agra College, Dr. B.R. Ambedkar University, Agra, India

[2]Department of Physics, Eritrea Institute of Technology, Asmara University, Asmara, Eritrea

[3]Department of Applied Sciences, Faculty of Engineering and Technology, R.B.S. College, Agra, U.P. Technical University, Lucknow, India

The well-established theory of ion-dependent quantum dielectrics is used to compute the temperature derivatives of optical refractive indices of II–VI and III–V covalent semiconductors. The ion characteristics of these materials vary a little from one another, due to variation in the plasma frequency of crystals and the d core effect. The computed values of the temperature derivatives of optical refractive indices are finally compared with the experimentally obtained values, and with the values predicted by some other workers. The correspondence between our theoretical predictions and the available, experimental data is shown, to be the most consistent to-date for a wide variety of crystals of interest.

Keywords: *optical refractive index; temperature dependence; d core effect*

1. Introduction

The model [1] for ion dependent quantum dielectrics, for ionic crystals, is now well established. This model produced multiple applications such as high resolution photographic lenses, optical instrumentation, and high power laser beams which are required to operate under a wide variety of temperature conditions. In this communication, we highlight a theory to study the effect of heat on the refractive indices of binary covalent semiconductors. The families under study are II–VI and III–V binary covalent semiconductors. The optical refractive properties of these dielectric compounds vary a little from one another, due to variation in plasma frequency and the d core effect. These properties depend upon the electric permittivities and optical refractive index of the crystal. Thus the study of the temperature dependence of refrac-

*Corresponding author, e-mail: gaurang_misra@rediffmail.com

tive indices for binary families is an integral part of the present study. The computed results have been thoroughly analyzed and a number of technological applications of the derivative have been presented.

It was noticed that in ionic solids, namely families of $A^N B^{8-N}$ compounds, with N increasing from 1 to 4, as we move from type I–VII to type IV–IV families a gradual transition from high ionicity to high covalency occurs [2]. The gradual change is from rock salt to wurtzite and zinc blende and finally to diamond structures.

The ionic compounds of I–VII binary crystals are purely ionic with a high percentage of heteropolar parts and a negligible homopolar part, showing pure cation dependent dielectric behaviour. However, solids belonging to the II–VI families have comparable homopolar and heteropolar parts. Thus, these solids may be considered as covalent as well ionic and hence show anion as well as cation dependent dielectric behaviour. The solids belonging to the III–V families are covalent in nature [1, 3]. Experimentally, it is also proved that the optical refractive properties of crystals vary with temperature. Therefore, after thermal treating of the solids, their optical refractive indices n and high frequency electric permittivity ε_∞ change, thereby varying their average energy gaps (E_g). Thus, we use our theory of ion-dependent dielectrics to compute the temperature derivatives of the refractive indices.

2. Theory

To study the temperature dependences of the optical refractive indices in the crystals under consideration, we will use the well established ion-dependent correlation [4, 5] between the optical refractive index and the average energy gap

$$n^2 = 1 + CE_g^k \tag{1}$$

where the parameter k is a family characteristic and the constant C is an ion characteristic for a given family. The parameter k is different for different binary families like II–VI and III–V etc., and is readily available in our base paper [3], whereas C is also found for different ions in different families.

Differentiation of Eq. (1) with respect to temperature leads to

$$\frac{1}{n}\left(\frac{dn}{dT}\right) = \frac{\left(n^2-1\right)}{2n^2}\left[\frac{k}{E_g}\left(\frac{dE_g}{dT}\right) + \frac{1}{C}\left(\frac{dC}{dT}\right)\right] \tag{2}$$

All terms in this equation are represented with unit per Kelvin and while deriving this correlation, the effect of core d electrons is neglected. In fact, the presence of core d electrons affects the number of free electrons per atom, which subsequently changes the plasma frequency by a small amount [6]. It is also noticed that the ion characteristic C varies a little from one ionic solid to another with the same cation, due to variation in the plasma frequency of the crystal [3].

3. Procedure

In order to compute the temperature derivatives of the optical refractive indices of various covalent semiconductors from the above model, we may rewrite Eq. (1) as:

$$\ln (n^2 - 1) = k \ln E_g + \ln C \tag{3}$$

Then, using the measured values of average energy gaps E_g [1] and the refractive indices n [6], a dependence of $\ln(n^2 - 1)$ on $\ln E_g$ is plotted and the parameter k, characteristic of the family, and the values of the parameter C, characteristic of the ion, are evaluated. Using these values, we have calculated the value of $(1/C)(dC/dT)$, which should remain constant for the same anion solids in the covalent families, and for the same cation solids in ionic families [7]. These data are listed in Table 1, along with the measured values of dE/dT for all representative compounds [8].

Table 1. Input parameters used for computing the temperature variation of refractive index

Family	Solid	E_g [1]	n [6]	k	$(1/C)(dC/dT)$ $\times 10^{-5}$/K	$-(dE_g/dT)$ $\times 10^{-5}$/K [8]
II–VI	ZnS	8.1	2.28	–1.000	2.012	5.00
	ZnSe	7.6	2.43	–1.000	2.012	5.40
	ZnTe	6.1	2.70	–1.000	2.012	6.30
III–V	GaP	5.3	2.92	–0.652	4.389	3.25
	InP	5.1	3.09	–0.652	4.389	4.00
	GaAs	5.0	3.30	–0.652	7.693	3.76
	InAs	4.7	3.51	–0.652	7.693	3.55
	GaSb	4.2	3.79	–0.652	11.726	3.80
	InSb	4.1	3.96	–0.652	11.726	3.46

Table 2. The computed values of $(1/n)(dn/dT)$, for various semiconductors along with the available experimental values and those computed through other theories

Family	Solid	Present model	Experimental value [10]	Other theories	
				[8]	[9]
II–VI	ZnS	3.3	3.3	4.3	–
	ZnSe	3.7	3.6	5.1	–
	ZnTe	5.3	5.2	8.3	–
III–V	GaP	3.7	3.7	4.2	2.2
	InP	4.2	4.0	6.2	3.6
	GaAs	5.8	5.6	5.8	5.4
	InAs	5.7	5.7	6.3	6.7
	GaSb	8.2	8.2	7.7	9.3
	InSb	12.7	12.9	8.0	15.0

These reference values are used to compute the values of $(1/n)(dn/dT)$ for the crystals, using Eq. (2). The computed values of $1/n)(dn/dT)$, namely the temperature derivatives of refractive indices, for various semiconductors in respective groups are given in Table 2, along with the available experimental values and those computed from other theories [8, 9], for comparison.

4. Conclusion

The computed values of $(1/n)(dn/dT)$ being the temperature derivatives of refractive indices, obtained through the present theoretical model are in better agreement with the available experimental values [10] than those predicted by Tsay et al. [8] and Yu et al. [9]. The predicted values of the temperature dependence of the refractive index may have a wide range of applications. Therefore, through this study we can obtain more data on behaviour of such crystals under application of heat. This property may be relevant to the field of photoelasticity, photoconductivity and solar cell technology [11]. Other applications of interest in this field are semiconductor electronics and high-power laser technology etc.

Acknowledgements

The authors are thankful to Dr. M.K. Rawat, Principal, Agra College, Agra, for providing the necessary facilities. We acknowledge Dr. K.P. Tiwari, Department of Physics, Agra College, Agra, for useful comments and suggestions. One of the authors, S.C.G., is thankful to the UGC for providing the financial assistance.

References

[1] SARKAR K.K., GOYAL S.C., Phys. Rev., 21 (1980), 279.
[2] PHILLIPS J.C., *Bonds and Bands in Semiconductors*, Academic Press, New York, 1973.
[3] SARKAR K.K., GOYAL S.C., J. Chem. Phys., 68 (1978), 3231.
[4] SINGH R.P., SINGH P., SARKAR K.K., Infrared Phys., 26 (1986), 1.
[5] SINGH R.P., SINGH P., SARKAR K.K., Infrared Phys., 26 (1986), 167.
[6] VAN VECHTEN J.A., Phys. Rev., 182 (1969), 921.
[7] FERNANDEZ A.O., SARKAR K.K., GOYAL S.C., Solid State Commun., 54 (1991), 633.
[8] TSAY Y.F., BENDOW B., MITRA S.S., Proc. Roy. Soc., A, 308 (1969), 473.
[9] YU P.Y., CORDONA M., Phys. Rev. B, 2 (1970), 3193.
[10] RUBLOFF G.W., Phys. Rev. B, 5 (1972), 662.
[11] RAVINDRA N.M., GANPATI P., CHOI J., Infrared. Phys. Tech., 50 (2007), 21.

Received 27 January 2009
Revised 8 May 2009

Materials Science-Poland, *Vol. 28*, *No. 1*, *2010*

Electrical conduction in $Ba(Bi_{0.5}Nb_{0.5})O_3$ ceramics Impedance spectroscopy analysis

K. PRASAD[1*], S. BHAGAT[1], K. AMARNATH[1], S.N. CHOUDHARY[1], K.L. YADAV[2]

[1] Materials Research Laboratory, University Department of Physics, T.M. Bhagalpur University, Bhagalpur 812 007, India

[2] Department of Physics, Indian Institute of Technology, Roorkee 247 667, India

A new lead free perovskite ceramics $Ba(Bi_{0.5}Nb_{0.5})O_3$ was fabricated by a conventional ceramic technique at 1185 °C and subsequent sintering at 1200 °C in air atmosphere. The XRD analysis of $Ba(Bi_{0.5}Nb_{0.5})O_3$ powder indicated the formation of a single-phase monoclinic structure. The ac conductivity data were found to obey the power law and showed a negative temperature coefficient for the resistance behaviour. The ac conductivity values were used to evaluate the density of states at the Fermi level, minimum hopping length and activation energy of the compound. The correlated barrier hopping model was found to successfully explain the mechanism of charge transport in $Ba(Bi_{0.5}Nb_{0.5})O_3$.

Keywords: *$Ba(Bi_{0.5}Nb_{0.5})O_3$; ceramics; ac conductivity; conduction mechanism; hopping model*

1. Introduction

$A(B'B'')O_3$ materials of the perovskite type exhibiting high dielectric permittivity ε' are of current interest due to their practical applications in various electronic/microelectronic devices. Most of the materials used for these applications are, in general, lead bearing compounds, e.g. $PbTiO_3$, $PbZr_{1-x}Ti_xO_3$, $PbMg_{1/3}Nb_{2/3}O_3$, $PbFe_{1/2}Nb_{1/2}O_3$, etc. With the aim of identifying alternatives to the lead-based materials, the electrical properties of $Ba(Fe_{1/2}Nb_{1/2})O_3$ [1–9], $Ba(Al_{1/2}Nb_{1/2})O_3$ [10], $Sr(Fe_{1/2}Nb_{1/2})O_3$ [5], $Ba(Fe_{1/2}Ta_{1/2})O_3$ [11], etc. have been investigated. One such ceramics in this series is perovskite $Ba(Bi_{0.5}Nb_{0.5})O_3$ having the tolerance factor $t = 0.8769$ estimated using the relation:

$$t = \frac{r_{Ba} + r_O}{\sqrt{2}}\left(\frac{r_{Bi} + r_{Nb}}{2} + r_0\right)^{-1}$$

*Corresponding author, e-mail: k.prasad65@gmail.com

where r_{Ba}, r_{Bi}, r_{Nb} and r_O are the ionic radii of the constituent ions. The material is mechanically tough and lead-free.

The complex impedance spectroscopy technique is widely recognized as a non-destructive but powerful technique for the study of the electrical properties of solids [12]. Thus, the dynamics of ionic movement and the contributions of various microstructure elements such as grain, grain boundary and interfacial polarization, to total electric response in polycrystalline solids can be identified by this technique. It also enables us to evaluate the nature of dielectric relaxation and the relaxation frequency of the material.

Despite an extensive literature survey, there has been no study of $Ba(Bi_{0.5}Nb_{0.5})O_3$ (BBN) so far, to the best of the author's knowledge. In the present work, structural, microstructural and ac conductivity studies of BBN have been described. An attempt has also been made to explain the conduction mechanism in the system.

2. Experimental

$Ba(Bi_{0.5}Nb_{0.5})O_3$ (BBN) was obtained from AR grade (99.9%+ pure) chemicals ($BaCO_3$, Bi_2O_3 and Nb_2O_5) by solid state synthesis using the following chemical reaction at 1185 °C for 4 h:

$$BaCO_3 + \frac{1}{4}Bi_2O_3 + \frac{1}{4}Nb_2O_5 \xrightarrow{\Delta} Ba(Bi_{0.5}Nb_{0.5})O_3 + CO_2$$

under controlled heating and cooling cycles. A circular disc shaped pellet, 9.99 mm in diameter and 2.192 mm thick was made by applying a uniaxial stress of ca. 650 MPa. The pellet was subsequently heated up to 1200 °C under air for 3h. The complete reaction and the formation of the desired compound were verified by X-ray diffraction analysis. The weights of the samples were monitored before and after heat treatments. The maximum difference was about 1.08 mg for 10 g of the sample. Therefore, the compositions of the samples were considered to be the same as the initial ones. The XRD spectra were taken on calcined powder of BBN with a X-ray diffractometer (XPERT-PRO) at room temperature, using CuK_α radiation (λ = 1.5405 Å), over a wide range of Bragg angles ($20° \le 2\theta \le 80°$) with a scanning speed of $2°\cdot min^{-1}$. The microstructure of the sintered BBN sample was taken on the fractured surface using a computer controlled scanning electron microscope (SEM Hitachi S-3400N, Japan). The identification of secondary phases present in the sample was carried out using an energy dispersive X-ray analyzer (Thermo Noran NSS200). Electrical impedance Z, phase angle θ, loss tangent $\tan\delta$ and capacitance C were measured in function of frequency (0.1 kHz–1 MHz) at various temperatures (30–500 °C) using a computer controlled LCR Hi-Tester (HIOKI 3532-50), Japan, attached with a microprocessor controlled dry temperature controller (DPI-1100), Sartech Intl., India on a symmetrical cell of type Ag|ceramics|Ag, where Ag is a conductive paint coated on either side of the pellet.

3. Results and discussion

Figure 1 shows the XRD profile of calcined BBN powder. A standard computer program (POWD) was utilized for the XRD profile analysis. Good agreement between the observed and calculated inter-planar spacing and no traces of any extra peaks due to constituent oxides were found, thereby suggesting the formation of a single phase compound having a monoclinic structure. The lattice parameters were estimated to be a = 4.320(6) Å, b = 4.238(8) Å, c = 3.001(6) Å and β = 90.659° with the estimated error of $\pm 10^{-4}$ Å. The unit cell volume was estimated to be 54.97 Å^3.

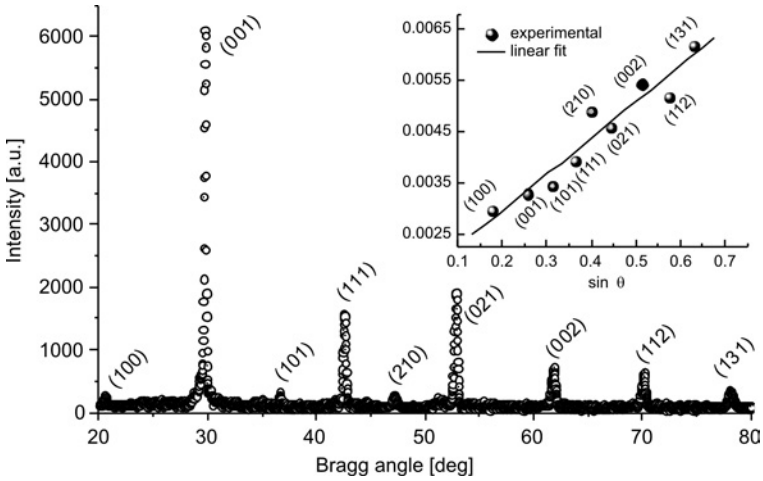

Fig. 1. X-ray diffraction pattern of calcined $Ba(Bi_{0.5}Nb_{0.5})O_3$ powder at room temperature. Inset shows the Williamson–Hall plot

The XRD pattern of BBN is found to be similar to that of $Ba(Fe_{0.5}Nb_{0.5})O_3$ [3, 6, 7, 9] with little shifts in peak positions. This may be due to the difference in the ionic radii of Fe^{3+} and Bi^{3+} ions. The criterion adopted for evaluating the robustness and accuracy of of the indexing and the structure of compound was the sum of differences in observed and calculated d values (i.e., $\sum \Delta d = \sum (d_{obs} - d_{calc})$), which were minimized using a least squares refinement technique. The apparent particle size and lattice strain of BBN were estimated by analyzing the broadening of the X-ray diffraction peak, using the Williamson–Hall approach [13]:

$$\beta \cos\theta = \frac{K\lambda}{D} + 2\frac{\Delta\xi}{\xi}\sin\theta \tag{1}$$

where D is the apparent particle size, β is the width of the diffraction peak at half intensity (FWHM), $\Delta\xi/\xi$ is the lattice strain and K is the Scherrer constant (K = 0.89). The term $K\lambda/D$ represents the Scherrer particle size distribution. The Gaussian model was applied to estimate the width of the diffraction peak at half intensity.

$$I = I_0 + \frac{A}{\eta\sqrt{\frac{\pi}{2}}}\exp\left(-2\left(\frac{\theta-\theta_c}{\eta}\right)^2\right) \tag{2}$$

where A and θ_c are the area and centre of the curve, respectively. The inset of Fig. 1 illustrates the Williamson–Hall plot for BBN. A linear least squares fitting of the $\beta\cos\theta$–$\sin\theta$ data provided the values of the apparent particle size and the lattice strain: these were found to be approximately 89 nm and 0.0035, respectively.

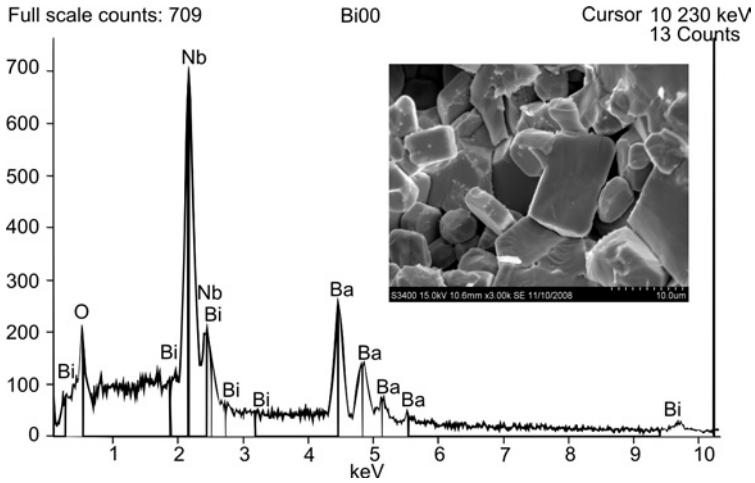

Fig. 2. EDAX spectrum and SEM micrograph of fractured surface of $Ba(Bi_{0.5}Nb_{0.5})O_3$ ceramics

To confirm the absence of a second phase, EDAX was carried out. Figure 2 shows the EDAX pattern for the constituent ions of BBN. All peaks in the pattern match perfectly with the elements present in $Ba(Bi_{0.5}Nb_{0.5})O_3$. This clearly indicated the purity and formation of BBN. The grain shapes (almost cuboid) are clearly visible in the SEM micrograph (inset of Fig. 2) of the sintered BBN sample, indicating the existence of a polycrystalline microstructure. Grains of unequal sizes (5–10 μm) appear to be distributed throughout the sample.

The ac electrical conductivity, which in most of the materials is due to localized states, is given by:

$$\sigma_{ac} = \sigma(0) + \sigma(\omega) \tag{3}$$

where $\sigma(0)$ and $\sigma(\omega)$ are the frequency independent and frequency dependent parts of the conductivity, respectively. Also, $\sigma(\omega)$ was found to satisfy the following equation in the frequency sensitive region: $\sigma(\omega) = A\omega^s$ with $0 \le s \le 1$, ω being the angular frequency of the applied ac field and $A = \pi N^2 e^2/6k_BT(2\alpha)$ is a constant, e is the electron charge, T – temperature, α – polarizability of a pair of sites, and N – the number of sites per unit volume among which hopping takes place. Such variation is associated

with displacement of carriers which move within the sample by discrete hops of the length R between randomly distributed localized sites. The term $A\omega^s$ can often be described based on two distinct mechanisms for carrier conduction: (i) quantum mechanical tunnelling (QMT) through the barrier separating the localized sites; and (ii) correlated barrier hopping (CBH) over the same barrier. In these models, the exponent s is found to have two different trends being a function of temperature and frequency. If the ac conductivity is related to QMT, s is predicted to be temperature independent but is expected to show a decreasing trend with ω

$$s = 1 + \frac{4}{\lg(\omega\tau_0)} \tag{4}$$

where τ_0 is the characteristic relaxation time. The ac conductivity is expected to be [14]

$$\sigma_{ac} = \frac{\pi^4}{24} e^2 \omega k_B T \left(N\left(E_f\right)\right)^2 \alpha^{-1} R_\omega^4 \tag{5}$$

where α^{-1} is the spatial decay parameter for the localized wave function, and R_ω is the tunnelling length at the frequency ω. If ac conductivity is related to CBH [15],

$$\sigma_{ac} = \frac{\pi}{3} e^2 \omega k_B T \left(N\left(E_f\right)\right)^2 \alpha^{-5} \left(\ln\frac{f_0}{\omega}\right)^4 \tag{6}$$

where $N(E_f)$ is the density of states at the Fermi level, f_0 the photon frequency and α is the localized wave function. The exponent s and minimum hopping length $R_{\min}$ can be expressed as [16, 17]

$$s = 1 - \frac{6k_B T}{W_m} \tag{7}$$

$$R_{\min} = \frac{2e^2}{\pi\varepsilon\varepsilon_0 W_m} \tag{8}$$

where W_m is the binding energy, which is defined as the energy required to remove an electron completely from one site to the another site. Figure 3 shows the log–log dependence of the electrical conductivity on frequency at various temperatures. The pattern of the conductivity spectrum shows dispersion throughout the chosen frequency range. The frequency dependence of ac conductivity satisfies [18]:

$$\sigma_{ac} = A_1\omega^{S_1} + A_2\omega^{S_2} \tag{9}$$

where A_1 and A_2 are the temperature dependent constants, and s_1 and s_2 are temperature as well as frequency dependent parameters. The values of s_1 and s_2 can be obtained from the slopes of the plots: $\lg\sigma_{ac}$ vs. $\lg\omega$ in the low and high frequency regions. The inset of Fig. 3 shows the temperature dependence of s_1 and s_2. It can be seen that the values of both s_1 and s_2 are always lower than 1. Also, the values of both s_1 as well as s_2 decrease with the rise in temperature. The value of $s_1 \to 0$ at higher

temperatures indicates that the dc conductivity dominates at higher temperatures in the low frequency region satisfying Eq. (3). The model based on correlated hopping of electrons over a barrier [19] predicts a decrease in the value of s_1 with the increase in temperature, and thus it is found to be consistent with the experimental results. Therefore, the conduction in the system could be considered due to the short range translational type hopping of charge carriers [18–20]. This indicates that the conduction process is thermally activated.

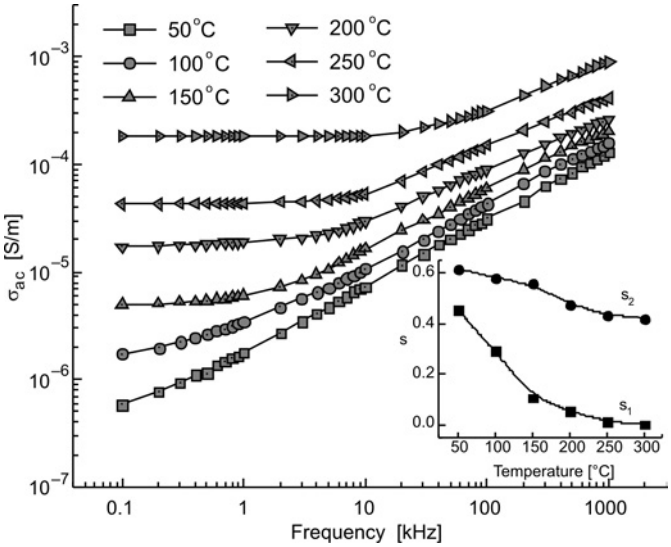

Fig. 3. Dependences of ac conductivity on frequency at various temperatures for $Ba(Bi_{0.5}Nb_{0.5})O_3$ ceramics. Inset figure illustrates the dependences of s_1 and s_2 on temperature

The hopping conduction mechanism is generally consistent with the existence of high density of states in the materials having a band gap similar to that of a semiconductor. Due to localization of charge carriers, formation of polarons takes place and the hopping conduction may occur between the nearest neighbouring sites. Figure 4 shows the dependence of ac conductivity on $10^3/T$. The activation energy for conduction was determined using the Arrhenius relationship:

$$\sigma_{ac} = \sigma_0 \exp\left(-\frac{E_a}{k_B T}\right) \tag{10}$$

where E_a is the activation energy of conduction and T is the absolute temperature. The variation profile shows the negative temperature coefficient of resistance (NTCR) behaviour of BNN. A linear least squares fitting of the conductivity data to Eq. (10) gives the value of the activation energy, E_a. The values of E_a were found to be 0.379 eV, 0.352 eV and 0.349 eV at 1 kHz, 10 kHz and 100 kHz, respectively.

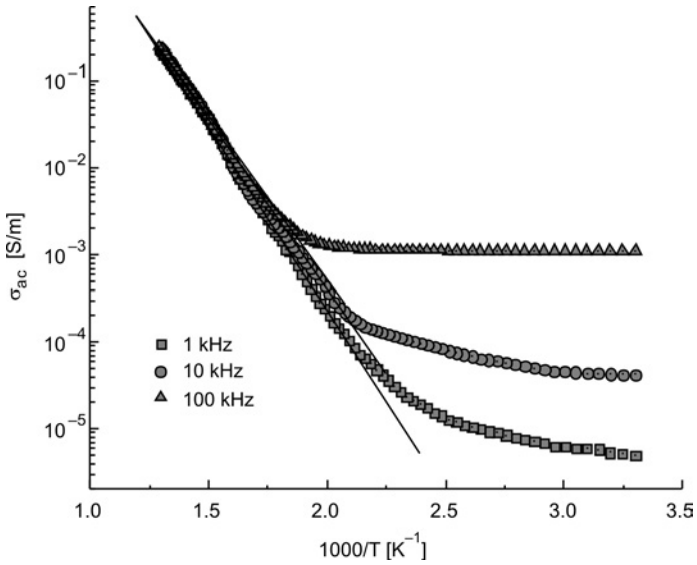

Fig. 4. Dependences of ac conductivity on inverse of temperature at various frequencies for $Ba(Bi_{0.5}Nb_{0.5})O_3$ ceramics

The activation energy decreases with the increase in frequency It can be seen that the ac conductivity is almost frequency insensitive in low temperature region. Also, the onset temperature shifts to higher temperature side with the increment in frequency. The low value of E_a may be due to the carrier transport through hopping between localized states in a disordered manner [21]. The increase in conductivity with temperature may be explained, taking into consideration that within the bulk the oxygen vacancies due to the loss of oxygen, are usually created during sintering and the charge compensation is described by the following reaction [22]:

$$\mathrm{O} \rightarrow \tfrac{1}{2}\mathrm{O}_2 \uparrow + V_0^{\bullet\bullet} + 2\mathrm{e}^-$$

which may leave behind free electrons, making them n type [23].

The values of $N(E_f)$ were estimated using Eq. (6) by assuming $f_0 = 10^{13}$ Hz, $\alpha = 10^{10}$ m^{-1} at various operating frequencies and temperatures. Figure 5 shows the frequency dependence of $N(E_f)$ at various temperatures. It can be seen that the values of $N(E_f)$ decrease with the increase in the operating frequency. Inset of Fig. 5 shows the variation of $N(E_f)$ with temperature at various frequencies. It is seen that the $N(E_f)$ simply increases with the increase in temperature. Therefore, at low frequencies the electrical conduction in the system is being affected by both frequency as well as temperature, whereas at higher frequencies the charge carriers are localized and being affected by thermal excitations. The reasonably high values of $N(E_f)$ suggest that the hopping between the pairs of sites dominates the mechanism of charge transport in BBN.

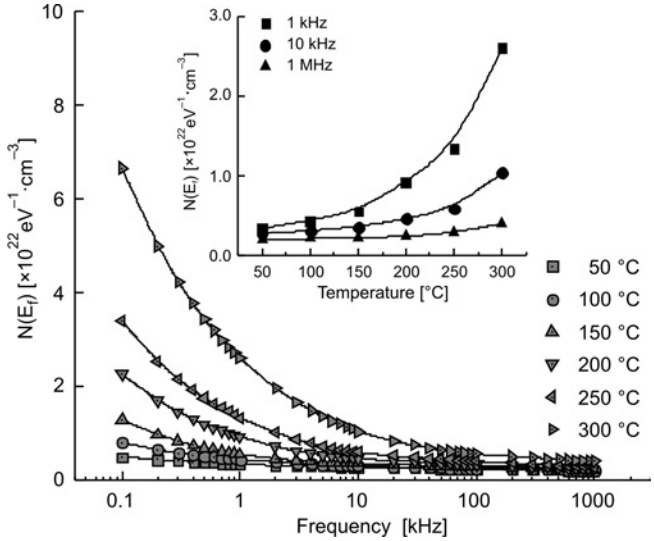

Fig. 5. Dependences of density of states at Fermi level of $(Ba(Bi_{0.5}Nb_{0.5})O_3$ ceramics on frequency at various temperatures. Inset figure shows the temperature dependence of $N(E_f)$ at various frequencies

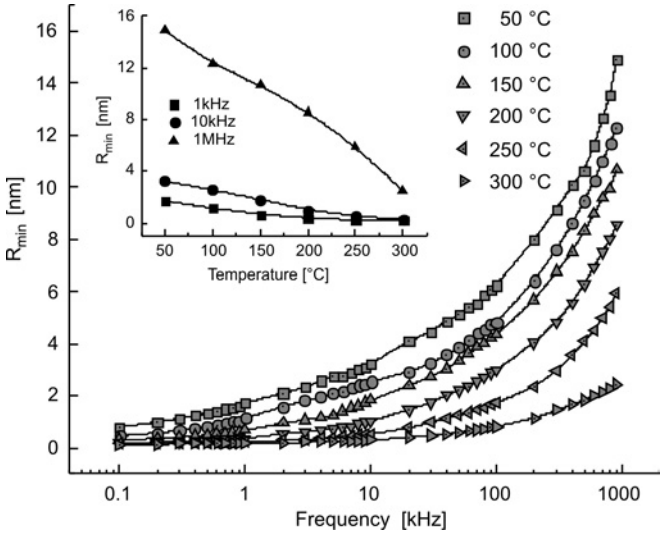

Fig. 6. Dependences of R_{min} of $Ba(Bi_{0.5}Nb_{0.5})O_3$ ceramics on frequency at various temperatures. Inset figure shows the variation of R_{min} on temperature at various frequencies

The values of the minimum hopping distance, R_{min} were calculated using Eq. (8). Figure 6 presents the variation of R_{min} with frequency at various temperatures. The values of R_{min} simply increase as the frequency increases at every temperature. Inset of Fig. 6 shows the variation of R_{min} with temperature at various frequencies. It can be seen that the values of R_{min} decrease with the increase in temperature. The value of R_{min} at room temperature was found to be 1.6 nm.

4. Conclusions

Polycrystalline $Ba(Bi_{0.5}Nb_{0.5})O_3$, fabricated through a high-temperature solid state reaction technique, was found to have a single phase perovskite type monoclinic structure. The ac conductivity is found to obey the universal power law and showed the NTCR character. The correlated barrier hopping model is found to successfully explain the mechanism of charge transport in BBN. Furthermore, the frequency dependent ac conductivity at various temperatures indicated that the conduction process is thermally activated.

Acknowledgements

The present work was supported by the Defense Research and Development Organization, New Delhi.

References

[1] REANEY I.M., PETZELT J., VOITSEKHOVSKII V.V., CHU F., SETTER N., J. Appl. Phys., 76 (1994), 2086.
[2] SAHA S., SINHA T.P., Phys. Rev. B, 65 (2002), 134103.
[3] RAEVSKI I.P., PROSANDEEV S.A., BOGATIN A.S., MALITSKYA M.A., JASTRABIK L., J. Appl. Phys., 93 (2003), 4130.
[4] CHUNG C.-Y., CHANG Y.-H., CHEN G.-J., J. Appl. Phys., 96 (2004), 6624.
[5] CHUNG C.-Y., CHANG Y.-H., CHEN G.-J., CHAI Y.-L., J. Cryst. Growth, 284 (2005), 100.
[6] EITSSAYEAM S., INTATHA U., PENGPAT K., TUNKASIRI T., Curr. Appl. Phys., 6 (2006), 316.
[7] WANG Z., CHEN X.M., NI L., LIU X.Q., Appl. Phys. Lett., 90 (2007), 022904.
[8] INTATHA U., EITSSAYEAM S., PENGPAT K., MACKENZIE K.J.D., TUNKASIRI T., Mater. Lett., 61 (2007), 196.
[9] KE S., HUANG H., FAN H., CHAN H.L.W., ZHOU L.M., Ceram. Int., 34 (2008), 1059.
[10] DUTTA A., SINHA T.P., J. Phys. Chem. Solids, 67 (2006), 1484.
[11] JUNG W.-H., LEE J.-H., SOHN J.-H., NAM H.-D., CHO S.-H., Mater. Lett., 56 (2002), 334.
[12] SUMAN C.K., PRASAD K., CHOUDHARY R.N.P., Adv. Appl. Ceram., 104 (2005), 294.
[13] WILLIAMSON G.K., HALL W.H., Acta. Metall., 1 (1953), 22.
[14] ELLIOTT S.R., Adv. in Phys., 36 (1987), 135.
[15] SHARMA G., ROY M., ROY M.S., Mater. Sci. Eng., B 104 (2003), 15.
[16] MOLLAH S., SOM K.K., BOSE K., CHAUDRI B.K., J. Appl. Phys., 74 (1993), 931.
[17] SALAM R., Phys. Stat. Sol. (a), 117 (1990), 535.
[18] FUNKE K., Prog. Solid State Chem., 22 (1993), 111.
[19] ELLIOTT S.R., Philos. Mag., B 37 (1978), 553.
[20] YOUSSEF AHMED A.A., Z. Naturforsch., A57 (2002), 263.
[21] PRASAD K., SUMAN C.K., CHOUDHARY R.N.P., Adv. Appl. Ceram., 105 (2006), 258.
[22] KRÖGER F.A., VINK H.J., Solid State Phys., 3 (1956), 307.
[23] PRASAD K., SUMAN C.K., CHOUDHARY R.N.P., Ferroelectrics, 324 (2005), 89.

Received 8 March 2009
Revised 4 June 2009

Materials Science-Poland, *Vol. 28*, *No. 1*, *2010*

Preparation and microwave absorption of M type ferrite nanoparticle composites

G.Z. SHEN[1*], G.S. CHENG[1], Y. CAO[1], Z. XU[2]

[1]College of Mathematics and Physics, Nanjing University of Information Science and Technology, Nanjing 210044, P.R. China

[2]School of Materials Science and Engineering, Tongji University, Shanghai 200092, P.R. China

The sol-gel method was used to obtain M type $BaFe_{12}O_{19}$ ferrite nanoparticles. Rod like and flake like ferrite nanoparticles can be successfully fabricated by controlling the heating process of the precursor. The phase attributes, morphology and grain size of $BaFe_{12}O_{19}$ ferrite were characterized by TEM and XRD. The complex permittivity and permeability of ferrite epoxy resin composites were measured in the Ku waveband (12.4–18 GHz). Ferrite composites containing short carbon fibres have also been fabricated in order to obtain higher complex permittivities of the composites. The reflectivities of these ferrite composites were calculated according to the measured electromagnetic parameters. The results show that the microwave absorption properties of ferrite composites can be effectively improved by filling them with short carbon fibres.

Keywords: *ferrite nanoparticles; sol-gel method; carbon fibres; microwave absorption*

1. Introduction

Electromagnetic wave absorbing materials in the GHz range have attracted much attention in recent years with the development of GHz microwave communication, radar detection and other industrial applications. These absorbing materials can be manufactured by a number of magnetic and dielectric materials in powder forms, loaded in various kinds of polymeric binders. Various electromagnetic wave absorbing materials can be designed by using the dispersion characteristic of the complex permittivity and permeability [1–5]. Ferrite is one of materials used as an electromagnetic

*Corresponding author, e-mail: shengz3@126.com

wave absorber, and a number of studies have been reported on the dependence of the electromagnetic wave absorption properties on their composition [6–12]. However, a pure ferrite microwave absorber is insufficient to achieve wideband absorption. In this work, emphasis has been laid on the synthesis of nanocrystalline $BaFe_{12}O_{19}$ ferrite powders and improving the dielectric properties of ferrite composites.

In the present study, M type ferrite nanoparticles were obtained by adopting the citrate sol-gel method. Various heating processes of the precursors were used to obtain different morphologies of nanoparticles. The flake-like nanoferrite was selected to produce ferrite epoxy resin composites. In order to improve the dielectric properties of ferrite composites, short carbon fibres (T700) were filled into the composites. The electromagnetic parameters of the ferrite composites were measured in the Ku wave-band by a network analyzer, and the microwave reflectivity of a single layer coating of the ferrite composites was calculated.

2. Experimental

M type $BaFe_{12}O_{19}$ hexaferrites were fabricated by the citrate sol-gel technique. The starting materials were $Ba(NO_3)_2$, $Fe(NO_3)_3{\cdot}9H_2O$ and citric acid. In a typical procedure for the preparation of $BaFe_{12}O_{19}$, firstly, aqueous solutions of barium and ferric salts were obtained separately by dissolving the salts in distilled water, and then added together in stoichiometric proportions. Solution of citric acid was added to the aqueous salt solution in an appropriate proportion under constant stirring and pH of the solution was adjusted to 7.0 with ammonia. The solution was then heated to 80 °C and maintained at that temperature for 3 h in a water bath. Finally, the solution was dried at 100 °C to form a dry gel. To obtain different structural features of ferrites, the dried gel precursor was treated by various heating methods in a muffle furnace. The precursor was heated to 900 °C at the rate of 50 °C/h, and then calcined at the same temperature for 4 h (sample A). Other samples were fabricated by a double heat-treatment method. First, the precursor was pre-heated at 450 °C for 3 h, and then the it was heated to 900 °C at the rate of 50 °C/h and calcined at 900 °C for 4 h to form ferrite sample B. Ferrite sample C was obtained by a similar method as sample B; the only difference was that the pre-heated product was rapidly heated to 900 °C.

The X-ray diffraction patterns of the ferrite powder were obtained with an X-ray powder diffractometer with CuK_α radiation (D/max-2550). The morphology of the crystal grain was observed under a transmission electron microscope (H-800). The electromagnetic parameters, complex permittivity and permeability, were measured by a network analyzer (Agilent E8363B) in the Ku waveband. In order to measure the electromagnetic parameters of composites, rectangular samples were made from the ferrite sample C and epoxy resin composite with 60 wt. % of ferrite. To obtain material of higher permittivity, ferrite composite samples containing 0.2 wt. % of short carbon fibres (3 mm long) were also obtained.

3. Results and discussion

3.1. Characterization of samples

XRD patterns of the ferrites samples synthesized by the sol-gel route are shown in Fig. 1. They show that the heating method affects the structural features of ferrite products. M type hexaferrite $BaFe_{12}O_{19}$ and α-Fe_2O_3 phases can be detected in sample A which fabricated by direct heating of dried precursors to 900 °C. Curves b and c in Fig. 1 show that pure crystalline M type ferrite can be obtained when the precursors are first preheated at 450 °C for 3 h, and then calcined at 900 °C.

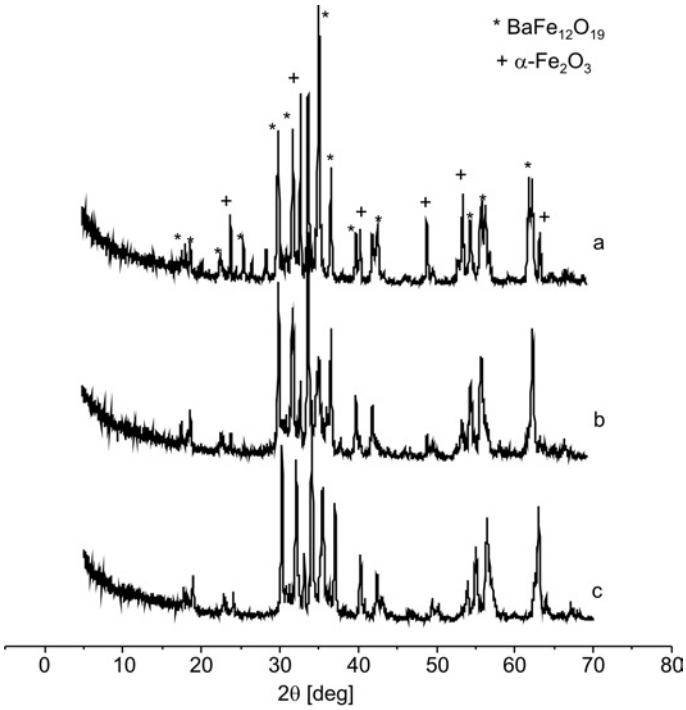

Fig. 1. XRD patterns of the ferrite samples: a) sample A, b) sample B, c) sample C

When the dried precursors are heated, the following reactions occur [8]:

$$\text{Dried precursors} \rightarrow \gamma\text{-}Fe_2O_3 + Ba^{2+}$$

$$\gamma\text{-}Fe_2O_3 + Ba^{2+} \rightarrow BaFe_2O_4$$

$$BaFe_2O_4 + 5\gamma\text{-}Fe_2O_3 \rightarrow BaFe_{12}O_{19}$$

First of all, precursors decompose and produce γ-Fe_2O_3, and then the reaction proceeds as shown in the above equations during the subsequent heat treatment. Finally,

the ferrite $BaFe_{12}O_{19}$ is obtained. However, when precursors are heated to 900 °C directly, α-Fe_2O_3 forms a stable phase and does not react with Ba^{2+} at 900 °C. As a result, a small amount of residual exists in sample A. However, the pre-heat treatment at 450 °C can effectively prevent precursors from producing α-Fe_2O_3 [13, 14].

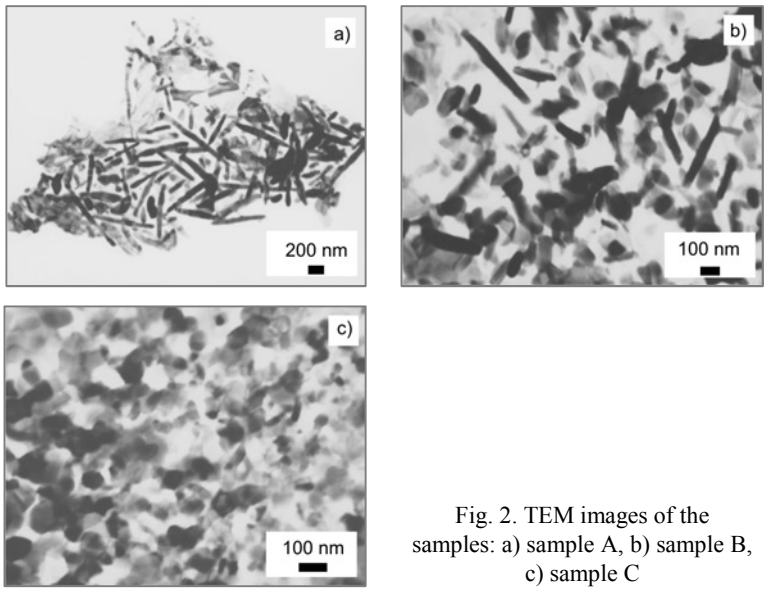

Fig. 2. TEM images of the samples: a) sample A, b) sample B, c) sample C

The morphology of the ferrite particles was examined by TEM. Homogeneous rod-like particles 60 nm in diameter, 0.7–1.0 μm long were found in sample A, as shown in Fig. 2a. Figure 2b shows that the particles of sample B are both rod-like and flake-like. However, the rod-like particles are not as homogeneous as sample A. The particles of sample C are mostly flake-like, and the average size of the grains is about 80 nm. The crystal morphology is determined by the growth rate of every crystal face, according to the crystal growth mechanism described in [15, 16]. Under slow heating, the crystallization time is enough long and the growth rate is higher along the long-axis for the hexaferrite. Thus a slow heating rate is conducive to fabrication of one-dimensional nanorods [17, 18] but a detailed mechanism of formation of the as-prepared rods and flakes is still under investigation.

3.2. Microwave absorption

The dependences of the complex permittivity and permeability of ferrite composites on frequency are shown in Figs. 3 and 4. Figure 3 represents the frequency dependences of the real part ε' and the imaginary part ε'' of the complex permittivity of the ferrite composite (M) and the ferrite composite filled with short carbon fibre (MC), respectively. The values of ε' and ε'' for the composite MC are higher than for the

composite M in the Ku waveband. The dielectric properties of polycrystalline ferrite composites arise mainly from the interfacial polarization and the intrinsic electric dipole polarization. However, the dielectric properties of the composite MC arise not only from the polarization of ferrite but also from the electric dipole polarization of short carbon fibres [19].

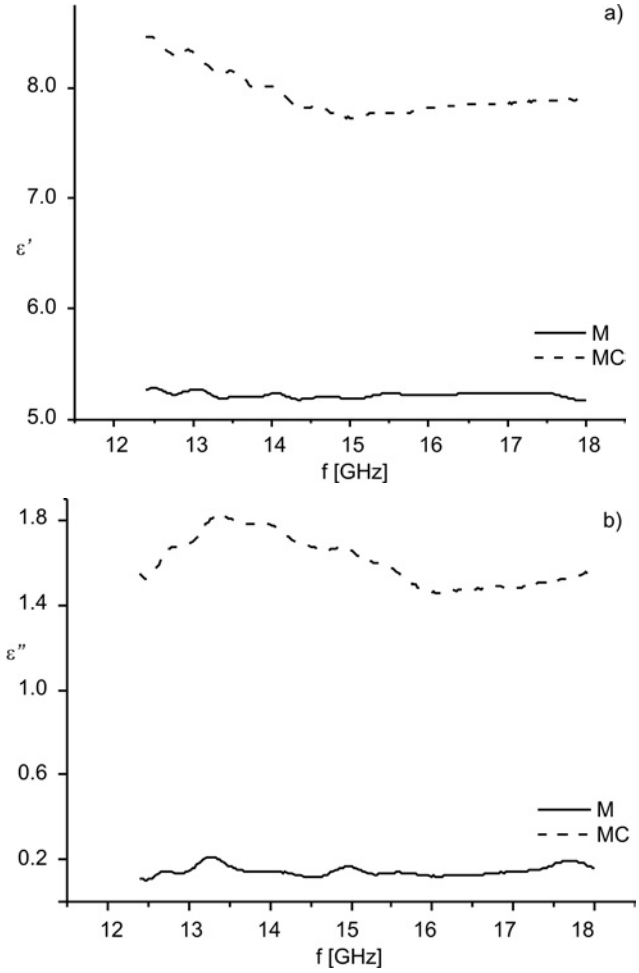

Fig. 3. Dependences of complex permittivity of ferrite composites on frequency: a) real part, b) imaginary part

It is seen from Fig. 4 that the values of μ' and μ'' of the complex permeability of the ferrite composite M and the composite MC are similar over the considered frequency range. The reason is that addition of carbon fibre has affects the magnetic properties of the composites.

The reflectivity of the incident electromagnetic wave normal to the planar single-layer coated on a metal plate is given as

$$R = 20\lg\left|\frac{\sqrt{\frac{\mu_r}{\varepsilon_r}}\tanh\left(j\frac{2\pi f}{c}\sqrt{\mu_r\varepsilon_r}d\right)-1}{\sqrt{\frac{\mu_r}{\varepsilon_r}}\tanh\left(j\frac{2\pi f}{c}\sqrt{\mu_r\varepsilon_r}d\right)+1}\right| \tag{1}$$

Here d, ε_r and μ_r are the thickness of the coating, the relative complex permittivity and the permeability of the composite, respectively [15].

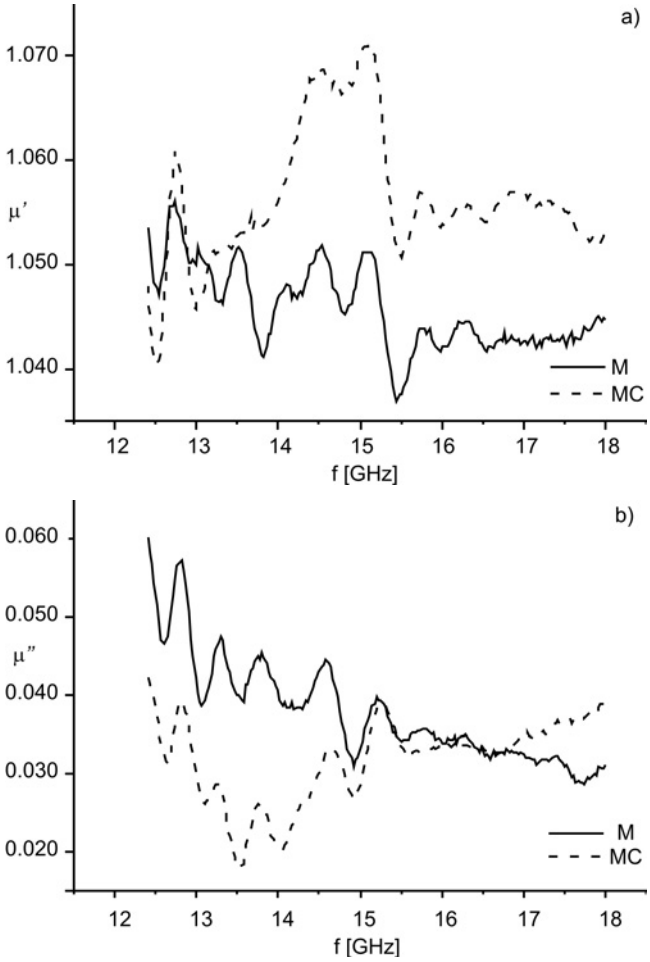

Fig. 4. Dependences of complex permeability of ferrite composites on frequency: a) real part, b) imaginary part

Figure 5 shows the predicted microwave absorption properties of a single layer coating 2 mm thick for the composite M and composite MC, according to Eqs. (1). It is observed that the reflective loss of the ferrite composite M is worse than that of MC.

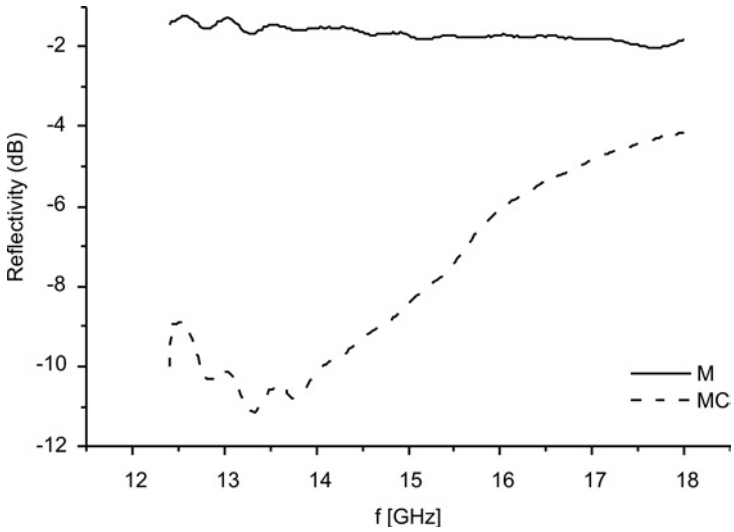

Fig. 5. Absorption curves of ferrite composite coatings

However, the absorption properties of the composite MC, which is filled with short carbon fibres, are improved obviously. Its reflectivity decreases as frequency increases, for frequencies below 13.3 GHz, and begins to increase gradually for frequencies above 13.3 GHz. The reflectivity is about –11.0 dB at 13.3 GHz, and –4.2 dB at 18 GHz. The absorption bandwidth lower than –10.0 dB is 1.4 GHz, which is from 12.7 GHz to 14.1 GHz. The reason that the absorption properties of the composite MC are better than those of the composite M is that short conductive carbon fibres in ferrite composite can act as electric dipoles and resonate with the incident wave. Adding short carbon fibres can increase the dielectric loss of the considered composites.

4. Conclusion

M type $BaFe_{12}O_{19}$ hexaferrite nanoparticles were successfully synthesized by the citrate sol-gel process. Rod like and flake like nanoparticles were obtained by various heating methods. Ferrite composites containing short carbon fibres were designed to test the electromagnetic parameters of the composites. The results show that addition of short carbon fibres can effectively improve the microwave absorption properties of M type ferrite nanocomposites. Absorption bandwidth lower than –10.0 dB of the composite is 1.4 GHz, between 12.7 GHz and 14.1 GHz. The method of preparation and design may potentially be applied to produce light weight and high performance absorption materials.

Acknowledgements

This work was supported by funding from the Nanjing University of Information Science and Technology (Grant No. 20080284).

References

[1] ZHANG B.S., LU G., FENG Y., XIONG J., LU H.X., J. Magn. Magn. Mater., 299 (2006), 205.
[2] LI D.S., HORIKAWA T., LIU J.R., ITOH M., MACHIDA K.I., J. Alloy Compd., 408–412 (2006), 1429.
[3] RAHUL SHARMA, AGARWALA R.C., VIJAYA AGARWALA, Mater. Lett., 62 (2008), 2233.
[4] DENG Y.D., LIU X., SHEN B., LIU L., HU W.B., J. Magn. Magn. Mater., 303 (2006), 181.
[5] PARK K.Y., LEE S.E., KIM C.G., HAN J.H., Compos. Sci. Tech., 66 (2006), 576.
[6] GHASEMI A., HOSSIENPOUR A., MORISAKO A., SAATCHI A., SALEHI M., J. Magn. Magn. Mater., 302 (2006), 429.
[7] SHEN G.Z., XU Z., LI Y., J. Magn. Magn. Mater., 301 (2006), 325.
[8] KIMURA S., KATO T., HYODO T., SHIMIZU Y., EGASHIRA M., J. Magn. Magn. Mater., 312 (2007), 181.
[9] ZHANG H.J., LIU Z.C., MA C.L., YAO X., ZHANG L.Y., WU M.Z., Mater. Chem. Phys., 80 (2003), 129.
[10] TABATABAIE F., FATHI M.H., SAATCHI A., GHASEMI A., J. Alloy Compd., 474 (2009), 206.
[11] LIMA U.R., NASAR M.C., NASAR R.S., REZENDE M.C., ARAUJO J.H., OLIVEIRA J.F., Mater. Sci. Eng. B, 151 (2008), 238.
[12] STEIER H.P., GALLAGHER P.K., J. Mater. Res., 14(1999), 3647.
[13] HUANG J.G., ZHUANG H.R., LI W.L., Mater. Res. Bull., 38(2003), 149.
[14] XU J.F., GUO F.F., XU Z., J. Tongji University., 32 (2004), 929.
[15] VEKILOV P.G., KUZNETSOV Y.G., CHERNOV A.A., J. Cryst. Growth., 121(1992), 643.
[16] TRACY S.L., WILLAMS D.A., JENNINGS H.M., J. Cryst. Growth, 193(1998), 374.
[17] WANG J.M., GAO L., J. Mater. Chem., 13 (2003), 2551.
[18] GUO L., JI Y.L., XU H.B., WU Z.Y., SIMON P., J. Mater. Chem., 13 (2003), 754.
[19] SHEN G.Z, XU M., XU Z., Mater. Chem. Phys., 105 (2007), 268.

Received 16 March 2009
Revised 4 August 2009

Materials Science-Poland, *Vol. 28*, *No. 1*, *2010*

Effect of thermal ageing on the evolution of microstructure and degradation of hardness of 2.25Cr-1Mo steel

B.B. JHA[1*], B.K. MISHRA[1], B. SATPATI[2], S.N. OJHA[3]

[1]Advanced Materials Technology Division, IMMT, Bhubaneswar-751013, India

[2]Materials Characterization Division, IMMT, Bhubaneswar-751013, India

[3]Department of Metallurgical Engineering, IT- BHU, Varanasi-221005, India

Thermal ageing of various durations and at various temperatures was performed in order to understand microstructural changes associated with precipitation and coarsening of carbides in 2.25Cr-1Mo steel. The severity of thermal ageing is expressed in terms of the Larson–Miller parameter (LMP). The microstructural examinations were carried out by optical and scanning electron microscopy techniques. A transmission electron microscope (TEM) and an electron probe micro analyzer (EPMA) were used to identify the carbide particles, and to analyse the shape, size and distribution of the precipitate phases. Influence of these precipitates on hardness degradation of the steel has been examined. The reasons for the variation in the microstructure and for the hardness degradation of steel arising from thermal ageing are discussed.

Keywords: *thermal ageing; microstructure; hardness degradation; 2.25Cr-1Mo steel*

1. Introduction

Ferritic 2.25Cr-1Mo steel is a popular engineering alloy used for high temperature applications such as heat exchangers, steam receivers, high temperature headers and piping in various power generating units [1]. As the service temperatures have been increasing to improve the thermal efficiency of power generating systems, materials having strong stability of microstructures and increased corrosion resistance at operating temperatures are needed for such applications. The main advantage of the steel under consideration is an improved high-temperature strength derived from molybdenum and chromium additions and the enhanced corrosion resistance derived from

*Corresponding author, e-mail: bbjha@immt.res.in

chromium [2]. The high temperature strength of this steel is derived mainly from two sources: solid solution strengthening of the ferrite matrix by carbon, molybdenum and chromium and precipitation hardening by carbides [3]. Due to its properties at elevated temperatures, this steel satisfies the safety criteria for operational use, as specified under section 3-ASME Case-47 of Ref. [4].

2.25Cr-1Mo ferritic steel has always been used in the normalized and tempered conditions or annealed conditions, depending upon the thickness of the component. Thin boiler tubes are made from steel in the annealed condition, whereas thick piping and headers are used mostly in the normalized and tempered conditions. Depending on cooling rates employed in these treatments, the microstructures of 2.25Cr-1Mo steel may vary from ferrite–pearlite aggregates to ferrite-bainite aggregates. The carbides obtained during the heat treatments are of the required morphology and distribution, so that the steel can maintain its strength at high temperature. However, due to the metastable nature of these precipitates, they undergo an undesirable transformation under operating conditions or during repair welding. Occasionally thermal transients can cause excessive local heating of the tubes, resulting in microstructural alteration [2, 5]. All these situations would result in microstructural variation of components quite different from the initial, optimized microstructure obtained in the normalized and tempered conditions, or after annealing.

2.25Cr-1Mo ferritic steel consists of bainite and ferrite containing iron carbides and fine M_2C type carbides in annealed condition. As the duration of ageing increases, a variety of secondary carbides like M_7C_3, $M_{23}C_6$ and M_6C gets precipitated [6, 7]. The precipitates also get coarsened with ageing. Such an evolution of precipitates, and their coarsening, influences the performance of this material at high temperatures. Although the microstructural instability of the steel, in terms of its cavity formation and its linkage under stress (leading to microcrack generation), is well documented [8, 9], but no systematic data is available on the microstructural deterioration due to carbide precipitation and coarsening. For this reason an investigation was made into microstructural degradation at various temperatures, together with subsequent analysis into how this influences hardness. Determination of the true state of degradation is an important consideration in the accurate assessment of the remaining operational lifetime of components.

2. Experimental

Materials. 2.25Cr-1Mo ferritic steel having nominal chemical composition (wt. %) C – 0.07, Mn – 0.42, Si – 0.019, S – 0.025, Cr – 2.28, P – 0.02, Mo – 0.98, Ni – 0.09, Fe – balance, has been used in the present investigation.

*Thermal ageing.*The starting material used in this study was shaped in the form of a plate 12 mm thick. From this plate strips measuring 12 ×12 × 250 mm^3 were cut using a power hacksaw and then machined to a size of 10 × 10 × 80 mm^3: the rolling directions were parallel to the length of the strips. These strips were then sealed in

evacuated quartz tubes and subject to annealing at 1223 K for 2 h. The temperature of the furnace was maintained constant, within an accuracy of ±1.0 K.

In order to study the microstructural degradation, these annealed strips were subject to ageing treatments at 873 K for 10 h, 923 K for 20 h, 973 K for 40 h and 973 K for 80 h using a tubular furnace. These treatments correspond to the values of the Larson–Miller parameter (LMP) of 33 012, 35 402, 37 846 and 38 374, respectively. Scales of the heat treated samples were then removed by coarse polishing on silicon carbide papers.

Metallography. Cubes of 10 × 10 × 50 mm^3 were cut from the heat treated samples, annealed and thermally aged to various degrees. These specimens were suitably mounted in a cold setting resin and were ground using successive grades of silicon carbide papers and then polished mechanically using 0.25 μ diamond paste for final, scratch-free polishing. Chemical etching was then done using a solution of 2 cm^3 HNO_3 in 100 cm^3 of methanol (i.e., 2% Nital) maximum for 10 s.

Chemically etched and dried specimens were examined under a Nikon make, metallurgical microscope (Model LV-150). Complete scanning was done at the lower magnification in order to extract the most representative microstructural features, which were then captured at higher magnification and presented as observations.

Scanning electron microscopy (SEM) and electron probe micro analysis (EPMA). All the heat treated samples, after chemical etching, were examined using a SEM (Joel Model-804 and a Hitachi Model S-3400 N) for phase identification. Energy dispersive X-ray Analysis (EDX) together with SEM was used for determination of the surface composition. An electron probe micro analyzer (Joel Model JXA-8100) was used to obtain the line scan profile showing the compositional variation of various elements in the matrix. X-ray images showing the elemental distribution of various elements in different phases was also obtained using EPMA. These analyses enabled identifying the concentration of solute atoms within the grains and at the grain boundaries: the state of deterioration of a given microstructure, namely the result of a particular ageing treatment, corresponded to a specific LMP value.

Transmission electron microscopy (TEM). For the transmission electron microscopy (TEM), very thin specimens ca. 0.5 mm thick were cut from various heat treated samples by electric discharge machining (EDM). These specimens were further thinned, using fine grade silicon carbide papers, up to a thickness of about 0.2 mm and then discs 3 mm in diameters were cut. They were further thinned by polishing both sides using silicon carbide papers and emery papers, up to the thickness of about 80 μ. The thickness of the discs was further reduced at the central portion, using a dimpler (M/s Gattan make), to a thickness of about 30 μ. Dimpled discs were then subject to ion milling till a fine perforated hole was made at the centre of the disc, enabling the adjacent area of the hole to be electron transparent.

A FEI make (model Tecnai G^2 20 twin) analytical transmission electron microscope operating at an accelerated voltage of 200 kV was used to identify carbides pre-

cipitated as a result of various degrees of ageing. Using this microscope it was possible to resolve the precipitates of size down to Angstrom level. Selected area diffraction (SAD) patterns from matrix containing precipitates, and also from precipitates alone, were obtained to ascertain the orientation difference of various carbide precipitates with that of the matrix. Microchemical analyses of precipitates were carried out using an EDX facility attached with TEM. The EDX attachment had a super ultra thin window with Si (Li) detector for analyzing the constituents. A combination of bright field and dark field imaging was carried out to ascertain a detailed morphology of the precipitates and their coarsening with respect to the increase in the degree of ageing.

Hardness measurement. Microhardness measurement of annealed (1223 K, 2 h) and aged specimens subject to various degrees of ageing, corresponding to LMP values of 33 012, 35 402, 37 846 and 38 374 was carried out using a microhardness tester (model RZD-00 of Leitz make). Indentations in both the phases were made with a diamond indenter using 0.5 N force and after measuring both the diagonals of the indentations, hardness values in VHN were obtained. Minimum of about five data points were taken for each measurement and the reported hardness values (Hv) in Table 1 are the average values of these five points. The maximum variation in the scatter of data was about 7.0%. This variation has also been indicated as an interval of confidence while plotting these hardness values in function of the L–M parameters.

3. Results and discussion

3.1. Microstructural analysis

Figure 1a shows the optical micrograph of 2.25Cr-1Mo steel in annealed conditions and Fig. 1b shows the same observed under SEM. The average initial grain size was measured and found to be 35 μm. Transmission electron micrographs of this sample showed fine precipitation of lenticular shaped carbides uniformly distributed within the grains of the bainitic matrix.

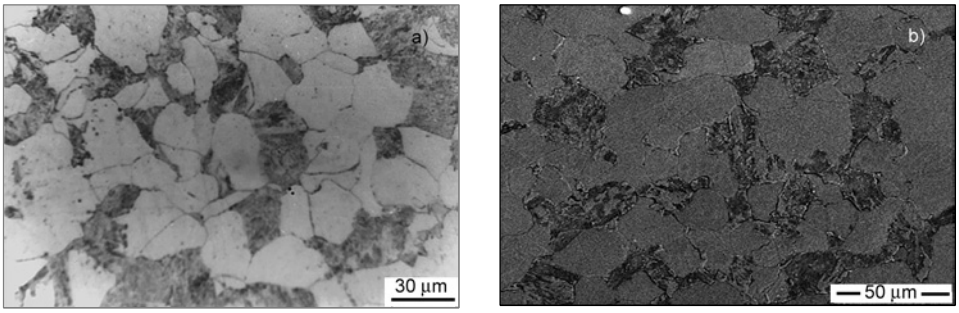

Fig. 1. Optical (a) and SEM (b) micrographs of 2.25Cr-1Mo steel showing bainite and ferrite phases after annealing (1223 K, 2h)

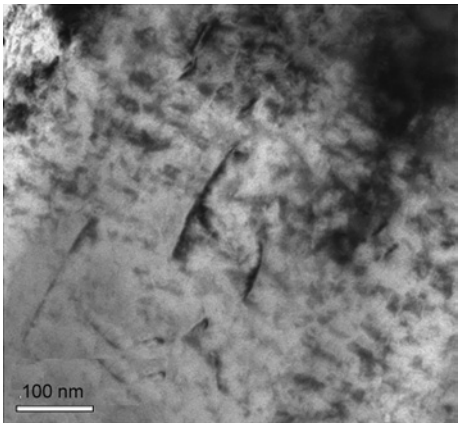

Fig. 2. Transmission electron micrograph of annealed 2.25Cr-1Mo steel showing lenticular precipitates of M_3C type in a bainite matrix

The shape of carbides is mostly lenticular, aligned parallel to each other along their axes, as shown in Fig. 2. It is observed that the size of these precipitates is of the order of about 100 nm. Figures 3a, b show the SAD pattern of a bainitic matrix containing these precipitates and their schematic indexing, respectively. The EDX results of 10–15 carbides showed them to be rich in iron. An EDX spectrum from typical carbide is shown in Fig. 4, which clearly revealed that these lenticular shaped carbides are of M_3C type, as observed by other workers [7, 10].

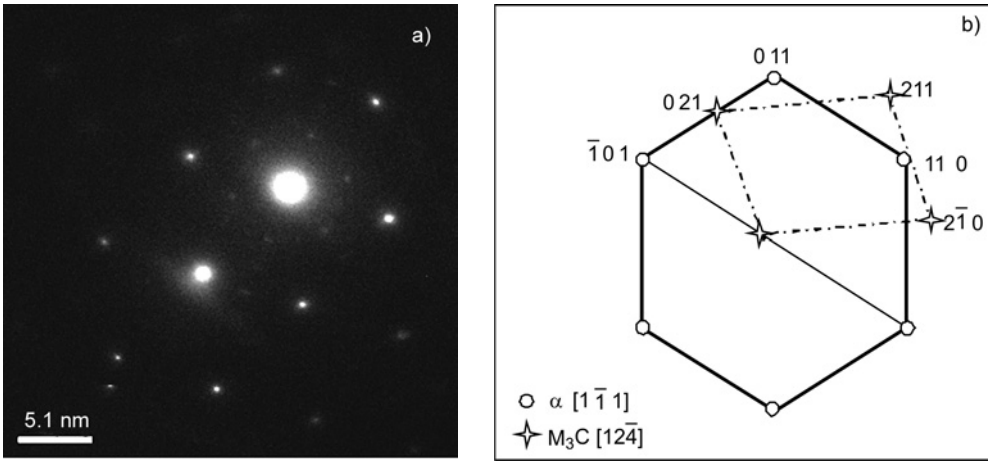

Fig. 3. SAD pattern of the bainitic matrix (a) containing precipitates of M_3C type in annealed 2.25Cr-1Mo steel and schematic indexing of a SAD pattern (b) shown in Fig. 3a

Transmission electron micrographs of the samples corresponding to the treatment of 873 K for 10 h (LMP = 33 012) showed the evolution of the needle type of precipitates, as shown in Fig. 5. The EDX results showed them to be rich in chromium with considerable iron contents. An EDX spectrum from typical carbide is shown in Fig. 6.

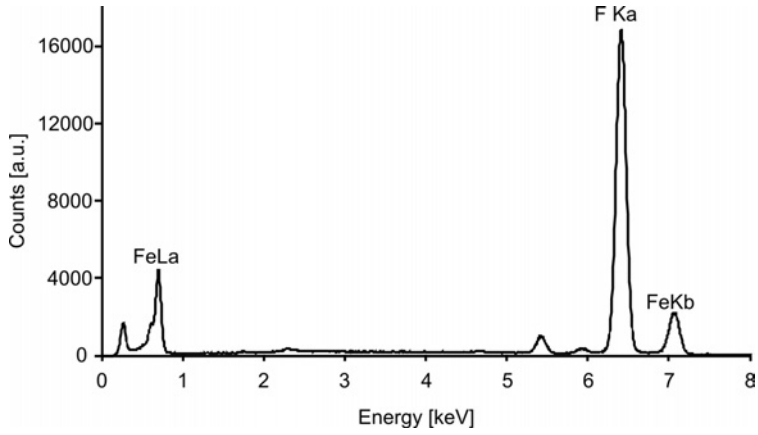

Fig. 4. Typical EDX spectrum of lenticular shaped iron rich carbide (M_3C type)

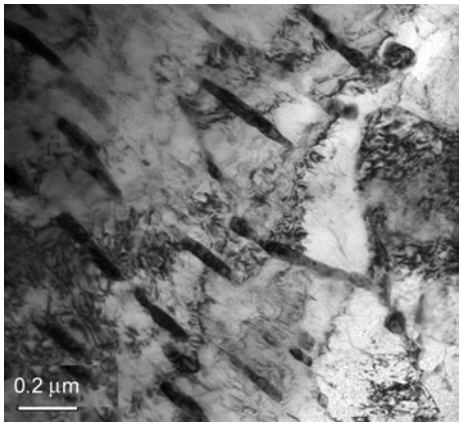

Fig. 5. Transmission electron micrograph of thermally aged 2.25Cr-1Mo steel (LMP = 33 012) showing precipitation of needle shaped carbides of a M_7C_3 type in a bainite matrix

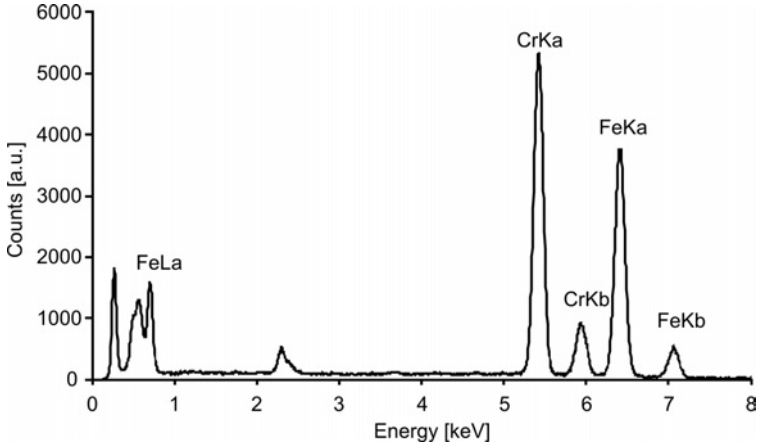

Fig. 6. Typical EDX spectrum of needle shaped carbide rich in chromium with considerable iron content (M_7C_3 type)

Selected area diffraction pattern, along with indexing of this kind of precipitates, showed a streaking pattern (Fig. 7) which is a typical characteristic of the M_7C_3 type of precipitates. These precipitates ca. 300 nm in size are also found to be oriented in the same direction.

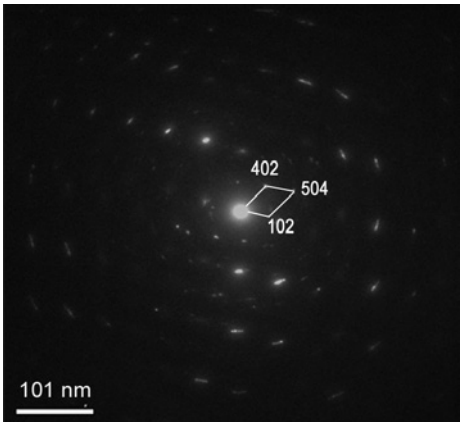

Fig. 7. SAD pattern of bainitic matrix containing precipitates of a M_7C_3 type showing streaking pattern along with indexing in thermally aged 2.25Cr-1Mo steel (LMP = 33 012)

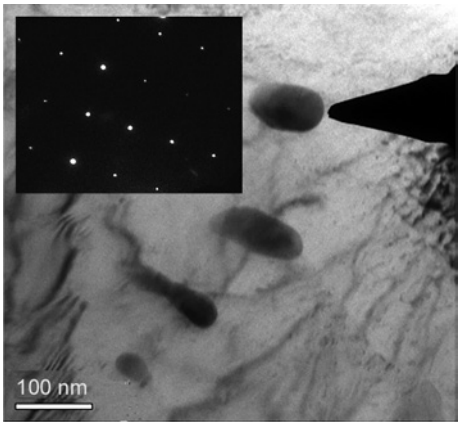

Fig. 8. Transmission electron micrograph of thermally aged 2.25Cr-1Mo steel (LMP = 35 402) showing precipitation of globular carbides of $M_{23}C_6$ type within the bainitic grain. The inset displays [100] zone of this phase

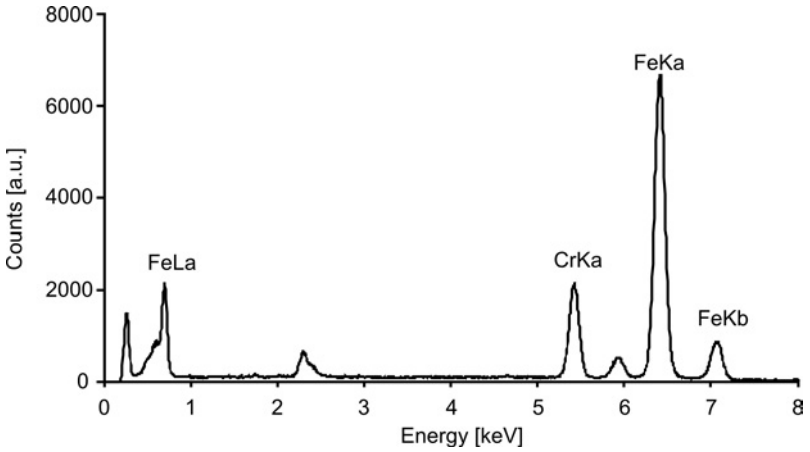

Fig. 9. Typical EDX spectrum of globular shaped carbide rich in iron with a considerable chromium content ($M_{23}C_6$ type)

Transmission electron micrographs of the samples corresponding to the treatment of 923 K for 20 h (LMP = 35 402) showed precipitation of globular carbides (size ca. 500 nm) within the bainitic matrix (Fig. 8). The inset of Fig. 8 also shows the SAD pattern from the precipitates along the zone axis [100]. The EDX results of these

globular shaped carbides showed them to be rich in iron with considerable chromium content. An EDX spectrum from typical globular shaped carbide is shown in Fig. 9. The spectrum revealed that these carbides are of $M_{23}C_6$ type, being at this stage rich in iron with a considerable chromium content. These observations suggest that globular precipitates evolved in bainitc matrix are different from those observed after the treatment at 873 K for 10 h (LMP = 33 012). The presence of $M_{23}C_6$ has also been reported by other workers [10] for this variety of steel and under this condition.

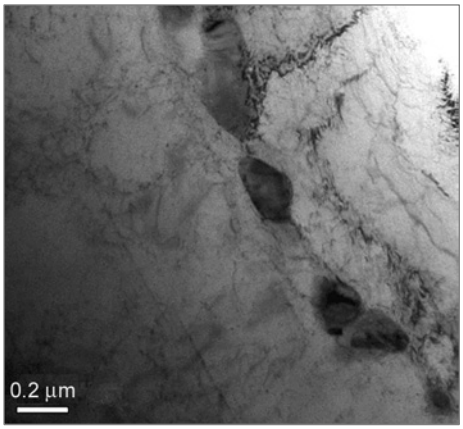

Fig. 10. Transmission electron micrograph showing precipitation of globular carbides of $M_{23}C_6$ type of at grain boundary in thermally aged 2.25Cr-1Mo steel (LMP = 37 846)

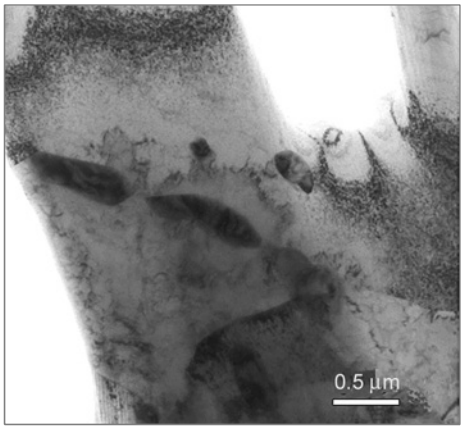

Fig. 11. Transmission electron micrograph showing precipitation of plate shaped carbides of M_6C type of at grain boundary in thermally aged 2.25Cr-1Mo steel (LMP = 37 846)

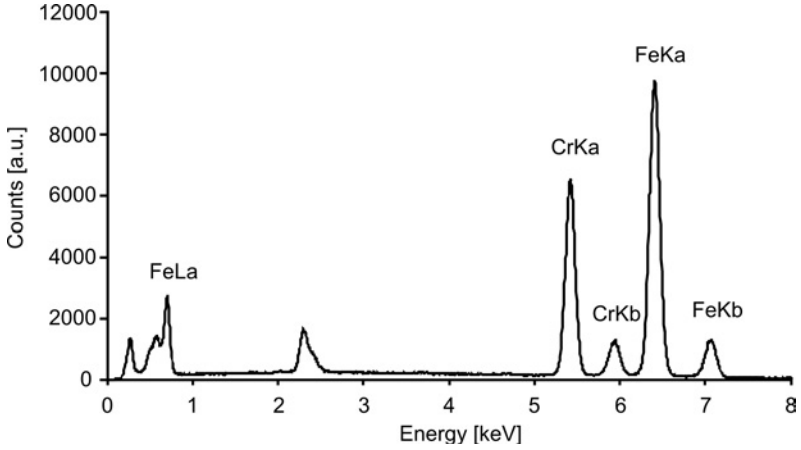

Fig. 12. Typical EDX spectrum of globular carbides rich in iron and chromium ($M_{23}C_6$ type)

Transmission electron micrographs of the specimen corresponding to the treatment at 973 K for 40 h (LMP = 37 846) are shown in Figs. 10 and 11. It is observed that by this treatment (LMP value of 37 846), the globular carbides have coarsened

and they are aligned at the grain boundaries. Their size has also increased (ca. 1 μ). Some plate shaped precipitates have also been observed (Fig. 11) as a result of this treatment. An EDX spectrum of typical globular shaped carbide is shown in Fig. 12. The spectrum indicates that these carbides contain a considerable amount of iron and chromium, being identified as $M_{23}C_6$ type. Figure 13 shows the EDX spectrum of the plate shaped precipitates shown in Fig. 11.

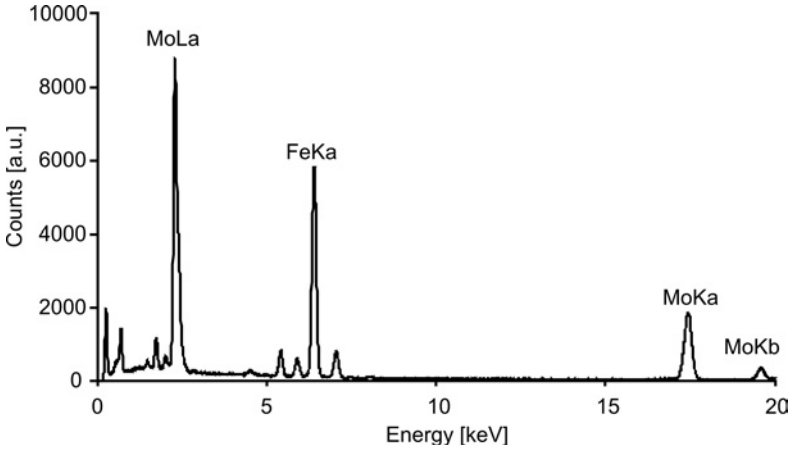

Fig. 13. Typical EDX spectrum of plate shaped carbide rich in molybdenum with a considerable iron content (M_6C type)

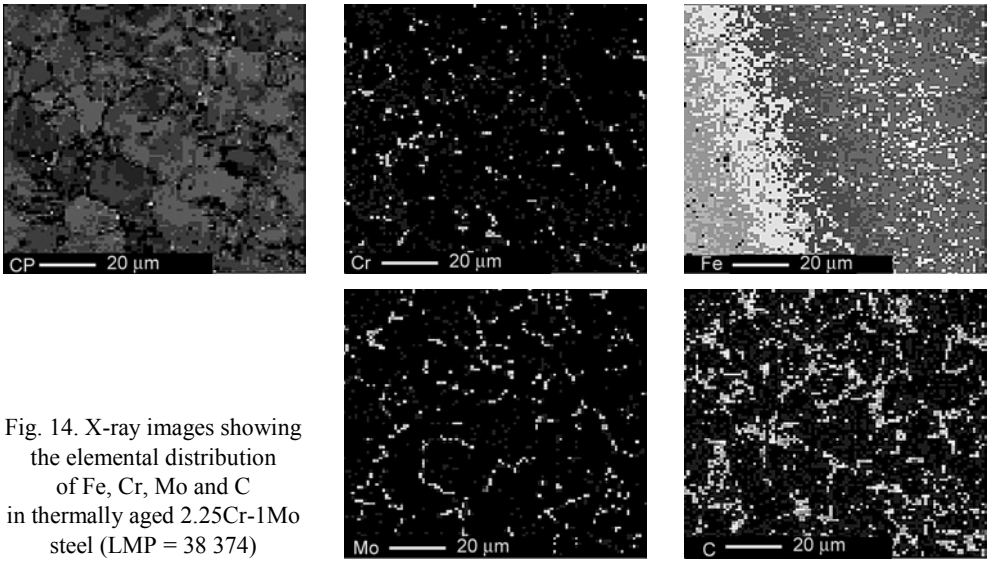

Fig. 14. X-ray images showing the elemental distribution of Fe, Cr, Mo and C in thermally aged 2.25Cr-1Mo steel (LMP = 38 374)

The spectrum indicates that the plate shaped precipitates are molybdenum rich with significant iron content. They are a typical M_6C type of precipitate [7, 10, 11]. Therefore, it is observed that at this stage of ageing, precipitated carbides are a mix-

ture of $M_{23}C_6$ and M_6C type. In this case, the $M_{23}C_6$ type of precipitate contains a greater amount of chromium as compared with the same precipitate having the LMP value 35 402. Observations of other workers [7, 10–12] have also showed that these globular carbides are of $M_{23}C_6$ type, rich in iron and chromium, and that the plate shaped carbides are of M_6C type, rich in molybdenum.

Figure 14 shows X-ray images of a specimen thermally aged at 973 K for 80 h, corresponding to the LMP value of 38 374. Precipitation of chromium and molybdenum carbides at grain boundaries is clearly evident in these figures. Thus, these micrographs very clearly show that as the exposure temperature or time is increased, molybdenum and chromium carbides get precipitated in the sequence of M_3C, M_7C_3, $M_{23}C_6$ and M_6C at the grain boundaries and within the grains themselves. Precipitates also get coarser as we increase the values of the L–M parameters.

3.2. Hardness degradation

The hardness values of both phases, i.e. bainite and ferrite in function of the Larson–Miller parameters are shown in Fig. 15 for both annealed (virgin) material (1223 K for 2 h) and thermally aged specimens. Degradation in hardness of bainitic phase is much stronger (62%) as compared with ferritic phase (12%).

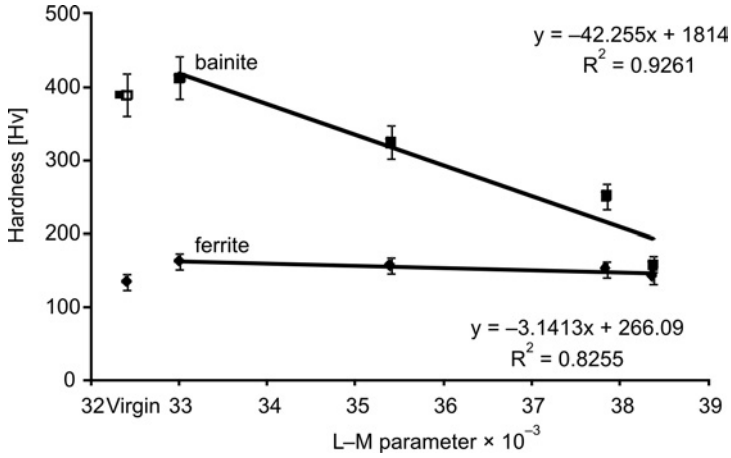

Fig. 15. Dependences of hardness variation of Virgin and thermally aged 2.25Cr-1Mo steel on the L–M parameter

Table 1 gives the hardness values for annealed and thermally aged specimens corresponding to various values of LMP. Hardness has been found to be a sensitive material degradation parameter, sufficient to predict the remaining life of components operating at higher temperatures. It has been reported [13, 14] that in low alloy ferritic steel, solute depletion and precipitate coarsening are the two predominant modes of material degradation during high temperature exposure.

Table 1. Hardness values of samples of annealed and thermally aged 2.25Cr-1Mo steel

Microstructural conditions	Bainite hardness [HV]	Ferrite hardness [HV]
Annealed (1223 K/2 hr)	397	138
Thermally aged (LMP 33.012)	412	162
Thermally aged (LMP 35.402)	324	156
Thermally aged (LMP 37.846)	251	152
Thermally aged (LMP 38.374)	157	141

Results on hardness measurements of samples of thermally aged 2.25Cr-1Mo steel indicate that solute depletion plays a minimum role in the degradation of hardness of this material. This is because the hardness degradation in the ferrite matrix is found to be only up to ca. 12.0%. This could be either because the amounts of solute atoms are very small or their diffusion with time and temperature is very fast. Hardness degradation of up to about 62.0% has been observed in the bainitic phase (Fig. 15). Microstructural examination of this steel at various degrees of ageing indicated a coarsening of carbide particles (Figs. 5, 8, 10 and 11) and a gradual change of their shapes and morphologies. All these observations, therefore, indicate that the predominant modes of hardness degradation in 2.25Cr-1Mo steel are due to a coarsening of alloy carbide precipitates, and a change in their shapes and morphologies. These phenomena are more predominant in bainitic phase, resulting in increased extent of hardness decline of this phase as compared with ferritic phase.

In addition, the variation of the hardness (of both the phases) could be applied to assess the life expectancy of components made out of this material, because the degradation of thermally aged specimens is expected to share similar features with the degradation profile of materials exposed to high temperatures under normal operating conditions. By measuring the hardness of any phase (preferably bainite) after certain, known, number of hours of service, one can ascertain the temperature at which the tube is actually operating. Then, by using the stress rupture plot of this steel, the remaining life of the tube can be estimated [8, 9] and preventive measures could then be taken to avoid potentially catastrophic component failures.

4. Conclusions

The present investigation indicated that in 2.25Cr-1Mo steel, as the ageing temperature or time is increased, molybdenum and chromium carbides get precipitated in the sequence of M_3C, M_7C_3, $M_{23}C_6$ and M_6C at the grain boundaries and within the grains. Precipitation of chromium and molybdenum carbides and coarsening of carbide precipitates are the main contributors of microstructural deterioration in this steel, as a result of increase in the severity of thermal ageing.

The hardness of the both phases (i.e., bainite and ferrite) degrades in function of the L–M parameters, and the hardness degradation of bainite is greater than that of the ferrite phase.

It has been observed that the coarsening of alloy carbide precipitates and the change in their shapes and morphologies are the two predominant factors influencing degradation of hardness in this variety of steel when exposed to service temperatures. Degradation of hardness in function of LMP could be used as a tool for predicting the lifetime of components made up of this steel and operating at higher temperatures.

References

[1] SANDERSON J., [In:] *Ferritic steels for high temperature applications*, Proc. Conf. ASM, A. Khare (Ed.), (1983), p. 178.
[2] PATTERSON S.R., KUNTZ T.A., MOSER R.S., VAILLANCOURT H., [In:] *Boiler tube failure metallurgical guide*, Vol. 1, Techn. Rep.(TR-102433), Electric Power Research Institute, Palo Alto, CA, (1993), p. 26.
[3] VISWANATHAN R., *Damage mechanisms and life assessment of high temperature components*, ASM Int., Metal Park, Ohio, (1989), p. 205.
[4] PATRIARCA D., [In:] *Topical conference on ferritic steels for use in nuclear technologies*, Metall. Soc. AMIE, J.W. Davies, D.J. Michel (Eds.), (1984), p. 107.
[5] THOMSON R.C., Bhadeshia H.K.D.H., Mater. Sci. Tech., 10 (1994), 193.
[6] GOPE N., MUKHERJEE T., SARMA D.S., Mater. Trans. JIM, 33 (1992), 110.
[7] SAROJA S., PARAMESWARAN P., VIJAYALAXMI M., RAGHUNATHAN V.S., Acta Metall. Mater., 43 (1995), 2985.
[8] VISWANATHAN R., PATTERSON S.R., GRUNLOH H., GEHL S., J. Press. Vessel Techn., 116 (1994), 1.
[9] CANE B.J., APLINE P.F., BREAR J.M., J. Press. Vessel Techn., 107 (1985), 295.
[10] JAYAN V., MANDAL P.K., HIRANI M., SANYAL S.K., Mater. Sci. Techn., 15 (1999), 1308.
[11] GANESAN V., RODRIGUEZ P., [In:] *Materials aging and life management*, B. Raj [Ed.], Proc. Int. Symp. Materials Ageing and Life Management, Kalpakkam, India, Allied Publishers Ltd., Chennai, (2000), p. 293.
[12] JAYAN V., KHAN M.Y., HUSAIN M., Mater. Lett., 58 (2004), 2569.
[13] FUJIAMA K., KIMURA K., MURAMATSU M., YAMADA M., ISIJ Int., 30 (1990), 869.
[14] GOPE N., CHATTERJEE A., MUKHERJEE T., SARMA D.S., Metall. Trans. A, 24 (1993), 315.

Received 20 March 2009
Revised 23 April 2009

Materials Science-Poland, *Vol. 28*, *No. 1*, *2010*

First-principles study of the elastic and mechanical properties of Ni_3Al under high pressure

S. BOUCETTA[1*], T. CHIHI[1], B. GHEBOULI[2], M. FATMI[3]

[1]Laboratoire d'Elaboration de Nouveaux Matériaux et Caractérisations (ENMC), Département de Physique, Université Ferhat Abbas, Sétif 19000, Algérie

[2]Laboratoire d'Etudes de Surfaces et Interfaces des Matériaux Solides (LESIMS), Département de Physique, Université Ferhat Abbas, Sétif 19000, Algérie

[3]Laboratoire de Physique et Mécanique des Matériaux Métalliques (LP3M), Département d'Optique et Mécanique de Précision, Université Ferhat Abbas, Sétif 19000, Algérie

A first-principles study of the structural and elastic properties of the intermetallic compound Ni_3Al was undertaken, exploiting density-functional theory and generalized gradient approximation (GGA). The elastic constants C_{11}, C_{12}, and C_{44} were shown to be sufficiently close to the density of the *k*-point mesh in the deformed Brillouin zone to conclude that the elastic anisotropy of the coefficient A increases as the pressure increases. Young's modulus of Ni_3Al along {100} is approximately two times higher than that along {111}. The computed elastic constants from first principles satisfy $C_{11} > C_{12} > C_{44}$, which are in good agreement with the experiment data. The cubic Ni_3Al possesses a bulk modulus of 312 GPa, comparable to that of cubic hafnium nitride. Theoretical calculations for Ni_3Al show that all elastic moduli increase monotonically as the pressure increases. These results suggest there are potential technological applications of such materials in extreme environments.

Keywords: *intermetallics; structural properties; elastic properties*

1. Introduction

Ni_3Al, an intermetallic compound, is representative of a class of systems exhibiting unique mechanical properties which make them attractive for structural applications. Hence Ni_3Al is a very promising material for high temperature and pressure applications [1]. In an early theoretical study on the Ni_3Al, Dobrina et al. [2] investigated its electronic structure and elastic properties by using the *ab initio* density func-

*Corresponding author, e-mail: boucetta_said02@yahoo.fr

tional theory and the FLMTO method. Sot and Kurzydłowski [3] studied the elastic properties of Ni_3Al, using the ab initio calculations for lower pressures. Hsu [21] studied electronic absorption spectra of Ni_3Al and Ni_3Ga. Sob et al. [22] investigated the magnetism of Ni_3Al and Fe_3Al under extreme pressure and shape deformation from ab initio study. Hsu and Wang [23] investigated optical properties of Ni_3Al, Ni_3Ga and Ni_3In. Guo et al. [24] studied the electronic structure, mechanical and magnetic properties of Ni_3Al, Ni_3Ga and Ni_3In from the first-principles and experimental studies. To the best of our knowledge, no other theoretical studies on Ni_3Al at high pressures have been reported.

In this paper, we report first-principles calculations of total energy electronic structure and the elastic constants of Ni_3Al. The elastic constants C_{ij} determine the response of the crystal to external forces, as characterised by the bulk modulus, shear modulus, Young's modulus, and Poisson's ratio, playing an important role in determining the strength of a material. The elastic constants are the measure of the shear and tensile strength of crystals in the long-wavelength limit. They provide valuable information on the bonding characteristics between adjacent atomic planes and the anisotropic character of the bonding. Here, we report a theoretical study of the equation of state, elasticity and mechanical properties of the intermetallic compound Ni_3Al.

2. Computational method

The use of computer simulation techniques is becoming more important in the understanding of the microscopic behaviour of materials. Our first-principles calculations are performed with the plane-wave pseudo potential (PWPP) method implemented with the CASTEP (Cambridge Serial Total Energy Package) simulation program [4]. This is based on the density functional theory (DFT) [5, 6] which is, in principle, an exact theory of the ground state. The generalized gradient approximation (GGA) method, proposed by Perdew and Wang, known as PW91 [7], is applied for determining the electronic exchange-correlation potential energy. The Coulomb potential energy caused by electron–ion interaction is described according to the ultrasoft scheme [8], in which the orbitals of Ni ($3d^8 4s^2$) and Al ($3s^2 p^1$), are treated as valence electrons. By the norm-conservation condition, the pseudo-wave function related to pseudopotential matches the plane wave function expanded with Kohn–Sham formation beyond the cut-off energy. Using high cut-off (660 eV) energy, accurate results can be obtained at the expense of long computational time. The cut-off energy for the plane wave expansion is 330 eV and the Brillouin zone sampling was carried out using an 8×8×8 set of the Monkhorst–Pack mesh [9].

The structural parameter a_0 of Ni_3Al was determined using the Broyden–Fletcher –Goldfarb–Shenno (BFGS) minimization technique. Therefore, the present parameters are sufficient to obtain well converged total energy and geometrical configurations.

3. Numerical results and discussion

3.1. Structural properties

The Ni_3Al is known to crystallize in a cubic lattice of Cu_3Au structure type with the space group $Pm\bar{3}m$, and the equilibrium lattice parameter is 3.572 Å [10–12]. Two inequivalent atomic sites, the aluminium atom is positioned at (0,0,0) and the nickel atoms at (1/2,1/2,0), (1/2,0,1/2) and (0,1/2,1/2) (Fig. 1).

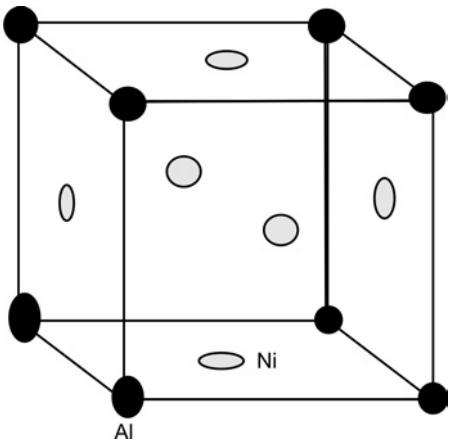

Fig. 1. The cubic structure of Ni_3Al

Table 1. Calculated and experimental values of the equilibrium lattice constant a_0 [Å], bulk modulus B_0 [GPa] and bulk derivative in cubic Ni_3Al compound.

a_0	B_0 [GPa]	B'$_0$	Source
3.558	130.13	8.67	This work
3.572[a] 3.56[b]	171[b]		Experiment
3.588[a] 3.48[b]	234[b]		Other

[a]Ref. [3].
[b]Ref. [2].

The lattice parameter of Ni_3Al calculated using the (PP-PW) method is given in Table 1, along with the available experimental and theoretical data. Our calculated equilibrium lattice parameter a_0 is in a good agreement with the experimental data. The calculated lattice constant a_0 is only 0.4% smaller than the experimental value. The calculated unit cell volume at an applied hydrostatic pressure in the range from 0 to 30 GPa were used to construct the equation of state (EOS), which was fitted to the third order Birch–Murnagham equation [13] (Fig. 2):

$$P=\frac{3}{2}B_0\left(\left(\frac{V}{V_0}\right)^{-7/3}-\left(\frac{V}{V_0}\right)^{-5/3}\right)\left(1+\frac{3}{4}\left(B'-4\right)\left(\left(\frac{V}{V_0}\right)^{-2/3}-1\right)\right)$$

With V_0 fixed at the value determined from the zero pressure data, we obtained by least-squares fitting the bulk modulus B_0 and its pressure derivative B_0' under zero pressure. These are listed in Table 1. We can see that the calculated value of the bulk modulus B_0 from the elastic constants $B_0 = (C_{11}+2C_{12})/3$ has nearly the same value as the one obtained from the EOS fitting. This might be an estimate of the reliability and accuracy of our calculated elastic constants for Ni_3Al.

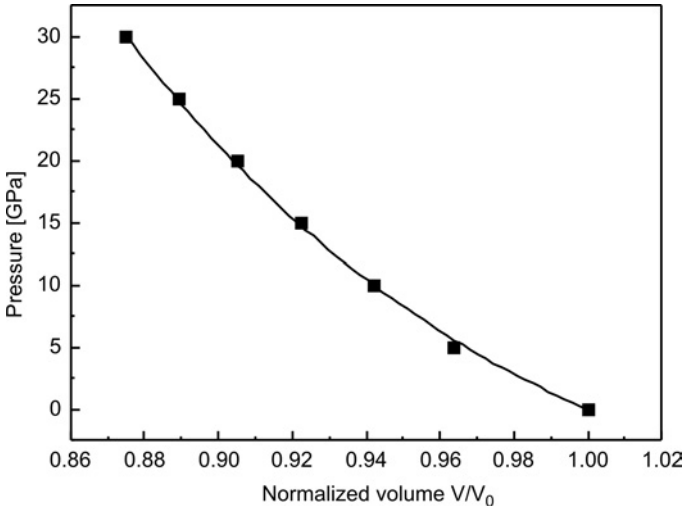

Fig. 2. Dependence of the calculated pressure on the normalized volume for Ni_3Al; the solid line is the plot of the Birch–Murnaghan equation of state with the parameters listed in Table 1

3.2. Elastic properties

The elastic constants are important parameters describing the response to an applied macroscopic stress. In Table 2, the calculated elastic constants and shear modulus of Ni_3Al under zero pressure are presented. We next study the pressure dependence of the elastic properties. In Figure 3, we present the variation of the elastic constants (C_{11}, C_{12} and C_{44}) and the bulk modulus B of Ni_3Al with respect to the variation of pressure. We observe a linear dependence in all curves in the considered range of pressure. It is easy to observe that the elastic constants C_{ij} and the bulk modulus B increase when the pressure is enhanced in this compound.

For a cubic crystal under a pressure P, the generalized elastic stability criteria [14, 15] are:

$$K=C_{11}+2C_{12}+P>0,\quad K_1=C_{44}-P>0,\quad K_2=C_{11}-C_{12}-2P>0$$

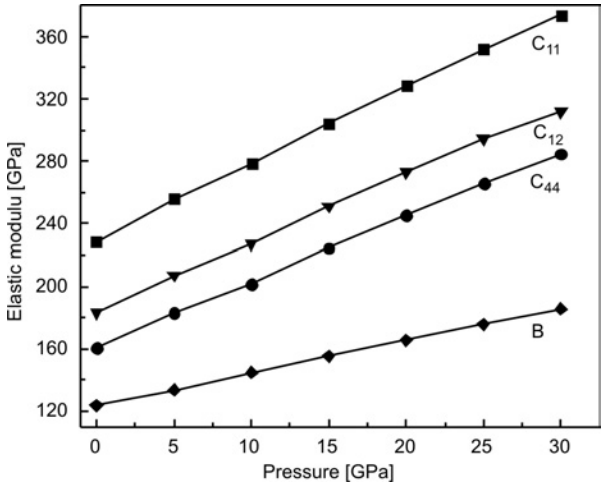

Fig. 3. Calculated pressure derivatives of the elastic constants C_{11}, C_{12} and C_{44} and the bulk modulus B_0 for Ni_3Al

Table 2. Calculated and experimental values of the elastic constants C_{ij} [GPa], shear moduli G [GPa], anisotropy factor A, Young's modulus E and Poisson's ratio ν in cubic Ni_3Al

C_{11}	C_{12}	C_{44}	G	A	E	ν	Source
228.4	160.41	123.75	34	3.64	96.04	0.41	This work
230[a] 221[b]	150[a] 146[b]	131[a] 124[b]	–	3.31[b]	–	0.40[b]	Experiment
230[a] 278[b]	139[a] 212[b]	123[a] 186[b]	–	5.64[b]	–	0.43[b]	Other

[a]Ref. [3].
[b]Ref. [2].

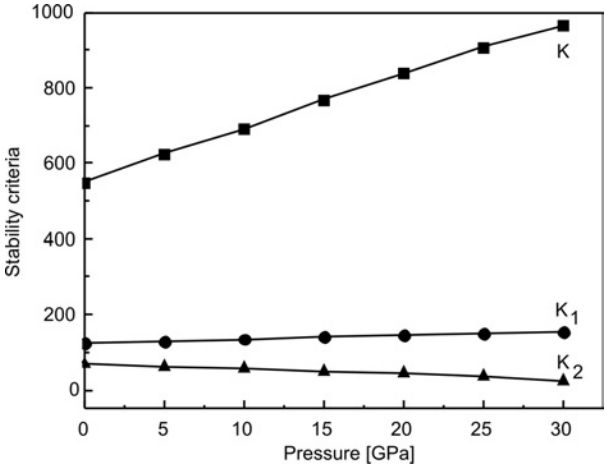

Fig. 4. Pressure dependences of the stability criteria

The obtained results are shown in Fig. 4. These criteria are satisfied in the studied pressure range. From our calculated C_{ij}, it is known that this compound is mechanically stable.

3.3. Mechanical properties

From the theoretical elastic constants, we computed the elastic wave velocities. The single crystal elastic wave velocities in different directions are given by the resolution of the Cristoffel equation [16]:

$$\left(C_{ijkl}n_j n_k - \rho v^2 \delta_{il}\right)u_l$$

where C_{ijkl} is the single crystal elastic constant tensor, n is the propagation direction, ρ is the density of material, u is the wave polarisation and v is the wave velocity. The solutions of this equation are of two types: a longitudinal wave with polarisation parallel to the direction of propagation v_l and two shear waves v_{T1} and v_{T2} with polarisations perpendicular to n. Another important parameter is the elastic anisotropy factor, A, which gives a measure of the anisotropy of the elastic wave velocity in a crystal. In a cubic crystal, the elastic anisotropy factor is given by [17]:

$$A = \frac{2C_{44} + C_{12}}{C_{11}} - 1$$

which is zero for an isotropic material. The plot of the elastic anisotropy factor is shown in Fig. 5.

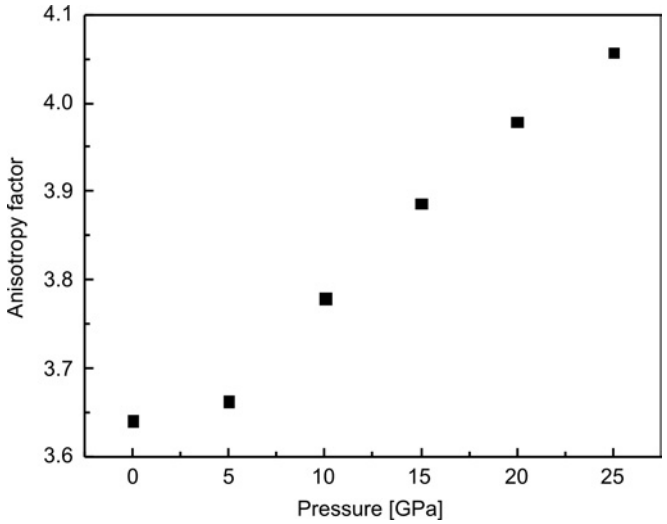

Fig. 5. Pressure dependence of the elastic anisotropy

The calculated elastic wave velocities along the [100], [110] and [111] directions for Ni_3Al under zero pressure are given in Table 3. Under zero pressure, longitudinal waves propagate faster along [111] and shear waves are slowest along [110] for Ni_3Al, which has a positive elastic anisotropy factor.

Table 3. The elastic wave velocities [$m \cdot s^{-1}$] for different propagation directions for Ni_3Al

Direction	v_L^{100}	v_{T1}^{100}	v_{T2}^{100}	v_L^{110}	v_{T1}^{110}	v_{T2}^{110}	v_L^{111}	v_{T1}^{111}	v_{T2}^{111}
Value	5733.18	4215.78	4215.78	6819.54	2211.83	4220.04	7077.49	3032.77	3032.77

Once the elastic constants are determined, we compare our results with experimental data, or predict what the elastic constants should be for a given experiment. For cubic systems, the isotropic bulk modulus B is given exactly by:

$$B = \frac{C_{11} + 2C_{12}}{3}$$

The bounds on the shear modulus are given by:

$$G_R = \frac{5C_{44}\left(C_{11} - C_{12}\right)}{4C_{44} + 3\left(C_{11} - C_{12}\right)}, \qquad G_V = \frac{C_{11} - C_{12} + 3C_{44}}{5}$$

We also calculated Young's modulus E and Poisson's ratio v which are frequently measured for polycrystalline materials when investigating their hardness. These quantities relate to the bulk modulus and the shear modulus by the following equations [18]:

$$E = \frac{9BG}{3B + G}, \qquad v = \frac{3B - E}{6B}$$

The shear moduli G_R and G_V, Young's modulus E and Poisson's ratio v for Ni_3Al calculated from the elastic constants are listed in Table 2.

3.4. Calculation of the Debye temperature

Having calculated Young's modulus E, the bulk modulus B and the shear modulus G, we can calculate the Debye temperature, which is an important fundamental parameter closely related to many physical properties such as elastic constants, the specific heat and the melting temperature. At low temperatures, the vibrational excitation arises solely from acoustic mode. Hence, at low temperatures, the Debye temperature calculated from the elastic constants is the same as that determined from specific heat measurements. One of the standard methods to calculate the Debye temperature θ_D is

based on the elastic data, since θ_D may be estimated from the average sound velocity v_m by the following equation [19]:

$$\theta_D = \frac{h}{k_B}\left(\frac{3n}{4\pi V_a}\right)^{1/3} v_m$$

where h is Planck's constant, k_B Boltzmann's constant and V_a the atomic volume. The average sound velocity in the polycrystalline material is given by [20]:

$$v_m = \left(\frac{1}{3}\left(\frac{2}{v_l^2}+\frac{1}{v_t^3}\right)\right)^{-1/3}$$

where v_l and v_t are the longitudinal and transverse sound velocities of an isotropic aggregate obtained using the shear modulus G and the bulk modulus B from Navier's equation [18]:

$$v_l = \left(\frac{3B+4G}{3\rho}\right)^{1/2} \quad \text{and} \quad v_t = \left(\frac{G}{\rho}\right)^{1/2}$$

The calculated sound velocity and Debye temperature as well as the density for Ni_3Al are given in Table 4.

Table 4. The calculated density ρ, the longitudinal, transverse and average sound velocity v_l, v_l and v_m calculated from polycrystalline elastic modulus, and the Debye temperatures θ_D calculated from the average sound velocity for Ni_3Al

Parameter	ρ [g cm^{-3}]	v_l [m·s^{-1}]	v_t [m·s^{-1}]	v_m [m·s^{-1}]	Θ_D [K]
Value	6.94882	6712.24	3590.82	4010.63	516.84

4. Conclusion

In this paper, the elastic and mechanical properties of the Ni_3Al intermetallic compound have been studied based on density functional theory (DFT), and the generalised gradient approximation (GGA) method. It has been shown that the equilibrium lattice parameter of the Ni_3Al compound is in excellent agreement with the available experimental data. It has also been shown that the elastic constants of Ni_3Al compound, obtained from the calculations, satisfy the criterion of mechanical stability in a cubic structure under an applied pressure. The computed results for the bulk and shear moduli suggest that the hardness of this material increases upon increasing pressure.

Acknowledgements

Professor L. Louail is acknowledged for providing the CASTEP software used to perform this calculations. This work is supported by the ENMC Laboratory, University of Setif.

References

[1] LAKHTINE I., *Métallographie et Traitement Thermiques des Métaux*, Mir, Moscow, 1982 (in French).
[2] DOBRINA I., KIOUSSIS N., SAY PENG LIM, Phys. Rev. B, 54 (1996), 14413.
[3] SOT R., KURZYDŁOWSKI K.J., Mater. Sci.-Poland, 23 (2005), 587.
[4] SEGALL M.D., LINDAN P.J.D., PROBERT M.J., PICKARD C.J., HASNIP P.J., CLARK S.J., PAYNE M.C., J. Phys. Cond. Matter., 14 (2002), 2717.
[5] HOHENBERG P., KOHN W., Phys. Rev. B, 136 (1964), 864.
[6] KOHN W., SHAM L.J., Phys. Rev. A, 140 (1965), 113.
[7] PERDEW J.P., CHEVARY J.A., VOSKO S.H., JACKSON K.A., PEDERSON M.R., SINGH D.J., FIOLHAIS C., Phys. Rev. B, 46 (1992), 6671.
[8] VANDERBILT D., Phys. Rev. B, 41 (1990), 7892.
[9] MONKHORST H.J., PACK J.D., Phys. Rev. B, 13 (1976), 5188.
[10] ICDD 09-0097, J. Met., 9 (1957), 865.
[11] SIMMONS G., WANG H., *Single Crystal Elastic Constants and Calculated Aggregate Properties: A Handbook*, MIT Press, Cambridge, MA, 1971.
[12] Smithells, Metals Reference Book, 6th Ed. E.A. Brandes (Ed.), Butterworths, London, 1983.
[13] BIRCH F., J. Geophys. Res., 83 (1978), 1257.
[14] YIP S., LI J., TANG M., WANG J., Mater. Sci. Eng. A, 317 (2001), 236.
[15] SINKO G.V., SMIMOV A., J. Phys. Cond. Matter., 14 (2002), 6989.
[16] KARKI B.B., STIXRUDE L., CLARK S.J., WARREN M.C., ACKLAND G.J., GRAIN J., J. Am. Mineral. Soc., (1997), 8251.
[17] BOUHEMADOU A., Model. Sim. Mater. Sci. Eng., 16 (2008), 055007.
[18] SCHREIBER E., ANDERSON O.L., SOGA N., *Elastic Constants and their Measurements*, McGraw-Hill, New York, 1973.
[19] WACHTER P., FILZMOSER M., REBISANT J., J. Phys. B, 293 (2001), 199.
[20] ANDERSON O.L., J. Phys. Chem. Solids, 24 (1963), 909.
[21] HSU L.-S., WANG Y.-K., TAI Y.L., LEE J.F., J. Alloys Compd., 413 (2006), 11.
[22] SOB M., LEGUT D., FRIAK M., FIALA J., J. Magn. Magn. Mater., 272 (2004), E205.
[23] HSU L.-S., WANG Y.-K., J. Alloys Compd., 377 (2004), 29.
[24] GUO G.Y., WANG Y.-K., HSU L.-S., J. Magn. Magn. Mater., 239 (2002), 91.

Received 13 May 2009
Revised 23 June 2009

Materials Science-Poland, *Vol. 28*, *No. 1*, *2010*

Density functional study of Mg_2FeH_6 complex hydride

J. ZHANG[1*], Y.N. HUANG[2], C.G. LONG[2], D.W. ZHOU[2], J.S. LIU[2]

[1]Institute of Automobile and Mechanical Engineering,
Changsha University of Science and Technology, Changsha 410114, China

[2]College of Materials Science and Engineering, Hunan University, Changsha 410082, China

[3]State Key Laboratory of Advanced Design and Manufacturing for Vehicle Body,
Hunan University, Changsha 410082, China

Mg_2FeH_6, which has the highest volumetric hydrogen density, is considered a promising hydrogen storage material. Within the framework of the density functional theory, the crystal structure, physical properties, electronic structure and formation capacity of Mg_2FeH_6 complex hydride have been investigated. The optimized structural parameters correspond closely with the experimental data from X-ray and neutron powder diffraction measurements. A detailed study of the electronic structures, including the energy band, density of states (DOS) and charge density distribution, reveals the orbital hybridization and bonding characteristics within this hydride. It was shown that Mg_2FeH_6 is a semiconductor with the energy gap of ca. 2.3347 eV, and that a mixed ionic-covalent bond between Fe and H in FeH_6 complexes is embedded in the matrix of Mg^{2+} cations. The calculated formation enthalpies of Mg_2FeH_6 , based on the possible synthesis routes, indicate that optimum conditions are achieved if this hydride is fabricated from pure elements, and that the preparation of other compounds would lead to inferior synthesis.

Keywords: *hydrogen storage materials; density functional theory; electronic structure; enthalpy of formation*

1. Introduction

With the growing pressure of energy shortage and environmental contamination, a common issue becomes to develop sustainable and clean energy sources. Hydrogen has been viewed as a highly appealing energy carrier for renewable energy because of its abundance and environmental friendliness. In the exploitation of hydrogen energy, hydrogen storage is one of the key challenges influencing the success of the hydrogen economy. Great efforts have been made to develop advanced hydrogen storage tech-

*Corresponding author, e-mail: zj4343@163.com

nology, and the solid state materials that chemically bind or physically adsorb hydrogen at volume densities higher than that of gas and liquid hydrogen are proved to be the most promising way of storing hydrogen. Mg and Mg based alloys have received great interest because of their high hydrogen volumetric-gravimetric capacity, light weight and low cost. However, a slow sorption kinetics and high dissociation temperature hamper their practical applications. Up to now, considerable research has been undertaken to identify a suitable material that absorbs hydrogen close to room temperature and desorbs it at temperatures low enough to use the waste heat of exhaust gas [1–3].

Complex hydrides are considered to be the most useful of all known hydrogen storage materials because they exhibit mixed ionic-covalent bonding between metal and the hydrogen complex, thereby making them adaptable and suitable for facilitating the hydrogenation/dehydrogenation process [4–6]. In particular, this makes them suitable for the storage of renewable fuel, which is used in both power cells as well as combustion engines. The ternary Mg_2FeH_6 hydride shows the highest volumetric hydrogen density, of 150 kg $H_2 \cdot m^{-3}$, among all the known transition metal complex hydrides and has a high gravimetric hydrogen density of 5.47 wt. %. Furthermore, this hydride is based on an inexpensive metallic element, Mg, and Fe, and its commercial price should be much lower than that of other complex hydrides, which makes it more appealing. However, this ternary hydride has the particularity that Mg and Fe do not form stable binary compounds themselves [7]. Therefore, the synthesis and study of Mg_2FeH_6 becomes difficult to carry out. Several investigations regarding Mg_2FeH_6 have been mainly focused on enhancing the hydride yield by adopting different preparation routes [8–12]. In order to improve effectively the performance of Mg_2FeH_6 involved in reversible hydrogenation/dehydrogenation processes for practical applications, beginning with an understanding of the fundamental physical properties of this complex hydride, is of key importance and great interest. Theoretical investigations into complex metal hydrides including calculations from first principles have been very common in recent years [13–15]. However, few studies on Mg_2FeH_6 as a potential hydrogen storage material have been reported. In the present work, first principle calculations based on density functional theory are conducted in a comprehensive study of the structural and electronic properties, as well as the formation ability, of Mg_2FeH_6 complex hydride. The results are expected to provide theoretical guidance for designing and improving this potential hydrogen storage material.

2. Models and method of calculations

X-ray and neutron powder diffraction experimental analysis showed that Mg_2FeH_6 has a K_2PtCl_6 type structure, as shown in Fig. 1a [8]. Its unit cell has the cubic symmetry, space group *Fm*3*m* (No. 225), and 36 atoms with the lattice constant $a = 6.443$ Å. Mg, Fe and H atoms occupy the 8*c*, 4*a* and 24*e* sites in the crystal, respectively. The

atomic coordinates in the unit cell are: Mg (8*c*) – (0.25, 0.25, 0.25); Fe (4*a*) – (0, 0, 0); H (24*e*): (*x*, 0, 0), $x \approx 0.24$.

Figure 1b presents the cluster model of Mg_2FeH_6. It is an octahedral FeH_6 complex, surrounded by 8 Mg atoms in a cubic configuration. These complexes are arranged on an fcc lattice such that each Mg atom is tetrahedrally surrounded by 4 FeH_6 complexes and has 12 H atoms as the nearest neighbours. The metal–hydrogen bond distances are d(Fe–H) = 1.556 Å and d(Mg–H) = 2.2739 Å, respectively. The shortest separations between the hydrogen atoms within (intra) and between (inter) the FeH_6 complexes are d^{intra}(H–H) = 2.201 Å and d^{inter}(H–H) = 2.346 Å, respectively. The primitive cell of Mg_2FeH_6 is used in the calculations as shown in Fig. 1c. It has 9 atoms, comprising 2 Mg atoms, 1 Fe atom and 6 H atoms.

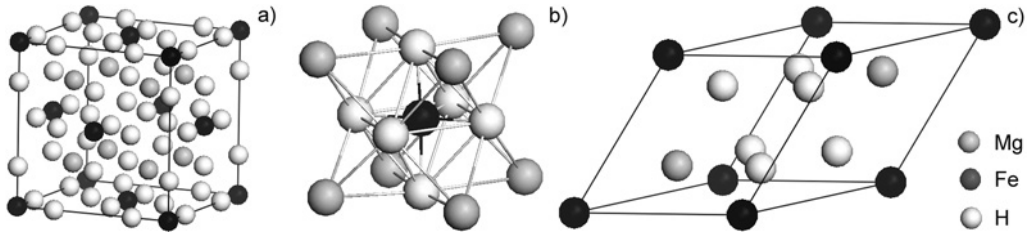

Fig. 1. Models of: a) a crystal cell, b) a cluster, c) primitive cell of Mg_2FeH_6

In the present work, the structural optimization and total energy calculations are performed with the DMol^3 package [16-18] which is based on the density functional theory (DFT) [19, 20], and the Perdew–Burke–Eruzerhof (PBE) exchange-correlation functional [21] is adopted for generalized gradient approximation (GGA) correction. All electron Kohn–Sham wave functions are expanded in a double numerical basis with a polarized orbital (DNP). The cell parameters, including lattice constants, and the atomic positions in the structure are fully relaxed to get the final structure with minimum total energy. The convergences criteria of optimization are 2.721×10^{-4} eV, 0.054eV/ Å and 0.005 Å for energy, gradient and atomic displacement, respectively.

3. Results and discussions

3.1. Parameters of crystal structure and physical properties

To assess the accuracy of the computational method, a series of preliminary calculations on crystal structure parameters and physical properties were performed on the related solids, such as hcp-Mg, bcc-Fe, rutile type α-MgH_2, and H_2 molecule. The corresponding results are listed in Table 1. It was found that their equilibrium lattice constants, atomic positions, interatomic distances and cohesive energies are all in good agreement with the experimental data. For example, the lattice constants *a*, *c* and

the c/a ratio of hcp-Mg are 3.1715 Å, 5.1504 Å and 1.6240, respectively, which are close to the experimental values [22] of $a = 3.21$ Å, $c = 5.21$ and $c/a = 1.623$, and the error of c/a ratio, calculated here relative to the experimental result, is about 0.06%. The calculated cohesive energy $E_{coh} = 1.4942$ eV/atom of hcp-Mg, which is close to the experimental value [22] of $E_{coh} = 1.51$ eV/atom, and the error of cohesive energy, calculated here relative to the experimental result, is about 1.05%. The lattice constant of bcc-Fe is 2.8619 Å, which is close to the experimental value [22] of $a = 2.87$ Å, and the error of the lattice constant calculated here relative to the experimental result, is about 0.28%.

Table 1. The equilibrium lattice constants a and c [Å], cohesive energy E_{coh} [eV/formula unit], bulk modulus B_0 [GPa], atomic positions and interatomic distance d [Å] for hcp-Mg, bcc-Fe, rutile type α-MgH_2, and H_2 molecule

Material	Property	This work	Experimental	Reference
hcp-Mg	a	3.1751	3.21	[22]
	c	5.1504	5.21	
	E_{coh}	1.4942	1.51	
	B_0	32.4579	35.4	
bcc-Fe	a	2.8619	2.87	[22]
	E_{coh}	5.4088	4.28	
	B_0	248.3762	168.3	
H_2	d(H–H)	0.7490	0.741	[23]
	E_{coh}	4.5502	4.74	
α-MgH_2	a	4..5124	4.501	[24]
	c	3.0240	3.010	
	E_{coh}	6.6185	-	
	B_0	47.7486	51	[25]
	u_H	0.3040	0.304	
Mg_2FeH_6	a	6.3977	6.443	[8]
	E_{coh}	24.9536	-	
	B_0	77.1010	-	
	Mg(8c)			
	x	0.2501	0.25	
	y	0.2500	0.25	
	z	0.2484	0.25	
	Fe(4a)			
	x	0	0	
	y	0	0	
	z	0	0	
	H(24e)			
	x	0.2456	0.24	
	y	0	0	
	z	0	0	
	d (Mg-H)	2.2667	2.2739	
	d (Mg-Fe)	2.7717	–	
	d (Fe-H)	1.5720	1.5560	
	d^{intra}(H-H)	2.2165	2.2010	
	d^{inter}(H-H)	2.3178	2.3460	

The bond length of a free H_2 molecule is 0.7490 Å, which is close to the experimental value [23] of $d_{H–H}$ = 0.741 Å, and the error of the bond length, calculated here related to the experimental result, is about 1.08%. The lattice constants a, c and c/a ratio of α-MgH_2 are 4.5124 Å, 3.0240 Å and 0.6702, respectively, which are close to the experimental values [24, 25] of a = 4.501 Å, c = 3.010 Å and c/a = 0.6687, the error of the c/a ratio, calculated here related to the experimental result, being about 0.22%. Evidently, a good agreement exists between the predictions based on calculations and experimental values. Although the calculated bulk moduli of solids such as Fe have larger errors relative to the experimental results [22], they are sufficiently acceptable for the purpose of the verifying calculations.

Next, the lattice constants, atomic positions and interatomic distances of Mg_2FeH_6 primitive cell are estimated from the minimized total energy. The final results are also listed in Table 1. It is found that the optimized structure of a Mg_2FeH_6 primitive cell maintains *Fm*3*m* symmetry, which is in good agreement with the experimental structure revealed by X-ray and neutron powder diffraction data [8]. The lattice constant of Mg_2FeH_6 is 6.3977 Å (the value is obtained by conversion of the lattice constant 4.5311 Å of the Mg_2FeH_6 primitive cell), which is close to the experimental value [8] of a = 6.443 Å, and the error of the lattice constant, calculated here with respect to the experimental result, is about 0.70%. The present positions of Mg, Fe, H atoms as well as interatomic distances in the Mg_2FeH_6 primitive cell are also in good agreement with the experimental results [8]. In particular, the hydrogen positions in Mg_2FeH_6 are precisely determined as to be (0.2456, 0, 0), which are very close to the deuterium positions (0.2420, 0, 0) in Mg_2FeD_6 obtained in the neutron diffraction measurement [8]. In addition, we also present the cohesive energy E_{coh} and bulk modulus B_0 of Mg_2FeH_6, and they are 24.9536eV per formula unit and 77.1010 GPa, respectively. Since no experimental values of E_{coh} and B_0 of Mg_2FeH_6 are available, no comparisons can be made with either of their theoretically computed values. However, the results of this paper are expected to be useful as a reference for future investigations into this complex hydride.

3.2. Electronic structure

The energy band structure and electronic density of states (DOS) of Mg_2FeH_6 are calculated and shown in Figs. 2, 3, respectively. Both of these figures exhibit an energy gap of about 2.3347 eV between valence and conduction bands, indicating that Mg_2FeH_6 hydride exhibits a semiconducting behaviour. The eight valence bands in Fig. 2 have a width of about 9.2519eV. From these figures it can be seen that the first valence band in the low energy range between –9.2519 and –6.1226eV mainly originates from the contribution of H(s), a few Mg(s) and a few Fe(s) orbitals, while the next seven interlapping valence bands in the higher energy range between –5.4423 and 0 eV are mainly from H(s) , Fe(p) and Fe (d) states. This suggests that there is a strong hybridization between H and Fe orbitals, while there is a weak one between H and Mg

orbitals. The conduction bands are mainly from Mg (and to lesser extent Fe and H) empty states. Mg has hardly any projection in the occupied states, as is shown in Fig. 3, indicating that each Mg donates two electrons to the FeH_6 complex [13]. Based on the analysis, it can be concluded that significant charge transfer leads to the formation of Mg^{2+} ions and a negatively charged FeH_6 complex, which constitutes the ionic bonding between them. At the same time, there exists a strong covalent bonding interaction between hydrogen and iron within the FeH_6 complex. The covalent bonding plays a comparatively more dominant role than ionic bonding in this complex hydride.

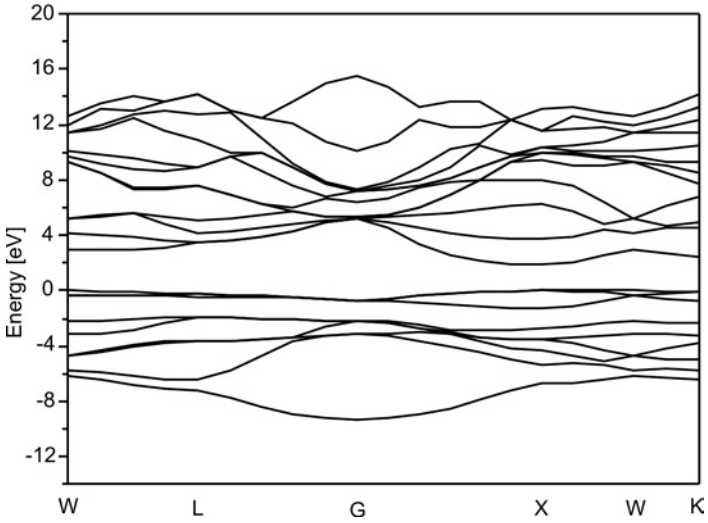

Fig. 2. Energy band structure of Mg_2FeH_6

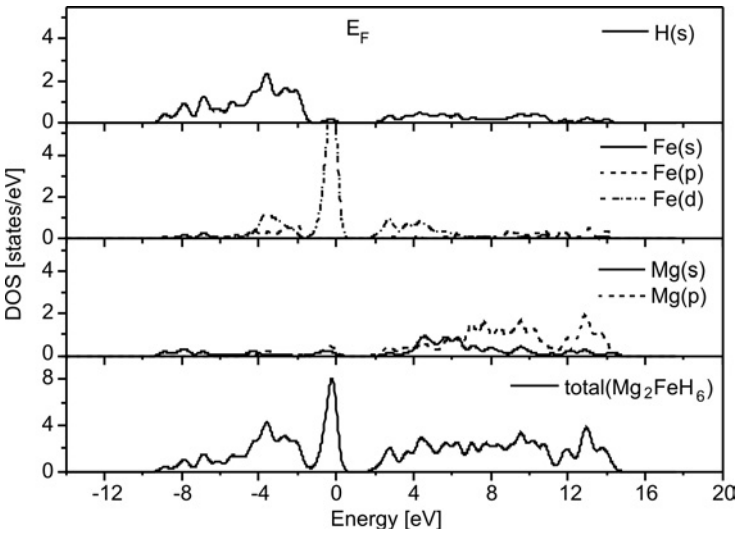

Fig. 3. Total and partial densities of states of Mg_2FeH_6

Further analysis of the charge distribution of Mg_2FeH_6 and the charge transfer in the FeH_6 complexes is performed. The total charge density $\rho(r)$ and the difference charge density $\Delta\rho(r)$ in the plane containing Mg, Fe, H atoms are shown in Figs. 4a, b. The difference charge density $\Delta\rho(r)$ [26] is defined as the difference between the total charge density of the solid and a superposition of atomic charge densities with the same spatial coordinates as in the solid. In Figure 4a, the total charge density plot shows that there is a strong bond between Fe and H atoms in FeH_6 complexes, while weak bonding interactions exist between Mg and FeH_6 complexes. The electron density is highest in the vicinity of FeH_6 complexes, which are consistent with the analytical results obtained from electronic density of states (DOS).

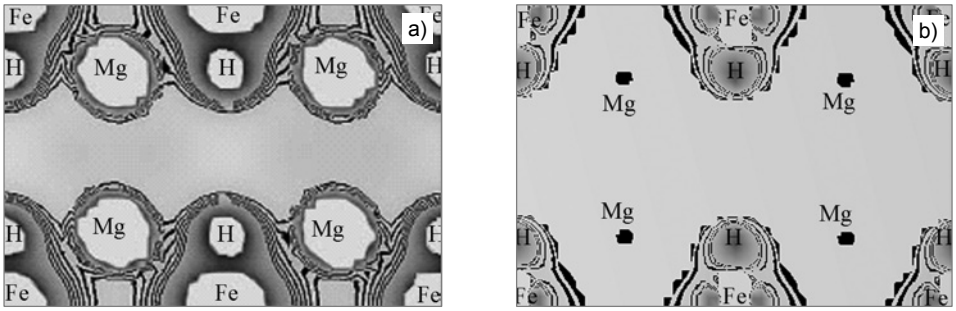

Fig. 4. Total (a) and difference (b) charge density plots of Mg_2FeH_6 in the (110) plane

From the difference density plot shown in Fig. 4b, it can be seen that there is significant charge transfer, leading to positively charged Mg and negatively charged FeH_6 complexes. For FeH_6 complexes, it was found that there is partial charge transfer from Fe to H, indicating that, besides the covalent bonding, there is also a weak ionic bonding interaction between Fe and H in FeH_6 complexes. These features are highly conducive to mixed ionic-covalent bonding between Fe and H in FeH_6 complexes embedded in the matrix of Mg^{2+} cations.

3.3. Enthalpy of formation

The enthalpy of formation is the most important thermodynamic parameter used to identify and classify hydrogen storage materials, since it determines the heat of the overall hydriding reaction, which, in turn, affects the temperatures of the reversible hydrogenation/dehydrogenation processes. It is the best aid to establish whether theoretically predicted phases are likely to be stable, and also such data may serve as guides for possible synthesis routes of materials. Commonly, the enthalpy of formation is negative, and the lower the enthalpy of formation, the greater the phase stability and the easier the synthesis of the material is [27]. As far as Mg_2FeH_6 is concerned, due to the absence of the binary Mg_2Fe compound, the synthesis of this complex hydride becomes very difficult. Experimentally, Mg_2FeH_6 are usually fabricated by ball

milling pure elements such as Mg and Fe or ball milling of other mixtures such as MgH_2 and Fe in an hydrogen atmosphere. In order to investigate the formation ability of Mg_2FeH_6 under various conditions of syntheses, it is necessary to calculate the enthalpy of formation. In the present work, three possible synthesis routes are considered as follows [8, 13]:

$$2MgH_2 + Fe + H_2 \rightarrow Mg_2FeH_6 \tag{1}$$

$$Mg + MgH_2 + Fe + 2H_2 \rightarrow Mg_2FeH_6 \tag{2}$$

$$2Mg + Fe + 3H_2 \rightarrow Mg_2FeH_6 \tag{3}$$

The corresponding enthalpy of formation (ΔH) is calculated according to the following expressions [28]:

$$\Delta H_1 = \frac{1}{3}\left(E_{\text{tot}}(Mg_2FeH_6) - 2E_{\text{tot}}(MgH_2) - E_{\text{tot}}(Fe_{\text{bcc}}) - E_{\text{tot}}(H_2)\right) \tag{4}$$

$$\Delta H_2 = \frac{1}{3}\left(E_{\text{tot}}(Mg_2FeH_6) - E_{\text{tot}}(Mg_{\text{hcp}}) - E_{\text{tot}}(MgH_2) - E_{\text{tot}}(Fe_{\text{bcc}}) - 2E_{\text{tot}}(H_2)\right) \tag{5}$$

$$\Delta H_3 = \frac{1}{3}\left(E_{\text{tot}}(Mg_2FeH_6) - 2E_{\text{tot}}(Mg_{\text{hcp}}) - E_{\text{tot}}(Fe_{\text{bcc}}) - 3E_{\text{tot}}(H_2)\right) \tag{6}$$

Here $E_{\text{tot}}(Mg_2FeH_6)$ refers to the total energy of the Mg_2FeH_6 primitive cell at the equilibrium lattice constant, $E_{\text{tot}}(Mg_{\text{hcp}})$, $E_{\text{tot}}(Fe_{\text{bcc}})$, $E_{\text{tot}}(MgH_2)$ are the single atomic energies of hcp-Mg, bcc-Fe in the solid states and α-MgH_2 in the primitive cell, respectively, and $E_{\text{tot}}(H_2)$ refers to the total energy of the gaseous H_2 molecule. In this paper, we calculate the single atomic energy of hcp-Mg and fcc-Fe by the following method: firstly, the energy of a pure metal crystal in the solid state is calculated, then the energy is divided by the number of atoms belonging to the crystal, and the result from the above calculation is just the energy of a single atom in the pure metal. The calculated values of $E_{\text{tot}}(Mg_2FeH_6)$, $E_{\text{tot}}(Mg_{\text{hcp}})$, $E_{\text{tot}}(Fe_{\text{bcc}})$, $E_{\text{tot}}(MgH_2)$ and $E_{\text{tot}}(H_2)$ are –45368.3726eV, –5442.5222eV, –34385.1223eV, –5474.8548eV and –31.6795eV, respectively. From Eqs. (1)–(3), the formation enthalpies of Mg_2FeH_6 based on various synthesis routes are estimated as ΔH_1 = –0.6204eV per H_2 molecule (i.e., –59.8200kJ/mol H_2), ΔH_2 = –0.8381eV per H_2 molecule (i.e., –80.9065kJ/mol H_2), ΔH_3 = –1.0558eV per H_2 molecule (i.e., –101.9929kJ/mol H_2). The calculated formation enthalpies are all negative, which indicates that these reactions are favourable from the thermodynamic point of view. By further comparing the values of ΔH, it is obvious that the route having the lowest reaction energy is the one that starts with pure elements. Hence, for the three considered synthesis routes, reaction (3) is clearly the optimum one. However, it should be noted that the kinetic aspects of these reaction pathways are not considered in the present calculation and this picture may be changed in a practical procedure. If there is no other compelling reason such as kinetics, the preparation of Mg_2FeH_6 the pure elements

should be the best synthesis route. This result is expected to be the guidance for enhancing the yield of Mg_2FeH_6 complex hydride.

4. Conclusions

The structural, electronic and formation ability of Mg_2FeH_6 complex hydride were investigated by using the first principles calculation based on density functional theory (DFT). The calculated structural parameters and physical properties are in good agreement with the experimental results, the hydrogen positions in Mg_2FeH_6 are precisely determined as (0.2456, 0, 0), being very close to the deuterium positions in Mg_2FeD_6 obtained in the neutron diffraction measurement. Detailed calculations of electronic structures suggest that the complex Mg_2FeH_6 hydride is a semiconductor with the energy band gap of about 2.3347 eV. The total and partial densities of states as well as the charge density plots indicate a significant charge transfer to Mg^{2+} ions and negatively charged FeH_6 complex. The bonding within the FeH_6 complex mainly involves the hybridization between Fe(p), Fe(d) and H(s) orbitals but exhibits a little ionic character for partial charge transfer from Fe to H. The calculations of formation enthalpy are used to estimate the heat change in hydrogenation process according to three possible synthesis routes. It is found that without considering the influence of kinetic aspects, the preparation of Mg_2FeH_6 is likely to perform via pure elements.

Acknowledgements

The work was supported by the Talents Foundation of Changsha University of Science and Technology (No. 20091026), the Hunan Provincial Innovation Foundation for Postgraduates (No. 521298294).

References

[1] TERZIEVA M., KHRUSSANOVA M., PESHEV P., RADEV D., Int. J. Hydrogen Energy, 20 (1995), 53.
[2] GARCÍA G.N., ABRIATA J.P., SOFO J.O., Phys. Rev. B, 59 (1999), 11746.
[3] LIANG G., HUOT J., BOILY S., SCHULZ R., J. Alloys Compd., 305 (2000), 239.
[4] ZÜTTEL A., Mater. Today, 6 (2003), 24.
[5] SEAYAD A., ANTONELLI D.M., Adv. Mater., 16 (2004), 765.
[6] FICHTNER M., Adv. Eng. Mater., 7 (2005), 443.
[7] *Binary Alloy Phase Diagrams*, 2nd Ed., T. Massalski, H. Okamoto, P. Subramanian, L. Kacprzak (Eds.), Am. Soc. Metals, Metals Park, OH,1990.
[8] DIDISHEIM J.-J., ZOLLIKER P., YVON K., FISCHER P., SCHEFER J., GUBELMANN M., WILLIAMS A.F., Inorg. Chem., 23 (1984), 1953.
[9] SELVAM P., YVON K., Int. J. Hydrogen Energy, 16 (1991), 615.
[10] SAI RAMAN S.S., DAVISON D.J., BOBET J.-L., SRIVASTAVA O.N., J. Alloys Compd., 333 (2002), 282.
[11] CASTRO F., GENNARI F.C., J. Alloys Compd., 375 (2004), 588.
[12] LI S., VARIN R.A., MOROZOVA O., KHOMENKO T., J. Alloys Compd., 384 (2004), 231.
[13] MYERS W.R., WANG L.-W., RICHARDSON T.J., RUBIN M.D., J. Appl. Phys., 91 (2002), 4879.
[14] VAN SETTEN M.J., DE WIJS G.A., POPA V.A., BROCKS G., Phys. Rev. B, 72 (2005), 073107.
[15] VELIKOKHATNYI O.I., KUMTA P.N., Mater. Sci. Eng. B, 140 (2007), 114.

[16] DELLEY B., J. Chem. Phys., 92 (1990), 508.
[17] DELLEY B., J. Chem. Phys., 94 (1991), 7245.
[18] DELLEY B., J. Chem. Phys., 113 (2000), 7756.
[19] HOHENBERG P.C., KOHN W., Phys. Rev. B, 136 (1964), 864.
[20] KOHN W., SHAM L.J., Phys. Rev. A, 140 (1965), 1133.
[21] PERDEW J.P., BURK K., ERNZERHOF M., Phys. Rev. Lett., 77 (2006), 3865.
[22] KITTEL C., *Introduction to Solid State Physics*, 6th Ed., Wiley, New York, 1986.
[23] FUKAI Y., *The Metal–Hydrogen System*, Vol. 21, of Springer Series in Mater. Sci., Springer, Berlin, 1993.
[24] BORTZ M., BERTHEVILLE B., BØTTGER G., YVON K., J. Alloys Compd., 287 (1999), 4.
[25] VAJEESTON P., RAVINDRAN P., KJEKSHUS A., FJELLVÅG H., Phys. Rev. Lett., 89 (2002), 175506.
[26] PELES A., ALFORD J.A., MA Z., YANG L., CHOU M.Y., Phys. Rev. B, 70 (2004), 165105.
[27] TAKAHASHI Y., YUKAWA H., MORINAGA M., J. Alloys. Compd., 242 (1996), 98.
[28] MEDVEDEVA M.I., GORNOSTYREV Y.N., NOVIKOV D.L., MRYASOV O.N., FREEMAN A.J., Acta Mater., 46 (1998), 3433.

Received 19 May 2009
Revised 23 July 2009

Contents

H. Eslami, M. Solati-Hashjin, M. Tahriri, F. Bakhshi, Synthesis and characterization of nanocrystalline hydroxyapatite obtained by the wet chemical technique 5

Q. -H. Chen, W.-J. Wang, W.-G. Zhang, Structure and optical properties of $(Alq_x)/Al_2O_3$ ethanol colloids 15

T. Zaremba, D. Witkowska, Methods of manufacturing of potassium titanate fibres and whiskers. A review 25

D. W. Zhou, J.S. Liu, J. Zhang, Z.G. Huang, P. Peng, Electronic mechanism of dehydrogenation of the Mg–Ge mixture during milling under hydrogen 43

N. Suresh, S. Venkateswaran, S. Seetharamu, Influence of cenospheres of fly ash on the mechanical properties and wear of permanent moulded eutectic Al–Si alloys 55

W.Z. Nie, J. Li, X.H. Sheng, Tribological properties of oxidation modified carbon fibre –reinforced polyamide 6 composites 67

L. Z. Pei, H.S. Zhao, W. Tan, H.Y. Yu, Q.-F. Zhang, Fabrication of core-shell Ge–GeO_2 nanoneedles 77

S. Vatansever, F. Öksüzömer, S. Naci Koç, M. Somer, H. Deligöz, M. A. Gürkaynak, Fabrication of yttria stabilized zirconia nanoparticles by the reverse microemulsion method for SOFC applications 85

N. Dukstiene, L. Tatariskinaite, M. Andrulevicius, Characterization of electrochemically deposited thin Mo–O–C–Se film layers 93

C. Ludwig, M.F. Beug, K.-H. Küsters, Advances in flash memory devices 105

K. Henkel, B. Seime, I. Paloumpa, K. Müller, D. Schmeisser, Optimization of MFIS structures containing poly(vinylidene-fluoride trifluoroethylene) for non-volatile memory applications 117

V. Tyrpek, J. Poltierová-Vejpravová, J. Plocek, D. Nižňanský, Preparation and characterization of SiO_2 microspheres doped with $CoFe_2O_4$ nanocrystals 129

K. Dehghani, A. Jafari, Finite element stress analysis of forging dies to improve their fatigue life.. 139

C. Wang, Z. Chen, Y. He, L. Li, D. Zhang, Raman scattering of ZnO films prepared by the laser molecular beam epitaxy 153

R. Sitek, J. Kamiński, P. Sallot, K.J. Kurzydłowski, Structure and properties of iron aluminide layers fabricated by the chemical vapour deposition on 316L steel 163

M.K. Halimah, W.M. Daud, H.A. A. Sidek, A.W. Zaidan, A.S. Zainal, Optical properties of ternary tellurite glasses 173

L. -P. Li, H.-Y. Zhang, J.-S. Pang, J. Lin, Fabrication and performance of carbon coated copper nanoparticles 181

R. I. Zhao, Y. Ma, J. Zhang, F. Li, W. Liu, Q. Cui, Nitrogen doped carbon nanotubes and curved lamellas produced via pyrolysis of melamine by direct current arc discharge 189

D. Pathak, R.K. Bedi, D. Kaur, Characterization of laser ablated $AgInSe_2$ films 199

B. Wang, Y. Guo, G. Hu, On the design of biodegradable hydrogels both thermosensitive and pH sensitive 207

M. Banski, A. Podhorodecki, J. Misiewicz, Influence of sol-gel matrices on the optical excitation of europium ions 217

D. W. Zhou, J.S. Liu, S.H. Xu, G.Y. Chen, First principles study on the improved dehydrogenating properties of MgH_2 systems with metal fluorides 229

I. S. El-Hallag, Characterization of electrodeposited nanostructured macroporous cobalt films using polystyrene sphere templates 245

A. Chorfa, M. Hamidouche, M.A. Madjoubi, F. Petit, Mechanical behaviour of glass during cyclic instrumented indentation 255

S. Sen, P. Sahu, K. Prasad, A novel technique for the synthesis of $CaCu_3Ti_4O_{12}$ ceramics 265
M. Jiang, X. Liu, H. Wang, J. Xu, Growth orientation transition and metal-like conductivity of Ti, Al co-doped ZnO films 273
S. Rani, P.K. Shishodia, R.M. Mehra, Enhancement of photovoltaic performance of quasi-solid state dye sensitized solar cell with dispersion of a hole conducting agent 281
K. Baltakys, E. Prichockiene, Influence of CaO reactivity on the formation of low-base calcium silicate hydrates 295
S. Bindra Narang, S. Bahel, Influence of frequency variations on the dielectric properties of Sm doped $Ba_4La_{9.33}Ti_{18}O_{54}$ dielectric ceramics at various temperatures 305
B. K. Sharma, G. Misra, S.C. Goyal, Quantum computations for temperature variation of refractive indices of covalent semiconductors 313
K. Prasad, S. Bhagat, K. Amarnath, S.N. Choudhary, K.L. Yadav, Electrical conduction in $Ba(Bi_{0.5}Nb_{0.5})O_3$ ceramics. Impedance spectroscopy analysis 317
G. Z. Shen, G.S. Cheng, Y. Cao, Z. Xu, Preparation and microwave absorption of M type ferrite nanoparticle composites 327
B. B. Jha, B.K. Mishra, B. Satpati, S.N. Ojha, Effect of thermal ageing on the evolution of microstructure and degradation of hardness of 2.25Cr-1Mo steel 335
S. Boucetta, T.Chihi, B. Ghebouli, M. Fatmi, First-principles study of the elastic and mechanical properties of Ni_3Al under high pressure 347
J. Zhang, Y.N. Huang, C.G. Long, D.W. Zhou, J.S. Liu, Density functional study of Mg_2FeH_6 complex hydride 357

Instructions for Authors

1. Submission of Manuscripts

Manuscripts can be sent by e-mail or by conventional mail. Submission of a manuscript to *Materials Science-Poland* implies that it is not being considered for publication elsewhere, and the authors have a necessary authorisation to publish the material contained in the paper.

1.1. First Submission

1.1.1. By Electronic Mail

Authors are encouraged to submit electronic versions of the manuscript to the e-mail address of the journal (*vide infra*). A single PDF file containing text, references, figures, tables etc. should be sent. When the size of such a file exceeds acceptable limits, the manuscript can be split into a few files (this should be clearly indicated in the covering letter). **Files in the DOC or RTF formats will be accepted only exceptionally.**

1.1.2. By Conventional Mail

The manuscripts can also be submitted by conventional mail. Authors are requested to send a CD with a PDF file containing a complete manuscript (text, references, tables, figures, etc.). The disk, accompanied by a covering letter, should be mailed to the Editor-in-Chief at his address given below.

1.2. Final Submission

After the manuscript has received preliminary acceptance, the authors will be requested to send the following material:
– A PDF file containing the complete manuscript (text, literature, tables, figures, etc). The file should be carefully checked as it will serve as a hard copy in case of doubts.
– A DOC or RTF file containing the text, references, tables and figure captions. The content of the file should be identical with that of the hard copy, and should exactly match the version seen and accepted be the referee(s).
– File(s) in appropriate formats containing figures. **Please consult Section 2.5 of this document.**
The files should be preferentially sent by e-mail, to the address of the Journal (*vide infra*), or by conventional mail, on a CD, to the Editor-in-Chief.
– **Additionally, the corresponding author is requested to send a copyright transfer form. The form should be copied from the web page of the Journal, filled out, signed and mailed to the Editor-in-Chief via conventional mail.**

2. Organisation of the Manuscript

The hard copy of the manuscript, submitted as a PDF file, should contain the material that can be reproduced in the A4 or letter size format, double spaced with ample margins throughout. All pages of the manuscript should be numbered consecutively, including references, figure captions and tables.

2.1. The First Page

The first page should be organised as follows:

Title of the paper

J.A. White[1], T.J. Brown[2*], M. Green[2**]
[1]Affiliation 1
[2]Affiliation 2
E-mail (only the corresponding author)

Abstract

An abstract of no more than 200 words

Key words

3 to 5 keywords, separated by semicolons (;)

* (**)Footnote(s)

2.2. Headings, Sub-headings

These should be placed in the main text as appropriate. The authors are encouraged to conform to the standard sequence of sections (e.g., Introduction; Experimental; Results; Discussion; Conclusions; etc.)

2.3. References

In the main text, references should be numbered consecutively by Arabic numerals in square brackets (e.g., [1]; [3, 4]; [7–11]). **Each reference should contain names of all authors.** The list of references should follow the main text and should be of the following format:

For a paper in a journal:

[1] KITAMURA T., YOKOYAMA M., J. Appl. Phys., 69 (1991), 821.

For a book:

[2] SWALIN R.A., *Thermodynamics of Solids*, Wiley, New York, 1962.

For a chapter in a book:

[3] WILD U.P., RENN A., *Spectral Hole-Burning*, [in:] H. Dürr and H. Bouas-Laurent (Eds.), *Photochromism. Molecules and Systems*, Elsevier, Amsterdam, 1990, p. 930.
Journal abbreviations should be in accordance with the standards of *Chemical Abstracts*.

GUIDELINES FOR AUTHORS

Manuscripts can be sent by conventional mail or by e-mail. Submission of a manuscript to *Materials Science-Poland* implies that it is not being considered for the publication elsewhere, and the authors have a necessary authorization to publish the material contained in the paper. **The manuscripts should conform to the formal standards of the Journal which may be found in the first issue of each volume and on the web page.**

Authors are encouraged to submit electronic versions of the manuscript by e-mail, to the address of the Journal. A single PDF file should be sent, containing text, references, figures, tables etc. Alternatively, the authors can submit the manuscript by conventional mail, sending a CD with the PDF file mentioned above, to the Editor-in-Chief at his address given below.

Each submitted manuscript will be reviewed, the final decision concerning its acceptance resting with the editors. Upon acceptance, the corresponding author will be requested to submit the following material (via e-mail or by conventional mail, on CD)

- A DOC or RTF file containing the final version of the text, references, tables and figure captions. The content of the file should be identical with that of the hard copy, and should exactly match the version seen and accepted be the referee(s).
- File(s) in appropriate formats containing figures. The required formats of the drawings (plots, schemes of technological processes) must be vector files such as XLS, OPJ, cdr (Excel, Origin, CorelDraw) which may also be exported as EPS, EMF or WMF files. Drawings submitted in tiff or jpg formats (bitmaps, raster graphics), even if exported as EPS, EMF or WMF files, will not be accepted. **Bitmaps are acceptable only in the case of photographs**. The photographs (only in grayscale) should have the resolution not lower than 300 dpi (estimated for the size in which they are expected to be reproduced).
- A PDF file containing the complete manuscript (text, literature, tables, figures, etc). The file should be carefully checked as it will serve as a hard copy in case of doubts. **The contents of the PDF file should exactly match the material in other files.**

Irrespective of whether the final version is submitted by e-mail or by conventional mail, the authors should also send **via conventional mail** a signed copy of the Copyright Transfer Agreement (available on the web page of the Journal).

For detailed information consult the first issue of each volume or the web page of the Journal.

The mail should be addressed to:

Professor Juliusz Sworakowski
Editor-in-Chief, Materials Science-Poland
Politechnika Wrocławska, W-3
Wybrzeże Wyspiańskiego 27
50-370 Wrocław, Poland

Electronic correspondence should be sent to: MatSci@pwr.wroc.pl
Web page of Materials Science-Poland: www.MaterialsScience.pwr.wroc.pl

The Publisher reserves the right to make necessary alterations to the text. Each corresponding author will be supplied with one free copy of the journal. Orders for additional offprints can be placed with the Publisher.